

UNIVERSITÀ DEGLI STUDI DI NAPOLI FEDERICO II
Scuola di Dottorato in Scienze della Terra, dell'Ambiente e delle Risorse

XXX Ciclo

Tesi di Dottorato in GIACIMENTI MINERARI

Ph.D. School in EARTH SCIENCES

XXX Cycle

Doctoral Thesis in ECONOMIC GEOLOGY



**GENESIS OF SUPERGENE NONSULFIDE ZINC
MINERALIZATIONS IN THE BONGARÀ (PERU) AND SKORPION-
ROSH PINAH (NAMIBIA) AREAS**

Ph.D. Student

Giuseppe Arfè

Supervisors

Prof. Maria Boni

Dr. Giuseppina Balassone

Dr. Nicola Mondillo

Table of contents

Abstract	5
Riassunto	13
Introduction	22
Chapter 1:	
Supergene nonsulfide Zn(Pb) deposits: classification, mineralogy, metallogenesis, climatic and structural controls	24
Classification and mineralogy of Zn(Pb) supergene nonsulfide deposits	25
<i>Direct replacement deposits</i>	<i>26</i>
<i>Wall rock-replacement deposits</i>	<i>27</i>
<i>Residual and karst-fill deposits</i>	<i>28</i>
Metallogenesis of Zn(Pb) supergene nonsulfide deposits	28
<i>Carbonate-hosted supergene zinc systems</i>	<i>28</i>
Tectonic and structural controls on supergene profile development	35
Climate controls on supergene profile and on geochemical and mineralogical models	36
Some aspects of mineral processing	38
Summary on supergene deposits	39
Chapter 2:	
Sampling and analytical methods	41
Sampling procedure	41
Analytical methods	42
<i>X-ray powder diffraction - XRPD</i>	<i>42</i>
<i>Optical and scanning electron microscopy and EDS-WDS microanalyses</i>	<i>47</i>
<i>AEM-Analytical Electron Microscopy</i>	<i>50</i>
<i>ZEISS Mineralogic Mining.....</i>	<i>51</i>
<i>Chemical analysis of major, minor and trace elements (ICP-AES and MS and XRF).....</i>	<i>53</i>
<i>Stable isotope geochemistry</i>	<i>55</i>
<i>Pb and Sr radiogenic isotope geochemistry.....</i>	<i>59</i>
Chapter 3:	
The karst-hosted Mina Grande nonsulfide zinc deposit, Bongará district (Amazonas region, Peru) .	61
Introduction	61
Geology of the Bongará district in the Pucará Basin.....	63
Climatic setting of the Bongará district.....	65
Main features of the Mina Grande deposit	66
Materials and analytical methods	70
Ore mineralogy and petrography.....	72
Major and minor elements geochemistry	81
Stable isotope geochemistry of carbonate minerals and waters	81
Discussion	85

<i>Mineralogy and paragenetic sequence of the deposit inferred from isotopic geochemistry</i>	85
<i>Conditions at the time of supergene alteration</i>	87
<i>Genetic model</i>	90
Conclusions	92
Chapter 4:	
The Cristal Zn prospect (Amazonas region, Northern Peru). Part I: New insights on the sulfide mineralization in the Bongará province	94
Introduction	94
Regional geological setting	96
Previous studies on sulfide mineralization in the Bongará area	98
Geology and sulfide mineralization in the Cristal area	100
Materials and Methods	102
Results	106
<i>Mineralogy and Petrography</i>	106
<i>Major and minor element geochemistry</i>	111
<i>Stable isotope geochemistry of sulfide and carbonate minerals</i>	115
<i>Lead and strontium isotope geochemistry</i>	116
Discussion	116
<i>Dolomitization in the Cristal area</i>	116
<i>Genesis of sulfide mineralization</i>	118
Conclusions	123
Chapter 5:	
The Cristal Zn prospect (Amazonas region, Northern Peru). Part II: An example of supergene zinc enrichments in tropical areas	125
Introduction	125
Geology of the Bongará Zn district	127
Climate evolution of the northern Andes from Miocene to Recent	130
Previous studies on the supergene mineralization in the Bongará area	131
Main features of the host rock and the Zn-nonsulfide mineralization in the Cristal area	132
Materials and Methods	135
Mineralogy and Petrography	140
<i>XRPD quantitative analyses and textural mineral associations</i>	140
<i>Mineral textures</i>	149
<i>Major and minor element geochemistry</i>	155
<i>Carbon and oxygen isotopes of supergene carbonate minerals</i>	163
Discussion	166
<i>Evolution from the hypogene sulfide mineralization to the “direct” and “wall rock” replacement supergene ores</i>	166
<i>Genesis and timing of the Cristal supergene nonsulfide mineralization</i>	170
Conclusions	173
Chapter 6:	

Identification of Zn-bearing micas and clays from the Cristal and Mina Grande - Bongará zinc deposits (Amazonas region, northern Peru)	175
Introduction	175
Geological setting	176
<i>Cristal prospect</i>	178
<i>Mina Grande deposit</i>	178
Materials and methods	179
Results	180
<i>XRPD analysis on oriented and randomly oriented mounts</i>	180
<i>Chemical composition and SEM observations</i>	183
Discussion	188
Conclusions	190
Introduction to the Namibian deposits - Why study them	191
Chapter 7:	
New C-O isotopic data on supergene minerals from the Skorpion and Rosh Pinah ore deposits (Namibia): Genetic and paleoclimatic Constraints	192
Introduction	192
Geological setting	193
<i>Regional geological setting</i>	193
<i>Rosh Pinah deposit</i>	195
<i>Skorpion deposit</i>	195
Materials and Methods	197
Results	198
Discussion	203
Conclusions	208
Chapter 8:	
Zn-clay minerals in the Skorpion Zn nonsulfide deposit (Namibia): identification and genetic clues revealed by HRTEM and AEM study	209
Introduction	209
Geology of the Skorpion zinc deposit area	210
Materials and Methods	213
Results	214
<i>Microtextures of clays and related minerals</i>	215
<i>Chemical composition</i>	223
Discussion and conclusions	229
Discussion and Conclusions	232
Acknowledgements	238
References	239

Abstract

Supergene Zn(Pb) nonsulfide deposits typically form via oxidation of sphalerite- and galena-rich sulfide bodies, under favorable weathering conditions. The resulting mineral assemblage mainly consists of smithsonite, hydrozincite, hemimorphite, sauconite, willemite, cerussite and anglesite, whose relative abundances generally depend on climate regime at the time of weathering and on the nature of host rocks.

The main object of this thesis is to increase the knowledge on the genetic processes of this kind of supergene ores by investigating all factors at the local scale, which may control the supergene profile genesis and development. To reach this aim, it was carried out an accurate study of the mineralogy and geochemistry of selected samples, which were collected along weathering profiles of supergene Zn deposits characterized by different geological and climatic conditions. Four deposits were considered: Mina Grande and Cristal in northern Peru (Bongará province), and Skorpion and Rosh Pinah in southern Namibia (Gariep Belt). Even if these districts show several common mineralogical features, they are completely different from the geo-climatic point of view. The genesis of nonsulfide mineralization in these deposits is probably related to similar weathering conditions that were active during the initial sulfides oxidation in both districts. Skorpion and Rosh Pinah deposits in Namibia are characterized by fossil supergene profiles that formed under humid conditions similar to those currently affecting those of the Bongará province. Subsequently, this tropical environment evolved toward the current arid conditions in southern Namibia, resulting in a different development of the supergene profiles in this area, compared to the Peruvian ones. Therefore, the identification of the features and possible genetic mechanisms in currently active supergene profiles, such as those occurring in the Bongará province, should fill the existing gaps for complete understanding of the various processes that are no more identifiable in no longer active (or fossil) supergene profiles.

The Mina Grande zinc nonsulfide deposit (Amazonas region, Peru) belongs to an ample mining concession corresponding to the “Bongará Project”, which covers an area of approximately 100 km². The deposit consists of several accumulations in karst cavities of Zn-oxide minerals, derived from the complete weathering of a Mississippi Valley-type deposit hosted in Mesozoic carbonate rocks (mainly limestones) of the Condorsinga Formation (Pucará Group). The karst cavities hosting the nonsulfide ores were developed in the Miocene, along northwest-southeast faults (avg. N40W/70SW) associated with regional structures, and locally along stratification joints (avg. N8E/26NW). Thus far, the Mina Grande Zn accumulations have been partially mined in two pits (named “Fase A” and “Fase B”) and explored in a third area, named “Fase C.” In 2008, the measured resources were as follows: Fase A = 160,000 metric tons (t) @ 21.2% Zn, Fase B = 36,400 t @ 28.9% Zn, and Fase C = 116,700 t @ 22.5% Zn. The nonsulfide mineral assemblage, consisting mostly of hydrozincite, smithsonite, and hemimorphite, is associated with few remnants of the hypogene ore (pyrite and sphalerite). Mineralogical

and petrographic studies revealed several texturally distinct smithsonite and hydrozincite generations, which are characterized by extremely negative $\delta^{13}\text{C}$ compositions, pointing to the prevailing contribution of an isotopically light carbon component from the oxidation of organic matter-derived carbon, and different $\delta^{18}\text{O}$ isotope compositions: 26.9 to 27.2 and 26.0 to 26.3‰ $\delta^{18}\text{O}$ VSMOW for smithsonite, and averages 24.6 and 23.7‰ $\delta^{18}\text{O}$ VSMOW for hydrozincite. These distinct $\delta^{18}\text{O}$ compositions indicate that smithsonite and hydrozincite precipitated at least during two depositional stages. These stages were probably related to several periods of uplift that occurred in the Bongará district since at least ~10 Ma, when the transition from the Pebas to Acre systems affected the Amazonas foreland basin in Miocene. The karst activity, to which the supergene mineralization is related, was restricted to the late Miocene and early Pliocene periods. Climatic conditions reconstructed from the ecosystems persisting in the region from Late Tertiary to Recent suggest that the Mina Grande supergene mineralization was associated with several weathering episodes that occurred under a climate resembling the present-day conditions.

The Cristal prospect is located 6 km north of the Mina Grande deposit, in the northernmost part of a wide mining district corresponding to the “Charlotte Bongará Zinc Project”, which covers an area of approximately 110 km². Differently from Mina Grande, at Cristal remnants of the primary Mississippi Valley-type mineralization are still in place. Indeed, the mineralized area of the Cristal Zn prospect contains both sulfide and nonsulfide mineralizations, which are locally mixed (sulfides + nonsulfides) or well separated (sulfides or nonsulfides). As in the case of Mina Grande, the mineralization is hosted by the lithologies of the Pucará Group (mainly dolostones), deposited in a Mesozoic extensional basin on the western margin of the Brazilian-Guyana shield. Zinc sulfides at Cristal occur in the roots of the nonsulfide concentrations, and are locally present also nearer to surface. The sulfide mineralization clearly postdates two hydrothermal dolomitization phases and the sulfides occur mainly in veins, cavity fillings or as disseminated mineralization, generally associated with sparry to saddle dolomite. They mostly consist of dark-brown sphalerite, associated with smaller amounts of pyrite. Sphalerite commonly displays Fe-zoning (it contains on average ca. 6 wt.% Fe), and is Ge-rich (mean concentration of 145 ppm, maximum of 383 ppm). Galena is rare. The Cristal sphalerite has sulfur isotopic compositions of $\delta^{34}\text{S} = 14$ to 15 ‰ VCDT. Oxygen isotopic compositions of dolomites are: $\delta^{18}\text{O} = 24.4$ to 24.7 ‰ VSMOW for early and 18.4 to 22 ‰ for late hydrothermal dolomites. The $\delta^{34}\text{S}$ and $\delta^{18}\text{O}$ values of Cristal sulfides and dolomites respectively are similar to those observed in two Mississippi Valley-type (MVT) deposits occurring in the region, namely the Florida Canyon and Florcita deposits. This is consistent with a single mineralization event at district scale. The Pb isotope ratios of sphalerite from two different areas of the property define two distinct data-point clusters (centered around averages of $^{206}\text{Pb}/^{204}\text{Pb} = 18.850 \pm 0.002$, $^{207}\text{Pb}/^{204}\text{Pb} = 15.685 \pm 0.002$, $^{208}\text{Pb}/^{204}\text{Pb} = 38.752 \pm 0.004$, and $^{206}\text{Pb}/^{204}\text{Pb} = 19.042 \pm 0.002$, $^{207}\text{Pb}/^{204}\text{Pb} = 15.712 \pm 0.002$, $^{208}\text{Pb}/^{204}\text{Pb} = 39.080 \pm 0.004$, respectively). This difference required distinct sulfide-bearing hydrothermal pulses in the mineralized area. The Pb isotopic compositions of the Cristal sulfides are intermediate between the

compositions of galena from the San Vicente and Shalypaico MVT deposits, and record a contribution from an old crustal component. The Marañon Complex basement, which has Pb isotopic ratios roughly matching those of dolomites and sulfides from Cristal and Charlita North areas, represents the most reliable candidate to be the main end-member source of the metals (e.g. Pb and Zn) for the Cristal sulfide mineralization. The second end-member, a Mesozoic or Tertiary magmatic source contributing Pb to the hydrothermal fluid, is elusive, as none of them has been documented in the Cristal area.

The Cristal nonsulfide ores are interpreted to be the product of weathering of primary MVT mineralization. The nonsulfide prospect spans over an area of approximately 2 x 1 km with nearly continuous zones of Zn enrichment that has been detected in soil and rock samples. The nonsulfide mineralization consists mainly of semi-amorphous orange to brown zinc “oxides” that include hemimorphite, smithsonite and Fe-(hydr)oxides. The most important mineralized areas are present in the Esperanza and Yolanda occurrences, which were also most densely explored. In both occurrences the supergene Zn-carbonates and silicates infill solution cavities, or replace the carbonate host rocks and/or the primary sulfides forming smithsonite- and hemimorphite-rich mineralizations. The analyzed drill cores are mainly from Esperanza, where the zinc content, associated with hemimorphite-rich layers can reach ~ 53 wt.% Zn; the average Zn grade is around 20 wt.%. Germanium concentrations are significant at Cristal, with values around 200 ppm measured on bulk rock, which are mostly related to the Ge-rich sphalerite, and to products of sulfides oxidation such as hemimorphite and goethite.

As already observed in the nearby Mina Grande deposit, the area experienced a prolonged phase of weathering from Miocene to Recent under tropical climatic conditions. In these climatic conditions, weathering processes affected many pre-existing sulfide deposits (e.g. Cristal, Florida Canyon, Mina Grande etc.), where supergene profiles were developed under locally different conditions, which are defined primarily on the basis of mineralogical and geochemical data. At Cristal, the occurrence of siderite paragenetically preceding smithsonite indicates that sulfide weathering took place under a transition from a reducing to an oxidizing environment. The mineralogy and geochemistry of the Bongará ore deposits is primarily conditioned at a local scale by two factors: (1) uplift rates, and (2) host rock lithology. The latter may favor the development of more (e.g. Mina Grande) or less (e.g. Cristal) alkaline supergene environments. As instance, Cd in the nonsulfide mineral assemblage of Mina Grande and Cristal deposits is respectively hosted in otavite and greenockite. The first mineral is indicative of alkaline conditions, whereas the second one is stable under weakly alkaline to near-neutral conditions. This difference in the geochemistry of the nonsulfide ores of the two deposits is also remarked by their Ge contents, which are much lower at Mina Grande than at Cristal. The absence of Ge at Mina Grande should reflect the limited capacity of some supergene minerals (e.g. goethite) to fix Ge in the lattice under highly alkaline conditions.

Supergene smithsonites and calcites show isotopically different generations. The $\delta^{18}\text{O}$ and $\delta^{13}\text{C}$ compositions of sulfide-replacing smithsonite range from 24.6 to 25.8‰ VSMOW and from -0.6 to -11.7‰ VPDB, respectively. The host rock-replacing smithsonite has a range of $\delta^{18}\text{O}$ values varying between 26.6 and 27.3‰ VSMOW,

whereas the $\delta^{13}\text{C}$ values are comparable with the $\delta^{13}\text{C}$ ratios of sulfide-replacing smithsonite. Late smithsonite veins show $\delta^{18}\text{O}$ and $\delta^{13}\text{C}$ values that are between 27.8 and 28.3‰ VSMOW and between 0.1 and -2.4‰ VPDB, respectively. The $\delta^{13}\text{C}$ values of supergene calcites occurring in late veins range between 0.7 to -7.4‰ VPDB, whereas the $\delta^{18}\text{O}$ values are around 24.7‰ VSMOW.

The uplift factor was mainly controlled by the activity of local faults, which allowed the exposure of sulfide protore at variable elevations in different periods of time and hydrological settings (e.g., the current superficial runoff rate is major at Mina Grande than at Cristal). Such different factors and settings may result in the precipitation of isotopically different supergene carbonates (e.g. smithsonites and calcites at Mina Grande and Cristal). Contrary to the Mina Grande deposit, the development of a karst network at Rio Cristal was quenched by a limited uplift rate, and the supergene alteration did not completely obliterate the roots of the original sulfide orebody.

In both Mina Grande and Cristal deposits, different Zn-bearing phyllosilicates were found in association with the principal Zn nonsulfide minerals (smithsonite, hemimorphite and hydrozincite). The XRD and SEM-EDS investigations revealed that the Zn-bearing micas occurring in both deposits mostly consist of I/S mixed layers of detrital origin, which have been partly altered or overprinted by sauconite during the supergene alteration of the sulfides. Sporadic hendricksite was also identified in the Cristal nonsulfide mineral assemblage, whereas at Mina Grande the fraipontite-zaccagnaite (3R-polytype) association was detected. The identified zaccagnaite polytype suggests that fraipontite and zaccagnaite are both genetically related to weathering processes. The hendricksite detected at Cristal may be instead considered a hydrothermal alteration product, formed during the emplacement of sulfides. The complex nature of the identified phyllosilicates is an evidence of the multiple hydrothermal and supergene processes that occurred in the Bongará district.

Skorpion and Rosh Pinah Zn(Pb) deposits are hosted in Neoproterozoic rocks that are part of a volcano-sedimentary sequence within the Gariep Belt (southwest Namibia). Skorpion is the largest Zn nonsulfide mineralization ever discovered and exploited. It mostly consists of Zn-oxidized minerals, derived from the weathering and oxidation of a volcanic-hosted massive sulfide (VMS) protore. Rosh Pinah is a hybrid Zn massive sulfide deposit, with both VMS and Broken Hill-type characteristics; it is partly weathered in the uppermost part of the massive sulfide lens.

A comparison between the deep oxidation processes that occurred at Skorpion and the limited weathering of the Rosh Pinah deposit was carried out by analyzing the carbon and oxygen isotope ratios of supergene carbonate minerals. Twenty-three smithsonite samples from the Skorpion deposit and six gossanous samples (containing both the host dolomite and smithsonite) from the uppermost levels of the Rosh Pinah mine have been analyzed. The Skorpion smithsonites form botryoidal crusts overgrown by euhedral calcite crystals. At Rosh Pinah all sampled smithsonites occur in veins within the host rock dolomite. Skorpion smithsonite is characterized by $\delta^{13}\text{C}$ values strongly variable between -9.1‰ and 0.1‰ VPDB and by a small range in $\delta^{18}\text{O}$ from 28.0 to 29.9‰ VSMOW. Calcite

shows a minor variation in $\delta^{13}\text{C}$, with values being generally positive (0-1.6‰ VPDB) and $\delta^{18}\text{O}$ values slightly lower than those of smithsonite (25.4-27.1‰ VSMOW). The analyses of the Rosh Pinah samples show that the host dolomite is characterized by $\delta^{18}\text{O}$ values ranging from 18.7 to 22.0‰ VSMOW, and by negative $\delta^{13}\text{C}$ values (-5.9 to -2.7‰ VPDB). The carbon isotope ratios of smithsonite, as in Skorpion, are negative (-2.8 to -1.9‰ VPDB) and they partly overlap with those of the host dolomites. The $\delta^{18}\text{O}$ values (26.7-29.0‰ VSMOW) are on average comparable with the values measured at Skorpion. The similar negative $\delta^{13}\text{C}$ values of smithsonite and dolomite at Rosh Pinah point to the involvement of both re-oxidized organic carbon and host dolomite inorganic carbon during smithsonite formation, whereas at Skorpion a larger contribution of isotopically light organic carbon is considered more probable. The comparable $\delta^{18}\text{O}$ compositions of smithsonite from the two deposits imply similar ore-forming fluids and/or similar temperature conditions during formation. In agreement with former studies, this research suggests that Skorpion smithsonite precipitated at an average temperature near 17°C from fluids depleted in ^{13}C , due to a high contribution of organic carbon from the soil, either during the first (Late Cretaceous-Paleocene) or the last humid climatic stage (early-middle Miocene). Even if the similarity between the $\delta^{18}\text{O}$ composition of Rosh Pinah and Skorpion smithsonites points to similar ore-forming fluids and/or similar conditions during formation, the relatively high $\delta^{13}\text{C}$ values of the Rosh Pinah smithsonites suggest a minor influence of isotopically light organic carbon and the absence of soils over this deposit. Combining these data with the limited thickness of the supergene zone over the Rosh Pinah orebody, it is likely that these smithsonites, together with the gossan in which they occur, formed at the end of the early-middle Miocene semi-humid period.

The $\delta^{18}\text{O}$ and $\delta^{13}\text{C}$ compositions of Skorpion calcite indicate that the precipitating supergene fluids remained roughly unchanged, but that the contribution of bicarbonate from the host rock became prevailing in them. This suggests that calcite formation occurred at the beginning of the late Miocene-Pliocene semi-arid period, when the host marbles were uplifted and karstified, thus promoting a higher bicarbonate contribution from dissolving host rock.

One of the main components of the Skorpion ore association is the Zn-smectite (“sauconite”). In fact, in the Skorpion orebody the trioctahedral Zn-bearing smectite predominates over the other Zn-oxidized minerals (e.g. smithsonite, hemimorphite and hydrozincite). A thorough study of the clay component has been focused on microtextural observation and chemical analyses of the clay nano-particles in the supergene nonsulfide ores from the Skorpion deposit, carried out for the first time using TEM/HRTEM and AEM. This approach helped to better understand the formation mechanism of the Skorpion Zn-clays and related phases down to the nanoscale. The microtextures of the Zn-clays suggest they formed from fluids, meteoric and/or hydrothermal in nature, in two textural contexts: the smectites can grow on previously deposited phyllosilicates (mica) (CCP texture), and/or directly nucleate from Zn-rich solutions (PCA texture). The Skorpion sauconite is chemically characterized by a greater homogeneity if compared with natural sauconites from other occurrences; it is quite stoichiometric, with Ca as

interlayer cation and limited quantities of Mg and Fe, with an average composition of $\text{Ca}_{0.14}\text{K}_{0.02}(\text{Zn}_{2.7}\text{Mg}_{0.09}\text{Al}_{0.14}\text{Fe}_{0.10})(\text{Si}_{3.4}\text{Al}_{0.6})\text{O}_{10}(\text{OH})_2 \cdot n\text{H}_2\text{O}$. At the micro- and nanoscale, also Zn-beidellite has been detected at Skorpion, though very subordinated. Chlorite and baileychlore also occur. Detrital micas are commonly the templates for epitaxial sauconite growth. The micro- and nano-features of the Skorpion mineral assemblage confirm the complex mineralogical nature of the smectite-rich nonsulfide (micro)systems, with remarkable implications for mineralogical evaluation and processing. In conclusion, typical supergene processes at ambient temperatures should be considered for the genesis of the Skorpion sauconite-bearing deposit, with some local contribution of low-T hydrothermal fluids.

In order to compare the evolution of the weathering profiles and the genetic characteristics of supergene deposits located in arid (Skorpion and Rosh Pinah) and humid (Cristal and Mina Grande) areas, parallel studies have been carried out. Carbon and oxygen stable isotope data have been useful to record long-lasting and short-term episodes of weathering. The first are mirrored by extreme differences between the $\delta^{13}\text{C}$ values of the host rock carbonates and those of the supergene minerals (e.g. smithsonite). The second are characterized by the homogeneity of carbon isotope ratios between the host rock and the weathering products. However, such homogeneity in supergene profiles that evolved in semi-arid conditions may also indicate long-lasting periods of weathering, during which the organic activity in the soil may have been negligible. Cristal and Mina Grande supergene carbonates, which formed and developed in uplifted areas under humid climate settings, show small variations of their isotopic compositional range that would suggest limited environmental changes. However, the extreme variation of the weathering conditions at local scale tells the exact opposite. Simultaneous changes of temperature and $\delta^{18}\text{O}$ composition of the supergene ore-forming fluids may result in similar oxygen isotope ratios of the various supergene carbonates belonging to different generations. However, the investigation on the constraints of the depositional conditions of supergene minerals in nonsulfide deposits cannot be conducted on the mineral association only. Once again, the involvement of several factors on the local scale may control the precipitation of the mineral phases (e.g. siderite instead of smithsonite, otavite instead of greenockite, sauconite instead of fraipontite). Additionally, the identification of environmental-proxy minerals such as kaolinite and smectite group minerals, which are found in tropical and arid soils respectively, might not be straightforward, since these minerals can also be precipitated from hydrothermal fluids (e.g. fraipontite and sauconite). The importance of local scale factors in humid and tropical uplifted areas is testified by the marked difference between the weathering profiles of Mina Grande and Cristal deposits. Such differences mainly reside on the capability of host rocks to store CO_2 under an acidic alteration environment (dolomite > calcite), which directly affects the pH of meteoric solutions, and on the altitude(uplift)-dependence of the runoff rates. The combination of these factors may result in a local preservation of sulfide minerals, as in the case of the Cristal prospect, or in a continuous supply of fresh meteoric water and deepening of the supergene profile, as recorded in the Mina Grande deposit. All these mechanisms control the genesis and development of supergene profiles in a restricted

range of pH-Eh conditions (from alkaline to near-neutral, and from weakly reducing to oxidizing), where the formation of a limited suite of minerals is favoured (mainly metal-bearing carbonates).

In conclusion, this study has confirmed that paleoclimatic switch-overs from seasonally humid/arid to hyperarid periods (e.g. in the Skorpion-Rosh Pinah district) might be the most favourable scenario for the formation and preservation of supergene world-class nonsulfide deposits. However, the present research has also denied some theories about the poor possibility of preserving supergene profiles under tropical weathering. The coexistence of many factors and their complex interplay during sulfide oxidation in modern tropical areas may generate local conditions of preservation (e.g. Cristal) or instability (e.g. Mina Grande). C-O stable isotope analyses are useful to roughly estimate these local conditions, but they do not provide data on the availability of water and its recharge capability. Therefore, any attempt to present paleoclimatic hypotheses, without considering the geological background (e.g. uplift and rainfall rates, host rock lithology) of the areas hosting nonsulfide deposits may result useless. The data provided by this study on this interesting topic could be applied to other (paleo)weathering profiles worldwide, in order to build more accurate geological and geochemical models.

The results of this study have been published in several papers on international Journals, and other manuscripts have been presented for publication. Several parts of this PhD thesis correspond to the content of the manuscripts quoted below:

Arfè, G., Boni, M., Balassone, G., Mondillo, N., Hinder, G., Joachimski, M., 2017. New C-O isotopic data on supergene minerals from the Skorpion and Rosh Pinah ore deposits (Namibia): Genetic and paleoclimatic constraints. *Journal of African Earth Sciences*, 126, 148-158.

Contributions of G. Arfè to the paper: samples preparation, petrological characterization, part of geochemical data collection, model interpretation of the data. G. Arfè wrote the first version of the manuscript that was revised and integrated by the co-authors.

Arfè G., Mondillo, N., Balassone G., Boni, M., Cappelletti, P., Di Palma, T., 2017. Identification of Zn-bearing micas and clays from the Cristal and Mina Grande - Bongará zinc deposits (Amazonas region, northern Peru). *Minerals*, 7, 214; DOI: 10.3390/min7110214.

Contributions of G. Arfè to the paper: on-site samples collection, samples preparation, petrological characterization, part of mineralogical geochemical data collection. G. Arfè strongly contributed to the interpretation of the data and to the drafting the first version of the manuscript, then revised and integrated by other co-authors.

Arfè, G., Mondillo, N., Boni, M., Balassone, G., Joachimski, M., Mormone, A., Di Palma, T., 2017. The karst-hosted Mina Grande nonsulfide zinc deposit, Bongará district (Amazonas region, Peru). *Economic Geology*, 112, 1089-1110.

Contributions of G. Arfè to the paper: on-site samples collection, samples preparation, petrological and mineralogical characterization, part of geochemical data collection. G. Arfè elaborated the interpretation of the data, and wrote the first version of the manuscript, then revised by other co-authors.

Arfè, G., Mondillo, N., Boni, M., Joachimski, M., Balassone, G., Mormone, A., Santoro L., Castro Medrano E. The Cristal Zn prospect (Amazonas region, Northern Peru). Part II: An example of supergene zinc enrichments in tropical areas. *Ore Geology Reviews*, (in press). DOI: 10.1016/j.oregeorev.2017.11.022.

Contributions of G. Arfè to the paper: on-site samples collection, samples preparation, petrological and mineralogical characterization, part of geochemical data collection. G. Arfè elaborated the interpretation of the data, and wrote the first version of the manuscript, then revised by other co-authors.

Balassone, G., Nieto, F., Arfè, G., Boni, M., Mondillo, N., 2017. Zn-clay minerals in the Skorpion Zn nonsulfide deposit (Namibia): Identification and genetic clues revealed by HRTEM and AEM study. *Applied Clay Sciences*, 150, 309-322.

Contributions of G. Arfè to the paper: samples selection and part of the mineralogical study (e.g. preliminary interpretation of XRD patterns).

Mondillo N., Arfè G., Boni M., Balassone G., Boyce A., Joachimski M., Villa I.M. The Cristal Zn prospect (Amazonas region, Northern Peru). Part I: New insights on the sulfide mineralization in the Bongará province. *Ore Geology Reviews*, (in press).

Contributions of G. Arfè to the paper: on-site samples collection, samples preparation, part of the mineralogical and petrological characterization, C-O stable isotope analyses. G. Arfè participated to data interpretation and to manuscript drafting with other co-authors.

Riassunto

I depositi a nonsolfuri di zinco(piombo) si formano generalmente attraverso l'ossidazione di giacimenti a solfuri ricchi in sfalerite e/o galena, in condizioni di *weathering* favorevoli. L'associazione mineralogica risultante da questo processo consiste principalmente in smithsonite, idrozincite, emimorfite, sauconite, willemite, cerussite ed anglesite, le cui abbondanze relative dipendono principalmente dal regime climatico al tempo dell'ossidazione e dalla natura delle rocce che ospitano il giacimento.

Il principale obiettivo di questa tesi è quello di incrementare le conoscenze sui processi genetici che portano alla formazione di questi particolari giacimenti, ponendo l'attenzione su tutti i fattori a scala locale che possono controllare la genesi e lo sviluppo del profilo di alterazione. Per tale scopo, è stato realizzato uno studio accurato della mineralogia e della geochemica di alcuni campioni che sono stati raccolti lungo i profili di *weathering* di depositi supergenici di zinco, caratterizzati da differenti condizioni geologiche e climatiche. Per lo studio sono stati considerati quattro depositi: Mina Grande e Cristal in Perù settentrionale (provincia di Bongará), e Skorpion e Rosh Pinah nel sud della Namibia (Gariep Belt). Sebbene questi distretti minerari mostrino molte caratteristiche comuni dal punto di vista mineralogico, essi sono completamente differenti dal punto di vista geo-climatico. La genesi della mineralizzazione a nonsolfuri di questi depositi è probabilmente legata a simili condizioni di *weathering* che erano attive durante l'iniziale ossidazione dei corpi a solfuri in entrambi i distretti. I depositi di Skorpion e Rosh Pinah sono caratterizzati da profili supergenici fossili che si sono formati in condizioni umide, le quali possono essere considerate analoghe a quelle che interessano attualmente la provincia di Bongará. Successivamente, questo ambiente tropicale è evoluto verso le attuali condizioni aride del sud della Namibia, risultando in un differente sviluppo dei profili supergenici di quest'area rispetto a quelli peruviani. Quindi, l'identificazione delle caratteristiche e dei possibili meccanismi genetici in profili supergenici attualmente attivi, come quelli che si presentano nella provincia di Bongará, dovrebbe colmare le lacune esistenti per una completa comprensione dei vari processi, non più identificabili, in profili supergenici non più attivi (o fossili).

Il deposito a nonsolfuri di zinco di Mina Grande (regione Amazonas, Perù) fa parte di una grande concessione mineraria che corrisponde al "Bongará Project", che comprende un'area di circa 100 km². Il deposito consiste in diversi accumuli di minerali ad ossidati di zinco in cavità carsiche, che sono derivati dalla completa alterazione di un deposito primario di tipo MVT (Mississippi Valley-type) ospitato in rocce carbonatiche mesozoiche (principalmente calcari) della Formazione del Condorsinga (Pucará Group). Le cavità carsiche che ospitano la mineralizzazione si sono sviluppate nel Miocene, lungo faglie con direzione NW-SE (230° di immersione e 70° di inclinazione) associate a strutture regionali, e localmente lungo giunti di strato (278° di immersione e 26° di inclinazione). Finora, le aree mineralizzate di Mina Grande sono state parzialmente coltivate attraverso due *open-pit*, chiamati "Fase A" e "Fase B". Una terza area, chiamata "Fase C" è in via di

esplorazione. Nel 2008, le risorse misurate furono le seguenti: Fase A = 160000 (t) @ 21.2% Zn, Fase B = 36400 t @ 28.9% Zn, e Fase C = 116,700 t @ 22.5% Zn. L'associazione mineralogica a nonsolfuri di zinco, che consiste in gran parte in idrozincite, smithsonite, ed emimorfite, è associata con poche rimanenze della mineralizzazione ipogenica (pirite e sfalerite). Studi mineralogici e petrografici hanno rivelato la presenza di più generazioni di smithsonite e idrozincite, tessituralmente differenti, che sono caratterizzate da composizioni di $\delta^{13}\text{C}$ estremamente negative, le quali evidenziano il prevalente contributo di una componente di carbonio isotopicamente leggera, legata all'ossidazione della materia organica. I due carbonati sono anche caratterizzati da diverse composizioni di $\delta^{18}\text{O}$, che variano mediamente da 26.9 a 27.2 e da 26.0 a 26.3‰ VSMOW per la smithsonite e sono mediamente uguali a 24.6 e 23.7‰ VSMOW per l'idrozincite. Queste distinte composizioni di $\delta^{18}\text{O}$ indicano che la smithsonite e l'idrozincite sono precipitate a seguito di almeno due fasi deposizionali. Queste fasi furono probabilmente connesse a diversi periodi di *uplift* che si sono verificati nell'area di Bongará a partite da almeno 10 milioni di anni fa, quando la transizione dall'ecosistema Pebas a quello Acre nel Miocene ha interessato il bacino amazzonico di avampaese. L'attività carsica, alla quale è connessa la mineralizzazione supergenica, può essere temporalmente collocata tra il Miocene superiore e il Pliocene inferiore. Le condizioni climatiche che sono state ricostruite a partire dagli ecosistemi che persistevano nella regione dal tardo Terziario al Recente suggeriscono che la mineralizzazione supergenica di Mina Grande era associata a diversi episodi di *weathering* che si verificarono in condizioni climatiche simili a quelle attuali.

Il deposito di Cristal si trova a circa 6 km nord dal deposito di Mina Grande nella parte più settentrionale di un ampio distretto minerario che corrisponde allo "Charlotte Bongará Zinc Project", il quale copre un'area di circa 110 km². Differentemente da Mina Grande, i resti della mineralizzazione primaria MVT di Cristal sono ancora in posto. Infatti, l'area mineralizzata del deposito di Cristal ospita sia mineralizzazioni a solfuri che a nonsolfuri, le quali localmente sono miste (solfuri + nonsolfuri) o ben separate (solfuri o nonsolfuri). Come nel caso di Mina Grande, la mineralizzazione è ospitata dalle litologie del Pucará Group (principalmente dolomie), che furono depositate in un bacino estensionale mesozoico sul margine ovest dello scudo brasiliano-guyanese. A Cristal i solfuri di zinco si trovano sia in corrispondenza delle radici delle mineralizzazioni a nonsolfuri che in zone prossimali alla superficie. La mineralizzazione a solfuri postdata chiaramente due fasi di dolomitizzazione idrotermale e si rinviene principalmente in vene, riempimenti di cavità o come mineralizzazione disseminata, generalmente associata con dolomite spatica o a sella. I solfuri consistono in gran parte di una sfalerite scura-marroncina, la quale è associata con minori quantitativi di pirite. Generalmente la sfalerite mostra una zonazione a ferro (contiene mediamente il 6% in peso di ferro), ed è ricca in germanio (la concentrazione media è di 145 ppm, mentre quella massima è di 383 ppm). La galena è rara. La sfalerite di Cristal ha una composizione isotopica dello zolfo ($\delta^{34}\text{S}$) che varia da 14 a 15‰ VCDT. Le composizioni isotopiche dell'ossigeno ($\delta^{18}\text{O}$) delle dolomiti variano da 24.4 a 24.7 ‰ VSMOW e da 18.4 a 22 ‰, rispettivamente per le dolomie idrotermali di prima e seconda generazione. I valori di $\delta^{34}\text{S}$ and $\delta^{18}\text{O}$ dei solfuri e delle dolomiti di

Cristal, rispettivamente, sono simili a quelli osservati in due depositi MVT presenti nella regione, che corrispondono ai depositi di Florida Canyon e Florcita. Questa similarità è consistente con un singolo evento mineralizzante alla scala del distretto. I rapporti isotopici della sfalerite proveniente da due diversi prospetti dell'area di Cristal definiscono due distinti *clusters* di dati (centrati intorno a medie di $^{206}\text{Pb}/^{204}\text{Pb} = 18.850 \pm 0.002$, $^{207}\text{Pb}/^{204}\text{Pb} = 15.685 \pm 0.002$, $^{208}\text{Pb}/^{204}\text{Pb} = 38.752 \pm 0.004$, and $^{206}\text{Pb}/^{204}\text{Pb} = 19.042 \pm 0.002$, $^{207}\text{Pb}/^{204}\text{Pb} = 15.712 \pm 0.002$, $^{208}\text{Pb}/^{204}\text{Pb} = 39.080 \pm 0.004$). Questa differenza richiede l'occorrenza di distinti impulsi idrotermali per la messa in posto dei solfuri nell'area di Cristal. Le composizioni isotopiche del piombo dei solfuri di Cristal sono intermedie tra le composizioni delle galene provenienti dai depositi MVT di San Vicente e Shalypaico, e registrano un contributo di una componente crostale antica. Il Marañon Complex che costituisce il basamento dell'area di Bongará, ha rapporti isotopici del piombo che fittano quasi del tutto le composizioni isotopiche delle dolomiti e dei solfuri delle diverse aree dello "Charlotte Bongará Zinc Project", e quindi rappresenta il candidato più realistico per essere il principale *end-member* delle sorgenti dei metalli della mineralizzazione a solfuri di Cristal. Il contributo di un secondo *end-member*, rappresentato da una sorgente magmatica mesozoica o terziaria, è elusivo, siccome nessun di questi magmatismi è stato documentato nell'area di Cristal.

La mineralizzazione a nonsolfuri di Cristal è stata interpretata come il prodotto del *weathering* della mineralizzazione primaria MVT. Il prospetto a nonsolfuri copre un'area di approssimativamente 2 x 1 km con zone di arricchimento in zinco quasi continue, che sono state identificate in campioni di suolo e roccia. La mineralizzazione a nonsolfuri consiste principalmente in ossidati di zinco semi-amorfi con colorazioni che vanno dall'arancione al marroncino. Questi includono emimorfite, smithsonite e idrossidi di ferro. Le zone mineralizzate più significative nell'area di Cristal sono denominate come Esperanza e Yolanda, che sono due prospetti densamente esplorati. In entrambi i prospetti i carbonati e i silicati supergenici di zinco riempiono cavità da dissoluzione, o sostituiscono i carbonati della roccia incassante e/o i solfuri primari formando mineralizzazioni ricche in smithsonite e emimorfite. Le carote analizzate provengono principalmente da Esperanza, dove i contenuti di zinco, associati a livelli ricchi in emimorfite, possono raggiungere valori del 53% in peso; Il tenore medio di zinco è intorno al 20%. A Cristal le concentrazioni di germanio sono significative, con valori del *bulk rock* intorno ai 200 ppm, i quali sono in gran parte relativi alla sfalerite, che è ricca in germanio, e ai prodotti dell'ossidazione dei solfuri come emimorfite e goethite.

Come già osservato per il deposito di Mina Grande, l'area di studio ha vissuto una prolungata fase di *weathering* dal Miocene al Recente in condizioni climatiche tropicali. In questo regime climatico, i processi di *weathering* hanno coinvolto molte mineralizzazioni a solfuri preesistenti (es. Cristal, Florida Canyon, Mina Grande ecc.), nelle quali i profili supergenici si sono sviluppati in condizioni localmente differenti, che sono state evidenziate principalmente sulla base di dati mineralogici e geochimici. A Cristal, la presenza di siderite che precede la smithsonite in paragenesi, indica che il *weathering* dei solfuri ha avuto luogo in una fase di transizione da un ambiente riducente ad uno ossidante. La mineralogia e la geochimica dei depositi dell'area di Bongará è stata

principalmente determinata, a scala locale, da due fattori: (1) i tassi di *uplift*, e (2) la litologia della roccia incassante. Questi ultimi possono favorire lo sviluppo di ambienti supergenici più (es. Mina Grande) o meno (es. Cristal) alcalini. Per esempio, il cadmio presente nelle mineralizzazioni supergeniche di Mina Grande e Cristal è rispettivamente ospitato nell'otavite e nella greenockite. Il primo è indicativo di condizioni alcaline, mentre il secondo è stabile in ambienti debolmente alcalini o caratterizzati da pH neutri. Questa differenza nella geochimica dei due depositi a nonsolfuri è anche rimarcata dai loro contenuti di germanio, i quali sono molto più bassi a Mina Grande rispetto a Cristal. L'assenza di germanio a Mina Grande dovrebbe riflettere la limitata capacità di alcuni minerali supergenici (es. goethite) di fissare questo elemento nella loro struttura in condizioni altamente alcaline.

Dal punto di vista isotopico, le smithsoniti e le calciti supergeniche sono caratterizzate da diverse generazioni. Le composizioni di $\delta^{18}\text{O}$ e $\delta^{13}\text{C}$ della smithsonite di sostituzione dei solfuri variano rispettivamente tra 24.6 e 25.8‰ VSMOW, e tra -0.6 e -11.7‰ VPDB. La smithsonite di sostituzione della roccia incassante è caratterizzata da valori di $\delta^{18}\text{O}$ che variano tra 26.6 e 27.3‰ VSMOW, mentre i valori di $\delta^{13}\text{C}$ sono comparabili con i rapporti di $\delta^{13}\text{C}$ della smithsonite di sostituzione dei solfuri. Vene tardive di smithsonite mostrano valori di $\delta^{18}\text{O}$ e $\delta^{13}\text{C}$ compresi rispettivamente tra 27.8 e 28.3‰ VSMOW, e tra 0.1 e -2.4‰ VPDB. I valori di $\delta^{13}\text{C}$ delle calciti supergeniche, che ricorrono come vene tardive, variano tra 0.7 e -7.4‰ VPDB, mentre i valori di $\delta^{18}\text{O}$ sono approssimativamente pari a 24.7‰ VSMOW.

Il fattore *uplift* è stato principalmente controllato dall'attività delle faglie locali, le quali hanno consentito l'esposizione dei corpi a solfuri a quote variabili in differenti periodi di tempo e condizioni idrogeologiche (es. l'attuale deflusso superficiale delle acque meteoriche è maggiore a Mina Grande che a Cristal). Queste differenti condizioni possono risultare nella precipitazione di carbonati supergenici che sono isotopicamente diversi (es. smithsoniti e calciti di Mina Grande e Cristal). Contrariamente a quanto osservato per il deposito di Mina Grande, a Cristal lo sviluppo di una rete carsica è stato smorzato da un limitato tasso di *uplift*, e l'alterazione supergenica non ha completamente obliterato le radici del corpo a solfuri originario.

Nei depositi di Mina Grande e Cristal sono stati trovati differenti Zn-fillosilicati in associazione con i principali minerali di Zn della mineralizzazione a nonsolfuri (smithsonite, emimorfite e idrozincite). Le analisi XRD e SEM-EDS hanno rivelato che le miche zincifere presenti in entrambi i depositi consistono principalmente in strati misti I/S di origine detritica, che sono stati parzialmente alterati o incrostatati da sauconite durante l'alterazione supergenica dei solfuri. Nell'associazione mineralogica dei minerali a nonsolfuri di Cristal è stata sporadicamente identificata l'hendricksite, mentre a Mina Grande è stata rilevata l'associazione fraipontite-zaccagnaite (politipo-3R). Il politipo identificato della zaccagnaite suggerisce che sia la fraipontite che la zaccagnaite sono geneticamente relative a processi di weathering. L'hendricksite rinvenuta a Cristal può essere invece considerata un prodotto dell'alterazione idrotermale, che si è formato durante la messa in posto dei solfuri. La complessa natura dei fillosilicati identificati è

un'evidenza di molteplici processi idrotermali e supergenici che sono ricorsi nel distretto di Bongará.

I depositi a Zn(Pb) di Skorpion e Rosh Pinah sono ospitati in rocce del Neoproterozoico che fanno parte di una sequenza vulcanosedimentaria del Gariep Belt nel sudovest delle Namibia. Skorpion è la più grande mineralizzazione a nonsolfuri di Zn mai scoperta. Quest'ultima si è formata dal *weathering* e conseguente ossidazione di un giacimento primario di tipo VMS (*Volcanic Massive Sulfides*) e consiste in gran parte di minerali ossidati di zinco. Rosh Pinah è un deposito ibrido a solfuri massivi di zinco, con caratteristiche che appartengono sia ad un VMS che ad un Broken Hill-*type*. Le parti più alte del corpo a solfuri mostrano segni evidenti dell'alterazione supergenica.

È stata realizzata una comparazione tra i processi di ossidazione profonda che si presentano a Skorpion e quelli che hanno prodotto il limitato *weathering* del deposito di Rosh Pinah, attraverso lo studio dei rapporti isotopici di carbonio e ossigeno dei carbonati supergenici. Sono stati analizzati ventitré campioni di smithsonite proveniente dal deposito di Skorpion e sei campioni ad ossidati di zinco (contenenti sia dolomite che smithsonite) provenienti dai livelli più alti della miniera di Rosh Pinah. Le smithsoniti di Skorpion formano croste botroidali che sono ricoperte da cristalli euedrali di calcite. A Rosh Pinah tutte le smithsoniti campionate si rinvenivano in vene all'interno della dolomite della roccia incassante. La smithsonite di Skorpion è caratterizzata da $\delta^{13}\text{C}$ molto variabili che sono compresi tra -9.1‰ e 0.1‰ VPDB e da un *range* ristretto di valori di $\delta^{18}\text{O}$ che variano da 28 a 29.9‰ VSMOW. La calcite mostra una minore variazione nella composizione di $\delta^{13}\text{C}$ con valori che sono generalmente positivi (da 0 a 1.6‰ VPDB), e valori di $\delta^{18}\text{O}$ leggermente inferiori rispetto quelli della smithsonite (da 25.4 a 27.1‰ VSMOW). Le analisi dei campioni di Rosh Pinah mostrano che la dolomite incassante è caratterizzata da valori di $\delta^{18}\text{O}$ che variano da 18.7 a 22.0‰ VSMOW, e da valori negativi di $\delta^{13}\text{C}$ (da -5.9 a -2.7‰ VPDB). I rapporti isotopici del carbonio della smithsonite, come a Skorpion, sono negativi (da -2.8 a -1.9‰ VPDB) e sono simili a quelli delle dolomiti della roccia incassante. I valori di $\delta^{18}\text{O}$ (26.7-29.0‰ VSMOW) sono mediamente comparabili con i valori della smithsonite di Skorpion. A Rosh Pinah, simili valori negativi di $\delta^{13}\text{C}$ della smithsonite e della dolomite suggeriscono il coinvolgimento sia di carbonio organico riossidato che di carbonio inorganico della dolomite della roccia incassante durante la formazione della smithsonite. Contrariamente, a Skorpion, un maggiore contributo di carbonio organico è considerato essere più probabile. Il fatto che le composizioni di $\delta^{18}\text{O}$ della smithsonite dei due depositi siano comparabili, implica che durante la formazione del minerale hanno agito fluidi precipitanti e/o condizioni di temperatura simili. In accordo con studi precedenti, questa ricerca suggerisce che la smithsonite di Skorpion è stata precipitata ad una temperatura media di circa 17°C da fluidi impoveriti in ^{13}C a causa dell'alto contributo del carbonio organico del suolo, o durante la prima (Cretacico Superiore-Paleocene) o l'ultima (Miocene inferiore-medio) fase climatica umida. Anche se la somiglianza tra le composizioni di $\delta^{18}\text{O}$ delle smithsoniti di Skorpion e Rosh Pinah indica che fluidi o condizioni simili persistevano durante la loro formazione, i valori relativamente più alti del $\delta^{13}\text{C}$ delle smithsoniti di Rosh Pinah suggeriscono una minore influenza di carbonio organico e l'assenza di un

suolo ben formato sopra il deposito. Combinando questi dati con il limitato spessore della zona supergenica soprastante il corpo mineralizzato di Rosh Pinah, è probabile che la smithsonite di questo deposito, insieme con il gossan nel quale essa ricorre, si sia formata alla fine del periodo semi-umido del Miocene inferiore-medio.

Le composizioni di $\delta^{18}\text{O}$ e $\delta^{13}\text{C}$ della calcite di Skorpion indicano che i fluidi supergenici precipitanti rimasero più o meno invariati ma che il contributo del bicarbonato della roccia incassante divenne prevalente. Questo suggerisce che la formazione della calcite è avvenuta all'inizio del periodo semi-arido del Miocene-Pliocene, quando i marmi incassanti furono sollevati e carsificati, favorendo quindi un più alto contributo del bicarbonato attraverso la dissoluzione della roccia incassante.

Uno dei principali componenti dell'associazione mineralogica di Skorpion è la Zn-smectite ("sauconite"). Infatti, nel corpo mineralizzato di Skorpion le smectiti zincifere triottaedriche sono prevalenti rispetto agli altri nonsolfuri di zinco (es. smithsonite, emimorfite e idrozincite). Uno studio approfondito della componente argillosa è stato concentrato sulle osservazioni microtessiturali e sulle analisi chimiche delle nanoparticelle dei minerali argillosi del corredo mineralogico supergenico del deposito di Skorpion. Tali osservazione ed analisi per questo deposito sono state realizzate per la prima volta utilizzando tecniche TEM/HRTEM e AEM. Questo approccio ha consentito una migliore comprensione dei meccanismi di formazione delle argille zincifere di Skorpion, e di fasi relative ad esse, fino alla nanoscala. Le microtessiture di queste argille suggeriscono che esse si sono formate da fluidi di natura meteorica e/o idrotermale, in due contesti tessiturali: le smectiti possono crescere su fillosilicati precedentemente depositati (miche) (tessitura CCP), e/o direttamente nucleare da soluzioni ricche in zinco (tessitura PCA). La sauconite di Skorpion è chimicamente caratterizzata da un'omogeneità maggiore se comparata con le sauconiti naturali provenienti da altri depositi. Quest'ultima è abbastanza stechiometrica, con Ca come catione *interlayer* e limitate quantità di magnesio e ferro. La composizione media della sauconite di Skorpion è la seguente:

$\text{Ca}_{0.14}\text{K}_{0.02}(\text{Zn}_{2.7}\text{Mg}_{0.09}\text{Al}_{0.14}\text{Fe}_{0.10})(\text{Si}_{3.4}\text{Al}_{0.6})\text{O}_{10}(\text{OH})_2 \cdot n\text{H}_2\text{O}$. Alla micro e nanoscala, è stata osservata anche la Zn-beidellite, ma il suo rinvenimento è molto subordinato, come nel caso della clorite e del baileychlore. Le miche detritiche sono comunemente il *template* per la crescita epitassiale della sauconite. Per la genesi della sauconite di Skorpion, e quindi di gran parte della mineralizzazione supergenica del deposito, dovrebbero essere considerati tipici processi supergenici a temperature ambiente, con alcuni locali contributi da parte di fluidi idrotermali di bassa temperatura. Le micro e nano caratteristiche dell'associazione mineralogica di Skorpion confermano la complessa natura mineralogica dei (micro)sistemi a nonsolfuri ricchi in smectite, con rimarcate implicazioni per definizione del modello mineralogico e del *work-flow* del *processing*.

Con lo scopo di comparare l'evoluzione dei profili di *weathering* e le caratteristiche genetiche dei depositi supergenici collocati in aree aride (Skorpion e Rosh Pinah) e umide (Mina Grande e Cristal), sono stati realizzati studi paralleli. I dati isotopici di carbonio e ossigeno sono stati utili per registrare episodi di *weathering* a lungo e a breve termine. I primi sono evidenziati da estreme differenze tra i valori di $\delta^{13}\text{C}$ dei carbonati della roccia

incassante e quelli dei minerali supergenici (es. smithsonite). I secondi sono caratterizzati da omogeneità nei rapporti isotopici del carbonio tra la roccia incassante i prodotti del *weathering*. Tuttavia, questa omogeneità nei profili supergenici che si sono evoluti in condizioni semi-aride, può anche indicare periodi prolungati di *weathering*, durante i quali l'attività organica nei suoli può essere stata trascurabile. I carbonati supergenici di Cristal e Mina Grande, i quali si sono formati e sviluppati in aree di catena in condizioni climatiche umide, mostrano piccole variazioni del loro *range* composizionale isotopico che suggerirebbero limitati cambiamenti ambientali. Tuttavia, le estreme variazioni delle condizioni di *weathering* a scala locale ci dicono l'esatto opposto. Cambiamenti simultanei della temperatura e della composizione di $\delta^{18}\text{O}$ dei fluidi supergenici possono risultare in rapporti isotopici simili dei carbonati supergenici che appartengono a differenti generazioni.

Tuttavia, le investigazioni sui vincoli delle condizioni deposizionali dei minerali supergenici nei depositi a nonsolfuri non possono essere esclusivamente condotte sull'associazione mineralogica. Una volta ancora, il coinvolgimento di molti fattori a scala locale può controllare la precipitazione delle diverse fasi mineralogiche (es. siderite invece di smithsonite, otavite invece di greenockite oppure sauconite invece di fraipontite). Inoltre, l'identificazione di minerali che possano essere usati come indicatori ambientali, come accade spesso per i minerali del gruppo della caolinite e delle smectiti, i quali sono rinvenuti rispettivamente in suoli tropicali e aridi, potrebbe non essere corretta siccome questi minerali possono anche essere precipitati da fluidi idrotermali (es. fraipontite e sauconite). L'importanza dei fattori a scala locale nelle aree umide-tropicali di catena è testimoniata dalla marcata differenza tra i profili di *weathering* dei depositi di Mina Grande e Cristal. Queste differenze dipendono principalmente dalla capacità delle rocce incassanti a trattenere la CO_2 in un ambiente di alterazione acido (dolomite > calcite), la quale influenza direttamente il pH delle soluzioni meteoriche, e dalla relazione che c'è tra quota (tassi di *uplift*) e tassi di *runoff*. La combinazione di questi fattori può risultare in una locale preservazione dei minerali a solfuri, come nel caso del deposito di Cristal, o in continuo apporto di acqua meteorica e approfondimento del profilo supergenico, come riscontrato nel deposito di Mina Grande. Tutti questi meccanismi controllano la genesi e lo sviluppo dei profili supergenici in un *range* ristretto di condizioni pH-Eh (da alcaline a neutre e da debolmente riducenti a ossidanti), le quali favoriscono la formazione di una suite limitata di minerali (principalmente carbonati metalliferi).

In conclusione, questo studio ha confermato che i passaggi paleoclimatici da periodi stagionali umidi/aridi a periodi iperaridi (es. il distretto di Skorpion-Rosh Pinah) potrebbe essere lo scenario più favorevole alla formazione e preservazione di giacimenti a nonsolfuri di zinco di una certa rilevanza economica. Tuttavia, la presente ricerca ha anche smentito alcune teorie circa la scarsa possibilità di preservare i profili supergenici in condizione di *weathering* tropicale. La coesistenza di molti fattori e la loro complessa relazione durante l'ossidazione dei solfuri in aree tropicali moderne può generare locali condizioni di preservazione (es. Cristal) o instabilità (es. Mina Grande). Le analisi degli isotopi stabili di carbonio e ossigeno sono utili per stimare approssimativamente queste condizioni locali ma esse non forniscono dati sulla disponibilità di acqua e sulla sua

capacità di ricarica. Quindi, ogni tentativo di presentare ipotesi paleoclimatiche, senza considerare il background geologico (es. tassi di *uplift* e delle precipitazioni, e litologia della roccia incassante) delle aree che ospitano i depositi a nonsolfuri può risultare privo di utilizzo. I dati forniti da questo studio su quest'interessante argomento potrebbero essere applicati ad altri profili di (paleo)*weathering* tropicali nel mondo, con lo scopo di costruire più accurati modelli geologici e geochimici.

I risultati di questo studio sono stati pubblicati in diversi articoli su riviste internazionali, e altri manoscritti sono stati presentati per la pubblicazione. Molte parti di questa tesi di dottorato corrispondono al contenuto dei manoscritti citati qui di seguito:

Arfè, G., Boni, M., Balassone, G., Mondillo, N., Hinder, G., Joachimski, M., 2017. New C-O isotopic data on supergene minerals from the Skorpion and Rosh Pinah ore deposits (Namibia): Genetic and paleoclimatic constraints. *Journal of African Earth Sciences*, 126, 148-158.

Contributi di G. Arfè al manoscritto: Ha condotto la preparazione dei campioni, la caratterizzazione petrologica, parte delle analisi geochemiche, ha elaborato il modello principale per l'interpretazione dei dati, ed ha completato la stesura della prima versione del manoscritto a cui hanno poi contribuito gli altri co-autori.

Arfè G., Mondillo, N., Balassone G., Boni, M., Cappelletti, P., Di Palma, T., 2017. Identification of Zn-bearing micas and clays from the Cristal and Mina Grande - Bongará zinc deposits (Amazonas region, northern Peru). *Minerals*, 7, 214; DOI: 10.3390/min7110214 .

Contributi di G. Arfè al manoscritto: Ha condotto la campionatura *in situ*, la preparazione dei campioni, la caratterizzazione petrologica e mineralogica, parte delle analisi geochemiche. Ha inoltre contribuito all'interpretazione dei dati, ed alla stesura della prima versione del manoscritto a cui hanno poi contribuito gli altri co-autori.

Arfè, G., Mondillo, N., Boni, M., Balassone, G., Joachimski, M., Mormone, A., Di Palma, T., 2017. The karst-hosted Mina Grande nonsulfide zinc deposit, Bongará district (Amazonas region, Peru). *Economic Geology*, 112, 1089-1110.

Contributi di G. Arfè al manoscritto: Ha condotto la campionatura *in situ*, la preparazione dei campioni, la caratterizzazione mineralogica e petrologica, parte delle analisi geochemiche. Ha inoltre elaborato l'interpretazione dei dati, ed ha completato la stesura della prima versione del manoscritto a cui hanno poi contribuito gli altri co-autori.

Arfè, G., Mondillo, N., Boni, M., Joachimski, M., Balassone, G., Mormone, A., Santoro L., Castro Medrano E. The Cristal Zn prospect (Amazonas region, Northern Peru). Part II: An example of supergene zinc enrichments in tropical areas. *Ore Geology Review*, (in press).

Contributi di G. Arfè al manoscritto: Ha condotto la campionatura *in situ*, la preparazione dei campioni, la caratterizzazione mineralogica e petrologica, parte delle analisi

geochimiche. Ha inoltre elaborato l'interpretazione dei dati, ed ha condotto la stesura della prima versione del manoscritto a cui hanno poi contribuito gli altri co-autori.

Balassone, G., Nieto, F., Arfè, G., Boni, M., Mondillo, N., 2017. Zn-clay minerals in the Skorpion Zn nonsulfide deposit (Namibia): Identification and genetic clues revealed by HRTEM and AEM study. *Applied Clay Sciences*, 150, 309-322.

Contributi di G. Arfè al manoscritto: Ha effettuato la scelta dei campioni e parte dello studio mineralogico (es. interpretazione preliminare dei patterns XRD).

Mondillo N., Arfè G., Boni M., Balassone G., Boyce A., Joachimski M., Villa I.M. The Cristal Zn prospect (Amazonas region, Northern Peru). Part I: New insights on the sulfide mineralization in the Bongará province. *Ore Geology Review*, (in press).

Contributi di G. Arfè al manoscritto: Ha parzialmente condotto la campionatura *in situ*, la preparazione dei campioni, la caratterizzazione mineralogica e petrologica, le analisi isotopiche C-O. Ha partecipato all'interpretazione dei dati ed alla stesura del manoscritto in collaborazione con gli altri co-autori.

Introduction

The main subject of this Ph.D. thesis is the study of two poorly known supergene Zn nonsulfide deposits in the Bongará area (Amazonas Region, northern Peru). The two deposits, namely Mina Grande and Cristal (Wright, 2010; Arfè et al., 2017b, in press), occur in an area affected by climatic conditions typical of humid tropical upland, characterized by both dry and rainy seasons. In order to improve the understanding of the genetic processes for the nonsulfide deposits in this pluvial area by comparing them with those occurring in more arid regions, the supergene profiles of the Zn-Pb Skorpion (nonsulfide) and Rosh Pinah (sulfide>>nonsulfide) deposits in Namibia were also studied.

The supergene nonsulfide zinc deposits can be hosted in both siliciclastic (Skorpion and Rosh Pinah; Fig. 1) and carbonate rocks (Cristal and Mina Grande; Fig. 2). The nonsulfide mineralizations are usually characterized by higher zinc grades than their sulfide progenitors, with average grades between 2 and 30% Zn (Paradis and Simandl, 2010). These deposit types show also sharp natural cut-off and tonnages ranging from <1 up to 50 Mt (Paradis and Simandl, 2010) that can be easily mined and exploited in open-pit mode.

Favorable climatic conditions are indispensable for the development and preservation of the supergene profiles of the Zn nonsulfide deposits. The two sets of studied deposits occur in two areas affected nowadays by very different climatic conditions, which have different influence on the development and/or preservation of their supergene profiles. However, most supergene profiles of the nonsulfide deposits worldwide are related to paleoweathering processes (Hitzman et al., 2003; Paradis and Simandl, 2010; Borg, 2015; Boni and Mondillo, 2015) and the current profiles are not active anymore. Many of the world-class supergene nonsulfide deposits recognized today (e.g. Skorpion; Borg et al., 2003; Kärner, 2006) were considered to have been formed and/or developed in semi-arid environments at temperatures constrained between 10 and 20°C (Gilg et al., 2008), and are currently hosted in fossil profiles. Reichert and Borg (2008) affirmed “*the oxidation under arid conditions is also the favoured scenario for an effective sulphide oxidation process and the formation of a non-sulphide orebody*”. In contrast, the recent review work of Boni and Mondillo (2015) on the carbonate-hosted supergene nonsulfide deposits of the “Calamine” type has stressed the importance of paleoclimatic switch-overs from seasonally humid/arid to hyperarid periods. Such switch-over periods have been considered as possessing the most favorable conditions for the formation and preservation of supergene nonsulfide deposits. Despite the latter considerations, some relatively recent supergene deposits formed either under prolonged warm and humid (e.g. Bongará; Arfè et al., 2017b, in press), cold-temperate (e.g. British Columbia; Paradis et al., 2011) and peri-glacial (e.g. Alaska; Santoro et al., 2015) climatic settings. Indeed, Boni and Mondillo (2015) recognized also that “*...at any case, the current location of many deposits does not reveal definitely the most favorable climate conditions for Zn-nonsulfide deposition and preservation*”. Therefore, the main purpose of this study was

to find the genetic relationships and the common aspects between the supergene nonsulfide deposits positioned in the tropical areas and those falling outside of the latter, in order to understand the real influence of climate conditions on the mineralogy, geochemistry and formation of nonsulfide Zn deposits.

The most important part of this study, which is at the base of the understanding of nonsulfide genesis and development, is the knowledge of the mineralogy of the deposits. Zn- bearing carbonates, silicates, oxides and hydroxides represent the prevailing species, followed by phosphates, secondary sulfides and, eventually, by remnants of primary sulfides. Most of the supergene Zn nonsulfide deposits are derived from the weathering of Mississippi Valley-type (MVT) and Carbonate Replacement Deposits (CRD), rather than from Irish-type, sedimentary exhalative (SEDEX) and volcanic-hosted massive sulfide (VHMS) deposits (Hitzman et al., 2003; Boni and Mondillo, 2015). Those formed from the supergene alteration of MVT are characterized by less complicated mineralogy than those derived from CRD deposits (Hitzman et al., 2003). Detailed descriptions of the mineralogy of MVT- or CRD-derived nonsulfide groups under humid or arid climate settings will be given in the next chapter. An additional complexity in the mineralogy can result from the climatic regime occurring at the time of supergene oxidation of the sulfide protores. For example, arid climate settings promote formation of smectite group minerals, such as saucroite (Zn-smectite), which is hardly recognized in notable amounts under humid climates where smithsonite is prevailing. The relative abundance of the carbonate phases is fundamental to perform stable isotopic studies on supergene minerals (mainly smithsonite, cerussite and calcite), which can be essential to develop the genetic models and to get paleoclimatic constraints. Indeed, smectite can be used to determine O and H isotopes, but it does not provide any data on C isotopes, which conversely are fundamental to reconstruct the environmental condition at the time of supergene minerals formation.

The secondary purpose of this study was to increase the knowledge of the geology and mineralogy of the still poorly known Mina Grande and Cristal deposits, which will be probably exploited in the near future. At this point, the exact knowledge of the mineral phases, and the deportment of several target elements (Zn-Pb-Ge) can be essential to optimize their recovery during the planned processing stages.

Chapter 1:

Supergene nonsulfide Zn(Pb) deposits: classification, mineralogy, metallogenesis, climatic and structural controls

The terms “nonsulfides” indicates a restricted group of deposits, which formed either from low temperature hydrothermal fluids, or from metal-carrying meteoric waters (e.g. groundwaters). The metal endowment of the latter waters derived from the weathering of preexisting Zn(Pb)-bearing sulfide ores. The sulfide progenitors are commonly Mississippi Valley-type (MVT), Sedimentary Exhalative (SEDEX), Carbonate Replacement (CRD), Volcanic-associated Massive Sulfides (VMS) and Skarn deposits worldwide. Hitzman et al. (2003) proposed an exhaustive classification of the nonsulfide deposits, reviewing and modifying previous classifications introduced by Penrose (1894), Emmons (1901), Lindgren (1913), Heyl and Bozion (1962) and Large (2001). In the above classification nonsulfide deposits are subdivided into hypogene and supergene (Fig 1.1), based on their geological setting, mineralogy and genesis. The supergene deposits are only a sub-category of the nonsulfide Zn(Pb) ores although the hypogene deposits are much less common than the supergene ones on global scale (Fig 1.2). The economic value of nonsulfide deposits mostly depends on factors such as: (1) mineralogy of the ore and gangue minerals, (2) tonnage and grade, and (3) geopolitical setting.

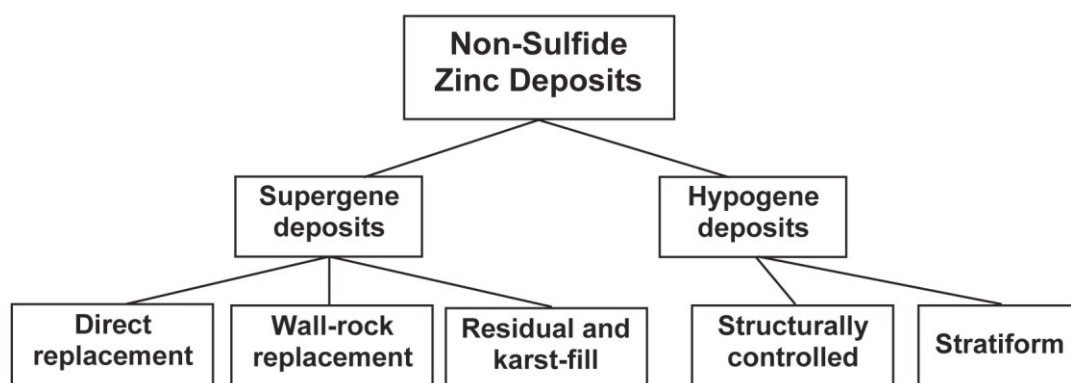


Figure 1.1. General classification of nonsulfide deposits (Hitzman et al., 2003).

The hypogene deposits mainly contain zinc silicates and oxides (e.g. franklinite, zincite, willemite, hematite and manganese-rich minerals), and minor sphalerite and gahnite. Smithsonite, hemimorphite, hydrozincite and sauconite are rare, except in near-surface exposures. In particular, deposits of the “structurally controlled” sub-category (Hitzman et al., 2003) are characterized by willemite-(sphalerite and ferromanganese-rich minerals)-bearing veins and pipes, whereas those of the “stratiform” sub-category contain more franklinite, zincite and gahnite. These types of nonsulfide deposits can be generated

from relatively high temperature Zn-rich and S-poor fluids that can be more or less reduced as function of different proportions with oxidized fluids.

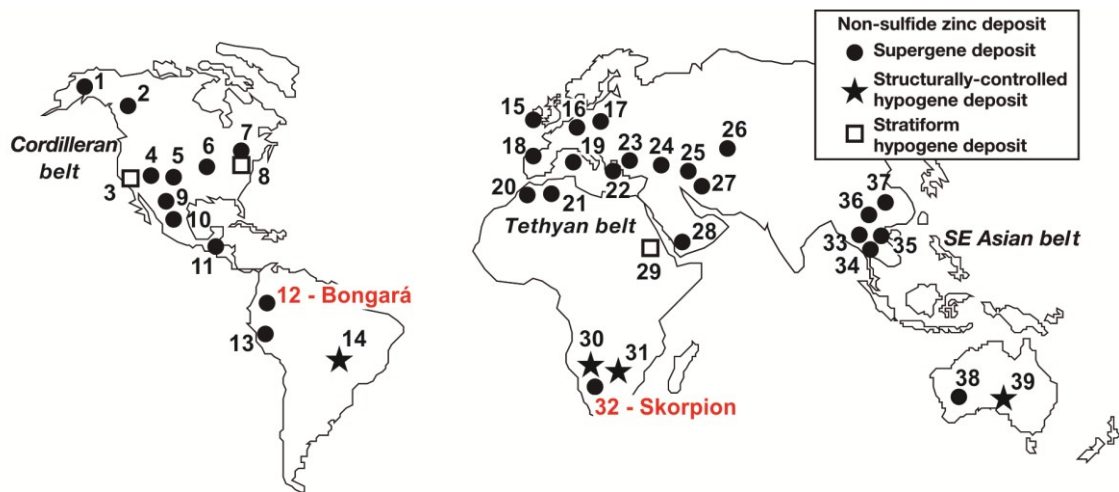


Figure 1.2. Distribution of principal nonsulfide deposits in the world (after Hitzman et al., 2003, and Boni and Mondillo, 2015). 1 = Reef Ridge, Alaska; 2 = Howards Pass, Canada; 3 = Desert View, United States; 4 = Tintic, United States; 5 = Leadville, United States; 6 = Upper Mississippi Valley district, United States; 7 = Balmat, United States; 8 = Franklin and Sterling Hill, United States; 9 = Sierra Mojada, Mexico; 10 = Santa Eulalia, Mexico; 11 = Torlon Hill, Guatemala; 12 = Bongará, Peru; 13 = Accha, Peru; 14 = Vazante, Brazil; 15 = Tynagh and Silvermines, Ireland; 16 = La Calamine, Belgium; 17 = Upper Silesian Mississippi Valley-type district, Poland; 18 = Reocin, Spain; 19 = Sardinian Zn-Pb district, Italy; 20 = Touissit, Morocco; 21 = Hamman N'Bails, Algeria; 22 = Larium and Thassos, Greece; 23 = Zambanti Zn-Pb district, central Turkey; 24 = Hakkari, Turkey; 25 = Angouran, Iran; 26 = Shaimerden, Kazakhstan; 27 = Mehdiabad, Iran; 28 = Jabali, Yemen; 29 = Abu Samar, Sudan; 30 = Berg Aukas and Abenab, Namibia; 31 = Kabwe and Star Zn, Zambia; 32 = Skorpion, Namibia; 33 = Padaeng (Mae Sot), Thailand; 34 = Long Keng, Myanmar; 35 = Cho Dien, Vietnam; 36 = Jinding (Lanping), China; 37 = Qiondong Shen, China; 38 = Magellan Pb, Australia; 39 = Beltana and Aroona, Australia.

Even if nonsulfide ores may be genetically associated with sphalerite-rich mineralizations in any rock type, both supergene and hypogene deposits occur preferentially in carbonate rocks. In the case of supergene ores this is due to the high reactivity of carbonate minerals with the acidic and zinc-rich fluids derived from weathering of sphalerite-bearing sulfide protore. Their hypogene (nonsulfide- or sulfide-bearing) progenitors and host rocks range from Late Proterozoic to Mesozoic, whereas the mineralization age spans from Cretaceous to Recent.

Classification and mineralogy of Zn(Pb) supergene nonsulfide deposits

Supergene Zn(Pb) deposits form mainly via oxidation of MVT and CRD sphalerite and galena)-bearing sulfide progenitors in a near surface environment, although some of them can also result from oxidation of a pre-existing hypogene nonsulfide ores (e.g. Vazante, Brazil; Monteiro et al., 2006, 2007).

The supergene deposits have been subdivided by Hitzman et al. (2003) in three groups: (1) “direct-replacement”, (2) “wall rock-replacement” and (3) “residual and karst-fill” (Fig. 1.3), based essentially on relationships between host rock, protore and supergene mineralization.

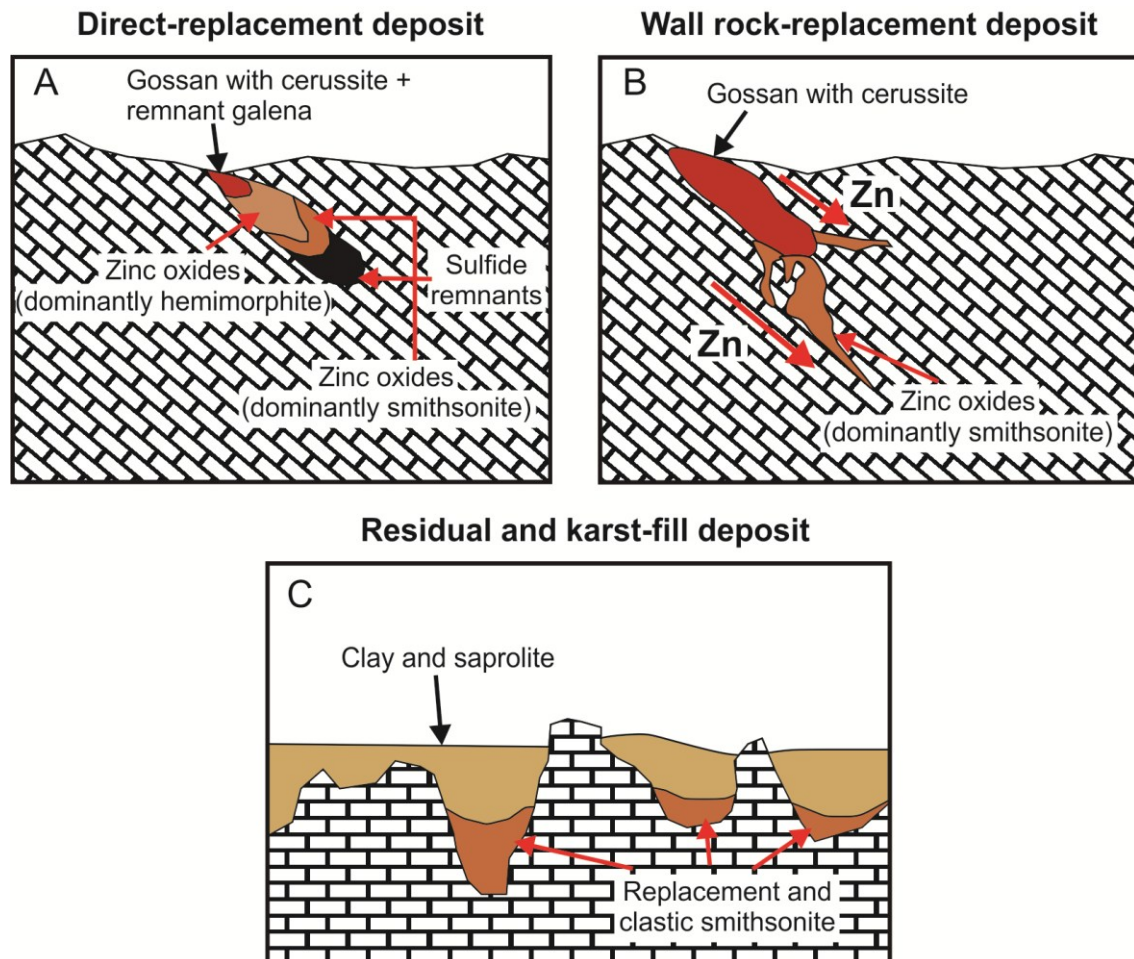


Figure 1.3. Schematic models of the formation of the different types of supergene zinc deposits (after Hitzman et al., 2003). A. Direct-replacement deposits form via replacement of sulfide minerals by hemimorphite and smithsonite. B. Wall rock-replacement deposits form via replacement of host rock-forming minerals (generally calcite and dolomite) by smithsonite (and hemimorphite). C. Residual and karst-fill deposit form via mechanical erosion and concentration of zinc oxide and silicate minerals in karst systems.

Direct replacement deposits

Direct-replacement deposits (Fig 1.3) result from in situ oxidation of sulfides and subsequent replacement with supergene minerals. Direct-replacement deposits from MVT ores are characterized by a relatively simple mineralogy, mostly consisting of smithsonite, hemimorphite and hydrozincite. Conversely, supergene deposits formed from sulfide progenitors of higher temperature (e.g. CRD ores), are characterized by a more complex mineral assemblage, in which smithsonite, hemimorphite and hydrozincite occur together with Mn-rich zinc minerals (e.g. hetaerolite and hydrohetaerolite,

chalcophanite etc.), copper carbonates and As-bearing minerals. Direct-replacement deposits are essentially Zn-rich gossans (Kelly, 1958), if pyrite does not occur in great quantity in sulfide protore. Indeed, since zinc is very mobile under supergene conditions (25°C and 1 atm), heavy production of acidic solutions during pyrite weathering would be able to completely leach zinc from the near-surface levels of the mineralized body, thus producing a vuggy jasperoid gossan with iron oxides, and less mobile Pb-bearing minerals (e.g. cerussite, plumbojarosite) and copper carbonates. As stated above, supergene deposit may also derive from oxidation of nonsulfide-bearing protores resulting in hemimorphite- and supergene willemite-rich bodies.

Even if occurrences of “pure” sub-categories are rare, there are some good examples of supergene deposits worldwide, mostly formed via direct-replacement processes: (1) the Tynagh and Silvermines deposits in Ireland (Clifford et al., 1986; Boland et al., 1992; Boni and Large, 2003; Balassone et al., 2008), (2) the Upper Silesian Mississippi Valley-type district of Poland (Sass-Gustkiewicz et al., 1982; Osika, 1986; Large, 2001; Boni and Large, 2003; Coppola et al., 2009), (3) the Accha deposit in Peru (Boni et al., 2009a), (4) the Jinding deposit in China (Li and Kyle, 1997), (4) the Reef Ridge deposit in Alaska (Santoro et al., 2015).

Wall rock-replacement deposits

Wall rock-replacement deposits (Fig. 1.3) are commonly associated with direct-replacement deposits, since sulfide bodies are progressively oxidized and zinc-bearing acidic groundwaters migrate into the calcareous wall rock that acts as a geochemical barrier (pH ~8), eventually allowing zinc carbonates to precipitate. Differently from direct replacement, the development of wall rock-hosted deposits is much more affected by tectonic setting and/or by fluctuations of the groundwater table. Indeed, both tectonic uplift and/or oscillation of the phreatic zone in permeable hosts can promote Zn-bearing meteoric fluids getting into contact with rocks surrounding the original sulfide deposit. This circulation may lead to a spatial distribution of the metals on the base of their different solubility. Therefore, zinc may be easily separated from lead, copper, silver, and iron (Sangameshwar and Barnes, 1983). Wall rock-replacement deposits appear to have a less complex mineralogy than direct-replacement deposits, even though it is affected by the composition of the protore type. Therefore, secondary deposits derived from MVT ores essentially contain “clean” smithsonite and only rarely zincian dolomite, whereas those deposits derived from Fe- and Mn-rich CRD consist generally of ferroan smithsonite with zincian dolomite and manganosiderite. The abundance of hemimorphite and other Zn-bearing silicates (e.g. sauconite and fraipontite) depends principally on the nature of the host rock (e.g. cherty limestones and carbonate rocks interbedded with siliciclastic rocks guarantee a certain SiO₂ availability in meteoric solutions) and multicyclic oxidation and leaching. Indeed, if there is availability of silica in the supergene system, repeated leaching of massive smithsonite occurrences may initially result in the formation of porous brown to reddish smithsonite with intergrown hemimorphite and, subsequently, in a mixture of hemimorphite, sauconite, Fe-(hydro) oxides, and hematitic chalcedonic silica, until to generate a barren goethite-chalcedonic

silica rock (Hitzman et al., 2003; Reichert and Borg, 2008; Paradis and Simandl, 2010; Boni and Mondillo, 2015)

Similarly to direct-replacement deposits, wall-rock replacement types are relatively common. Some wall rock-dominated examples include: (1) the Iglesias district of Sardinia (Moore, 1972; Boni et al., 1996; Boni et al., 2003), (2) most Turkish deposits (Sağuroğlu, 1988; Yılmaz et al., 1992; Ceyhan, 2003; Yigit, 2009; Santoro et al., 2013), (3) the Laurium district in Greece (Skarpelis and Argyraki, 2009), the Jabali deposit in Yemen (Al Ganad et al., 1994; Mondillo et al., 2011, 2014a) and the Skorpion deposit in Namibia (Corrans et al., 1993; Borg et al., 2003; Kärner, 2006).

Residual and karst-fill deposits

Residual and karst-fill supergene deposits (Fig. 1.3) result from physical-chemical transport and concentration of zinc minerals in karstic depressions or in cave systems, which are far from the original location of supergene-weathered sulfide bodies. Tectonic uplift, combined with wet conditions on site (tropical climate and/or wet periods in temperate areas), can enhance karst development and high-grade smithsonite accumulation within cavities. Hydrozincite can be very abundant in these conditions. Renewed uplift phases in association with repeated leaching of the first supergene products, can lead to downward migration of the supergene weathering profile and to the deepening of the karst system that can eventually collapse and produce a “collapse breccia”, suitable for the deposition of successive generations of Zn-bearing minerals.

This type of deposit is relatively uncommon. Examples of residual and karst-fill-dominated occurrences described so far by Hitzman et al. (2003) are the Cho Dien deposit in Vietnam and the Padaeng deposit in Thailand

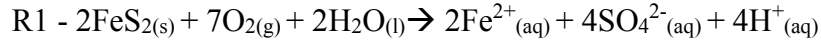
Metallogenesis of Zn(Pb) supergene nonsulfide deposits

The genesis of Zn supergene deposits is controlled by the interaction between host rocks, hypogene sulfides, and meteoric fluids (Takahashi, 1960; Sangameshwar and Barnes, 1983; Reichert, 2009; Reichert and Borg 2008; Boni and Mondillo, 2015; Borg, 2015). On this base, supergene deposits can be divided in carbonate- and siliciclastic rock-hosted supergene zinc systems, which are subjected to different genetic processes.

Carbonate-hosted supergene zinc systems

This type of deposits is also known as “Calamine” (Boni and Large, 2003), which is a term indicating a supergene Zn-mineralization (mainly consisting of smithsonite + hemimorphite) hosted in carbonate rocks. The name “Calamine” is associated with the small town of La Calamine, today named Kelmis in Belgium, which was the first site where the characteristics of the carbonate-hosted supergene deposits have been described (Coppola et al., 2008). The supergene evolution in this system develops through two geochemically and mineralogically different stages: (1) sulfide oxidation stage, and (2) post-oxidation stages.

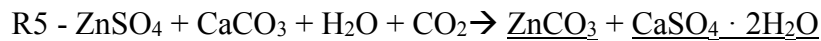
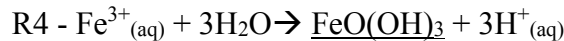
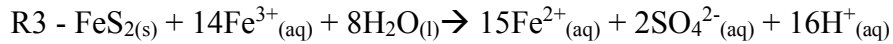
Oxidation stage - During this first stage, the alteration process of pyrite/marcasite via oxidizing meteoric waters results in low-pH sulfate-bearing solutions (R1), able to carry metal cations.



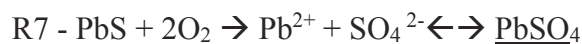
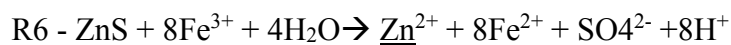
The oxidation of Fe^{2+} (R2) located into pyrite/marcasite crystalline structure is very limited under pH ~ 4 if exclusively via chemical oxidation (Battaglia et al., 1998; Boon and Heijnen, 1998; Rimstidt and Vaughan, 2003).



However, the oxidation process of ferrous iron can be accelerated (up to 10-20 times) through the action of Fe-oxidizing bacteria (e.g. *Thiobacillus ferrooxidans* and *Thiobacillus thiooxidans*), which are commonly present in the oxidation zone (Singer and Stumm, 1970; Schippers, 2003). Generally, the abundance of pyrite improves the amount of weathering process, because it provides more SO_4^{2-} than sphalerite or galena (Williams, 1990). The high availability of SO_4^{2-} and Fe^{3+} (R3) in this acidic solution (@ pH between 3 and 4) in the early oxidation stage results in the initial precipitation of Fe-(hydr)oxides (R4) and gypsum (rather than smithsonite; R5). The formation of these minerals inhibits a fast neutralization reaction of the acidic solutions in proximity of the sulfide protore causing an “armouring effect” (Evangelou et al., 1992; Reichert and Borg, 2008).



Under pH of ~ 5.5 , the Fe-(hydr)oxides adsorb most Pb and less than 3% of the dissolved Zn from the acidic meteoric solutions (Rutherford, 2002; Dyer et al., 2003; Reichert and Borg, 2008), which become progressively more Pb-depleted (zinc adsorption starts to be significative at pH values from 5.5 to 7.5; Dzombak and Morel, 1990). Moreover, in the oxidation stage between 25°C and 60 °C under oxidizing and acidic conditions (Fig. 1.4) Zn^{2+} remains in aqueous solutions (R6), whereas Pb^{2+} tends to form sulfate (R7) and carbonate minerals (R8) (e.g. anglesite and cerussite; Sangameshar and Barnes, 1983; Faure, 1998).



rock-derived carbon is mirrored by similar $\delta^{13}\text{C}$ composition between host rock-forming carbonate minerals and smithsonite (Gilg et al., 2008).

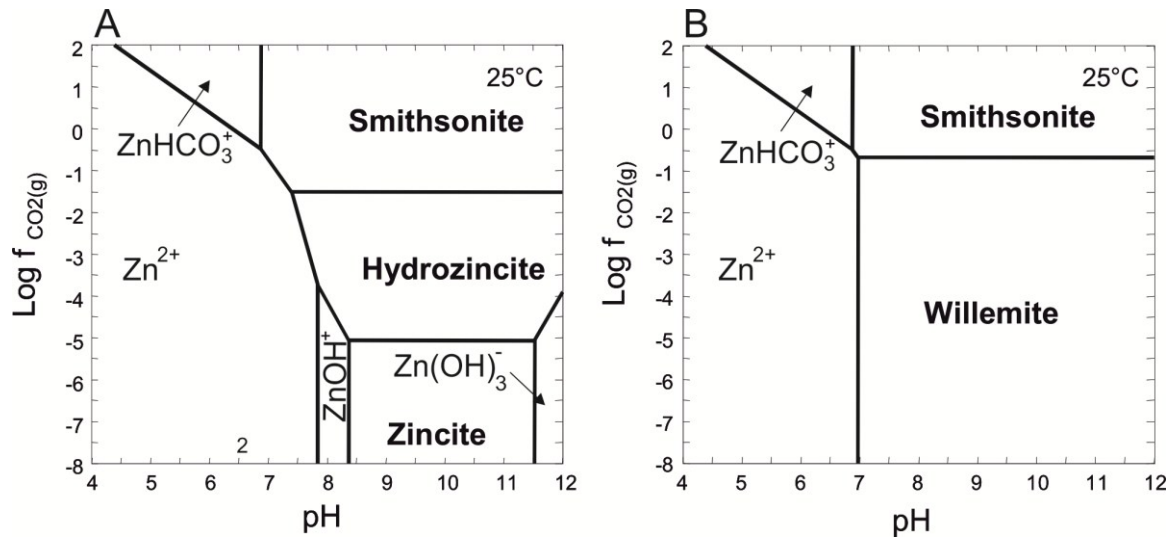


Figure 1.5. Zinc mineral stabilities in the chemical system Zn-O-H-C at 25°C under silica-free (A) and -saturated (B) conditions. The activity of Zn^{2+} is 10^{-5} . Atmospheric $\text{CO}_2(\text{g})$ is $\log f_{\text{CO}_2(\text{g})} = -3.5$ (McPhail et al., 2003).

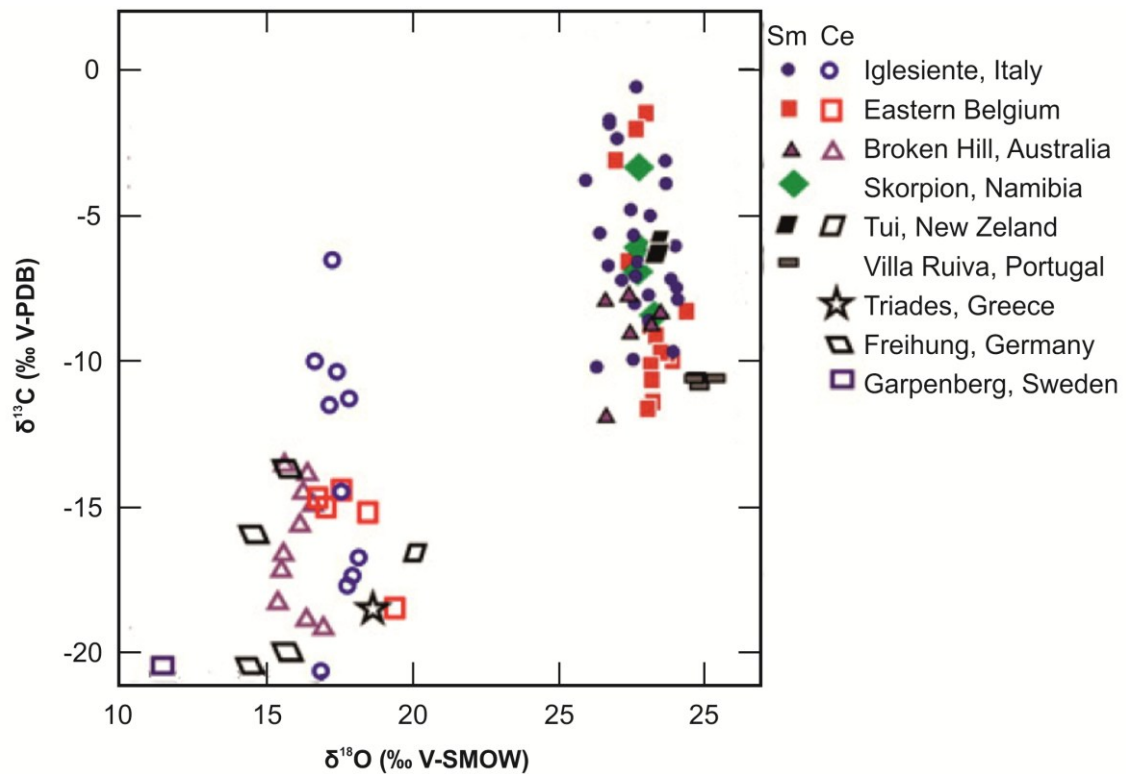


Figure 1.6. Carbon and oxygen isotope compositions of smithsonite (sm) and cerussite (ce) from supergene Zn-Pb deposits worldwide (Gilg et al., 2008).

The minimum smithsonite-precipitating conditions (0.4 KPa at 298.2 K) in near-surface levels tend to naturally rebalance when the oxidation and neutralization processes stop, whereas they persist in deep and/or water-saturated levels. Under oxidizing conditions at 1 atm and 25°C and 60°C with near-neutral pH values, smithsonite and hydrozincite can form indiscriminately (Sangameshwar and Barnes, 1983; Fig. 1.4). Therefore, relatively far from the oxidation site, precipitation of Zn-carbonates is mostly controlled by CO₂ partial pressure rather than by pH values (Fig 1.5).

In this alkaline environment, the distribution of potentially toxic elements (As, Sb and Hg) is limited, due to their inclusion as trace component in major secondary minerals (e.g. As in smithsonite and Se in cerussite), and/or as major constituents of minor secondary minerals, such as Sb in bindheimite and Hg in cinnabar (Stavinga et al., 2017). Another phenomenon that can occur in distal and/or deeper zones is a widespread replacement of host-rock dolomites by secondary Zn-bearing dolomite phases. Well-studied examples of this process have been described for the deposits of Yanque in Peru (Mondillo et al., 2014b), Jabali in Yemen (Mondillo et al., 2011, 2014a) and for those belonging to the Sardinian district (Boni et al., 2011). In these secondary deposits, the reaction of (Zn)-carrying and O-rich meteoric fluids with preexisting dolomite bodies hosting Zn-bearing sulfide protore, resulted in the progressive substitution of Mg²⁺ with Zn²⁺ in the dolomite lattice and formation of zincian dolomite (pure minrecordite is very rare) as intermediate product between dolomite and smithsonite.

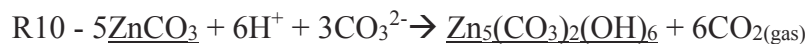
During the oxidation stage, the precipitation of Zn-bearing silicates (e.g. hemimorphite and willemite) is limited due to the low H₄SiO_{4(aq)} concentration in carbonate-buffered solutions (R9).



The solubility of silica phases (Dove and Rimstidt, 1994) in this environment increases drastically from crystalline quartz ($9.6 \cdot 10^{-4} \text{ mol} \cdot \text{l}^{-1}$) to amorphous silica ($2.0 \cdot 10^{-3} \text{ mol} \cdot \text{l}^{-1}$; Reichert and Borg, 2008). Therefore, the possibility to precipitate Zn-silicates is strictly dependent by the availability of opal within the oxidation site.

Post-oxidation stage - Complete or almost complete oxidation of the sulfide protore results in the end of acidic solution production and neutralization processes that lead to the increase of sulfate (e.g. gypsum and anglesite) solubility, due to decrease of SO₄²⁻ concentrations in water solutions (Sangameshar and Barnes, 1983; Reichert and Borg, 2008). The increase of sulfate solubility and pH values toward slightly alkaline conditions (from 6 to 8), coupled with desorption of Pb²⁺ from Fe-(hydr) oxides recrystallization, culminates with progressive removal of gypsum with time and replacement of anglesite with cerussite (R8), which can also form in late-stage fractures and as open space fillings. In this newly formed Fe-(hydr)oxide rich zone, zinc is immobile and will form secondary zinc minerals such as hydrozincite, smithsonite or Zn-bearing silicates. Under lower P_{CO2(g)} values (i.e. water-undersaturated and/or near-surface conditions and P_{CO2(g)} rebalance to atmospheric values with log $f_{\text{CO2(gas)}} = -3.5$), the smithsonite formed during early oxidation stages become unstable (Brugger et al., 2003; Hitzman et al., 2003;

McPhail et al., 2003; Reichert, 2009; Reichert and Borg, 2008) and it is rapidly replaced by (hydroxy-)carbonate minerals, namely hydrozincite (R10), and/or Zn-bearing silicates (e.g. hemimorphite and willemite).



Data provided by Takahashi (1960), McPhail et al. (2003) and Ingwersen (1990) show that hemimorphite and willemite under near-neutral pH values and atmospheric $\text{P}_{\text{CO}_2(\text{g})}$, are the least soluble and most stable Zn-bearing minerals. Therefore, during the $\text{P}_{\text{CO}_2(\text{g})}$ rebalance from the oxidation to post-oxidation stages, hydrozincite and hemimorphite can co-precipitate if there is availability of SiO_2 , as in the case of Mina Grande in Peru (Arfè et al., 2017b), which will be discussed in the following chapters of this thesis, and of Mehdi-Abad in Iran (Reichert et al., 2003).

Siliciclastic rock-hosted supergene zinc systems

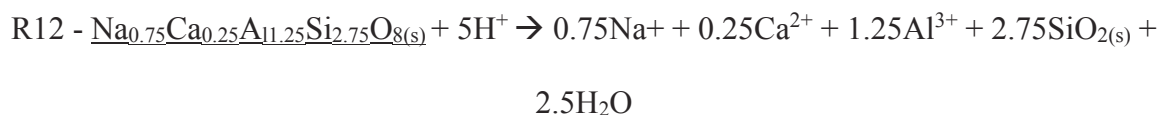
These types of deposits are much less common compared to the carbonate-hosted, although there are two prominent examples (Skorpion and Yanque), which have contributed to a better understanding of this peculiar supergene types.

Both deposits derived from the oxidation of polymetallic Zn-Pb-bearing protorees that resulted in acidic and metal-carrying supergene fluids, which percolated through immature siliciclastic and volcanoclastic rocks consisting of conglomerate and sedimentary breccia at Yanque (Mondillo et al., 2014b) and of volcanoclastic arkose at Skorpion (Borg et al., 2003; Kärner, 2006). The interaction between the acidic fluids with highly reactive feldspars and mica-group minerals of the host rocks, converted the silicates to sauconite and minor hemimorphite via loss of ions from existing mineral structures. Some smithsonite occurrences can result from CO_2 liberated from dissolving carbonate cements of the siliciclastic units (Kärner, 2006).

Weathering of feldspars and mica group minerals can also result in a wide variety of clay minerals including illite, kaolinite, vermiculite, smectite, palygorskite, and sepiolite (Keller, 1970; Singer, 1979; Vicente-Hernández et al., 1983; Wilson, 1987; Borchardt, 1989; Aoudjit et al., 1995; Galán, 2006). However, the formation of these clay minerals can also derive from direct precipitation of ions from percolating solutions (e.g. neogenetic smectite; Borchardt, 1989). For instance, zincian smectite can precipitate at temperatures ranging between 20° and 200°C from solutions of silicic acid, which are variously mixed with Zn compounds (Zn chloride, Zn oxide, or Zn hydroxide), Na compounds, and Al compounds, with pH values comprised between 6 and 12 (Tiller and Pickering, 1974; Harder, 1977; Klopogge et al., 1999; Higashi et al., 2002; Petit et al., 2008; Pascua et al., 2010).

Dissolution of feldspars can result from hydrolysis reactions of orthoclase (R11) and plagioclase (R12), leading to the formation of supergene silicates and aluminosilicates.





Weathering of feldspar is not directly linked with formation of secondary clay minerals, but is considered only a preparatory stage favoring the microfracturing and intergranular porosity of the host rock (Borg, 2003; Kärner, 2006). This process starts with orthoclase weathering and develops even better with advanced plagioclase dissolution, which results in enhanced inter- and intragranular pore space development, and in precipitation of secondary clay minerals that replace the primary phase. Dissolution of mica group minerals (e.g. muscovite; R13) also supports saunonite and vermiculite or mixed layered clay minerals (e.g. illite-smectite) formation. Supergene Zn-rich fluids produce a progressive Zn enrichment into the muscovite/illite lattice and/or their dissolution and partial replacement with secondary Zn smectite. Conversion from illite to smectite depends on availability of mica group mineral and on the activity of K^+ , Al^{3+} (low), silica, Ca^{2+} , and Mg^{2+} (high) within soil systems characterized by neutral to alkaline pH (Borchardt, 1989; Aoudjit et al., 1995; Galán, 2006). Mica group mineral (e.g. biotite) dissolution become fundamental for producing KOH and NaOH, which are two strong bases able to buffer the pH of the supergene fluids (Sherman, 2001) inducing mineral precipitation. Transformation of kaolinite to smectite can occur in near-surface (25°C and 1 atm) environment, when groundwaters percolating through kaolinitic soils undergo modification processes of their salinity (Bennetts et al., 2006; Taylor et al., 2012), or when solutions of silicic acid, Ca oxide, Mg hydroxide, and Na silicate react for long time (~54 years; Imasuen et al., 1989) with kaolinite.

Since the siliciclastic rocks hosting these kind of supergene deposits also consist of variable amounts of P-bearing accessory minerals (e.g. apatite, monazite and xenotime), their dissolution may result in the release of phosphorous in the supergene fluid and its eventual precipitation as zinc-bearing phosphates, such as tarbuttite and scholzite (Borg, 2003; Kärner, 2006). The apatite dissolution (R13) process can occur in both acid and neutral environments (pH from 4 to 7, respectively) but the dissolution rates are greater at low pH conditions compared to near-neutral environments (Valsami-Jones et al. 1998). The dissolution of apatite produces Ca in solution (R13), and contributes to the alkalinity of the meteoric fluid due to the release of OH^- .



Besides the weathering of sulfides, acidity of meteoric solutions is also favored by constant percolation of supergene meteoric fluids in presence of high amounts of organic matter in advanced state of decomposition (i.e. production of organic acids; Nagao et al., 1998; Pourrett et al., 2007; Goyne et al., 2010; Aide and Aide, 2012). In these conditions REE released during monazite and xenotime dissolution tend to form stable complexes with organic acids, so that this may be a major pathway for REE mobility (Goyne et al., 2010) in these types of supergene system, even if other inorganic complexing agents (e.g. carbonate, phosphate and fluorine anions) also support the process (Santana et al., 2015).

Summarizing the processes occurring in the siliciclastic rock-hosted deposits, here the supergene fluids can be neutralized by the break-down and weathering of feldspar, micas and minor carbonates. Conversion of the dissolved minerals to zincian clays is controlled by metal-depleted meteoric solutions, which can eventually leave the supergene oxidation site and reach impermeable units such as the Skorpion marbles (Borg, 2003; Kärner, 2006; Borg, 2015) and the highly-cemented sandstones at Yanque (Mondillo et al., 2014a). The impermeable units act as hydrological barriers and prevent the barren supergene fluid from migrating further.

Tectonic and structural controls on supergene profile development

Since supergene weathering occurs in near-surface environments, uncapping of barren covers of the sulfide bodies becomes essential. Crust uplift is the main process to archive the exhumation of a buried sulfide protore, and subsequent trigger of oxidation, remobilization and, eventually, metals re-precipitation and fixation. In contrast, as opposite effect, the crustal uplift can also result in extremely deep erosion leading to complete removal of the sulfide protore. The best compromise is achieved when the rate of sulfide body exhumation is fast enough to avoid dispersion of mobile elements (e.g. Zn and S) under near-surface conditions (Borg, 2015). Indeed, as stated previously, under acidic and oxidizing conditions zinc and sulfur result so much soluble that they can be easily dissolved and transported via groundwater flow from the “vadose zone” toward the “phreatic zone” and/or to more distal areas from the oxidation site. If the exhumation process is slow, sulfur and zinc can undergo strong dilution, which minimizes the chances to re-precipitate zinc, and thus to form a Zn-bearing supergene ore. The exhumation process plays also another important role in generating and maintaining the oxidizing conditions to turn the Zn-bearing sulfide protore into a supergene Zn nonsulfide ore. The oxidizing conditions can only occur in the water-unsaturated “vadose zone” located above the groundwater table (Thomber, 1975a,b). Therefore, the amounts of oxidized materials is function of the size of the sulfide protore portion that is uplifted in the “vadose zone”, of time span during which this uplifted position is maintained, and of meteoric water supply (e.g. seasonal rainwaters). Poor dynamic conditions of the underlying water-saturated “phreatic zone” favor a chemically reducing environment and thus metals re-precipitation as “enriched” sulfides (e.g. supergene sphalerite, covellite and chalcocite; Sillitoe, 2005) and not as nonsulfide minerals. The so-called “enriched zone” is well studied in the porphyry-Cu-superimposed supergene systems (Ague and Brimhall, 1989; Sillitoe, 2005; Reich et al., 2009). The position of the water table (i.e. water-saturated vs. water-unsaturated conditions) is not only controlled by tectonic evolution but it also depends on variable capability to retain groundwaters of certain lithotypes, such as karstified limestone and poorly-cemented carbonate breccias and conglomerates, on landscape morphology (high relief vs. low relief), as well as on climate (Hitzman et al., 2003; Boni and Mondillo, 2015; Borg, 2015).

Tectonically induced local-scale structural and karst-related conduits also favor the supply of descending and oxidizing meteoric waters, as well as the metal zonation and

distribution. Fault zones at near-surface levels are relatively permeable (especially in lithotypes susceptible to weathering e.g. carbonates), due to dissolution of rock-forming minerals. In extreme cases, they allow the supergene weathering process to extend down to depths greater than 1 km (e.g. Tsumeb mine in Namibia; Borg, 2009). Since during the oxidation process Zn is far more mobile than Pb under acidic pH conditions (from 4 to 7), the fault-related conduits control much better the development of supergene Zn deposits (especially wall rock- and direct-replacement types), than that of the Pb-rich occurrences (Borg, 2009). Juxtaposition between the sulfide protore and porous and permeable rocks through fault zones can result in a perfect condition, in which meteoric fluids can leach metals from formerly impermeable rocks (e.g. shales and schists) and transport them to the juxtaposed reservoir rocks such as dolomitized limestones (e.g. Iran-Kuh mine in Iran; Ghazban et al., 1994; Borg, 2009). Moreover, if the juxtaposition occurs between permeable sulfide-host rock and porous but not permeable rocks, the latter can act as fault-related geochemical barriers (e.g. Angouran mine in Iran; Boni et al., 2007; Borg, 2009), inducing zinc to precipitate along the fault zone that separate the two lithotypes. Considering all these mechanisms, it becomes clear that fracturing, faulting and karstification constitute a sort of “early” and/or “syngenetic” ground preparation for mineralizing supergene fluids. Generation of these secondary permeability features in presence of water-unsaturated conditions results in dynamic hydrogeological systems that can be defined “open” systems. Conversely, low permeability of rocks coupled with water-saturated conditions (e.g. saturated portion of capillary fringe zone) lead to generation of hydrogeological “closed” systems. As stated above, the precipitation of supergene carbonate minerals is affected by equilibrium conditions of CO₂ partial pressure between supergene solutions and atmosphere. Within the ‘open’ systems, supergene solutions are able to equilibrate continuously with the atmosphere, whereas, in the “closed” systems, conditions of disequilibrium are established.

Climate controls on supergene profile and on geochemical and mineralogical models

Another factor that controls the position and the thickness of the “vadose zone” is climate. Generally, in the arid to hyper-arid areas, the water table is located at topographic levels deeper than those that would occur if the same supergene system would have been originated in a humid climate setting. Thus, in a dry setting, a larger portion of the sulfide protore will be affected by supergene weathering. In contrast, in humid climate the efficiency of the supergene weathering is higher, due to the major supply of meteoric water. However, if there is not seasonality in water supplying, constant percolation of metal (Zn)-carrying meteoric fluids leads to the dispersion and loss of most zinc and sulfur in the subsurface and groundwater (Hitzman et al., 2003; Reichert and Borg, 2008; Borg, 2015). Indeed, a favourable scenario would consist in seasonal rainfall settings characterized by “wet” and “dry” periods, in which metals can be leached (wetter periods) and re-precipitated (drier periods), followed by a switch to hyper-arid conditions during which supergene profile development stops and can be

preserved (Large, 2001; Hitzman et al., 2003; Reichert and Borg, 2008). Such conservation features coupled with protective rock cover, which avoids mechanical erosion, are typical for many supergene deposits. Some examples of climate-controlled supergene profiles come from the Coastal Cordillera and the Central Depression of the Andean mountain chain (e.g. most supergene profiles in the Atacama Region stop at ~ 14 Ma, with the onset of the hyper-arid climate; Sillitoe and McKee, 1996; Hartley and Rice, 2005; Arancibia et al., 2006; Bissig and Riquelme, 2010; Arfè et al., 2016), from the mountain ranges in the Middle East and from the escarpment of the Southern African deserts.

During the oxidation stage, in which the meteoric solutions are acidic because the neutralization processes are still inactive, the equilibrium conditions of CO_2 partial pressure between atmosphere and meteoric solutions become an important factor in mineral precipitation. These fleeing equilibrium-disequilibrium conditions are mainly affected by climate and hydrogeological settings (e.g. humid vs. arid climate and “open” vs. “closed” systems, respectively). Reichert and Borg (2008) described the most important mechanisms of geochemical and mineralogical controls occurring in the humid and arid scenarios as follows.

Humid and wet scenario - Dissolution of carbonates (e.g. calcite) from the host rock consumes great quantity of $\text{CO}_{2(g)}$. In “opened” humid systems, characterized by a well-developed soil covers, the consumed gases will be rapidly supplied by $\text{CO}_{2(g)}$ from the overlying soil and/or atmosphere (Palmer and Palmer, 1995). This process will not cause a significant increase in the pH, therefore favoring the precipitation of minerals stable at acidic conditions (e.g. smithsonite rather than hydrozincite). In contrast, if the system is “closed” (i.e. small fissures and low permeability), during the dissolution process most of the $\text{H}_2\text{CO}_{3(aq)}$ dissolved in the pore water will be consumed, and because the lack of supply of atmospheric $\text{CO}_{2(g)}$ a rapid increase of pH values will result in the meteoric solutions (i.e. precipitation of minerals under less acidic conditions; e.g. hydrozincite rather than smithsonite).

The isotopic signature of smithsonite can be used as vector to determine under what kind of climate it formed. Indeed, the microbiological activity within soils of humid climates can result in P_{CO_2} increase, and consequent precipitation of smithsonite with marked isotopically light carbon component. Appreciable amounts of kaolinite group minerals and gibbsite also indicate deep weathered supergene profile formed under humid and wet conditions. However, quantities more or less abundant of both minerals can result from many other processes occurring under a variety of conditions (e.g. Gerrard, 1994; Woodward et al., 1994; Sherman, 2001; Fig. 1.7).

Arid and dry scenario - Within arid climate settings, the availability of water is low (i.e. low dynamicity) and soil covers are scarce or not well developed. As a consequence, biological activity is poor and values of $\text{CO}_{2(g)}$ and $\text{O}_{2(g)}$ partial pressures are similar to those of the atmosphere. This implies a low rate increment of pH values and O_2 -rich meteoric solutions, due to the scarcity of O_2 -consuming organisms within the soil. Conversely, within “closed” arid systems, the pH values increase for the same reasons occurring in humid contexts. On the base of this geochemical model, Reichert and Borg

(2008) argue that arid climates promote better than humid climates the oxidation process of sulfide protores for the presence of more oxidizing solutions. However, there are some examples contradicting this theory, such as the Zn-nonsulfide occurrences in the Bongará district in northern Amazonian Peru (Boni and Mondillo, 2015; Arfè et al., 2017b, in press), which formed under climate regime not so different from today. Therefore, it is possible to get favorable oxidation conditions in both arid and humid climate settings with the only difference that in arid climates the oxidation products are well preserved and do not undergo multicyclic oxidation and leaching as in the case of those formed in humid climates.

Smectite formation in soils is generally associated with low-lying topography, high pH values of meteoric solutions, high silica activity, and abundance of basic cations (Borchardt, 1989; Gerrard, 1994) under dry and poorly-drained systems (Sherman, 2001; Fig. 1.7). However, these factors can be present under very different climates when drainage conditions (e.g., occurrences of topographic lows and/or low permeability host rock) determine a limited leaching of soil (Galán, 2006).

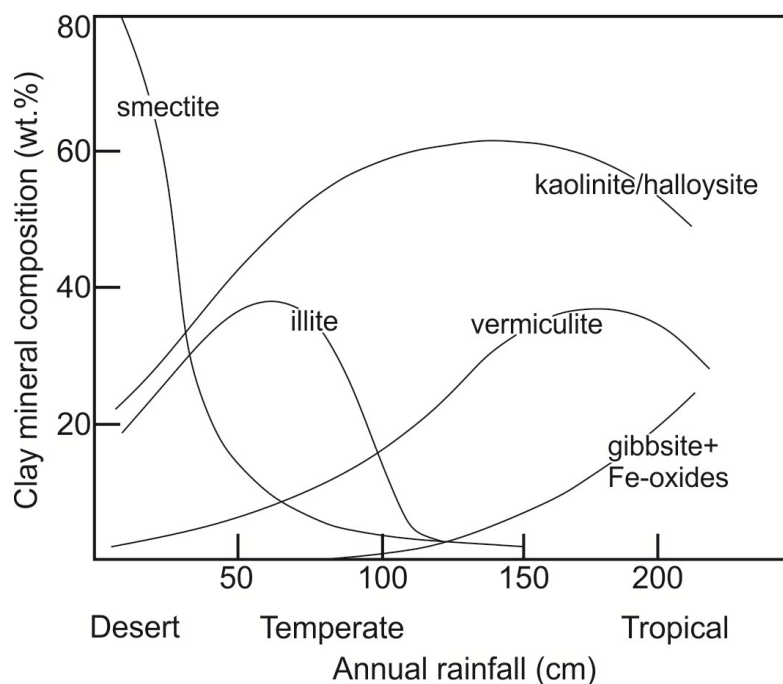


Figure 1.7. Mineralogy of soil clay fraction in desert, temperate and tropical climates, which are characterized by different annual rainfall rates (from Sherman, 2001).

Some aspects of mineral processing

Looking at the extraction processes, the choice of the best method to maximize the recovery resides in a correct evaluation of the mineralogical components, particle size and their spatial distribution in the ore material. As instance, if the nonsulfide ore body is hosted in rocks whose carbonate matrix is prevailing (the most common case) over other components, a treatment with acid leaching (H_2SO_4) is not recommended. Since both

calcite and dolomite are highly reactive to acid leaching (Frenay, 1985), an underestimation of the carbonate minerals in the gangue material can lead to high acid consumption, which would lead to high production costs. To overcome this issue some mining companies have been carried out many attempts of applying some methods of mineral separation (e.g. heavy liquid separation and flotation) before the leaching of the ore (e.g., de Wet and Singleton, 2008). On the other hand, the silicate-rich nonsulfide deposits (hemimorphite and sauconite > smithsonite), are subject to several problems during the leaching stages consisting mainly in the precipitation of silica gels (Dufresne, 1976; Matthew and Elsner, 1977, Frenay, 1985) and the detrimental effect of sauconite. Minerals belonging to smectite and vermiculite groups produce many problems during gravity separation and flotation phases (Boni et al., 2009b; Rollinson et al., 2011; Kademli and Gulsoy, 2012). These problems can be bypassed extracting the zinc by calcination and subsequent precipitation of the zinc-rich fumes as oxides prior to acid leaching (Rosenqvist, 2004). Additionally, alkaline leaching (Zhao and Stanforth, 2000) and zinc volatilization in a Waelz rotary kiln (Cross and Read, 1970; Clay and Schoonraad, 1976; Porter, 1991; Mager et al., 2000) have been also proposed as an alternative to the calcination.

Summary on supergene deposits

When sulfide bodies are exposed to near-surface environments (Fig. 1.8), the following processes take place:

- The descending meteoric waters oxidize many sulfide minerals, producing acidic solvents that further dissolve both ore and gangue minerals;
- In the “oxidation” site, the sulfide body becomes oxidized and generally stripped of most valuable mobile components (e.g. zinc and copper). In the distal or deeper levels, metal cations in meteoric solutions can re-precipitate as nonsulfide minerals (above the groundwater table), or as enriched sulfide minerals (below the groundwater table);
- The lowermost, unaffected part of the sulfide body is called the hypogene zone.
- The efficiency of these processes depends on:
 - Rate of exhumation (by tectonic uplift) vs rate of erosion;
 - Availability of water and/or prolonged seasonal deep weathering;
 - Reactivity of the host-rock forming minerals (e.g. calcite and feldspars)
 - Permeable host rocks to allow for groundwater percolation;
 - Trap sites for the newly formed supergene minerals;
 - Local hydrologic parameters that do not allow the dispersion of Zn-bearing fluids;
 - Local structural parameters that control meteoric solutions pathway and metal re-distribution;
 - Local climate parameters that control the evolution of the supergene profile;

- Possibility to preserve the newly formed supergene mineralization with adequate rock covers.

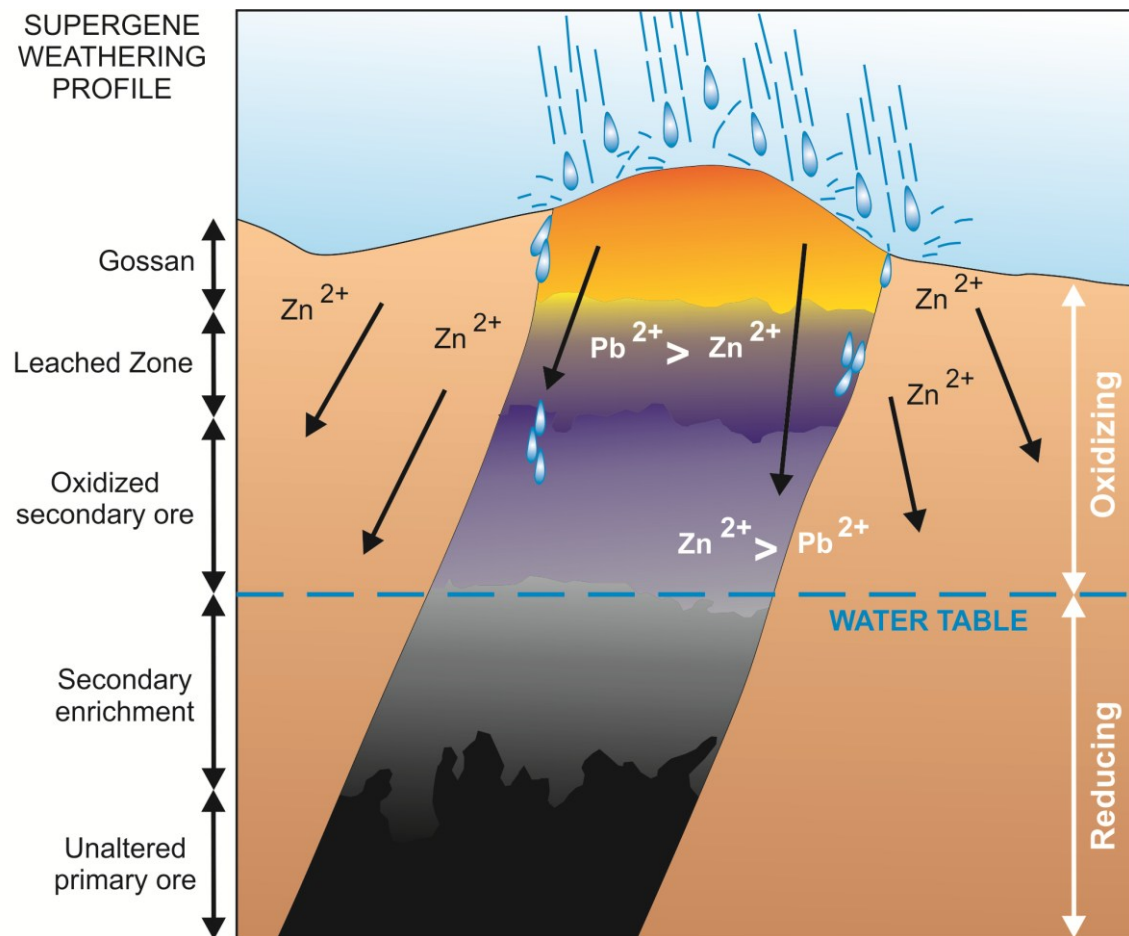


Figure 1.8. Typical supergene weathering profile of a Zn-Pb protore showing zinc and lead zonation and secondary minerals precipitation. Generally, the Leached Zone is characterized by lower Zn contents than the Oxidized Zone and adjacent host rocks.

Chapter 2:

Sampling and analytical methods

Sampling procedure

For the study of Mina Grande and Cristal deposits (Bongará), a significant number of samples were collected from outcrop and drill cores, following the criteria below:

1. availability of mineralized and assayed drill cores;
2. representativity of geological features and ore grade of the ore deposit;
3. distinct mineralogical assemblages of sulfides and/or nonsulfides;
4. major and/or peculiar gangue minerals.

In particular, the study regarding the Mina Grande deposit has been carried out on 13 outcrop samples and on 2 drill core samples representative of the horizons below the exploited deposit. The samples were selected during a geological campaign (August 2015), in which field data have been also collected, in order to evaluate the structural and geological controls on the mineralization. The analysis of the field data has allowed to recognize karst structures developed along NW-SE striking faults, which host most of the Zn-nonsulfide mineral assemblage at Mina Grande. The study mostly involved representative samples of the karst breccias (clasts and matrix), and concretionary structures typical of the karst environment.

Regarding the Cristal deposit, in order to quantify the ore grade and relative abundances of the mineral phases occurring in this deposit, the sampling has involved mostly drill core samples. More in detail, the study has been carried out on 55 core samples, collected approximately each meter of mineralized core, keeping the same interval of the chemical assays.

With the purpose of estimating the possible $\delta^{18}\text{O}$ composition of the fluids that generated the nonsulfide minerals of Mina Grande and Cristal, also 2 water samples, one from the Rio Cristal river (RC-M) and one from one of its tributary (RC-T), were collected for isotope analysis of the surface waters. To prevent evaporation of the water samples, 100 ml HDPE plastic bottles with inner seal and parafilm around the cap were used. Few drops of HgCl_2 (solubility = 74 g/l) were added to the collected samples, to stop any microbial activity.

For the study of Namibian deposits, 6 gossanous samples were collected from the uppermost levels of the Rosh Pinah mine. Twenty-three specimens from the Skorpion deposit were obtained mostly from private collections (A. Johr and G. Hinder), and in limited amount sampled from the open pit of the mine during a field trip in summer 2014. Since the Namibian study is focused on C-O stable isotope analysis and on study of clay component, the sampling mainly involved mineral assemblages consisting of different

generations of carbonate minerals (e.g. several calcite and smithsonite generations or co-precipitated carbonates) and of phyllosilicates.

Analytical methods

Before performing specific analyses for distinct purposes, the samples from the mentioned deposits underwent common treatments. Small slabs from the most representative samples were cut and soaked in “Araldite D” and “Raku Hardener EH 2950”, in order to prepare polished thin sections (30µm) for optical microscopy (OM), scanning electron microscopy with energy dispersive X-ray spectroscopy (SEM-EDS), and/or wavelength dispersion spectrometry (full WDS) studies. The remaining portions of the samples were crushed and then quartered until representative amounts were obtained. From the remaining quartered materials, a quantity of ~ 20 g is subsequently pulverized for mineralogical X-ray powder diffraction (XRPD) and whole rock chemical analyses. It is worth to note that XRPD and chemical analyses were performed on the same powdered quarter, in order to obtain comparable mineralogical and chemical results. Whole rock chemical analyses were only performed on the samples collected in the Bongará area, because Skorpion and Rosh Pinah deposits already had large datasets.

After the common treatments, the samples underwent additional specific analysis that will be listed in the following paragraphs.

X-ray powder diffraction - XRPD

X-ray generation and features (Klug and Alexander, 1954; Bertin, 1970; Attwood 2016)

The X-rays are the electromagnetic radiations comprised between the UV rays and γ rays with wavelength (λ) between 0.1 and 100 Å and frequency between 106 and 109 Hz.

The X-rays are emitted when an accelerated electron hitting an atom loses kinetic energy and turns it into radiation. In the laboratory, a tungsten filament is heated to produce electrons, which are then accelerated in a vacuum by a high electric field in the range of 20-60 kV towards a metal target, which being positive is called the anode. At atomic scale, when the electron of the exciter beam hits an electron of the “K” layer, the first one moves away the second from the atom and, consequently, an electron from the outer layers, with major energy, falls on the “K” layer to bring it back to the ground state. This quantum leap gives rise to an emission of energy in the form of radiation. The radiation, in terms of wavelength (λ) emitted from the stricken atom, is partially function of the energy of the incident electron beam. Indeed, until a certain threshold excitation, this radiation will result in production of a continuous spectrum of X-rays known as “white” radiation (Fig. 2.1).

The maximum energy lost, $E(\text{max})$, determines the shortest wavelength, $\lambda(\text{min})$, that can be obtained according to the Plank’s law:

$$E \text{ (Joule)} = e \cdot V = h \cdot c / \lambda \text{ (m)}$$

where (e) is the charge on the electron, (V) is the accelerating voltage, (h) is Planck's constant ($6.63 \cdot 10^{-34}$ Js), and c is the speed of light ($3 \cdot 10^8$ m/s).

Over a certain threshold excitation, which depends on the metal anode, the radiation emitted from the stricken atom will be independent from the incident radiation and it will assume wavelength values that are characteristic of the atom and, therefore, of the emitting element. This second type of spectrum, which is superimposed on top of the “white” radiation, is called the “characteristic” radiation (Fig 2.1).

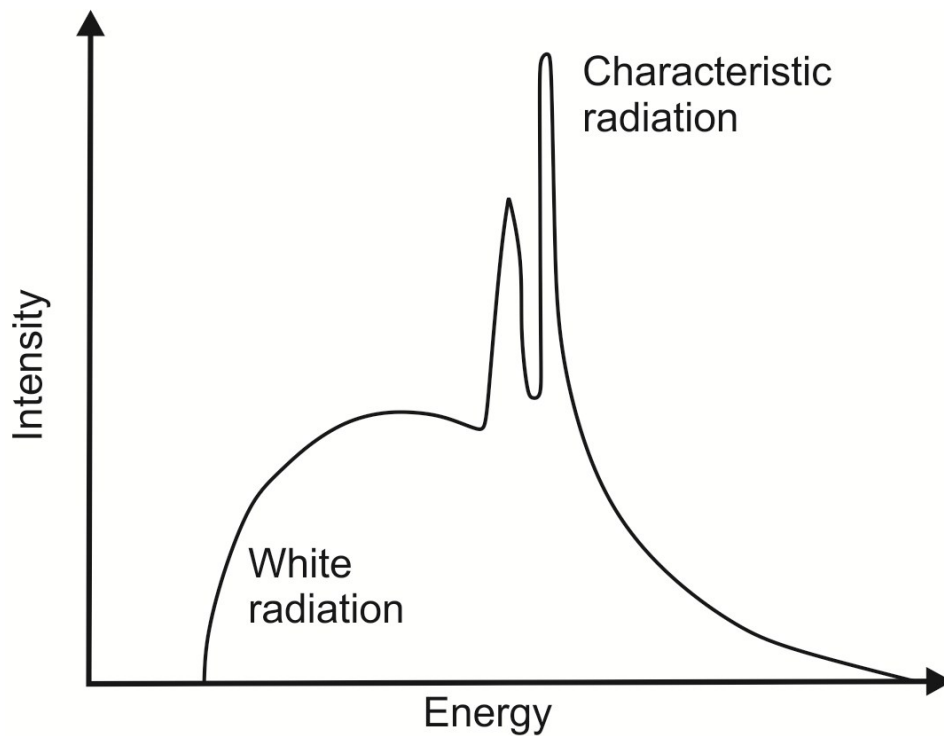


Figure 2.1. Typical X-ray spectrum showing “white” radiation underneath “characteristic” radiation.

X-ray diffraction (Klug and Alexander, 1954; Warren, 1969)

The X-ray diffraction is based on the possibility of the atoms constituting crystalline material to become a source of X-rays, when stricken by X-rays beam derived from another source. This possibility to obtain “diffracted” X-rays can occur only if some conditions are satisfied. The best way to represent them is the Bragg’s law:

$$2d \cdot \sin\theta = n \cdot \lambda$$

where (d) is the lattice spacing, (θ) is the diffraction angle, (n) is an integer and (λ) is the X-ray wavelength (Fig. 2.2)

To simplify the process, the diffraction is interpreted as reflection. Therefore, if the angle and wavelength of the incident X-ray beam are known, the only unknown value in the equation is represented by the lattice spacing (d), which is characteristic of the crystalline material.

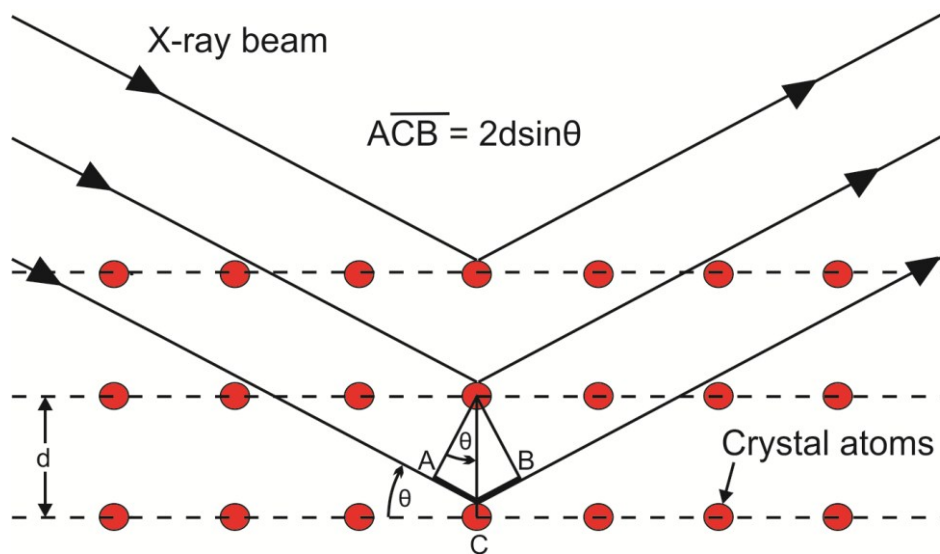


Figure 2.2. Diffraction geometry of an incident X-ray beam, after Bragg's law.

X-ray measuring instrument

The most used measuring instrument for X-ray analysis is the powder diffractometer. In this instrument, the X-ray beam is produced from the metallic anode, located within an X-ray tube). The metallic anodes are generally constituted by Cu, Mo for heavily adsorbing samples, Co for iron-rich samples, and less frequently by Fe, W, Cr. The X-ray beam is initially filtered and collimated to reduce the divergent angle and then it is brought to hit a powdered sample of the material of interest, located on a plane sample order. There are two possible arrays of sample holder vs detector vs X-ray tube that are defined “ θ - 2θ ” and θ - θ ” couplings. In the θ - 2θ array, the sample rotates on its axis and diffracts the X-rays according to the Bragg's law. The diffracted rays, collimated again, hit a detector that rotates with double angular velocity respect to the sample holder and the X-ray tube does not move. In the θ - θ array, the sample holder does not move, whereas, the detector and the X-ray tube rotate with the same angular velocity. In both arrays, the geometry of sample holder vs detector vs X-ray can be vertical or horizontal (Fig. 2.3), but the analytical procedure is the same. The output data consist in sequential graphical registrations of the diffraction effects produced by the sample over time, which are expressed in 2θ angles. Each deviation of the graphic pattern corresponds to a diffraction effect, with intensity that is proportional to the height of the obtained peak.

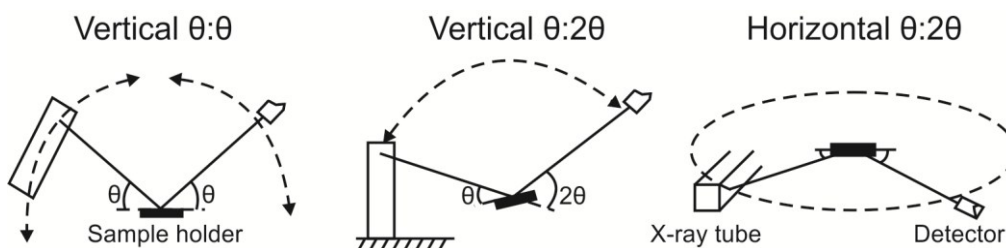


Figure 2.3. Diffractometer geometries.

Uses of XRPD analysis

The XRPD analysis is used to identify the mineral phases occurring in the material of interest. The analysis can be performed to obtain qualitative or quantitative data. In the latter case, the Rietveld Quantitative Analysis (Rietveld, 1969; Bish and Howard, 1988; Bish and Post, 1993; Hill, 1991) is a powerful method for determining the quantities of crystalline and amorphous components in multiphase powdered mixtures. The method is based on the standard deviation between observed (or measured) and calculated spectra (Fig. 2.4).

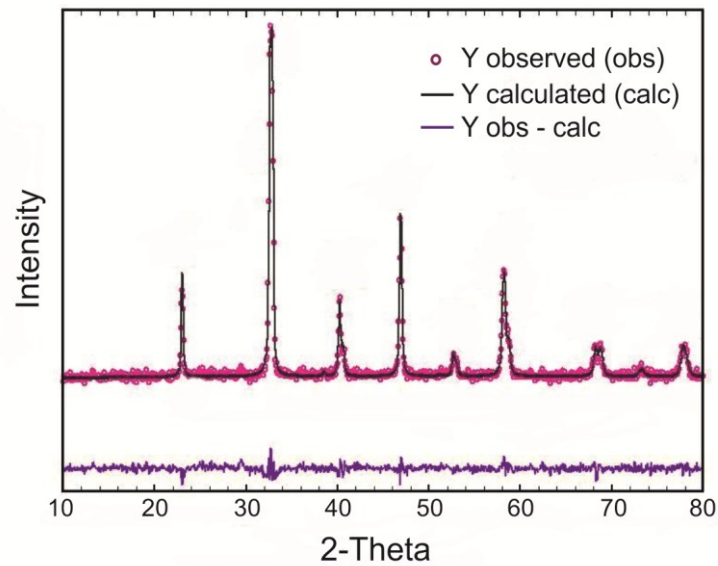


Figure 2.4. Example of Rietveld Quantitative Analysis.

The method to produce a calculated spectrum relies on the simple relationship:

$$W_p = S_p \cdot (Z \cdot M \cdot V)_p / \sum_{i=1}^n S_i (Z \cdot M \cdot V)_i$$

where (W) is the relative weight fraction of phase (p) in a mixture of (n) phases, and (S), (Z), (M), and (V) are, respectively, the Rietveld scale factor, the number of formula units per cell, the mass of the formula unit (in atomic mass units) and the unit cell volume (in Å³). Therefore, for this method of mineral phase quantification, it is fundamental to know the crystallographic information of the mineral phases constituting the powdered mixture.

Analytical details

The XRPD analyses have been carried out to obtain information on the mineralogy of bulk material and of specific phases collected by hand picking.

The samples were crushed and then quartered until a representative amount is obtained. From the remaining quartered materials, quantities of ~10 g from each sample are subsequently pulverized either manually in an agate pestle or in a ball mill until

homogeneous for mineralogical X-ray powder diffraction (XRPD). Pulverization using the ball mill was performed at the Osservatorio Vesuviano-INGV (Napoli, Italia).

X-ray diffraction semi-quantitative analyses on samples from Skorpion and Rosh Pinah deposits were performed at the Dipartimento di Scienze della Terra, dell'Ambiente e delle Risorse, Università di Napoli Federico II (DiSTAR, Italy). From the quartered material, a quantity of ~10 g was previously ground in a pestle in order to obtain granulometrically homogeneous powders (fraction <200 μm). The XRPD measurements were performed on a Seifert-GE ID3003 diffractometer with $\text{CuK}\alpha$ radiation, Ni-filtered at 40 Kv and 30 Ma, 3-80 $^{\circ}2\theta$ range, step scan 0.02 $^{\circ}$, time 10 sec/step, and the RayfleX (GE) software package. The identification of the mineral phases was carried out by means of the X Powder software (www.xpowder.com), coupled with JCPDS PDF-2 database.

X-ray diffraction on the samples from Mina Grande and Cristal deposits was carried out at the Osservatorio Vesuviano-INGV (Napoli, Italia) with a Panalytical X'pert PRO diffractometer equipped with a pyrolytic graphite analyzer crystal; we used an unfiltered $\text{CuK}\alpha$ radiation (40 KV, 40 mA) in the 3 $^{\circ}$ -70 $^{\circ}$ 2θ range, steps size of 0.01 $^{\circ}$ 2θ counting time of 30 s/step, 0.5 mm divergence slit, 1 mm receiving slit, and 0.5 $^{\circ}$ anti-scattered slit. Diffraction patterns for obtaining semi-quantitative (Mina Grande) and qualitative (Cristal) analyses were interpreted using the High Score Plus software and JCPDS PDF-2 database. Quantitative phase analysis was carried out only for the core samples of the Cristal deposit, in order to evaluate the average mineralogical composition of the orebody. The data have been elaborated using the Rietveld method and tested with data from whole rock chemical analyses.

To analyze the clay fraction a quantity of 30 gr of crushed material (~1 mm) was added in a plastic beaker with 450 ml of deionized water. The suspension underwent ultrasonic treatment for 15 minutes to disaggregate the particles. At the end of the ultrasonic treatment, it was necessary to energetically mix the material and wait for one minute. At the end of the minute, the suspension was decanted in a glass beaker, whereas, the remaining portion, on the bottom of the plastic beaker, was recovered in a Petri dish and then put to dry in a sand bath. This schedule was repeated after 5 minutes, 1 hour and 17 hours (Over/ Night) according to the Stokes' law. After 17 hours, the overnight suspension/supernatant was decanted in another glass beaker, and the remaining residue was treated with the previously described procedure. Subsequently, it was possible to start with the centrifugation of the suspension/supernatant. The latter underwent two cycles of centrifugation running at 5000 rpm for 5 minutes and, then, at 8000 rpm for 40 minutes. After each cycle of centrifugation, the residue attached on the walls and on the bottom of the capsules was recovered in a "watch-glass". The suspension recovered after the two cycles of centrifugation was used to prepare the oriented clay mineral aggregate, whereas, all the material heated in the Petri dishes, was used for XRPD analyses.

To prepare the oriented clay mineral aggregates we followed the "Glass Slide Method" (Moore and Reynolds, 1997). There was prepared three different kinds of aggregates:

1. Normal Oriented Aggregate (AON).

An eye dropper was used to add the suspension on the glass slide so that the liquid was able to cover the entire surface of the slide. After this procedure it is necessary to wait for the drying of the suspension “en plein” air so that the clay minerals settle producing a thin films. Then it is possible to proceed with the acquisition of the XRPD patterns.

2. “Glycolated” Oriented Aggregate (AOG)

The solvation occurs by the exposition of the sample (AON) to the vapor of the reagent for 8 hours at 60°C.

3. Heated Oriented Aggregate (AOR).

After the acquisition of the AOG, the same sample is heated at 375°C to observe the collapse of Smectite.

Optical and scanning electron microscopy and EDS-WDS microanalyses

Optical microscopy

Before to perform advanced technique of microscopy discussed in the next paragraph, all polished thin sections were investigated under transmitted and reflected light to observe the general features of non-metallic (carbonate, silicates etc.) and metallic (sulfides, oxides etc.) mineral assemblages. For the isotope study, hand picking of the mineral phases has been carried using a stereoscopic microscope to get greater enlargements of selected rock fragments (Fig 2.5)



Figure 2.5. Smithsonite crystals from Skorpion deposit.

Scanning electron microscopy (SEM; Goldstein et al., 2012) and energy-wavelength dispersive X-ray Spectrometry (EDS-WDS; Goldstein et al., 2012)

The SEM (Fig. 2.6) is an instrument of microphotography that works both on thin section (2D images) and on massive samples (3D images), and it is able to achieve enlargements up to $\sim 2 \mu\text{m}$. The sample must be opportunely metallized (with gold or graphite) to implement the conductivity of the surface samples. An electronic beam (ΔV between 5 and 50 kV) produced by a tungsten filament, is focalized by magnetic lenses toward the sample holder that can be moved horizontally. The interaction between the electronic beam and the surface of the sample will result in emission of several radiations, which include characteristic X-rays, backscattered electrons, secondary electrons, Auger electrons and visible light.

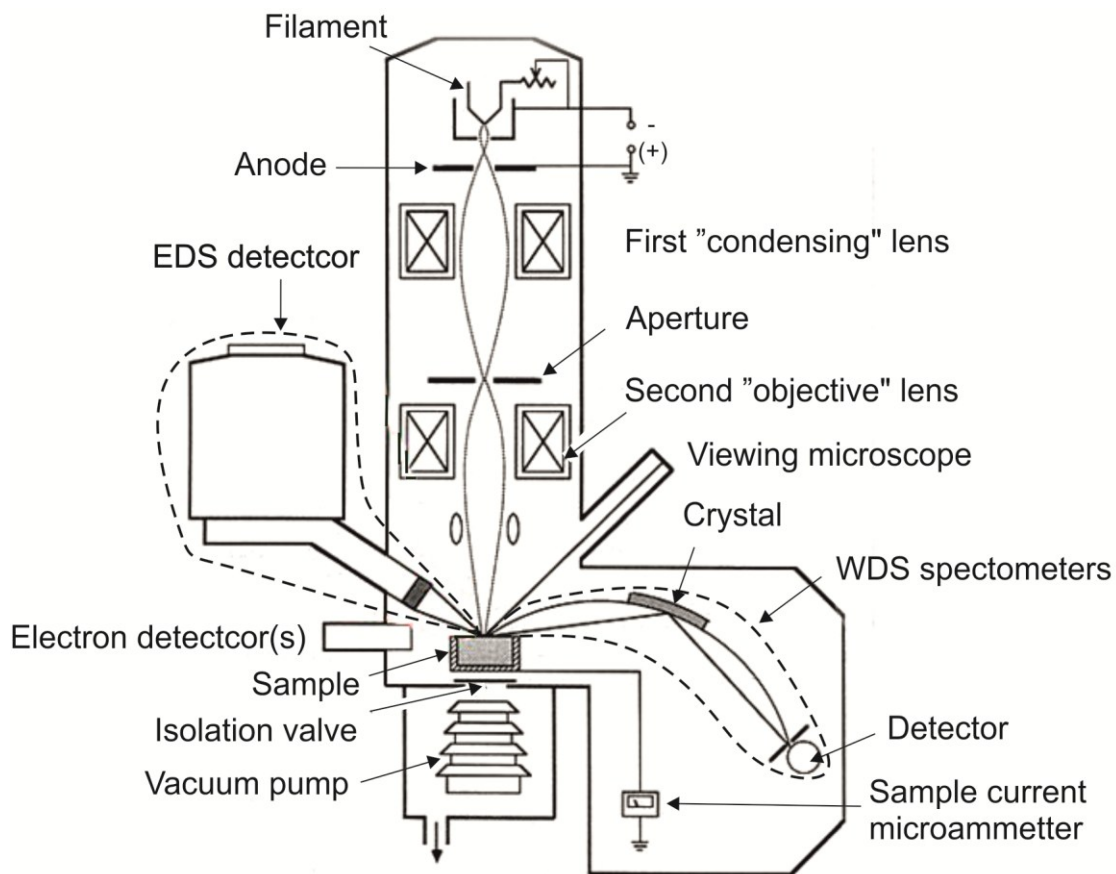


Figure 2.6. Generic components scheme of EMP/SEM instrument.

The scanning image of specimen surface is provided by the secondary electrons, whereas, backscattered electrons provide an image contrast (BSE image) that is function of the mean atomic number and topography of the specimen. For instance, material with higher atomic number will result brighter than material with lower atomic number.

The X-ray emitted from the sample hits a detector (Fig. 2.6), which will produce an electrical reply that is proportional to the energy of photon X. The intensity of energy and

wavelength of photon X depend on the atomic species constituting the investigated material according to the Planck's law. Therefore, if an electron microprobe is coupled to the scanning electron microscope, it is possible to determine qualitative-quantitative chemical composition of polished surface of specimen, point by point.

The detectors installed on the electron microprobe that can measure either the energy or the wavelength of the emitted X-rays and therefore, the two different arrays (Fig. 2.6) are called, respectively, energy-dispersive spectroscopy (EDS) and wavelength-dispersive spectroscopy (WDS). A comparison between the technical features of the two measuring systems is given in the following table:

Technical features	EDS	WDS
Sensitivity	ca. 10000 c/s/Na	1000 c/s/Na
Beam current	0.5 Na	1-100 Na
Measure time	50-100 s	20 s
(15 keV)	(all elements)	(per element)
Analyzed elements (Z)	Na(11) - U(92)	Be(4)-U(92)
Resolution	(MnK α ca. 5.9 keV) 150 Ev	(quartz 1011) 6 Ev
Peak/background ratio	10-100	100-1000
Detection limit	1000 ppm	100 ppm

Analytical details

SEM observations were performed on graphite-metallized polished thin sections and massive specimens by means a JEOL JSM5310 at the Dipartimento di Scienze della Terra, dell'Ambiente e delle Risorse (DiSTAR), Università degli Studi di Napoli Federico II (Italy). The analytical conditions were: 20 mm objective lens to specimen working distance, 15 kV accelerating voltage with a tilt angle of 0°. Element mapping and qualitative energy dispersive (EDS) investigations were carried out with the INCA X-stream pulse processor and the 4.08 version Inca software (Oxford Instruments detector), interfaced with the Jeol JSM 5310. The following reference standards were used for quantitative microanalysis: albite (Si, Al, Na), orthoclase (K), wollastonite (Ca), diopside (Mg), almandine (Fe), rutile (Ti), barite (Ba), strontianite (Sr), eskolaite (Cr), rhodonite (Mn), pyrite (S), sphalerite (Zn), galena (Pb), pure silver (Ag), arsenopyrite (As), fluorite (F), apatite (P), sylvite (Cl), pure vanadium (V) and Corning glass (Th, U). Analytical errors are 1% rel. for major elements and 3% rel. for minor elements.

Wavelength dispersion spectrometry (WDS) was performed to obtain high quality quantitative analyses on selected samples from Cristal and Mina Grande deposits. The analyses were performed at the Natural History Museum, London (UK), by the use of a Cameca SX50 electron microprobe operating at 15 Kv, 15 Na, and 10 μ m spot size. The following reference standards were used: jadeite (Na), diopside (Mg, Si), potassium bromide (K), wollastonite (Ca), aragonite (Ca), pyrophanite (Ti, Mn), eskolaite (Cr), hematite (Fe), bunsenite (Ni), corundum (Al), smithsonite (Zn), celestine (Sr, S), vanadinite (Pb), barite (Ba), greenockite (Cd). Detection limits for WDS are in the order of 0.01 wt%. The CO₂ contents in carbonates and water content in hydrated carbonates

and silicates were overestimated and, therefore, they have been calculated by stoichiometry.

AEM-Analytical Electron Microscopy

Similarly to the SEM-EDS-WDS analytical methods, the analytical electron microscopy (AEM) technique is based on collection of various signals generated from interaction of an incident electron beam with the sample in a transmission electron microscope (TEM). These signals can be used to identify and quantify the concentration of the elements present in the analyzed area, map their distribution in the sample with high spatial resolution (down to 1 nm or better), as well as to determine their chemical state. The two main techniques at the core of AEM are widely described by Botton, (2007). The latter are based on the detection of X-ray signals generated in the sample by the primary incident electrons with the technique called energy dispersive X-ray spectroscopy (EDXS) and the measurement of the energy lost by the incident electrons with electron energy loss spectroscopy (EELS). These techniques are used within a TEM (Fig. 2.7) equipped with EDXS, EELS detectors, and other detectors to record TEM images, diffraction patterns, and other signals that can be combined to form other images containing additional information on the chemical nature and structure of the sample.

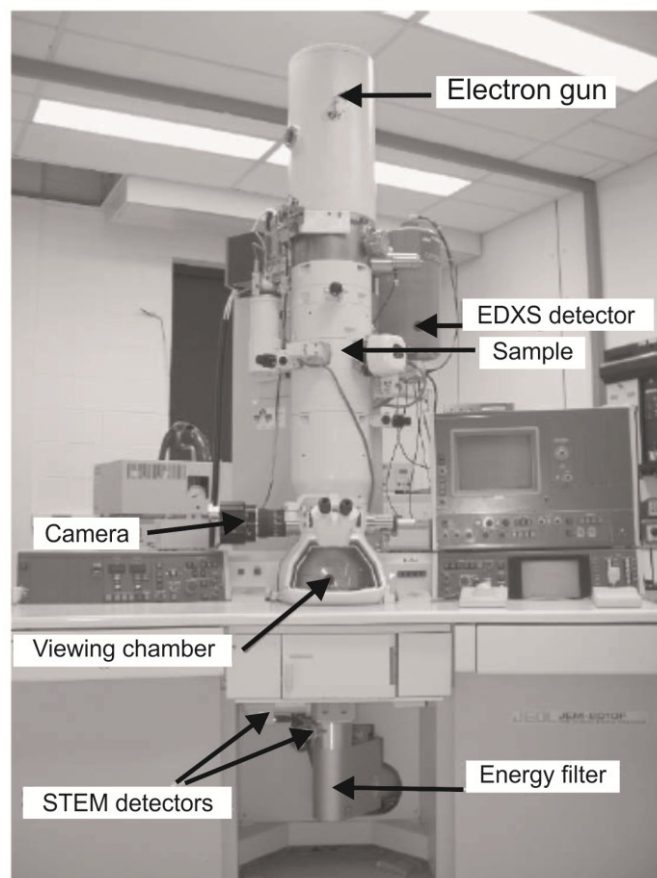


Fig. 2.7. Example of TEM instrumentation where the energy dispersive X-ray (EDXS) detector, the energy loss spectrometer (in post-column energy filter), and digital cameras and detectors are indicated (modified from Botton, 2007)

The transmission electron microscope for conventional TEM, high-resolution (HR)-TEM, and AEMs can be equipped with two types of electron sources: (1) thermionic and (2) field emission. Thermionic sources are represented from both tungsten filaments and refractory crystals. These sources operate at high temperature and emit electrons that are subsequently accelerated by the anode potential (100-200 kV or more). The thermionic sources are heated either by a flow of current through the emitting material itself (for the filament) or by thermal contact of a low-workfunction emitter material such as the refractory crystals and resistive heating of a W wire supporting material. The field-emission gun (FEG) source operates on the principles of electron tunneling from the tip to vacuum following the application of a strong electric field ($\approx 10^9$ V/m) generating a very large electric field gradient at the tip of the cathode. Modern instruments are able of working in two different modes: (1) the conventional TEM and (2) the FEG-scanning transmission electron microscope (STEM). The electron optical configuration required for STEM imaging and analysis is achieved, in a TEM-STEM instrument capable of both operation modes and with the combination of the Cm condenser lens (called “condenser minilens” or “minicondenser”) optically switched off and the subsequent focus of the nearly parallel beam into a small source image by the upper OL field. The latter consists of a strong magnetic field before the sample (i.e., a prefield) generated by an objective lens (OL).

Analytical details

The TEM-AEM analyses were performed on 3 samples aluminosilicate-rich samples from the Skorpion mine. The HRTEM study was conducted at the CIC of the University of Granada (Spain) to investigate the texture of clays at micro- and nano-scale. For this study a Titan TEM with XFEG emission gun was used. The instrument was equipped with spherical aberration corrector and HAADF detector, working at 300 kV, with a resolution of 0.8 Å in the TEM mode and 2 Å in the STEM mode. EDX spectra for qualitative identification of minerals and chemical maps were obtained using the Super-X system.

ZEISS Mineralogic Mining

ZEISS Mineralogic Mining is an automated mineralogy and petrological analyzer, designed to provide a technological and methodological advance over traditional automated mineralogy techniques. Mineralogic Mining combines a scanning electron microscope with one or more EDS detectors, a mineral analysis engine and the Mining software plug-in. The instrument is equipped of five analysis modes (Fig. 2.8), each of which is fully user-configurable: (1) line scan; (2) mapping; (3) Back Scatter Electron (BSE) only; (4) spot centroid; (5) feature scan (Graham et al., 2015).

Line scan - This mode is able to provide data on bulk mineralogy by performing fast and statistically valid modal analysis. EDS analyses are collected at pre-determined points across a single line through the center of each grain. Line scan is another extremely fast measurement mode, which also provides an indication of relative texture (size, liberation, association). Moreover, it is useful when non-unique BSE values for minerals limit the use of spot-centroid.

The mapping (full map) - In this mode, the user can set an EDS pixel size (step size) and magnification for the analysis, and the Mining software will draw the analysis grid over the sample. The analysis will provide a spatially resolved mineralogical data set consisting of quantitative and statistically valid values of ore mineral amounts and associations, particle size and shape distributions.

The Back Scatter Electron (BSE) only mode - In this analytical mode, the mineral phase occurring in the analyzed material is detected by using the BSE electron grey scales (0-255). The BSE-only mode is the fastest mode of analysis, since it does not use any EDS analysis. Indeed, the efficiency of the process relies on the unique BSE value of each mineral grain to identify the mineral phase present.

Spot centroid - This analysis performs a BSE image partition in progressively smaller segments, in order to find each individual mineral grain. From the calculated geometric center of each grain a single EDS analysis is collected and the chemical composition of this one analytical spot is assigned to the grain. Compared to the mapping mode, this is an extremely fast mode of measurement, due to fewer analyzed points. In contrast, it does not take into the account minerals having a discrete BSE, and does not report changes of elemental department within grains (as only one point on each grain is analyzed rather than many).

Feature scan - This mode of analysis follows a workflow, which is halfway between the spot centroid and full mapping modes. Indeed, it uses the same BSE function to identify the mineral grains and, subsequently, it rasters the beam across the surface of the grain and sums the X-rays collected to calculate the average composition of the grain. This mode will provide an analysis faster than the full mapping, but a good average composition of mineral grains.

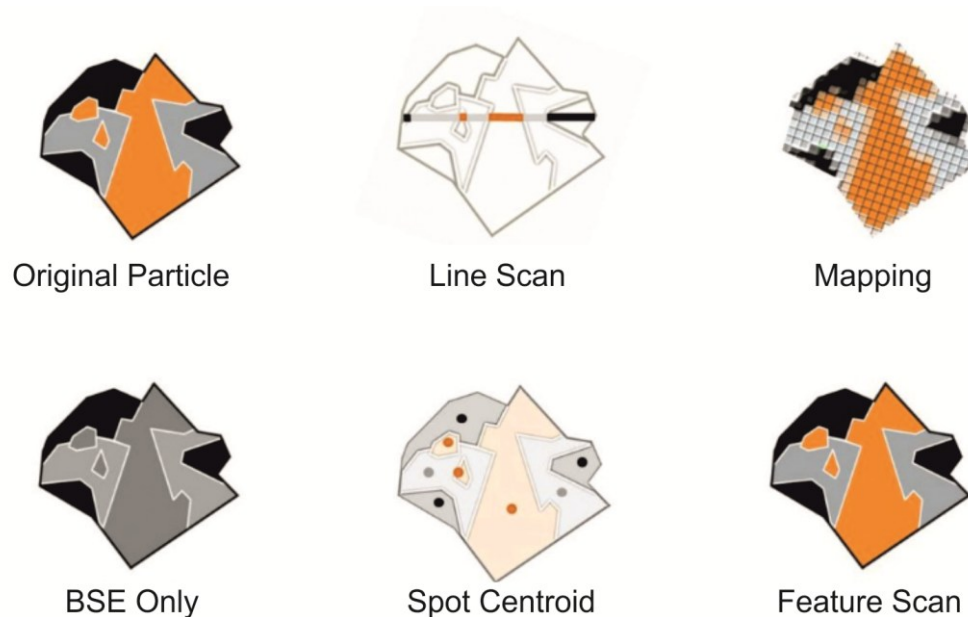


Figure 2.8. Graphical representation of analysis modes of ZEISS Mineralogic Mining instrument.

Analytical details

The Modal Mineralogy analysis by automated scanning electron microscope (SEM) was carried out for three representative core samples from the Cristal deposit, in order to make a comparison with the data obtained from quantitative XRPD analysis, and to get information on the mineral association in the selected samples. The Modal Mineralogy of the samples was investigated on polished blocks, which incorporate crushed material that has been previously sieved to achieve particle sizes around 1 mm. The analysis was performed at the Natural History Museum, London (UK) using the Mineralogic system, on an automated ZEISS EVO•50 scanning electron microscope (SEM), equipped with two Bruker xFlash 5010 Energy Dispersive Spectrometers (EDS) detectors. The analyses were carried out with an acceleration voltage of 20 kV with 13 mm working distance, 0.050 s dwell time corresponding to ~3000 EDS counts per spectra. The calibration of the EDS detectors was carried out every 60 minutes, using a Cu standard (Cu K α peak). The analyses were carried out adopting the “full map” analytical mode, in order to obtain high-resolution distribution maps of the occurring mineral phases, correlated with a database containing statistical information of the samples.

Chemical analysis of major, minor and trace elements (ICP-AES and MS and XRF)

The concentration of major, minor and trace elements in natural samples of rock, water and gas can be measured by using spectrometric analytical techniques. The latter exploit natural or induced electromagnetic radiations of variable wavelength (X-ray, γ -ray, light and etc.) absorbed or emitted by the elements.

X-ray fluorescence spectroscopy (XRF)

The XRF is a non-destructive method for determining the chemical composition of minerals and rocks by exploiting secondary emission of X-rays from atomic species contained in the sample, when other X-rays of high energy excite these atoms (Bertin, 1970). The exciting X-rays beam does not have an electronic charge and, therefore, it does not interact with electrons of the atoms that constituted the specimen. As consequence, the X-rays beam does not provide a continuous spectrum but if it is sufficiently energetic, it exclusively favors the emission of characteristic spectra. Therefore, by varying the intensity of the incident X-rays beam, it is possible to obtain “fluorescence spectra”, which may contain the characteristic responses of all “L” and “M” layers of a determined atom, and not contain those of the “K” layer that, for example, would require higher energy.

A spectrometer for the XRF analysis is constituted by:

- X-rays polychromatic generator of strong energy;
- sample holder (solid samples can be analyzed rather than liquid ones). Indeed, the radiation depends on the type and not on the three-dimensional distribution of the atoms;

- one or more crystal analyzers, both flat and curved, which are cut according to the precise crystallographic directions, in order to obtain the surface parallel to a family of lattice planes, of which the equidistance “d” is known;
- one or more detectors collecting and converting the X-ray reflections into pulses;
- a system of discrimination and counting of electrical pulses.

Inductively Coupled Plasma (ICP) - Atomic Emission Spectrometry (AES) and Mass Spectrometry (MS)

AES (Manning and William, 1997) - This method of analysis relies on quantitative measurement of the electromagnetic radiation emitted from excited atoms to determine the elemental concentrations. Atomic emission requires a means to convert a solid, liquid, or solution analyte into a free gaseous atom (atomization). The most common methods are flames and plasmas, both of which are useful for liquid or solution samples. Solid samples can be analyzed by dissolving them in a solvent, and using a flame or plasma atomizer. These high-temperature atomization sources provide sufficient energy to promote the atoms into high energy levels. The atoms decay then back to lower levels by emitting light. Since the transitions are between distinct atomic energy levels, the emission lines in the spectra are narrow. The spectra of multi-elemental samples can be very congested, and spectral separation of nearby atomic transitions requires a high-resolution spectrometer.

MS (Montaser, 1998) - This analytical technique employs the principles of motion of charged particles (ions) through electric and magnetic field, where the ions can be sorted according to their mass/charge ratio. The method relies on the following equation:

$$B = \frac{143.95}{r} \cdot \sqrt{\frac{m \cdot V}{e}}$$

where (B) is the magnetic field (Gauss), (r) is the radius (cm), (e) is the electronic charge units, (m) is the atomic mass units (a.m.u.) and V is the potential difference (volts). Generally, (r) is proportional to \sqrt{m} .

Part of the factors that should be considered in the choice of a particular analytical technique over another one, could be summarized as follows:

- To establish the analytical requirements for the technique in question that will depend on the specific application (geochemical survey vs chemical composition of minerals);
- What range of trace elements needs to be analyzed, and if the user is also interested in the organic matter contents or both;
- Effective cost of the instrumental procedure;
- Easy access/operation;
- Time required to obtain the final results;
- Detection limit of the instrument;
- Precision and accuracy of the instrument.

Analytical details

For the outcrop samples from Mina Grande and the drill core samples from Cristal whole rock chemical analyses of major and minor elements were carried out. A quantity of ~10 g for each samples of powdered material was shipped to the Bureau Veritas Commodities Canada Ltd. (Vancouver, Canada), which performed the analysis. The powders were collected from the same powdered portions used for the XRPD analyses. For major elements analysis, the samples were fused in presence of borate fluxes, and the solutions analyzed by means of XRF method. Conversely, minor elements were assayed by using ultratrace ICP-MS technique. Loss on ignition (LOI) was also evaluated. The minimum detection limits were 0.01 ppm to 0.01 %.

Whole-rock chemical analyses of the CR-13-08 and part of the CR-18-08 drill core samples were carried out at the Natural History Museum, London (UK). Approximately 50 mg of each powdered rock sample were dissolved in HCl and HNO₃ mixture. The solutions were analyzed with ICP-MS method using an Agilent 7700x mass spectrometer. The instrument was calibrated using multi-elements standards (Inorganic Ventures), typically with a 4-point calibration with a correlation coefficient of > 0.9999. Accuracy was monitored by analyzing certified reference materials JLk-1 (Lake sediment, GSJ) and SdAR-1 (Modified river sediment, IAG), at the beginning and at the end of the run. All values were found to be within the uncertainty of the published data. The limits of quantification were calculated as 10 times the standard deviation of HNO₃ blank solution analyzed at least 10 times during the run. This analytical method is very different from the one described above, therefore the resulting two chemical datasets are not directly comparable. For this reason, in the text it is shown the specific detection limit (DL) of each element measured with the two methods of analysis. The specific analytical errors are included in the “Materials and Methods” section of the chapters and in each table showing the two distinctive datasets.

Stable isotope geochemistry

Stable isotope geochemistry studies the variation of isotope ratios that are unrelated to the radioactive decay and undergo significant isotopic fractionation (Hoefs, 1987; Sharp, 2007)). During physical and chemical processes, the ratios between isotopic abundance of heavy elements (e.g. ⁸⁷Sr/⁸⁶Sr) do not vary, whereas those of light elements (e.g. ¹⁸O/¹⁶O) do vary. The isotopic fractionation occurs when one isotope of an element is either depleted or enriched compared to another isotope. Hydrogen, carbon, oxygen and sulfur represent the elements of major interest in the stable isotope geochemistry, and are characterized by common features reported below:

- they have low atomic mass;
- there is a large mass difference among their isotopes;
- they form strong covalent bonds;
- they occur in more than one oxidation stage (e.g. C and S), or they form a great variety of compounds (e.g. O);
- the abundance of their isotopes is large enough to favor the analysis.

Since after the fractionation process the differences in isotopic abundance of the elements are small, it is necessary to adopt a normalization to report the value of the isotope ratios as follow:

$$\delta^hE = \left[\frac{\left(\frac{h_E}{l_E} \right)_{sample} - \left(\frac{h_E}{l_E} \right)_{standard}}{\left(\frac{h_E}{l_E} \right)_{standard}} \right] \cdot 10^3$$

where (^hE) is the heavy isotope of the element, (^lE) is the light isotope of the element and (δ) is expressed in permil (‰), positive or negative, deviation from a standard of reference. δ^hE can be expressed as Standard Mean Ocean Water (SMOW) or as Pee Dee Belemnite (PDB) for carbon and oxygen, and as Canyon Diablo Troilite (CDT) standard for sulfur.

C - O stable isotope analysis on carbonate minerals

An accurate isotopic study of the carbonate minerals in supergene deposits plays a very important role in distinguishing supergene from hypogene base metal carbonate deposits, in evaluating the effects of oxidative heating and the role of microbes during sulfide oxidation (Gilg et al., 2008). Moreover, it may be useful to characterize the type and temperature of fluid (meteoric or seawater) involved in sulfide oxidation and mineral precipitation, to obtain indirect information on the duration of the oxidation period (e.g. deduced from changes of isotope compositions of meteoric waters), to distinguish between direct- and wall rock-replacements, to trace metal enrichments versus dilution and to gain paleoclimatic constraints. Indeed, unless bacterial sulfate reduction (BSR) processes are involved, the sulfur isotope ratios from S-bearing supergene minerals (e.g. sulfates and/or sulfides; Gavelin et al., 1960; Field, 1966), as well as δ⁶⁶Zn values from supergene carbonates (Maréchal et al., 1999), do not show significant fractionation compared to the precursor sulfides. In order to achieve a correct interpretation of the stable isotope data, the following two prerequisites are needed:

- accurate measurement of the C and O isotopic composition of the carbonate minerals (e.g. mass spectrometry);
- knowledge of fractionation factors between mineral and fluids as function of temperature.

Given two phases (A) and (B), if (R) indicates the ratio between two isotopes of a light element (e.g. O or H), the fractionation factor α is defined as follow:

$$\alpha_{A-B} \equiv \frac{R^A}{R^B}$$

or

$$\Delta_{A-B} = \delta_A - \delta_B$$

where the relationship between (Δ) and (δ) is given by $\Delta \sim 10^3 \cdot \ln \alpha$, and (α) is temperature-dependent so that $\ln \alpha = A + B/T^2$ (where A and B are two constants).

Following this reasoning, the equation describing the oxygen isotope fractionation between CO₂ liberated from calcite, for example, during reaction with phosphoric acid and carbonate ($\alpha^{\text{phos}}_{\text{CO}_2\text{-carbonate}}$), can be reported as follows;

$$1000 \ln \alpha^{\text{phos}}_{\text{CO}_2\text{-calcite}} = 3.95 + 5.53 \cdot 10^5 / T^2 \text{ (Gilg et al., 2003)}$$

(T) is in Kelvin

Analytical details

Carbon and oxygen isotope analyses of carbonate specimens, and hydrogen and oxygen analyses of water samples were performed at the GeoZentrum Nordbayern of Erlangen (Germany).

More than 100 carbonate specimens (calcite, smithsonite and dolomite) from Skorpion, Rosh Pinah, Mina Grande and Cristal deposits were analyzed for the C-O isotope analysis.

The carbonate powders were made to react with 100% phosphoric acid at 70°C using a Gasbench II connected to a ThermoFisher Delta V Plus mass spectrometer. All values are reported in per mil relative to V-PDB. The $\delta^{18}\text{O}$ values are reported for calcite, therefore, the oxygen isotope values of dolomite and smithsonite were corrected using the phosphoric acid fractionation factors given by Kim et al. (2007), Rosenbaum and Sheppard (1986) and Gilg et al. (2008) respectively. Reproducibility and accuracy was monitored by replicate analysis of laboratory standards calibrated by assigning $\delta^{13}\text{C}$ values of +1.95‰ to NBS19 and -46.6‰ to LSVEC and $\delta^{18}\text{O}$ values of -2.20‰ to NBS19 and -23.2‰ to NBS18. Reproducibility for $\delta^{13}\text{C}$ and $\delta^{18}\text{O}$ was $\pm 0.0\text{x}$ and $\pm 0.0\text{y}$, respectively.

For the H-O isotope analysis, water samples from the Cristal area were analyzed for $\delta^{18}\text{O}$ by an automated equilibration unit (Gasbench II; Thermo Fisher Scientific, Bremen, Germany) in continuous flow mode, coupled to a Delta plus XP isotope ratio mass spectrometer (Thermo Fisher Scientific, Bremen, Germany). All samples were measured in duplicates and the reported value is the mean value. The data sets were corrected for instrumental drift during the run, and normalized to the VSMOW/SLAP (Standard Light Antarctic Precipitation) scale by assigning a value of 0 ‰ and -55.5 ‰ ($\delta^{18}\text{O}$) to VSMOW2 and SLAP2, respectively (Brand et al., 2014). For normalization two laboratory standards that were calibrated directly against VSMOW2 and SLAP2, were measured in each run. External reproducibility based on repeated analyses of a control sample was better than 0.1‰ (± 1 sigma) for $\delta^{18}\text{O}$. The same water samples were analyzed for $\delta^2\text{H}$ by liquid injection into a modified high temperature pyrolysis unit (Thermo TC/EA with CTC PAL autosampler), coupled in continuous flow mode to a Delta V plus isotope ratio mass spectrometer (Thermo Fisher Scientific, Bremen, Germany). The TC/EA unit was converted into an online chromium reduction system based on the principle outlined by Morrison et al. (2001). Temperature were set to 840°C (reactor temperature) and 85°C (GC column). Injection volume was 0.2 μL by using a 0.5

uL syringe (SGE Analytical Science, Australia). The output value is the mean value of 4 injections. The data sets were corrected for memory and instrument drift during the run and normalized to the VSMOW/SLAP (Standard Light Antarctic Precipitation) scale by assigning a value of 0‰ and -427.5‰ ($\delta^2\text{H}$) to VSMOW2 and SLAP2, respectively. Sequence setup and post-run correction procedures were adopted from the procedure described by van Geldern and Barth (2012) for laser isotope instruments. For scale normalization two laboratory standards that were calibrated directly against VSMOW2 and SLAP2, were measured in each run. External reproducibility based on repeated analyses of a control sample was better than 1‰ (± 1 sigma) for $\delta^2\text{H}$.

Sulfur isotopes analysis on sulfides

Sulfur has five valence states, which are +6 (BaSO_4), +4 (SO_2), 0 (S), -1 (FeS_2) and -2 (H_2S). This great variety of valence states and compounds favors the isotopic fractionation. Generally, $\delta^{34}\text{S}$ values of rocks may be very different from those of the natural reservoirs (natural sources of sulfur on earth). The most isotopically homogeneous natural reservoirs of sulfur are mantle basalts ($\delta^{34}\text{S} \sim 0\text{‰}$) and sea-water ($\delta^{34}\text{S} \sim +20\text{‰}$). All other natural reservoirs are less homogeneous, making the S stable isotope geochemistry somewhat complex. However, individual deposits or districts may have more than one source of sulfur including sulfate-bearing evaporates, connate seawater, diagenetic sulfides, sulfur-bearing organic material, H_2S reservoir gas and reduced sulfur in anoxic waters of stratified basins. The most frequent sources of sulfur for many ore deposits correspond to seawater sulfate contained in the sediments and/or reduced connate waters (Sangster, 1990). The most common $\delta^{34}\text{S}$ values of sulfides in many MVT deposits are lower than $\delta^{34}\text{S}$ values of seawater contemporaneous in age with the host rocks (Sangster, 1990). This discrepancy depends on many factors and processes, which are summarized as follows:

- the isotopic composition of oceanic sulfate varies considerably with the age;
- the mechanism of sulfate reduction (Ohmoto and Rye, 1979 and references therein) such as Thermochemical Sulfate Reduction (TSR) vs Bacterial Sulfate Reduction (BSR);
- reduction occurring in “open” or “closed” systems;
- H_2S derived from organic material or not;
- mixing processes among more sources;
- isotopic fractionation as function of the mineralogy and kinetic effects between mineral pairs.

Analytical details

Sulfur stable isotope analysis was carried out by N. Mondillo at SUERC-Scottish Universities Environmental Research Centre, on 4 sphalerite specimens from the Cristal deposit. Sulfides were prepared for conventional isotopic analysis by standard heavy liquid, magnetic, diamond micro-drilling and hand picking techniques. Around 5 to 10 mg were utilized for isotopic analysis. Minor contamination by non S-bearing phases was tolerated, and has no isotopic effect on the final data. Sulfides were analysed by standard

techniques (Robinson and Kusakabe, 1975), in which SO₂ gas was liberated by combusting the sulfides with excess Cu₂O at 1075°C, in vacuo. The liberated gases were analysed on a VG Isotech SIRA II mass spectrometer, and standard corrections applied to raw δ SO₂ values to produce true $\delta^{34}\text{S}$. The standards employed were the international standards NBS-123 and IAEA-S-3, and the SUERC standard CP-1. Repeated analyses of these standards gave $\delta^{34}\text{S}$ values of +17.1‰, -32‰ and -4.6‰ respectively, with a standard error around $\pm 0.2\text{‰}$ during the execution of the analyses. The sulfur data are reported in $\delta^{34}\text{S}$ notation as per mil (‰) variations from the Vienna Cañon Diablo Troilite (V-CDT) standard.

Pb and Sr radiogenic isotope geochemistry

The isotopes of lead occurring in nature are: ²⁰⁴Pb, ²⁰⁶Pb, ²⁰⁷Pb and ²⁰⁸Pb. The ²⁰⁶Pb, ²⁰⁷Pb and ²⁰⁸Pb derived from a complex radioactive decay of ²³⁸U, ²³⁵U and ²³²Th, respectively, and are therefore radiogenic. Heavy isotopes such as those of lead and strontium (⁸⁶Sr and ⁸⁷Sr) do not fractionate as strongly as the light isotopes of O and C. Therefore, the importance of studying the geochemistry of Pb- and Sr-isotopes relies on the possibility to preserve their isotopic signature during some geological processes linked to ore deposits formation. Indeed, it has been observed that lead isotope ratios of ore minerals can reflect the isotopic signatures, both for igneous host rock in volcanic arc and rift settings (Church et al., 1986; LeHuray et al., 1988), and for basement source, from which lead derived, in continental and subsiding basin settings (Zartman, 1974; Andrew et al., 1984; LeHuray et al., 1987). Since the isotopic signature is preserved during geological processes affecting ore deposits, it is possible to detect, for example, the presence of one or more sources of lead, and the direct connection between primary sulfides and secondary supergene minerals. Moreover, it is also possible to discriminate between hydrothermal vs supergene alteration overprint (e.g. sericitization vs supergene formation of illite/smectite), or to characterize the type of ore deposits (e.g. MVT vs CRD; Mondillo et al., 2014b). Looking at the Sr-isotopes, the relative mass difference is not sufficient to justify fractionation of ⁸⁶Sr from ⁸⁷Sr as mineral precipitation takes place. Consequently, a mineral bears rather the same Sr isotope composition as its mother fluid (Clauer and Chaudhuri, 1992; Hoefs, 1997). ⁸⁶Sr does not take part of any decay series and its abundance is constant, whereas ⁸⁷Sr generate by radioactive decay of ⁸⁷Rb and its abundance increases with time. Carbonates can host large amounts of Sr, but they cannot host Rb in their lattice structure. As consequence, the amount of ⁸⁷Sr in a carbonate phase does not vary with time and the ⁸⁷Sr/⁸⁶Sr ratio remains relatively constant. Therefore, the Sr isotope ratios of carbonates generally reflect the composition either of the fluids from which they precipitated, or of the fluids through which they subsequently reequilibrated. As instance, the Sr isotope composition of dolomites can be an excellent proxy to deduce the composition and nature of dolomitizing fluids.

Lead and strontium isotope analysis of rock samples were generally performed by using ICP-MS techniques.

Analytical details

Analyses of the Pb and Sr isotope ratios of sulfides and carbonate minerals from the Cristal and the Mina Grande deposits were performed at the Laboratory of Isotope Geology at the University of Bern (Switzerland), by I. Villa. The analysis involved a Nu InstrumentsTM multicollector inductively coupled plasma mass spectrometer (MC-ICP-MS). To analyze Sr isotope ratios, the carbonate specimens were dissolved in HNO₃ and Sr was purified using the Sr•SpecTM cation exchange resin, according to the procedure of Villa et al. (2006). On the other hand, for measuring Pb isotope ratios sulfides and carbonates were dissolved in *Aqua Regia* and purified using the Sr•SpecTM cation exchange resin according to Villa (2009) analytical procedure.

Chapter 3:

The karst-hosted Mina Grande nonsulfide zinc deposit, Bongará district (Amazonas region, Peru)

Published in "Economic Geology"

Reference: Arfè, G., Mondillo, N., Boni, M., Balassone, G., Joachimski, M., Mormone, A., Di Palma, T., 2017. The karst-hosted Mina Grande nonsulfide zinc deposit, Bongará district (Amazonas region, Peru). Economic Geology, 112, 1089-1110.

Introduction

The Pucará basin (Late Triassic-Early Jurassic) is host of various types of strata-bound mineralizations in central and northern Peru (Kobe, 1977, 1982, 1990a; Dalheimer, 1990; Fontboté, 1990; Reid, 2001). These mineralization types include Zn-Pb-(Cu-Ag) porphyry-related epithermal polymetallic ("Cordilleran") and Mississippi Valley-type (MVT) Zn-Pb deposits. The principal producing mines hosted in the Pucará Group carbonates are San Vicente and Shalipayco (Fontboté, 1990; Fontboté and Gorzawski, 1990; Gorzawski et al., 1990; Moritz et al., 1996; Spangenberg et al., 1996, 1999), Cerro de Pasco (Baumgartner and Fontboté, 2008; Baumgartner et al., 2009; Rottier et al. 2016), San Gregorio in the Colquijirca District (Bendezú and Fontboté 2009), and the mines located in the Yauli dome (e.g., San Cristobal, Carahuacra, and Morococha; see Dalheimer, 1990; Kobe, 1990b; Beuchat et al. 2004; Catchpole et al. 2015). Interesting areas of exploration are also located in northern and eastern parts of the Pucará basin, including the Bongará district (Fig. 3.1A), which is the subject of this paper. The Bongará district is located approximately 740 km north of Lima and 245 km northeast of the coastal city of Chiclayo, on the western edge of the Subandean foreland basin of northern Peru and within the mountainous terrain of the Subandean fold-and-thrust belt (Fig. 3.1B). The major mineral occurrences of the area are the following (Fig. 3.1A): the Charlotte Bongará deposits (including Bongará-Mina Grande) in the north, and the Bongará-Florida Canyon occurrence in the south. All of these deposits consist of strata-bound Zn-Pb nonsulfide/sulfide concentrations (Wright, 2010; Boni and Mondillo, 2015). Field observations, mineralogy, mineral paragenesis, and fluid inclusion characteristics indicate that the Zn-Pb sulfide mineralization in the Bongará district is MVT (Reid, 2001; Basuki, 2006; Basuki and Spooner, 2008, 2009). The most intensive exploration was carried out in the Florida Canyon area (Pedro Ruiz-Chachapoyas district; Reid, 2001), in order to estimate its economic potential. The Florida Canyon orebody (owned by Votorantim/Milpo) is hosted in the carbonates of the Chambará Formation, and contains up to 7 Mt of ore averaging ~7% Zn + Pb (Reid, 2001). The high-grade Zn occurrences of Charlotte Bongará, known today as Mina Grande, Mina Chica, and Cristal, were discovered in 1973 (Brophy et al., 2012) and are nonsulfide-type mineralizations. These types of ore deposits mostly consist of oxidized Zn-P minerals (i.e., carbonates and silicates; Hitzman et al., 2003). In 2005 the estimated resource at Mina Grande was 1

million metric tons (Mt) at 23.4% Zn and 1.6% Pb, with a 10% Zn cutoff grade (Corianta S.A.C.). Corianta S.A.C. mined high-grade zinc nonsulfides at this mine site, producing zinc calcines from 2007 until 2008, when the operation was shut down due to low zinc prices. The property produced approximately 25,000 t of zinc. A number of historical resource estimates have been calculated on the Bongará Zinc Mine since 2008, including the latest one by Corianta S.A.C. in 2011: total resources (measured + indicated) are: 1,007,796 tons @ 21.6% Zn.

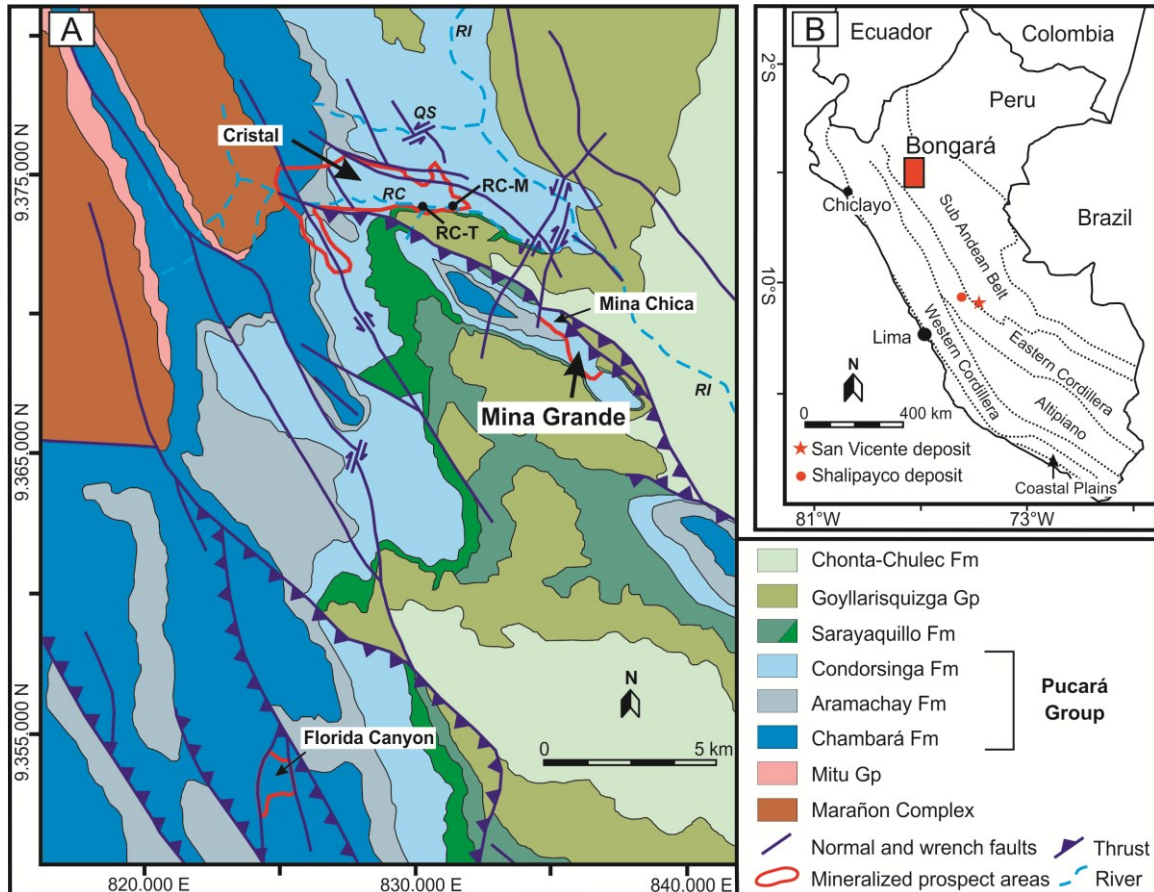


Figure 3.1. Geologic map (A) and location of the Bongará district within the Northern Andes morphostructural units (B) (modified from Basuki et al., 2008, and Brophy, 2012). QS = Quebrada Seca river, RC = Rio Cristal river, RI = Rio Imasa river. Black dots = river water sampling sites, RC-M = Rio Cristal river, RC-T = Rio Cristal tributary.

Nonsulfide ore deposits commonly form after weathering and alteration of exhumed sulfide bodies, but they can be also genetically associated with direct precipitation from oxidizing hydrothermal fluids (Hitzman et al., 2003; Boni and Mondillo, 2015; Borg, 2015). Mina Grande, Mina Chica, and Cristal nonsulfide deposits are hosted by Mesozoic limestone and dolomite (Pleinsbachian- Toarcian) of the Pucará Group (Condorsinga Formation), and are considered to be genetically related to supergene processes (Boni and Mondillo, 2015, and references therein; Arfè et al., 2017b, in press). In the area there are other not yet developed mineral concentrations (e.g., Mina Chica and Bongarita) with zinc ores of the same type. The formation of supergene nonsulfide deposits depends on

(1) the tectonic evolution of an area, which promotes uplift, uncapping, and alteration of sulfide orebodies, and (2) the climatic conditions existing at the time of sulfide alteration, which favor the formation of certain oxidized minerals, rather than others (Hitzman et al., 2003; Boni and Mondillo, 2015; Borg, 2015). Considering that the Mina Grande deposit is an important supergene Zn mineralization of Peru (see Hitzman et al., 2003, table 1; Boni and Mondillo, 2015, and references therein), the objective of our research is to provide a comprehensive mineralogical, petrographic, and geochemical characterization of this nonsulfide occurrence, to better constrain its genesis in the frame of tectonic and climatic evolution of the region.

Geology of the Bongará district in the Pucará Basin

The Andes experienced two important orogenic cycles (Benavides-Cáceres, 1999): the pre-Andean (Precambrian to Paleozoic) and Andean (Early Jurassic to Present) cycles. In the Eastern Cordillera of Peru, these two cycles were separated by a Late Permian to Triassic rifting period (Laubacher, 1978; Mégard, 1978; Noble et al., 1978; Dalmayrac et al., 1980; Kontak et al., 1985; Rosas and Fontboté, 1995; Rosas et al., 1997; Jacay et al., 1999; Sempere et al., 2002). During the Late Triassic to Early Jurassic an extensional postrift sedimentary basin developed in the Eastern Cordillera, within a NW-trending sinistral shear zone (Mégard, 1987; Benavides-Cáceres, 1999; Rosas et al., 2007). Prior to the onset and during the deposition of the Mesozoic Pucará Group, the sedimentary basin underwent a fault-controlled subsidence (Middle to Late Triassic), followed by a gradual transition to widespread regional subsidence (Late Triassic to Early Jurassic) associated with NW- to NNW-trending shear zones (Rosas et al., 2007). The basin started to be filled with up to ~3,000-m-thick continental siliciclastics of the Mitu Group (Middle to Late Triassic; Spikings et al. 2016). From Late Triassic to Early Jurassic, the basin was filled with marine carbonates of the Pucará Group (Fontboté, 1990; Reid, 2001; Rosas et al., 2007), which unconformably overly the sediments of the Mitu Group (see Fig. 3.2). The Pucará Group consists of the Chambará, Aramachay, and Condorsinga Formations of the Triassic to Jurassic. The Norian-Rhaetian Chambará Formation (Mathalone and Montoya, 1995; Rosas et al., 2007) was deposited in a progressively deepening carbonate environment (Brophy et al., 2012). The Chambará Formation is overlain by the Aramachay Formation (Reid, 2001; Rosas et al., 2007; Basuki et al., 2008; Brophy et al., 2012) that consists of thinly bedded limestone and silty shale, intercalated with bituminous silty mudstone of the late Rhaetian-Sinemurian (Rosas et al., 2007). The uppermost unit of the Pucará Group, the Condorsinga Formation (Pliensbachian-Toarcian) consists of bioclastic and cherty limestone, locally with a shaly to sandy component (Brophy et al., 2012). The Upper Jurassic to Cretaceous Sarayaquillo Formation, consisting of red shale, sandstone, and marl, overlies the Condorsinga Formation with an angular unconformity (Fontboté, 1990; Instituto Geológico Minero y Metalurgico-INGEMMET, 1995; Rosas et al., 2007). The Lower Cretaceous Goyllarisquizga Group overlies the Sarayaquillo Formation (Brophy et al., 2012). In the

Bongará area the youngest rocks belong to the Early Cretaceous Chonta-Choulec Formation (Fig. 3.2).













Quaternary				Polymictic river gravels.
Cretaceous	Upper		Chonta Fm	Limestones and marls interbedded with silty mudstones.
	Lower		Goyllarisquizga Gp 300-500 m	Quartzitic sandstones and conglomerates with minor intercalations of siltstones and mudstones.
Jurassic	Upper		Sarayaquillo Fm +/- 200 m	Subaerial-lacustrine sandstones and silty mudstones. Limestones boulder conglomerates.
	Lower		Condorsinga Fm +/- 300 m	Pelletal calcite mudstones and wackestones. Dolomitized packstones and wackestones.
			Aramachay Fm +/- 200 m	Laminated beds of calcitic mudstones. Thinly-bedded bituminous limestones and mudstones with ammonites.
Triassic	Upper		Chambará Fm > 1000 m	Micrites and biomicrites with fossiliferous horizons. Micrites with chert nodules. Bituminous packstones, locally dolomitized. Dolomitic grainstones. Thickly-bedded micrites and biomicrites.
	Middle		Mitu Gp	Continental red-bed sandstones, mudstones and polymictic conglomerates.
Paleozoic			Marañon Complex	Foliated greenish micaschists and metasediments cut by magmatic dykes.
<div>  Mina Grande and Cristal deposits  Florida Canyon deposit  Faults  Facies heteropy </div>				

Figure 3.2. Stratigraphic column of the succession in the Bongará area (modified from Brophy, 2012).

The Pucará basin has been affected by the Andean tectonics since Late Cretaceous, and the most important deformation events were associated with the Andean compressive phase (40 Ma) (Mégard et al., 1984). In the area of interest for this study, the front of deformation migrated from the Western Cordillera to the Subandean thrust belt during the Quechua phase in late Oligocene (Pfiffner and Gonzalez, 2013). The latter deformation phase affected the entire orogen, lasted at least until the Pliocene, and is still active. In fact, as documented by many authors (Mégard et al., 1984; Gil et al., 1999; Gregory-Wodzicki, 2000; Mora et al., 2010; Pfiffner and Gonzalez, 2013), the northeastern part of the Peruvian morphostructural units experienced a Neogene phase of deformation from 20.5 to 1.6 Ma, which is expressed by a northeast vergent thrust system, mainly responsible for the rise of the Eastern Cordillera. The Oligocene-Holocene phase of deformation produced most of the uplifts of the Andean Plateau and all the uplift of the Subandean zone (Sempere et al., 1990; Jordan et al., 1997). On the basis of apatite fission tracks and paleosurfaces analysis, many authors (Laubacher and Naeser, 1994; Alcmán and Marksteiner, 1997; Garver et al., 2005; Montario, 2006) argued that the onset of the

uplifts in both the Eastern Cordillera and the Subandean zone may be traced back to late Oligocene-early Miocene, whereas the most intensive uplift phases occurred between 15 to 10 and 4 to 5 Ma, and from 4 to ~2.7 Ma. Indeed, during the latter stages the uplift rates reached maximum values of 0.05 and 3.0 mm/yr, respectively (Gregory-Wodzicki, 2000). Moreover, both Gregory-Wodzicki (2000) and Hooghiemstra and Van der Hammen (2004) argued that the easternmost domains of the northern Andes were located at the 25 and 30% of their modern elevation at 20 and ~14 Ma, respectively, and that at 10 Ma the height of the northern Andes was less than half of their modern elevation. An additional rapid increase in elevation (0.6 mm/yr) occurred in Pliocene (~4-5 Ma), whereas the current elevation was eventually reached in Pleistocene (~2.5 Ma; Hooghiemstra and Van der Hammen, 2004).

The most important MVT deposits in the Bongará area occur in the Chambará and Condorsinga Formations, but also in the topmost parts of the Goyllarizquisga Formation (Reid, 2001). Their exact ages, not well constrained, are either Campanian (Reid, 2001; Basuki, 2006) or younger. If younger, their genesis can be linked with one of three compressive Incaic phases (dated respectively at 59-55, 43-42, and 30-27 Ma) or with the deformations related to the Quechua period (20.5-1.6 Ma; Mégard, 1984; Mégard et al., 1984; Benavides-Cáceres, 1999; Zúñiga y Rivero et al., 2010).

Climatic setting of the Bongará district

In the Bongará area the average annual temperature varies between 23° and 25°C with high humidity values. At altitudes >2,000 m.a.s.l. strong diurnal variations are common and temperatures range from 7° to ~30°C. Most rainfalls occur between November and April reaching average annual values of 100 cm (Workman and Breede, 2016). These humid conditions that are able to sustain a rainforest ecosystem in this part of Peru have been present during the last ~20 Ma (Savin et al., 1975; Monsch, 1998). Between late Oligocene and Miocene, the western Amazonia basin experienced two particularly humid periods: (1) the Pebas (~23-10 Ma), during which wetlands, shallow lakes, and swamps formed; and (2) the Acre (~10-7 Ma), during which fluvial-tidal-dominated wetland (onset of the transcontinental Amazon River systems) developed (Lundberg et al., 1998; Wesselingh and Salo, 2006; Hoorn et al., 2010). Kaandorp et al. (2005) also suggested that the hydrologic cycle active during the Miocene Climate Optimum (MCO) was comparable to the system currently affecting the northern Amazonia region of Peru in terms of seasonality, and that the oxygen isotope composition of precipitation might have been comparable.

Main features of the Mina Grande deposit

The Mina Grande mineralized body is 1.5 km long, 0.4 km wide, and extends to depths of 20 to 60 m below surface. The deposit lies on the crest of a tight and overturned ramp anticline (Mina Grande anticline), in the hanging wall of the Chiriaco reverse fault (Fig. 3.3).

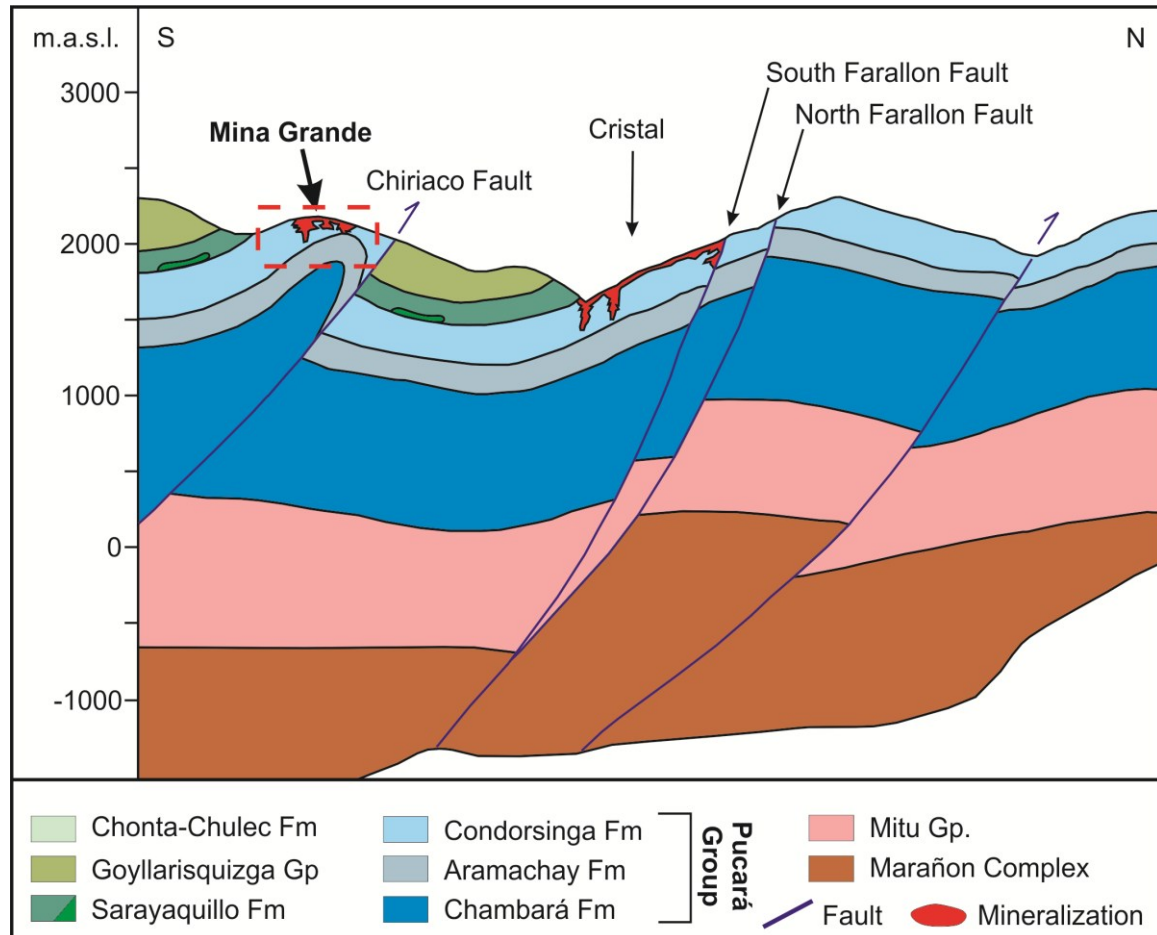


Figure 3.3. Schematic section of the Mina Grande (dashed red square) and Cristal mineralized districts (modified from Brophy, 2012).

The mining permit has been divided into three areas: “Fase A,” “Fase B,” and “Fase C” (Fig. 3.4), whose altitudes vary between 1,920 and 2,260 m.a.s.l. Diamond drilling has identified the mineralization to a depth of 27 m. Measured resources in 2008 were as follows: Fase A = 160,000 t @ 21.2% Zn; Fase B = 36,400 t @ 28.9% Zn; Fase C = 116,700 t @ 22.5% Zn. The Mina Grande resources have been partially mined in two pits to this date, and are thus in lesser amount in respect to the above mentioned resources. The Mina Chica area has not been developed; although, measured resources are 16,120 t @ 20.2% Zn (Corianta S.A.C.). Resource estimates currently existing for the Bongarita deposit are 38,400 t @ 23.5% Zn.

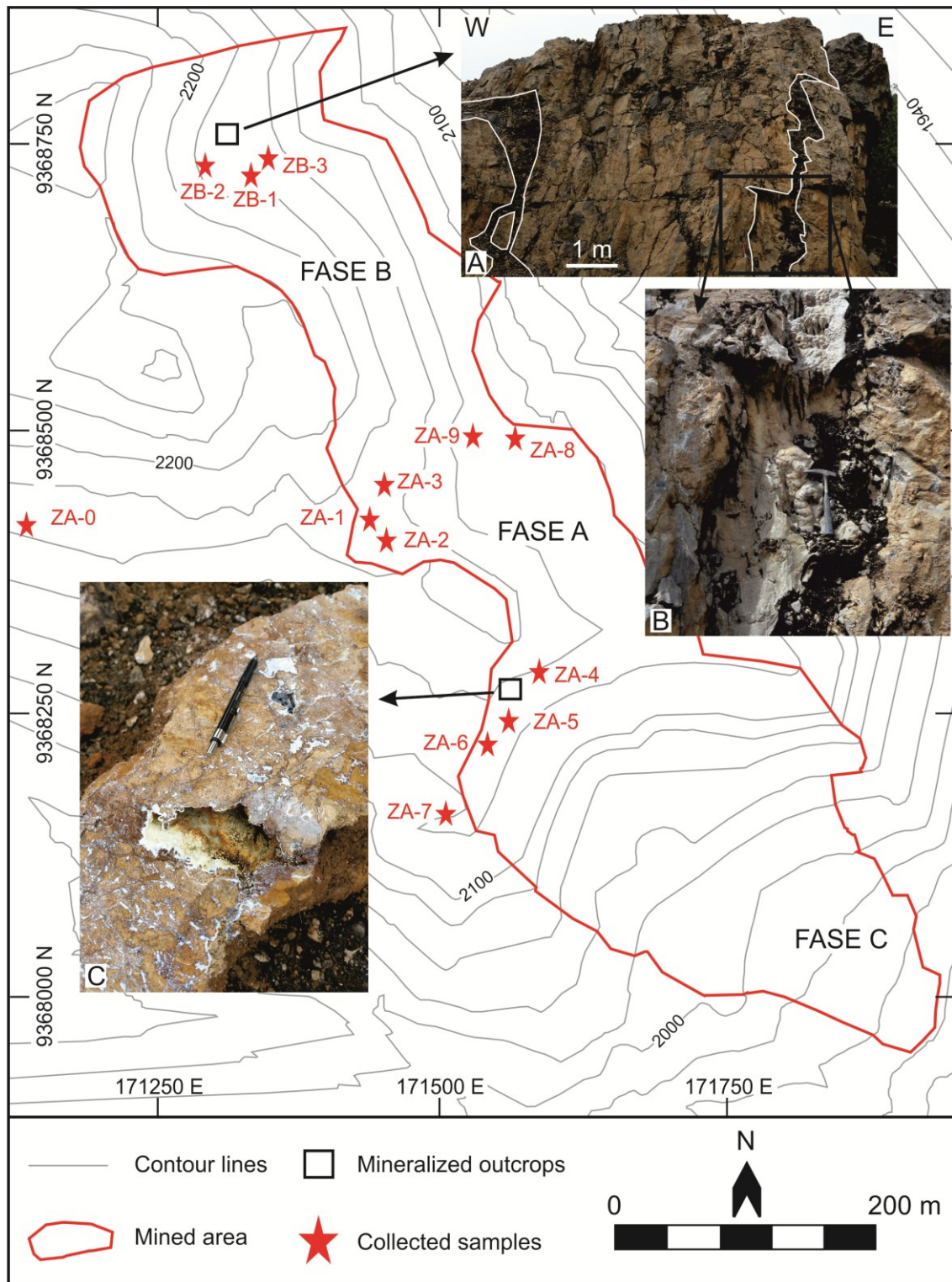


Figure 3.4. Topographic map of the Mina Grande mining area, showing Fase A, Fase B, and Fase C. A. Solution cavities following early joints striking northwest-southeast, developed perpendicular to the bedding. B. Concretionary aggregates of calcite, hydrozincite, and Mn-(hydr)oxides on the walls of the karst cavities. C. Supergene Zn minerals (smithsonite, hemimorphite, and hydrozincite), with crustiform structures. Location of the collected samples (red stars).

At Mina Grande the nonsulfide ore is associated with karst cavities (Fig. 3.4A, B), which developed and deepened mainly along several NW-trending faults (avg N40W/70SW), controlled by the regional fault network and locally by stratification joints (avg N8E/26NW). The best evidence of faulting and karstification is recognized in the Fase B area, where supergene Zn-bearing minerals (smithsonite, hemimorphite, and hydrozincite) occur as cement of collapse breccias (Arfè et al., 2017b) and as concretionary features, similar to typical karst speleothems (Fig. 3.4B, C). Breccia clasts consist mainly of dolomite and calcite, and only locally of siliciclastic lithologies. Rare remnants of sphalerite and galena have been observed in the limestone at the base of the nonsulfide-filled cavities. Calcite stalactites and stalagmites, showing vertical orientations relative to today's morphological surface, also occur in karst cavities. The walls of the cavities are covered by concretionary aggregates of calcite and hydrozincite, followed in turn by Mn-(hydr)oxides (Fig. 3.4B). Most recent hydrozincite has grown on waste dumps and stockpile mounds in both Fase A and Fase B. Mina Grande Fase B is partially overlain by a goethite-rich ferricrete (gossan-style). Angular, centimeter-scale fragments of goethite from the ferricrete are locally cemented by hydrozincite, creating a mosaic-style breccia (Workman and Breede, 2016). Possible NW-trending mineralized faults might occur in the Fase C area, but its colluvial nature (Workman and Breede, 2016) does not allow an accurate geologic characterization.

To provide a three-dimensional image of the Mina Grande mineralization (Fases A, B, and C), geologic (Fig. 3.5) and geochemical (Fig. 3.6) models have been constructed based on 69 drill cores (Corianta S.A.C.).

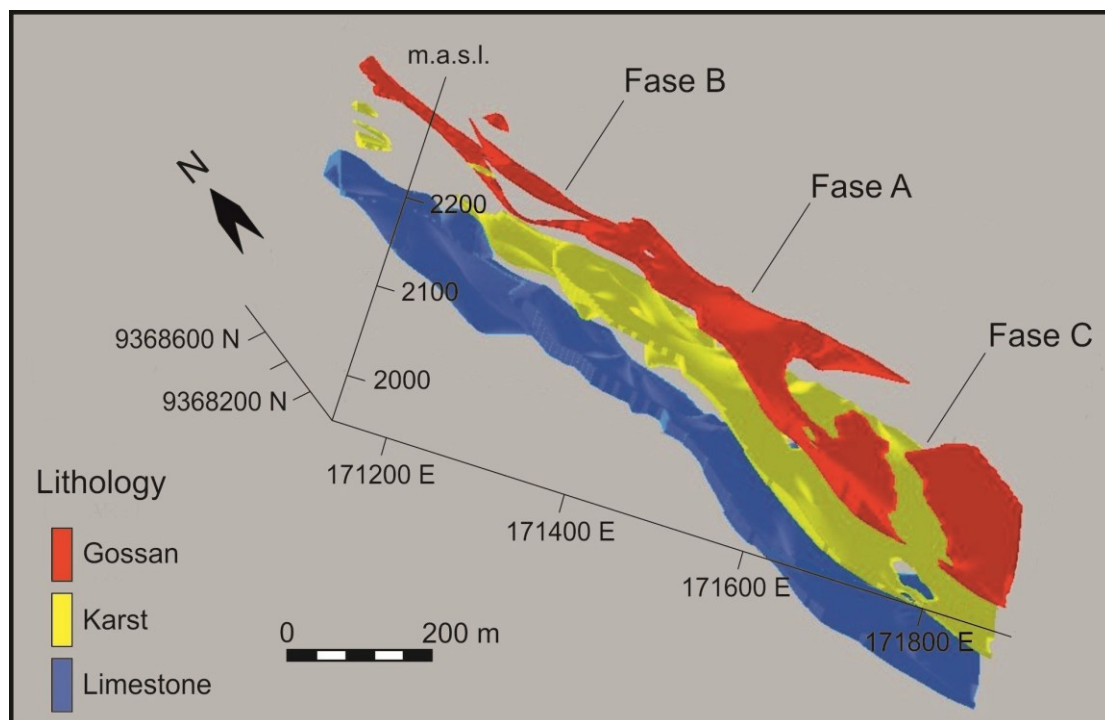


Figure 3.5. Three-dimensional lithologic model of the Mina Grande area based on 69 drill cores; Karst = karst fillings; Limestone = host limestone. The drill core data were interpolated, using a Kriging algorithm in Rockworks/15 software (RockWare).

Karstic effects on the footwall carbonates of the Mina Grande area are visible at the top of the Condorsinga Formation limestone. The karst-filling materials are especially visible in the Fase A area. The uppermost parts of the karst fill are characterized by a gossanous lithology. High-grade zones follow the direction of the northwest-southeast anticlinal axis (Fig. 3.6). The patches where the mineral occurrences lie on top of the current topography have been mined since 2008 (corresponding to an average thickness of at least 17 m of exploited ore and gangue material). Below the current topographic surface is shown the remaining bulk ore.

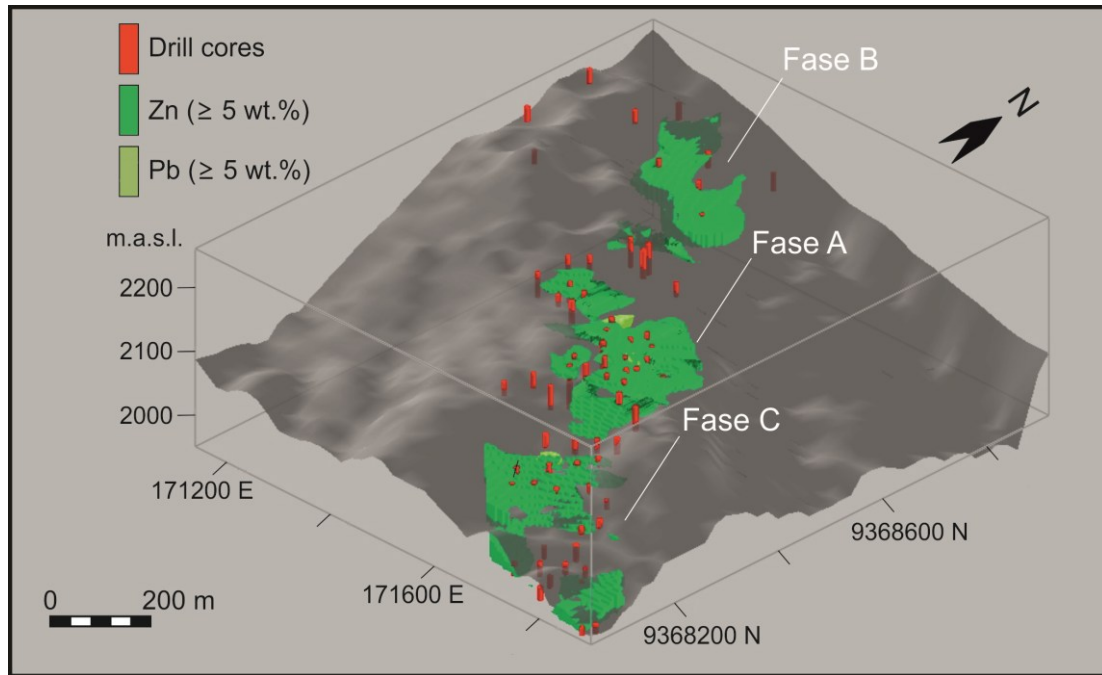


Figure 3.6. Three-dimensional geochemical model of the zinc and lead orebodies (with metal concentrations ≥ 5 wt %) at Mina Grande, based on 69 drill cores. The drill core data were interpolated with a Kriging algorithm, using Rockworks/15 software (RockWare).

Materials and analytical methods

Our mineralogical and geochemical studies were performed on 13 representative specimens (Fig. 3.7A-F) collected from several outcrops from the Mina Grande deposit (Fase A, samples ZA-0-ZA-9; Fase B, samples ZAB-1-ZAB-3, ZABT1, ZAB-T2), and on two drill core fragments sampled below the mineralized outcrops of the Condorsinga (sample ZB-T1) and the Aramachay (sample ZB-T2) Formations.

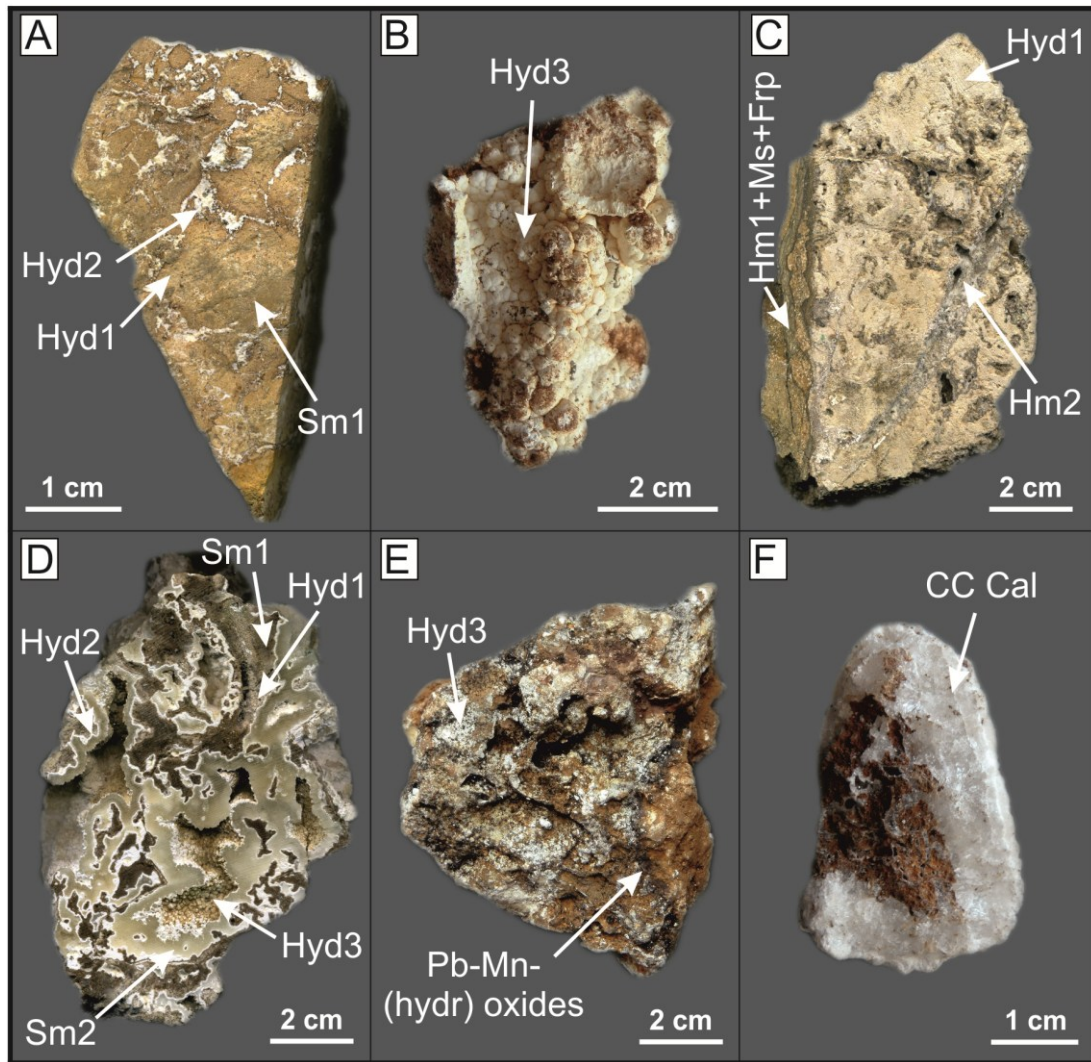


Figure 3.7. Most representative nonsulfide samples. A. Early smithsonite (Sm1) replacing host rock, replaced in turn by spongy hydrozincite (Hyd1), cut by veinlets of compact hydrozincite (Hyd2); sample ZA-5. B. Hydrozincite crust with concretionary texture (Hyd3); sample ZA-7. C. Late hemimorphite veinlet (Hm2), cutting a mass of spongy hydrozincite (Hyd1) with patches of early hemimorphite (Hm1), mica group minerals (Ms) and fraipontite (Frp); sample ZB-2. D. Late smithsonite (Sm2) and compact to spongy hydrozincites (Hyd2 and Hyd3, respectively) cementing clasts of a collapse breccia consisting of early smithsonite (Sm1), replaced by spongy hydrozincite (Hyd1); sample ZB-3. E. Hemimorphite-rich gossanous material covered by crusts of concretionary hydrozincite (Hyd3) and manganous (hydr)oxides (mostly ranciéite); sample ZA-0. F. Concretionary calcite growing on a goethite-impregnated material; sample ZA-9.

Polished thin sections were prepared for optical microscopy (OM), scanning electron microscopy with energy dispersive X-ray spectroscopy (SEM-EDS), and wavelength dispersion spectrometry (full WDS) studies. Portions of the samples were crushed and pulverized for mineralogical X-ray powder diffraction (XRPD) and wall-rock chemical analyses.

SEM observations were carried out with a JEOL JSM5310 at the Dipartimento di Scienze della Terra, dell'Ambiente e delle Risorse (DiSTAR), Università degli Studi di Napoli Federico II, Italy. Analytical conditions were the following: 20-mm objective lens to specimen working distance, and 15-kV accelerating voltage with a tilt angle of 0°. Element mapping and qualitative EDS investigations were carried out with an INCA X-stream pulse processor and the 4.08 version Inca software (Oxford Instruments detector), interfaced with the Jeol JSM 5310. Reference standards used for quantitative microanalysis were the following: albite (Si, Al, Na), orthoclase (K), wollastonite (Ca), diopside (Mg), almandine (Fe), rutile (Ti), barite (Ba), strontianite (Sr), eskolaite (Cr), rhodonite (Mn), pyrite (S), sphalerite (Zn), galena (Pb), pure silver (Ag), arsenopyrite (As), fluorite (F), apatite (P), sylvite (Cl), pure vanadium (V), and Corning glass (Th, U). Analytical errors are 1% relative for major elements and 3% relative for minor elements. Quantitative data sets of selected samples were obtained by full WDS, using a Cameca SX50 electron microprobe operating at 15-kV, 15-nA, and 10- μ m spot size at the Natural History Museum, London, UK. WDS detection limits for each element are mostly on the order of 0.01 wt %.

X-ray powder diffraction (XRPD) semiquantitative analyses on outcrop samples were performed with X'Pert PRO diffractometer by PANalytical at the Istituto Nazionale di Geofisica e Vulcanologia-Osservatorio Vesuviano, Napoli, Italy, with a high-speed PIXcel detector, Ni-filtered, CuK α radiation, pyrolytic graphite crystal monochromator, at 40 kV and 40 mA in a 3 to 70° 2 θ range with 0.02° steps at 8 s/step. Diffraction patterns were interpreted using the HighScore Plus software and JCPDS PDF-2 database. Whole-rock chemical analyses of major (Zn, Fe, Ca, Mg, Si, Al, Na, K, P, Mn) and minor elements (Mo, Cu, Pb, Ni, Co, As, U, Th, Sr, Cd, Sb, V, La, Cr, Ba, Sc, Ti, Se, Ga, Ge, Rb, Sn, Zr, Y, Ce, Li in ppm, and Au, Ag, Hg in ppb) were carried out at Bureau Veritas Commodities Canada Ltd., Vancouver, Canada, on identical powder splits to those used for XRPD analyses. In each case, 10 g of pulp was used for chemical analysis on the LF725 package (fusion/X-ray fluorescence spectroscopy (XRF)). Samples with high Zn (greater than 24%) were run for overlimits with the LF726 package. Minor elements were analyzed by using the AQ250-EXT (ultratrace aqua regia/ICP-AES and MS) package, except Ga and Ge, which were analyzed using the GC204-Ge and Ga package.

Both geologic and geochemical models were generated using the Rockworks/15 software (RockWare).

Carbon and oxygen isotope analyses were performed on the Toarcian dolomitized limestone of the Condorsinga Formation hosting the mineralization, on calcite veins, hostrock replacement smithsonites, and on several specimens of hydrozincite, smithsonite, and supergene calcite. Stable isotope analyses were carried out at the University of Erlangen-Nuremberg, Germany. Pure carbonate minerals (concretionary

calcite and hydrozincite, fracture-filling calcite, smithsonite and host-rock dolomite and calcite) were isolated by handpicking. Powdered samples were allowed to react for at least 36 h with phosphoric acid at 70°C, using a GasBench II connected to a ThermoFinnigan Five Plus isotope ratio mass spectrometer. The acid fractionation factor of the hydrozincite has not yet been determined and we used the closest acid fractionation factor of smithsonite (Gilg et al., 2008). Carbon and oxygen isotope values are reported relative to the Vienna Pee Dee belemnite (VPDB) and Vienna standard mean ocean water (VSMOW), respectively, by assigning a $\delta^{13}\text{C}$ value of +1.95‰ and a $\delta^{18}\text{O}$ value of -2.20‰ to standard NBS19. Reproducibility, determined by replicate analysis of laboratory standards, was better than $\pm 0.07\text{‰}$ (1σ) for both carbon and oxygen isotope analyses. Oxygen isotope values were corrected using the phosphoric acid fractionation factors given by Kim et al. (2007), Rosenbaum and Sheppard (1986) for dolomite, and by Gilg et al. (2008) for smithsonite.

Two water samples, one from the Cristal river (RCM) and one from a tributary (RC-T), were collected for the oxygen isotope analyses of surface waters. The water samples were analyzed in duplicate for $\delta^{18}\text{O}$ by an automated equilibration unit (Gasbench II) in continuous flow mode coupled to a ThermoFisher Delta Plus XP isotope ratio mass spectrometer. All values are reported in the standard delta notation (‰) versus Vienna Standard Mean Ocean (VSMOW). Data were normalized to the VSMOW/SLAP (standard light Antarctic precipitation) scale by assigning a value of 0 and -55.5‰ ($\delta^{18}\text{O}$) to VSMOW2 and SLAP2, respectively (Brand et al., 2014). For normalization, two laboratory standards, calibrated directly against VSMOW2 and SLAP2, were measured in each run. The external reproducibility based on repeated analyses of a control sample was better than 0.1‰ ($\pm 1\sigma$) for $\delta^{18}\text{O}$.

Ore mineralogy and petrography

XRPD analyses show that hydrozincite is the most abundant ore mineral in the analyzed materials (Table 3.1), with the highest amounts (>60 wt %) measured in samples ZA-6 and ZA-7. Hydrozincite is generally associated with hemimorphite (samples ZA-0, ZA-1, ZA-5, ZA-6, and ZB-2) and minor smithsonite (samples ZA-3 and ZA-5), which is abundant in only one sample (40-60 wt % in sample ZB-3). Calcite and dolomite were detected in fragments of the host rock (samples ZA-2, ZA-4, ZA-8, ZB-1, ZB-T1, and ZB-T2), and in concretionary samples (e.g., sample ZA-9). Otavite (CdCO_3) is rare (samples ZA-5 and ZA-6). Goethite is ubiquitous, whereas traces of Mn-(hydr)oxides have been detected in sample ZA-0. Samples ZB-1 and ZB-2 consist mostly of quartz and silicate minerals (e.g., mica group minerals and fraipontite).

Remnants of pyrite occur in drill core samples ZB-T1 and ZB-T2, together with traces of barite and celestite. Chemical compositions of the Zn-bearing nonsulfide minerals, obtained from EDS and WDS analyses, are reported in Tables 3.2, 3.3, 3.4 and 3.5.

TABLE 3.1. Bulk mineralogy of the Mina Grande samples, deduced from semiquantitative XRPD analyses.

Sample ID	Py	Dol	Cal	Sm	Otv	Hyd	Qz	Ms	Frp	Hm	Brt	Clt	Ap	Gth	Rac
ZA-0	-	-	-	-	-	XXXX	-	-	-	XXXX	-	-	-	-	X
ZA-1	-	-	-	-	-	XX	-	-	-	XXXXXX	-	-	-	-	-
ZA-2	X	-	XXXXX	-	-	-	-	-	-	-	X	X	-	X	-
ZA-3	-	-	-	XXX	-	XXXX	-	-	-	-	-	-	-	X	-
ZA-4	-	-	XXXXX	-	-	-	-	-	-	-	X	-	-	X	-
ZA-5	-	-	-	XX	X	XXXX	-	-	-	XXX	-	-	-	X	-
ZA-6	-	-	-	-	X	XXXX	-	-	-	XX	-	-	-	XX	-
ZA-7	-	-	-	-	-	XXXXX	-	-	-	-	-	-	-	-	-
ZA-8	-	XXXXX	-	-	-	-	-	-	-	-	-	-	-	X	-
ZA-9	-	-	XXXXX	-	-	X	-	-	-	X	-	-	-	X	-
ZB-1	-	XX	XX	-	-	XXX	-	XX	XX	-	-	-	-	-	-
ZB-2	-	-	-	-	-	XXXX	XX	XX	XX	XXX	-	-	-	-	-
ZB-3	-	-	-	XXXXX	-	XXX	-	-	-	-	-	-	-	-	-
ZB-T1	X	XXX	XXX	-	-	-	-	-	-	-	-	X	-	-	-
ZB-T2	XX	-	XXXX	-	-	-	XX	-	-	-	-	XX	X	XX	-

Note: Py, pyrite; Dol, dolomite; Cal, calcite; Sm, smithsonite; Otv, otavite; Hyd, hydrozincite; Qz, quartz; Ms, mica group minerals; Frp, fraipontite; Hm, hemimorphite; Brt, barite; Clt, celestine; Ap, apatite; Gth, goethite; Rac, rancieite (mineral abbreviations after Whitney and Evans, 2010). "-" not found; x < 5 wt%; 5 wt% < xx < 20 wt%, 20 wt% < xxx < 40 wt%, 40 wt% < xxxx < 60 wt%, xxxxx > 60 wt%.

Hydrozincite occurs with textures from compact to spongy, and to needle-shaped in concretions. Spongy hydrozincite (Hyd1, Table 3.2) is the most common and abundant type occurring together with goethite (Fig. 3.8A). Compact hydrozincite (Hyd2) forms veinlets cutting spongy hydrozincite (Fig. 3.7A), but also occurs as zoned crusts in fractures and cavities (Fig. 3.8A, B). Needle-shaped hydrozincite (Hyd3) was the latest hydrozincite to form. It typically occurs as aggregates of fine crystals in the concretionary samples (Fig. 3.7B) and on the surface of cavities carved in smithsonite, dolomite, and Zn/Cd-bearing calcite (Fig. 3.8C, D).

TABLE 3.2. Chemical composition (EDS) and structural formulae (apfu) of hydrozincite from Mina Grande deposit.

Sample ID	ZA-3	ZA-4	ZA-5	ZA-5	ZA-5	ZA-7
Mineral phase	Hyd1	Hyd1	Hyd1	Hyd1	Hyd2	Hyd3
wt. %						
FeO	0.14	3.11	0.07	0.15	N.D.	N.D.
MnO	0.11	N.D.	0.14	0.16	N.D.	0.26
MgO	0.05	0.14	0.12	0.38	0.11	N.D.
CaO	N.D.	N.D.	N.D.	0.24	0.18	0.21
PbO	0.49	0.21	0.88	N.D.	0.42	N.D.
ZnO	74.99	71.06	71.74	74.01	72.90	73.71
CdO	0.16	0.42	N.D.	N.D.	N.D.	N.D.
CuO	0.44	N.D.	N.D.	0.14	N.D.	N.D.
CO ₂ ¹	16.44	16.30	15.68	16.34	15.90	16.07
H ₂ O ¹	10.09	10.00	9.62	10.03	9.76	9.86
TOTAL	102.91	101.24	98.25	101.45	99.26	100.12
on the basis of (CO ₃) ₂ (OH) ₆						
Fe	0.01	0.23	0.01	0.01	-	-
Mn	0.01	-	0.01	0.01	-	0.02
Mg	0.01	0.02	0.02	0.05	0.01	-
Ca	-	-	-	0.02	0.02	0.02
Pb	0.01	0.00	0.02	-	0.01	-
Zn	4.93	4.71	4.95	4.90	4.96	4.96
Cd	0.01	0.03	-	-	-	-
Cu	0.02	-	-	0.01	-	-

Note: Hyd1 = spongy hydrozincite; Hyd2 = compact hydrozincite; Hyd3 = needle-shaped hydrozincite; ¹Calculated from stoichiometry: "N.D." not detected and "-" not determined

Two generations of hemimorphite have been observed (Table 3.3). The early phase (Hm1) is fairly abundant and fills fractures in the footwall together with spongy hydrozincite (Hyd1). In siliciclastic layers, it also occurs as cement of detrital quartz fragments (Fig. 3.8E) in association with aluminosilicates, such as mica group minerals and fraipontite (Figs. 3.7C, 3.8F).

TABLE 3.3. Chemical composition (EDS) and structural formulae (apfu) of hemimorphite from Mina Grande deposit.

Sample ID	ZB-2	ZB-2	ZA 9	ZA-5	ZB-2	ZB-2
Mineral phase	Hm1	Hm1	Hm1	Hm1	Hm2	Hm2
wt. %						
FeO	1.00	0.08	0.11	0.40	N.D.	N.D.
CaO	N.D.	N.D.	0.71	N.D.	0.15	N.D.
ZnO	66.18	66.83	66.08	69.54	66.69	67.87
SiO ₂	25.58	25.49	24.53	24.16	26.12	25.97
H ₂ O ¹	7.55	7.52	7.39	7.49	7.61	7.64
TOTAL	100.31	99.91	98.82	101.59	100.57	101.48
on the basis of O ₇ (OH) ₂						
Fe	0.07	0.01	0.01	0.03	-	-
Ca	-	-	0.06	-	0.01	-
Zn	3.88	3.93	3.95	4.11	3.88	3.93
Si	2.03	2.03	1.99	1.93	2.06	2.04

Note: Hm1 = early hemimorphite; Hm2 = late hemimorphite; ¹Calculated from stoichiometry: "N.D." not detected and "-" not determined

Late hemimorphite (Hm2) consists of fan-shaped aggregates of platy crystals (Fig. 3.9A, B), and fills open spaces both in spongy hydrozincite, Hyd1 (Fig. 3.7C), and in goethite-rich earthy-looking material.

Two distinct smithsonite phases have been detected at Mina Grande (Table 3.4): early (Sm1) and late (Sm2) smithsonites. The early smithsonite generally replaces the host rock (Fig. 3.7D) and is replaced in turn by spongy hydrozincite, Hyd1 (Fig. 3.8G). Late smithsonite (Sm2) occurs as crustiform layers alternated with compact hydrozincite, Hyd2 (Figs. 3.7D, 3.8H, 3.9C, D). Sm2 fills vugs in the Zn-bearing calcite but is not associated with Cd calcite (Fig. 3.8C, I).

The cadmium carbonate otavite has been detected (Table 3.4) as scattered spots on the Fe-(hydr)oxides (Fig. 3.10A). It also fills vugs and fractures in early hemimorphite, Hm1 (Fig. 3.10B). Rare descloizite crystals occur within spongy hydrozincite (Fig. 3.10C).

The Fe-(hydr)oxides, consisting mostly of goethite, are relatively abundant in all samples. Fe-(hydr)oxides replace pyrite/ marcasite crystals locally, or form concretionary aggregates associated with all smithsonite and hydrozincite generations. Fe-(hydr)oxides are also detected as vein fillings cutting dolomite and calcite (Fig. 3.10D). Fe-(hydr)oxides have variable compositions, with iron ranging between 45 and 75 wt % FeO, and they also contain SiO₂ and Al₂O₃ with concentrations varying between 0.2 and 5 wt % (max 10 wt % SiO₂ and 6.5 wt % Al₂O₃). Zinc concentrations in Fe-(hydr)oxides commonly range between 0.2 and 15 wt % ZnO, rarely reaching 25 wt % ZnO (sample ZA-5A). Lead contents in Fe-(hydr)oxides vary between 0.1 and 13 wt % PbO. Mn-(hydr)oxides (possibly consisting of ranci  ite; Figs. 3.7E, 3.10E) contain variable proportions of Mn, Pb, Zn, and Fe (~20-34 wt %; MnO; ~13-29 wt % PbO; ~7-23 wt % ZnO; ~2-10 wt % FeO).

Calcite, the main component of the carbonate host rock (HR Cal), is locally replaced by saddle dolomite (Dol). Saddle dolomite contains manganese and iron (below 3 wt % MnO and ~1 wt % FeO) and is commonly replaced by early smithsonite, Sm1 (Fig. 3.10F). Sparry calcite occurs also as vein fillings (FF Cal) in both limestone and dolomite host rocks, and as concretions (CC Cal; Fig. 3.7F) associated with the Zn oxide minerals in karsts, as well as festooning recent solution cavities (Fig. 3.9E, F). Concretionary calcite (CC Cal) may be chemically zoned, with alternating zinc- and cadmium-rich bands (Fig. 3.8C; Table 3.4). Some calcite layers are also interbedded with compact hydrozincite (Hyd2; Fig. 3.9E, F)

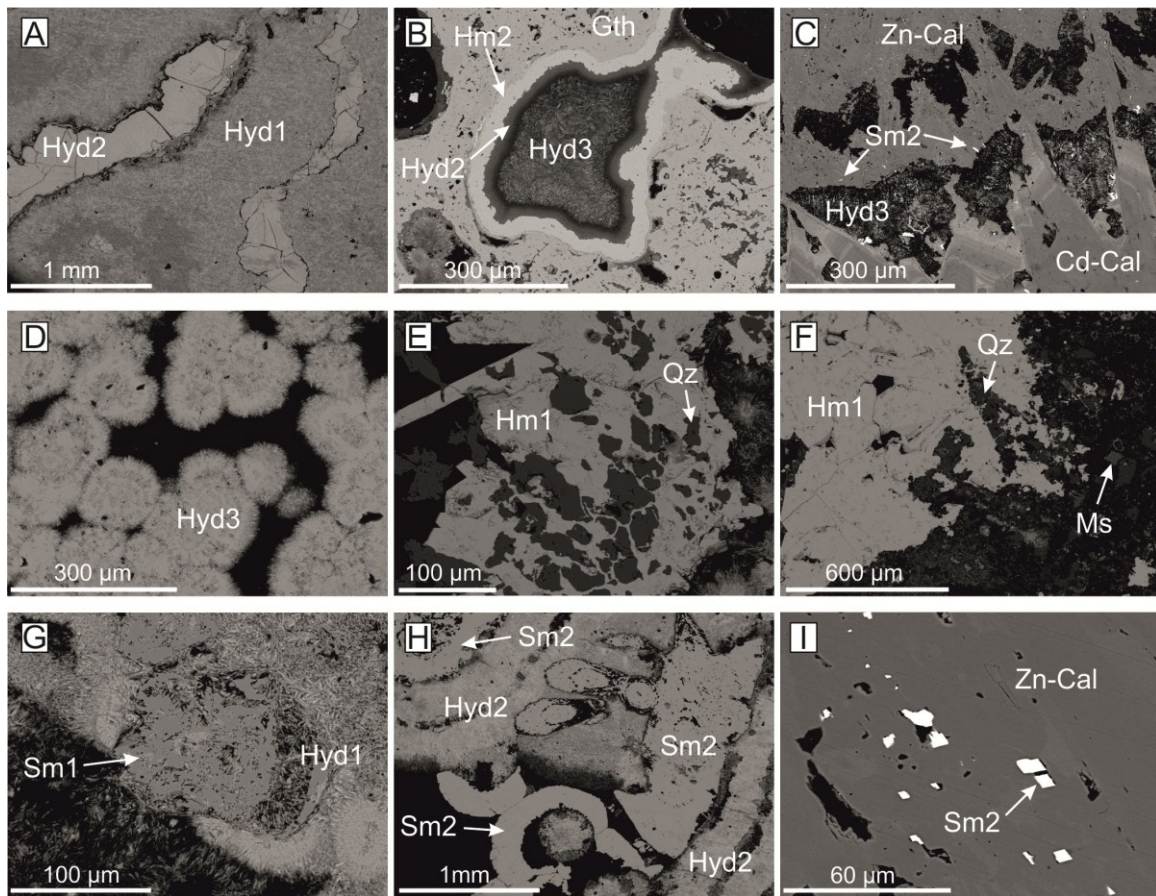


Figure 3.8. Backscattered electron images (BSE) of the most common Zn-bearing nonsulfide minerals. A. Compact hydrozincite (Hyd2) filling microcavities in the spongy variety (Hyd1); sample ZA-5. B. Crusts of late hemimorphite (Hm2) on the rim of goethite-rich zones (Gth), precede a layer of compact hydrozincite (Hyd2). Needle-shaped hydrozincite (Hyd3) fills the cavity; sample ZA-6. C. Needle-shaped hydrozincite (Hyd3) fills vugs into Cd- and Zn-rich layers of concretionary calcite with smithsonite (Sm2) remnants; sample ZA-9. D. Concretionary aggregates of needle-shaped hydrozincite (Hyd3); sample ZA-7. E. Early hemimorphite (Hm1) cementing quartz fragments; sample ZB-2. F. Early hemimorphite (Hm1) occurring in association with quartz (Qz) and muscovite (Ms) fragments; sample ZB-2. G. Spongy hydrozincite (Hyd2) replaces early smithsonite (Sm1); sample ZA-3. H. Crustiform layers of late smithsonite (Sm2) and compact hydrozincite (Hyd2); sample ZB-3. I. Late smithsonite (Sm2) filling vugs in Zn-rich concretionary calcite; sample ZA-2.

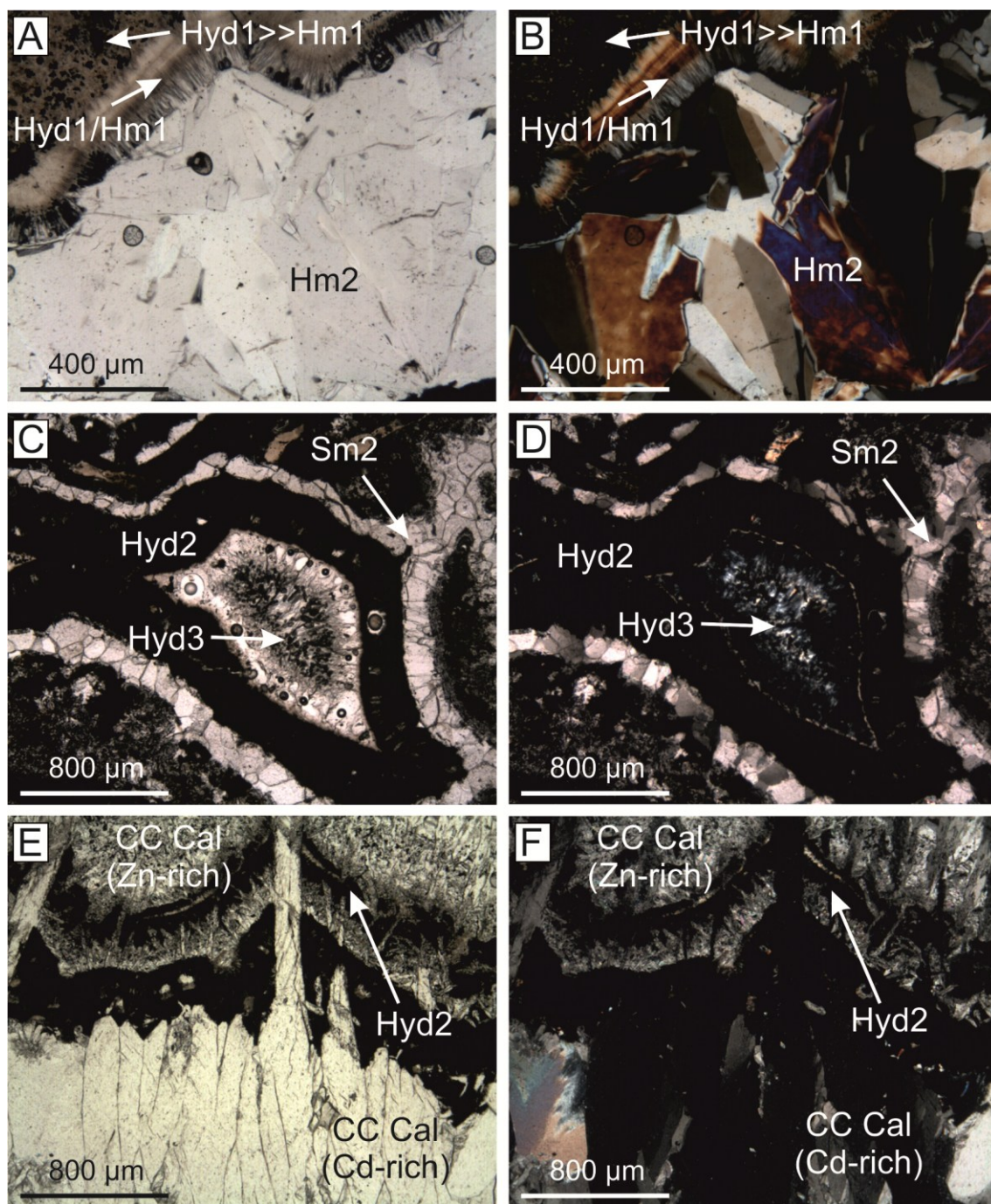


Figure 3.9. Textures of hemimorphite, smithsonite, and calcite in thin sections. A, B. Fan-shaped aggregates of platy hemimorphite crystals filling fracture in spongy hydrozincite (Hyd1)/early hemimorphite (Hm1) mixture; sample ZB-2 (N II, N+). C, D. Crustiform layers of late smithsonite (Sm2) alternated with compact hydrozincite (Hyd2). Needle-shaped hydrozincite fills final porosity; sample ZB-3 (N II, N+). E, F. Compact hydrozincite (Hyd2) interbedded with Cd- and Zn-rich layers of concretionary calcite (CC Cal); sample ZA-9 (N II, N+).

TABLE 3.4. Chemical composition and structural formulae (apfu) of smithsonite (EDS), concretionary calcite (WDS) and otavite (EDS) from the Mina Grande deposit.

	Smithsonite						Concretionary calcite				Otavite	
Sample ID	ZA-6	ZB-3	ZB-3	ZA-5	ZB-3	ZB-3	ZA-9	ZA-9	ZA-9	ZA-9	ZA-6	ZA-5
Mineral phase	Sm1	Sm1	Sm1	Sm2	Sm2	CC Cal	CC Cal	CC Cal	CC Cal	CC Cal	Otv	Otv
wt. %												
FeO	1.30	0.35	0.18	0.07	N.D.	N.D.	N.D.	N.D.	0.13	N.D.	N.D.	0.17
MgO	0.20	0.19	0.33	0.30	N.D.	0.22	0.04	0.04	0.10	0.12	N.D.	N.D.
CaO	0.57	0.10	1.36	0.20	0.04	0.10	55.45	54.69	48.97	53.83	1.14	7.28
PbO	0.16	0.19	N.D.	0.05	0.83	0.41	N.D.	N.D.	N.D.	N.D.	N.D.	N.D.
ZnO	62.72	64.46	61.45	65.02	63.90	63.12	0.51	2.46	3.03	2.10	6.69	2.57
CdO	N.D.	0.17	0.28	0.14	0.14	N.D.	N.D.	N.D.	4.66	0.77	64.17	60.79
CuO	0.16	0.45	0.22	0.27	N.D.	N.D.	N.D.	N.D.	N.D.	0.21	1.10	0.23
CO ₂ ¹	35.49	35.69	34.97	35.88	34.79	34.52	43.83	44.28	41.84	43.88	27.11	28.16
TOTAL	100.59	101.60	98.78	101.93	99.70	98.38	99.83	101.47	98.74	100.92	100.21	99.20
on the basis of CO ₃												
Fe	0.02	0.01	0.00	0.00	-	-	-	-	0.00	-	-	0.00
Mg	0.01	0.01	0.01	0.01	-	0.01	0.00	0.00	0.00	0.00	-	-
Ca	0.01	0.00	0.03	0.00	0.00	0.00	0.99	0.97	0.92	0.96	0.03	0.20
Pb	0.00	0.00	-	0.00	0.00	0.00	-	-	-	-	-	-
Zn	0.96	0.98	0.95	0.98	0.99	0.99	0.01	0.03	0.04	0.03	0.13	0.05
Cd	-	0.00	0.00	0.00	0.00	-	-	-	0.04	0.01	0.81	0.74
Cu	0.00	0.01	0.00	0.00	-	-	-	-	-	0.00	0.02	0.00

Note: Sm1 = host rock-replacing smithsonite; Sm2 = concretionary smithsonite; CC Cal = concretionary calcite; Otv = otavite; ¹Measured for calcite and calculated from stoichiometry for smithsonite and otavite; "N.D." not detected and "-" not determined

TABLE 3.5. Chemical composition and structural formulae (apfu) of Zn-bearing micas (see text) analysed in WDS, and fraipontite (EDS) from the Mina Grande deposit.

Sample ID	Micas					Fraipontite		
	ZB-2	ZB-2	ZB-2	ZB-2	ZB-2	ZB-1	ZA-3	ZB-2
wt. %								
SiO ₂	48.15	48.41	47.44	46.40	48.84	19.62	26.05	24.07
TiO ₂	0.91	0.15	0.09	0.15	0.05	N.D.	0.11	0.17
Al ₂ O ₃	25.37	26.14	24.93	25.67	23.31	22.63	10.42	19.99
Fe ₂ O ₃	1.04	1.53	2.29	1.06	2.37	0.41	13.93	1.89
MgO	2.89	2.96	3.35	2.64	3.77	0.07	0.42	0.24
K ₂ O	7.10	7.45	7.00	7.17	7.78	N.D.	0.65	0.66
ZnO	8.14	8.91	10.04	9.15	6.55	46.57	38.15	44.73
PbO	0.30	0.23	0.26	0.23	0.21	N.D.	N.D.	N.D.
H ₂ O ¹	4.29	4.36	4.30	4.21	4.26	9.77	9.89	10.23
TOTAL	98.19	100.15	99.70	96.67	97.14	99.08	99.62	101.97
		on the basis of O ₁₀ (OH) ₂				on the basis of O ₅ (OH) ₄		
Si	3.37	3.33	3.31	3.31	3.44	1.20	1.58	1.41
Al ^{IV}	0.63	0.67	0.69	0.69	0.56	0.80	0.42	0.59
Σ _{tetr}	4.00	4.00	4.00	4.00	4.00	2.00	2.00	2.00
Al ^{VI}	1.46	1.44	1.36	1.46	1.38	0.84	0.32	0.79
Ti	0.02	0.00	0.00	0.00	0.00	-	0.00	0.00
Fe	0.05	0.08	0.12	0.06	0.13	0.02	0.64	0.08
Mg	0.30	0.30	0.35	0.28	0.40	0.01	0.04	0.02
Zn	0.42	0.45	0.52	0.48	0.34	2.11	1.71	1.93
Pb	0.01	0.00	0.00	0.00	0.00	-	-	-
Σ _{oct}	2.26	2.29	2.35	2.29	2.24	2.97	2.70	2.83
K _{interlayer}	0.63	0.65	0.62	0.65	0.70	-	0.05	0.05

¹Calculated from stoichiometry; "N.D. not detected and "-" not determined

Sulfides are rare. Iron-rich sphalerite (~9 wt % Fe) was detected in a dolomite clast in a Sm-cemented karst breccia (Fig. 3.10F). Pyrite veins associated with celestite and barite have been found in drill core fragments of dolomitized host rock (Fig. 3.10G). Celestite has been found together with pyrite in the deepest drill core samples, and together with barite as scattered spots in calcite. Celestite is chemically zoned, with bands of low to high barium (<6 wt % BaO), whereas barite contains traces of strontium (<4 wt % SrO). Fraipontite (Table 3.5), a Zn-bearing phyllosilicate belonging to the kaolinite-serpentine group and detected in some outcrop samples (Fig. 7C), occurs with quartz, muscovite, and Zn-bearing mica (Fig. 10H, I), or as alteration rims around muscovite and Zn-bearing mica. Zn-bearing micas show chemical compositions between those of muscovite and the hydrothermal Zn-bearing mica hendricksite (Fig. 3.11; Table 3.5).

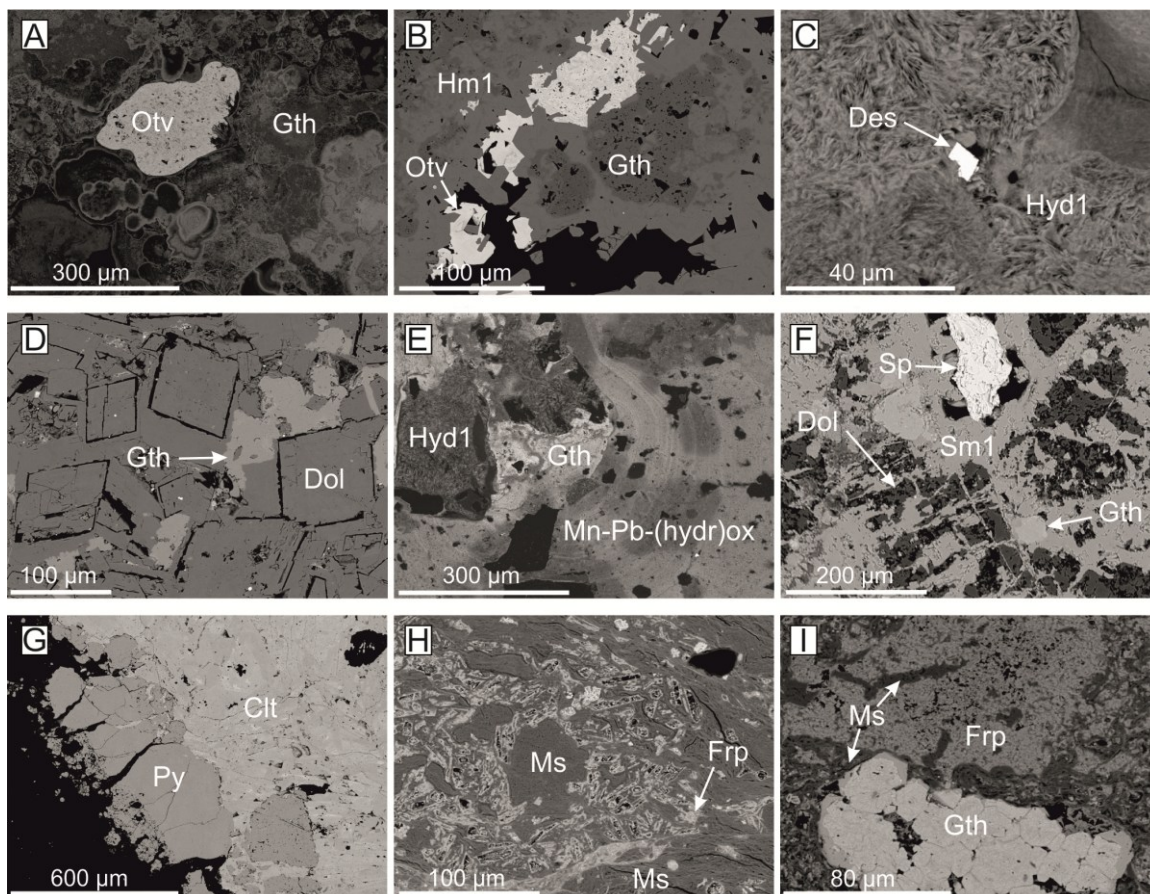


Figure 3.10. Backscattered electron images (BSE) of minor Zn-bearing minerals. A. Otavite (Otv) in goethite (Gth); sample ZA-5. B. Otavite (Otv) filling vugs in early hemimorphite (Hm1) associated with goethite (Gth); sample ZB-2. C. Descloizite (Des) crystal growing in spongy hydrozincite (Hyd1); sample ZA-5. D. Goethite veinlets (Gth) in the cement of saddle dolomite (Dol); sample ZB-T1. E. Concretions of Mn-Pb-(hydr)oxides and goethite growing around remnants of spongy hydrozincite (Hyd1); sample ZA-3. F. Sphalerite (Sp) remnant in a network of early smithsonite (Sm1), which replaces host-rock dolomite (Dol) along fractures; sample ZA-6. G. Pyrite growing on edges of a celestite vein (Clt); sample ZB-T2. H. Fraipontite (Frp) as alteration of Zn-bearing mica (Ms); sample ZB-2. I. Fraipontite (Frp) replacing Zn-bearing mica (Ms) in the groundmass; goethite (Gth) replaces euhedral pyrite; sample ZB-2.

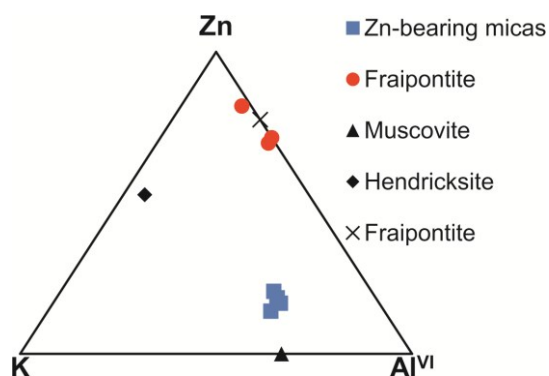


Figure 3.11. Zn-bearing aluminosilicates composition in the system Zn-K-AlVI, based on apfu calculated. Compositions of muscovite (triangle), hendricksite (diamond), and fraipontite (X) are from Deer et al. (1963), Evans and Strens (1966), and Cesàro (1927), respectively.

Major and minor elements geochemistry

Zinc concentrations (Table 3.6) of bulk ore samples generally range from 15 to 54 wt %. High zinc contents, between 50 and 54 wt %, have been measured in samples ZA-0, ZA-3, and ZB-3. The highest zinc contents (>60 wt %) were detected in sample ZA-7, which corresponds to a crust of concretionary hydrozincite. Dolostone (samples ZA-8 and ZB-T1) and limestone (samples ZA-2 and ZB-T1) show zinc amounts ranging from 0.3 to 2.6 wt %, which are mostly related to the zinc content of supergene calcite veinlets. On average, iron concentrations vary between 0.1 and 8 wt %, except in sample ZA-6 where iron reaches 33 wt %. Silica contents range from 0 to 16 wt % SiO₂, reaching a maximum value of 26.4 wt % in sample ZB-1. Aluminum oxide, mostly contained in fraipontite and mica group minerals, is relatively low in all samples (from 0.1-1.5 wt % Al₂O₃), except in sample ZB-1 (~4 wt % Al₂O₃). Lead concentrations are low, generally ranging between 16 and 7,000 ppm. The highest lead value is in sample ZA-3 (7,287 ppm), which contains Mn-Pb-(hydr)oxides. Barium and strontium values are generally below 300 ppm, whereas cadmium can exceed 2,000 ppm.

The cadmium concentration is positively correlated with zinc content. All other analyzed elements (i.e., Mo, Sb, Rb, Th, Sn, etc.) rarely reach values higher than 10 ppm.

Stable isotope geochemistry of carbonate minerals and waters

The $\delta^{13}\text{C}$ and $\delta^{18}\text{O}$ values for the limestone (HR Cal) hosting the mineralization are between -1.5 and -4.0‰ VPDB and 22.5 and 24.2‰ VSMOW, respectively (Fig. 3.12; Table 3.7). Two samples of sparry calcite (FF Cal) from the veins cutting the host carbonates have $\delta^{18}\text{O}$ values around 22‰ VSMOW and $\delta^{13}\text{C}$ values close to 0‰ VPDB. Saddle dolomite (Dol) shows $\delta^{18}\text{O}$ values of about 23.0‰ VSMOW, and $\delta^{13}\text{C}$ values of 0.1‰ VPDB in sample ZB-T1 and 2.4‰ VPDB in sample ZB-8 (Fig. 3.12; Table 3.7). The $\delta^{18}\text{O}$ composition of concretionary calcite (CC Cal) in karst cavities ranges from 24.0 to 24.9‰ VSMOW, and the $\delta^{13}\text{C}$ values are relatively low, ranging from -9.5 to -14.2‰ VPDB (Fig. 3.12; Table 3.7). The $\delta^{18}\text{O}$ composition of early smithsonite (Sm1) is between 26.9 and 27.2‰ VSMOW, with an average value of 26.9‰ VSMOW. In contrast, the $\delta^{13}\text{C}$ values of smithsonite (Sm1) show large variations, ranging from -7.8 to -12.5‰ VPDB. Late generation concretionary smithsonite (Sm2) has $\delta^{18}\text{O}$ values slightly lower than those of early smithsonite, varying between 26.0 and 26.3‰ VSMOW, with $\delta^{13}\text{C}$ values ranging from -8.1 to -12.9‰ VPDB, comparable to those of the early smithsonite (Sm1). Hydrozincite oxygen isotope ratios vary between 22.2 and 25.3‰ VSMOW (Fig. 3.12; Table 3.7). The $\delta^{18}\text{O}$ compositions of the spongy hydrozincite (Hyd1) are between 24.0 and 25.3‰ VSMOW, whereas $\delta^{18}\text{O}$ of compact (Hyd2) and needle-shaped hydrozincite (Hyd3) vary from 22.2 to 22.5 and from 23.6 to 23.7‰ VSMOW, respectively. A mixed phase containing small amounts of the three hydrozincites has a $\delta^{18}\text{O}$ value of 23.8‰ VSMOW and a $\delta^{13}\text{C}$ value of -9.0‰ VPDB. The $\delta^{13}\text{C}$ ratios are relatively lower than those of smithsonite, being between -4.1 and -

17.0‰ VPDB. The low $\delta^{13}\text{C}$ value of -4.1‰ of sample ZB-1, compared with those of the other hydrozincites, is explained by a contribution of host-rock calcite (Fig. 3.12).

River waters sampled in the Rio Cristal (RC-M) and from one of its tributaries (RC-T) have similar average $\delta^{18}\text{O}$ compositions: -8.5 and -7.9‰ VSMOW, respectively (Table 3.7)

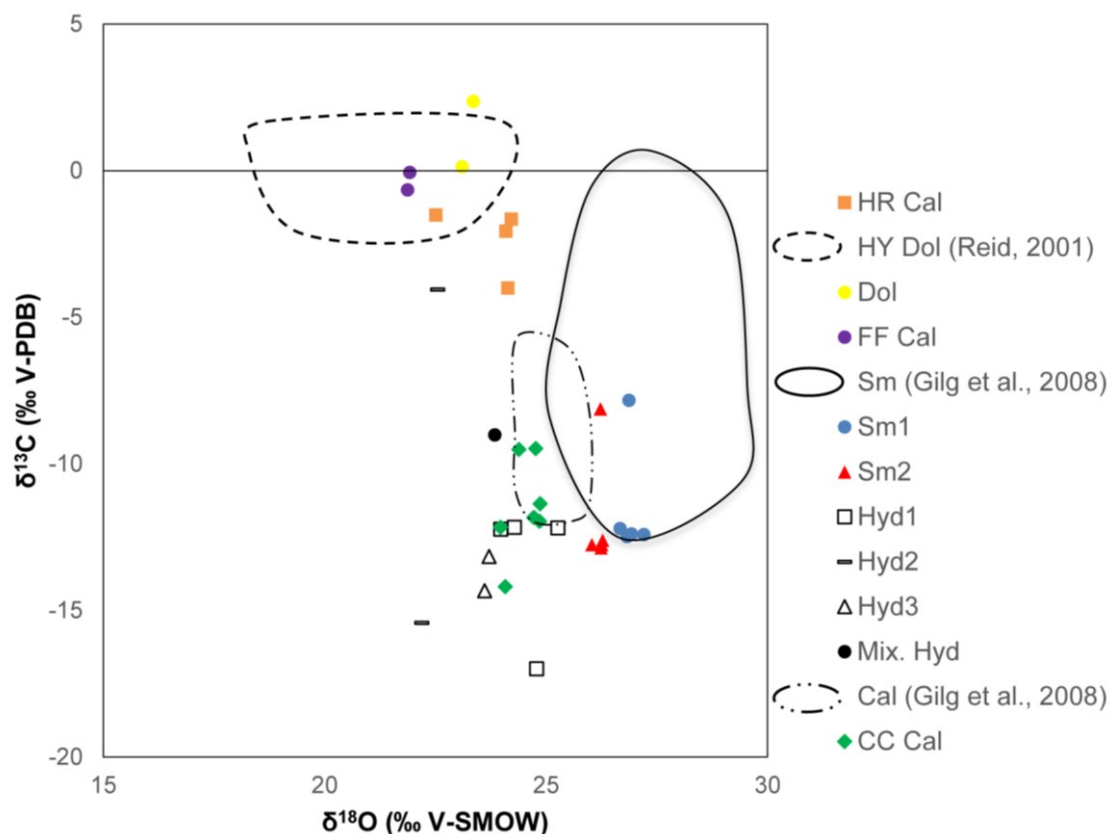


Figure 3.12. $\delta^{13}\text{C}$ and $\delta^{18}\text{O}$ values of carbonate minerals at Mina Grande, and comparison with published isotope values. Cal = supergene calcite in Zn nonsulfide deposits field (Gilg et al., 2008); CC Cal = concretionary calcite; Dol = saddle dolomite; FF Cal = fracture filling calcite paragenetically following sphalerite (Reid, 2001); HR Cal = host rock calcite; HY Dol = hydrothermal dolomite in the Bongará district (Reid, 2001); Hyd1 = spongy hydrozincite; Hyd2 = compact hydrozincite; Hyd3 = needle-shaped hydrozincite; Mix. Hyd = mixture of Hyd1, 2, and 3; Sm = supergene smithsonite field (Gilg et al., 2008); Sm1 = host-rock replacive smithsonite; Sm2 = concretionary smithsonite.

TABLE 3.6. Major (wt.%), minor and trace (ppm and ppb) element concentrations in the samples from the Mina Grande deposit.

	Sample ID	ZA-0	ZA-1	ZA-2	ZA-3	ZA-4	ZA-5	ZA-6	ZA-7	ZA-8	ZA-9	ZB-1	ZB-2	ZB-3	ZB-T1
Wt. %	MDL (Minimum Detection Limit)														
SiO ₂	0.01	13.49	13.20	0.81	8.02	0.16	3.84	2.09	<0.01	<0.01	0.43	26.43	16.68	0.48	3.55
Al ₂ O ₃	0.01	1.66	1.16	0.40	3.03	0.08	0.64	0.18	<0.01	0.03	0.26	16.85	6.09	0.25	0.86
MgO	0.01	0.09	5.88	0.30	0.26	0.79	1.47	0.06	<0.01	21.26	0.10	1.44	0.44	0.04	9.49
Fe ₂ O ₃	0.01	3.24	5.29	3.95	4.59	2.32	12.39	47.47	0.19	1.16	3.39	3.75	1.91	0.42	1.91
CaO	0.01	0.05	9.50	50.83	0.24	50.84	2.08	0.13	0.65	30.24	52.02	10.38	0.15	0.31	40.33
Na ₂ O	0.01	0.60	0.45	<0.01	0.50	0.03	0.49	0.33	0.46	<0.01	0.01	0.22	0.43	0.47	<0.01
K ₂ O	0.01	0.26	0.27	0.09	0.13	0.01	0.08	<0.01	<0.01	<0.01	0.06	3.07	1.07	0.08	0.21
MnO	0.01	0.14	0.31	0.14	0.43	0.11	0.24	0.04	<0.01	0.14	0.12	0.02	0.13	0.03	0.1
P ₂ O ₅	0.01	0.06	0.06	0.03	0.03	<0.01	0.04	0.01	<0.01	<0.01	0.01	0.15	0.11	0.02	0.07
LOI	-5.11	16.23	21.85	40.60	21.74	42.01	23.16	17.29	26.30	46.53	41.73	16.16	16.15	32.96	42.11
Zn	0.1	52.50	34.40	1.33	50.10	2.56	45.30	26.30	>60	0.34	1.30	15.63	47.10	54.20	0.42
ppm															
Mo	0.01	0.23	1.49	3.62	3.66	0.76	4.79	4.61	0.06	0.11	1.11	0.41	0.33	0.3	0.17
Cu	0.01	5.31	4.92	2.56	39.45	1.09	13.5	5.81	0.99	0.48	1.46	58.2	22.61	3.1	2.29
Pb	0.01	2163.08	492.78	73.95	7287.02	160	3275.34	2168.62	4218.01	18.5	15.57	3285.34	3771.52	2062.82	17.13
Ni	0.1	70.8	25.1	5.5	72.5	6.1	51.5	12.0	26.3	1.1	3.2	59.0	57.0	21.1	6.4
Co	0.1	1.2	1.5	2.2	3.7	1.0	2.5	0.7	<0.1	0.6	1.1	21.9	17.4	1.7	1.2
As	0.1	1.6	3.6	5.7	4.7	0.7	6.0	20.8	0.1	<0.1	1.5	13.8	5.2	1.2	0.7
U	0.1	0.2	0.7	0.4	2.2	0.2	0.9	1.0	0.2	0.2	0.3	0.2	0.3	1.0	0.1
Th	0.1	0.4	0.7	0.2	1.1	<0.1	0.3	0.1	<0.1	<0.1	0.1	1.7	0.9	0.2	0.3
Sr	0.5	10.2	25.9	261.3	186.1	180.2	19.4	6.1	2.6	69.3	241.4	55.5	3.9	4.6	129.2
Cd	0.01	394.08	>2000.00	32.29	346.52	465.32	1216.04	664.2	410.38	11.38	803.89	27.16	132.26	>2000.00	37.66
Sb	0.02	0.12	0.31	2.55	0.61	0.63	1.14	1.44	0.05	0.03	0.09	0.37	0.42	0.18	0.16
V	2	7	13	7	20	4	14	12	<2	5	3	58	23	3	10
La	0.5	3.7	2.5	0.6	34	0.7	2.3	0.8	108.2	<0.5	0.6	7.6	12.9	4.5	2.1
Cr	0.5	2.4	3.9	2.8	9.1	0.8	3.8	1.3	<0.5	0.8	1.2	8.8	4	1.8	2.3
Ba	0.5	14.7	222.4	38.2	35.3	171.9	41.5	14.9	4.2	13.7	293.6	11.5	12.5	4.2	58.2
Sc	0.1	1.0	1.2	0.9	1.2	0.5	0.8	0.4	0.1	0.2	0.8	10	4.4	0.7	1.0
Tl	0.02	1.01	1.01	0.58	2.94	0.53	1.22	0.49	0.05	0.03	0.25	0.61	0.56	0.07	0.32
Se	0.1	6.6	7.6	0.9	6	4.6	7.1	6.9	8	0.6	1.3	2.5	5.8	8.3	0.3
Ga	1	2	2	<1	14	<1	3	2	<1	<1	<1	16	7	<1	<1
Ge	1	3	10	<1	29	<1	13	4	<1	<1	<1	5	5	<1	<1
Rb	0.1	0.8	1.3	0.5	1.7	0.1	0.4	<0.1	<0.1	<0.1	0.4	6.1	2.5	0.4	1.2
Sn	0.1	0.1	0.3	0.2	1.9	<0.1	0.6	0.5	<0.1	<0.1	<0.1	0.8	0.4	0.1	<0.1
Zr	0.1	0.6	1.2	0.5	1.8	0.3	1.2	0.8	<0.1	0.2	0.5	1.2	0.8	0.5	0.5
Y	0.01	6.85	3.3	1.73	30.62	0.82	3.92	1.11	124.38	1.02	1.99	30.33	22.52	15.52	3.12
Ce	0.1	5.2	5	1.4	13.6	1.1	3.8	0.5	0.1	0.8	1.2	3.5	13.6	3.6	4.8
Li	0.1	0.4	0.9	0.3	2.7	<0.1	0.3	<0.1	<0.1	0.2	0.2	5.9	1.7	0.2	1.1
ppb															
Au	0.2	0.4	<0.2	0.7	0.7	0.2	<0.2	1.8	<0.2	1	<0.2	0.9	3.1	<0.2	<0.2
Ag	2	1496	1308	90	2447	24	1546	353	309	7	216	1288	964	312	9
Hg	5	38	52	8	281	8	77	99	<5	30	8	19	20	<5	31

TABLE 3.7. (a) Carbon and oxygen isotope compositions of dolomite, smithsonite, calcite and hydrozincite from the Mina Grande deposit; (b) oxygen isotope compositions of river waters from the Rio Cristal and its tributary.

(a) Rock samples				
Sample ID	Sub-sample ID	Mineral phase	$\delta^{13}\text{C}$ (‰ VPDB)	$\delta^{18}\text{O}$ (‰ VSMOW)
ZA-0	ZA-0_Hyd	Mix Hyd	-9.01	23.84
ZA-1	ZA-1_HydA	Hyd2	-15.42	22.20
	ZA-1_HydB	Hyd3	-14.33	23.61
ZA-2	ZA-2_CalA	HR Cal	-1.51	22.51
	ZA-2_CalB	CC Cal	-11.36	24.86
	ZA-2_CalC	CC Cal	-9.48	24.76
ZA-3	ZA-2_CalD	CC Cal	-9.51	24.39
	ZA-3_Hyd	Hyd1	-12.18	25.27
	ZA-4_CalA	HR Cal	-4.00	24.13
ZA-4	ZA-4_CalB	CC Cal	-11.96	24.85
	ZA-4_CalC	CC Cal	-11.82	24.73
	ZA-4_Hyd	Hyd1	-16.99	24.79
ZA-5	ZA5_SmA	Sm1	-7.83	26.87
	ZA5_SmB	Sm2	-8.13	26.22
ZA-6	ZA-6_Hyd	Hyd1	-12.23	23.98
ZA-7	ZA-7_Hyd	Hyd3	-13.15	23.71
ZA-8	ZA-8_Dol	Dol	2.37	23.35
	ZA-8_Cal	FF Cal	-0.65	21.87
ZA-9	ZA-9_CalA	CC Cal	-12.16	23.97
	ZA-9_CalB	CC Cal	-14.19	24.08
ZB-1	ZB-1_Cal	HR Cal	-1.65	24.22
	ZB-1_Hyd	Hyd2	-4.05	22.55
ZB-2	ZB-2_Hyd	Hyd1	-12.16	24.29
	ZB-3_SmA	Sm1	-12.21	26.67
	ZB-3_SmB	Sm1	-12.47	26.83
ZB-3	ZB-3_SmC	Sm1	-12.41	27.21
	ZB-3_SmD	Sm1	-12.39	26.93
	ZB-3_SmE	Sm2	-12.60	26.27
	ZB-3_SmF	Sm2	-12.76	26.04
	ZB-3_SmG	Sm2	-12.87	26.24
	ZB-3_SmH	Sm2	-12.76	26.26
ZB-T1	ZB-T1_Cal	HR Cal	-2.06	24.10
	ZB-T1_Dol	Dol	0.13	23.11
ZB-T2	ZB-T2_Cal	FF Cal	-0.06	21.92
(b) Water samples				
RC-M	RC-M_river	-	-	-8.84
RC-T	RC-T_river	-	-	-7.49

Note: Mix Hyd = mixed spongy, compact and needle-like hydrozincite; Hyd1 = spongy hydrozincite; Hyd2 = compact hydrozincite; Hyd3 = needle-shaped hydrozincite; HR Cal = hostrock-forming calcite; Dol = saddle dolomite; FF Cal = hydrothermal calcite; Sm1 = host rock-replacing smithsonite; Sm2 = concretionary smithsonite; CC Cal = concretionary calcite; RC-M = Rio Cristal river; RC-T = Rio Cristal tributary; "-" not determined

Discussion

Mineralogy and paragenetic sequence of the deposit inferred from isotopic geochemistry

The mineralogical and textural characteristics of the analyzed samples confirm that a hypogene sulfide mineralization originally occurred in the Mina Grande area, and preceded the deposition of nonsulfide supergene minerals (Fig. 3.13).

	HOST ROCK	HYDROTHERMAL ALTERATION AND MINERALIZATION	SUPERGENE MINERALIZATION
Host rock calcite (HR Cal)	—————		
Saddle Dolomite (Dol)		—————	
Celestine		—————	
Barite		—————	
Pyrite/marcasite		—————	
Sphalerite		—————	
Galena		—————	
Calcite (FF Cal)		—————	
Goethite			—————
Early smithsonite (Sm1)			—————
Early hemimorphite (Hm1)			—————
Spongy hydrozincite (Hyd1)			—————
Descloizite			—————
Otavite			—————
Concretionary calcite (CC Cal)			—————
Late hemimorphite (Hm2)			—————
Compact hydrozincite (Hyd2)			—————
Late smithsonite (Sm2)			—————
Needle-shaped hydrozincite (Hyd3)			—————
Mn-Pb-(Zn-Fe) hydroxides			—————
	Pleinsbachian-Toarcian	Post-Cretaceous/Early Tertiary ? (Reid, 2001; Basuki et al., 2006)	Late Miocene to Recent

Figure 3.13. Paragenesis and timing of the hydrothermal and supergene minerals in the Mina Grande deposit. Hm1 = hemimorphite after the first oxidation stage; Hyd1 = stage 1 hydrozincite after the first oxidation stage; Hm2 and Hyd2 = later hemimorphite and hydrozincite after the postoxidation stage 1; Sm1 = smithsonite of stage 1 replacing the host rock; Sm2 = concretionary smithsonite of oxidation stage 2.

The host limestone (HR Cal) of the Condorsinga Formation is patchily dolomitized by saddle dolomite (Dol) of clear hydrothermal origin (Radke and Mathis, 1980). HR Cal is also cut locally by calcite veins (FF Cal). Traces of sphalerite occur in between the crystals of saddle dolomite, and rare pyrite and galena are the only other sulfides. Hypogene barite and celestite have been observed as well. Carbon and oxygen isotope

ratios of saddle dolomite (Dol) and calcite veins (FF Cal) are similar to those reported by Reid (2001) for hydrothermal dolomite and calcite associated with the Florida Canyon Zn-Pb MVT deposit, which is considered to be Late Cretaceous in age (Reid, 2001; Basuki et al., 2008). This similarity suggests that the original hypogene mineralization at Mina Grande was a MVT deposit equivalent to other Zn-Pb sulfide bodies in the Bongará area. Fraipontite and Zn-bearing mica could have formed during the hydrothermal alteration of siltstone or sandstone interbedded with the host limestone, associated with the emplacement of sulfides. However, the genesis of these Zn-bearing aluminosilicates remains questionable, and more specific analyses are needed to discriminate if they are “hydrothermal” or “supergene”.

Supergene minerals formed at the expense of the hypogene mineral assemblage (Fig. 3.13). Smithsonite (Sm1), associated with hemimorphite (Hm1) and a first hydrozincite phase (spongy hydrozincite, Hyd1), precedes the deposition of concretionary calcite (CC Cal). CC Cal is accompanied by compact hydrozincite (Hyd2), a second generation of hemimorphite (Hm2), and by other trace minerals such as descloizite and otavite. Late concretions of smithsonite (Sm2) and needle-shaped hydrozincite (Hyd3), together with goethite and Mn-(hydr)oxides, fill cavities and the porosity of the previous assemblage. To firmly establish that the supergene minerals are derived from the hypogene mineralization in nonsulfide deposits, Mondillo et al. (2014) compared lead isotope compositions of hypogene galena and supergene minerals in the Yanque deposit (Peru). This comparison was not carried out in the Mina Grande deposit, because any attempt to isolate galena or sphalerite for lead isotope analysis was unsuccessful.

The isotopic compositions of Mina Grande smithsonite and calcite are similar to those measured on supergene smithsonites and calcites in other nonsulfide deposits worldwide (Gilg et al., 2008; Fig. 3.12). Therefore, both smithsonite and calcite are thought to have been precipitated by meteoric waters and groundwaters. Hydrozincite, smithsonite, and concretionary calcite show narrow $\delta^{18}\text{O}$ ranges, indicating relatively uniform isotopic compositions for the descending O_2 -rich meteoric water and comparable low temperatures during the precipitation of supergene minerals (Gilg et al., 2008). However, there are significant differences among the isotopic ratios of the various generations of supergene carbonates at Mina Grande. Early (Sm1) and late (Sm2) smithsonites have different $\delta^{18}\text{O}$ ratios (26.9-27.2 and 26.0-26.3‰ VSMOW, respectively), suggesting distinct oxidations of the deposit by distinct fluids. The average oxygen isotope ratios of spongy (Hyd1) and needle-shaped (Hyd3) hydrozincite (24.6 and 23.7‰ VSMOW, respectively) are relatively similar to that of concretionary calcite (CC Cal; 24.5‰ VSMOW). Since the fractionation factors of hydrozincite and calcite are different, they must have been formed at different temperatures during the oxidation process and/or from different fluids. Contrarily, the $\delta^{18}\text{O}$ values of compact hydrozincite (Hyd2) are low and do not overlap with those of concretionary calcites. Based on the oxygen isotope ratios, both the spongy and needle-shaped hydrozincites may have resulted from oxidations of early and late smithsonites, respectively, whereas compact hydrozincite may be linked to the formation of the calcite concretions.

The negative $\delta^{13}\text{C}$ composition of all generations of smithsonite, hydrozincite, and supergene calcite clearly indicates the prevailing contribution of isotopically light carbon derived from the oxidation of soil-derived carbon associated with microbial activity, as mentioned by Gilg et al. (2008) for other supergene nonsulfide deposits. However, a contribution of carbonate carbon from the host rock, with $\delta^{13}\text{C}$ values as low as -4‰ VPDB, is also possible.

Hitzman et al. (2003) and Brugger et al. (2003) reported that, at 25°C and quartz undersaturated, in the supergene environment hydrozincite is stable at lower log $f\text{CO}_{2(\text{gas})}$ than smithsonite (e.g., under atmospheric conditions with log $f\text{CO}_{2(\text{gas})} = -3.5$). Moreover, with an increase in pH from 6 to 8, the hydrozincite stability field increases and remains stable at low log $f\text{CO}_{2(\text{gas})}$. McPhail et al. (2003), Reichert and Borg (2008), and Reichert (2009) also reported the impossibility of precipitating smithsonite from a meteoric solution in equilibrium with geologically recent atmospheres, due to the low atmospheric $p\text{CO}_{2(\text{g})}$. In order to attain and maintain high $\text{CO}_{2(\text{g})}$ levels enabling smithsonite precipitation and preservation, it is necessary to have water-saturated environments and/or a deep supergene alteration. However, at the beginning of the oxidation process in a carbonate environment, acidic solutions are readily buffered and neutralized, and $\text{CO}_{2(\text{g})}$ is added to the system from dissolving the host rock. This increment results in a temporarily increase of the CO_2 partial pressure, which, if the availability of SiO_2 is low, can initiate smithsonite deposition (Reichert and Borg, 2008). If geochemical conditions are subsequently reequilibrated, i.e., the CO_2 partial pressure returns to atmospheric values, smithsonite is rapidly hydrated to form hydrozincite (Reichert, 2009). Further, hemimorphite may precipitate together with hydrozincite if SiO_2 is available in the system. At Mina Grande, the formation of two texturally and isotopically different smithsonites (Sm1 and Sm2), both replaced by several generations of isotopically different hydrozincite (Hyd1, Hyd2, and Hyd3), point to two distinct oxidation stages, each followed by a postoxidation phase. A reestablishment of the CO_2 partial pressure to near-present-day levels, coupled with repeated leaching events, typical of a humid environment, would have favored the transformation of smithsonite to hydrozincite.

Conditions at the time of supergene alteration

The climatic conditions responsible for the weathering regime and formation of the Mina Grande nonsulfide zinc deposit are strictly related to major events occurring in the western Amazonia basin from Oligocene to Present, when Andean deformation migrated toward the current Subandean zone and the rocks of the Pucará Group were repeatedly uplifted and eroded (Mora et al., 2010; Pfiffner and Gonzales, 2013). The geochemistry of the meteoric waters and the seasonality of hydrogeologic cycle characterizing the wet period of transition from Pebas to Acre systems from the middle to late Miocene were already comparable with the ecosystem currently affecting the Bongará area. If so, the humid climate in the study area was also characterized by several intervals of moderate precipitation (Kaandorp et al., 2005; Workman and Breede, 2016). In the Mina Grande area, these relatively dryer periods would have been limited to the intervals from May to October, during which Zn oxide minerals might have been easily precipitated. Thin

hydrozincite blankets, deposited on waste dumps during the last 10 years, clearly indicate that the mobilization and relatively rapid reprecipitation of zinc are still active under present-day atmospheric conditions.

As in several supergene nonsulfide deposits (Gilg et al., 2008), in the Mina Grande deposit smithsonite and calcite do not contain measurable fluid inclusions, and precipitation temperatures can be only estimated by considering the $\delta^{18}\text{O}$ composition of the ore-forming fluids, as well as the oxygen isotope ratios of calcite and smithsonite. The average 0.7‰ difference in $\delta^{18}\text{O}$ between early (Sm1) and late (Sm2) smithsonite may be explained by the precipitation of late smithsonite at slightly different temperatures, and/or by lower $\delta^{18}\text{O}$ values for late smithsonite-forming fluids during a distinctly late uplift stage. If we admit that (1) these supergene minerals precipitated from subsurficial paleogroundwaters, (2) it is difficult to know the exact $\delta^{18}\text{O}$ of the precipitating waters, and (3) the hydrologic cycle in this area of Peru has remained stable for the last 20 Ma (Kaandorp et al., 2005), we could assume that the oxygen isotope composition of paleogroundwaters was comparable to modern groundwaters. Considering that the Rio Cristal river is mostly supplied by subterranean groundwater (Brophy et al., 2012), the $\delta^{18}\text{O}$ composition of its water (-8‰ VSMOW) can be considered analogous to that of modern groundwater in the area, and can be used to estimate the precipitation temperature of supergene minerals. Since groundwater in carbonate terranes is recharged by direct infiltration, the isotope composition of contemporary groundwater commonly corresponds to that of the annual average incident precipitation (Gat, 1996). Taking into account that the oxygen isotope composition of rainwater is altitude-dependent, we used the $D\delta^{18}\text{O} = 0.24 \text{ ‰}/100 \text{ m}$ gradient for rainwater in the South American Andes (Poage and Chamberlain, 2001) to calculate the composition of the paleogroundwater at the probable time of supergene deposition, when the area was at a lower altitude than at the present time. The paleoelevation of the Mina Grande area was estimated on the basis of the paleoelevation model for the easternmost domains of the Andean Cordillera (Gregory-Wodzicki, 2000). From these calculations, we obtained the following $\delta^{18}\text{O}$ values of the paleogroundwater in the study area: (1) in late Oligocene-early Miocene (onset of the first main uplift stage) the Mina Grande area was at ~25% of the present altitude (2,100 m.a.s.l.), corresponding to an altitude of ~525 m.a.s.l., and $\delta^{18}\text{O}$ of paleogroundwaters is calculated as -4.2‰ VSMOW; (2) in middle to late Miocene (first increase of the uplift rates; ~14-10 Ma), the Mina Grande area was at ~50% of the current altitude, corresponding to an altitude of ~1,050 m.a.s.l., and the $\delta^{18}\text{O}$ value of the paleogroundwater can be estimated as -5.5‰ VSMOW; (3) in Pliocene-early Pleistocene (final stages of the main uplift; ~5- 2.5 Ma) the Mina Grande area reached its current altitude (avg 2,100 m.a.s.l.), and the $\delta^{18}\text{O}$ values of the paleogroundwater are assumed to be comparable to modern groundwater (~-8‰ VSMOW).

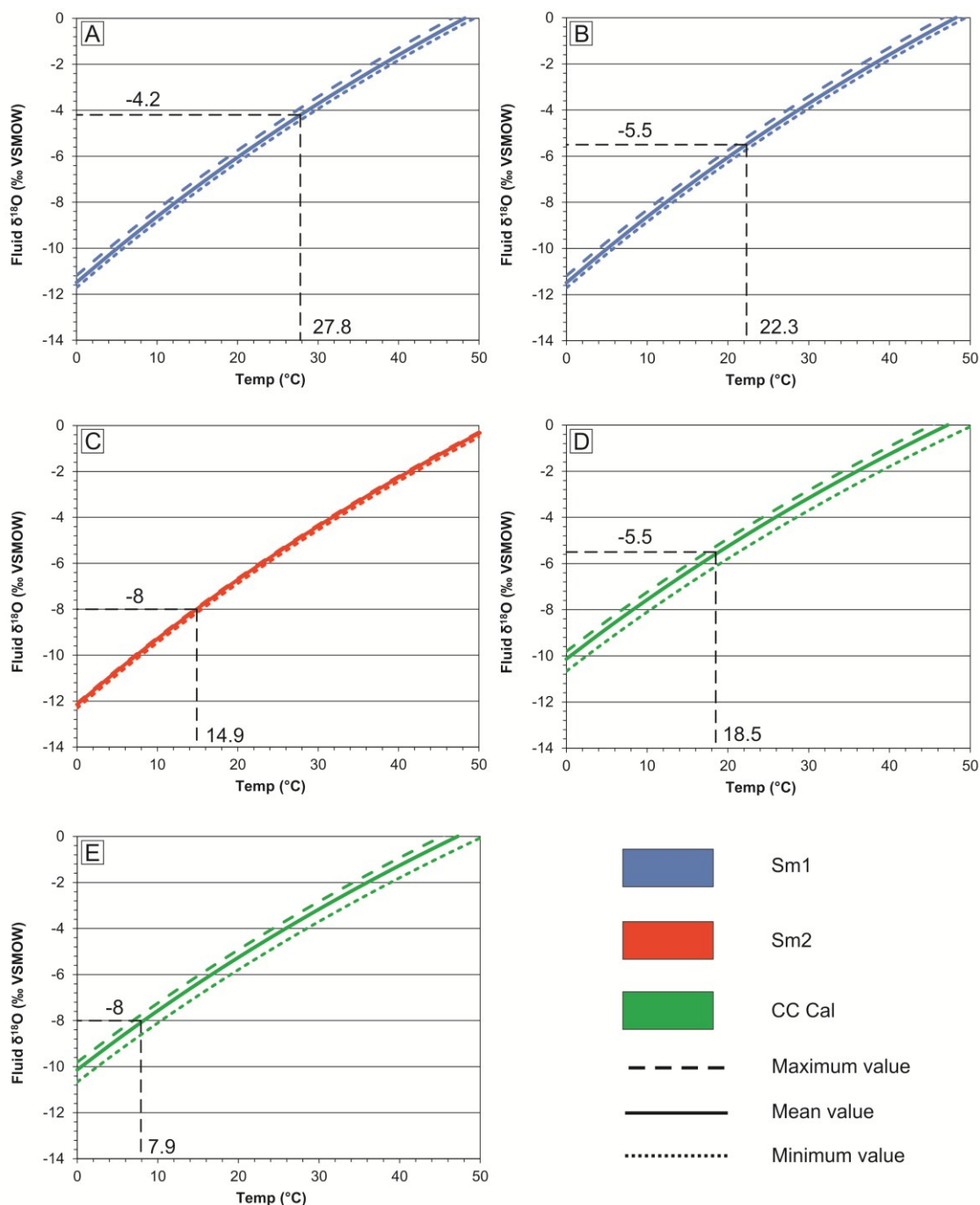


Figure 3.14. Oxygen isotope equilibrium curves for Mina Grande smithsonite and concretionary calcite, after smithsonite-water fractionation factors of Gilg et al. (2008) and calcite-water fractionation factors of O'Neil et al. (1969). A, B, C. Average precipitation temperatures calculated for early (Sm1) and late (Sm2) smithsonites during late Oligocene-early Miocene (A, B), middle to late Miocene and Pliocene-early Pleistocene (C) stages when Mina Grande area was at ~525, ~1,050, and ~2,100 m.a.s.l., respectively. D, E. Average precipitation temperatures calculated for concretionary calcite (CC Cal) during middle to late Miocene (D) and Pliocene-early Pleistocene (E) stages. The $\delta^{18}\text{O}$ for the fluid (groundwater) was assumed in the 525, 1,050, and 2,100 m.a.s.l. cases to have been -4.2, -5.5, and -8‰ VSMOW, respectively, by using $D\delta^{18}\text{O} = 0.24\text{‰}/100\text{ m}$ gradient valid for the South American Andes (Poage and Chamberlain, 2001).

Using the $\delta^{18}\text{O}$ of the paleogroundwater calculated for 525 m.a.s.l and the mean $\delta^{18}\text{O}$ value of early-stage smithsonite (Sm1: 26.9‰ VSMOW), a precipitation temperature of $\sim 28^\circ\text{C}$ has been calculated (Fig. 3.14A). The same calculation for an altitude of 1,050 m.a.s.l results in a precipitation temperature of $\sim 22^\circ\text{C}$ (Fig. 3.14B). The precipitation temperatures calculated for the late smithsonite (Sm2), using the mean $\delta^{18}\text{O}$ value of late stage smithsonite (Sm2: 26.2 ‰ VSMOW) at the current altitude of 2,100 m.a.s.l., are $\sim 15^\circ\text{C}$ (Fig. 3.14C). Since temperatures of approximately 28°C are too high for smithsonite formation in a karstic environment, the precipitation of Zn carbonate during the late Oligocene-early Miocene uplift stages seems unrealistic. In contrast, an average temperature of 22°C is absolutely compatible with a karstic supergene environment. Therefore, we suggest that Sm1 may have precipitated between ~ 14 and 10 Ma, in conjunction with the middle to late Miocene uplift. Moreover, an average temperature of 15°C is also realistic for the late smithsonite (Sm2) precipitated in the Mina Grande area, which preceded the deposition of needle-shaped hydrozincite (Hyd3).

To calculate the temperature of formation of supergene concretionary calcite (CC Cal), we used the same $\delta^{18}\text{O}$ values for the paleogroundwater and a mean measured $\delta^{18}\text{O}$ value of 24.5‰ VSMOW for this calcite. Assuming that calcite deposition also occurred in the middle to late Miocene, the formation temperature would have been 18.5°C (Fig. 3.14D), whereas if considering a deposition from the Pliocene to early Pleistocene, the precipitation temperature would have been 7.9°C (Fig. 3.14E). Since concretionary calcite (CC Cal) paragenetically followed early smithsonite (Sm1) and preceded late smithsonite (Sm2), it is confirmed that the karstic activity to which all these supergene minerals are related can be restricted to a period of time between the late Miocene and early Pliocene.

Genetic model

On the basis of this study and considering the existing literature on other zinc-lead deposits in the Bongará area (e.g., Reid, 2001; Basuki et al., 2008), we propose the following model for the mineralization process at Mina Grande (Fig. 3.15). Compelling evidence suggests that originally a hypogene sulfide mineralization must have been present at Mina Grande, considering the occurrence of hydrothermal saddle dolomite and of remnant galena and sphalerite in the nonsulfide ore. By analogy with the Florida Canyon deposit, primary mineralization should have been of the MVT, formed between Late Cretaceous and Early Tertiary (Fig. 3.15A). In uplifted areas characterized by humid climatic conditions, karst-related nonsulfide deposits are well developed. For example, the oxidation of sulfide bodies would have resulted in the formation of oxidized acidic solutions favorable to the development and enhancement of karsts (Thornber and Taylor, 1992). Considering that the early stages of Andean uplift commencing during the late Oligocene (Gregory-Wodzicki, 2000; Mora et al., 2010; Pfiffner and Gonzalez, 2013) could have produced a progressive denudation and uncapping of the original orebody, it is possible that intense sulfide weathering started only in the middle to late Miocene (~ 14 -10 Ma), during the transition from the Pebas to Acre wet periods (Horn et al., 2010).

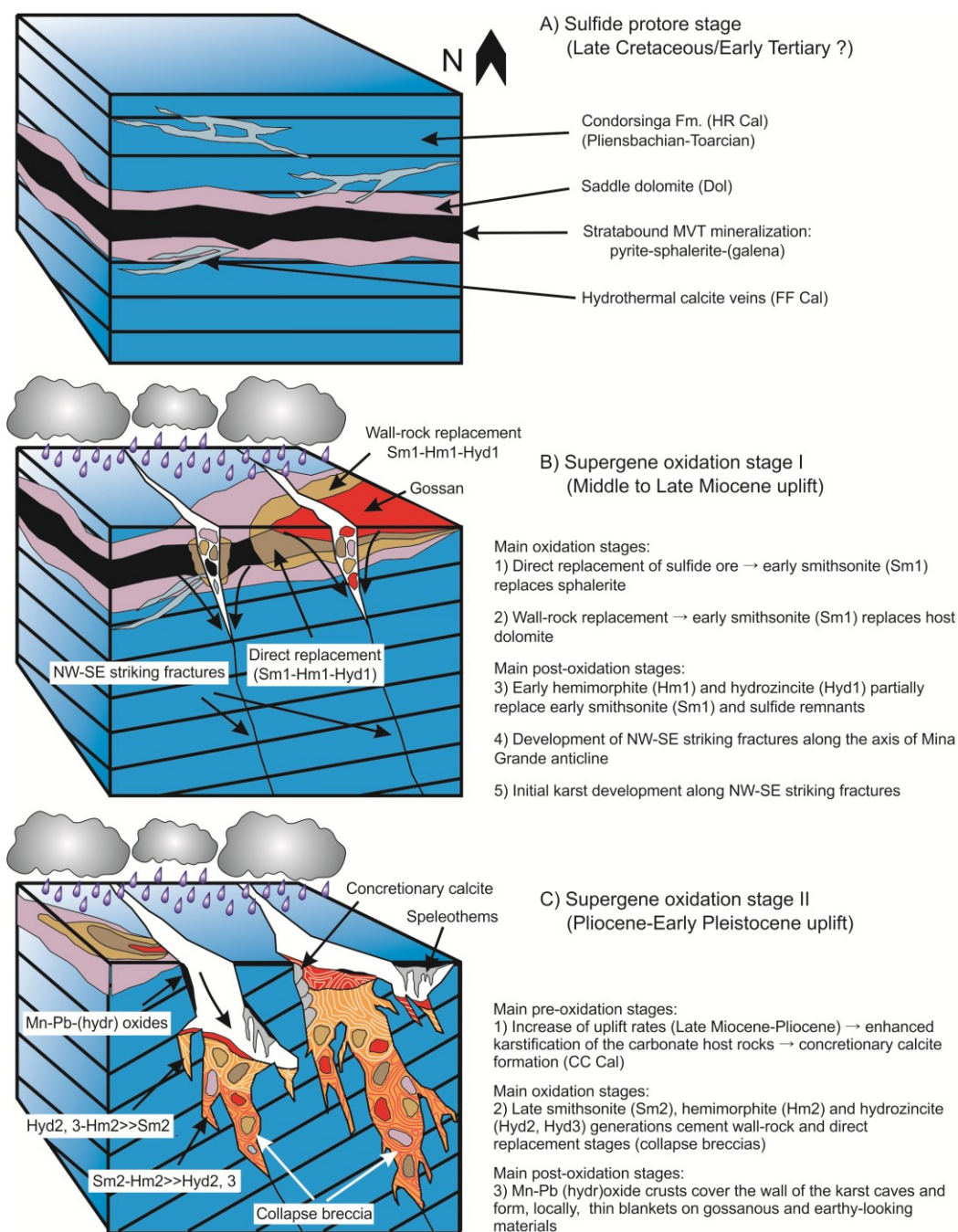


Figure 3.15. Geologic sketches of development stages for the Mina Grande Zn nonsulfide ore deposit. A. Strata-bound MVT mineralization in patchily dolomitized packstone and wackestone of the upper units of the Condorsinga Formation. Hydrothermal calcite veins cut the Condorsinga carbonate rocks. B. Miocene compression (Quechua stage) promotes uplift and tilting of strata. This uplift results in deep weathering of the sulfide protore and onset of supergene oxidation followed by “wall rock” and “direct replacement” mineralization sensu Hitzman et al. (2003); early smithsonite formation and its partial replacement by early generations of hydrozincite and hemimorphite. To accommodate the Mina Grande anticline formation, NW-SE-striking faults and fractures develop and are subsequently filled by weathering products. C. The increase of uplift rates since late Miocene, associated with a renewed oxidation phase (Pliocene-early Pleistocene) enhances the karst development along the same structures and deposits concretionary calcite. Late generations of smithsonite, hemimorphite, and hydrozincite, generally occurring as cement of collapse breccias, are related to the above phase. The most recent karst evolution resulted in the vertical growth of stalactites.

Uplift rates increased during this time interval and karstification of the uppermost Condorsinga units would have been enhanced along NW-SE-striking fractures (Fig. 3.15B). Early smithsonite (Sm1), the first product of sulfide oxidation at Mina Grande, was then partially replaced by early hemimorphite (Hm1) and hydrozincite (Hyd1; Fig. 3.15B). The second oxidation stage, determined through paragenetic studies and confirmed by the isotopic ratios of the various generations of smithsonite and hydrozincite, probably occurred after a renewed and more intense uplift phase that lasted from Pliocene to early Pleistocene (Fig. 3.15C). Deepening and widening of uplift-related fracture zones contributed to increase the permeability of host rocks and favored a deeper weathering of sulfides and a large-scale dispersion of the highly soluble Zn cations (Borg, 2009). Wide karst systems formed along fault and fracture zones, and first-stage nonsulfide mineral assemblages were brecciated and sedimented into karst cavities. Late smithsonite, hemimorphite, and hydrozincite generations, deposited as cements of the karst breccias, can be considered products of this second uplift and oxidation (Fig. 3.15C). The increase of the uplift rates between oxidation stages can be confirmed by the strong development of concretionary calcites, resulting from the increased calcium carbonate solution and precipitation as a consequence of the enhanced karstification of the host limestone.

Conclusions

The Mina Grande deposit (Peru) consists of several areas, where mineralization occurs as Zn nonsulfides (avg 23% Zn in partly exploited resources). The primary mineralization is considered to have been a MVT deposit hosted by carbonate rocks of the Condorsinga Formation (Pucará Group), whose formation was probably linked to one of three late- to post-Cretaceous Incaic tectonic phases. Hydrothermal saddle dolomite and vein calcite at Mina Grande are isotopically similar to those measured in other MVT deposits of the Bongará area. Nonsulfide mineralization, mostly consisting of hydrozincite (prevailing) with lesser amounts of smithsonite and hemimorphite, is concentrated in uplift-related karstic cavities with concretionary calcites and, locally, a gossanous cap. The karst morphology developed and deepened mainly along several NW-trending faults, associated with a regional network of faults and local stratification joints. Zinc occurs also partly in other minerals such as goethite, calcite, mica group minerals, and fraipontite. Lead is scarce or absent.

The paragenetic study reveals several stages of alteration and mineral formation, which have been confirmed by carbon and oxygen isotope analyses of the carbonate minerals. The extremely negative $\delta^{13}\text{C}$ compositions of all supergene carbonates clearly indicate an important contribution of isotopically light carbon from the oxidation of organic matter. At least two distinct generations of smithsonite, hydrozincite, and hemimorphite have been recognized. These ore-forming stages are interpreted to be related to distinct periods of uplift that occurred in the area since at least ~10 m.y. ago, when the transition from the Pebas to Acre climatic systems affected the Amazonas foreland basin.

The karstic activity, to which the supergene minerals are related, can be constrained to a period comprised between late Miocene and early Pliocene. Climatic models of the ecosystems persisting in the region from Late Tertiary to Recent time suggest that the Mina Grande supergene mineralization was related to several weathering episodes that occurred under conditions not much different from today's climate.

Chapter 4:

The Cristal Zn prospect (Amazonas region, Northern Peru). Part I: New insights on the sulfide mineralization in the Bongará province

Submitted to “Ore Geology Reviews”

Reference: Mondillo N., Arfè G., Boni M., Balassone G., Boyce A., Joachimski M., Villa I.M. The Rio Cristal Zn prospect (Amazonas region, Northern Peru). Part I: New insights on the sulfide mineralization in the Bongará province. Ore Geology Reviews, (in press).

Introduction

The Cristal Zn prospect consists of a mixed sulfide and nonsulfide mineralization located approximately 245 km northeast of the coastal city of Chiclayo and 740 km north of Lima, in the Bongará province (Amazonas region, northern Peru) (Fig. 4.1).

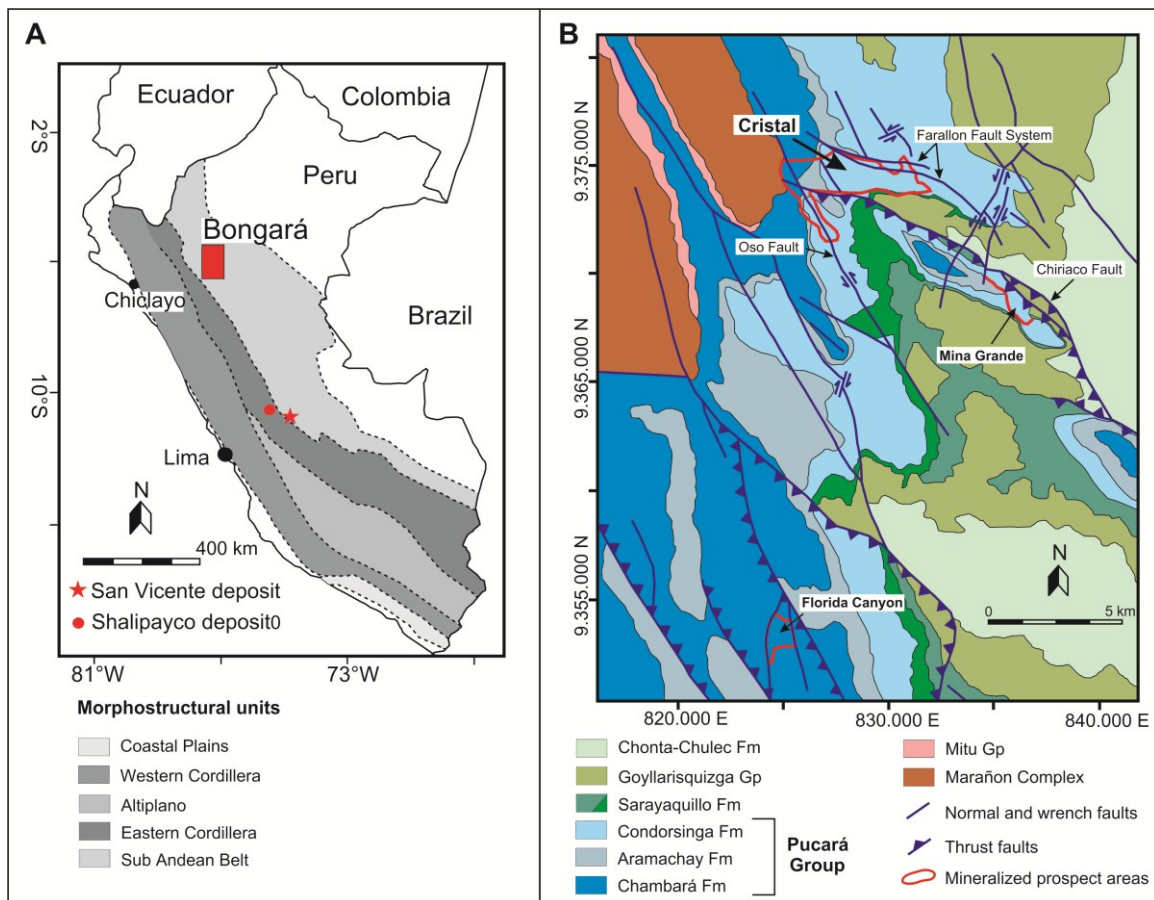


Figure 4.1. (A) Location of the Bongará district within the Andean morphostructural units of northern Peru. (B) Geological map of the Bongará district (from Arfè et al., 2017b, modified).

The Cristal mining license (currently owned by Zinc One Resources Inc.) covers an area of ca. 400 km² and is entirely located in the Yambrasbamba district. The economic value of this prospect resides in its prevailing surficial Zn oxidized mineralization, which has still not been fully quantified as required by the CIM standards (Boni and Mondillo, 2015; Workman and Breede, 2016). The Cristal mineralization is hosted by the lithologies of the Pucará Group, a Mesozoic sedimentary succession typical of central and northern Peru, deposited in an extensional basin on the western margin of the Brazilian-Guyana shield (Rosas et al., 2007). The Pucará Group hosts several types of Zn-Pb deposits, which can be spatially and genetically grouped as follows: (1) Mississippi Valley-type (MVT) deposits, especially located in the eastern and central outcropping areas of the Pucará Group (e.g. San Vicente and Shalipayco, Fig. 4.1A; Fontboté, 1990; Fontboté and Gorzawski, 1990; Gorzawski et al., 1990; Moritz et al., 1996; Spangenberg et al., 1996, 1999); (2) polymetallic Zn-Pb-Ag-Cu-Bi deposits, predominantly located in the central part of the former Pucará basin (e.g. Cerro de Pasco; Baumgartner and Fontboté, 2008; Baumgartner et al., 2009; Rottier et al. 2016); and (3) deposits genetically associated with the Tertiary magmatic activity (e.g. Zn-Pb-(Ag)-Domo de Yauli district; Beuchat et al., 2001; Dalheimer, 1990; Kobe, 1990a, b; Beuchat et al. 2004; Catchpole et al. 2015).

The geology and emplacement conditions of the sulfide bodies in the Bongará province have been only described for the Florida Canyon and Florcita Zn deposits (Basuki et al., 2008; Basuki and Spooner, 2009; Reid, 2001). The mineralogical, petrographic and geochemical features of the Florida Canyon deposit suggest that MVT-like fluids, associated with two hydrothermal dolomitization phases, emplaced the sulfides. Moreover, Reid (2001) argued that a common mineralizing hydrothermal system, with a structurally controlled interconnected plumbing network, was active at the district scale, similarly to the MVT- hydrothermal regime responsible for the San Vicente deposit (Fontboté et al., 1990). Basuki and Spooner (2009) calculated relatively high homogenization temperatures (160-220°C) for both hydrothermal dolomite and sphalerite at Florida Canyon and Florcita, which are very close to the upper limit of the “typical” temperature range for MVT-forming fluids (Leach et al., 2005).

Here we present the results of a study on the characteristics of the Cristal hypogene sulfide mineralization (the nonsulfide mineralization has been described in Arfè et al., in press). To determine the primary mineral association and paragenesis, as well as the average composition of the ore minerals, we carried out a comprehensive mineralogical, petrographic and geochemical study mainly focusing on drill core samples. The geochemical characterization was combined with Pb isotope and stable carbon, oxygen and sulfur isotope analyses on sulfides and carbonates of the hypogene mineral assemblage, to determine the possible sources of metals, and to investigate the relationships between hydrothermal dolomitization and ore deposition. The data presented address some genetic issues and open a new field for the discussion on the nature of the sulfide ores in the Bongará district.

Regional geological setting

From Permian to Triassic times, transtensional tectonics and rifting in the easternmost domains of the Peruvian Cordillera, including the Bongará area, controlled the inset of the Pucará basin (Fig. 4.1A and B; Dalmayrac et al., 1980; Jacay et al., 1999; Kontak et al., 1985; Laubacher, 1978; Mégard, 1978; Noble et al., 1978; Rosas and Fontboté, 1995; Rosas et al., 1997; Sempere et al., 2002). From the Middle to Late Triassic (Rosas et al., 2007; Spikings et al., 2016) the Pucará basin was filled by the sediments of the Mitu Group that include polymict conglomerates, red sandstones, mudstones and rare pyroclastic volcanics (Fig. 4.2), which overlie horst-and-graben structures of the Paleozoic basement (Figs. 4.3A and B). During the same time period, the sedimentary basin underwent a fault-controlled subsidence, which from Late Triassic to Early Jurassic was gradually followed by a more widespread regional subsidence associated with NW to NNW-trending sinistral shear zones (Benavides-Cáceres, 1999; Mégard, 1984; Rosas et al., 2007; Figs. 4.1 and 4.3).

Age	Stratigraphic units	Thickness (m)	Description
Upper Cretaceous	Chonta Fm.		Limestones, marls and silty mudstones
Lower Cretaceous	Goyllarisquizga Gp.	300 - 500	Quartzitic sandstones and conglomerates
Upper Jurassic - Lower Cretaceous	Sarayaquillo Fm.	+/- 200	Continental redbeds and lacustrine lithotypes Limestones boulder conglomerates
Upper Triassic - Lower Jurassic	Condorsinga Fm.	+/- 300	Micritic limestones and dolomitized wackestones and packstones
	Aramachay Fm.	+/- 300	Bituminous calcareous and silty mudstones
	Chambará Fm.	> 1000	Micritic and biomicritic with chert nodules; locally dolomitic grainstones and packstones
Middle - Late Triassic	Mitu Gp.	> 1000	Continental red-bed sandstones, mudstones and polymictic conglomerates
Paleozoic	Marañón Complex		Foliated micaschists and metasediments cut by magmatic dykes

Figure 4.2. Schematic stratigraphy of the sedimentary rocks in the Bongará area. Red star = Cristal and Mina Grande deposits host rock; black star = Florida Canyon deposit host rock (from Arfè et al., 2017b).

During the Late Triassic and Early Jurassic, the shallow- to deep-water marine carbonates of the Pucará Group were deposited unconformably over the sediments of the Mitu Group (Fontboté, 1990; Reid, 2001; Rosas et al., 2007) (Figs. 4.2 and 4.3C). The Pucará Group consists of the basal Chambará (Norian-Rhaetian), and by the overlying Aramachay (Rhaetian-Sinemurian) and Condorsinga (Pliensbachian-Toarcian) formations. In the Toarcian, a regional uplift promoted erosion and karstification of the uppermost

carbonate sediments (Condorsinga Formation). Following these tectonic events, the continental sediments of the Sarayaquillo Formation (Upper Jurassic to Cretaceous) were locally deposited in various colluvial, alluvial and lacustrine environments together with gypsum beds (Fig. 4.3D; Rosas et al., 2007). The upper part of the Sarayaquillo Formation is overlain by the siliciclastic rocks of the Goyllarisquizga Group, deposited during a first major marine transgression of Early Cretaceous age (Figs. 4.2). This transgression led to the deposition of the youngest rocks in the Bongará area, which belong to the Lower-Upper Cretaceous Chonta-Choulec Formation, and are represented by thinly bedded limestones and argillaceous limestones intercalated with nodular silty mudstones (Figs. 4.3E and F).

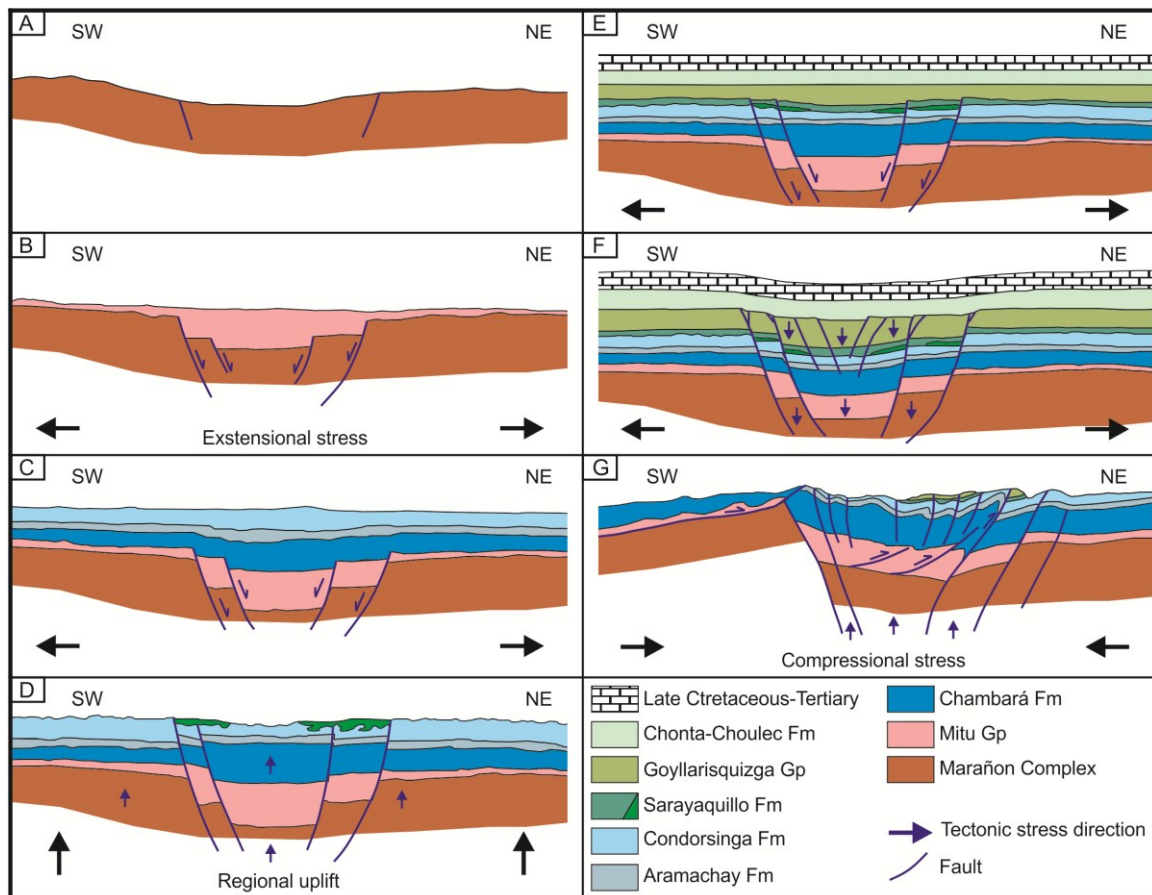


Figure 4.3. Tectonic evolution of the Bongará area (from Anglo Peruana, 2005, modified). (A) Late Permian-Early Triassic - basement faulting. (B) Middle to Late Triassic - Mitu Group deposition over horst-and-graben structures of the Precambrian basement. (C) Late Triassic to Early Jurassic - Pucará Group deposition unconformably over the Mitu Group. (D) Middle to Late Jurassic - deposition of the continental sediments of the Sarayaquillo Formation. (E), (F) Early Cretaceous to Early Tertiary - marine transgression and deposition of the Goyllarisquizga Group and of the Chonta-Choulec Formation. (G) Late Oligocene to Early Miocene - the northeastern part of the Pucará basin was affected by the Andean tectonics since (Quechua 1 Phase - 20.5 to 12 Ma).

At the district scale the development of the Pucará basin led to the formation of a localized pull-apart basin in the Bongará area, named Pomacochas Pull Apart Basin

(PPAB), mostly confined by NNW-SSE and WNW-ESE basement faults (Fig. 4.1; Anglo Peruana, 2005). In the western parts of the Bongará area metric-sized boulders of red-beds, polymictic conglomerates containing sub-rounded schists and volcanics clasts, granite fragments and red sandstones with a calcareous sandy matrix occur in the upper portion of the Mitu Group (Anglo Peruana, 2005). These rocks are exposed in the Marañon Geoanticline structural high, where also the Paleozoic basement has been brought to the surface toward the west. In the PPAB the Mitu Group has mostly less than 1000 m thickness, and is directly overlain by an evaporitic succession deposited at the base of the Chambará Formation. Moreover, evaporites are known to occur regionally also within the Mitu Group (Basuki et al., 2008).

Since late Oligocene to early Miocene, the northeastern part of the Pucará basin was affected by the first phase of the Andean tectonics (Quechua I Phase-20.5 to 12 Ma; Fig. 4.3G; Klein et al., 2011; Mégard et al., 1984; Pfiffner and Gonzalez, 2013). Subsequently, at 8-7 Ma (Quechua II Phase), at 5-4 Ma (Quechua III Phase) and at 2-1.6 Ma (Quechua IV Phase), the Quechua compression developed as several tectonic pulses (Klein et al., 2011).

Previous studies on sulfide mineralization in the Bongará area

In the Bongará province important Zn sulfide mineralizations, owned by Milpo/Votorantim, occur in the Florida Canyon and Florcita areas, located ca. 20-30 km south of Cristal (Fig. 4.1). Field observations, mineralogical assemblages, paragenetic relationships, and fluid inclusion studies (Basuki et al., 2008; Basuki and Spooner, 2009; Reid, 2001) indicate that the Zn-Pb mineralization in the Bongará area is of Mississippi Valley-type. Three different styles of mineralization have been recognized in the whole area (Basuki and Spooner, 2009; Reid, 2001). The first and most common style are stratabound layers, replacing the carbonate host rock or occurring as open space fillings. The second type is a collapse breccia-hosted mineralization, where sulfide minerals partially replace breccia fragments and matrix, and fill the open spaces between fragments. The third type, which is less common, occurs in veins, crackle and mosaic breccia; this kind of occurrence has been mostly observed in the upper part of the Chambará Formation. Two dolomite generations can be distinguished: an early generation with fine- to coarse rhombohedral crystals, which replaces fossiliferous float- and rudstones, and a late sparry dolomite (generally “saddle” type) occurring as medium- to coarse-grained crystals (Basuki et al., 2008; Reid, 2001). The earliest dolomite generation preceded sulfide emplacement, and can be interpreted as early pre-mineralization ground preparation before the main mineralization event. The late dolomite generation is roughly coeval with sulfide deposition, with some sulfides also postdating this late dolomite phase (Basuki et al., 2008; Reid, 2001).

The Florida Canyon deposit, located about 13 km northwest of the small town of Pedro Ruiz, is the collective name given to a number of Zn-sulfide and -nonsulfide orebodies, which have a total of measured plus indicated resources of 2.78 Mt with 12.77% Zn, 1.78% Pb and 18.2 g/t Ag (SRK, 2014). The Florida Canyon sulfide mineralization is

preferentially hosted in dolomitized volumes of the Chambará Formation, in a gently folded and faulted sector of the carbonate succession. Zinc mineralization mostly occurs as massive sphalerite, but is locally oxidized to smithsonite and hemimorphite. Lead occurs as galena (locally Ag-bearing), cerussite and anglesite. Low amounts of pyrite have been detected locally (SRK, 2014). The Florcita orebody, located 15 km south of Pedro Ruiz, is hosted in the upper dolomitized part of the Condorsinga Formation as well as in the lower part of the Goyllarisquizga Formation, near the unconformity contact with the Condorsinga Formation.

Two sphalerite types occur at Florida Canyon: a first dark-reddish brown and a late pale yellow variety. The dark-reddish sphalerite (ca. 1-3 mm grain size, up to ca. 5 mm) is the most abundant between the two phases, and was precipitated during the main mineralization stage as replacement and open-space filling. The pale yellow sphalerite (ca. 1-2 mm grain size), postdating sphalerite-1 and galena, occurs in veinlets and is locally associated with dissolution breccias. At Florcita, sphalerite commonly occurs as open-space filling in association with white sparry dolomite. An early black sphalerite typically occurs on the border of the cavities and is followed by a late brown sphalerite filling the open spaces (Basuki et al., 2008). Fluid inclusion measurements (Basuki, 2006; Basuki and Spooner, 2009) on early and late dolomite and on sphalerite specimens indicate that the fluids responsible for both dolomitization and mineralization are compatible with warm and saline MVT brines (homogenization temperatures of ca. 80 to 190 °C, corresponding to pressure-corrected temperatures of ca. 110 to 225 °C; salinity of ca. 15 to 24 wt % CaCl_2 equivalent).

The $\delta^{34}\text{S}$ values (Basuki et al., 2008) of early sphalerite from Florida Canyon range from -13.7 to +14.2 ‰ VCDT (mean = $+1.0 \pm 4.8$ ‰), with 90% of the data falling between -6 and +6 ‰ VCDT. Late sphalerite is isotopically heavier than early sphalerite, with $\delta^{34}\text{S}$ ranging between -0.3 to +17.6 ‰ (mean = $+5.2 \pm 6.9$ ‰) (Basuki et al., 2008). Early sphalerite from Florcita gives $\delta^{34}\text{S}$ values ranging from +11.1 to +19.3 ‰ VCDT (mean = $+15.5 \pm 1.8$ ‰; Basuki et al., 2008). These values indicate that H_2S for metal precipitation is derived from thermochemical reduction of dissolved sulfate (TSR) (Basuki et al., 2008). After the latter authors, the possible sources of sulfate include (1) Late Cretaceous seawater ($\delta^{34}\text{S}$ from ca. 18 to 21 ‰; Paytan et al., 2004) and (2) Middle Triassic-Late Jurassic evaporitic sulfate minerals from the Chambará and Condorsinga Formations ($\delta^{34}\text{S}$ from ca. 12 to 15 ‰; Claypool et al., 1980) and/or from the Late Jurassic Sarayaquillo Formation (Reid, 2001; Rosas, 1994). Reduced sulfur from thermal cracking of organosulfuric compounds, and probably also remnants of H_2S derived from bacterial sulfate reduction (BSR) might have played a role during the Florida Canyon metal precipitation (Basuki et al., 2008). The sulfide mineralization event at Florida Canyon seems to have occurred in association with the initial stages of the Andean orogeny, between the Late Cretaceous and early Tertiary (Basuki, 2006; Basuki and Spooner, 2009; Reid, 2001).

Geology and sulfide mineralization in the Cristal area

The Cristal area is located in the footwall of the Chiriaco reverse fault and in the hanging wall of the South Farallon normal fault (Fig. 4.1B). The Zn and Pb occurrences are hosted in dolomitized shallow-water platform mud-, pack- and wackestones of the upper units of the Condorsinga Formation (Fig. 4.2) (Anglo Peruana, 2005; Brophy, 2012; Reid, 2001). On the basis of sedimentary and diagenetic facies, Anglo Peruana (2005) subdivided the Condorsinga Formation in this area in three units (Lower, Middle and Upper unit). The lower unit consists of cm-laminated calcitic mudstones, with an overall estimated thickness of 100 m. These limestones are barren of ore and have only local infills of sparry calcite. The middle unit (120 m thick) consists of wacke- and packstones and is characterized by pervasive dolomitization, which does not affect the underlying lower unit. This unit is an important host rock for Zn-Pb mineralization. The upper unit (80 m thick) consists of thinly bedded (10-30 cm) micritic limestones with intercalated thin shale-sandstone horizons (Brophy, 2012). The higher units of the Condorsinga Formation are extensively karstified, with reworked carbonate material occurring as layered infillings in solution cavities and extensive cave systems. These Early Jurassic karsts and cave-infill deposits subsequently acted as pathways for later fluids depositing the sulfide mineralization (L. Oldham, pers. comm. 2017).

Within the Cristal property, the middle and upper units of the Condorsinga Formation are mostly characterized by a compact, fine-grained dolomicrite. This dolomitization can be followed along a belt up to 1.5 km wide between Cristal and the North Farallon Fault, which extends 7 km westward from the Cristal old mining camp to the contact of the Chambará Formation with the underlying Paleozoic basement (Fig. 4.1B). The dolomitization front continues south-southeastwards for more than 600 meters along the strike of the Oso Fault. Additionally, in the upper part of the Rio Cristal Valley, the dolomitization affects both the Aramachay and Chambará carbonates (Anglo Peruana, 2005). In the fault intersection and in the high permeable layers of the central part of the Cristal area, the widespread dolomicrite facies is patchily replaced by sparry dolomite (or dolosparite), which is less abundant in other mineralized areas. Locally, undolomitized remnants of the original calcitic mud-, wacke- and packstones of the Condorsinga Formation also occur. The overlying Sarayaquillo Formation has been seldom found in the area, because it is easily eroded. However, in more sheltered areas such as the southern flanks of the Rio Cristal Valley, the Sarayaquillo Formation occurs undisturbed keeping almost its original thickness. The overall northeast-southwest stratification of the Condorsinga Formation at Cristal does not correspond with the east-west strike of the contact with the overlying Sarayaquillo Formation, implying that the sediments of the Pucará Group were gently folded and tilted to the southeast during the tectonic adjustments that took place at the end of Pucará Group deposition, accompanied by uplift and erosion. It also implies that the unconformable base of the Sarayaquillo Formation truncates not only the upper part of the Condorsinga Formation progressively to the northwest, but also the crests of its gentle anticlinal structures, leading to the preservation of an incomplete stratigraphy of the Condorsinga Formation.

In the Bongará area, the Neogene deformation produced an imbricate fracturing and faulting system, which follows NNW-SSE, WNW-ESE and NNE-SSW structural trends (Anglo Peruana, 2005). The NNW- and NNE-trending faults confine the mineralized area to a sigmoidal zone (Fig. 4.1B). The Cristal mineralized belt is approximately 1.5 km long and 0.5 km wide, distributed in many occurrences scattered in the area (Brophy, 2012). The mixed sulfide and nonsulfide mineralization in these occurrences displays different geological features. In general, the orebodies in the belt are associated with: (1) paleo-karst; (2) veins and/or fault-related systems; (3) collapse breccias; (4) stratabound layers. Zinc sulfides at Cristal occur in the roots of the nonsulfide concentrations, and are locally present as unaltered patches also nearer to surface. Sulfides mostly consist of disseminated dark-brown sphalerite, which is associated with smaller amounts of pyrite and galena. They occur mainly within veins, as cavity fillings or disseminated mineralization, associated with sparry dolomite that generally follows the same trends of solution cavities and vertical or steeply dipping faults and fractures (Anglo Peruana, 2005), with trends including N-S to NNW-SSE (ca. N30°W) and WNW-ESE (ca. 120°). Drill cores at Cristal have encountered both near-surface primary base metal sulfides (only in traces), and oxidized mineralization at depths of over 50 m down-hole, with grades of up to 20 to 30 % Zn (Brophy, 2012). It is possible that significant sulfide bodies are present in greater depth, along the major tectonic structures (Brophy, 2012).

The most extended mineralized bodies are located in two intensively explored areas in the center of Cristal property, namely at Esperanza and Yolanda. The Esperanza occurrence covers an area approximately 150 m long and 90 m wide. The host rocks consist of dolomitized wacke- and packstones of the Condorsinga Formation, which have been weathered, showing Fe-oxy-hydroxides staining. The carbonate layers have an overall NE-SW strike similar to the dominant trend at Cristal, but dip northwestward at angles comprised between 30° and 60° (Anglo Peruana, 2005). The former Company Rio Cristal Resources collared 14 diamond drill holes at Esperanza, for a total of ca. 1,073 m (Brophy, 2012). The drill holes defined a mineralized area with a surface of approximately 11,200 m². The mineralized horizons have returned Zn grades between 22.5 and 29.7 wt.% Zn, mostly associated with the nonsulfide mineralization. The Yolanda occurrence can be followed in an E-NE-trending outcrop of earthy oxides, which is 50 m long and 10 m wide. Fe-oxy-hydroxides that display massive and botryoidal textures were detected in residual soils. Locally, saddle dolomite with disseminated fine cubic pyrite and bitumen replaces the calcareous grainstone host rock (Anglo Peruana, 2005). At Yolanda Rio Cristal Resources collared 14 diamond drill holes, covering a total area of ca. 12,000 m² and a total of ca. 735 m. The mineralized horizons have returned Zn grades that are ca. 17 wt.% Zn.

Structural studies by Anglo Peruana (2005) and other data reported in Brophy (2012) suggest that the age of sulfide mineralization in the Cristal area could be younger than Late Cretaceous-early Tertiary as proposed for the Florida Canyon deposit. The reason for this younger age is related to the situation of the mineralized occurrences within the Condorsinga Formation being associated with faults and fractures striking in a N-S direction. These faults were probably generated by combined dextral movements along

NNW-SSE and WNW-ESE faults, produced by a northeast-directed compression during the Miocene Quechua Phase (Anglo Peruana, 2005).

Materials and Methods

The mineralogical and geochemical studies were performed on 35 drill core samples from the Esperanza orebody. In detail, 12 samples from the CR-13-08 drill core (latitude 9.374.355, longitude 831.039), and 23 samples from the CR-18-08 drill core (latitude 9.374.369, longitude 831.043) were collected approximately at each meter of mineralized rock (Table 4.1, Fig. 4.4). The study also included: two specimens of sphalerite associated with galena (CN; CNBZ), and one massive pyrite specimen (ACR) from an area located in the northern sector of the Cristal property, called Charlita North, several limestone specimens of the Condorsinga Formation from the south-east part of the Cristal property, called Anita and Erika, and two dolomite and one smithsonite specimens from the CR07 drill core, also located in the Esperanza area. Polished thin sections were prepared for optical microscopy (OM), scanning electron microscopy with energy dispersive X-ray spectroscopy (SEM-EDS), and wavelength dispersion spectrometry (full WDS) studies. Portions of samples were crushed and pulverized for whole rock chemical analyses.

Table 4.1. List of the drill core samples and drill holes details.

Drill Hole	Easting (UTM)	Northing (UTM)	Azimuth	Dip	Depth (m)	Sample	From (m)	To (m)
CR-13-08	831,040	9,374,356	270	-60	56.90	CR13-1	16.35	18.00
						CR13-2	18.00	18.95
						CR13-3	18.95	19.85
						CR13-4	19.85	21.50
						CR13-5	21.50	23.10
						CR13-6	23.10	24.30
						CR13-7	24.30	25.35
						CR13-8	25.35	26.40
						CR13-9	26.40	27.40
						CR13-10	29.70	29.70
						CR13-11	30.50	30.50
						CR13-12	48.70	48.70
CR-18-08	831,043	9,374,369	270	-60	56.20	CR18-1	5.65	6.85
						CR18-2	6.85	8.15
						CR18-3	8.15	8.90
						CR18-4	8.90	10.00
						CR18-5	10.00	10.95
						CR18-6	10.95	11.90
						CR18-7	11.90	13.20
						CR18-8	13.20	14.70
						CR18-9	14.70	16.20
						CR18-10	16.20	17.65

Table 4.1. Continue....

CR-18-08	831,043	9,374,369	270	-60	56.20	CR18-11	17.65	18.65
						CR18-12	18.65	19.65
						CR18-13	19.65	20.65
						CR18-14	20.65	21.50
						CR18-15	21.50	22.70
						CR18-16	22.70	24.00
						CR18-17	24.00	25.30
						CR18-18	25.30	26.30
						CR18-19	26.30	27.30
						CR18-20	32.35	33.70
						CR18-21	33.70	34.35
						CR18-22	34.35	35.10
						CR18-23	36.70	38.30

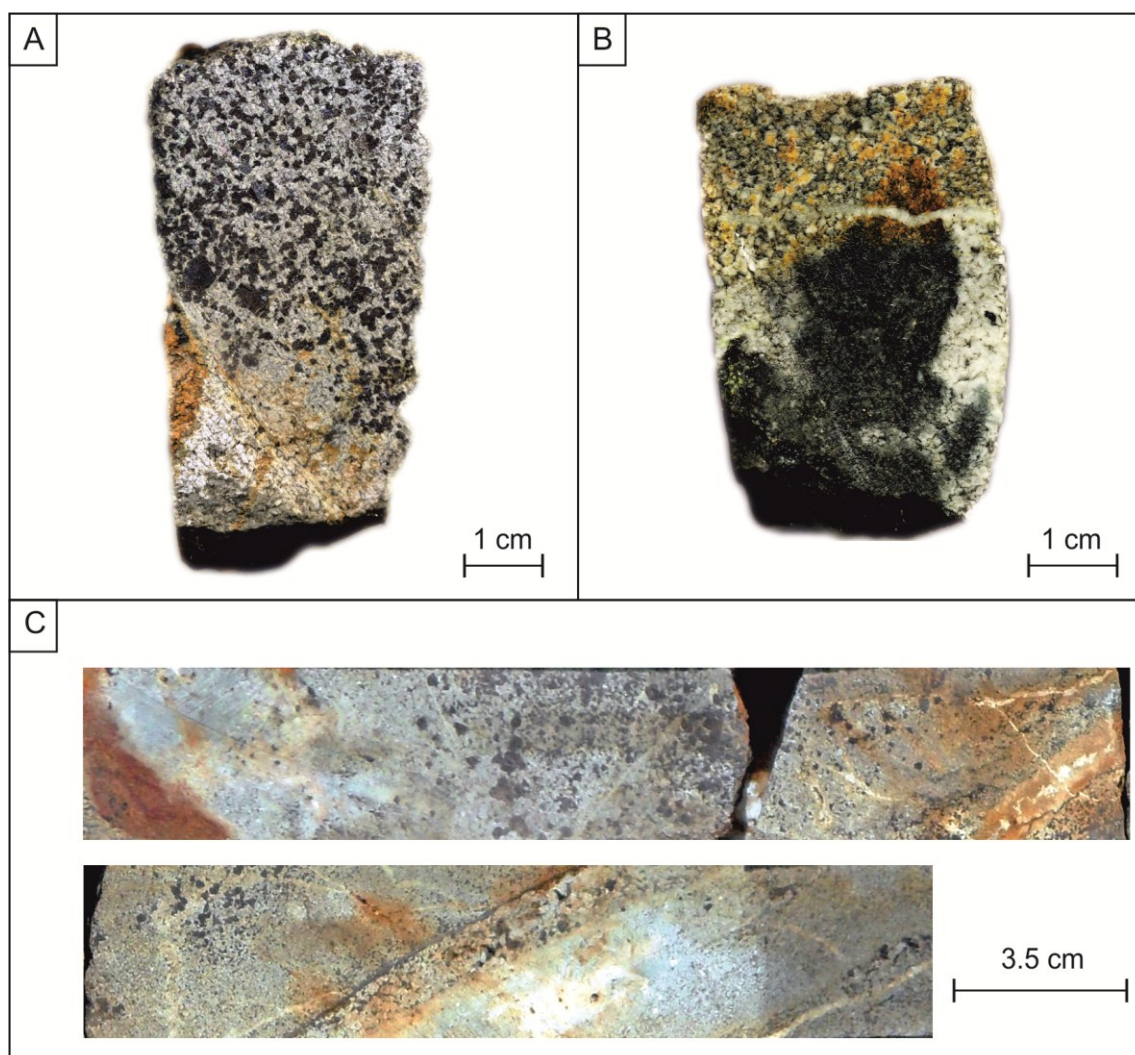


Figure 4.4. Examples of drill core samples used for this study. (A), (B) Specimens from the CR18-5 and CR18-15 samples. (C) Sample CR18-5.

SEM observations were carried out with a JEOL JSM5310 at the Dipartimento di Scienze della Terra, dell'Ambiente e delle Risorse (DiSTAR), Università degli Studi di Napoli Federico II (Italy). The analytical conditions were: 20 mm objective lens to specimen working distance, 15 kV accelerating voltage with a tilt angle of 0°. Element mapping and qualitative EDS investigations were carried out with the INCA X-stream pulse processor and the 4.08 version Inca software (Oxford Instruments detector), interfaced with the Jeol JSM 5310. Reference standards used for quantitative microanalysis were: albite (Si, Al, Na), orthoclase (K), wollastonite (Ca), diopside (Mg), almandine (Fe), rutile (Ti), barite (Ba), strontianite (Sr), eskolaite (Cr), rhodonite (Mn), pyrite (S), sphalerite (Zn), galena (Pb), pure silver (Ag), arsenopyrite (As), fluorite (F), apatite (P), sylvite (Cl), pure vanadium (V) and Corning glass (Th, U). Analytical errors are 1% relative for major elements and 3% relative for minor elements. Quantitative data sets of selected samples were obtained by full WDS, using a Cameca SX50 electron microprobe operating at 15 kV, 15 nA, and 10 µm spot size (Natural History Museum, London, UK). WDS detection limits for each element are mostly in the order of 0.01 wt%.

Whole-rock chemical analyses of major elements (Zn, Fe, Ca, Mg, Si, Al, Na, K, P, Mn) and minor elements (Mo, Cu, Pb, Ni, Co, As, U, Th, Sr, Cd, Sb, V, La, Cr, Ba, Sc, Tl, Se, Ga, Ge, Rb, Sn, Zr, Y, Ce, Li in ppm, and Au, Ag, Hg in ppb) of the CR18 drill core samples (CR18-1 to 20) were carried out at Bureau Veritas Commodities Canada Ltd. (Vancouver, Canada). About 10 g pulp for each sample were used for chemical analysis of the LF725 package (fusion/X-ray fluorescence spectroscopy "XRF"). Samples with high Zn (> 24 %), were run for overlimits with the LF726 package. Minor elements were analyzed by using the AQ250-EXT (ultratrace aqua regia/ICP-AES and MS) package, except Ga and Ge, which were analyzed using the GC204-Ge & Ga package.

Whole-rock chemical analyses of major (Zn, Fe, Mg, Al, K) and minor (Cu, Ni, Co, As, Cd, Sb, V, Ba, In, Ga, Ge, Ag) elements of the CR13 drill core samples (CR13-1 to 13) were carried out at Natural History Museum, London, UK. Approximately 50 mg of powdered rock sample was dissolved in Savillex 60 ml fluoropolymer vessels. 2-4.5 ml HCl and 0.05-0.25 ml HNO₃ were added to all samples and the mixture was shortly heated up to 70°C and the temperature rose to 100°C once the reaction had subsided. After samples were cooled down, 1 ml HNO₃, 1 ml HClO₄ and 2 ml HF was added to each, the vessels were capped and heated overnight at 100°C. Then the solutions were evaporated down at 150°C and reconstructed in 50 ml of ca. 0.6 M HNO₃ with traces of H₂O₂. The solutions were analyzed by ICP-MS using an Agilent 7700x mass spectrometer. To minimize polyatomic interferences, the instrument was run with 5 ml/min He (99.9995% purity) in the collision-reaction octopole cell (CRC) as well as with no collision gas entering the CRC. Ga (71Ga) was determined in the 'no gas' mode while all other elements were determined in the 'He mode'. To minimize the contamination of the instrument with high lead concentrations the solutions were further diluted 100-fold with ca. 0.7 M HNO₃. The instrument was calibrated using multi-elements standards (Inorganic Ventures) typically with a 4-point calibration with a correlation coefficient of > 0.9999. Accuracy was monitored by analyzing certified reference materials Jlk-1 (Lake sediment, GSJ) and SdAR-1 (Modified river sediment,

IAG) at the beginning and at the end of the run. All values were found to be within the uncertainty of the published data. The limits of quantification were calculated as 10 times the standard deviation of HNO₃ blank solution analyzed at least 10 times during the run. Carbon and oxygen isotope analyses were performed on the pure limestone and the dolomitized limestone of the Condorsinga Formation hosting the mineralization. Stable isotope analyses were carried out at the University of Erlangen-Nürnberg (Germany). Pure carbonate minerals (fracture-filling calcites, and host-rock dolomites and calcites) were separated by handpicking. The powdered samples were allowed to react for at least 36 hours with phosphoric acid at 70°C using a GasBench II connected to a ThermoFinnigan Five Plus isotope ratio mass spectrometer. Carbon and oxygen isotope values are reported relative to the Vienna Peedee belemnite (VPDB) and Vienna standard mean ocean water (VSMOW), respectively, by assigning a $\delta^{13}\text{C}$ value by assigning $\delta^{13}\text{C}$ values of +1.95 ‰ to NBS19 and -46.6 ‰ to LSVEC, and $\delta^{18}\text{O}$ values of -2.20 ‰ to NBS19 and -23.2 ‰ to NBS18. Reproducibility was checked by replicate analysis of laboratory standards and was better than ± 0.07 ‰ (1σ) for both carbon and oxygen isotope analyses. Oxygen isotope values were corrected using the phosphoric acid fractionation factors given by Kim et al. (2007) for dolomite, and Rosenbaum and Sheppard (1986) for calcite.

Sulfur stable isotope analyses were performed on 4 sphalerite specimens from drill core CR18-18-08 (CR18-5 and CR18-15) and from Charlita North area (CNBZ and CN). The samples were analyzed at the SUERC-Scottish Universities Environmental Research Centre. Sulfide specimens were prepared for conventional isotopic analysis by standard heavy liquids, magnetic, diamond micro-drilling and hand picking techniques. Around 5 to 10 mg was utilized for isotopic analysis. Minor contamination by non S-bearing phases was tolerated, and has no isotopic effect on the final data. Sulfides were analyzed by standard techniques reported in Robinson and Kusakabe (1975). Liberated gases were analyzed on a VG Isotech SIRA II mass spectrometer, and standard corrections applied to raw δSO_2 values to produce true $\delta^{34}\text{S}$. The standards employed were the international standards NBS-123 and IAEA-S-3, and the SUERC standard CP-1. Repeat analyses of these standards gave $\delta^{34}\text{S}$ values of +17.1 ‰, -32 ‰ and -4.6 ‰ respectively, with a standard error around ± 0.2 ‰ during the execution of these. Data are reported in $\delta^{34}\text{S}$ notation as per mil (‰) variations from the Vienna Cañon Diablo Troilite (VCDT) standard.

Lead isotope analyses were performed on Cristal sulfides, dolomites and smithsonite, and Sr isotope analyses on dolomites. Lead isotope analyses were also carried out on 5 samples of smithsonite from the Mina Grande deposit, which is analogous to the Cristal mineralization (Arfè et al., 2017b). The analyses were carried out by using a Nu Instruments™ multicollector inductively coupled plasma-mass spectrometer at the Laboratory of Isotope Geology at the University of Bern (Switzerland). For Sr isotopes, the carbonates were dissolved in HNO₃ and Sr was purified using the Sr•Spec™ cation exchange resin, according to the procedure of Villa et al. (2006). The measured values of the NIST SRM 987 standard required a bias correction of 0.000015, smaller than the in-run measurement uncertainty. For Pb, the samples were dissolved in *aqua regia* and

purified using the Sr•Spec™ cation exchange resin, based on the procedure of Villa (2009). All samples were spiked with thallium for correction of mass bias. The measured values of the NIST SRM 981 standard are coincident with those reported by Rehkämer and Mezger (2000); further bias corrections were unnecessary. Errors indicated for individual analyses are calculated as the square root of the square in-run error plus the square of the dispersion of the standard measurements for the corresponding day of analysis.

Results

Mineralogy and Petrography

The host rock samples from the Anita and Erika occurrences consist of limestone containing coarse-grained calcite (HR Cal), with halos of sparry dolomite and quartz. In the analyzed Esperanza drill cores no limestone has been detected, and the host rock consists only of dolomite alternating with sandstone and shale layers, containing detrital muscovite/illite, quartz, apatite, monazite, xenotime, rutile, zircon and orthoclase. In the Esperanza drill cores dolomite is displayed in a variety of fabrics and crystal forms. A commonly barren, early dolomite generation with a fine-grained texture, called DST (e.g. samples CR13-9 and CR18-23) has been observed (Fig. 4.5A). This early dolomite has been overprinted by a second fine-grained dolomite (Dol1), which locally replaces and mimics the textures of the early dolomite generation (DST) (Fig. 4.5B). DST has been detected either in the deepest levels of the drill cores (e.g. CR18-23), or in contact zones with shale horizons (e.g. CR13-9). DST exhibits a homogeneous mosaic texture and is relatively porous, especially where overprinted by Dol1. Pyrite, goethite and rutile occur in the solution cavities of this dolomite. The replacive dolomite (Dol1) is partly associated with Zn-mineralization, and it is generally obliterated by a much later coarse-grained sparry to saddle dolomite (Dol2), which mostly occurs in veins and fills open spaces (Fig. 4.5C and D). Dol2 is host for the sulfide mineralization (Figs. 4.5E, F and 4.6A, B, C). From the geochemical point of view, the fine-grained dolomites (DST and Dol1) are relatively stoichiometric, compared to the coarse-grained dolomite (Dol2) (Table 4.2; Fig. 4.6A). Dol2 crystals are commonly zoned, with alternating bands characterized by high Fe (up to 10 wt. % FeO) and/or significant Mn contents (up to 1.4 wt. % MnO) (Table 4.2). These dolomite crystals also have Zn-rich rims where ZnO can reach values up to 3 wt. %. Locally, Dol2 is accompanied by white sparry calcite veins (Sp Cal; Fig. 4.6B), and by occasional euhedral quartz crystals. The calcite veins are paragenetically late and may contain variable amounts of Mg and Zn.

The sphalerite crystals occur between Dol2 crystals and in geodes (Figs. 4.5E and F, 4.6A and 4.6C), and always contain significant amounts of Fe (on average ca. 6 wt.% Fe); maximum values around 12 wt.% Fe have been locally measured by EDS and WDS (Table 4.3). At high microscope enlargements (20 µm), Fe-Zn chemical zoning of sphalerite is easily appreciable (Figs 4.6E and F). This sphalerite is also Ge-rich: the mean content is around 145 ppm, but maximum values of 383 ppm have also been

measured (Mondillo et al., 2018). Galena is rare. Pyrite has been found in the Charlita North samples, in association with sparry calcite veins (Sp Cal) and in the dolomite halos, whereas in drill core samples it occurs mainly as remnants in goethite. Stibnite inclusions have been occasionally observed in pyrite. Celestine was locally detected in geodes or veins in the quartz-rich zones. In the sandstone intercalations muscovite is locally altered to the Zn-Mn-mica variety hendricksite $[K(Zn,Mg,Mn^{2+})_3(Si_3Al)O_{10}(OH)_2]$ (Table 4.4; Fig. 4.6D).

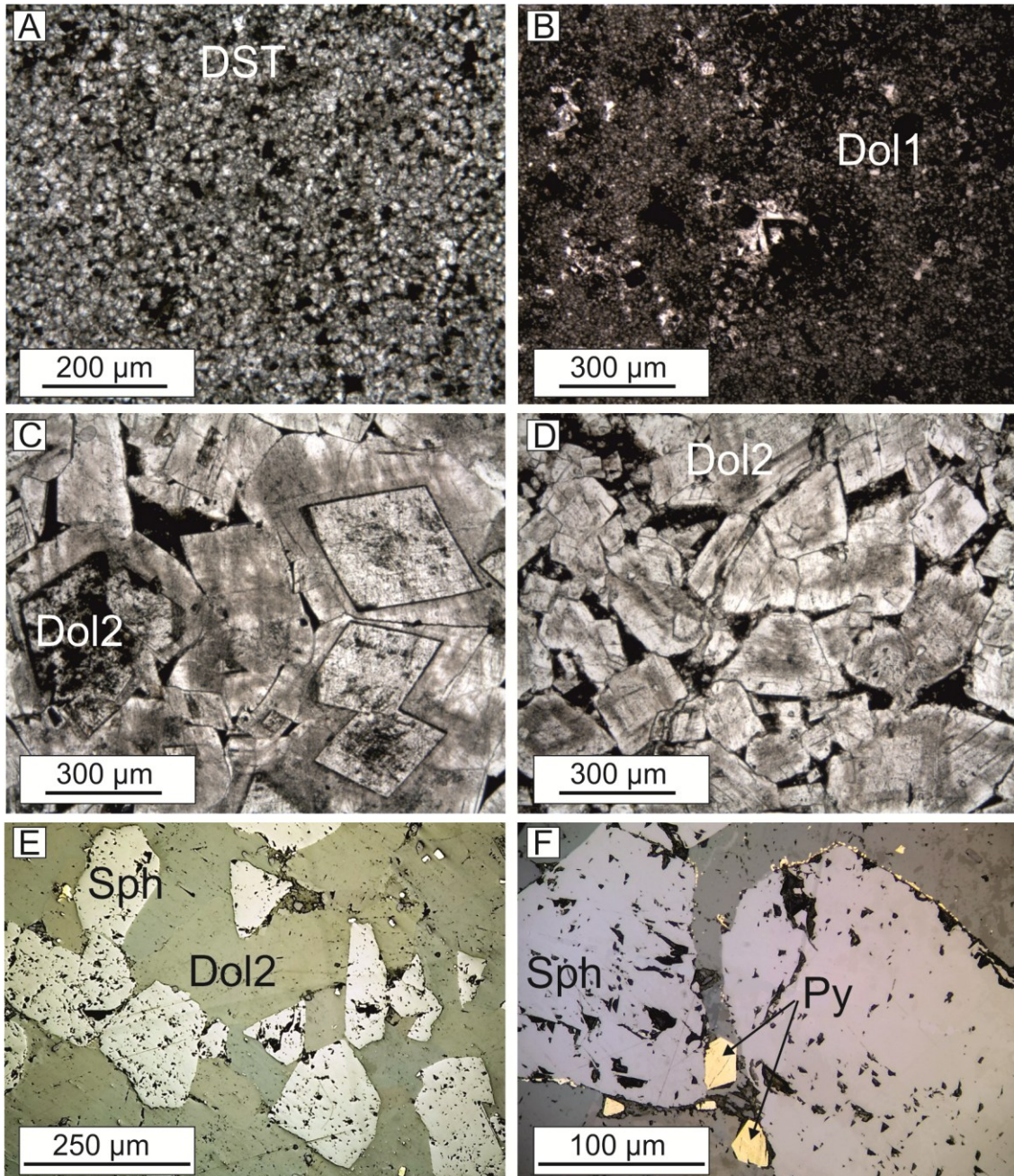


Figure 4.5. Textures of dolomite and sulfides in the studied samples. (A) DST dolomite (Samples CR13-9). (B) Dol1 dolomite (Sample CR18-23). (C), (D) Zoned Dol2 sparry dolomite crystals having different sizes (Sample CR18-15). (E) Sphalerite (Sph) filling voids in Dol2 (Sample CR18-5). (F) Small pyrite grains associated with sphalerite (Sample CR18-4).

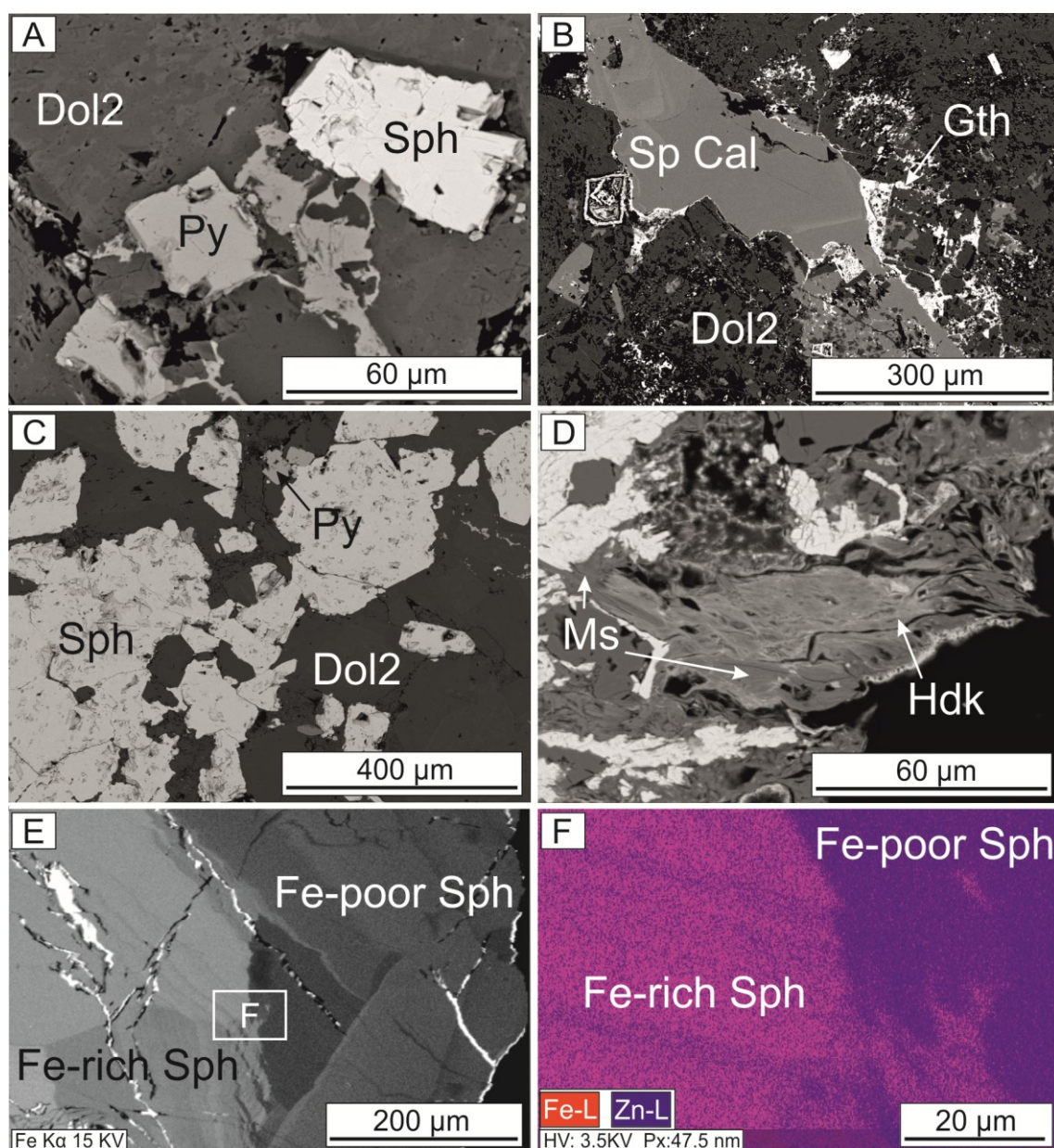


Figure 4.6. SEM-BSE-EDS and -WDS images of the hypogene assemblage. (A) Dol2 showing a mottled texture (Fe-rich areas are light gray), enclosing sulfides (Sample CR18-14). (B) Sparry calcite (Sp Cal) vein cutting Dol2 (Sample CR13-10). (C) Sphalerite showing no chemical zoning at SEM-BSE-EDS (Sample CR18-16). (D) Hendricksite replacing muscovite (Sample CR13-6). (E) Sphalerite showing Fe zoning at SEM-BSE-WDS (Sample CR18-4). (F) Enlargements of "F" portions of figure E showing Fe-Zn chemical mapping of sphalerite (Sample CR18-4)

TABLE 4.2. Representative chemical composition and structural formulae (apfu) of dolomite from the Cristal prospect.

Sample ID	CR13-9	CR13-9	CR07-7	CR13-3	CR13-5	CR13-10	CR18-3	CR18-4	CR18-5	CR18-14	CR18-14	CR18-14	CR18-15	CR18-16
wt. %	DST	DST	Dol2	Dol2	Dol2	Dol2	Dol2	Dol2	Dol2	Dol2	Dol2	Dol2	Dol2	Dol2
FeO	1.34	0.53	1.00	0.11	0.35	2.65	0.59	0.69	1.87	0.41	4.96	3.61	-	-
MnO	0.63	-	1.21	0.44	0.32	0.20	0.43	0.27	0.20	-	0.12	0.40	0.43	1.04
MgO	19.26	20.92	20.04	20.93	20.71	21.31	21.10	21.04	21.02	21.37	18.66	19.64	19.87	20.80
CaO	30.43	30.06	30.56	29.39	28.96	28.16	29.09	28.83	29.24	27.84	29.54	29.16	31.81	30.04
ZnO	0.42	1.07	-	0.94	2.02	-	0.76	1.78	0.91	3.06	0.73	0.81	-	-
CO ₂ ¹	46.11	46.75	47.22	46.25	45.74	47.10	46.48	46.18	47.16	45.42	46.65	46.77	46.92	46.91
Total	98.18	99.34	100.04	98.06	98.10	99.43	98.44	98.80	100.41	98.09	100.66	100.38	99.03	98.78
On the basis of (CO ₃) ₂														
Fe	0.04	0.01	0.03	0.00	0.01	0.07	0.02	0.02	0.05	0.01	0.13	0.09	0.00	0.00
Mn	0.02	0.00	0.03	0.01	0.01	0.01	0.01	0.01	0.01	0.00	0.00	0.01	0.01	0.03
Mg	0.91	0.98	0.93	0.99	0.99	0.99	0.99	0.99	0.97	1.03	0.87	0.92	0.92	0.97
Ca	1.04	1.01	1.02	1.00	0.99	0.94	0.98	0.98	0.97	0.96	0.99	0.98	1.06	1.00
Zn	0.01	0.02	0.00	0.02	0.05	0.00	0.02	0.04	0.02	0.07	0.02	0.02	0.00	0.00

Note: Dol1 = diagenetic dolomite; Dol2 = hydrothermal dolomite; ¹calculated from stoichiometry; - not detected.

TABLE 4.3. Selected chemical composition and structural formulae (apfu) of sphalerite from the Cristal prospect.

Sample ID	CR13-2	CR13-2	CR13-3	CR18-4	CR18-14	CR18-14	CR18-14	CR18-14	CR18-15	CR18-15	CR18 18
wt %											
Zn	59.77	67.87	60.50	59.80	62.15	60.67	54.44	60.68	60.34	63.40	
Fe	7.40	0.63	7.30	6.00	6.27	6.83	12.33	6.77	6.66	4.34	
S	32.72	32.02	32.56	33.04	32.54	32.61	33.43	32.20	31.24	31.88	
Total	99.89	100.51	100.36	98.84	100.96	100.10	100.20	99.65	98.24	99.63	
on the basis of 1 S											
Zn	0.90	1.04	0.91	0.89	0.94	0.91	0.79	0.92	0.95	0.98	
Fe	0.13	0.01	0.12	0.11	0.11	0.12	0.21	0.12	0.11	0.07	

TABLE 4.4. Chemical composition and structural formulae (apfu) of Zn-Mn-bearing micas from Cristal prspect.

Sample ID	CR13-6	CR13-6	CR13-7	CR13-7
wt. %				
SiO ₂	34.86	38.99	35.01	40.79
TiO ₂	-	0.17	0.21	-
Al ₂ O ₃	20.15	23.13	20.62	23.75
FeO	1.56	0.73	0.62	0.34
MnO	10.89	7.85	12.53	7.64
ZnO	16.85	13.15	10.69	11.32
MgO	1.64	1.67	1.66	1.83
CaO	0.11	0.17	0.22	0.17
K ₂ O	5.61	6.86	5.89	6.47
PbO	1.18	0.57	5.67	1.72
H ₂ O ¹	3.43	3.64	3.40	3.71
Total	96.28	96.93	96.52	97.73
On the basis of O ₁₀ (OH) ₂				
Si	2.87	3.03	2.89	3.09
Al ^{IV}	1.13	0.97	1.11	0.91
Σ _{TETR}	4.00	4.00	4.00	4.00
Al ^{VI}	0.83	1.16	0.90	1.21
Ti	0.00	0.01	0.01	0.00
Fe ²⁺	0.11	0.05	0.04	0.02
Mn	0.76	0.52	0.88	0.49
Zn	1.03	0.76	0.65	0.63
Mg	0.20	0.19	0.20	0.21
Pb	0.03	0.01	0.13	0.04
Σ _{OCT}	2.95	2.70	2.81	2.60
K	0.59	0.68	0.62	0.62
Ca	0.01	0.01	0.02	0.01
Σ _{INT}	0.60	0.69	0.64	0.63
OH	1.88	1.87	1.88	1.87
□ _{CATIONS}	7.55	7.39	7.45	7.23

Note: ¹Calculated from stoichiometry; - not detected.

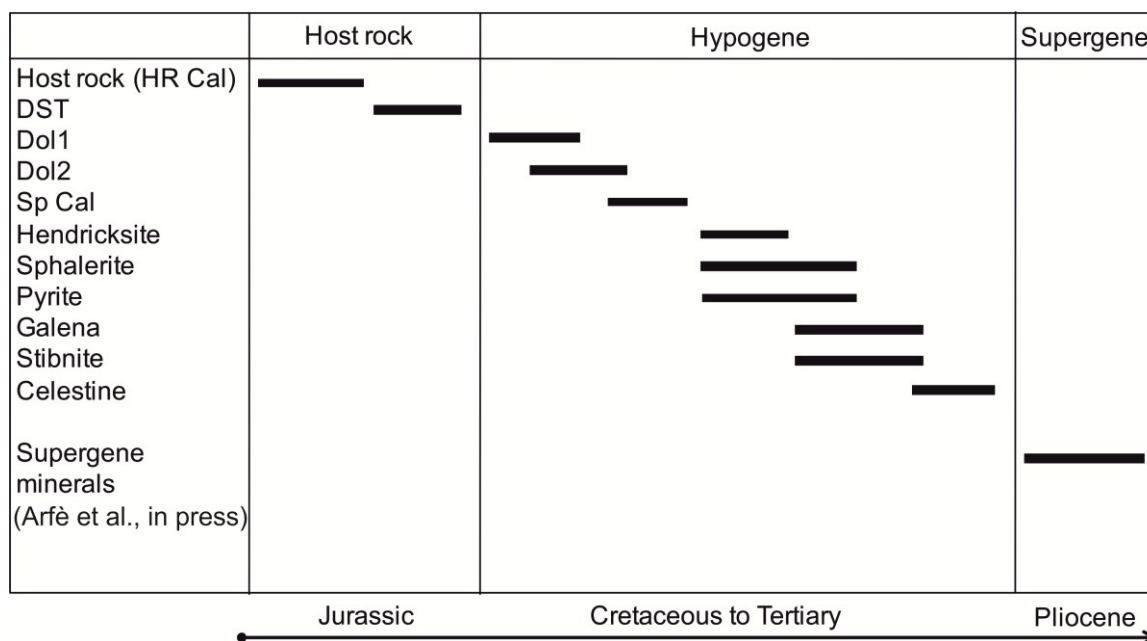


Figure 4.7. Paragenetic scheme of the hypogene mineralization in the Cristal area.

Major and minor element geochemistry

Whole rock chemical analyses of the samples from the Cristal cores are shown in Table 4.5. In the best-mineralized samples, the Zn content varies from 15 to ca. 53 wt. %, and is on average around 20 wt.% Zn. However, the highest Zn values are not associated with sulfides, but with the zones containing nonsulfide minerals, which also show high Cd contents (e.g. presence of supergene greenockite). Lead concentrations are low, generally under 2000 ppm but in some samples they can reach values close to 1 wt. %. Copper concentrations rarely exceed 200-300 ppm.

Iron concentrations vary from ca. 2 to 83 wt. % Fe (mean 26 wt. % Fe). The highest Fe values are associated with Fe-oxy-hydroxides; however, amounts comprised between 5 and 10 wt. % of the total Fe can be associated with saddle dolomite, sphalerite and aluminosilicate minerals. Manganese can reach maximum values of ca. 3 wt. % MnO, mostly contained in Mn-oxy-hydroxides (Table 4.5).

The mean concentrations of Y and Co are around 70 ppm (only in CR-18-08) and 94 ppm, respectively. Yttrium can be quite anomalous (up to 174 ppm) in a few samples of drill core CR18, where large modal amounts of xenotime have been observed. Cobalt anomalies have been found in many samples of drill core CR18. A maximum Co concentration of 294 ppm was measured in drill core CR13, possibly in association with hydroxides. Concentrations of critical elements like Ge are not negligible, because bulk rock values near 220 ppm of germanium (on average ca. 90 ppm) have been measured in most cores. Mondillo et al. (2018) reported high Ge values associated not only with sphalerite, but also with nonsulfide (hemimorphite and goethite) minerals. The average concentrations of all other analyzed elements (Mo, Sb, Rb, Th, Sn, etc.) rarely reach 40 ppm.

Table 4.5. Chemical composition of the studied samples.

	detect. limit*	CR13-1	CR13-2	CR13-3	CR13-4	CR13-5	CR13-6	CR13-7	CR13-8	CR13-9	CR13-10	CR13-11	CR13-12
wt. %													
SiO ₂													
Al ₂ O ₃	0.01	1.87	0.48	0.93	1.58	2.11	3.10	6.47	5.22	4.00	2.32	0.76	0.20
Fe ₂ O ₃	0.01	83.98	17.21	12.08	31.53	25.30	19.55	9.29	35.76	14.25	7.14	1.77	5.09
CaO													
MgO	0.01	4.90	7.85	17.02	5.72	2.99	0.35	0.65	0.50	9.14	17.22	19.78	18.77
Na ₂ O													
K ₂ O	0.01	1.11	0.58	1.11	1.65	2.20	3.25	7.77	6.03	4.62	2.88	0.93	<0.01
MnO	0.01	1.50	0.30	0.41	0.64	1.08	0.74	0.65	3.01	0.45	0.43	0.13	0.41
TiO ₂													
P ₂ O ₅													
Cr ₂ O ₃	0.01	<0.01	<0.01	<0.01	<0.01	<0.01	<0.01	<0.01	<0.01	<0.01	<0.01	<0.01	<0.01
Pb	0.01	0.83	<0.01	0.01	0.01	0.03	0.08	0.06	0.09	0.01	<0.01	<0.01	<0.01
Zn	0.10	5.65	28.62	15.76	21.54	31.35	53.03	35.99	17.33	17.67	0.49	0.23	0.04
LOI													
Total													
TOT/C													
TOT/S													
ppm													
Mo													
Cu	7	140	318	116	43	44	24	18	23	14	<7	<7	<7
Ni	1.5	22.7	14.0	10.2	29.1	84.7	72.0	46.9	48.7	31.1	7.9	4.8	<1.5
Co	1	139	149	91	60	13	14	17	294	35	2	1	<1
As	1.5	19.6	15.3	8.1	14.9	10.4	7.8	10.3	50.7	54.1	7.3	1.8	4.4
Cd	1	179	996	732	355	558	178	133	209	214	4	12	<1
Sb	0.4	1.7	2.2	1.9	1.8	2.3	4.2	3.9	3.0	4.4	2.1	1.1	1.0
V	1	65.0	39.2	43.1	51.8	86.7	84.4	164	144	100	32.5	13.6	9.1
Ba	3.9	95.5	22.0	17.3	144	132	72.6	83.9	298	108	44.0	16.9	24.6
In	0.6	1.1	12.8	6.0	<0.6	<0.6	<0.6	<0.6	<0.6	<0.6	<0.6	<0.6	<0.6
Ga	0.4	5.9	14.1	8.9	6.4	11.1	6.5	12.0	14.9	10.2	4.5	1.5	0.6
Ge	12	163	216	84	103	91	138	62	65	41	<12	<12	<12
Ag	1	5	7	11	<1	5	2	2	2	<1	<1	<1	<1

Note: < = below detection limits; * Analyses carried out at the Natural History Museum London; ** Analyses carried out at the Bureau Veritas Commodities Canada Ltd. (analytical details are given in the text).

Table 4.5 (continue)....

	detect. limit**	CR18-1	CR18-2	CR18-3	CR18-4	CR18-5	CR18-6	CR18-7	CR18-8	CR18-9	CR18-10	CR18-11	CR18-12	CR18-13	CR18-14	CR18-15	CR18-16	CR18-17	CR18-18	CR18-19	CR18-20
wt. %																					
SiO ₂	0.01	1.29	2.17	1.35	2.28	2.11	1.26	2.04	3.35	7.07	4.46	2.09	3.61	4.36	7.01	4.16	7.57	6.96	7.66	11.99	7.38
Al ₂ O ₃	0.01	0.12	0.21	0.22	0.58	0.55	0.25	0.33	0.84	1.26	0.41	0.47	0.64	0.95	1.01	0.76	1.24	1.1	1.44	1.09	0.87
Fe ₂ O ₃	0.01	39.03	56.87	17.84	9.12	9.44	12.54	12.02	26.73	47.64	25.18	18.24	17.28	34.27	12.17	8.19	10.88	43.04	22.38	35.99	50.12
CaO	0.01	0.16	0.1	20.37	18.16	18.84	22.04	6.77	0.1	0.05	0.19	0.12	0.2	0.24	6.74	19.36	16.38	4.33	9	2.26	1.09
MgO	0.01	0.51	0.28	14.46	12.68	11.83	15.19	4.69	0.17	0.14	0.26	0.19	0.3	0.39	4.5	12.22	10.47	2.78	5.82	1.51	0.86
Na ₂ O	0.01	0.27	0.14	<0.01	0.06	0.1	<0.01	0.26	0.31	0.19	0.32	0.38	0.36	0.28	0.29	0.06	0.09	0.13	0.17	0.21	0.15
K ₂ O	0.01	0.03	0.05	0.08	0.18	0.18	0.08	0.12	0.24	0.35	0.13	0.16	0.21	0.52	0.32	0.24	0.38	0.28	0.42	0.3	0.25
MnO	0.01	0.8	0.55	0.53	0.39	0.3	0.52	0.43	0.48	0.45	0.6	0.4	0.31	1.22	0.4	0.37	0.46	0.88	0.5	0.39	0.72
TiO ₂	0.01	<0.01	<0.01	<0.01	0.01	0.01	<0.01	<0.01	0.02	0.04	<0.01	<0.01	0.02	0.03	0.03	0.02	0.03	0.03	0.05	0.03	0.03
P ₂ O ₅	0.01	0.01	0.01	0.01	0.02	0.01	<0.01	0.01	0.01	0.04	0.02	0.01	0.01	0.03	0.03	0.03	0.04	0.04	0.04	0.05	0.06
Cr ₂ O ₃	0.01	<0.01	<0.01	<0.01	<0.01	<0.01	<0.01	<0.01	<0.01	<0.01	<0.01	<0.01	<0.01	<0.01	<0.01	<0.01	<0.01	<0.01	<0.01	<0.01	<0.01
Pb	0.01	0.09	0.06	0.01	<0.01	<0.01	<0.01	0.18	0.79	0.38	0.05	0.08	0.02	0.02	0.02	<0.01	0.01	0.12	0.04	0.04	0.02
Zn	0.1	28.9	17.4	6.0	15.3	16.7	6.8	33.8	34.8	18.9	35.2	41.1	41.5	29.3	32.1	14.8	14.7	16.5	21.4	25.7	18.0
LOI	-	22.76	17.03	37.02	26.4	10.18	38.21	32.34	24.82	17.63	25.93	28.72	27.54	22.57	27.71	24.02	32.37	19.4	19.79	15.12	15.86
Total		99.49	99.17	99.3	88.89	74.38	98.56	99.28	98.54	98.76	98.77	99.65	99.59	99.81	98.3	87.92	98.19	99.69	93.91	99.17	99.86
ppm																					
TOT/C	0.02	5.12	2.88	9.25	9.46	8.28	10.36	8.53	5.85	2.25	6.08	7.26	6.7	4.62	7.27	8.59	8.76	3.35	5.5	1.96	1.81
TOT/S	0.02	<0.02	<0.02	0.09	5.02	11.81	0.38	0.09	0.1	5.27	<0.02	0.03	0.19	0.08	0.55	5.2	0.64	0.03	2.4	0.04	<0.02
Mo	0.01	0.57	0.45	0.36	0.74	0.26	0.17	0.28	0.54	5.28	0.68	0.74	2.77	1.33	1.76	1.05	2.33	2.55	1.41	0.94	2.24
Cu	0.01	115.31	13.89	33.58	107.04	169.76	80.26	200.42	221.92	78.71	42.54	89.5	341.55	123.36	131.11	112.68	75.55	43.5	120.81	110.97	6.62
Ni	0.1	23.1	17.9	4.8	4.9	2.1	3.8	18.7	41.9	37.9	29	17.9	14	20.7	10	4.8	9.2	24.4	11.5	13.6	29.7
Co	0.1	129	51.8	41.6	89.5	118.5	51	110.9	92.2	43.1	68.4	153.6	228.8	169.7	290.4	95.4	69.7	86.5	124.6	137.8	64.3
As	0.1	4.2	2.2	9.9	2.9	3	2.4	3.2	5.7	16.3	6.6	2.7	4.1	2.6	7.6	1.8	3.4	7	12.5	8.1	5
Cd	0.01	967.28	574.29	525.59	917.94	1150.87	475.66	1662.74	1541.16	723.95	1086.3	1459.27	1792.1	945.7	1484.31	745.4	613.4	586.68	795.09	519.39	694.77
Sb	0.02	0.25	0.15	0.28	0.26	0.36	0.18	0.32	0.65	0.67	0.71	0.16	0.32	0.23	0.41	0.25	0.36	0.26	0.29	0.18	0.19
V	2	17	29	16	15	17	10	14	28	20	17	10	16	13	9	13	17	20	11	22	29
Ba	0.5	48	32.7	27.8	9.2	1.3	22.2	17.1	18	29.5	45.7	22.4	42.3	67.3	36.6	9.4	20.9	48.6	28.4	27	109.9
In	0.02	3.56	0.15	3.22	7.66	9.75	7.59	27.75	11.24	4.59	6.27	3.86	34.56	7.41	15.42	6.15	1.06	1.1	6.52	7.29	0.09
Ga	1	4	<1	2	6	7	3	17	16	9	19	14	72	17	13	5	8	4	11	8	2
Ge	1	92	56	38	112	138	65	87	124	64	66	94	112	96	87	69	47	57	89	129	77
Ag	0.002	3.470	1.908	2.366	17.536	15.186	3.052	10.383	37.176	13.153	1.389	9.232	27.762	6.908	4.541	3.828	4.269	1.106	5.653	4.859	0.503

Note: < = below detection limits; * Analyses carried out at the Natural History Museum London; ** Analyses carried out at the Bureau Veritas Commodities Canada Ltd. (analytical details are given in the text).

TABLE 4.6. Lead, strontium and sulfur isotope compositions of sulfide and carbonate minerals from Cristal, Charlita North and Mina Grande deposits.

Sample ID	Sub-sample ID	Mineral *	²⁰⁶ Pb/ ²⁰⁴ Pb	2σ	²⁰⁷ Pb/ ²⁰⁴ Pb	2σ	²⁰⁸ Pb/ ²⁰⁴ Pb	2σ	²⁰⁷ Pb/ ²⁰⁶ Pb	2σ	²⁰⁸ Pb/ ²⁰⁶ Pb	2σ	⁸⁷ Sr/ ⁸⁶ Sr	2σ	δ ³⁴ S (VCDT)
Cristal															
CR07-1	CR07-1_sm	Smithsonite	18.9163	0.0010	15.6709	0.0011	38.8605	0.0040	0.82843	0.00003	2.05429	0.00013	-	-	-
CR07-3	CR07-3_sm	Smithsonite	18.9946	0.0016	15.6871	0.0016	38.9361	0.0052	0.82588	0.00003	2.04995	0.00012	-	-	-
CR07-7	CR07-7_dol2	Dol2	19.0083	0.0005	15.6896	0.0005	38.8814	0.0015	0.82541	0.00001	2.04550	0.00004	0.708817	0.000016	-
CR13-2	CR13-2_dol2	Dol2	19.0126	0.0203	15.6465	0.0175	38.7565	0.0458	0.82296	0.00020	2.03847	0.00096	0.708324	0.000010	-
CR13-9	CR13-9_dst	DST	19.7667	0.0026	15.7188	0.0013	38.7446	0.0062	0.79519	0.00008	1.96013	0.00021	0.708340	0.000012	-
CR18-4	CR18-4_sp	Sphalerite	18.9735	0.0006	15.6895	0.0006	38.9267	0.0021	0.82691	0.00001	2.05159	0.00005	-	-	-
	CR18-5_dol2	Dol2	18.9665	0.0015	15.6839	0.0015	38.8500	0.0044	0.82693	0.00003	2.04835	0.00011	0.708281	0.000010	-
CR18-5	CR18-5_spA	Sphalerite	19.2611	0.0011	15.7945	0.0009	39.8142	0.0064	0.82002	0.00003	2.06725	0.00008	-	-	-
	CR18-5_spB	Sphalerite	19.0043	0.0039	15.6970	0.0035	38.8827	0.0101	0.82596	0.00005	2.04596	0.00020	-	-	-
	CR18-5_spC	Sphalerite	-	-	-	-	-	-	-	-	-	-	-	-	14.0
CR18-9	CR18-9_py	Pyrite	18.9537	0.0089	15.6690	0.0069	38.8622	0.0228	0.82668	0.00002	2.05055	0.00008	-	-	-
CR18-11	CR18-11_sm	Smithsonite	18.9639	0.0027	15.6904	0.0022	38.9386	0.0056	0.82736	0.00002	2.05332	0.00009	-	-	-
CR18-12	CR18-12_sm	Smithsonite	19.1209	0.0050	15.7540	0.0040	39.2392	0.0112	0.82397	0.00007	2.05225	0.00023	-	-	-
	CR18-15_dol2	Dol2	19.0848	0.0015	15.6953	0.0010	38.8769	0.0077	0.82238	0.00002	2.03718	0.00007	0.708402	0.000008	-
CR18-15	CR18-15_spA	Sphalerite	18.9754	0.0006	15.6908	0.0006	38.9223	0.0018	0.82690	0.00001	2.05120	0.00004	-	-	-
	CR18-15_spB	Sphalerite	19.0282	0.0033	15.7089	0.0029	39.0195	0.0116	0.82556	0.00005	2.05082	0.00015	-	-	-
	CR18-15_spC	Sphalerite	-	-	-	-	-	-	-	-	-	-	-	-	15.0
	CR18-15_py	Pyrite	18.9841	0.0010	15.6870	0.0011	38.9232	0.0039	0.82632	0.00002	2.05036	0.00008	-	-	-
CR18-17	CR18-17_py	Pyrite	19.2234	0.0006	15.9862	0.0007	39.9156	0.0021	0.83161	0.00001	2.07640	0.00006	-	-	-
CR18-18	CR18-18_sp	Sphalerite	19.0143	0.0038	15.6911	0.0041	38.9139	0.0124	0.82520	0.00007	2.04640	0.00030	-	-	-
CR18-23	CR18-23_dol1	Dol1	19.1633	0.0014	15.6924	0.0014	38.8602	0.0048	0.81888	0.00002	2.02791	0.00009	0.708259	0.000009	-
Charlita North															
CNBZ	CNBZ_spA	Sphalerite	18.8279	0.0009	15.6868	0.0008	38.7403	0.0047	0.83317	0.00002	2.05768	0.00011	-	-	-
	CNBZ_spB	Sphalerite	18.9175	0.0012	15.6995	0.0010	38.8867	0.0030	0.82991	0.00002	2.05558	0.00008	-	-	-
	CNBZ_sp	Sphalerite	-	-	-	-	-	-	-	-	-	-	-	-	14.9
CN	CN_sp	Sphalerite	18.8034	0.0009	15.6696	0.0008	38.6298	0.0027	0.83333	0.00001	2.05445	0.00006	-	-	-
	CN_sp	Sphalerite	-	-	-	-	-	-	-	-	-	-	-	-	14.2
	CN_gn	Galena	18.7531	0.0012	15.6604	0.0011	38.5409	0.0033	0.83509	0.00002	2.05519	0.00008	-	-	-
ACR	ACR_py	Pyrite	18.8166	0.0027	15.6696	0.0025	38.7005	0.0062	0.83273	0.00003	2.05677	0.00008	-	-	-
Mina Grande															
ZA-5	ZA-5_sm	Smithsonite	18.9160	0.0012	15.6799	0.0014	38.8530	0.0044	0.82891	0.00002	2.05395	0.00011	-	-	-
	ZA-3_smA	Smithsonite	18.9071	0.0017	15.6779	0.0019	38.8423	0.0058	0.82920	0.00005	2.05440	0.00017	-	-	-
ZA-3	ZA-3_smB	Smithsonite	18.9360	0.0010	15.6785	0.0011	38.8482	0.0035	0.82796	0.00002	2.05154	0.00007	-	-	-
	ZB-3_smA	Smithsonite	18.9600	0.0012	15.6821	0.0011	38.8571	0.0036	0.82713	0.00002	2.04949	0.00009	-	-	-
ZB-3	ZB-3_SmB	Smithsonite	18.9373	0.0014	15.6783	0.0016	38.8477	0.0046	0.82791	0.00003	2.05145	0.00009	-	-	-

Note: * Dol1 = early hydrothermal dolomite; Dol2 = late hydrothermal dolomite; DST = diagenetic dolomite.

Stable isotope geochemistry of sulfide and carbonate minerals

Sulfur isotope analyses have been carried out on sphalerite samples from Esperanza and Charlita North areas (Table 4.6). The samples from the CR18-15 and CR18-5 drill cores (Esperanza) have $\delta^{34}\text{S}$ values of 15 and 14 ‰ VCDT, respectively. The sphalerites from Charlita North (samples CNBZ and CN) show $\delta^{34}\text{S}$ values of 14.9 and 14.2 ‰ VCDT, respectively.

Carbon and oxygen isotope analyses were performed on carbonate minerals (dolomite and calcite), and on the limestone host rock of Erika and Anita (Table 4.7). The $\delta^{13}\text{C}$ and $\delta^{18}\text{O}$ values of the barren limestone (HR Cal) hosting the mineralized horizons range between -0.2 and -7.2 ‰ VPDB and 22.5 and 24.2 ‰ VSMOW, respectively (Table 4.7). Two samples of sparry calcite (Sp Cal) from veins cutting the host dolomite and limestone have $\delta^{13}\text{C}$ values between 0.1 and 2.6 ‰ VDPB and $\delta^{18}\text{O}$ values between 18.6 and 20.9 ‰ VSMOW.

The early dolomite generation (DST) is characterized by a narrow range in $\delta^{13}\text{C}$ (2.2 to 2.6 ‰ VPDB) and in $\delta^{18}\text{O}$ (26.2 to 27 ‰ VSMOW). Dolomite Dol1 shows a limited variation in $\delta^{18}\text{O}$, with values ranging from 24.4 to 24.7 ‰ VSMOW. Conversely, the $\delta^{13}\text{C}$ values of Dol1 are in a wide range, varying from 0.6 to 3.3 ‰ VPDB. Saddle dolomite (Dol2) has $\delta^{18}\text{O}$ values from 18.4 to 22 ‰ VSMOW, and $\delta^{13}\text{C}$ values between -0.2 and 2.0 VPDB (Table 4.6).

TABLE 4.7. Carbon and oxygen isotope compositions of dolomite and calcite from the Cristal prospect.

Sample ID	Sub-sample ID	Mineral*	$\delta^{13}\text{C}$ (‰ VPDB)	$\delta^{18}\text{O}$ (‰ VSMOW)
CR03-4	CR03-5_Dol	Dol2	1.98	19.67
CR07-8	CR07-9_Dol	Dol1	3.33	24.68
CR13-2	CR13-2_DolA	Dol2	1.54	22.02
	CR13-2_DolB	Dol2	1.40	19.82
CR13-9	CR13-9_DSTA	DST	2.57	26.97
	CR13-9_DSTB	DST	2.58	27.05
CR13-10	CR13-10_Cal	Sp Cal	0.10	20.90
CR18-4	CR18-4_Dol	Dol2	1.33	18.84
CR18-5	CR18-5_Dol	Dol2	0.80	19.02
CR18-15	CR18-15_DolA	Dol2	1.33	20.05
	CR18-15_DolB	Dol2	-0.16	18.39
CR18-16	CR18-16_Dol	Dol2	0.86	20.33
CR18-18	CR18-18_Dol	Dol2	0.92	18.92
CR18-22	CR18-22_Dol	Dol2	1.65	19.45
	CR18-23_DolA	DST	2.24	26.25
CR18-23	CR18-23_DolB	Dol1	0.62	24.45
	CR18-23_DolC	Dol2	1.53	19.59
ANITA	ANITA_A	HR Cal	0.26	22.51
	ANITA_B	Sp Cal	-2.59	18.56
ERIKA	ERIKA	HR Cal	-7.17	24.20

Note; * DST = dolostone-forming dolomite; Dol1 = early hydrothermal dolomite; Dol2 = late (sparry) hydrothermal dolomite; Sp Cal = sparry calcite; HR Cal = host rock calcite.

Lead and strontium isotope geochemistry

The Pb isotope composition (PbIC) of early dolomite DST (Table 4.7) is very different from that of dolomite Dol1 (Table 4.7). DST is characterized by $^{206}\text{Pb}/^{204}\text{Pb} = 19.767 \pm 0.002$, $^{207}\text{Pb}/^{204}\text{Pb} = 15.719 \pm 0.001$, $^{208}\text{Pb}/^{204}\text{Pb} = 38.745 \pm 0.006$, whereas Dol1 has $^{206}\text{Pb}/^{204}\text{Pb} = 19.163 \pm 0.001$, $^{207}\text{Pb}/^{204}\text{Pb} = 15.692 \pm 0.001$, and $^{208}\text{Pb}/^{204}\text{Pb} = 38.860 \pm 0.005$. The average PbIC of saddle dolomite Dol2 ($^{206}\text{Pb}/^{204}\text{Pb} = 19.018 \pm 0.006$, $^{207}\text{Pb}/^{204}\text{Pb} = 15.679 \pm 0.005$, $^{208}\text{Pb}/^{204}\text{Pb} = 38.841 \pm 0.015$; Table 4.7) is slightly lower than that of Dol1. The PbIC of sphalerite and pyrite from the Esperanza drill cores (Table 4.6) is similar to that of dolomite Dol2. The least radiogenic sulfide PbIC is $^{206}\text{Pb}/^{204}\text{Pb} = 18.954 \pm 0.009$, $^{207}\text{Pb}/^{204}\text{Pb} = 15.669 \pm 0.007$ and $^{208}\text{Pb}/^{204}\text{Pb} = 38.862 \pm 0.023$. The most radiogenic PbIC ($^{206}\text{Pb}/^{204}\text{Pb} = 19.261 \pm 0.001$, $^{207}\text{Pb}/^{204}\text{Pb} = 15.986 \pm 0.001$ and $^{208}\text{Pb}/^{204}\text{Pb} = 39.916 \pm 0.002$) was found in the only measured pyrite specimen from the Cristal area.

The PbIC of sphalerite, galena and pyrite from the Charlita North orebody is less radiogenic than that of the sulfides from Esperanza drill cores (Table 4.7). The measured Charlita North ratios are between $^{206}\text{Pb}/^{204}\text{Pb} = 18.753 \pm 0.001$, $^{207}\text{Pb}/^{204}\text{Pb} = 15.669 \pm 0.007$ and $^{208}\text{Pb}/^{204}\text{Pb} = 38.541 \pm 0.003$, and $^{206}\text{Pb}/^{204}\text{Pb} = 18.918 \pm 0.001$, $^{207}\text{Pb}/^{204}\text{Pb} = 15.699 \pm 0.001$ $^{208}\text{Pb}/^{204}\text{Pb} = 38.887 \pm 0.003$.

Cristal smithsonite has an average Pb isotope composition very similar to those of sphalerite: $^{206}\text{Pb}/^{204}\text{Pb} = 18.999 \pm 0.002$, $^{207}\text{Pb}/^{204}\text{Pb} = 15.701 \pm 0.002$, $^{208}\text{Pb}/^{204}\text{Pb} = 38.994 \pm 0.006$. These values are also similar to the Pb isotope compositions of smithsonite from the Mina Grande nearby deposit: $^{206}\text{Pb}/^{204}\text{Pb} = 18.931 \pm 0.001$, $^{207}\text{Pb}/^{204}\text{Pb} = 15.679 \pm 0.001$, $^{208}\text{Pb}/^{204}\text{Pb} = 38.850 \pm 0.004$.

$^{87}\text{Sr}/^{86}\text{Sr}$ in dolomites varies between 0.708259 ± 0.000009 and 0.708817 ± 0.000016 (Table 4.7). DST shows a $^{87}\text{Sr}/^{86}\text{Sr}$ composition similar to Dol1, whereas the maximum $^{87}\text{Sr}/^{86}\text{Sr}$ (0.708817) ratio has been measured in Dol2 (Table 4.6).

Discussion

Dolomitization in the Cristal area

In the Cristal area the hypogene sulfide mineralization, consisting almost exclusively of sphalerite and pyrite with minor galena, is hosted in strongly dolomitized members of the Condorsinga Formation. The original host limestone (HR Cal) was only observed in the outcrop samples of the Erika and Anita occurrences. Similarly to the nearby Florida Canyon Zn sulfide deposit (Basuki et al., 2008; Reid, 2001), in the most mineralized samples of the Cristal prospect we distinguished early and late dolomite generations (DST, Dol1 and Dol2), cut by successive sparry calcite veins (Sp Cal). The first dolomite generation (DST) shows textures typical of dolomite genetically related to shallow- to deep-burial diagenesis, which produces a pervasive recrystallization locally destroying the depositional fabric of the original limestones (Warren, 2000). DST is overprinted by two successive dolomite phases: Dol1, which mimics the textures of the DST dolomite, and Dol2, which is coarser-grained from sparry to saddle. These textures are typical of

hydrothermal dolomites (Radke and Mathis, 1980), and are similar to those observed in the host rock of the nearby Florida Canyon sulfide deposit, where dolomite was considered to have been formed through two separate hydrothermal stages, preceding the emplacement of sulfide mineralization (Basuki et al., 2008; Reid, 2001). Using SEM-EDS and WDS analyses, the late dolomite generation at Cristal (Dol2) was shown to be Fe- (up to 10 wt. % FeO) and Mn-rich (up to 1.4 wt. % MnO). These Mn and Fe contents are much higher than those observed in the hydrothermal dolomites of the San Vicente MVT deposit (where the maximum Fe and Mn contents are up to 5000 and 3000 ppm, respectively; Spangenberg et al., 1999).

The carbon and oxygen isotope ratios of the remnants of the host limestone at Cristal ($\delta^{13}\text{C} = -0.2$ to -7.2 ‰ VPDB, $\delta^{18}\text{O} = 22.5$ to 24 ‰ VSMOW; Fig. 4.8) are similar to those of the Jurassic host limestone at Mina Grande (Arfè et al., 2017b), but not compatible with the $\delta^{18}\text{O}$ and $\delta^{13}\text{C}$ of marine carbonates of the same age (Jenkyns et al., 2002). This suggests that the limestone lost the original marine isotopic signature during diagenetic alteration. The various dolomite generations have similar C isotopic compositions (DST has $\delta^{13}\text{C}$ of 2.2 and 2.6 ‰ VPDB, Dol1 has $\delta^{13}\text{C}$ varying from 0.6 to 3.3 ‰ VPDB, and Dol2 has $\delta^{13}\text{C}$ values between -0.2 and 2.0 VPDB), but show very different O isotopic compositions (Fig. 4.8): DST has average $\delta^{18}\text{O}$ of 26.8 ‰ VSMOW, Dol1 has $\delta^{18}\text{O}$ between 24.4 and 24.7 ‰ VSMOW, and Dol2 has $\delta^{18}\text{O}$ between 18.4 and 22 ‰ VSMOW.

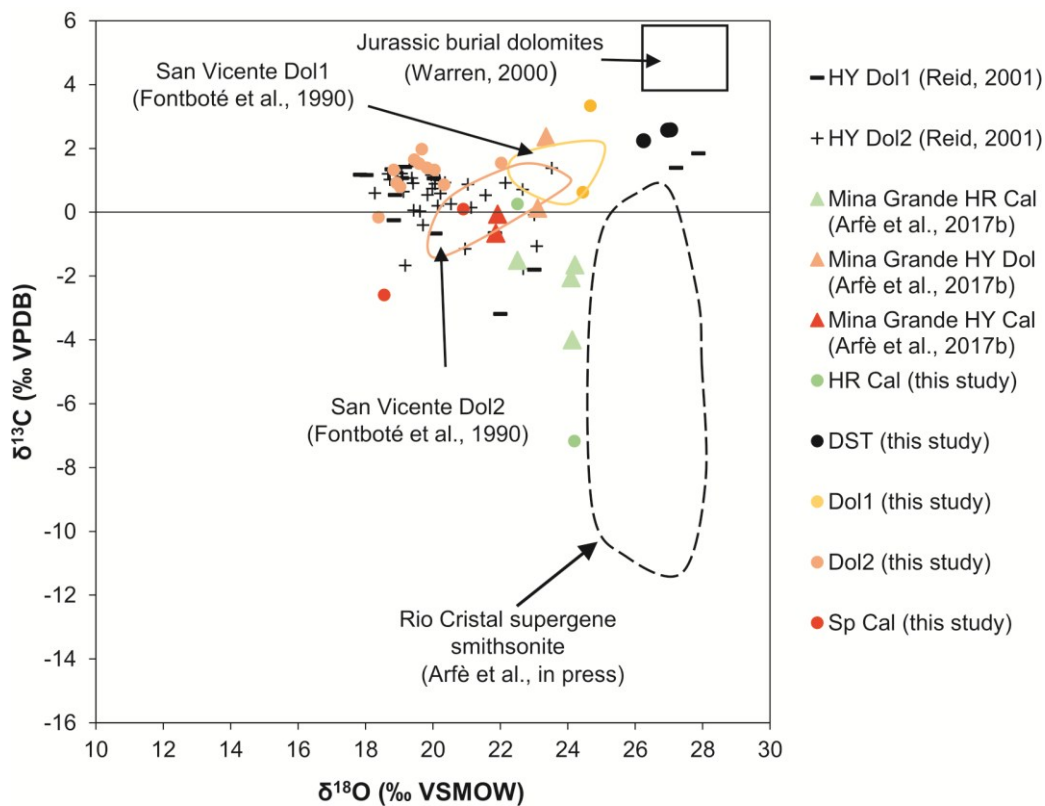


Figure 4.8. Carbon and oxygen stable isotope compositions of dolomite and calcite from the Cristal area, compared with dolomite and calcite from the Mina Grande deposit (Arfè et al., 2017b), and dolomites from Florida Canyon (Reid, 2001) and San Vicente (Fontboté et al., 1990).

$^{87}\text{Sr}/^{86}\text{Sr}$ of the different dolomite generations is quite similar (around 0.7083 in DST and Dol1), but the highest $^{87}\text{Sr}/^{86}\text{Sr}$ (0.708817) was measured in Dol2. Though DST has textures compatible with shallow diagenetic processes, its C, O and especially Sr isotopic compositions do not match with those of Pliensbachian-Toarcian marine or shallow burial dolomites ($^{87}\text{Sr}/^{86}\text{Sr}$ from 0.7070 to 0.7074; McArthur and Howarth, 2004). This suggests that DST likely formed during a deep burial dolomitization process (Dera et al., 2009; Warren, 2000). The C, O and Sr isotopic compositions of Dol1 and Dol2 are perfectly compatible with a hydrothermal genesis, in agreement with their textures (sparry to saddle crystals) and chemical compositions (Dol2 is Fe- and Mn-bearing). The ^{18}O depletion observed in Dol2 relative to Dol1 likely reflects the progressive increase in temperature during precipitation of Dol2. The similarity in $\delta^{13}\text{C}$ and $^{87}\text{Sr}/^{86}\text{Sr}$ between DST and Dol1 suggests that the early hydrothermal dolomite Dol1 inherited the carbon and strontium isotopes from DST (this confirming the replacive character of Dol1 over DST), compared to the late Dol2 (where open space filling prevailed), which was more affected by carbon and strontium contributions from other sources.

In the nearby Florida Canyon and Florcita deposits, several generations of dolomite have been described (Reid, 2001; Basuki et al., 2008), but none of these generations has textures and chemical compositions similar to the DST. The Florida Canyon and Florcita dolomites are texturally and compositionally similar to the Cristal Dol1 and Dol2 phases (Reid, 2001). Comparing the above data with the dolomites measured in other ore deposits from the Pucará basin, we could observe that Dol1 and Dol2 also match the oxygen isotope composition of the hydrothermal dolomites from the San Vicente MVT deposit (central Peru; Fontboté et al., 1990). This suggests similar conditions during the formation of the Cristal dolomites and the dolomites of other Peruvian MVT deposits (e.g. Florida Canyon and San Vicente).

Genesis of sulfide mineralization

The sulfide association observed at Cristal is very similar to the associations recorded in the Florida Canyon and Florcita deposits (Basuki et al., 2008). Cristal mineralization is dominated by sphalerite and clearly postdates the Dol2 dolomite phase. Similarly to the Florida Canyon deposit, the sulfides occur in cavities and geodes in Dol2. Cristal sphalerite is always enriched in Fe (up to 12 wt. %), as well as in Ge (up to 383 ppm; Mondillo et al., 2018). This uncommon chemical signature of the Cristal sphalerite has been observed only in few MVT deposits worldwide, because Ge and Fe are generally inversely correlated: low-temperature hydrothermal sphalerites (e.g., in carbonate-replacement MVT deposits) are characterized by high Ge and low Fe concentrations, whereas high Fe and low Ge concentrations have been assigned to high-temperature sphalerites in skarns, epithermal and massive sulfide deposits (Cook et al., 2009; Frenzel et al., 2016). As no detailed geochemical data are available for the Florida Canyon and Florcita sphalerite, it was not possible to compare the Ge-Fe correlation in the other sphalerite occurrences from the Bongará district. The first geochemical data for Fe-rich sphalerite in MVT deposits were reported by Song (1984) and Song and Tan (1996) for the Fankou deposit in China, where sphalerite contains from 3.8 to 6.2 wt. % Fe, and Ge

values range from 80 to 110 ppm. Other Fe-rich sphalerites in MVT deposits were described from the Tres Marias Mine in Mexico (Saini-Eidukat et al., 2009) and from the Saint-Salvy deposit in France (Belissant et al., 2014). In the Tres Marias Mine, Fe-rich sphalerite (ca. 10 wt.% Fe) contains more Ge (ca. 800 ppm) than the Fe-poor (5.5 wt.% Fe) sphalerite (470 ppm Ge). In contrast, at Saint-Salvy, sphalerite with high amounts of Fe (ca. 11.7 wt.%) contains less Ge (ca. 0.4 ppm) than Fe-poor sphalerite (2.6 wt. % Fe and 1363 ppm Ge). These characteristics are seldom associated with low-temperature MVT deposits, but have been recognized in high-temperature ores, such as the Kipushi deposit (Democratic Republic of Congo), which formed at temperatures > 300 °C (Schneider et al., 2007). The Kipushi sphalerite has Fe contents around 5 wt. % and average Ge amounts around 200 ppm. By using the geothermometer of Frenzel et al. (2016), based on trace elements composition in sphalerite, Mondillo et al. (2018) obtained a homogenization temperature of 230 ± 50 °C for the Cristal sphalerite. This temperature is slightly higher than those measured in the other MVT deposits of the Bongarà district (homogenization temperatures of ca. 80 to 190 °C, corresponding to pressure-corrected temperatures of ca. 110 to 225 °C; Basuki and Spooner 2009), but also higher than average formation temperatures of typical MVT deposits (Frenzel et al., 2016 and references therein; Leach et al., 2005).

Another peculiar feature of the Cristal mineralization is the strong in situ hydrothermal alteration of detrital muscovite locally transformed into hendricksite, a Zn-Mn mica only recorded from the Zn-Mn-bearing mineral assemblages of high temperature metamorphism-related hypogene nonsulfide Zn deposits (Evans and Strens, 1966; Frondel and Ito, 1966; Hitzman et al., 2003). This kind of alteration is also associated with the high Mn contents detected in the bulk rock analyses. In fact, at Cristal maximum values of ca. 3 wt. % MnO have been measured, as well as high concentrations of other elements (e.g Fe and Co) that are commonly considered more typical of “polymetallic” mineralizations than of MVT deposits (Hitzman et al., 2003 and references therein; Leach et al., 2005).

The sulfur isotopic compositions of the Cristal sphalerite ($\delta^{34}\text{S}$ between 14 to 15 ‰ VCDT; mean value 14.5 ‰ VCDT; Fig. 4.9) are isotopically heavier than sulfur isotopic compositions derived from primary magmatic sources (from -3 to 3 ‰ VCDT; Ohmoto and Rye, 1979). However, the S isotopic compositions of the sphalerites from Cristal are considerably different from the $\delta^{34}\text{S}$ values measured on sphalerites from the Florida Canyon deposit (-13.7 to 17.6 ‰ VCDT; mean value ca. 1 ‰ VCDT; Basuki et al., 2008; Fig. 4.9), but comparable with the positive values measured on sphalerites from the Florcita deposit (11.4 to 19.3 ‰ VCDT; mean value ca. 15.5 ‰ VCDT; Basuki et al., 2008; Fig.4.9). The $\delta^{34}\text{S}$ values of sphalerite from Cristal are also comparable to the mean $\delta^{34}\text{S}$ value of sphalerite from San Vicente (10.3 ± 2.5 ‰; Fontboté et al., 1990).

Despite the differences in the S isotopic composition of sphalerite from Florida Canyon, Florcita, and the San Vicente deposit, Basuki et al. (2008) suggest that the observed $\delta^{34}\text{S}$ values are consistent with thermochemical sulfate reduction (TSR): the dissolved sulfate in the metals-bearing fluids reacted with organic matter in carbonate host rocks at temperatures >120°C, producing H₂S which quickly reacted precipitating sulfides (Basuki

et al., 2008). TSR is common in mineral deposit settings at temperatures ranging from 100 to 180°C (Machel, 2001 and references therein). Considering that Cristal sphalerite shares several features with the Florida Canyon, Florcita, and the San Vicente sphalerites (i.e. the petrographic characteristics, and the position in the paragenesis of the mineralization), and has high Fe-contents, suggesting high deposition temperatures, it could form after H₂S production through TSR in analogy to the above-mentioned deposits. For the Florida Canyon and Florcita sphalerite, Basuki et al. (2008) suggested two possible sulfate sources: (1) Late Cretaceous seawater ($\delta^{34}\text{S}$ from ca. 18 to 21 ‰; Paytan et al., 2004) and (2) Middle Triassic-Late Jurassic evaporitic sulfate minerals from the Chambará and Condorsinga Formations ($\delta^{34}\text{S}$ from ca. 12 to 15 ‰; Claypool et al., 1980). This could be valid also for the Cristal sulfides. The Florcita mineralization occurs near the stratigraphic contact between the Condorsinga and Goyllarisquizga Formations (Basuki et al., 2008), similarly to Cristal sulfides. Its sulfur isotopic composition is similar to that of Cristal, which suggests that Cristal and Florcita could be related to the same MVT mineralization event, acting at a district scale.

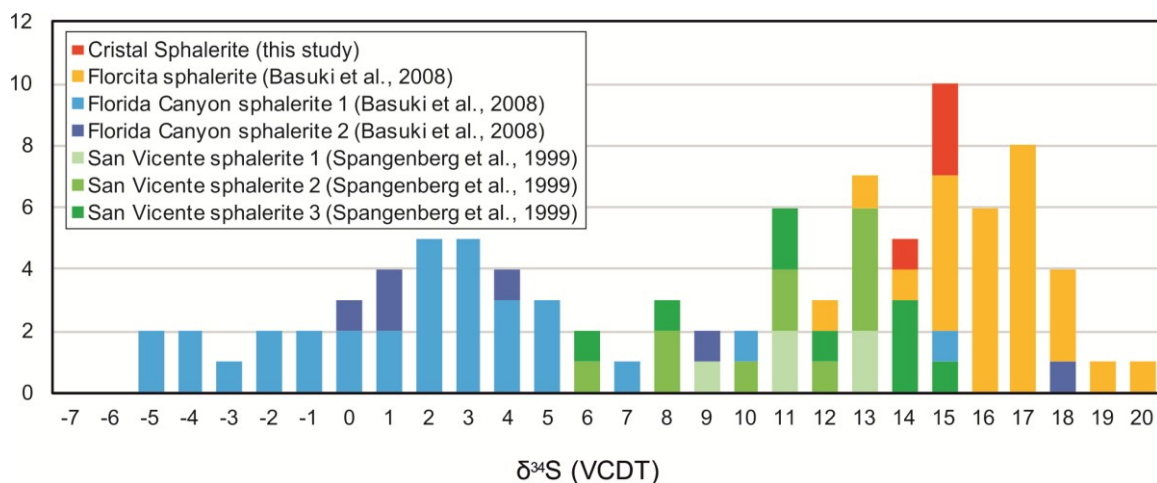


Figure 4.9. Sulfur stable isotope compositions of Cristal sphalerite, compared with compositions of sulfides occurring in other deposits hosted in the Pucará Group.

The PbIC of the sphalerite specimens define two data clusters: more radiogenic values were measured for a set of samples from the Cristal prospect *stricto sensu*, whereas less radiogenic values were obtained on samples from the Charlita North occurrence (Fig. 4.10). The PbIC difference requires at least two distinct sulfide-bearing hydrothermal pulses in the broader Cristal area. This implies that Cristal and Charlita North mineralizations formed at different times. The PbIC of the early dolomite generation (DST) is different from that of both sulfides and late stage dolomites (Dol1 and Dol2). This indicates that the first dolomitization (DST) of the host rock at Cristal is not related to the same (hydrothermal) system that precipitated sulfides. The required different origin is in agreement with the data from C, O and Sr isotope analyses.

The Cristal sulfides (Fig. 4.10A) have PbIC mostly lying in the field occupied by the galena specimens from other deposits hosted in the Pucará Group carbonates, namely the

San Vicente and Shalypaico MVT deposits (Spangenberg et al., 1999). In contrast, sulfides from Charlita North show Pb isotopic compositions similar to those observed in the galenas from the Hualgayoc area (Macfarlane and Petersen, 1990), Dome de Yauli (Gunnesch et al., 1990) and Cerro de Pasco (Kulp et al., 1959), whose mineralizations have been genetically associated with Tertiary volcanic intrusions (Baumgartner and Fontboté, 2008; Baumgartner et al., 2009; Beuchat et al., 2001; Macfarlane and Petersen 1990).

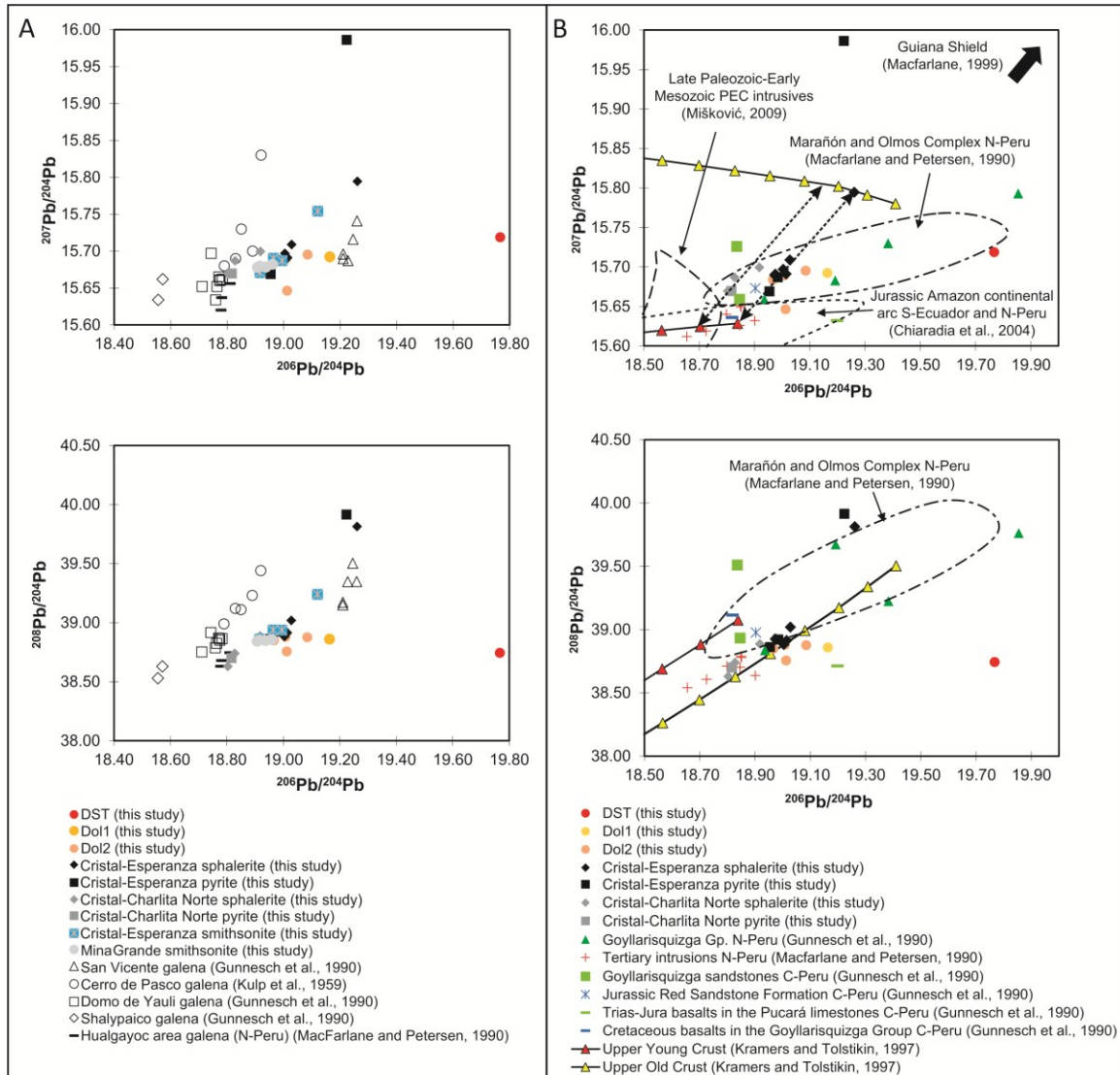


Figure 4.10. Lead isotopic compositions of Cristal sulfides, dolomites and smithsonite. Compositions of minerals from other deposits hosted in the Pucará Group, and of igneous and metamorphic basement rocks of northern Peru, are plotted for reference. The model curves for the Young and Old Upper Crust of Kramers and Tolstikhin (1997) are marked by red and yellow triangles, respectively. Each triangle represents a 200 Ma age increase from right to left, zero age being the rightmost point of each curve.

Figure 4.10B presents the Pb isotopic data in a broader context. It includes literature data for Late Paleozoic-to-Tertiary igneous rocks and for older metamorphic basement rocks. In terms of the Pb evolution model of Kramers and Tolstikhin (1997), the Jurassic and

Tertiary igneous rocks plot close to the model curve representing the young/juvenile upper crust (YUC), whereas the basement rocks plot close to, or extend to more uranogenic and thorogenic values than the model curve representing the old/reworked upper crust (OUC). Most of the sulfides from Esperanza and Charlita North lie between YUC and OUC, as do most deposits worldwide. This reflects the obvious truism that metals in most mineralizations derive from the continental crust.

The PbIC can help constrain the derivation of the Bongará metals. Firstly, it is observed that several data-points from Esperanza (black symbols) define a linear trend in Fig. 4.10B top, and several data-points from Charlita North (grey symbols) also define a linear trend, albeit a distinct one (Fig. 4.10B top). Linear trends in common-denominator isotope correlation diagrams are evidence of binary mixing, in the present case suggesting the derivation of Pb (and other metals) partly from a YUC-like source and partly from an OUC-like source (the grey and the black linear arrays converge towards an Esperanza sphalerite point on the OUC curve with a Late Paleozoic model age). The OUC-like end-member can be accounted for by admixture of Pb from the crustal basement underlying the Andean chain. This crystalline basement, represented by the Paleozoic Marañon Complex, also crops out in the western and upper parts of the Bongará area. Its Pb isotopic composition reaches extremely radiogenic $^{206}\text{Pb}/^{204}\text{Pb}$ ratios, as expected of old U-bearing crustal rocks. The radiogenic Pb isotope ratios of the basement roughly match all dolomite and sulfide compositions from Cristal and Charlita North area. This correspondence suggests that the Marañon Complex is a likely source of the Pb occurring in the sulfides. If the MVT mineralization model is valid for the Bongará region, the Marañon Complex could have been leached of metals by hot brines traveling through basement faults, which at a certain point migrated upward in the Pucará Group carbonates, precipitating the sulfides through TSR. The brines possibly originated from seawater or groundwater migrating downward through basement faults, and heated at depth (Basuki et al., 2008).

The thermal engine pushing the brines through the basement is not well constrained. As suggested by Basuki et al. (2008), it could have been the change of the geothermal gradient related to the Late Cretaceous-early Tertiary Andean tectonics. Alternatively, the required heat could have been provided by a pluton. A magmatic heat source would have the attractive property of accounting for the PbIC, as in Peru the Mesozoic and Tertiary magmatic rocks normally have compositions close to the YUC (e.g. Chiaradia et al., 2004; Gunnesch et al., 1990; Macfarlane and Petersen, 1990; Mišković, 2009). It would also explain the high homogenization temperature of sphalerite, the high Mn contents in the rocks, and the presence of hendricksite, but would contrast with sulfur isotope systematics, which supports a sedimentary non-magmatic origin of the sulfur. Moreover, Tertiary intrusions have not been recorded in the Bongará area so far (Instituto Geológico Minero y Metalúrgico-INGEMMET, 1995) and evidence of Tertiary igneous activity has been found only in the relatively near Bagua basin (ca. 60 Km to the west), where volcanic tuffs of Paleocene to Miocene age are intercalated at different levels in the Tertiary continental sequence of the Bagua syncline (Naeser et al., 1991). As very long-distance transport of Pb via hydrothermal systems is unlikely, the existence of a Tertiary

magmatic end-member for the mixing process involved in the metal supply to the Cristal hydrothermal system remains speculative. An older igneous source is possibly suggested by the Charlita North array, whose less radiogenic end-member lies at the intersection of the literature field of the Late Paleozoic-Early Mesozoic intrusives of the Peruvian Eastern Cordillera, with the field of the Jurassic N-Peru magmatic arc.

One Esperanza pyrite contains more radiogenic Pb than the OUC model curve, this requiring an additional source of metal. In this area of Peru rocks characterized by $^{207}\text{Pb}/^{204}\text{Pb}$ ratios higher than those of the Marañón Complex are represented by the sediments derived from the Brazilian-Guyana shield occurring in the western part of the Pucará basin (Rosas et al., 2007), which due to the ancient age (ca. 3 Ga) of the shield have $^{207}\text{Pb}/^{204}\text{Pb}$ ratios up to 17 (Macfarlane, 1999 and references therein). A similar case was reported by Fontboté et al. (1990) for the San Vicente deposit, where the main source of Pb was considered to be the clastic components eroded from the Precambrian upper crust of the Brazilian Shield, which occur in the Red Sandstone Formation underlying the Pucará carbonate sequence in that area.

The observation that PbIC varies among sulfides of the same drill core (and even more so between Esperanza and Charlita North) and the absence of a single, tight linear trend mean that the Pb isotope record cannot be accounted for by a simple binary mixing between one well-defined YUC-like and one well-defined OUC-like end-member. If one single plumbing system, or a single source for the metals had been involved, the PbIC should be the same in the two occurrences. Instead, what is required is a plurality of pulses of broadly similar fluids, which tapped multiple metal sources and were variable both in space and in time. This pattern is consistent with the observation by MacFarlane et al. (1990) that sedimentary-hosted ore deposits have very different PbIC, even when they insist on the same formation, as several metal sources contributed to the final sulfides. Since Pb isotope compositions are mostly preserved during the alteration from sulfides to nonsulfides (Mondillo et al., 2014b), the similarities between the Pb isotopic compositions of the Cristal sphalerite and smithsonite and the Mina Grande smithsonite suggest that the protores of the two deposits were originally similar.

Conclusions

1. The sulfide association observed at Cristal is similar to those recorded in the Florida Canyon and Florcita MVT deposits from the same Bongará district (Basuki et al., 2008). The Cristal mineralization is dominated by the Zn-sulfide sphalerite and clearly postdates two hydrothermal dolomitization phases, which favored the emplacement of sulfides by increasing the porosity of the host rock. The sulfides occur in cavities and geodes mainly associated with saddle dolomite, similarly to the Florida Canyon mineralization.
2. Cristal sphalerite is enriched both in Fe (up to 12 wt. % Fe), and Ge (up to 383 ppm Ge). This positive correlation is uncommon and points to a high-temperature origin of sphalerite.

3. The Mn-Zn-mica hendricksite is formed by hydrothermal alteration of detrital muscovite. This is a fairly uncommon phase and confirms the high temperature depositional environment.
4. The sulfur isotopic composition of the Cristal sphalerite (from 14 to 15 ‰ VCDT) is isotopically heavier than the sulfur isotope ratios derived from primary magmatic sources. This sulfur isotopic composition is similar to that measured in the Florcita deposit.
5. The Pb isotopic compositions of sphalerite are heterogeneous. In the Esperanza area Pb is more radiogenic than at Charlita North. This difference requires chemically (and possibly temporally) distinct pulses of hydrothermal fluids. The mineralizing fluids transported metals derived from at least three different sources: the Marañón basement complex, which has Pb isotopic ratios that match the dolomite and sulfide compositions from the Esperanza and Charlita North areas; a minor detrital component from the Precambrian Brazil-Guyana craton; an elusive igneous source, isotopically identical to the Peruvian igneous rocks of Paleozoic to Tertiary age.
6. The overall context suggests that Cristal and the other deposits of the Bongará region could be related to the same MVT mineralization event, acting at the district scale.

Chapter 5:

The Cristal Zn prospect (Amazonas region, Northern Peru). Part II: An example of supergene zinc enrichments in tropical areas

Published in “Ore Geology Reviews”

Reference: Arfè, G., Mondillo, N., Boni, M., Joachimski, M., Balassone, G., Mormone, A., Santoro L., Castro Medrano E. The Cristal Zn prospect (Amazonas region, Northern Peru). Part II: An example of supergene zinc enrichments in tropical areas. Ore Geology Reviews, (in press).

Introduction

The Cristal Zn prospect is located in the Bongará area (Amazonas region, northern Peru, 740 km north of Lima and 245 km northeast of the coastal city of Chiclayo), at the northern extremity of a carbonate belt that extends for 900 km along the eastern flank of the Andean Cordillera, from the Ecuador border to the south (Fig. 5.1). This belt is on the western margin of the Subandean Foreland Basin and within the Subandean Fold-and-Thrust Belt domain (Fig. 5.1) of the Amazonas Region in Peru. The study area is at the junction of the 1:100.000 topographic sheets 12-g (Bagua Grande) and 12-h (Jumbilla) of the Instituto Geográfico Nacional (IGN) of Peru. The geographic UTM coordinates of the center of the area correspond to 826,200E and 9,375,000N (Zone 17, Datum WGS 84).

The Cristal prospect is situated in the northernmost part of a wide mining district, corresponding to the so-called “Charlotte Bongará Zinc Project” (ZincOne Resources Inc.), which covers an area of approximately 110 km² (Fig. 5.1). The mineralized area consists of many Zn occurrences that contain mixed sulfide and nonsulfide ores (Anglo Peruana, 2005; Wright, 2010). The nonsulfide ores are interpreted to be the product of weathering of primary sulfide bodies (Anglo Peruana, 2005; Wright, 2010; Brophy, 2012), which have the characteristics of a Mississippi Valley-type mineralization (Reid, 2001; Basuki, 2006; Basuki and Spooner, 2008; Basuki and Spooner, 2009; Mondillo et al., in press).

Supergene nonsulfide ores are developed when sulfide bodies are exposed to meteoric alteration (Hitzman et al., 2003). Recent studies (Reichert and Borg, 2008; Reichert, 2009) suggested that arid climate conditions represent the most favorable conditions for oxidation and formation of nonsulfide ore bodies. Under an arid climate, enhanced sulfide oxidation has been attributed to scarce biogenic activity within the soil and to the low rates of dilution, dispersion and removal of metals. Such features are mostly related to the low levels of the water table in arid regions. The possibility of developing supergene enrichment in tropical climates has been already discussed by Hitzman et al. (2003) and by Boni and Mondillo (2015), who reported that supergene zinc deposits are commonly found in both arid and tropical modern as well as paleo-environments. Under tropical

weathering with high rainfall rates, the oxidation of sulfide bodies results in the formation of acidic and oxidized solutions favoring karst development (Thornber and Taylor, 1992). These solutions become progressively zinc-enriched because zinc is more readily separated from other metals (Rose et al., 1979; Sangameshwar and Barnes, 1983). Significant amounts of smithsonite (and less hemimorphite, hydrozincite and Zn-clays) may precipitate within karst cavities, thus making karst-hosted deposits the most common nonsulfide occurrence in this climate setting. Only a few technical reports from mining and consulting companies (Anglo Peruana, 2005; Brophy, 2012; Workman and Breede, 2016) had described the Zn-nonsulfide occurrences in the Charlotte Bongará area. Arfè et al. (2017b) presented the first comprehensive study of the Mina Grande nonsulfide deposit, located 6 km SE from the Cristal area (Fig. 5.1).

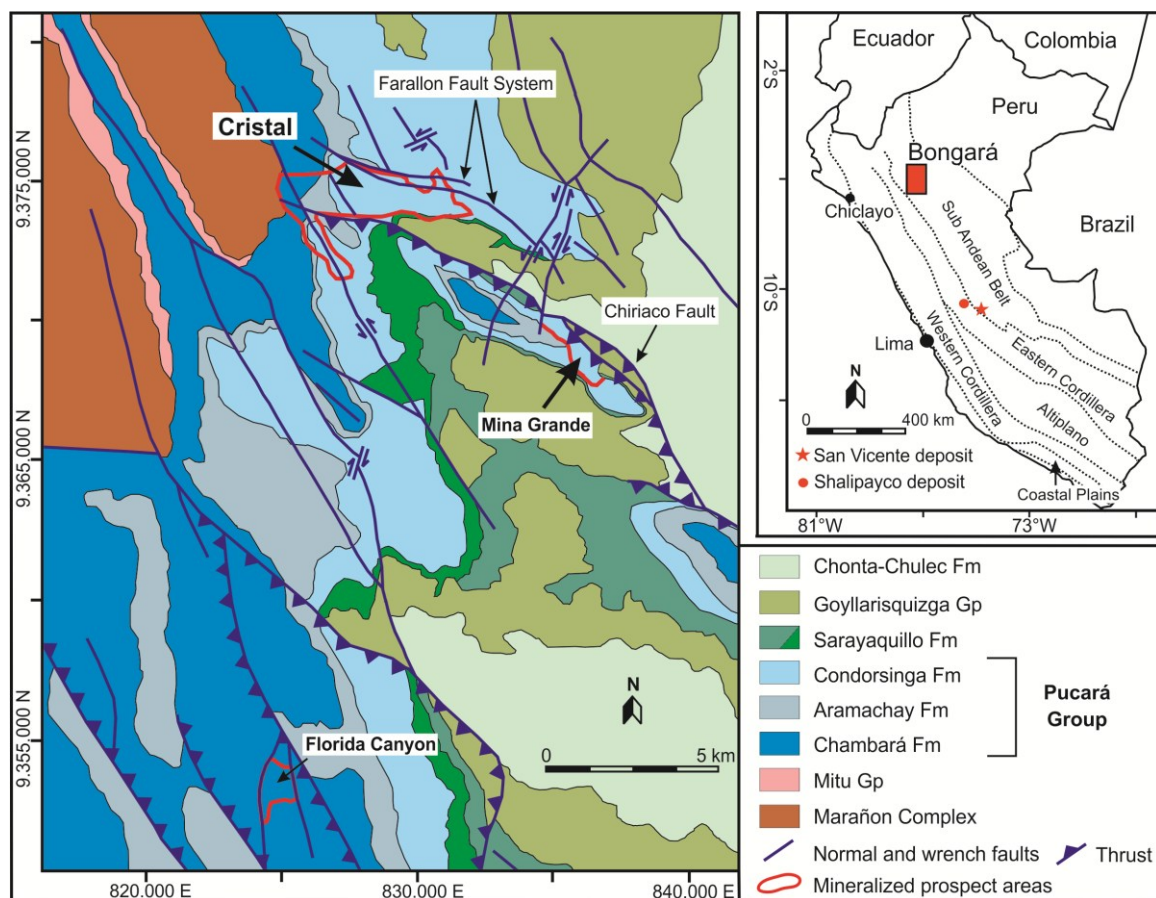


Figure 5.1. Geologic map (A) and location of the Bongará district within the Andean morphostructural units of northern Peru (B) (from Arfè et al., 2017b, modified).

Hydrozincite, smithsonite and hemimorphite are common in the ore minerals association of Mina Grande, and occur mostly in collapse breccias derived from the weathering of a sphalerite-rich protore in carbonate host rocks (Arfè et al., 2017b). However, hydrozincite also occurs as thin blankets on waste dumps throughout the mine site: this is indicative of a recent precipitation under present-day climatic conditions, and of still active weathering. At Cristal, the presence of sulfides still in place (Mondillo et al., in press) and

the absence of obvious recent karstic activity suggest that supergene alteration has acted in two different ways at Mina Grande and Cristal.

The main objective of this study is to document the geological, mineralogical and geochemical features of the Zn-nonsulfide mineralization in the Cristal area that may provide new paleoclimatic, as well as time constraints for the genesis of the supergene deposit. This work also aims to extend the knowledge about the supergene evolution from sulfides to nonsulfides in tropical climate conditions by comparing the Mina Grande and the Cristal mineralizations. For this purpose, we selected several samples from the best-mineralized drill cores at Cristal that are representative of the bulk ore. These samples were studied for whole rock chemistry, mineralogical composition and carbon and oxygen isotope geochemistry of the supergene carbonates.

Geology of the Bongará Zn district

The Zn mineralized zones of the Bongará area are hosted in the carbonate rocks belonging to the Pucará Group (Figs. 5.1 and 5.2). This group overlies the metamorphic units of the Marañon Complex (Fig. 5.2) that represent the Paleozoic basement of the Pucará Basin (Mišković et al., 2009). The Pucará depositional basin was developed in a post-rift phase during Late Triassic and Early Jurassic along a NNW-SSE shear zone (Rosas et al., 2007). In the Bongará area, the sedimentary sequences that are representative of the rift phase consist of polymictic continental conglomerates (with clasts of schists, volcanics, and granite; Fig. 5.2) and of red sandstones of the Middle-Late Triassic Mitu Group (Mathalone and Montoya, 1995; Basuki, 2006; Basuki and Spooner, 2008; Spikings et al., 2016). The units of the Pucará Group are stratigraphically subdivided (Fig. 5.2) into platform carbonates of the Chambará Formation (Late Triassic), deeper water shaly limestones partly rich in organic matter of the Aramachay Formation (Late Triassic-Early Jurassic), and platform carbonates of the Condorsinga Formation (Early Jurassic).

During Early to Middle Jurassic, regional uplift, karstification and erosional phases marked the end of the Condorsinga carbonate sedimentation and the onset of the overlying Upper Jurassic-Cretaceous Sarayaquillo Formation (Fig. 5.2; INGEMMET, 1995; Mathalone and Montoya, 1995; Reid, 2001). The latter formation consists of continental sequences of colluvial, alluvial and possibly lacustrine deposits, which commonly display abrupt facies changes (Loughman and Hallam, 1982; Reid, 2001). The entire Sarayaquillo Formation is thought to have a thickness of around 200 m (Fig. 5.2), which may vary locally. The first major Cretaceous transgression resulted in the sedimentation of the sandstones and conglomerates of the Goyllarisquizga Group (Lower Cretaceous). The Chonta-Chulec Formation was deposited afterward (Fig. 5.2), and consists mostly of shallow marine limestones and marls interbedded with silty mudstones. Late Cretaceous and Tertiary sequences are not exposed in the study area because they have been completely eroded after late Andean uplift and erosion.

Late Andean tectonics affected the Bongará area since the late Oligocene-early Miocene when the Quechua 1 compressional phase occurred (20.5 to 12 Ma; Klein et al., 2010;

Pfiffner and Gonzalez, 2013). Further tectonic pulses were recognized in Miocene (~ 8-7 Ma; Quechua II Phase) and early Pliocene (~5-4 Ma; Quechua III Phase), respectively. The last effects of late Andean tectonics occurred in the early Pleistocene, in correspondence to the Quechua IV Phase (2-1.6 Ma).



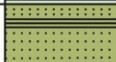










Quaternary				Polymictic river gravels.
Cretaceous	Upper		Chonta Fm	Limestones and marls interbedded with silty mudstones.
	Lower		Goyllarisquizga Gp 300-500 m	Quartzitic sandstones and conglomerates with minor intercalations of siltstones and mudstones.
Jurassic	Upper		Sarayaquillo Fm +/- 200 m	Subaerial-lacustrine sandstones and silty mudstones. Limestones boulder conglomerates.
	Lower		Condorsinga Fm +/- 300 m	Pelletal calcite mudstones and wackestones. Dolomitized packstones and wackestones. Laminated beds of calcitic mudstones.
			Aramachay Fm +/- 200 m	Thinly-bedded bituminous limestones and mudstones with ammonites.
			Chambará Fm > 1000 m	Micrites and biomicrites with fossiliferous horizons. Micrites with chert nodules. Bituminous packstones, locally dolomitized. Dolomitic grainstones. Thickly-bedded micrites and biomicrites.
Triassic	Middle		Mitu Gp	Continental red-bed sandstones, mudstones and polymictic conglomerates.
			Marañon Complex	Foliated greenish micaschists and metasedimentary rocks cut by magmatic dykes.
		 Mina Grande deposit and Cristal mineralization  Florida Canyon deposit		 Faults  Facies heteropy

Figure 5.2. Schematic stratigraphy of the succession in the Bongará area and stratigraphic position of the main ore deposits (from Arfè et al., 2017b, modified).

During the Quechua compressional phase a localized SSW–NNE stress promoted an inversion of the basement faults (Hermoza et al., 2006, 2007), which in Cristal area were developed as the Chiriaco and Farallon Faults (Fig. 5.3). On the other hand, in the Subandean belt the chain relaxation subsequent to the Quechua compression favored a partial re-inversion that can be observed in the normal dip slip movements of the Farallon fault (Fig. 5.3; Anglo Peruana, 2005).

Apatite fission tracks dating and on paleosurfaces (Laubacher and Naeser, 1994; Alcmán and Marksteiner, 1997; Garver et al., 2005; Montario, 2006) indicate that the onset of the uplift in both the Eastern Cordillera and Subandean zone may have commenced during late Oligocene-early Miocene. The constant growth of the easternmost domains of the Eastern Cordillera and the formation of the Subandean Fold-and-Thrust Belt of the Central Andes were accompanied by significant amounts of erosion (Isacks, 1988).

Masek et al. (1994) estimated that 2-6 km of erosion occurred in the last 10 Ma north of 19°S, which would indicate between 200 and 1200 m of isostatic rebound. No mass-balance studies have been carried out for the Eastern Cordillera of the Northern Andes, but a similar degree of erosion probably also occurred in this tropical wet zone (Gregory-Wodzicki, 2000). Gregory-Wodzicki (2000) and Hooghiemstra and Van der Hammen (2004) suggested that at 20 and 14 Ma the easternmost domains of northern Andes were located at 25% and 30% of their modern elevation, respectively. Additionally, at 10 Ma the height of the northern Andes was less than half of the today measured elevation, and only in the Pleistocene (~2.5 Ma) the northern Andes eventually reached their current altitudes (Hooghiemstra and Van der Hammen, 2004). From the paleo-elevation data of the Eastern Cordillera, Gregory-Wodzicki (2000) calculated rates of uplift from 0.03 to 0.05 mm/yr between middle Miocene (15 Ma) to early Pliocene (4-5 Ma), and from 0.6 mm/yr up to a maximum of 3 mm/yr between early and late Pliocene (from 4.5 to 2.7 Ma). Therefore, most of the uplift in the easternmost domains of the northern Peruvian Andes probably occurred from middle Miocene to Pliocene, with short-term pulses of great intensity in the latest stages.

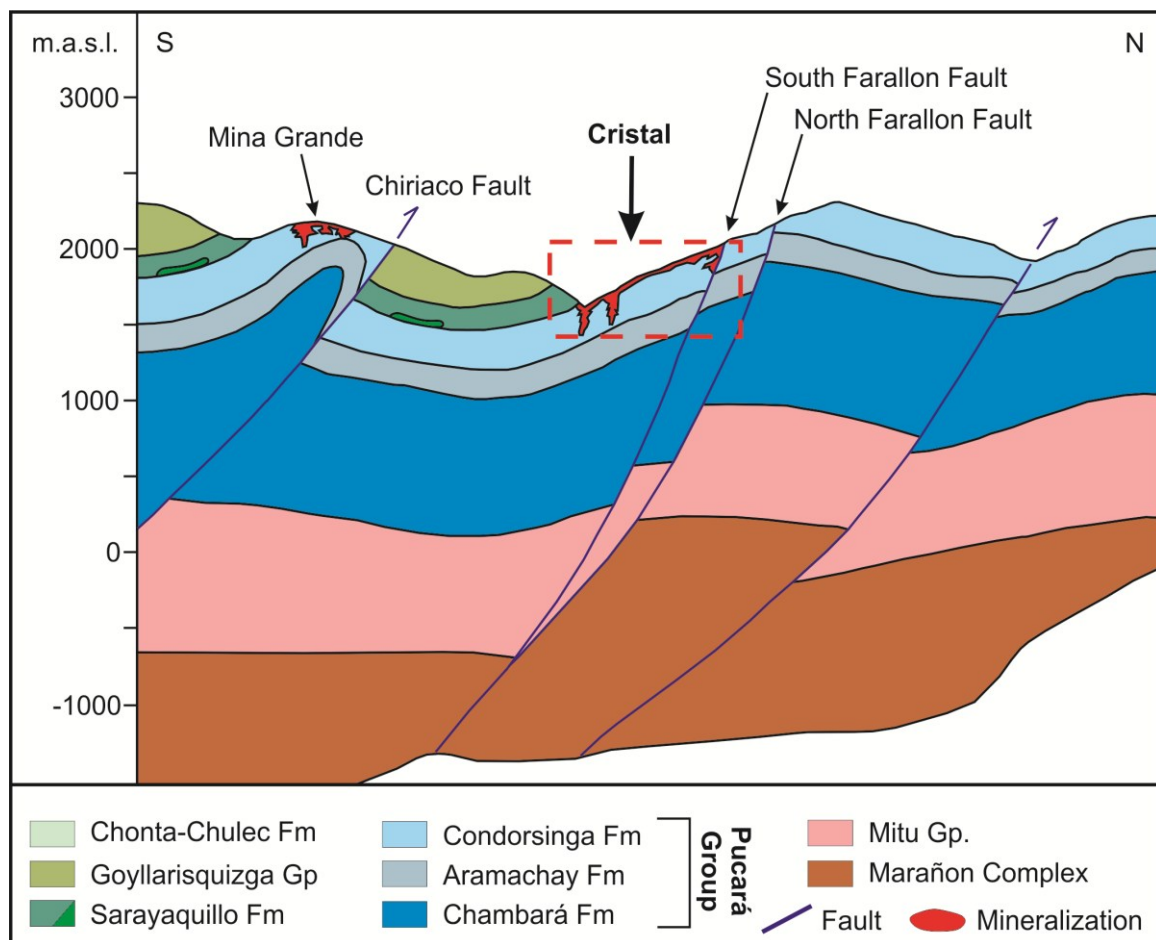


Figure 5.3. Schematic section of the Mina Grande and Cristal (dashed red squares) mineralized areas (from Arfè et al., 2017b, modified).

Climate evolution of the northern Andes from Miocene to Recent

Research on marine paleotemperatures (Savin et al., 1975; Hays et al., 1989; Dowsett et al., 1996; King, 1996) estimated from stable isotope geochemistry of Amazonian bivalves (Wesselingh et al., 2002; Kaandorp et al., 2003, 2005), coupled with relatively recent paleontological, palaeobotanical and palynological studies (Hoorn, 1994; Wijninga, 1996; Monsch, 1998; Gregory-Wodzicki, 2000) were used to reconstruct the climatic evolution of this sector of the Andes. Most authors argued that climatic conditions in the northeastern domains of the Amazonian South American Andes (e.g. Northern Peru, Ecuador and Colombia) were similar during the last ~20 Ma, if compared to present-day climate. From pollen records, Hoorn (1994) demonstrated that a rainforest ecosystem already existed in the Amazonian Andes in the Miocene. Later studies (Kaandorp et al., 2005) confirmed this interpretation and provided evidence that the seasonal rainfall patterns in the middle of the Miocene Climate Optimum (MCO = ~16 Ma; Flower, 1999; Zachos et al., 1994) were identical to those currently affecting the Amazonian Andes in Northern Peru. Additionally, these authors affirm that the oxygen isotope compositions of rainwaters during MCO were comparable to the values of present-day precipitation, suggesting comparable climatic conditions.

Hoorn et al. (2010) documented the Tertiary environmental evolution of the Amazonian region of Peru during a prolonged humid climate episode. From the Late Oligocene (~23 Ma) to the beginning of the Late Miocene (~10 Ma), a large wetland called “Pebas” (Fig. 5.4A) developed in the Western Amazonia basin.

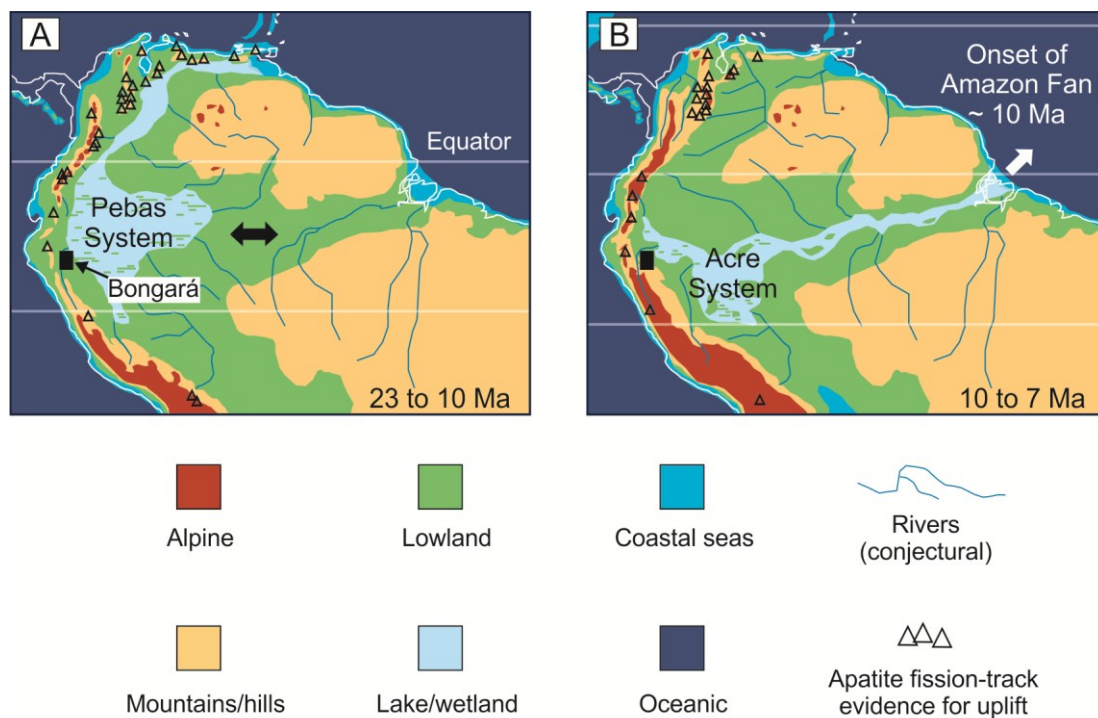


Figure 5.4. Paleogeographic maps of the North Andes, showing the transition from “Pebas” to “Acre” megawetlands and location of the Bongará district (from Horn et al., 2010, modified).

The “Pebas” ecosystem consisted of shallow lakes and swamps that prograded toward west after 12 Ma, contemporaneously with the constant growth of the Central and Northern Andes. Subsequently, the uplift of the Northern Andes at about 10 Ma promoted the onset of the transcontinental Amazon River system (Lundberg et al., 1998; Wesselingh and Salo, 2006; Hoorn et al., 2010), during which a fluvial-tidal-dominated wetland, the so-called “Acre” (Fig. 5.4B), developed. After 7 Ma the Acre wetland disappeared and the current rainforests ecosystem expanded (Hoorn et al., 2010).

Currently, the climatic conditions in the Bongará area resemble those of typical humid tropical uplands, having both drier and wetter seasons. The Cristal mineral occurrences are located between 1,600 m.a.s.l. and 2,000 m.a.s.l. (Fig. 5.3), where average annual temperatures range from 23° to 25°C and precipitation may not exceed average annual rainfall of 145 mm (Anglo Peruana, 2005). At altitudes > 2,000 m.a.s.l., the average annual rainfall may exceed 1,000 mm and the temperature varies from 7 to 29°, with strong thermal differences between day and night.

Previous studies on the supergene mineralization in the Bongará area

Some examples of supergene nonsulfides derived from the weathering of primary sulfide bodies in the Bongará district have been described for the Florida Canyon (owned by Votorantim/Milpo) and Mina Grande (owned by Zinc One) deposits (de Oliveira et al., 2015; Arfè et al., 2017b). These supergene ores have been classified as a combination of “wall rock” and “direct” replacement occurrences (after Hitzman et al., 2003). The Florida Canyon deposit (16 km SSE from Cristal; Fig. 5.1) is hosted in a broad anticline structure consisting of dolomitized limestones of the Chambará Formation. The ore deposit contains both hypogene (sphalerite, galena, pyrite, marcasite) and supergene (mainly smithsonite and hemimorphite) mineral assemblages. Smithsonite and hemimorphite occur as in situ replacement of sphalerite, of which they generally preserve the original texture. Cerussite and anglesite are generally less common. The oxidized mineralization mostly occurs as manto-like replacement of primary stratabound sulfide bodies. However, faults and fault-related karst conduits also control the shape of sulfide, nonsulfide and mixed ores that can have the form of variably extended “Christmas-trees” (SRK Consulting, 2014). The karst activity at Florida Canyon affected the carbonate rocks of the Chambará Formation during pre- and post-ore stages (SRK Consulting, 2014). The post-ore structures and karstification also partially controlled the remobilization of the oxidized orebodies at depth. Contrary to Florida Canyon, the Mina Grande prospect, hosted in the Condorsinga carbonate rocks, is completely weathered (Arfè et al., 2017b). Mina Grande is located at 6 km E-SE from the Cristal area (Fig. 5.1) in the hanging wall of the Chiriaco reverse fault, on the crest of an overturned ramp anticline (Fig. 5.3). It consists of several mineralized areas (named “Fase(s)”), where the ore occurs as Zn-nonsulfides mostly along fault-and fracture-related karst conduits. Arfè et al. (2017b) suggested that several successive uplifts since the late Oligocene could have produced the progressive denudation and uncapping of the original Mina Grande orebody. The nonsulfide ore was formed during two different oxidation stages, in which

early smithsonite, hemimorphite and hydrozincite generations (stage I) were partially replaced and cemented by a late generation of hemimorphite and by hydrozincite (stage II), which paragenetically follow concretionary calcite. These different oxidation stages might have occurred after the major periods of uplift (middle-late Miocene and early Pliocene-early Pleistocene), and were comprised in a time span between late Miocene (stage I) and late Pliocene (stage II) (Arfè et al., 2017b), under a climate not very different from today (see Kaandorp et al., 2005).

Main features of the host rock and the Zn-nonsulfide mineralization in the Cristal area

The rock hosting the Cristal mineralization is represented by carbonates and interbedded siliciclastic layers of the Condorsinga Formation (Fig. 5.5), which are exposed in the entire Cristal area, with a NE-SW strike and a prevailing dip toward SE.

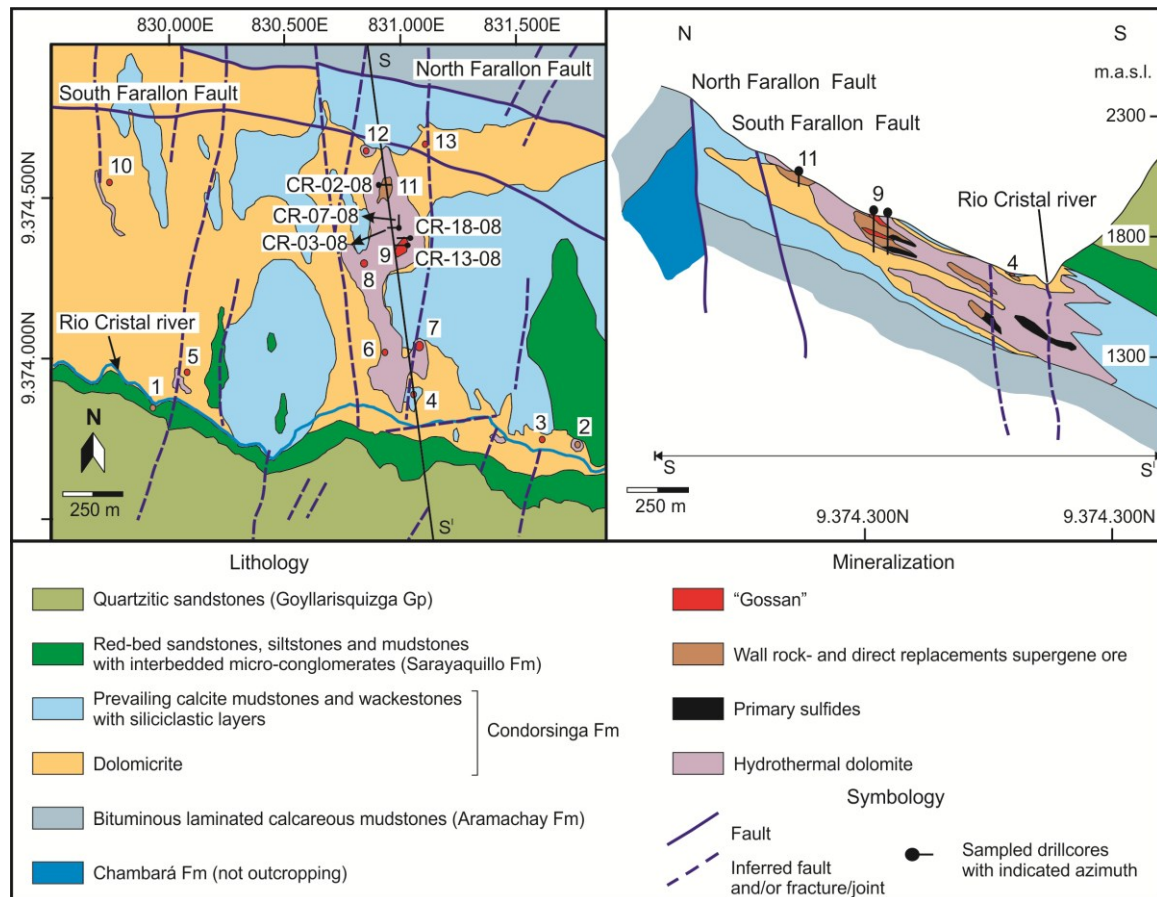


Figure 5.5. Geological map of the Cristal area showing the Zn(Pb) occurrences and prospects (indicated from numbers 1 to 13: 1 = Charlita, 2 = Anita, 3 = Erika, 4 = Kenita, 5 = El Aguila, 6 = Lupita, 7 = Marita, 8 = Nenita, 9 = Esperanza, 10 = Charlita North, 11 = Yolanda, 12 = Gigi, 13 = Juanita), the projections of the sampled drill cores, and the S-S' section with a conceptual model of the mineralizations (modified from Brophy, 2012).

The overall NE-SW strike does not correspond to the E–W strike of the contact with the overlying Sarayaquillo Formation, this implying that the Pucará Group was gently folded and tilted to the southeast during end-Pucará tectonic adjustments, which were accompanied by uplift and erosion (Wright, 2010). The latter processes resulted in an extensive karstification of the higher strata of the Condorsinga Formation. Layered reworked carbonates infill the pre-Sarayaquillo solution cavities and cave systems (Reid, 2001; Wright 2010; Brophy, 2012). As observed both in outcrop and drill cores, the basal units of the Condorsinga Formation are limestones passing upward into dolomitized wacke- and packstones (Fig. 5.2) that have a maximum thickness of 120 m. In the Cristal area, these upper horizons host the majority of the Zn nonsulfide occurrences (Fig. 5.5). At the contact with the eroded and karstified horizons of the uppermost units of the Condorsinga Formation, the carbonate clasts within the polymictic conglomerates of the overlying Sarayaquillo Formation are weakly dolomitized. Locally, these horizons host small sulfide occurrences, as in the Anita and Charlita areas (Fig. 5.5; Anglo Peruana, 2005; Wright, 2010; Brophy, 2012).

At Cristal the nonsulfide mineralization is confined between the footwall of the Chiriaco reverse fault and the hangingwall of the South Farallon normal fault (Figs. 5.3 and 5.5). The Cristal prospect extends over an area of approximately 2 x 1 km, and consists of many zinc occurrences (Fig. 5.5): Anita, Erika, Marita, Lupita, Esperanza, Yolanda, Juanita, Gigi, El Aguila, Charlita and Charlita North. Zn-nonsulfide ores outcrop in the following locations: Gigi, Yolanda, Nenita, Esperanza, Lupita, Marita and Kenita, with a nearly continuous zone of Zn enrichment having been detected in soil (>500 ppm; Wright, 2010; Brophy, al., 2012) and rock samples (>2500 ppm; Wright, 2010; Brophy, 2012). The nonsulfide mineralization consists mainly of semi-amorphous orange to brown zinc “oxides” that mostly include hemimorphite, smithsonite and Fe-(hydr)oxides (Fig. 5.6). The textural features of the secondary minerals may resemble those of their sulfide and carbonate progenitors. However, clear examples of smithsonite replacing dolomite crystals are difficult to observe in hand specimens (Fig. 5.6) for the following reasons: (1) replacive smithsonite generally shows the same texture as the host dolomite, (2) smithsonite can be intergrown with Fe-(hydr)oxides and can be misinterpreted as “oxidized” dolomite, as observed in many other nonsulfide deposits in the world (e.g. Accha and Yanque in southern Peru, Boni et al. 2009, Mondillo et al. 2014a; or Yemen, Mondillo et al. 2014b). Some examples of this kind of replacement can be recognized in several outcrops of the Cristal prospect.

The most significant mineralized areas are present in the Esperanza and Yolanda occurrences (Fig. 5.5), which were also most intensely explored. At both Esperanza and Yolanda, residual soils occur in outcrop, with large proportions of Fe-(hydr)oxides that display massive and/or botryoidal textures (Fig. 5.6). The supergene Zn-carbonates and silicates may infill the cavities within the botryoidal Fe-(hydr)oxides (Anglo Peruana, 2005) or occur along with massive goethite layers (Fig. 5.6). The nonsulfide layers have an overall NE-SW strike similar to the dominant trend at Cristal, but dip northwest at angles between 30° and 60° (Anglo Peruana, 2005).

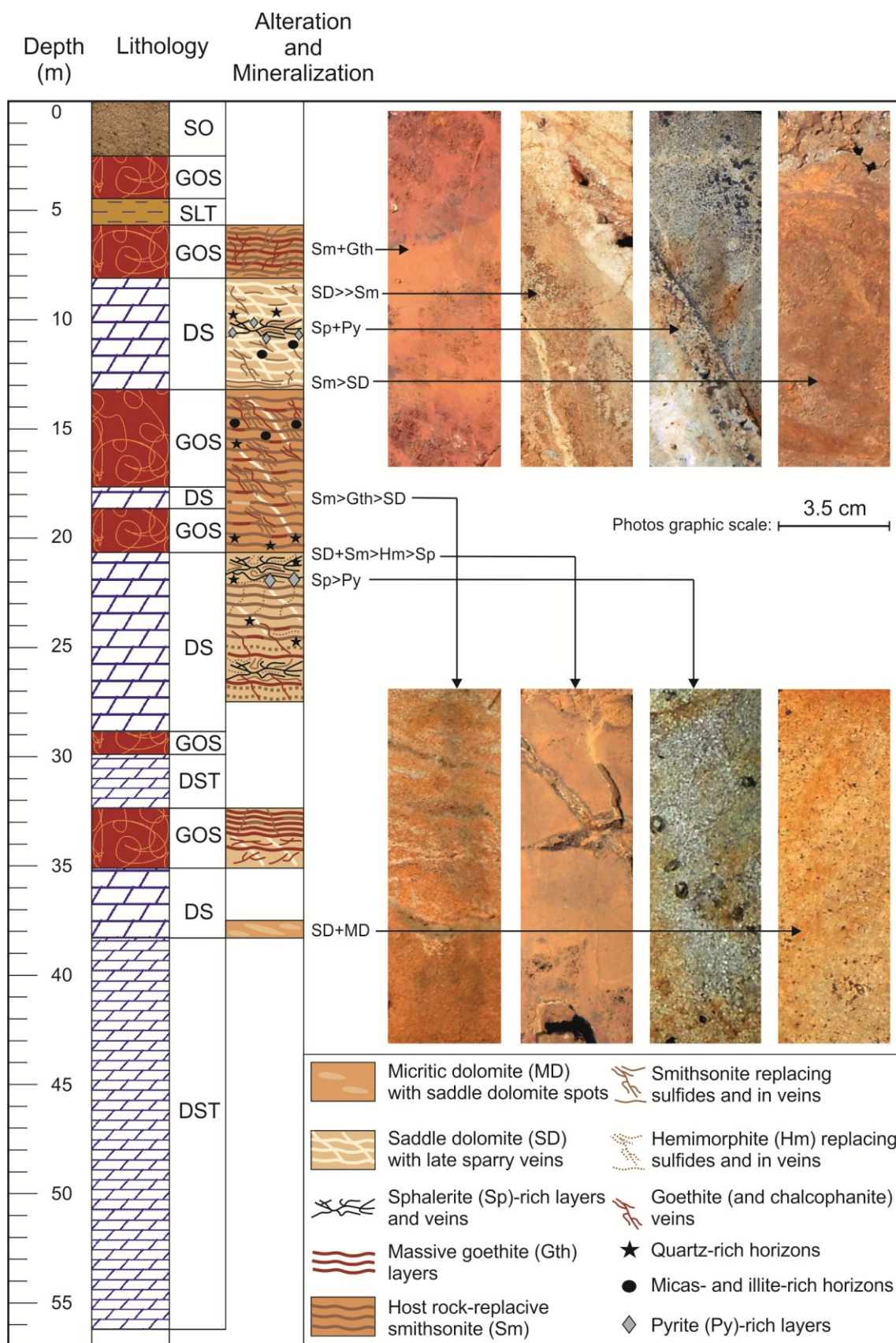


Figure 5.6. Examples of sulfide and nonsulfide occurrences and textures occurring in drill core CR-18-08. The stratigraphic logs were modified on the basis of data from Rio Cristal Resources Corp. Abbreviations: DS = Dolosparite; DST = Dolostone; GOS = Gossan; SO = Soil; SLT = Siltstone.

Rio Cristal Resources collared 28 diamond drill holes and recognized several significantly mineralized horizons having mean grades from 22.5 and 29.7 wt.% Zn at Esperanza, and around 17 wt.% Zn at Yolanda, which are mostly related to the nonsulfide ore. At Erika, the Zn carbonates replace sphalerite- and pyrite-rich layers (Anglo Peruana, 2005). At Marita, the nonsulfide minerals occur as massive replacement of sphalerite with laminar and colloform textures, visible both in outcrops and in collapsed blocks. At Lupita, both sulfides and nonsulfides occur preferentially in solution cavities of the dolomitic packstone, and can be traced over a strike length of 60 m (Anglo Peruana, 2005). Throughout the Lupita area, there is evidence that the solution cavities may have followed early joints and faults developed perpendicularly to bedding (Anglo Peruana, 2005; Brophy, 2012) and locally penetrated as deep as the intermediate unit. Arfè et al. (2017b) also recognized similar features in the nearby Mina Grande deposit, where the development of NW-trending solution cavities was instrumental for the formation of the karst-hosted nonsulfide bodies. The northernmost occurrence of Charlita North (Fig. 5.5) displays strong meteoric alteration, which is reflected in the high amount of Fe-(hydr)oxides and Zn carbonates, showing as sub-millimeter films along the strata joints.

Materials and Methods

The mineralogical and geochemical analyses were performed on 54 core samples from diamond drill holes, collared by Rio Cristal Resources in the 2008. The samples were collected approximately at one meter interval in the mineralized zones from the Esperanza (CR-03-08, CR-07-08, CR-13-08 and CR-18-08 drill holes) occurrence, and one sample was taken from the Yolanda (CR-02-08 drill hole) occurrence. A complete list of the sampled specimens is reported in Table 5.1.

Polished thin sections of slabs of mineralized core specimens (3 cm wide x 5 cm long) were prepared for optical microscopy (OM), scanning electron microscopy with energy dispersive X-ray spectroscopy (SEM-EDS), and wavelength dispersion spectrometry (full WDS) analyses. Parts of the samples were crushed and pulverized for mineralogical X-ray powder diffraction (XRPD) and whole rock chemical analyses.

SEM observations were carried out with a JEOL JSM5310 at the Dipartimento di Scienze della Terra, dell'Ambiente e delle Risorse (DiSTAR), Università degli Studi di Napoli Federico II (Italy). The analytical conditions were: 20 mm objective lens to specimen working distance, 15 kV accelerating voltage with a tilt angle of 0°. Element mapping and qualitative EDS investigations were performed with the INCA X-stream pulse processor and the 4.08 version Inca software (Oxford Instruments detector), interfaced with the Jeol JSM 5310. Reference standards used for quantitative microanalysis were: albite (Si, Al, Na), orthoclase (K), wollastonite (Ca), diopside (Mg), almandine (Fe), rutile (Ti), barite (Ba), strontianite (Sr), eskolaite (Cr), rhodonite (Mn), pyrite (S), sphalerite (Zn), galena (Pb), pure silver (Ag), arsenopyrite (As), fluorite (F), apatite (P), sylvite (Cl), pure vanadium (V) and Corning glass (Th, U). Analytical errors are 1% relative for major elements and 3% relative for minor elements. Quantitative data sets of selected samples were obtained by full WDS, using a Cameca SX50 electron microprobe

operating at 15 kV, 15 nA, and 10 μm spot size at the Natural History Museum (London, UK). WDS detection limits for each element are mostly in the order of 0.01 wt.%.

The mineralogical association of the main ore minerals (smithsonite and hemimorphite) was investigated with the Mineralogic system (ZEISS), on crushed/grinded material from three drill core samples (CR18-13, CR13-7; CR07-4). For these analyses five grams of 1 mm-sifted material were mounted on polished blocks. The analyses were carried out at the Natural History Museum (London, UK) on the Mineralogic system, which is an automated ZEISS EVO•50 scanning electron microscope (SEM), equipped with two Bruker xFlash 5010 Energy Dispersive Spectrometers (EDS) detectors. The analyses required an acceleration voltage of 20 kV with 13 mm working distance, 0.050 s dwell time corresponding to ~ 3000 EDS counts per spectra. The calibration of the EDS detectors was carried out every 60 minutes using a Cu standard (Cu K α peak). The “full map” analytical mode has been adopted, in order to obtain high-resolution distribution maps of the occurring mineral phases, correlated with a database containing the statistical information on the samples. Not recognized phases have been reported as “unclassified” in the mineral list.

The mineralogical characterization and quantitative analyses of the drill core samples have been performed by X-Ray Powder Diffraction (XRPD) on micro-milled bulk rocks at the INGV-Osservatorio Vesuviano, (Naples, Italy). The instrument was a Panalytical X'pert PRO diffractometer equipped with a pyrolytic graphite analyzer crystal; we used an unfiltered CuK α radiation (40 KV, 40 mA) in the 3° - 70° 2θ range, steps size of 0.01° 2θ , counting time of 30 s/step, 0.5 mm divergence slit, 1 mm receiving slit, and 0.5° anti-scattered slit. All samples have been side-loaded to minimize eventual preferred orientation effects. A search-match software (High Score Plus software) and the ICDD PDF2 database were used to identify the mineralogical phases and to elaborate the acquired spectra using the Rietveld method. The refining procedure accuracy was based on the agreement indices GOF (Goodness of Fit), Rwp (weighted agreement factor), and Rp (Profile agreement factor) following Bish and Post (1993).

Whole-rock chemical analyses (A) of major (Zn, Fe, Ca, Mg, Si, Al, Na, K, P, Mn) and minor elements (Mo, Cu, Pb, Ni, Co, As, U, Th, Sr, Cd, Sb, V, La, Cr, Ba, Sc, Tl, Se, Ga, Ge, Rb, Cs, Sn, Zr, Y, Ce, In, Li in ppm, and Au, Ag, Hg in ppb) of the CR-02-08, CR-03-08, CR-07-08 and CR-18-08 drill cores were carried out at Bureau Veritas Commodities Canada Ltd. (Vancouver, Canada), on identical powder splits to those used for the XRPD analyses. In each case, 10 g of pulp was used for chemical analysis on the LF725 package (fusion/X-ray fluorescence spectroscopy “XRF”). Samples with high Zn amounts (greater than 24%) were run for overlimits with the LF726 package, in which the samples are fused in presence of $\text{Li}_2\text{B}_4\text{O}_7/\text{LiBO}_2$ fluxes to be subsequently analyzed by XRF. Minor elements were assayed by using the AQ250-EXT (ultratrace *aqua regia*/ICP-AES and MS) package, except Ga and Ge, which were analyzed using the GC204-Ge & Ga package. The latter involves a closed vessel procedure, to prevent element loss during the HF + AR digestion, followed by ICP-MS analysis.

Whole-rock chemical analyses (B) of major (Zn, Fe, Mg, Al, K) and minor (Cu, Ni, Co, As, Cd, Sb, V, Ba, In, Ga, Ge, Ag) elements of the CR-13-08 drill core and some samples

from CR-18-08 drill core were carried out at Natural History Museum (London, UK). Approximately 50 mg of powdered rock sample was dissolved in Savillex 60 ml fluoropolymer vessels. 2-4.5 ml HCl and 0.05-0.25 ml HNO₃ were added to all samples and the mixture was shortly heated up to 70°C and the temperature rose to 100°C once the reaction had subsided. After samples were cooled down, 1 ml HNO₃, 1 ml HClO₄ and 2 ml HF was added to each of them, and the vessels were capped and heated overnight at 100°C. Then the solutions were evaporated down at 150°C and reconstructed in 50 ml of ca. 0.6 M HNO₃ with traces of H₂O₂. The solutions were analyzed by ICP-MS using an Agilent 7700x mass spectrometer. To minimize polyatomic interferences, the instrument was run with 5 ml/min He (99.9995% purity) in the collision-reaction octopole cell (CRC), as well as with no collision gas entering the CRC. Gallium (71Ga) was determined in the 'no gas' mode while all other elements were determined in the 'He mode'. To minimize the contamination of the instrument with high lead concentrations, the solutions were further diluted 100-fold with ca. 0.7 M HNO₃. The instrument was calibrated using multi-elements standards (Inorganic Ventures), typically with a 4-point calibration with a correlation coefficient of >0.9999. Accuracy was monitored by analyzing certified reference materials JLk-1 (Lake sediment, GSJ) and SdAR-1 (Modified river sediment, IAG) at the beginning and at the end of the run. All values were found to be within the uncertainty of the published data. The limits of quantification were calculated as 10 times the standard deviation of HNO₃ blank solution analyzed at least 10 times during the run.

Carbon and oxygen isotope analyses were performed on several specimens of early host-rock replacement smithsonite and on smithsonite and calcite of younger generations, separated from the bulk rock by handpicking. Stable isotope analyses were carried out at the University of Erlangen-Nuremberg (Germany). The powdered samples were allowed to react for at least 36 hours with phosphoric acid at 70°C using a GasBench II connected to a ThermoFinnigan V Plus isotope ratio mass spectrometer. The acid fractionation factor of the hydrozincite has not yet been determined; we used the closest acid fractionation factor of smithsonite (Gilg et al., 2008). Carbon and oxygen isotope values are reported relative to the Vienna Peedee belemnite (VPDB) and Vienna standard mean ocean water (VSMOW), respectively, by assigning $\delta^{13}\text{C}$ values of +1.95‰ to NBS19 and -46.6‰ to LSVEC and $\delta^{18}\text{O}$ values of -2.20‰ to NBS19 and -23.2‰ to NBS18. Reproducibility was checked by replicate analysis of laboratory standards and was better than $\pm 0.07\text{‰}$ (1 σ) for both carbon and oxygen isotope analyses. Oxygen isotope values were corrected using the phosphoric acid fractionation factors given by Kim et al. (2007) for calcite, Rosenbaum and Sheppard (1986) for dolomite and by Gilg et al. (2008) for smithsonite.

TABLE 5.1. List of the drill cores samples and drill holes details.

Drill Hole	Target occurrence	Easting (UTM)	Northing (UTM)	Azimuth	Dip	Depth (m)	Sample	From (m)	To (m)
CR-02-08	Yolanda	830,910	9,374,537	90	-75	22.90	CR02	11.70	12.30
CR-03-08	Esperanza North	830,998	9,374,403	270	-60	62.75	CR03-1	53.95	55.35
							CR03-2	57.50	57.90
							CR03-3	58.30	59.15
							CR03-4	59.15	59.70
							CR03-5	59.70	60.10
CR-07-08	Esperanza North	831,001	9,374,405	0	-60	70.05	CR07-1	16.90	18.55
							CR07-2	18.55	20.20
							CR07-3	20.20	22.05
							CR07-4	22.05	23.95
							CR07-5	23.95	25.05
							CR07-6	25.05	26.45
							CR07-7	26.45	28.05
							CR07-8	32.30	32.30
							CR07-9	44.35	45.90
							CR07-10	45.90	47.80
							CR07-11	49.00	50.90
							CR07-12	50.90	52.30
							CR07-13	52.30	53.50
							CR07-14	54.85	56.70
CR-13-08	Esperanza East	831,040	9,374,356	270	-60	56.90	CR13-1	16.35	18.00
							CR13-2	18.00	18.95
							CR13-3	18.95	19.85
							CR13-4	19.85	21.50
							CR13-5	21.50	23.10
							CR13-6	23.10	24.30
							CR13-7	24.30	25.35
							CR13-8	25.35	26.40

TABLE 5.1 (continue)....

Drill Hole	Target occurrence	Easting (UTM)	Northing (UTM)	Azimuth	Dip	Depth (m)	Sample	From (m)	To (m)
							CR13-9	26.40	27.40
							CR13-10	29.70	29.70
							CR13-11	30.50	30.50
							CR13-12	48.70	48.70
CR-18-08	Esperanza East	831,043	9,374,369	270	-60	56.20	CR18-1	5.65	6.85
							CR18-2	6.85	8.15
							CR18-3	8.15	8.90
							CR18-4	8.90	10.00
							CR18-5	10.00	10.95
							CR18-6	10.95	11.90
							CR18-7	11.90	13.20
							CR18-8	13.20	14.70
							CR18-9	14.70	16.20
							CR18-10	16.20	17.65
							CR18-11	17.65	18.65
							CR18-12	18.65	19.65
							CR18-13	19.65	20.65
							CR18-14	20.65	21.50
							CR18-15	21.50	22.70
							CR18-16	22.70	24.00
							CR18-17	24.00	25.30
							CR18-18	25.30	26.30
							CR18-19	26.30	27.30
							CR18-20	32.35	33.70
							CR18-21	33.70	34.35
							CR18-22	34.35	35.10
							CR18-23	36.70	38.30

Mineralogy and Petrography

XRPD quantitative analyses and textural mineral associations

The results of the XRPD quantitative analyses of the mineral associations on considered drill core samples are reported in Tables 5.2 (see Table 5.1 for the identification of the core intervals from which the samples were taken). The most relevant results of our study are summarized below.

From the XRPD analyses we recognized two different types of Zn-bearing nonsulfide mineralization: I) smithsonite-rich bodies and II) hemimorphite-rich horizons (e.g. smithsonite in CR-03-08, CR-07-08, CR-18-08, and hemimorphite in CR-13-08).

The smithsonite-rich (from ~30 to ~93 wt.%) mineralization consists of stratabound bodies (Fig. 5.7; from 12.6 down to 22.1 m), which occur between dolomitic horizons locally separated by quartz- and muscovite-bearing siliciclastic layers (from ~14 to ~53 wt.% of quartz, and from 2 to 24 wt.% of muscovite) (Fig. 5.9). In this mineralization type, smithsonite occurs in stoichiometric form, but also as Fe-smithsonite and Mg-smithsonite (Table 5.3). In gossanous horizons, the smithsonite phases are mainly associated with Zn-bearing goethite (e.g. CR-18-08 drill core; Figs. 5.10 and 5.11). On the contrary, where the siliciclastic horizons prevail, smithsonite is commonly found in association with quartz and Zn clays (e.g. CR-07-08 drill core; Figs. 5.10 and 5.11). In the smithsonite-rich bodies hemimorphite rarely shows abundances greater than 3 wt.% (Table 5.3; Fig. 5.11).

The hemimorphite-rich mineralizations commonly occur within quartz- and muscovite-bearing layers, intercalated with dolomitic host rock (Fig. 5.8; from 20.7 down to 26.9 m), and are quite detached from the smithsonite-rich bodies. These hemimorphite-rich mineralizations contain from 23 to 83 wt.% hemimorphite, from 8 to 17 wt.% quartz and from 3 to 12 wt.% muscovite (Fig. 5.8). However, hemimorphite-rich mineralization could be also associated with gossan-like horizons, containing up to ~64 wt.% goethite (Fig. 5.9). In the gossan-like mineralization hemimorphite occurs mainly in contact with Zn-clays (up to 36%) and quartz (up to 23%) (Table 5.3; Fig. 5.11). In the hemimorphite-rich body smithsonite amounts are below 4 wt.%.

In both mineralization types, other nonsulfide minerals occur with amounts comprised between 1 and 5 wt.%. They consist of Zn-bearing smectite, Zn-bearing illite, and Zn-Mn-(hydr)oxides, namely chalcophanite, and/or hetaerolite. The highest illite (up to ~4 wt.%) and smectite (up to ~5 wt.%) amounts are contained in the siliciclastic layers.

Sulfide minerals, mostly consisting of dolomite-hosted sphalerite and pyrite solely occur the CR-18-08 and CR-13-08 drill cores. The highest sphalerite abundances (up to ~ 11 wt.%) were detected in the CR-18-08 core, where no Zn-nonsulfide minerals have been detected.

TABLE 5.2. Mineralogical composition (XRPD quantitative analyses) of drill core samples from the Cristal prospect.

Sample ID	Mean depth (m)	Dolomite	Smithsonite	Goethite	Hemimorphite	Quartz	Calcite	Muscovite	Illite	Smectite	Chalcophanite	Siderite	Sphalerite	Pyrite	Total
CR02	12.0	-	9.1	31.9	1.5	43.3	-	9.8	4.4	-	-	-	-	-	100
														-	
CR03-1	54.7	-	-	47.4	-	45.0	-	7.6	-	-	-	-	-	-	100
CR03-2	57.7	-	45.2	36.3	1.5	15.2	-	1.8	-	-	-	-	-	-	100
CR03-3	58.7	0.8	78.6	8.2	-	12.1	-	0.3	-	-	-	-	-	-	100
CR03-4	59.4	16.9	74.7	-	-	5.0	-	3.4	-	-	-	-	-	-	100
CR03-5	59.9	48.3	44.8	-	-	5.0	-	1.9	-	-	-	-	-	-	100
														-	
CR07-1	17.7	-	74.2	4.9	-	20.1	-	-	-	0.8	-	-	-	-	100
CR07-2	19.4	-	7.2	52.9	-	39.4	-	-	-	0.5	-	-	-	-	100
CR07-3	21.1	-	89.6	2.1	-	6.3	-	-	-	0.4	-	1.6	-	-	100
CR07-4	23.0	30.8	62.3	1.9	-	4.5	-	-	-	0.5	-	-	-	-	100
CR07-5	24.5	-	45.2	35	-	18.8	-	-	-	1.0	-	-	-	-	100
CR07-6	25.8	1.1	82.6	3.8	-	11.3	-	-	-	1.2	-	-	-	-	100
CR07-7	27.3	50.2	11.7	11	-	6.3	20.4	-	-	0.4	-	-	-	-	100
CR07-8	32.3	50.6	-	1.3	-	3.6	44.3	-	-	0.2	-	-	-	-	100
CR07-9	45.1	-	60.6	24.4	-	14.0	-	-	-	1.0	-	-	-	-	100
CR07-10	46.9	2.4	9.2	53.4	-	24.2	-	9.8	-	1.0	-	-	-	-	100
CR07-11	50.0	-	44.1	1.9	-	47.0	-	2.2	4.2	0.6	-	-	-	-	100
CR07-12	51.6	-	42.2	3.6	-	49.2	-	4.2	-	0.8	-	-	-	-	100
CR07-13	52.9	-	19.1	3.7	-	53.1	-	24.1	-	-	-	-	-	-	100
CR07-14	55.8	-	26.2	2.7	-	47.4	-	23.7	-	-	-	-	-	-	100
														-	
CR13-1	17.2	33.4	-	64.2	-	2.0	-	-	-	0.4	-	-	-	-	100
CR13-2	18.5	47.8	37.9	12.4	1.2	-	-	-	-	-	-	-	0.7	-	100
CR13-3	19.4	82.7	13.1	-	1.0	2.4	-	0.3	-	-	-	-	0.5	-	100
CR13-4	20.7	50.8	3.9	25.1	18.9	-	-	1.3	-	-	-	-	-	-	100
CR13-5	22.3	24.5	3.5	23.9	46.8	-	-	0.4	-	0.9	-	-	-	-	100
CR13-6	23.7	-	-	4.8	83.2	8.0	-	-	-	4.0	-	-	-	-	100
CR13-7	24.8	-	-	-	66.4	16.6	-	12.1	-	4.9	-	-	-	-	100
CR13-8	25.9	-	-	38.4	34.0	16.4	-	7.1	-	-	4.1	-	-	-	100
CR13-9	26.9	66.5	-	-	23.0	7.4	-	3.1	-	-	-	-	-	-	100
CR13-10	29.7	88.9	-	-	-	9.7	0.4	-	-	1.0	-	-	-	-	100
CR13-11	30.5	96.4	-	0.1	-	2.4	-	0.7	-	0.4	-	-	-	-	100
CR13-12	48.7	89.6	-	1.6	-	-	8.5	-	-	0.3	-	-	-	-	100

Note: - not detected.

TABLE 5.2. Continue....

Sample	Mean depth (m)	Dolomite	Smithsonite	Goethite	Hemimorphite	Quartz	Calcite	Muscovite	Illite	Smectite	Chalcophanite	Siderite	Sphalerite	Pyrite	Total
CR18-1	6.3	-	65.4	33.7	-	-	-	-	-	0.9	-	-	-	-	100
CR18-2	7.5	-	42.2	56.8	-	0.7	-	-	-	0.3	-	-	-	-	100
CR18-3	8.5	90.6	7.2	2.2	-	-	-	-	-	-	-	-	-	-	100
CR18-4	9.5	78.0	13.4	-	0.5	-	-	-	-	0.1	-	-	8.0	-	100
CR18-5	10.5	80.9	-	-	-	0.9	-	-	-	-	-	-	10.8	7.4	100
CR18-6	11.4	87.2	6.8	2	-	-	-	-	4.0	-	-	-	-	-	100
CR18-7	12.6	40.3	56.8	2	0.9	-	-	-	-	-	-	-	-	-	100
CR18-8	14.0	0.4	78.1	21.5	-	-	-	-	-	-	-	-	-	-	100
CR18-9	15.5	-	29.9	33.7	-	-	-	20.4	-	-	-	-	-	16.0	100
CR18-10	16.9	-	74.1	21.1	0.4	3.1	-	1.3	-	-	-	-	-	-	100
CR18-11	18.2	-	83.6	15.7	-	0.7	-	-	-	-	-	-	-	-	100
CR18-12	19.2	-	92.8	3.4	3.0	-	-	0.8	-	-	-	-	-	-	100
CR18-13	20.2	-	58.9	37.3	1.2	2.6	-	-	-	-	-	-	-	-	100
CR18-14	21.1	50.4	39.4	2.3	3.6	3.5	-	-	-	0.2	-	-	0.6	-	100
CR18-15	22.1	87.4	5.9	-	0.9	-	-	-	-	0.1	-	-	5.7	-	100
CR18-16	23.4	78.7	13.5	1.2	1.3	4.7	-	0.4	-	0.2	-	-	-	-	100
CR18-17	24.7	50.4	-	44.3	4.2	0.6	-	0.5	-	-	-	-	-	-	100
CR18-18	25.8	73.6	17.1	-	3.9	-	-	-	1.1	-	-	-	4.3	-	100
CR18-19	26.8	31.0	8.2	31.3	29.5	-	-	-	-	-	-	-	-	-	100
CR18-20	33.0	17.3	15.2	62.8	4.7	-	-	-	-	-	-	-	-	-	100
CR18-21	34.0	3.9	9.2	86.3	0.6	-	-	-	-	-	-	-	-	-	100
CR18-22	34.7	77.1	0.2	22.2	0.5	-	-	-	-	-	-	-	-	-	100
CR18-23	37.5	97.8	-	1.8	0.4	-	-	-	-	-	-	-	-	-	100

Note: - not detected

TABLE 5.3. Textural mineral association of representative drill core samples as determined with Mineralogic system (Zeiss).

Sample ID	Target Mineral	Al contamination	Background	Dolomite	Fe-Dolomite	Zn-dolomite	Calcite	Smithsonite	Fe-smithsonite	Mg-smithsonite	Hemimorphite	Goethite	Goethite (Zn)
CR07-4	Fe-smithsonite	0.07	8.83	-	-	-	0.01	59.25	-	0.02	2.07	4.18	16.28
CR07-4	Mg-smithsonite	-	4.06	-	-	-	-	71.88	1.88	-	3.75	2.50	7.19
CR07-4	Smithsonite	0.48	23.31	-	-	-	0.01	0.00	5.94	0.07	6.59	6.51	28.42
CR07-4	Hemimorphite	0.08	9.60	-	1.71	-	-	54.45	-	0.03	-	3.15	12.97
CR13-7	Fe-smithsonite	0.10	5.43	-	-	-	0.06	1.98	-	-	53.19	2.11	12.16
CR13-7	Mg-smithsonite	-	5.68	15.34	0.85	6.82	1.14	2.27	-	-	39.20	0.85	3.69
CR13-7	Smithsonite	0.06	17.62	0.02	0.01	0.02	0.02	-	0.14	0.02	43.53	0.72	2.89
CR13-7	Hemimorphite	0.12	12.99	0.03	0.01	0.02	0.07	4.87	0.41	0.03	-	0.67	5.34
CR18-13	Fe-smithsonite	0.01	5.81	-	-	-	-	30.06	-	-	1.74	3.48	54.21
CR18-13	Mg-smithsonite	-	6.50	-	-	-	-	68.50	-	-	4.00	1.00	17.00
CR18-13	Smithsonite	0.05	15.58	-	-	-	-	-	5.36	0.05	5.74	3.61	53.65
CR18-13	Hemimorphite	0.05	13.29	-	-	-	-	41.50	2.25	0.02	-	1.15	20.69

Note: - not detected

TABLE 5.3. Continue...

Sample ID	Target Mineral	Pyrite	Sphalerite	Cerussite	Chalcophanite	Hetaerolite	Quartz	Muscovite	Kaolinite	Zn-clays	Gypsum	Unclassified
CR07-4	Fe-smithsonite	-	-	-	-	0.59	0.89	0.47	0.01	1.43	-	5.90
CR07-4	Mg-smithsonite	-	-	-	-	0.31	1.25	0.31	-	2.19	-	4.69
CR07-4	Smithsonite	-	0.01	0.01	-	2.01	3.56	2.05	0.01	4.60	-	16.37
CR07-4	Hemimorphite	-	-	0.01	-	1.03	3.22	1.68	0.01	5.61	-	6.45
CR13-7	Fe-smithsonite	-	-	-	-	0.42	4.18	2.08	0.03	15.33	-	2.94
CR13-7	Mg-smithsonite	-	-	-	-	0.85	5.40	1.14	0.28	13.07	-	3.41
CR13-7	Smithsonite	-	-	-	0.01	2.40	9.43	4.06	0.05	11.36	-	7.66
CR13-7	Hemimorphite	-	-	-	-	0.85	23.08	8.23	0.03	36.03	-	7.23
CR18-13	Fe-smithsonite	-	-	-	0.01	0.47	0.08	0.29	0.01	0.01	-	3.84
CR18-13	Mg-smithsonite	-	-	-	-	-	-	-	-	-	-	3.00
CR18-13	Smithsonite	0.02	-	-	0.02	1.00	0.53	1.02	0.02	0.02	-	13.31
CR18-13	Hemimorphite	-	-	-	0.01	1.20	5.93	1.37	0.03	0.11	0.01	12.39

Note: - not detected

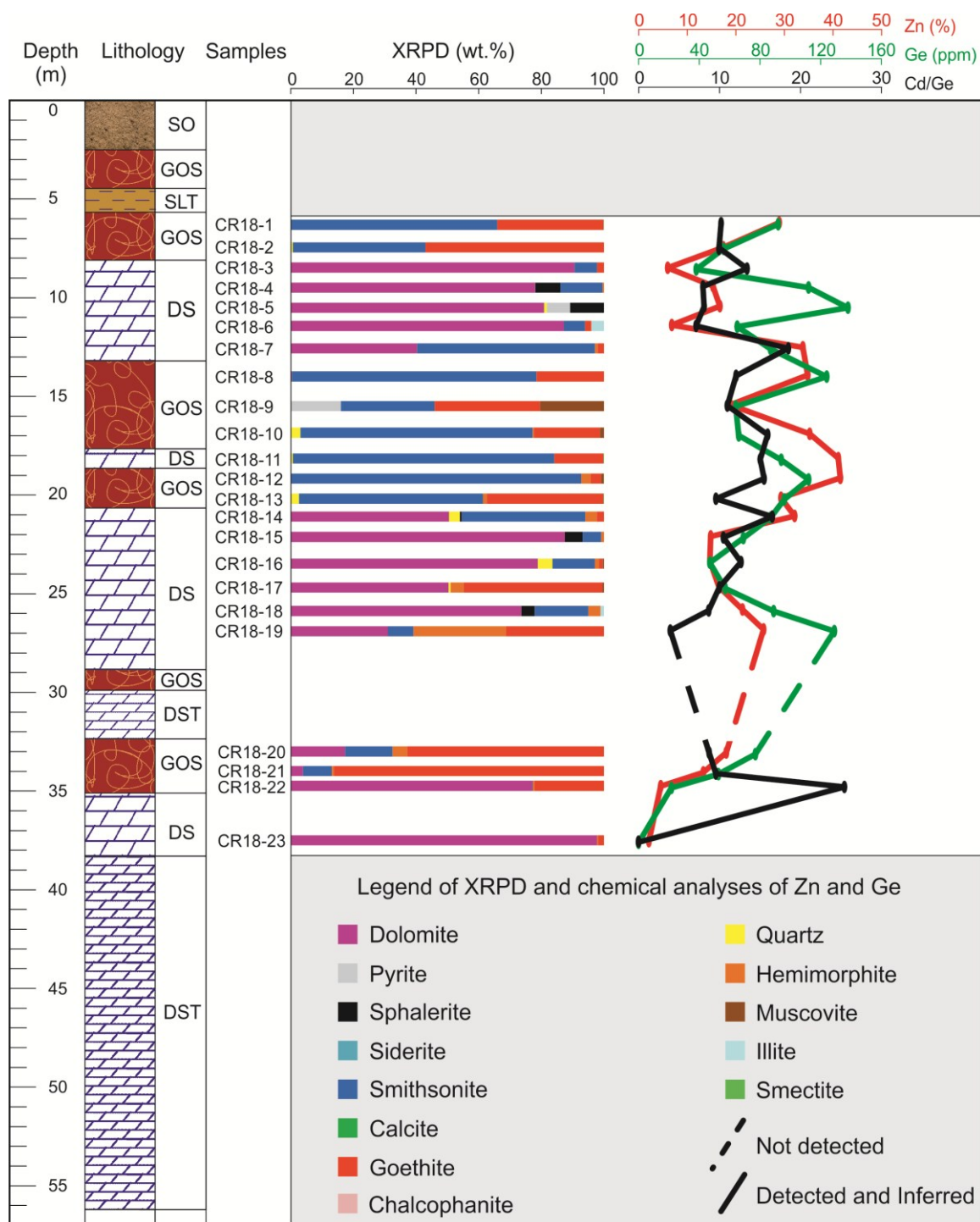


Figure 5.7. Stratigraphic log of the CR-18-08 drill core with related bulk XRPD quantitative analyses, Zn (%) and Ge (ppm) grades, and Cd/Ge ratios of the collected samples. The legend of the XRPD analyses refers to all drill core samples analyzed (i.e. some mineral phases may not really occur in this drill core, see Table 5.2 for more details). The grey colored areas refer to not-sampled portions of the drill core. The stratigraphic log was modified on the basis of data from Rio Cristal Resources Corp. Abbreviations: DS=Dolospirite; DST=Dolostone; GOS=Gossan; SO=Soil; SLT=Siltstone .

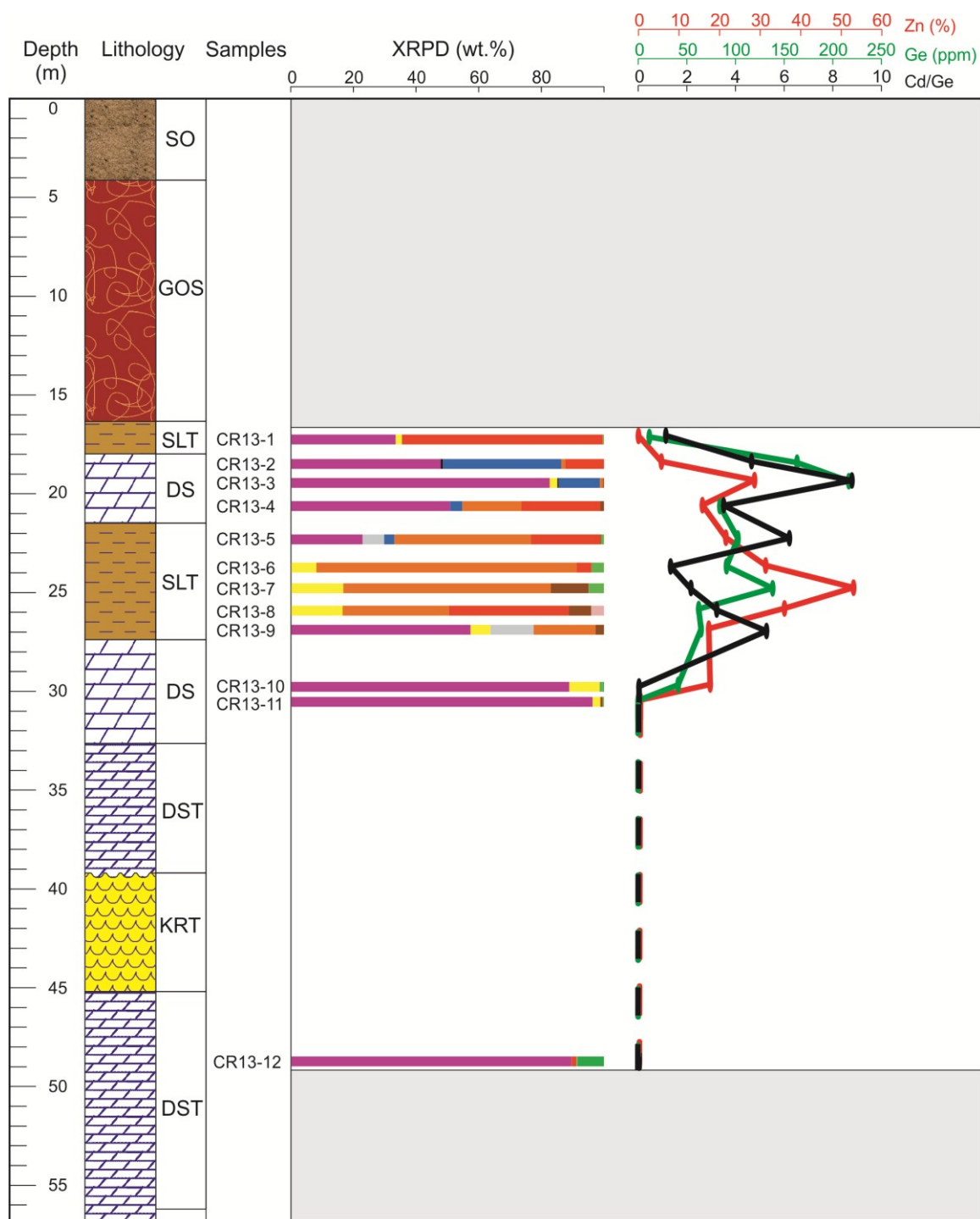


Figure 5.8. Stratigraphic log of the CR-13-08 drill core, with related bulk XRPD quantitative analyses, Zn (%) and Ge (ppm) grades, and Cd/Ge ratios of the collected samples. The grey colored areas refer to not-sampled portions of the drill core (see legend in Fig. 5.7). The stratigraphic log was modified on the basis of data from Rio Cristal Resources Corp. Abbreviations: DS=Dolosparite; DST=Dolostone; GOS=Gossan; KRT=Karst; SO=Soil; SLT=Siltstone.

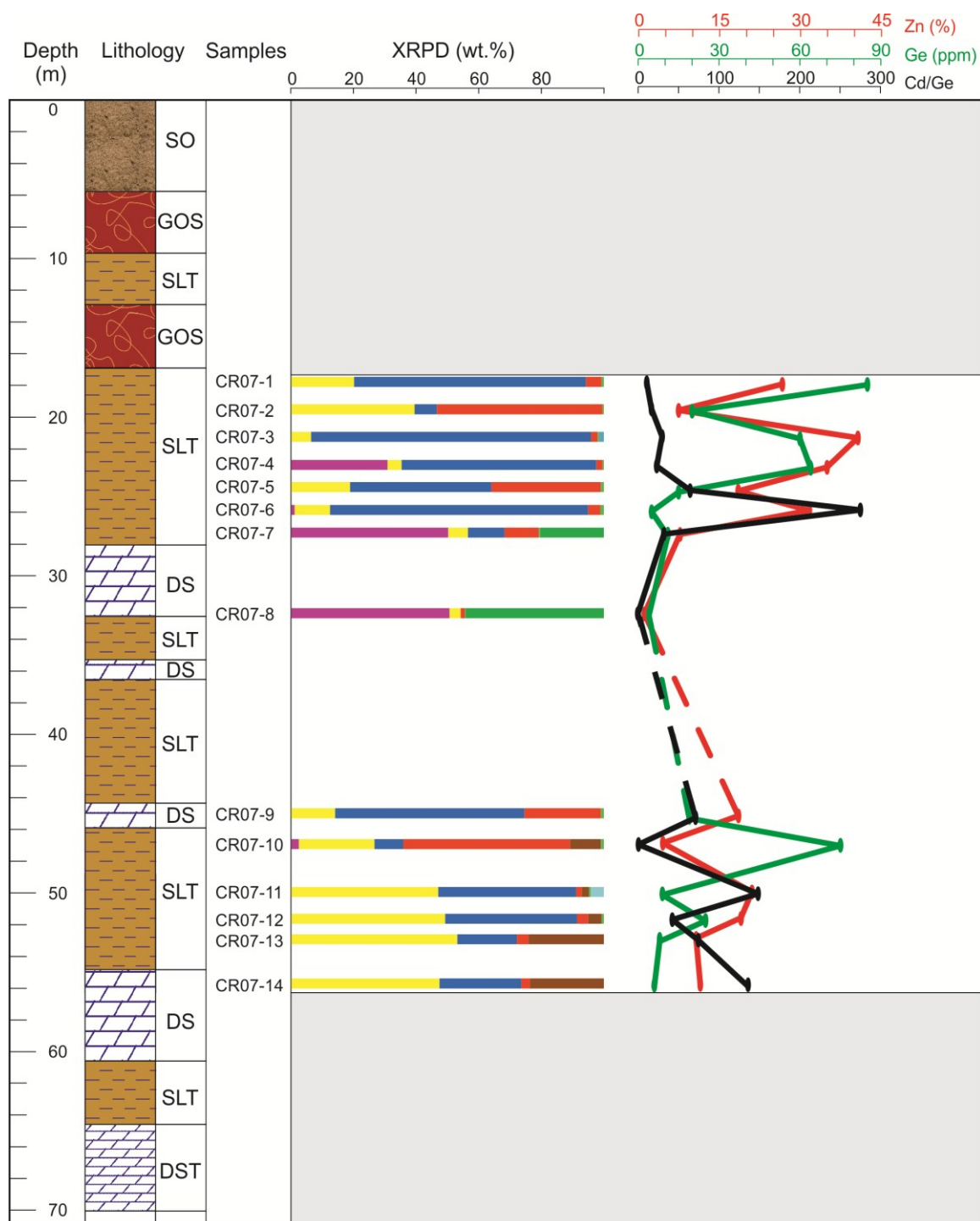


Figure 5.9. Stratigraphic log of the CR-07-08 drill core with related bulk XRPD quantitative analyses, Zn (%) and Ge (ppm) grades, and Cd/Ge ratios of the collected samples. The grey colored areas refer to not sampled portions of the drill core (see legend in Fig. 5.7). The stratigraphic log was modified on the basis of data from Rio Cristal Resources Corp. Abbreviations: DS=Dolosparite; DST=Dolostone; GOS=Gossan; SO=Soil; SLT=Siltstone .

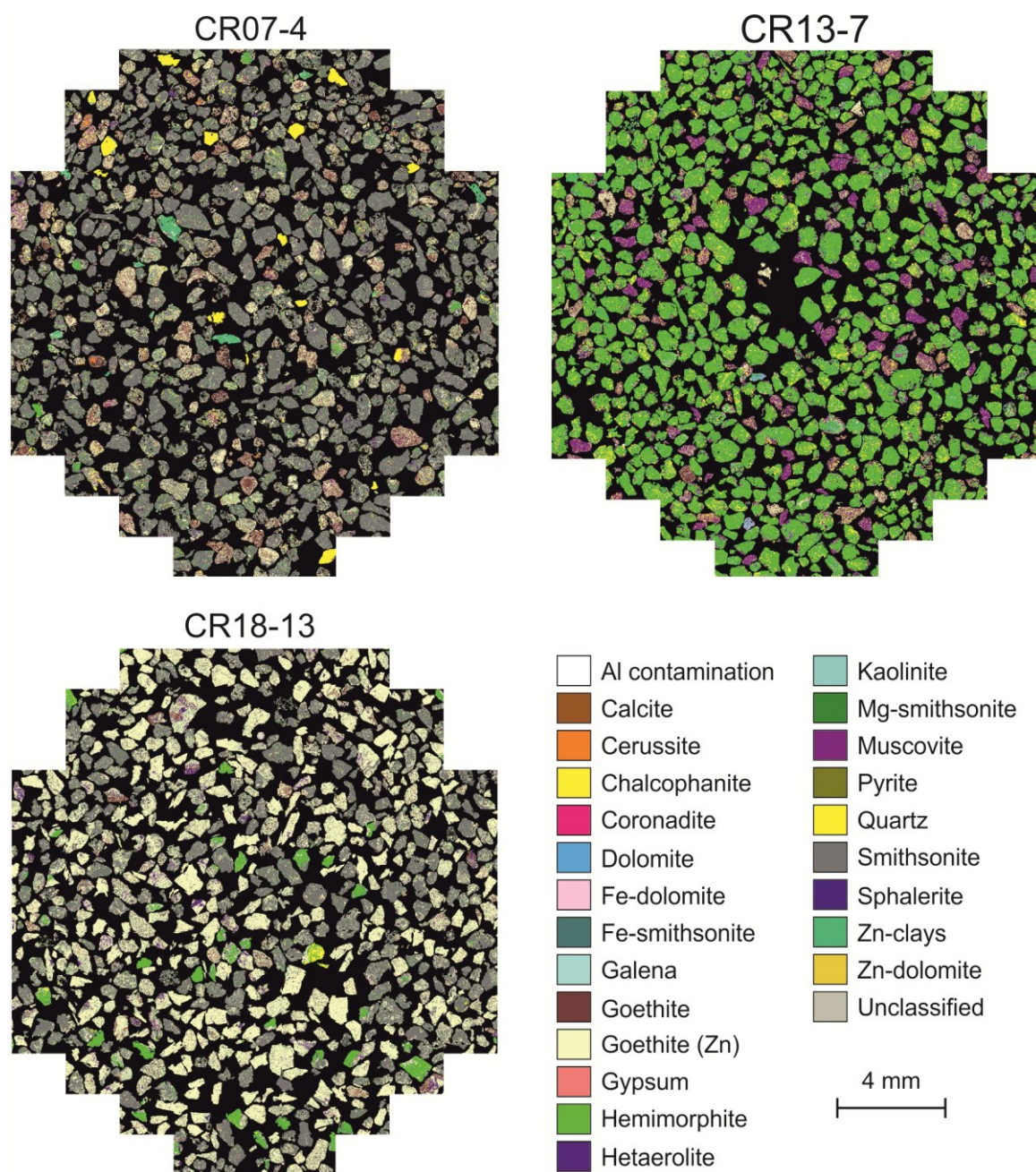


Figure 5.10. Mineralogic false color fieldscan images of CR07-4, CR18-13 and CR13-7 drill core samples, which are representative of smithsonite- (CR07-4 and CR18-13) and hemimorphite- (CR13-7) rich mineralizations .

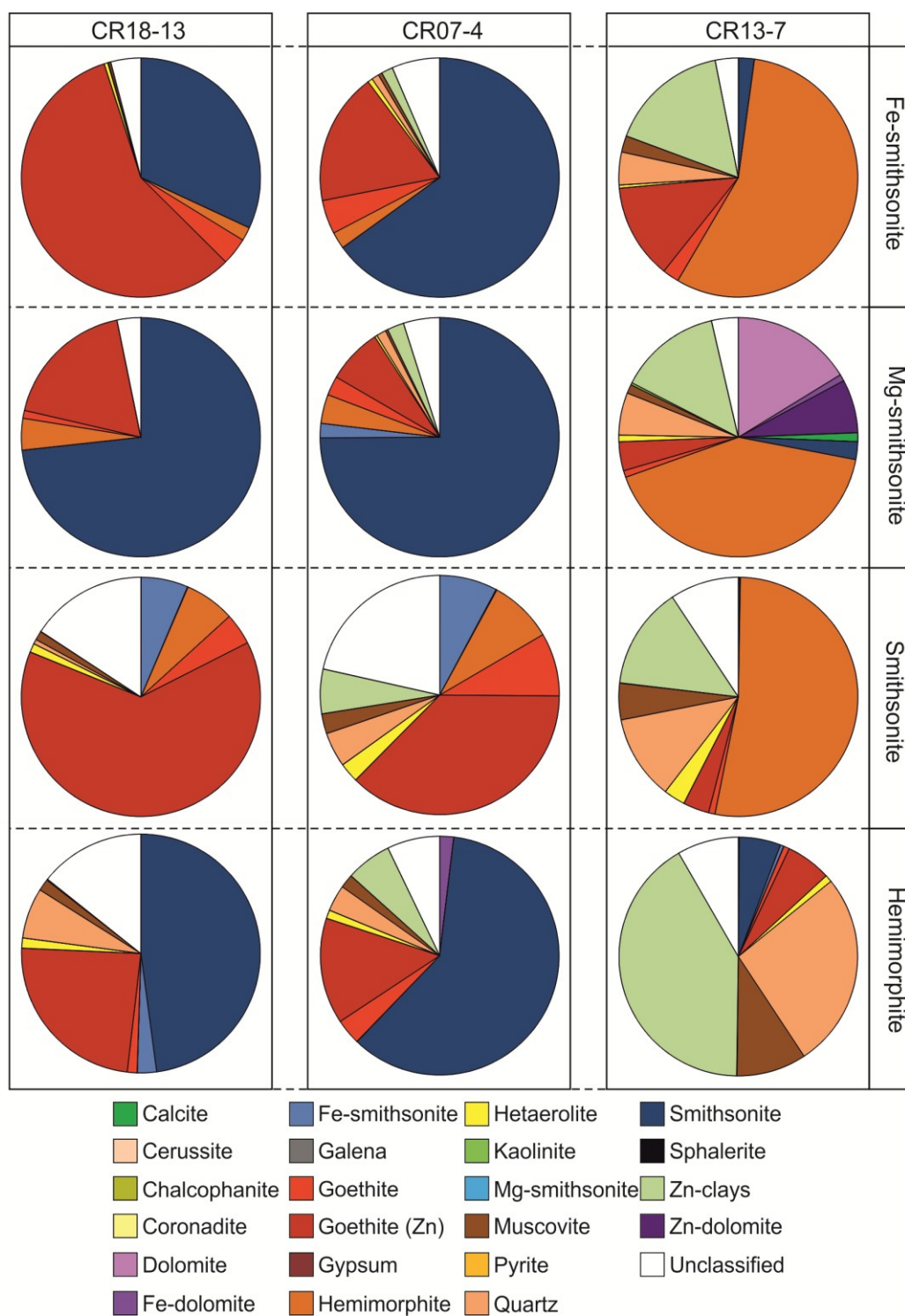


Figure 5.11. Pie charts showing the textural mineral associations (i.e. % of contacts between minerals) of Fe-smithsonite, Mg-smithsonite, smithsonite (stoichiometric) and hemimorphite in the samples from CR18-13, CR07-4 and CR13-7, detected by automated scanning electron microscopy .

Mineral textures

The richest samples of the smithsonite- and hemimorphite-rich bodies do not show macroscopically different textures, being both represented by rather massive smithsonite and hemimorphite. A few brecciated horizons can occur along the contact zones between the mineralized bodies and host lithologies (see CR-18-08 and CR-13-08 drill cores). In these zones, smithsonite and hemimorphite mainly occur as cement of clasts consisting of dolomite and quartz, originated from the interbedded dolomite and siliciclastic layers. This texture is much more common in the CR-07-08 and CR-03-08 drill cores, where smithsonite also occurs in small fractures and cavity filling. Such textural features make the stratabound smithsonite body very irregular in this zone that corresponds to a small portion of the Esperanza occurrence.

Remnants of the primary mineral assemblage (dolomite, pyrite and sphalerite) (Mondillo et al., in press) have been recognized mostly in the CR-18-08 and CR-13-08 drill cores. However, the large amounts of goethite occurring as perfectly cubic crystals (pseudomorphs formed after pyrite replacement) and in veins from several CR-07-08 drill core samples suggest that sulfides should have been also present in this part of the Esperanza body. The sulfide mineralization is clearly followed by several generations of nonsulfide minerals. From micro-textural observations, different generations of smithsonite and hemimorphite have been recognized at Cristal. Early stages consist of sulfide- and host rock-replacive generations, whereas late stages are generally represented by open space filling generations.

Early smithsonite (Sm1) commonly replaces sphalerite and pyrite (Figs. 5.12A, B, C, and D), and in the earlier stages is associated with siderite patches. Specifically, siderite and early smithsonite have been observed as filling a few altered zones in sphalerite grains (Fig. 5.12A), and in veins within dolomite (Fig. 5.12B). The veins are generally characterized by a siderite outer zone and a smithsonite inner core (Fig. 5.12B), this indicating at large scale, a first precipitation of the Fe-carbonate followed by the Zn-carbonate. Sm1 has a high Fe content, generally reaching ~3 wt.% FeO (Fig. 5.12D; Table 5.4).

Smithsonite of the second generation (Sm2) mainly occurs as part of an extensive replacement front of the dolomite host rock, consisting of an intricate fracture system (Fig. 5.12E). In the siliciclastic layers interbedded to the dolomite host rock, commonly containing detrital minerals as quartz, rutile, ilmenite and fluorapatite, Sm2 is associated with sauconite, Zn-Mn-bearing micas, goethite and chalcophanite. The boundary between the barren host dolomite and Sm2 is very irregular. When replacing microcrystalline dolomite, Sm2 has a very fine texture, conversely, when replacing saddle dolomite, it mimics perfectly the form of the rhombohedral dolomite crystals. Sm2 has commonly a stoichiometric composition, rarely characterized by FeO contents reaching 1 wt.%. Greenockite (CdS) occurs as tiny spots filling the microporosity of Sm1 and Sm2 (Fig. 5.12H).

The late smithsonite generation (Sm3) is represented by a pure phase, occurring as thin veins in the host rock (Fig. 5.12F), and as crusts in cavities, previously festooned by concretionary goethite (Fig. 5.12G).

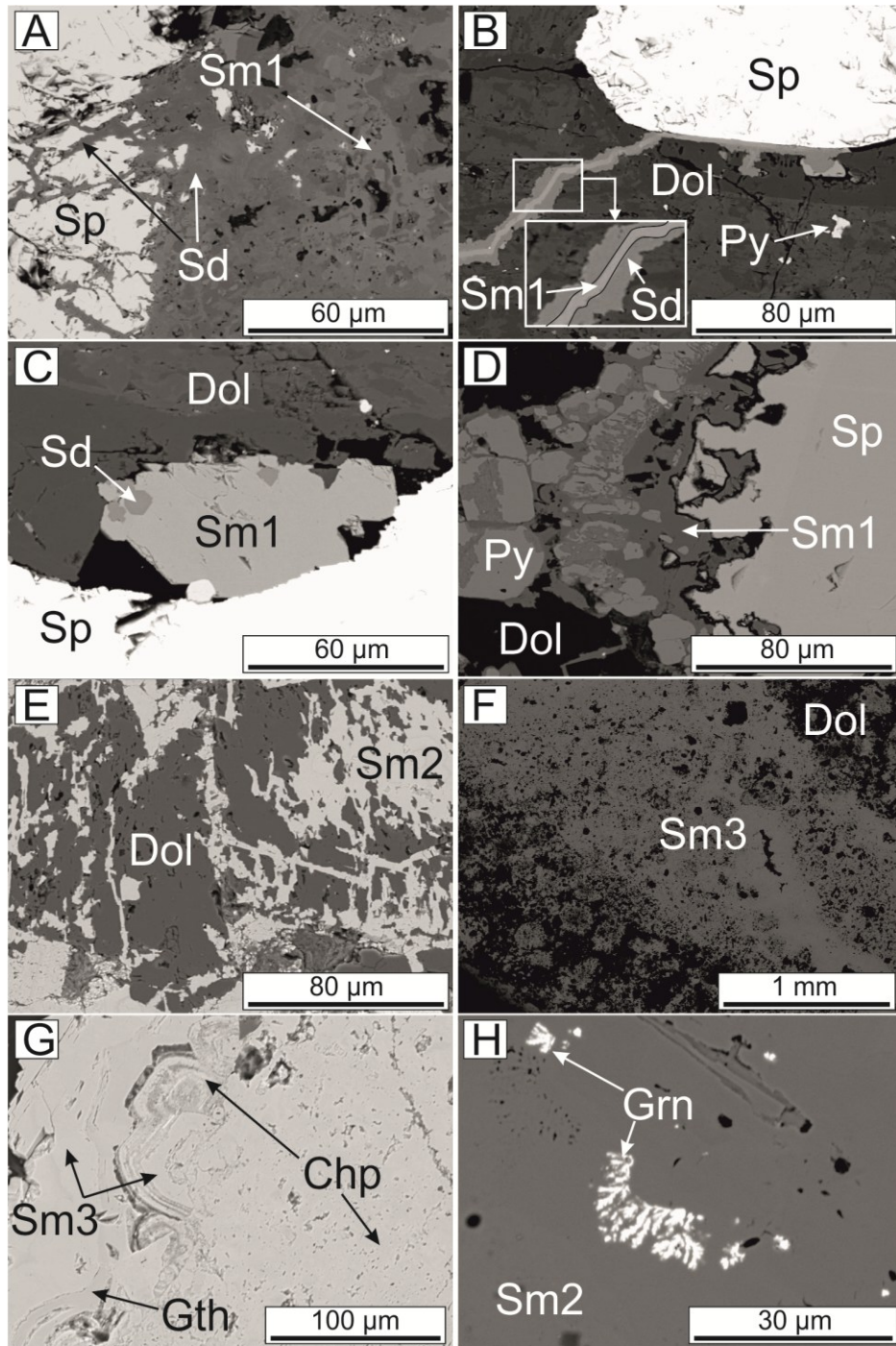


Figure 5.12. Backscattered electron images (BSE) of sulfides and paragenetically early nonsulfide minerals. A. Smithsonite (Sm1) is associated with siderite (Sd), which replaces sphalerite (Sp); sample CR18-5. B. Carbonate-filled vein cutting dolomite (Dol) with pyrite (Py) remnants. The vein is characterized by a smithsonite (Sm1)-rich inner part and by a siderite-rich outer part; sample CR18-5. C. Patches of siderite in a smithsonite (Sm1) crystal, at the contact between dolomite and sphalerite; sample CR18-5. D. Smithsonite (Sm1) that replaces sphalerite and pyrite in vein; sample CR18-4. E. Smithsonite (Sm2) replacing host rock dolomite along fractures and inter-crystalline porosity; sample CR03-5. F. Late smithsonite vein (Sm3) cutting dolomite and filling cavities; sample CR03-5. G. Late generation of smithsonite (Sm3) occurring as crustiform bands along the walls of the cavities, which have been previously festooned and filled by concretionary goethite (Gth) and chalcophanite (Chp); sample CR07-1. H. Greenockite filling vugs in Sm2 smithsonite; sample CR18-13.

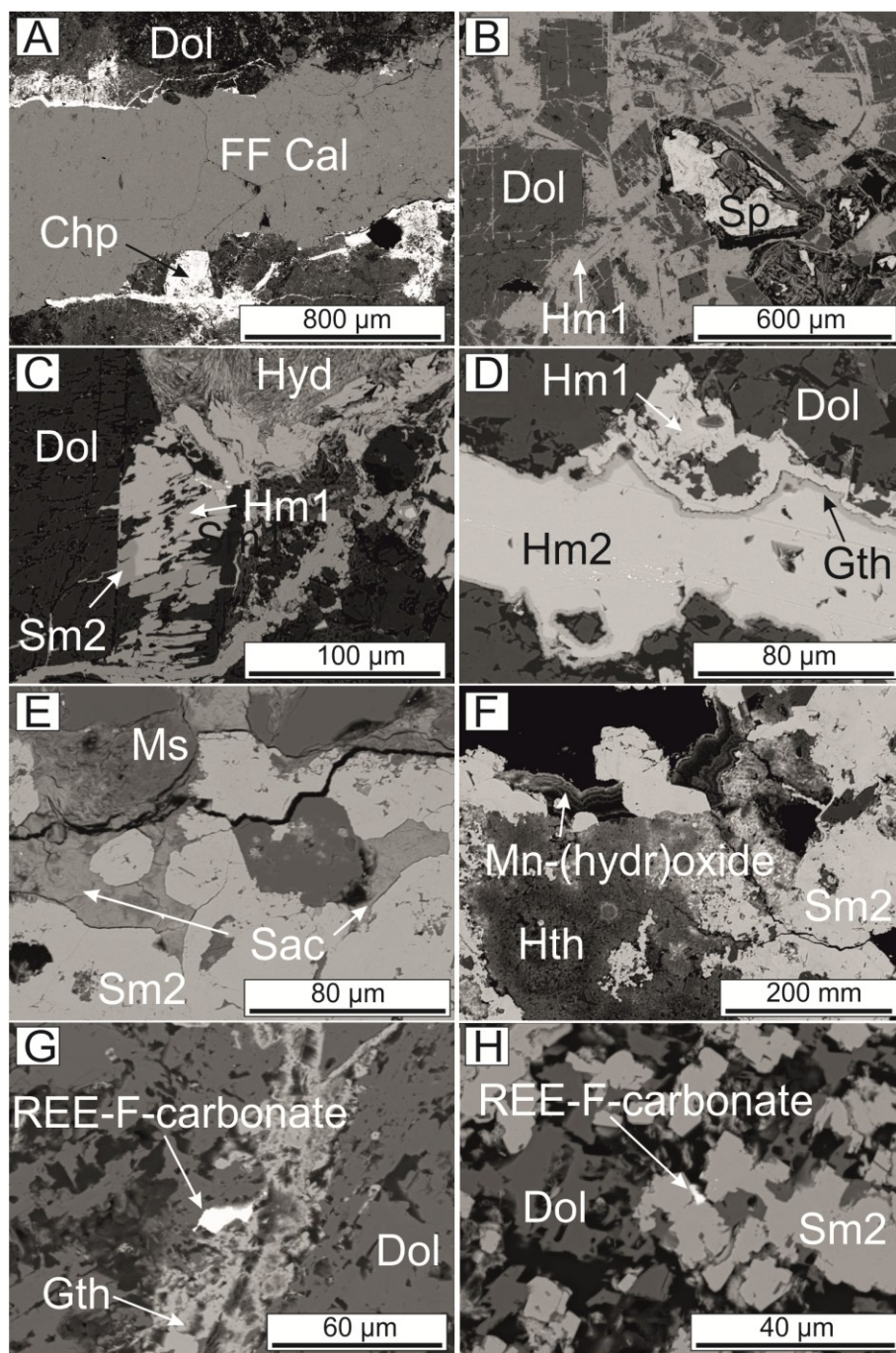


Figure 5.13. Backscattered electron images (BSE) of sulfides and paragenetically late nonsulfide minerals. A. Late calcite (FF Cal) vein cutting dolomite breccia, occurring together with chalcophanite (Chp) veins; sample CR07-8. B. Hemimorphite (Hm1) replacing rhombic dolomite (Dol) crystals and sphalerite (Sp); sample CR18-14. C. Hemimorphite (Hm1) replacing dolomite-replacive smithsonite (Sm2). Hydrozincite (Hyd) that replaces hemimorphite (Hm1) and shows spongy to needle-shaped texture; sample CR18-14. D. Late hemimorphite (Hm2) vein cutting dolomite. The outer part of the vein consists of goethite, in contact with a paragenetically earlier hemimorphite (Hm1); sample CR13-9. E. Sauconite (Sac) replacing muscovite (Ms) and filling fractures within smithsonite (Sm2); sample CR03-3. F. Concretions of amorphous Mn-(hydr)oxides growing on smithsonite (Sm2), which is partially replaced by hydrohetaerolite (Hth); sample CR03-3. G. REE-F-carbonate (synchysite) occurring together with goethite (Gth) in vein cutting dolomite; sample CR18-6. H. REE-F-carbonate (synchysite) occurring at the border of smithsonite (Sm2); sample CR18-3.

TABLE 5.4. Representative chemical composition (EDS) and structural formulae (apfu) of smithsonite from the Cristal prospect.

Sample ID	CR18-5	CR18-6	CR18-6	CR13-3	CR18-11	CR18-14	CR03-4
Mineral phase ID	Sm1	Sm1	Sm1	Sm2	Sm2	Sm1	Sm3
wt. %							
ZnO	58.17	59.46	59.60	63.06	62.64	62.21	63.29
FeO	2.38	2.83	2.37	0.67	N.D.	0.78	0.07
MnO	0.02	0.43	0.54	N.D.	0.79	N.D.	0.05
MgO	1.82	1.22	0.96	0.77	0.16	0.47	0.17
CaO	0.89	0.15	0.79	N.D.	0.34	0.38	0.20
CdO	N.D.	N.D.	N.D.	0.15	N.D.	0.22	0.56
CO ₂ ¹	35.60	35.58	35.67	35.38	34.79	34.99	34.82
Total	98.88	99.66	99.93	100.03	98.72	99.05	99.17
on the basis of CO ₃							
Zn	0.88	0.90	0.90	0.96	0.97	0.96	0.98
Fe	0.04	0.05	0.04	0.01	-	0.01	-
Mn	-	0.01	0.01	0.00	0.01	-	-
Mg	0.06	0.04	0.03	0.02	-	0.01	0.01
Ca	0.02	-	0.02	-	0.01	0.01	-
Cd	-	-	-	-	-	-	0.01

Note: Sm1 = sulfide-replacive smithsonite; Sm2 = dolomite-replacive smithsonite; Sm3 = open space filling smithsonite; ¹calculated from stoichiometry; N.D. not detected; - not determined

The late calcite veins (FF Cal; Fig. 5.13A) have a coarse- to finer-grained texture, which is similar to that of the younger smithsonite generation (Sm3). These veins also cut a few breccia intervals in calcite and dolomite host rock. The breccia contains detrital quartz, visible as clasts within a goethite and clay matrix. The late calcite veins are cut in turn by goethite and chalcophanite veinlets (Fig. 5.13A).

Early stage hemimorphite (Hm1; Figs. 5.13B and C; Table 5.5) has been observed in cm-size agglomerates of tabular crystals that replace sphalerite, dolomite (Fig. 5.13B) and Sm2 (Fig. 5.13C). A late hemimorphite generation (Hm2; Fig. 5.13D; Table 5.5) occurs locally as vein fillings and as crustiform bands along fractures and cavities, where it shows the same texture of Sm3. Hemimorphite has Ge content with mean values from 39 to 137 ppm and maximum values of 258 ppm (Mondillo et al., 2018).

Sauconite can be found as mica replacement (Fig. 5.13E), as well as in vugs and fracture fillings in smithsonite, in the silicate- and aluminosilicate-rich intercalations (abundant in CR-13-08 drill core). Hydrozincite is quite rare at Cristal. When present, it occurs as halos around both smithsonite and hemimorphite (Fig. 5.13C) in the deepest parts of the drill cores, or as concretionary fillings in vugs, where it shows a needle-shaped texture. In the aluminosilicate-rich samples, hydrozincite replacing smithsonite (both Sm1 and Sm2) and hemimorphite (Hm1) has also been locally detected.

TABLE 5.5. Representative chemical composition (EDS) and structural formulae (apfu) of hemimorphite from the Cristal prospect.

Sample ID	CR13-3	CR13-4	CR13-5	CR13-6	CR18-14	CR18-15	CR13-5	CR13-9	CR18-15
Mineral phase ID	Hm1	Hm1	Hm1	Hm1	Hm1	Hm1	Hm2	Hm2	Hm2
wt. %									
SiO ₂	23.30	25.48	22.86	25.93	24.44	25.50	23.60	24.47	24.55
Al ₂ O ₃	N.D.	1.75	0.06	1.83	N.D.	1.16	0.25	0.46	0.12
FeO	0.60	0.26	0.69	1.17	0.62	N.D.	0.11	0.05	N.D.
ZnO	69.47	64.16	68.31	63.42	68.22	66.38	68.69	67.68	68.05
H ₂ O ¹	7.37	7.61	7.25	7.71	7.47	7.64	7.37	7.47	7.46
Total	100.74	99.26	99.18	100.07	100.75	100.68	100.02	100.13	100.18
on the basis of O ₇ (OH) ₂									
Si	1.89	2.01	1.89	2.02	1.96	2.00	1.92	1.96	1.97
Al	0.00	0.16	0.01	0.17	0.00	0.11	0.02	0.04	0.01
Fe	0.04	0.02	0.05	0.08	0.04	0.00	0.01	0.00	0.00
Zn	4.17	3.73	4.17	3.64	4.04	3.84	4.12	4.01	4.04
OH	1.99	1.99	1.99	2.00	1.99	1.99	2.00	2.00	2.00

Note: Hm1 = early hemimorphite; Hm2 = late hemimorphite; ¹calculated from stoichiometry; N.D. not detected; - not determined.

TABLE 5.6. Chemical composition (WDS) and structural formulae (apfu) of synchysite from the Cristal prospect (CR18-4 core).

wt. %					
La ₂ O ₃	2.05	1.31	0.80	0.66	0.70
Ce ₂ O ₃	8.40	7.89	6.53	6.12	6.22
Pr ₂ O ₃	2.39	2.21	2.05	2.04	1.96
Nd ₂ O ₃	18.79	19.66	17.85	18.75	17.36
Sm ₂ O ₃	9.96	10.58	11.95	11.95	11.67
Gd ₂ O ₃	6.83	7.25	9.63	9.36	9.67
Dy ₂ O ₃	0.91	0.84	1.40	1.26	1.46
Tb ₂ O ₃	0.47	0.42	0.67	0.54	0.62
Ho ₂ O ₃	0.10	0.09	0.15	0.08	0.17
CaO	17.38	17.36	17.43	17.18	17.47
Fe ₂ O ₃	0.25	0.76	0.20	0.92	0.38
SiO ₂	0.15	0.16	0.14	0.20	0.18
Y ₂ O ₃	1.94	1.33	2.58	2.03	3.04
CO ₂ ¹	27.62	27.76	28.12	28.18	28.15
F	7.02	4.89	4.62	5.06	4.98
F ¹	5.96	5.99	6.07	6.08	6.08
O=F ₂	2.96	2.06	1.95	2.13	2.10
O=F ₂ ¹	2.51	2.52	2.56	2.56	2.56
Total	101.32	100.46	102.15	102.21	101.93
On the basis of (CO ₃) ₂ F					
La	0.04	0.03	0.02	0.01	0.01
Ce	0.16	0.15	0.12	0.12	0.12
Pr	0.05	0.04	0.04	0.04	0.04
Nd	0.36	0.37	0.33	0.35	0.32
Sm	0.18	0.19	0.21	0.21	0.21
Gd	0.12	0.13	0.17	0.16	0.17
Dy	0.02	0.01	0.02	0.02	0.02
Tb	0.01	0.01	0.01	0.01	0.01
Ho	-	-	-	-	-
ΣREE	0.93	0.93	0.93	0.92	0.91
Ca	0.99	0.98	0.97	0.96	0.97
Fe	0.01	0.03	0.01	0.04	0.01
Si	0.01	0.01	0.01	0.01	0.01
Y	0.05	0.04	0.07	0.06	0.08

Note: ¹ calculated from stoichiometry; - not determined.

The Fe-(hydr)oxides (goethite) at Esperanza contain not only FeO, but also ZnO (up to 16 wt.%), PbO (up to 2 wt.%), SiO₂ (up to 12 wt.%) and Ge (mean values 100 to 229 ppm, max 511 ppm, Mondillo et al. 2018). Similarly, most Zn-Mn-Pb-(hydr)oxides occur generally as pure phases (e.g. chalcophanite, hetaerolite and coronadite), rather than as amorphous phases containing Zn-Mn-Pb-Fe in variable proportions (ZnO ~10-20 wt.%;

MnO ~30 wt.%; PbO ~0-10 wt.%; FeO ~0-30 wt.%). Chalcophanite, which is the most recurrent Mn-bearing hydroxide, occurs in concretions together with an amorphous Mn-phase (Fig. 5.13F), or in association with Sm3 and FF Cal as crustiform bands (Fig. 5.12G). Generally, all hydroxides occur in veinlets cutting smithsonite and hemimorphite, or as crusts on the zincian secondary minerals and on mica-bearing layers.

In the more weathered and oxidized zones, Y- and REE-sulfophosphates and Ca-REE-fluorocarbonates (synchysite; Table 5.6) commonly occur together with Mn-(hydr)oxides and goethite (Fig. 5.13G) at the border of smithsonite crystals (Fig. 5.13H). Average fluorocarbonate composition generally comprehends: Ca (~17 wt.% CaO), Nd (~19 wt.% Nd₂O₃), Sm (~11 wt.% Sm₂O₃), Ce (~7 wt.% Ce₂O₃), Gd (~8 wt.% Gd₂O₃), F (~5 wt.%), Pr (~2 wt.% Pr₂O₃), Y (~2 wt.% Y₂O₃), La (~1 wt.% La₂O₃), Dy (~1 wt.% Dy₂O₃) and Fe, Tb and Ho (<1 wt.% Fe₂O₃, Tb₂O₃ and Ho₂O₃).

Major and minor element geochemistry

Whole rock chemical analyses of the samples from the Cristal drill cores are shown in Tables 5.7 and 5.8. In the samples characterized by amounts of smithsonite and hemimorphite higher than 90 wt.%, the zinc content is between ~40 and ~50 wt.% Zn (Tables 5.7). The highest Zn values (up to 53 wt.% Zn) are associated with the hemimorphite-rich layers of the CR-13-08 drill core (Table 5.7). However Zn concentration is also high in the silicate- and aluminosilicate-rich samples (e.g. CR07 and CR03 samples; Table 5.8), where dolomite is not abundant or completely replaced by smithsonite. This means that Zn/Si ratio is not useful to distinguish among smithsonite- and hemimorphite-rich mineralizations, which instead can be easily identified by looking at the Cd/Ge ratio. In fact, Cd and Ge have different deportments in the two minerals: Cd is strictly related to smithsonite, being commonly hosted in the lattices of Sm1 and Sm2 (Table 5.4) and in greenockite, which is also commonly associated with smithsonite, whereas Ge is preferentially hosted in hemimorphite and goethite (Mondillo et al. 2018). Moreover the elements concentrations are significant at Cristal, with bulk rock values of >2000 Cd and up to 200 ppm Ge (Table 5.7). In the smithsonite-rich mineralization from the CR-18-08 and CR-07-08 drill cores, the Cd/Ge ratios (Tables 5.7 and 5.8; Figs. 5.7 and 5.9) are mostly comprised between ~7 and ~25, and ~20 and ~150, respectively. The lower ratios measured in the CR-18-08 drill core samples are associated with higher amounts of Ge-bearing goethite as well as sphalerite, which are not equally abundant in other smithsonite-rich drill core samples (e.g. CR07 and CR03). In the hemimorphite-rich mineralization from the CR-13-08 drill core, instead, the values of Cd/Ge ratio are < 8 for almost of the analyzed samples (Table 5.7; Fig. 5.8).

Lead concentrations are low, generally below 2000 ppm, and rarely reach values around 1 wt.% (Tables 5.7 and 5.8). The highest Pb values are associated with hydroxides-rich layers, where Pb-bearing goethite, chalcophanite and hydrohetaerolite are the main lead hosts. Copper is scarce, with values that seldom exceed 150 ppm. Iron concentrations in the smithsonite- and hemimorphite-rich bodies are similar, varying from ~1 to ~80 wt.% (Table 5.7). The highest Fe amounts are generally associated with the presence of goethite. The environmentally dangerous thallium is very scarce at Cristal, with values

always <1 ppm. Yttrium is enriched (100 - 235 ppm) in a few samples from the CR-18-08 and CR-07-08 drill cores of the smithsonite-rich mineralization (Tables 5.7 and 5.8), where high concentrations of xenotime have been detected. High contents of Co have been detected in many samples from the CR-18-08 and CR-03-08 drill cores, although, the highest Co concentration (max value ~294 ppm) has been measured in the CR-13-08 drill core of the hemimorphite-rich body, where it is possibly associated with Fe-Mn(hydr)oxides (goethite, chalcophanite and hydrohetarolite). All other analyzed elements (i.e., Mo, Sb, Rb, Th, Sn, etc.) rarely reach average values higher than 40 ppm.

TABLE 5.7. Major (wt.%), minor and trace (ppm, ppb) element concentrations of CR-18-08 and CR-13-08 drill cores (Esperanza).

	Sample ID	CR18-1	CR18-2	CR18-3	CR18-4	CR18-5	CR18-6	CR18-7	CR18-8	CR18-9	CR18-10	CR18-11	CR18-12	CR18-13	CR18-14	CR18-15	CR18-16	CR18-17	CR18-18	CR18-19	CR18-20
wt. %	MDL (A)																				
SiO ₂	0.01	1.29	2.17	1.35	2.28	2.11	1.26	2.04	3.35	7.07	4.46	2.09	3.61	4.36	7.01	4.16	7.57	6.96	7.66	11.99	7.38
Al ₂ O ₃	0.01	0.12	0.21	0.22	0.58	0.55	0.25	0.33	0.84	1.26	0.41	0.47	0.64	0.95	1.01	0.76	1.24	1.10	1.44	1.09	0.87
MgO	0.01	0.51	0.28	14.46	12.68	11.83	15.19	4.69	0.17	0.14	0.26	0.19	0.30	0.39	4.50	12.22	10.47	2.78	5.82	1.51	0.86
Fe ₂ O ₃	0.01	39.03	56.87	17.84	9.12	9.44	12.54	12.02	26.73	47.64	25.18	18.24	17.28	34.27	12.17	8.19	10.88	43.04	22.38	35.99	50.12
CaO	0.01	0.16	0.10	20.37	18.16	18.84	22.04	6.77	0.10	0.05	0.19	0.12	0.20	0.24	6.74	19.36	16.38	4.33	9.00	2.26	1.09
Na ₂ O	0.01	0.27	0.14	<0.01	0.06	0.10	<0.01	0.26	0.31	0.19	0.32	0.38	0.36	0.28	0.29	0.06	0.09	0.13	0.17	0.21	0.15
K ₂ O	0.01	0.03	0.05	0.08	0.18	0.18	0.08	0.12	0.24	0.35	0.13	0.16	0.21	0.52	0.32	0.24	0.38	0.28	0.42	0.30	0.25
MnO	0.01	0.80	0.55	0.53	0.39	0.30	0.52	0.43	0.48	0.45	0.60	0.40	0.31	1.22	0.40	0.37	0.46	0.88	0.50	0.39	0.72
TiO ₂	0.01	<0.01	<0.01	<0.01	0.01	0.01	<0.01	<0.01	0.02	0.04	<0.01	<0.01	0.02	0.03	0.03	0.02	0.03	0.03	0.05	0.03	0.03
P ₂ O ₅	0.01	0.01	0.01	0.01	0.02	0.01	<0.01	0.01	0.01	0.04	0.02	0.01	0.01	0.03	0.03	0.03	0.04	0.04	0.04	0.05	0.06
LOI	-5.11	22.76	17.03	37.02	26.4	10.18	38.21	32.34	24.82	17.63	25.93	28.72	27.54	22.57	27.71	24.02	32.37	19.4	19.79	15.12	15.86
Zn	0.1	28.9	17.4	6.0	15.3	16.7	6.8	33.8	34.8	18.9	35.2	41.1	41.5	29.3	32.1	14.8	14.7	16.5	21.4	25.7	18.0
S	0.02	<0.02	<0.02	<0.02	2.75	8.07	0.13	0.05	0.10	4.53	<0.02	0.03	0.19	0.07	0.35	3.32	0.32	<0.02	1.21	<0.02	<0.02
ppm																					
Mo	0.01	0.57	0.45	0.36	0.74	0.26	0.17	0.28	0.54	5.28	0.68	0.74	2.77	1.33	1.76	1.05	2.33	2.55	1.41	0.94	2.24
Cu	0.01	115.31	13.89	33.58	107.04	169.76	80.26	200.42	221.92	78.71	42.54	89.50	341.55	123.36	131.11	112.68	75.55	43.50	120.81	110.97	6.62
Pb	0.01	798.73	504.70	91.34	45.99	35.69	90.12	1867.66	8271.48	3918.25	340.95	594.30	103.39	86.49	99.02	25.35	83.82	1047.32	269.36	318.68	133.19
Ni	0.1	23.1	17.9	4.8	4.9	2.1	3.8	18.7	41.9	37.9	29.0	17.9	14.0	20.7	10.0	4.8	9.2	24.4	11.5	13.6	29.7
Co	0.1	129.0	51.8	41.6	89.5	118.5	51.0	110.9	92.2	43.1	68.4	153.6	228.8	169.7	290.4	95.4	69.7	86.5	124.6	137.8	64.3
As	0.1	4.2	2.2	9.9	2.9	3.0	2.4	3.2	5.7	16.3	6.6	2.7	4.1	2.6	7.6	1.8	3.4	7.0	12.5	8.1	5.0
U	0.1	0.6	0.7	0.2	0.1	0.2	0.1	0.3	0.5	0.4	0.4	0.3	0.3	0.4	0.4	0.6	0.3	0.9	0.5	0.8	1.1
Th	0.1	0.1	<0.1	<0.1	0.1	0.1	<0.1	<0.1	0.2	0.4	0.2	<0.1	0.2	0.3	0.3	0.2	0.2	0.5	0.4	0.5	0.5
Sr	0.5	2.5	2.5	151.7	87.3	73.4	70.5	42.0	1.0	1.2	1.5	0.8	0.8	7.2	31.3	85.2	102.5	14.5	48.1	16.7	10.6
Cd	0.01	967.28	574.29	525.59	917.94	1150.87	475.66	1662.74	1541.16	723.95	1086.30	1459.27	1792.10	945.70	1484.31	745.40	613.40	586.68	795.09	519.39	694.77

Note: MDL = minimum detection limit; for (A) see methods; - not detected.

TABLE 5.7 (continue)....

	Sample ID	CR18-1	CR18-2	CR18-3	CR18-4	CR18-5	CR18-6	CR18-7	CR18-8	CR18-9	CR18-10	CR18-11	CR18-12	CR18-13	CR18-14	CR18-15	CR18-16	CR18-17	CR18-18	CR18-19	CR18-20
ppm	MDL (A)																				
Sb	0.02	0.25	0.15	0.28	0.26	0.36	0.18	0.32	0.65	0.67	0.71	0.16	0.32	0.23	0.41	0.25	0.36	0.26	0.29	0.18	0.19
V	2	17	29	16	15	17	10	14	28	20	17	10	16	13	9	13	17	20	11	22	29
La	0.5	5.8	4.3	5.6	4.8	0.9	4.0	3.1	13.2	12.2	4.5	5.3	5.0	2.9	1.5	1.5	1.8	3.2	2.6	2.1	4.4
Cr	0.5	2.3	2.5	1.6	1.6	2.3	1.2	1.8	4.9	4.9	1.8	1.8	5.0	3.5	2.9	2.4	3.4	3.9	2.6	4.1	6.0
Ba	0.5	48.0	32.7	27.8	9.2	1.3	22.2	17.1	18.0	29.5	45.7	22.4	42.3	67.3	36.6	9.4	20.9	48.6	28.4	27.0	109.9
Sc	0.1	1.4	1.9	1.3	1.1	0.8	0.9	0.9	1.9	1.7	1.2	1.7	3.3	2.1	2.0	2.2	2.1	1.8	1.7	2.1	1.2
Tl	0.02	0.11	0.09	0.08	0.20	0.12	0.08	0.15	0.24	0.33	0.36	0.17	0.20	0.29	0.17	0.10	0.24	0.32	0.23	0.29	0.76
Se	0.1	1.0	2.4	0.5	1.8	3.2	0.3	1.2	1.0	1.0	1.0	1.0	7.8	2.2	3.7	2.6	3.8	2.4	1.0	0.8	0.8
Ga	1	4	<1	2	6	7	3	17	16	9	19	14	72	17	13	5	8	4	11	8	2
Ge	1	92	56	38	112	138	65	87	124	64	66	94	112	96	87	69	47	57	89	129	77
Rb	0.1	0.2	0.3	0.3	0.6	0.5	0.3	0.4	0.8	1.2	0.5	0.6	0.6	0.9	1.2	0.8	1.1	1.0	1.3	1.3	1.0
Cs	0.02	0.02	0.04	0.05	0.11	0.10	0.05	0.07	0.14	0.24	0.06	0.09	0.09	0.10	0.13	0.10	0.13	0.13	0.16	0.14	0.12
Sn	0.1	0.4	0.1	0.2	0.6	0.5	0.4	1.4	1.9	0.7	0.3	0.8	5.7	1.1	0.9	0.5	0.4	<0.1	0.5	0.4	<0.1
Zr	0.1	<0.1	0.2	0.1	0.3	0.3	<0.1	0.2	0.4	1.3	1.5	0.4	0.3	0.6	0.9	0.6	1.1	0.9	1.2	1.0	1.3
Y	0.01	59.26	76.44	67.80	44.27	42.28	69.48	73.53	135.66	174.55	101.18	59.57	88.52	64.74	33.92	35.52	44.40	64.88	47.03	61.53	38.94
Ce	0.1	34.7	24.6	39.0	34.7	8.2	29.0	10.1	8.3	9.8	11.6	7.6	5.9	13.6	9.0	7.7	9.5	16.2	13.6	14.0	10.2
In	0.02	3.56	0.15	3.22	7.66	9.75	7.59	27.75	11.24	4.59	6.27	3.86	34.56	7.41	15.42	6.15	1.06	1.10	6.52	7.29	0.09
Li	0.1	0.3	0.1	0.2	0.3	0.3	0.2	0.2	0.3	0.4	0.2	0.3	0.2	0.4	0.3	0.4	0.3	0.3	0.2	0.4	0.4
ppb																					
Au	0.2	<0.2	<0.2	0.9	<0.2	<0.2	<0.2	<0.2	<0.2	0.6	<0.2	<0.2	<0.2	<0.2	<0.2	<0.2	<0.2	<0.2	1.9	1.4	<0.2
Ag	2	3470	1908	2366	17536	15186	3052	10383	37176	13153	1389	9232	27762	6908	4541	3828	4269	1106	5653	4859	503
Hg	5	95	70	61	229	358	156	448	447	243	98	247	1603	287	497	281	189	25	260	206	12
Zn/Pb		361.8	345.4	652.5	3320.3	4682.0	754.5	181.0	42.1	48.1	1032.4	691.6	4013.9	3387.7	3241.8	5846.2	1749.0	157.6	792.6	806.5	1354.5
Zn/Fe		1.1	0.4	0.5	2.4	2.5	0.8	4.0	1.9	0.6	2.0	3.2	3.4	1.2	3.8	2.6	1.9	0.5	1.4	1.0	0.5
Cd/Ge		10.5	10.3	13.8	8.2	8.3	7.3	19.1	12.4	11.3	16.5	15.5	16.0	9.9	17.1	10.8	13.1	10.3	8.9	4.0	9.0

Note: MDL = minimum detection limit; for (A) see methods; - not detected.

TABLE 5.7 (continue)...

	Sample ID	CR18-21	CR18-22	CR18-23	CR13-1	CR13-2	CR13-3	CR13-4	CR13-5	CR13-6	CR13-7	CR13-8	CR13-9	CR13-10	CR13-11	CR13-12
wt. %	MDL (B)															
SiO ₂	-	-	-	-	-	-	-	-	-	-	-	-	-	-	-	-
Al ₂ O ₃	0.03	1.69	2.41	2.44	3.74	0.95	1.86	3.15	4.21	6.19	12.94	10.43	7.99	4.64	1.51	0.39
MgO	0.01	0.37	13.55	22.93	4.90	7.85	17.02	5.72	2.99	0.35	0.65	0.50	9.14	17.22	19.78	18.78
Fe ₂ O ₃	0.004	73.445	36.977	13.891	83.982	17.208	12.080	31.535	25.299	19.555	9.288	35.766	14.246	7.138	1.771	5.089
CaO	-	-	-	-	-	-	-	-	-	-	-	-	-	-	-	-
Na ₂ O	-	-	-	-	-	-	-	-	-	-	-	-	-	-	-	-
K ₂ O	0.1	0.5	0.7	0.8	0.6	0.3	0.6	0.8	1.1	1.6	3.9	3.0	2.3	1.4	0.5	<0.1
MnO	0.001	1.208	1.047	0.502	1.495	0.297	0.407	0.636	1.081	0.740	0.647	3.014	0.452	0.431	0.132	0.407
TiO ₂	-	-	-	-	-	-	-	-	-	-	-	-	-	-	-	-
P ₂ O ₅	-	-	-	-	-	-	-	-	-	-	-	-	-	-	-	-
LOI	-	-	-	-	-	-	-	-	-	-	-	-	-	-	-	-
Zn	0.001	13.303	4.538	2.102	5.650	28.618	15.759	21.542	31.350	53.026	35.991	17.332	17.673	0.490	0.227	0.035
S	-	-	-	-	-	-	-	-	-	-	-	-	-	-	-	-
ppm																
Mo	1	3	2	2	2	2	2	1	1	3	3	4	3	2	<1	<1
Cu	7	<7	<7	<7	140	318	116	43	44	24	18	23	14	<7	<7	<7
Pb	12	108	51	33	8306	25	70	118	303	785	626	909	95	20	<12	<12
Ni	1.5	30.3	22.2	11.3	22.7	14.0	10.2	29.1	84.7	72.0	46.9	48.7	31.1	7.9	4.8	<1.5
Co	1	125	30	13	139	149	91	60	13	14	17	294	35	2	1	<1
As	1.5	5.5	9.3	5.5	19.6	15.3	8.1	14.9	10.4	7.8	10.3	50.7	54.1	7.3	1.8	4.4
U	0.5	2.4	2.5	2.6	2.2	1.2	1.7	2.5	3.0	2.9	5.3	5.6	5.4	3.6	1.4	1.0
Th	1	<1	<1	<1	<1	<1	<1	1	1	2	3	2	2	1	<1	<1
Sr	6	14	89	121	40	48	80	42	13	7	15	40	42	180	86	104
Cd	1	518	568	194	179	996	732	355	558	178	133	209	214	4	12	-

Note: MDL = minimum detection limit; for (B) see methods; - not detected.

TABLE 5.7 (continue)....

	Sample ID	CR18-21	CR18-22	CR18-23	CR13-1	CR13-2	CR13-3	CR13-4	CR13-5	CR13-6	CR13-7	CR13-8	CR13-9	CR13-10	CR13-11	CR13-12
ppm	MDL (B)															
Sb	0.4	1.5	2.5	1.9	1.7	2.2	1.9	1.8	2.3	4.2	3.9	3.0	4.4	2.1	1.1	1.0
V	1	36	44	23	65	39	43	52	87	84	164	144	100	32	14	9
La	-	-	-	-	-	-	-	-	-	-	-	-	-	-	-	-
Cr	18	<18	<18	<18	<18	<18	<18	<18	18	<18	31.8	31.6	22.4	20.8	<18	<18
Ba	3.9	109.2	107.3	38.5	95.5	22.0	17.3	144.3	132.0	72.6	83.9	298.0	108.4	44.0	16.9	24.6
Sc	-	-	-	-	-	-	-	-	-	-	-	-	-	-	-	-
Tl	1	<1	<1	<1	<1	<1	<1	<1	1	1	1	11	1	<1	<1	<1
Se	-	-	-	-	-	-	-	-	-	-	-	-	-	-	-	-
Ga	0.4	2.0	2.5	2.4	5.9	14.1	8.9	6.4	11.1	6.5	12.0	14.9	10.2	4.5	1.5	0.6
Ge	12	53	22	<12	163	216	84	103	91	138	62	65	41	<12	<12	<12
Rb	1	4	8	9	5	2	7	9	12	19	51	37	26	19	6	2
Cs	0.3	0.4	0.7	0.7	0.5	0.6	0.6	1.1	1.7	1.6	2.9	2.6	2.0	1.2	0.3	<0.3
Sn	4	<4	<4	<4	<4	<4	<4	<4	<4	<4	<4	<4	<4	<4	<4	<4
Zr	-	-	-	-	-	-	-	-	-	-	-	-	-	-	-	-
Y	-	-	-	-	-	-	-	-	-	-	-	-	-	-	-	-
Ce	-	-	-	-	-	-	-	-	-	-	-	-	-	-	-	-
In	0.6	<0.6	<0.6	<0.6	1.1	12.8	6.0	<0.6	<0.6	<0.6	<0.6	<0.6	<0.6	<0.6	<0.6	<0.6
Li	-	-	-	-	-	-	-	-	-	-	-	-	-	-	-	-
ppb																
Au	-	-	-	-	-	-	-	-	-	-	-	-	-	-	-	-
Ag	-	-	-	-	-	-	-	-	-	-	-	-	-	-	-	-
Hg	-	-	-	-	-	-	-	-	-	-	-	-	-	-	-	-
Zn/Pb		1232.0	886.3	636.2	6.8	11369.0	2264.2	1818.4	1033.0	675.1	575.2	190.6	1865.6	241.8	-	-
Zn/Fe		0.3	0.2	0.2	0.1	2.4	1.9	1.0	1.8	3.9	5.5	0.7	1.8	0.1	0.2	-
Cd/Ge		9.8	26.3	-	1.1	4.6	8.7	3.5	6.2	1.3	2.1	3.2	5.2	-	-	-

Note: MDL = minimun detection limit; for (B) see methods; - not detected

TABLE 5.8. Major (wt.%), minor and trace (ppm and ppb) element concentrations of CR-07-08 and CR-03-08 from Esperanza, and CR-02-08 from Yolanda.

	Sample ID	CR07-1	CR07-2	CR07-3	CR07-4	CR07-5	CR07-6	CR07-7	CR07-8	CR07-9	CR07-10	CR07-11	CR07-12	CR07-13	CR07-14	CR03-1	CR03-2	CR03-3	CR03-4	CR03-5	CR02
wt. %	MDL (A)																				
SiO ₂	0.01	11.05	27.93	6.66	7.37	18.50	11.32	9.87	5.29	25.41	21.02	40.16	35.92	52.93	46.82	35.17	8.26	7.73	6.89	7.40	31.98
Al ₂ O ₃	0.01	1.66	3.47	1.59	1.47	3.50	2.45	2.06	1.12	11.08	5.40	4.05	4.08	5.69	10.73	4.17	3.61	0.91	2.18	1.67	4.04
MgO	0.01	0.32	0.30	0.25	0.36	0.36	1.24	6.80	6.69	0.87	4.30	0.40	0.46	0.56	0.98	0.31	0.22	0.37	2.58	8.02	0.34
Fe ₂ O ₃	0.01	31.23	44.93	13.00	20.61	31.35	18.12	17.51	7.98	17.15	36.17	8.58	15.96	13.26	10.70	47.84	0.74	1.26	3.74	4.56	41.44
CaO	0.01	0.16	0.08	0.17	0.13	0.18	1.59	20.86	37.70	0.19	5.82	0.30	0.27	0.28	0.54	0.07	0.92	0.87	3.58	11.45	0.26
Na ₂ O	0.01	0.37	0.08	0.48	0.42	0.28	0.45	0.10	0.02	0.24	0.08	0.26	0.27	0.14	0.15	0.04	0.41	0.50	0.45	0.33	0.12
K ₂ O	0.01	0.45	0.98	0.26	0.36	1.01	0.73	0.59	0.33	3.00	1.46	1.18	1.21	1.70	2.83	1.11	0.18	0.30	0.69	0.49	1.15
MnO	0.01	0.93	1.65	0.61	1.10	1.97	1.14	0.92	0.53	1.36	2.01	1.00	0.77	0.93	0.70	0.34	0.12	0.20	0.42	0.29	0.40
TiO ₂	0.01	0.06	0.16	0.03	0.04	0.15	0.11	0.08	0.03	0.20	0.14	0.21	0.19	0.29	0.42	0.22	<0.01	0.03	0.06	0.06	0.23
P ₂ O ₅	0.01	0.05	0.20	0.03	0.02	0.05	0.05	0.06	0.02	0.14	0.18	0.10	0.16	0.19	0.29	0.24	0.04	0.03	0.09	0.09	0.15
LOI	-5.11	21.43	10.27	28.07	25.38	17.13	24.83	31.14	38.52	16.43	17.27	16.46	16.26	9.98	10.66	7.95	30.36	31.67	32.03	34.99	9.61
Zn	0.1	26.6	7.4	40.6	34.9	18.4	31.6	7.7	1.0	18.5	4.5	21.0	18.9	10.6	11.4	1.3	46.3	46.4	39.8	25.8	6.8
S	0.02	0.07	0.13	0.11	0.02	<0.02	<0.02	<0.02	<0.02	<0.02	<0.02	<0.02	<0.02	<0.02	<0.02	0.04	<0.02	<0.02	<0.02	<0.02	0.03
ppm																					
Mo	0.01	1.49	2.69	1.26	1.02	1.48	0.54	0.84	0.84	8.65	18.72	4.85	7.14	7.19	5.27	9.18	0.65	0.46	0.56	0.69	6.47
Cu	0.01	91.68	23.57	41.00	75.22	31.69	7.54	12.86	2.08	15.64	137.98	12.13	67.09	20.38	25.31	84.54	132.40	134.67	55.41	37.61	28.13
Pb	0.01	1134.74	290.45	2008.83	6783.53	>10000	389.65	725.00	13.02	133.91	1039.03	57.81	537.42	283.40	50.76	5334.97	6.50	5.10	12.50	14.34	>10000
Ni	0.1	50.5	71.5	68.4	68.1	56.1	68.8	31.7	9.2	59.1	36.4	66.3	63.8	138.7	57.0	24.0	60.1	26.3	34.2	39.6	30.4
Co	0.1	138.5	28.2	51.0	85.1	31.9	11.2	19.3	6.2	7.0	58.3	27.1	41.1	16.2	37.3	22.8	116.4	140.2	116.1	40.4	21.4
As	0.1	8.7	13.0	6.3	5.8	6.9	3.0	3.4	1.2	13.3	22.0	23.0	14.5	10.2	12.1	98.0	<0.1	1.2	2.8	3.7	13.0
U	0.1	0.7	0.7	0.6	0.7	0.8	0.4	0.5	0.2	0.9	1.3	0.7	0.8	0.6	0.9	0.4	0.6	0.2	0.1	0.1	1.1
Th	0.1	0.5	0.9	0.3	0.3	1.0	0.8	0.6	0.4	2.6	1.5	2.1	2.1	2.9	3.9	0.9	0.3	0.4	0.4	0.6	1.1
Sr	0.5	2.2	4.0	1.9	2.3	4.0	10.3	30.8	38.8	5.6	16.0	9.5	7.1	5.8	13.6	1.5	38.3	5.4	13.2	29.4	5.8
Cd	0.01	1139.91	383.66	1939.01	1643.15	1003.06	1383.36	379.09	9.49	1396.77	244.95	1355.74	1121.52	615.49	827.80	27.41	1689.32	>2000	>2000	1066.66	305.99

Note: MDL = minimun detection limit; for (A) see methods;

TABLE 5.8 (continue)...

	Sample ID	CR07-1	CR07-2	CR07-3	CR07-4	CR07-5	CR07-6	CR07-7	CR07-8	CR07-9	CR07-10	CR07-11	CR07-12	CR07-13	CR07-14	CR03-1	CR03-2	CR03-3	CR03-4	CR03-5	CR02
ppm	MDL (A)																				
Sb	0.02	0.79	1.01	0.46	0.46	0.69	0.29	0.35	0.13	0.88	0.93	0.56	0.89	0.45	0.80	2.03	0.08	0.13	0.26	0.44	1.39
V	2	32	68	18	27	54	31	28	17	25	37	21	32	33	40	59	5	5	12	13	28
La	0.5	2.7	4.8	2.7	4.5	7.3	4.7	2.6	1.4	9.9	8.3	20.0	7.0	5.6	15.8	0.8	12.1	5.2	2.8	3.9	6.6
Cr	0.5	6.0	8.3	3.7	5.4	8.2	6.1	5.4	3.8	6.1	11.0	12.1	12.1	11.6	11.8	21.1	2.0	1.6	3.2	10.7	11.3
Ba	0.5	56.9	166.7	43.5	62.1	115.2	88.3	32.6	10.8	375.4	253.4	155.3	162.8	128.0	149.0	148.8	55.1	15.9	54.9	32.4	33.1
Sc	0.1	1.5	2.2	1.4	1.5	2.9	2.0	2.7	1.8	2.2	3.4	2.8	3.7	2.6	5.5	1.6	5.0	1.6	3.6	2.2	2.6
Tl	0.02	0.84	2.21	0.56	0.61	0.95	1.34	0.44	0.78	0.80	0.69	0.37	0.55	0.68	0.68	0.59	0.12	0.12	0.31	0.25	0.65
Se	0.1	6.8	2.3	8.2	7.8	7.1	7.4	2.7	0.7	4.6	4.6	5.2	5.6	3.1	2.4	2.0	9.1	6.9	8.4	9.3	9.5
Ga	1	6	6	5	8	7	4	3	1	13	12	7	8	7	14	22	1	2	3	2	9
Ge	1	85	20	60	64	15	5	11	4	19	75	9	25	8	6	29	1	<1	<1	<1	24
Rb	0.1	2.0	2.9	1.1	1.4	3.4	3.2	2.4	1.4	5.0	3.5	3.8	3.8	4.7	7.7	2.8	1.6	1.8	2.7	3.1	3.1
Cs	0.02	0.29	0.45	0.22	0.23	0.45	0.44	0.34	0.22	1.61	0.74	0.91	0.73	0.76	1.84	0.51	0.46	0.40	0.45	0.37	0.32
Sn	0.1	0.9	0.2	0.5	0.6	0.2	0.1	0.1	<0.1	0.3	0.8	0.2	0.8	0.5	0.7	0.6	0.1	0.2	0.1	<0.1	0.5
Zr	0.1	1.0	1.7	0.9	0.8	1.7	1.3	1.1	0.8	1.2	1.6	2.6	2.2	2.5	2.0	3.8	0.5	0.6	0.9	1.1	1.7
Y	0.01	35.28	68.95	47.31	67.97	111.62	77.86	48.77	27.55	234.44	151.84	96.97	63.65	32.74	43.54	3.51	67.87	51.04	30.10	27.39	81.67
Ce	0.1	15.2	20.5	12.8	25.1	29.0	11.7	14.0	8.0	10.8	40.7	46.0	27.4	26.3	46.4	2.9	44.3	14.7	10.7	5.8	17.4
In	0.02	2.41	0.22	2.55	9.14	0.39	0.28	0.51	0.06	0.07	3.29	0.04	1.12	0.35	0.16	14.23	<0.02	<0.02	0.02	<0.02	0.11
Li	0.1	0.5	0.5	0.4	0.4	1.3	0.9	0.6	0.2	0.3	1.5	0.7	3.8	1.3	1.9	0.4	2.1	0.6	0.6	1.0	0.6
ppb																					
Au	0.2	<0.2	2.3	<0.2	<0.2	<0.2	<0.2	<0.2	<0.2	<0.2	<0.2	<0.2	2.8	0.3	2.2	1.6	<0.2	<0.2	<0.2	<0.2	1.1
Ag	2	30208	13751	36172	63192	5520	5658	8200	138	1453	9623	912	3777	975	259	5402	1052	423	407	553	16301
Hg	5	235	30	77	154	26	9	20	<5	15	117	10	59	30	46	63	12	9	<5	19	66
Zn/Pb		234.4	254.4	202.1	51.4	-	811.0	105.5	798.8	1378.5	43.0	3629.1	352.4	375.1	2243.9	2.4	71230.8	90980.4	31840.0	17991.6	-
Zn/Fe		1.2	0.2	4.5	2.4	0.8	2.5	0.6	0.2	1.5	0.2	3.5	1.7	1.1	1.5	-	89.5	52.7	15.2	8.1	0.2
Cd/Ge		13.4	19.2	32.3	25.7	66.9	276.7	34.5	2.4	73.5	3.3	150.6	44.9	76.9	138.0	0.9	1689.3	-	-	-	12.7

Note: MDL = minimum detection limit; for (A) see methods

Carbon and oxygen isotopes of supergene carbonate minerals

The majority of calcite and smithsonite specimens measured for stable isotope analyses were collected from the smithsonite-rich mineralization (only one specimen has been collected from the hemimorphite-rich horizon).

The $\delta^{18}\text{O}$ composition of sulfide-replacing smithsonite (Sm1) is between 24.6 and 25.8‰ VSMOW (Table 5.9; Fig. 5.14), with an average value of 25.1‰ VSMOW. In contrast, the $\delta^{13}\text{C}$ values of this smithsonite show a very large variation, ranging from -11.7‰ to -0.6 ‰ VPDB.

TABLE 5.9. Carbon and oxygen isotope compositions of supergene smithsonites and calcites from the Cristal prospect.

Sample ID	Sub-sample ID	Mineral phase ID	$\delta^{13}\text{C}$ (‰ VPDB)	$\delta^{18}\text{O}$ (‰ VSMOW)
CR03-3	CR03-3_Sm	Sm2	0.10	26.80
CR03-5	CR03-5_Sm	Sm3	0.43	27.89
CR07-3	CR07-3_Sm	Sm1	-11.71	25.40
CR07-4	CR07-4_Sm	Sm3	0.14	27.85
CR07-6	CR07-6_Sm	Sm2	-11.44	26.76
CR07-8	CR07-8_Cal	FF Cal	-7.41	24.72
CR07-9	CR07-9_SmA	Sm2	-11.69	26.75
	CR07-9_SmB	Sm2	-11.63	26.87
CR13-12	CR13-12_Sm	FF Cal	0.76	24.72
CR18-3	CR18-3_Sm	Sm2	-2.05	26.60
CR18-4	CR18-4_Sm	Sm1	-0.65	24.62
CR18-6	CR18-6_Sm	Sm1	-1.18	24.79
CR18-7	CR18-7_Sm	Sm1	-6.38	25.80
CR18-8	CR18-8_Sm	Sm2	-9.06	27.34
CR18-10	CR18-10_Sm	Sm2	-7.29	27.29
CR18-11	CR18-11_SmA	Sm3	-2.40	27.85
	CR18-11_SmB	Sm3	-2.36	28.30
CR18-12	CR18-12_Sm	Sm2	-9.74	27.11
CR18-13	CR18-13_Sm	Sm2	-5.59	26.82

Note: Sm1 = sulfide-replacive smithsonite; Sm2 = dolomite-replacive smithsonite; Sm3 = open space filling smithsonite; FF Cal = open space filling calcite.

The host rock-replacing smithsonite Sm2 (Table 5.9) has $\delta^{18}\text{O}$ values varying between 26.6 and 27.3‰ VSMOW (mean 26.9‰). These values are higher by ~ 2‰ than those recorded for Sm1 smithsonite. Conversely, the $\delta^{13}\text{C}$ values of both Sm1 and Sm2 are comparable, with the $\delta^{13}\text{C}$ ratios of the latter, ranging from 0.1 to -11.7‰ VPDB (Table 5.9). The late smithsonite generation (Sm3) has $\delta^{18}\text{O}$ values that are between 27.8 and

28.3‰ VSMOW; these values are respectively 1‰ and 3‰ higher than the average $\delta^{18}\text{O}$ of Sm2 and Sm3. The $\delta^{13}\text{C}$ values of Sm3 are between 0.1 and -2.4‰ VPDB, and thus in a narrower range compared to those measured in the previous smithsonite generations (Sm1 and Sm2). The $\delta^{13}\text{C}$ and $\delta^{18}\text{O}$ values of the supergene calcite veins (FF Cal) are 0.7 and -7.4‰ VPDB, and around 24.7‰ VSMOW, respectively (Table 5.9; Fig. 5.14).

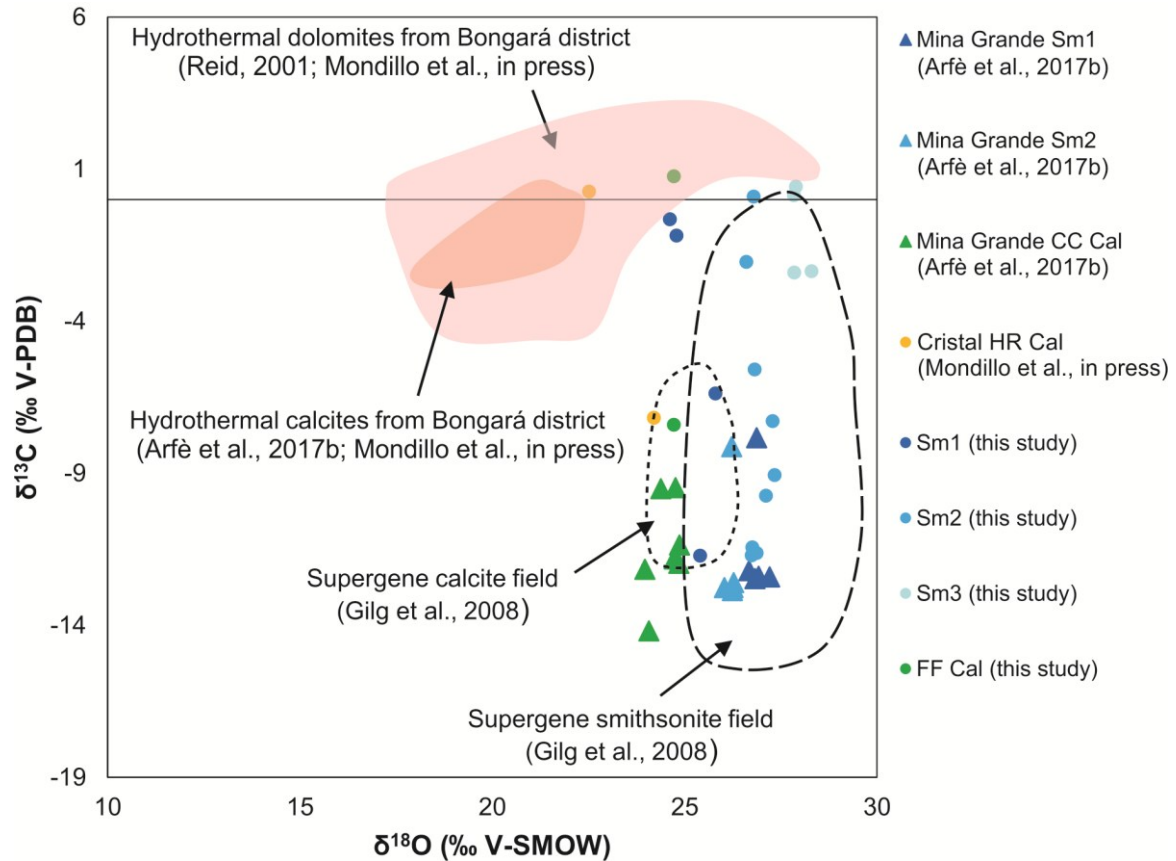


Figure 5.14. $\delta^{13}\text{C}$ and $\delta^{18}\text{O}$ values of supergene carbonate minerals at Cristal, and comparison with published isotope values of supergene smithsonites and calcites (Supergene smithsonite and calcite fields; Gilg et al., 2008), and of hydrothermal dolomites and calcites from the Bongará district (data from Reid 2001; Arfè et al., 2017b; Mondillo et al., in press). Mina Grande Sm1 = host-rock replacive smithsonite of Mina Grande oxidation stage I (Arfè et al., 2017b); Mina Grande Sm2 = concretionary smithsonite of Mina Grande oxidation stage II (Arfè et al., 2017b). Mina Grande CC Cal = Mina Grande concretionary calcite; Cristal HR Cal = weathered limestone of the Condorsinga Formation (Mondillo et al., in press); Sm1 = Cristal sulfide-replacive smithsonite; Sm2 = Cristal dolomite-replacive smithsonite; Sm3 = Cristal late smithsonite veins and concretions; FF Cal = fracture-filling calcite paragenetically associated with Sm3.

The $\delta^{13}\text{C}$ and $\delta^{18}\text{O}$ compositions of the supergene carbonate minerals (Table 5.9) vary with the host lithologies and in presence of texturally different mineral generations, but they do not show appreciable variations between the different macro-textures (e.g cements of breccias or massive bodies). Different $\delta^{13}\text{C}$ values of texturally comparable calcites and smithsonites are associated with different host rocks. The most negative $\delta^{13}\text{C}$ values of smithsonite (-11.7‰ VPDB) and calcite (-7.4‰ VPDB) have been measured into the specimens sampled in the siltstones and sandstones of the CR-07-08 drill core, whereas the most positive $\delta^{13}\text{C}$ values (0.7 and 0.1‰ VPDB for calcite and smithsonite,

respectively) have been detected into specimens from dolomite-rich layers of CR-18-08 and CR-13-08 drill cores.

$\delta^{13}\text{C}$ variations are not significant among the different mineral generations, but smithsonite is characterized by $\delta^{18}\text{O}$ values becoming progressively higher from the early to the late generations (Figure 5.15A). Additionally, the sulfide- and dolomite-replacive smithsonite generations (Sm1 and Sm2) show a clear variation of the $\delta^{18}\text{O}$ values within the mineralized body: the $\delta^{18}\text{O}$ values of smithsonite in the center of the body are higher than those measured at the lower and upper boundaries with the host rock, and are roughly positively correlated to the smithsonite abundances (Figures 5.15A and B).

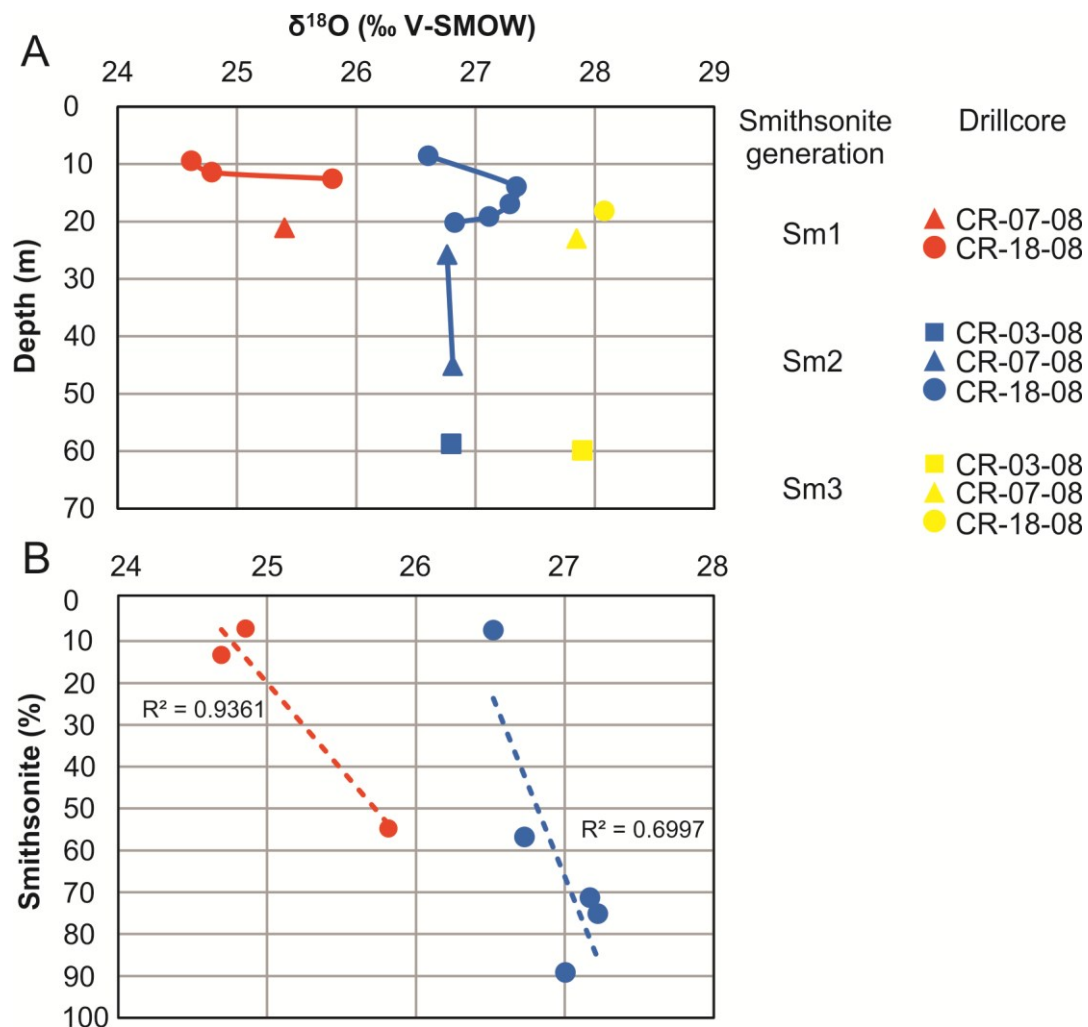


Figure 5.15. (A) $\delta^{18}\text{O}$ variation with depth of the texturally different smithsonite generations in the CR-03-08, CR-07-08 and CR-18-08 drill cores. (B) Correlation between $\delta^{18}\text{O}$ values and the abundance of replacive smithsonite generations (Sm1 and Sm2) in the stratabound smithsonite body visible in the CR-18-08 drill core .

The offset in the mean $\delta^{18}\text{O}$ values (3.3‰) between the youngest smithsonite generation (Sm3) and supergene calcite (FF Cal) indicates that the two minerals co-precipitated at an average temperature of $\sim 20^\circ\text{C}$ from a fluid with a $\delta^{18}\text{O}$ value around -5.1‰ VSMOW (Fig. 5.16).

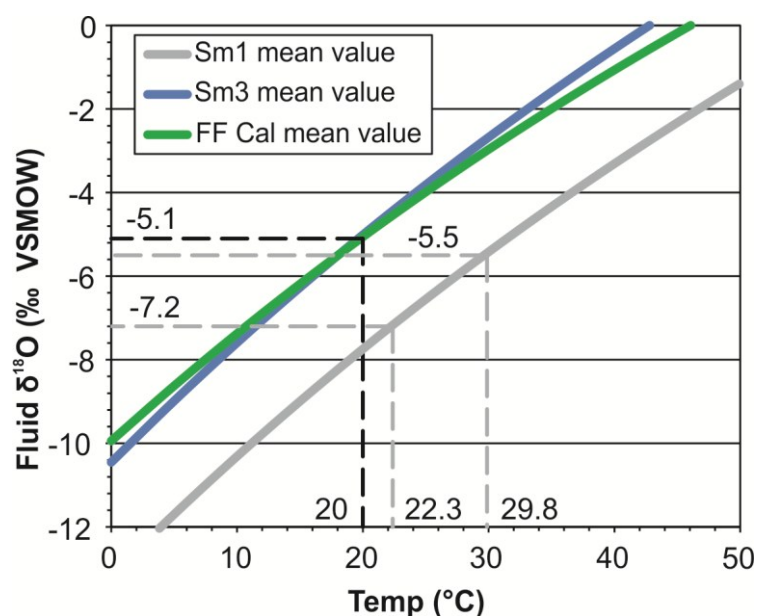


Figure 5.16. Oxygen isotope equilibrium curves for Cristal Sm1 and Sm3 smithsonites, and calcite (FF Cal), after smithsonite- and calcite-water fractionation factors of Gilg et al. (2008) and of O’Neil et al. (1969), respectively. The diagram shows the average precipitation temperature (29.8°C) and fluid composition (-7.2‰ VSMOW), calculated for early (Sm1) smithsonite, if the latter was precipitated either under the same temperature (22°C) or the same kind of fluid ($\delta^{18}\text{O} = -5.5\text{‰ VSMOW}$) of Mina Grande Sm1 smithsonite, and the intersection point ($T_{\text{fluid}} \sim 20^\circ\text{C}$ and $\delta^{18}\text{O}_{\text{fluid}} = -5.1\text{‰ VSMOW}$) of the Sm3 and FF Cal curves. Such intersection indicates that the two minerals co-precipitated in the supergene realm under the above conditions.

Discussion

Evolution from the hypogene sulfide mineralization to the “direct” and “wall rock” replacement supergene ores

The Cristal Zn nonsulfide mineralization postdates the deposition of the hypogene sulfides. The Zn nonsulfides occur in the upper parts of the Condorsinga Formation (Brophy, 2012), as two different types of mineralization consisting of smithsonite- and hemimorphite-rich assemblages, in which goethite is ubiquitous and appears locally concentrated in gossanous horizons. Both mineralization types mainly occur as manto-like bodies, mostly replacing the preexisting sulfides and the dolomite host rock (e.g. CR-18-08 and CR-13-07 drill cores), and/or as open-space filling (e.g. CR-18-08, CR-07-08 and CR-03-08). Locally, smithsonite-rich bodies are also hosted in brecciated horizons (e.g. CR-07-08 and CR-03-08 drill cores), where the ore distribution is controlled by fractures and by inherited karst cavities of Lower to Middle Jurassic age (Brophy, 2012). The latter style of mineralization is similar to both the Florida Canyon (SRK Consulting, 2014) and Mina Grande (Arfè et al., 2017b) deposits nearby, which, also present Zn nonsulfide orebodies filling karst cavities of tertiary age (i.e. formed contemporaneously to the mineralization), that are absent at Cristal.

The supergene mineral paragenesis at Cristal, comprising sulfide and nonsulfide minerals is shown in Figure 5.17. Smithsonite and hemimorphite occur as paragenetically distinct generations that replace hypogene sulfides in veins (first generations), saddle dolomite in the host rock (second generations), and as late veins cutting the previously precipitated phases (third generations).

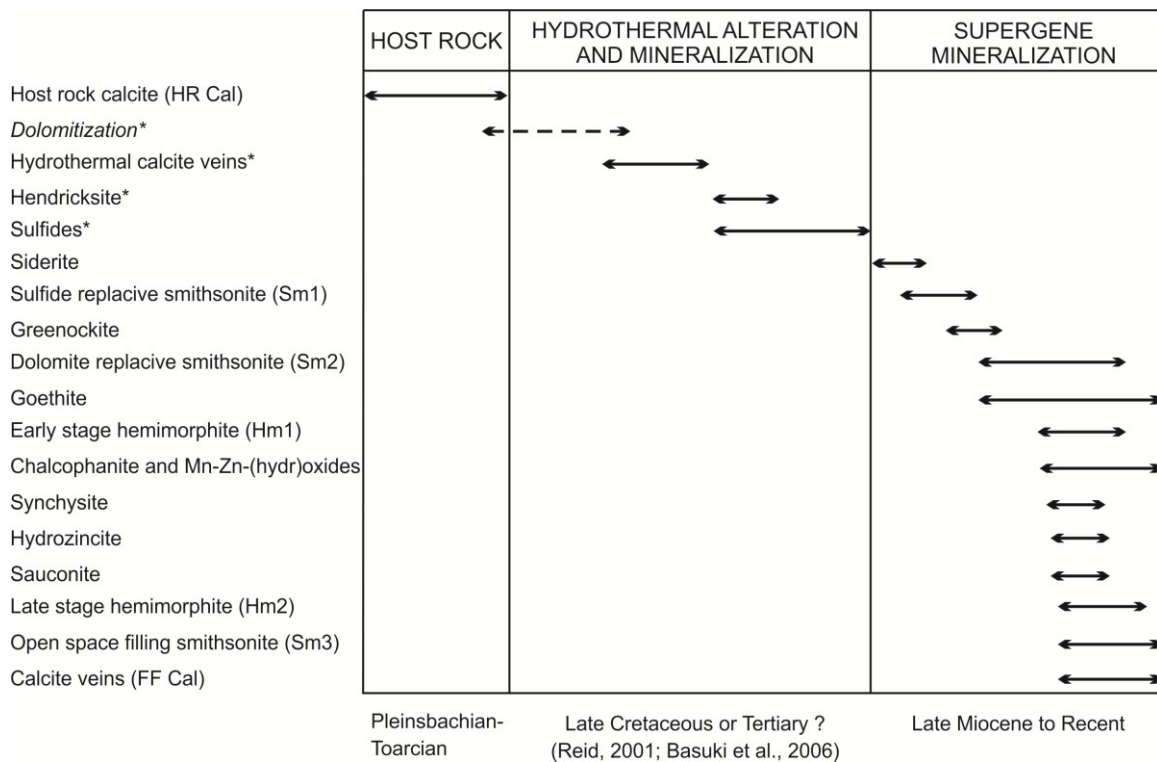


Figure 5.17. Paragenesis and timing of hydrothermal (* data from Mondillo et al., in press) and supergene minerals in the Cristal mineralization. Sm1 = smithsonite of stage 1 replacing sulfides; Sm2 = smithsonite of stage 2 replacing host rock dolomite; Sm3 = late smithsonite veins and concretions of oxidation stage 3; Hm1 = hemimorphite replacing smithsonite of the second oxidation stage; Hm2 = late hemimorphite veins occurring together with late smithsonite and calcite (FF Cal) veins of the oxidation stage 3.

At Cristal Sm1 seems to be paragenetically preceded by siderite, which occurs either in veins or as tiny patches in smithsonite, suggesting that this Fe-carbonate had a supergene origin. This would reflect Eh variations from slightly reducing to oxidizing conditions of the supergene solutions (McSween et al., 2004) during the initial stages of sulfide weathering in the Cristal area. The reducing conditions necessary for siderite precipitation in a supergene environment can be produced by microbial activity in subsurface sediments, or by local oscillation of the water table in association with seasonal climatic changes or tectonic activity (Mortimer et al., 1997; Zhang et al., 2001; Roh et al., 2003). Even though in other mineralized areas of the Bongará district, a siderite texturally similar to the Cristal ones was interpreted as a product of late hydrothermal processes acting after sulfides emplacement (Basuki et al., 2008), the presence of the supergene sulfide greenockite (occurring as crusts coating sphalerite) is another indicator of a transition from reducing to oxidizing conditions during the initial stages of sulfide

alteration. In the nearby Mina Grande deposit the Cd-carbonate otavite is common, whereas greenockite has not been detected (Arfè et al., 2017b). This difference is probably due to the less oxidizing and alkaline weathering conditions that were present at Cristal during initial supergene mineral precipitation, which favored greenockite stability over otavite. Under poorly acidic to near neutral pH, coupled with slightly reducing to oxidizing environmental conditions, smithsonite can coexist with greenockite (Takahashi, 1960).

The formation of either preferentially hemimorphite-rich or smithsonite-bearing bodies is commonly controlled by several factors that include: the presence of original sulfides, the host rock lithology, the water/rock ratio, and the depth of emplacement. Acidic solutions deriving from sulfide oxidation can contain high amounts of dissolved metallic (Cd^{2+} , Mn^{2+} , Zn^{2+} , Pb^{2+} , and Fe^{2+}) and bicarbonate (HCO_3^-) ions. If the buffering effect of the carbonate rocks prevails in the system, carbonate and bicarbonate may react and bond with the metallic cations, triggering the precipitation of an ample suite of supergene carbonate minerals (Takahashi, 1960; Sangameshwar and Barnes, 1983; Hitzman et al., 2003; Reichert and Borg, 2008). If the buffering effect is produced by silica-rich host rocks, or if silica is present in the solutions, hemimorphite or Zn-bearing clay minerals prevail in the supergene assemblage (Hitzman et al., 2003). Fractures and other types of secondary porosity, in presence of water-unsaturated conditions, create a dynamic “open” hydrogeological system (Borg, 2015). In an open system, the meteoric solutions are able to equilibrate continuously with the atmosphere, and thus the physical conditions that control chemical equilibrium of the typical reaction $\text{CaCO}_3 + \text{H}_2\text{CO}_3$ (deposition) \leftrightarrow $\text{Ca}^{2+} + 2\text{HCO}_3^-$ (weathering) are mostly related to the amounts of CO_2 dissolved in the fluid (Reichert and Borg, 2008 and references therein). The consumption of great quantities of $\text{CO}_{2(g)}$ derived from the dissolution of host rock carbonates (e.g. dolomite) can be rapidly supplied by $\text{CO}_{2(g)}$ from the overlying soil and/or atmosphere (Palmer and Palmer, 1995). This continuous process results in relatively constant amounts of dissolved CO_2 (as H_2CO_3) in the aqueous solutions, which thus maintain a quite stable pH. This condition would favor the precipitation of minerals stable at more neutral to acidic conditions (e.g. smithsonite rather than hydrozincite; Sangameshwar and Barnes, 1983). Water-saturated environments and/or deep supergene alteration favor the achievement and maintenance of high $\text{CO}_{2(g)}$ levels, enabling smithsonite precipitation and preservation. Under water-undersaturated and/or near-surface conditions, characterized by $P_{\text{CO}_{2(g)}}$ rebalance to atmospheric values ($\log f_{\text{CO}_{2(\text{gas})}} = -3.5$), the $P_{\text{CO}_{2(g)}}$ values in the meteoric solutions are low and hydroxy-carbonate minerals (e.g. hydrozincite) and/or Zn-bearing hydrosilicates (e.g. hemimorphite) can rapidly replace smithsonite precipitated during earlier oxidation stages (Brugger et al., 2003; Hitzman et al., 2003; McPhail et al., 2003; Reichert and Borg, 2008; Reichert, 2009).

In the Cristal case, the smithsonite-rich horizons occurring at different depths in the drill cores within dolomite host rock are always associated with sulfide remnants or pseudomorphic textures inherited from the original sulfides (i.e. cubic goethite formed as direct alteration of pyrite). This fact would suggest that metal-bearing solutions did not migrate so much from the original source of metals (i.e. the sulfide bodies), probably

because the acidic solutions mostly deriving from pyrite alteration were immediately buffered by the dolomite host rock. This reaction favored the formation of smithsonite for direct replacement of sulfides and the only local replacement of the dolomite host rock. The $\delta^{13}\text{C}$ composition of all smithsonite generations clearly indicates a mixed contribution of both isotopically heavy (from carbonate host rocks; Fig. 5.14), and isotopically light (from organic matter and soils) carbon. This compositional variation in $\delta^{13}\text{C}$ values of the Cristal supergene carbonates is consistent with sulfide oxidation processes occurring in an “open-system”, characterized by a continuous supply of new oxidized organic soil and wall rock carbon into the meteoric solutions (Gilg et al., 2008). It is interesting to observe that Sm1, Sm2 and Sm3 smithsonites hosted in dolomite show a greater contribution from an isotopically heavy carbon source, identifiable with the dolomite host rock, than from a light source, indicating the presence of organic carbon, possibly suggesting that the buffering effect of the host rock had a greater impact than the oxidation of organic matter in supplying carbonate for smithsonite precipitation. An exception to this model can be observed in the siltstones-hosted smithsonite of the CR-07-08 drill core, which shows the most negative smithsonite $\delta^{13}\text{C}$ values measured in the Cristal prospect, clearly indicating that most of the carbonate of this smithsonite derived from the oxidation of soil-derived organic carbon (Gilg et al., 2008). This “anomaly” was probably due to the absence of dolomite and to the presence of neutral to basic conditions unfavorable to hemimorphite precipitation, which only allowed Zn to precipitate as smithsonite utilizing the organic carbon occurring in the solution. However, in agreement with the models reported in the literature and cited before (e.g. Hitzman et al., 2003), hemimorphite-rich bodies at Cristal commonly occur in siltstones and sandstones interbedded with the dolomite, and also contain Zn-clays, obviously suggesting that hemimorphite formed in the more silica-rich lithologies.

Looking at the $\delta^{18}\text{O}$ compositions of smithsonite occurring in the Cristal stratabound/manto-type bodies, it is possible to observe that the smithsonite $\delta^{18}\text{O}$ values increase from the boundaries to the core zones of the mineralized layers (Fig. 5.15A). This trend may reflect a smithsonite-precipitating fluid with $\delta^{18}\text{O}$ compositions progressively buffered through water-rock exchange with the saddle dolomite host. However, maximum difference in $\delta^{18}\text{O}$ between these zones is 0.7‰ VSMOW permil, and thus not really large to clearly support this process. Additionally, the correlation of $\delta^{18}\text{O}$ and smithsonite percentage (or abundance; Fig. 5.15B) suggests a mixing of another end-member, which is probably represented by dolomite and/or goethite occurring as micro-inclusions in less pure smithsonite grains of the outer zones.

During the emplacement of the generations of replacive smithsonite and hemimorphite, Zn^{2+} and Mg^{2+} cations from the supergene solutions underwent a partial interchange in the lattices of Fe-dolomite and smithsonite: the results of this process are Mg-rich smithsonites and slightly Zn-bearing dolomites. At the same time, the partial dissolution of the Zn-Mn-bearing micas and of the host dolomite (which contains up to 1 wt.% Mn), may have produced an increase in the Mn^{2+} content in circulating groundwaters, thus favoring the precipitation of the Mn-(hydr)oxide chalcophanite that is commonly associated with smithsonite. In the Mina Grande deposit the most abundant Mn-

(hydr)oxide is ranciéite (Arfè et al., 2017b). The presence of ranciéite rather than chalcophanite generally depends on the level of supergene oxidation (Nimfopoulos et al., 1997). More specifically, the precipitation of ranciéite starts under continuous percolation of Ca-saturated and Zn-bearing meteoric solutions after a progressive acid dissolution of other Mn-(hydr)oxides (e.g. chalcophanite), which were formed during earlier stages of the oxidation process. The equilibration of the acid solution with the carbonate host rocks and the consequent increase in pH toward neutral values can favor ranciéite precipitation. Therefore, the presence of ranciéite indicates that the Mina Grande deposit was subjected to a deeper and more prolonged weathering process than the Cristal occurrence.

Hydrozincite, which is a typical mineral of the post-oxidation stage (*sensu* Reichert and Borg, 2008), is relatively scarce at Cristal, but it is extremely abundant in the nearby Mina Grande deposit (Arfè et al., 2017b), where it is related to the high runoff rate through the karst network. This resulted in a downward migration of the supergene front, with accumulation of smithsonite in the deepest levels of the profile and the formation of hydrozincite in near-surface horizons. Therefore, the absence of hydrozincite at Cristal may suggest that in this area, the nonsulfide concentrations were not affected by further significant alteration during the post-oxidation stages.

Mondillo et al. (2018) have shown that both hemimorphite and goethite at Cristal host discrete amounts of Ge (50-200 ppm), which could have been incorporated in these minerals at 25°C and a pH between 5 and ~9. As reported in Arfè et al. (2017b), Ge does not occur at Mina Grande. Considering that the comparison between the mineralogy of the two nonsulfide mineralizations suggests that the weathering conditions were more alkaline at Mina Grande than at Cristal, it is possible that Ge was completely leached from the Mina Grande ore during supergene alteration. In fact, the high hydrozincite amounts in the Mina Grande deposit indicate that the percolating meteoric solutions were characterized by pH values >9, which allow Ge remaining in solution and to be dispersed in the environment (Mondillo et al., 2018).

The presence of supergene REE-bearing minerals (i.e. synchysite and Y-sulfophosphate) within the smithsonite- and goethite-rich mineralization should not be considered unusual, because they are probably derived from the alteration of detrital apatite, monazite and xenotime occurring within the siliciclastic lithologies of the host Condorsinga Formation.

Genesis and timing of the Cristal supergene nonsulfide mineralization

The three generations of smithsonite (Sm1, Sm2 and Sm3; Fig. 5.14) detected at Cristal differ in their oxygen isotope compositions, and specifically the diverse smithsonite generations have $\delta^{18}\text{O}$ compositions increasing from the oldest (Sm1) generation to the youngest (Sm3) (Fig. 5.14), which is opposite to the $\delta^{18}\text{O}$ decreasing trend observed in the smithsonites from the Mina Grande deposit (Arfè et al., 2017b). This fact may be indicative of distinct oxidizing events.

During middle Miocene, the western Amazonia foreland basin was located close to the equator (Scotese, 2001) and the climate was characterized by low annual variations of surface air temperature, which is a condition not very different from the current one. In

the Bongará area, the average annual temperatures between 1,000 and 2,000 m.a.s.l. are between 23° and 25°C, whereas at an altitude between 2,000 and 3,600 m.a.s.l. they are between ~16 and 18°C (Anglo Peruana, 2005). Arfè et al. (2017b) postulated that the earliest smithsonite generation in the Mina Grande deposit (in this text called “MG Sm1”) was precipitated during the Middle Miocene-Early Pliocene uplift, in association with the switch from the “Pebas” to “Acre” mega-wetland ecosystems (~ 10 Ma; Hoorn et al., 2010), when the joint activities of uplift and erosional processes were able to bring the sulfide bodies of the Bongará district to near-surface conditions (Figs. 5.18A, B and C). The same authors also affirmed that MG Sm1 precipitated from a fluid with $\delta^{18}\text{O}$ values around -5.5‰ VSMOW, at a temperature of 22.3°C, when this area had an altitude of 1050 m.a.s.l. These conditions ($\delta^{18}\text{O}_{\text{fluid}} = -5.5\text{‰ VSMOW}$, temperature = 22 °C) are incompatible with the precipitation of Cristal first smithsonite generation (Sm1 $\delta^{18}\text{O} = 25.1\text{‰ VSMOW}$), which might have instead precipitated either at the above-mentioned temperature from a fluid with a $\delta^{18}\text{O}$ value of -7.2‰ VSMOW, or from a fluid with a composition of -5.5‰ VSMOW at a temperature of 29.8°C (Fig. 5.16). The 29.8°C temperature is too high for being considered reliable (see Arfè et al., 2017b). On the contrary, the -7.2‰ VSMOW fluid value is consistent with the $\delta^{18}\text{O}$ reconstruction of the surface waters (Pebas; -7 and -8‰ VSMOW) from the Miocene mollusc shells in western Amazonas (Vonhof et al., 1998). Taking into account that the first smithsonite generation (Sm1) at Cristal follows in the paragenesis the deposition of the supergene siderite pointing to local reducing conditions (i.e. water-saturated and low dynamic environment), it is possible that Cristal Sm1 was precipitated in a hydrogeological setting different from the MG Sm1, for example between 10 and 7 Ma, during the interval between the low dynamic Pebas and the high dynamic Acre periods (Fig. 5.18C), before the disappearance of these mega-wetlands in Northwestern Amazonia at ~7 Ma (Hoorn et al., 2010). In other words, from our observations, it seems that the first smithsonite generation at Cristal (Sm1) formed between 10 and 7 Ma at temperatures around 22.3°C from a fluid with $\delta^{18}\text{O}$ values similar to those of the waters that characterized the Pebas ecosystem, whereas the first generation at Mina Grande (MG Sm1) formed later, probably after ~7 Ma. This interpretation might be reliable assuming that the Cristal and Mina Grande sulfide protores occurred at the same depth below the base of the Sarayaquillo Formation (Figs. 5.18A or B), and that the zone containing the Cristal sulfide body was uplifted, and consequently weathered, before the area where the Mina Grande orebody was located (Fig. 5.18C).

From 7 to 5-4 Ma (Fig. 5.18D), the Bongará region was subjected to the Quechua II pulse of the major Andean tectonic phases (8-7 Ma; Klein et al., 2010), and underwent the Middle Miocene-Early Pliocene uplift, which produced a further increase of 150 m in altitude (Gregory-Wodzicki, 2000). This uplift resulted in a strong uncapping of the residual rock cover, and subsequently in the formation of the first generation of smithsonite at Mina Grande (MG Sm1) (Arfè et al., 2017b). The similar mean $\delta^{18}\text{O}$ values (26.9‰ VSMOW), measured in the MG Sm1 and in the second generation of Zn carbonates (Sm2) at Cristal, which result in a calculated fluid temperature of 22° C, and a

fluid $\delta^{18}\text{O}$ of -5.5‰ VSMOW, strongly suggest that MG Sm1 and Cristal Sm2 formed at the same time, under the same hydrological conditions and roughly at the same altitude.

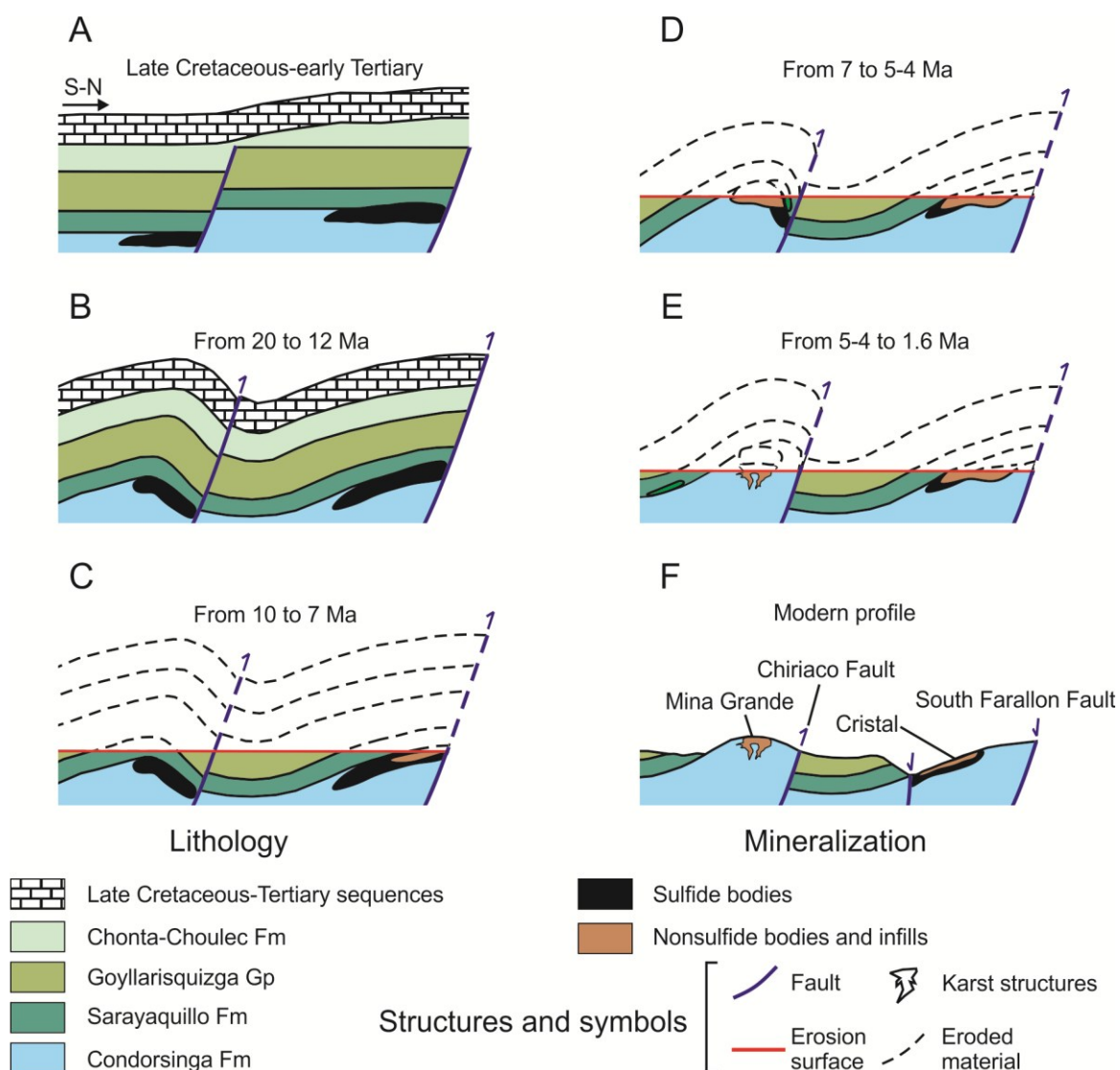


Figure 5.18. History of the oxidation stages of Cristal hypogene ore by comparison with those occurring in the nearby Mina Grande deposit (Stage I = Mina Grande Sm1 and Stage II = Mina Grande Sm2; Arfè et al., 2017b). A. Sulfide bodies were emplaced during late Cretaceous-early Tertiary. B. Sulfide bodies were deformed during the early stages of Miocene Quechua Phase. C. Cristal sulfide protore was brought to near-surface conditions earlier than the Mina Grande one, this resulting in the formation of the first smithsonite generation (Sm1) at Cristal, from fluids with $\delta^{18}\text{O}$ composition (-7.2‰ VSMOW) similar to those characterized the megawetlands ecosystem. D. Megawetlands disappeared and Mina Grande sulfide protore was brought to near-surface conditions, resulting in the formation of Mina Grande Sm1 smithsonite and subsurface precipitation of the second smithsonite generation (Sm2) at Cristal under the same hydrological and topographic conditions. E. The last smithsonite generation (Sm3) at Cristal formed in the earliest stages of the Pliocene-early Pleistocene uplift, before the onset of the Mina Grande Sm2 precipitation. F. The undisturbed presence of the Sarayaquillo and Goyllarisquiza Formations in the southern flank of the modern profile of the Cristal valley also supports the different weathering processes that occurred in the two areas.

The last two tectonic pulses (Quechua III and IV), dated at 5-4 and 2-1.6 Ma respectively (Fig. 5.18E) and the increasing uplift rates (up to 3 mm/yr) caused an enhanced weathering activity in the entire Bongará area. At Mina Grande, the weathering processes produced a renewed oxidation phase that intensified the karst development, and resulted in the formation of concretionary calcite followed by a late generation of smithsonite (called in this text “MG Sm2”; Arfè et al., 2017b). At Cristal and surroundings, there is no clear evidence of a strong karstic activity; therefore, it is likely that the Cristal area was less uplifted than Mina Grande (e.g. the Chiriaco fault was more active than the Farallon fault system). This difference in the weathering processes is also well supported by geological evidence, such as the undisturbed presence of the Sarayaquillo and Goyllarisquiza Formations in the southern flank of the Rio Cristal valley, and the absence of both formations in the Mina Grande anticline (Fig. 5.18F). It is therefore likely that the Cristal area remained for longer time under conditions that caused the subsurface precipitation of the second smithsonite generation (Sm2).

In the Cristal mineralization, the youngest smithsonite generation (Sm3) and supergene calcite (FF Cal) co-precipitated at an average temperature of ~20°C from a fluid with a $\delta^{18}\text{O}$ value around -5.1‰ VSMOW (Fig. 5.16), under the same conditions as the supergene concretionary calcite in the Mina Grande deposit (MG CC Cal; 24.5‰ VSMOW; Arfè et al., 2017b).

Conclusions

The Bongará district, where both the Cristal and Mina Grande mineral occurrences are located, experienced a prolonged phase of weathering lasting from Miocene to Recent under humid tropical climatic conditions. Under such a prolonged climate setting, weathering processes in this area involved many pre-existing sulfide bodies (e.g. Cristal, Florida Canyon, Mina Grande etc.), where supergene profiles have been developed under locally different conditions. The mineralogy of the nonsulfide bodies was mainly controlled by two factors at the local scale: (1) uplift rates, and (2) host rock lithology. Uplift is mainly controlled by the activity of local faults, which in the Bongará area allowed the exposure of the sulfide protorees at different altitudes in distinct time periods. Altitude in a tropical weathering regime is a fundamental factor for the development of supergene profiles, since in humid tropical uplands the runoff rate varies significantly with the increase of the average altitude. For this reason, sulfide weathering in the Mina Grande and Cristal areas, which were affected by different uplift rates, started under similar conditions but evolved in distinctive ways due to the local availability of water. The greater availability of water at Mina Grande than at Cristal resulted in deeper weathering of the Mina Grande sulfide progenitors and in the formation of a well-developed karst system. At Cristal the karst development was suppressed by the “limited” uplift rate, and supergene alteration did not obliterate the roots of the original sulfide body, which are still in place.

The type of host lithology (e.g. limestone vs. dolostone), the possibility to have sulfide-rich horizons and a continuous recharge of fresh water determined the buffering of the

acid metal-carrying solutions, and triggered the precipitation of a suite of supergene minerals. At Cristal, these local scale factors resulted in the formation of hemimorphite- and smithsonite-rich mineralizations that may locally result in continuous mineralized bodies of prospective economic interest.

Chapter 6:

Identification of Zn-bearing micas and clays from the Cristal and Mina Grande - Bongará zinc deposits (Amazonas region, northern Peru)

Published in “Minerals”

Reference: Arfè G., Mondillo, N., Balassone G., Boni, M., Cappelletti, P., Di Palma, T., 2017. Identification of Zn-bearing micas and clays from the Cristal and Mina Grande - Bongará zinc deposits (Amazonas region, northern Peru). Minerals, 7, 214; DOI: 10.3390/min7110214.

Introduction

The Zn-nonsulfide deposits have been genetically associated to both hypogene (hydrothermal) and supergene (weathering) processes (Hitzman et al., 2003; Boni and Mondillo, 2015; Borg, 2015). The geological setting, the nature of the protore and climate are the main controls on the genesis and mineral association of supergene deposits. The most common mineral phases in the Zn-nonsulfide deposits are smithsonite, hydrozincite, hemimorphite and sauconite, with local cerussite and anglesite occurrences (Hitzman et al., 2003). Minor components can be represented by phosphates, vanadates and Fe-oxy-hydroxides. Zinc-rich clay minerals are seldom the prevailing economic species in nonsulfide ores, with the exception of the peculiar case of the Skorpion deposit in Namibia (Borg et al., 2003; Kärner, 2006). In fact, their presence is commonly considered a disadvantage in the first steps of mineral processing (Connelly, 2011; Lim, 2011). The particle size and fabric of minerals belonging to smectite and vermiculite groups can be a problem during gravity separation and flotation processing (Boni et al., 2009b; Rollinson et al., 2011; Kademli and Gulsoy, 2012). This generally results in a slower flotation kinetics (Bayraktar et al., 1998; Fuerstenau et al., 2007) and detrimental effects on the leaching techniques, due to “undesired” increments of pulp viscosity. Therefore, to understand the nature of clays occurring in the paragenesis of nonsulfide ores is a crucial issue, when planning the right workflow and mineral processing procedure, in order to avoid any loss during base and critical metal extraction and recovery. Huge steps forward in the field of nonsulfide exploitation and recovery have been done since the discovery of the Skorpion deposit, where the main nonsulfide mineral is represented by sauconite (Zn-smectite). In the above deposit, the solvent extraction technique (Gnoinski, 2007), coupled with several electrowinning and leaching steps (de Wet and Singleton, 2008; Abkhoshk et al., 2014) was applied to overcome the mentioned processing issues, and maximize the zinc recovery.

Even though the nature of clays is crucial information for the mining industry dealing with nonsulfide deposits, the knowledge of the genesis of such minerals is also an interesting issue from the scientific point of view. Zn-smectite (e.g. sauconite) is

commonly related to the hydrolysis of aluminosilicate minerals, as micas and feldspars (Borg et al., 2003; Kärner, 2006) under meteoric conditions ($T = 20\text{--}25^{\circ}\text{C}$ and atmospheric pressure; Tiller and Pickering, 1974; Harder, 1977) and at neutral pH or nearly below 7 in prevailingly arid climate settings (Kittrick, 1969; Sherman et al., 2001). However, experimental studies on the synthesis and stability of sauconite (Roy and Mumpton, 1956; Klopogge et al., 1999; Higashi et al., 2002; Petit et al., 2008; Pascua et al., 2010) revealed that it can also form at $T = 200^{\circ}\text{C}$ and pH up to 12. Kaolinite, usually formed under tropical climates, acidic conditions and high water/rock ratios (Garrels and Christ, 1990; Sherman et al., 2001), is rare in nonsulfide deposits. Less uncommon, instead, is fraipontite that is a mineral belonging to the kaolinite-serpentine group (Coppola et al., 2008; Choulet et al., 2016). Fraipontite can be hydrothermal in origin, as in the case of the Preguiça mine in southern Portugal (Will et al. 2014), or associated with late stages of the supergene evolution (Coppola et al., 2008; Choulet et al., 2016). Since neither the kaolinite-serpentine minerals, nor the clays belonging to the smectite group are really useful in discriminating between supergene or hydrothermal origin, in several studies (Choulet et al., 2016; Mondillo et al., 2015; Buatier et al., 2016; Balassone et al., 2017) where a clear identification of the Zn-bearing clay minerals has been provided, several doubts still remain on their formation. On the contrary, the Zn- and Mn-bearing micas may be a precious source of genetic information for nonsulfide Zn deposits, because they commonly form through hydrothermal processes at high temperatures ($>150^{\circ}\text{C}$). In fact, the synthesis of Mn-bearing micas has been achieved only under hydrothermal conditions at temperature around 200°C (Choi et al., 2009). In magmatic and metamorphic environments, zincian trioctahedral micas (Zn-Mn-bearing fluorophlogopite, hendricksite) are seldom observed and, when present, indicate skarn conditions and/or low $f\text{S}_2$, high $f\text{O}_2$, high alkalinity and high volatiles content in their parental magma (Sharygin, 2015 and references therein).

The main aim of this study is to identify the Zn-bearing phyllosilicates occurring in the Mina Grande and Cristal sulfide and nonsulfide deposits, located in the Bongará area, belonging to the Subandean fold and thrust belt of northern Peru (Fig. 6.1). Sulfide minerals are mostly represented by sphalerite and less pyrite that have been weathered to a nonsulfide assemblage, consisting of goethite, smithsonite, hemimorphite, and hydrozincite. Minor amounts of various Zn-bearing phyllosilicates were also identified in these deposits (Arfè et al., 2017b, in press), but no specific analyses on clay minerals have been carried out yet.

Geological setting

The Cristal and Mina Grande mineralizations are hosted by the sedimentary successions of the Pucará Group (Fig. 6.1), which lie on top of the continental sequences of the Mitu Group (Middle to Late Triassic; Rosas et al., 2007; Spikings et al., 2016), in turn overlying the Paleozoic metamorphic basement (i.e. the Marañon Complex; Reid, 2001; Mišković et al., 2009). The Pucará Group is subdivided in three prevailingly carbonate formations that from the stratigraphic base to the top are as follows (Fig. 6.1): (1) Upper

Triassic Chambará Formation, (2) Upper Triassic-Lower Jurassic Aramachay Formation, (3) Lower Jurassic Condorsinga Formation (Mégard, 1968; Szekely and Grose, 1972; Rosas and Fontboté, 1995; Rosas et al., 2007). The Chambará and Condorsinga Formations are dominated by shallow-water platform facies in contrast with the Aramachay Formation, which is deeper basinal. The Pucará successions are followed by continental sequences of the Sarayaquillo Formation (Upper Jurassic - Cretaceous; Mathalone and Montoya, 1995; Rosas, 2007; Fig. 6.1), and by the marine lithologies of the Lower Cretaceous Goyllarisquizga Group and the Chonta-Chulec Formation (INGEMMET, 1995). The study area was affected by Neogene tectonics, characterized by late Miocene and Pliocene-early Pleistocene uplift phases, corresponding to the Andean and Quechua tectonic pulses (Gregory-Wodzicki, 2000; Klein et al., 2011; Pfiffner and Gonzalez, 2013).

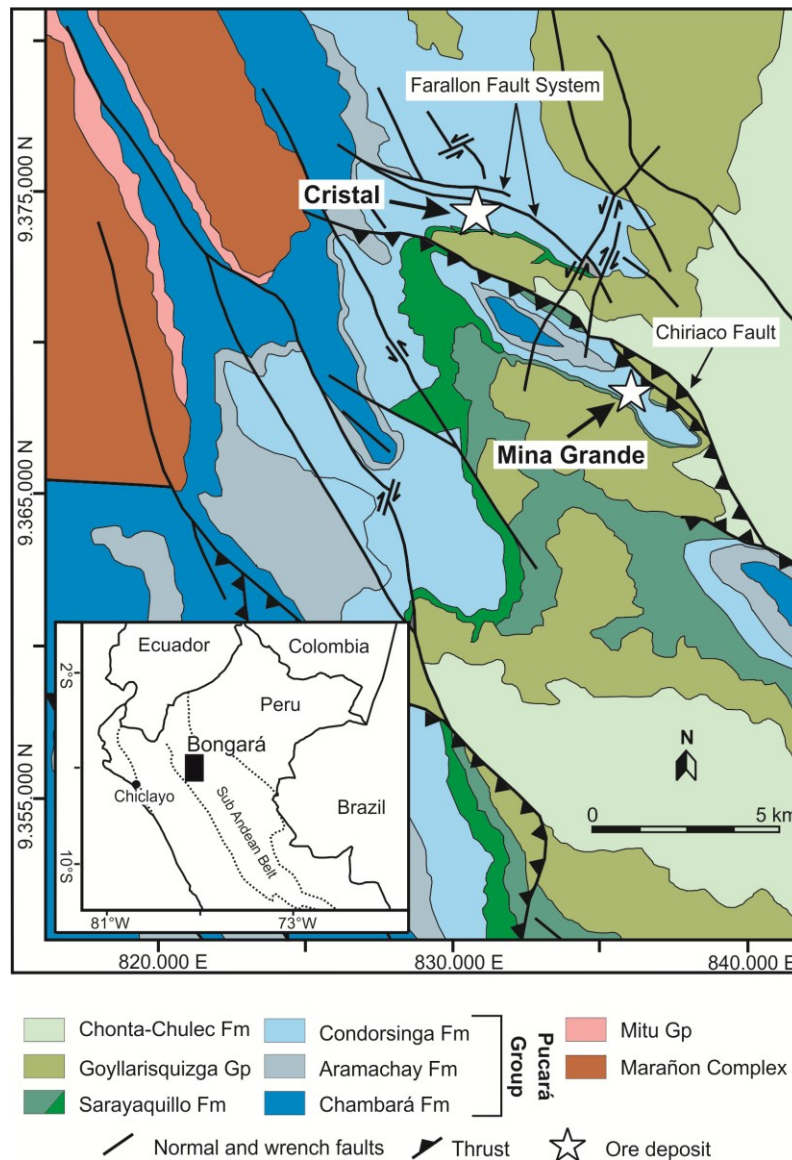


Figure 6.1. Location of the Bongará province within the Sub Andean Belt and geological map of the Mina Grande and Cristal areas (modified from Arfè et al. 2017b).

Cristal prospect

The Cristal prospect is located in a faulted block, bordered by the Chiriaco reverse fault and the South Farallon normal fault (Fig. 6.1). The zinc occurrences consist of both sulfide and nonsulfide bodies (Brophy, 2012; Mondillo et al., in press; Arfè et al., 2017b), discontinuously cropping out over an area of ca. 2 km². The mineralized bodies are mainly hosted by dolomitized limestone of the upper levels of the Condorsinga Formation, alternated with clayey horizons (Basuki et al., 2008; Basuki and Spooner, 2008, 2009; Brophy, 2012). Limestone is extensively karstified, with reworked carbonate material in form of layered infills to fossil solution cavities and cave systems. The clayey layers consist of quartz, feldspar, mica, and clays, associated with detrital monazite, xenotime and zircon. The bulk mineralogy of the drill core samples (Arfè et al., in press) is characterized by ubiquitous quartz and micas, which have been firstly classified as muscovite- and illite-type micas. The mineralogy of the sulfide bodies is relatively simple, and mostly consists of disseminated dark-brown and Fe-rich sphalerite (Mondillo et al., 2018, in press), with lesser amounts of pyrite and galena. The nonsulfide mineral association is quite complex, being represented by a wide suite of supergene minerals: smithsonite, hemimorphite, hydrozincite, chalcophanite, goethite and greenockite (Arfè et al., in press). Smithsonite prevails over hemimorphite with abundances that are between 10 and 70 wt.%, whereas hemimorphite ranges from 5 to 60 wt.%. Goethite has concentrations that vary between ~2 and ~35 wt.%. In addition, in the Cristal drill cores, sauconite (< 5 wt.%), as well as minor amounts of a Zn-Mn-bearing mica, tentatively identified as hendricksite, were also detected (Arfè et al., in press).

Mina Grande deposit

The Mina Grande deposit is located ~6 km south of Cristal, on top of an anticlinal ramp in the hangingwall of the Chiriaco reverse fault (Workman and Brede, 2016; Arfè et al., 2017b; Fig. 6.1). Compared to the Cristal deposit, the zinc occurrences at Mina Grande consist almost exclusively of Zn-oxidized minerals, whereas sulfides are very rare. The host rock of the nonsulfide mineralization is predominantly a limestone belonging to the upper levels of the Condorsinga Formation with intercalations of siliciclastic material: quartz and feldspar, with minor monazite, xenotime, and zircon (Arfè et al., 2017b). The nonsulfide mineralization occurs as accumulations in karst depressions and cavities, commonly in form of collapse breccias. The karst cavities developed during the Miocene-Pliocene Andean tectonics, along northwest-southeast fractures and faults and locally along stratification joints, and overprinted the Cretaceous karstified surface of the Condorsinga Formation. Nonsulfide association consists of hydrozincite, hemimorphite, smithsonite, and Fe-(hydr)oxides (Arfè et al., 2017b). In the samples analyzed for this study, hydrozincite (from 25 to 45 wt.%) prevails over hemimorphite and smithsonite (between 5 and 40 wt.%). At Mina Grande the Zn-phyllosilicate fraipontite was tentatively identified, commonly occurring as alteration rims around muscovite and other type of undetermined Zn-bearing micas (Arfè et al., 2017b).

Materials and methods

The analyses were conducted on 12 clay-rich samples from several drill cores of the Cristal prospect (CR02, CR03-3, CR03-4, CR07-9, CR07-11, CR07-13, CR07-14, CR13-5, CR13-6 and CR13-7) and on mineralized outcrop samples (ZB-1 and ZB-2) from the Mina Grande deposit (Fig. 6.2).

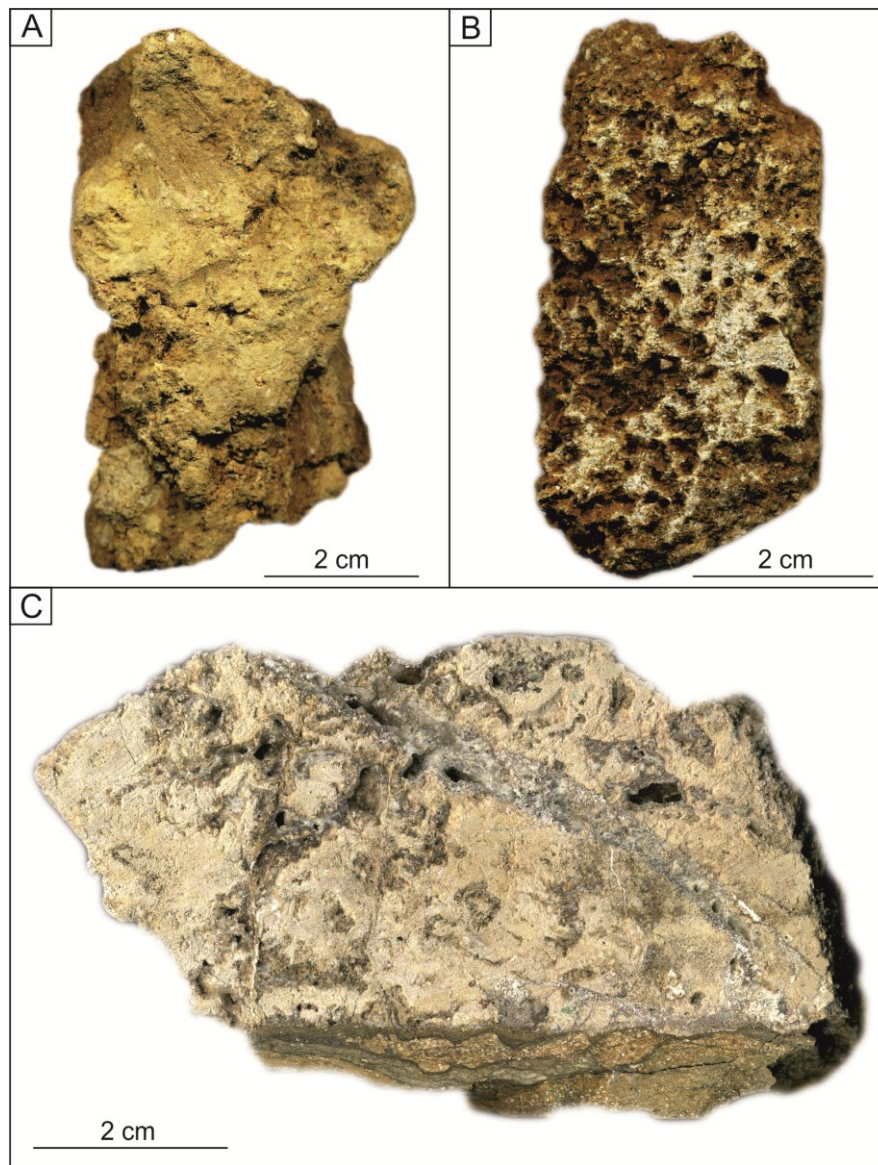


Figure 6.2. Examples of analyzed specimens from Cristal (A, CR07-14; B, CR13-7) and Mina Grande (C, ZB-2) deposits.

The samples were cut in small slabs for the preparation of polished thin sections used for optical microscopy (OM) and scanning electron microscopy with energy dispersive X-ray spectroscopy (SEM-EDS). SEM and backscattered electron (BSE) observations on thin sections were performed on a JEOL JSM5310 at DiSTAR (Department of Earth Sciences, Environment and Resources Sciences, Università di Napoli Federico II). The analytical

conditions were: 20 mm objective lens to specimen working distance, 15 kV accelerating voltage with a tilt angle of 0°. Analytical errors are 1% relative for major elements and 3% relative for minor elements. Element mapping and qualitative energy dispersive (EDS) investigations were carried out with the INCA X-stream pulse processor and the 4.08 version Inca software (Oxford Instruments detector), interfaced with the JEOL JSM 5310.

X-ray powder diffraction (XRPD) analyses on oriented clay aggregates were conducted on the clay fraction of 7 samples (CR02, CR07-11, CR07-13, CR07-14, CR13-7, ZB1 and ZB2). To obtain the clay fraction, according to the Moore and Reynolds (1997) procedure, the samples were milled and ground, and about 30 gr of grained material (grain size <1 mm) was blended with 500 ml of deionized water in a plastic beaker to be subjected to ultrasonic disaggregation for about 15 minutes. The <2 µm fraction was separated from the whole sample via four steps of progressive sedimentation (1 min, 5 min, 1 h and 17 h “overnight”), and two cycles of centrifugation with a Hettich Rotina centrifuge (5 min at 5000 rpm and 40 min at 8000 rpm). The final suspension resulted was too dilute and thus, for the preparation of oriented aggregates (mounts), we used the suspended material obtained after the first or the second cycle of centrifugation, depending on the quantity of material. This material was smeared on glass slides and left drying at ambient temperature (air-dried). The slides were firstly solvated with Ethylene-glycol (EG) at 80 °C for 24 h (Brunton, 1955) and then heated at 350°C for 2 h. Subsequently, the presence of kaolinite was investigated by heating the slides at 550°C for 1 h (Moore and Reynolds, 1997). XRPD analysis was performed on (i) the overnight residues of randomly oriented mounts (labelled “O/N”), (ii) air-dried oriented mounts (labelled “AON”), (iii) glycolated (EG) oriented samples (labelled “AOG”), and (iv) oriented samples heated at 350 and 550°C, respectively labelled as “AOR” or “AORR”. The XRPD analyses were carried out on a Seifert GE ID3003 diffractometer (DiSTAR), with CuKα radiation, Ni-filtered at 40 kV and 30 mA, 3-70° 2θ range, step scan 0.02°, time 10 s/step, and the RayfleX (GE) software package; a silicon wafer was used to check the instrumental settings.

In order to obtain morphologic SEM images of clayey material, representative chips (ca. 5 x 5 mm in dimension) were directly removed from the AON oriented aggregate slides and mounted on Agar stubs using Carbon conductive double-sided adhesive tape.

Results

XRPD analysis on oriented and randomly oriented mounts

Random XRPD patterns of the O/N overnight residues (Figs. 6.3A and B) show that, after the first three steps of progressive sedimentation, the samples still contain quartz, calcite, goethite, smithsonite, hydrozincite and hemimorphite, in addition to the layered silicates. The XRD patterns of the AON (air-dried) slides show that 10 Å-spaced phyllosilicates mainly occur in the samples CR02, CR07-11, CR07-13, CR07-14 and CR13-7, whereas 15 Å-spaced phyllosilicates are dominant in the samples CR07-14 and CR13-7 (Fig. 6.4).

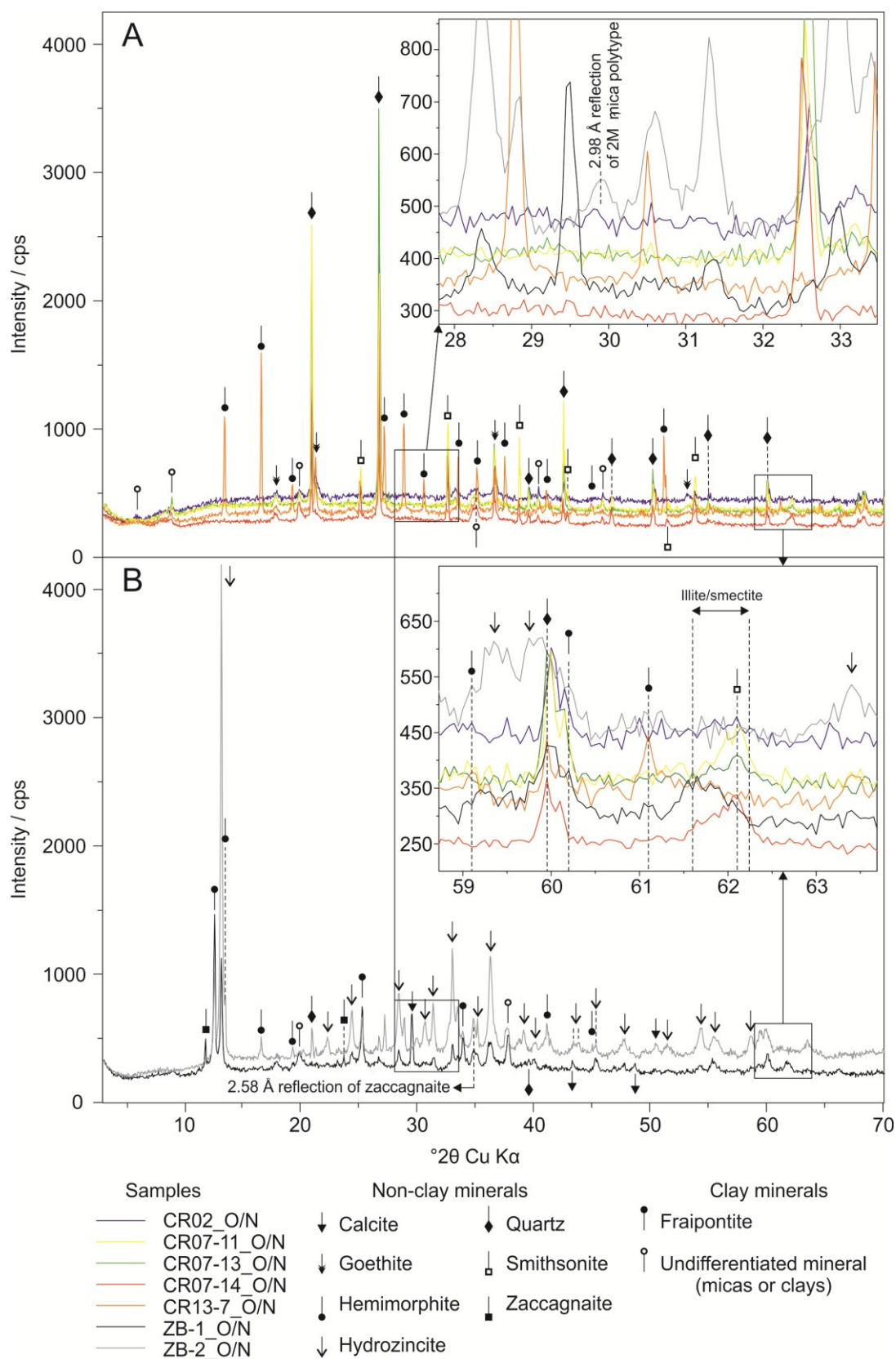


Figure 6.3. XRPD patterns of randomly oriented (O/N) residues of Cristal (A) and Mina Grande (B) samples, which show the main reflections of the detected minerals, those corresponding to the 060 spacings and the diagnostic 2.98 Å peak of the 2M1 mica polytype.

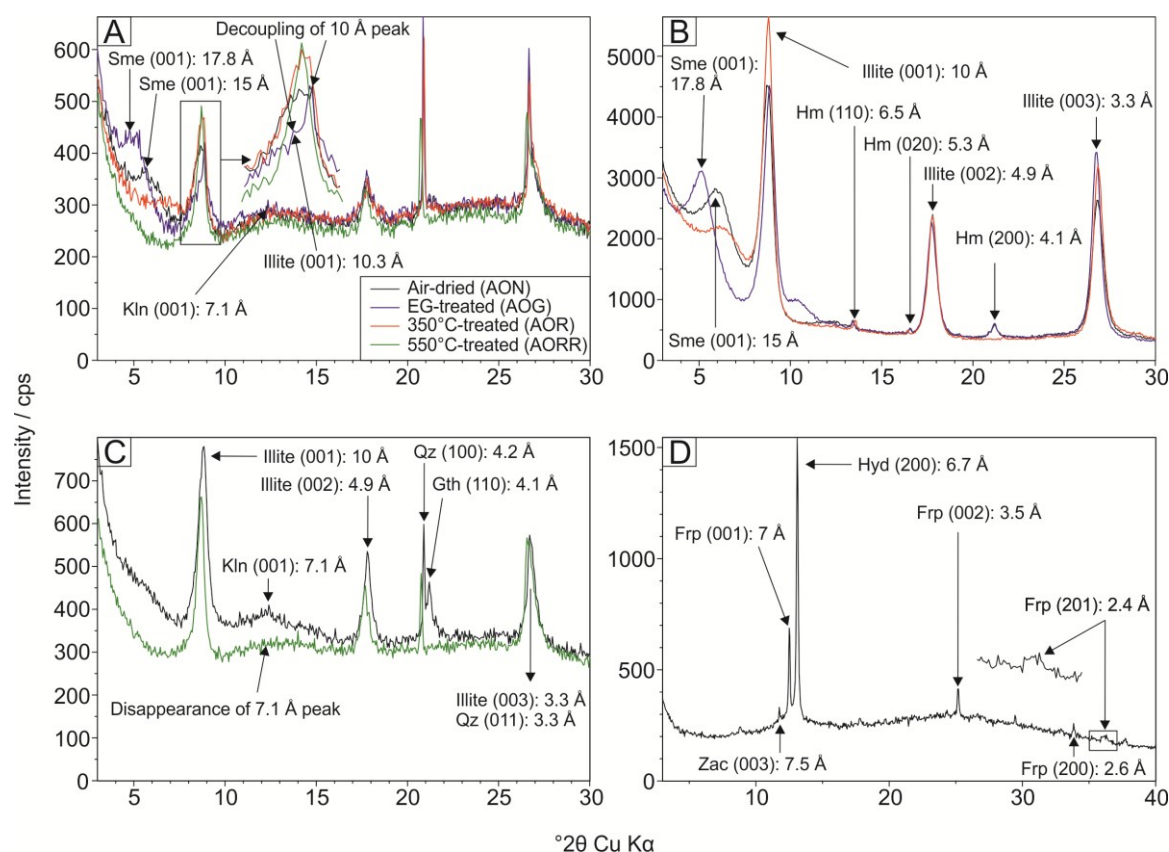


Figure 6.4. XRPD patterns of AON, AOG, AOR and AORR oriented aggregates from residues of 5 min/5000 rpm and 40 min/8000 rpm centrifugation cycles. (A) The XRPD patterns of the EG-treated aggregate (AOG) show the decoupling of the 10 Å peak (AON) into 10.3 (left) and 9.97 (right) Å reflections (sample CR07-14_5/5000). (B) Example of I/S mixed layers in the Cristal samples. Hemimorphite (Hm) residues are still detected in the sample (CR13-7_40/8000). (C) The XRPD patterns of the AOR oriented aggregate show the disappearance of the 7.1 Å reflection of kaolinite (Kln) (sample CR02_5/5000). (D) The XRPD pattern of the AON oriented aggregate shows the diagnostic reflections of fraipontite (Frp) and the 003 spacing of zaccagnaite (Zac) in a hydrozincite-rich sample from the Mina Grande deposit (sample ZB-1_5/5000).

The AOG EG-treated patterns of the CR07-14 and CR13-7 samples (Figs. 6.4A and B, respectively) show a shift in the reflection at 15 Å toward 17.8 Å, due to the swelling typical of the smectite clays. In the AOG EG-treated pattern of the sample CR07-14, a decoupling of the ~ 10 Å peak into the 10.3 and 9.97 Å reflections was also observed (Fig. 6.4A). After a treatment at 350°C, the decoupling disappeared and a single reflection appeared at ~ 10 Å, sharper than the previous one observed in the AON (air-dried) pattern (Fig. 6.4A). This behavior suggests that the original reflection at 10 Å could correspond to a mixed layer illite-smectite (I/S), and that the narrow shoulder appearing at 10.3 Å in the EG-treated pattern likely represented the (001) illite reflection. The ~ 10 Å position of the I/S mixed layer reflection indicates a long-range ordering (*Reichweite value* “R” > 1) and a high percentage of illite (>90%) in the mixed-layer I/S (e.g. Moore and Reynolds, 1997). Sample CR13-7 does not show this decoupling (Fig. 6.4B). The AON, AOG and AOR patterns of samples CR07-14 and CRO2 (Figs. 6.4A and C, respectively) show the presence of a peak around 7.1 Å, which is very weak or absent in

other samples (e.g. samples CR13-7). The disappearance of the 7.1 Å-peak in the AORR pattern (550 °C-heated slides) of both CR07-14 and CR02 samples suggests that the reflection can be likely attributable to the presence of kaolinite, rather than chlorite (Moore and Reynolds, 1997).

In the air-dried samples from the Mina Grande deposit (e.g. sample ZB-1; Fig. 6.4D) the main reflections are related to hydrozincite (i.e. 6.66 Å). Minor reflections occur at 3.03, 7.07, 7.53 and 10 Å. The 7.07 Å reflection represents the basal spacing 001 of fraipontite, whereas the 7.53 Å reflection corresponds to the 003 spacing of zaccagnaite [$\text{Zn}_4\text{Al}_2(\text{CO}_3)(\text{OH})_{12}\cdot 3\text{H}_2\text{O}$], a mineral belonging to the hydrotalcite-manasseite group (Drits et al., 1987; Merlino and Orlandi, 2001; Lozano et al., 2012). The occurrence of fraipontite and zaccagnaite is confirmed by the distinct presence of other diagnostic reflections for both fraipontite (d_{002} at 3.53 Å and d_{201} at 2.48 Å) and zaccagnaite (d_{006} at 3.76 Å, d_{012} at 2.58 Å) (Figs. 6.3B and 6.4D). The XRPD pattern of zaccagnaite occurring in the O/N overnight residue of sample ZB-1 (Figure 6.3B) belongs to the zaccagnaite-3R polytype (Lozano et al., 2012).

In the Mina Grande samples (ZB-1 and ZB-2), the 060 spacings occurring in the O/N (overnight residues) patterns (Fig. 6.3B) between 1.53 and 1.54 Å are consistent with the presence of trioctahedral species of the serpentine (fraipontite) group. In both Mina Grande and Cristal samples (ZB-1 and CR07-14, respectively), broader 060 reflections between 1.49 and 1.50 Å may correspond to dioctahedral phyllosilicates as kaolinite, muscovite, or also to species of the smectite group or to illite/smectite mixed layers (Figure 6.3B). The 2.98 Å ($30^\circ 2\theta$) reflections, which are visible in both Cristal (CR02) and Mina Grande (ZB-2) samples (Fig. 6.3A) suggest the presence of the $2M_1$ mica polytype (Moore and Reynolds, 1997).

Chemical composition and SEM observations

In the analyzed samples, the most common micas, occurring together with detrital apatite, rutile and quartz in a Zn- and Mn-bearing clayey matrix (Fig. 6.5A), commonly show SiO_2 and Al_2O_3 contents (Table 6.1) respectively higher and lower than the values reported for the muscovite classified by International Mineralogical Association (IMA). These micas also have FeO_t (total iron) and MgO contents ranging from 0 to 5 wt.%, and from 0 to 3 wt.%, respectively, and concentrations of interlayer cations varying from 6 to 11 wt.% for K_2O and <1 wt.% for CaO. Several Bongará micas are also Zn-bearing (up to 12 wt.% ZnO; Table 6.1). These compositions are not compatible with proper muscovite, and could evidence the presence of illite or I/S mixed layers.

In the mica-rich samples, it was possible to detect Zn-Mn-bearing phyllosilicates with compositions close to hendricksite [$\text{K}(\text{Zn,Mg,Mn})_3\text{Si}_3\text{AlO}_{10}(\text{OH})_2$], which locally replace Zn-bearing illite or I/S mixed layers (Fig. 6.5B) and occur also as thin interstratifications within the mica flakes (Figs. 6.5C and D). However, the ZnO, SiO_2 and Al_2O_3 contents (Table 6.2) detected in the Zn-Mn-bearing phyllosilicates do not coincide exactly with theoretical hendricksite (IMA database). Generally, the SiO_2 and Al_2O_3 contents of Bongará hendricksite-like phases are higher and the ZnO contents lower than the in IMA hendricksite, as well as its $\text{SiO}_2/\text{Al}_2\text{O}_3$ ratio (2.30 for IMA hendricksite and 1.73 for

Cristal Zn-Mn-bearing micas). The common association of Zn-Mn-bearing phyllosilicates with Mn-(hydr)oxides, sometimes finely intergrown with layered minerals, makes difficult to discriminate by SEM-EDS the Mn content related to each phase (Figs. 6.5C and D). However, qualitative SEM-EDS analyses, performed on small portions of the clay fraction apparently free of Mn-(hydr)oxides (Figs. 5E and F), led to confirm that the phyllosilicates in the clay fraction were free of Mn-(hydr)oxides, thus corroborating the occurrence of Zn-Mn-bearing phyllosilicates.

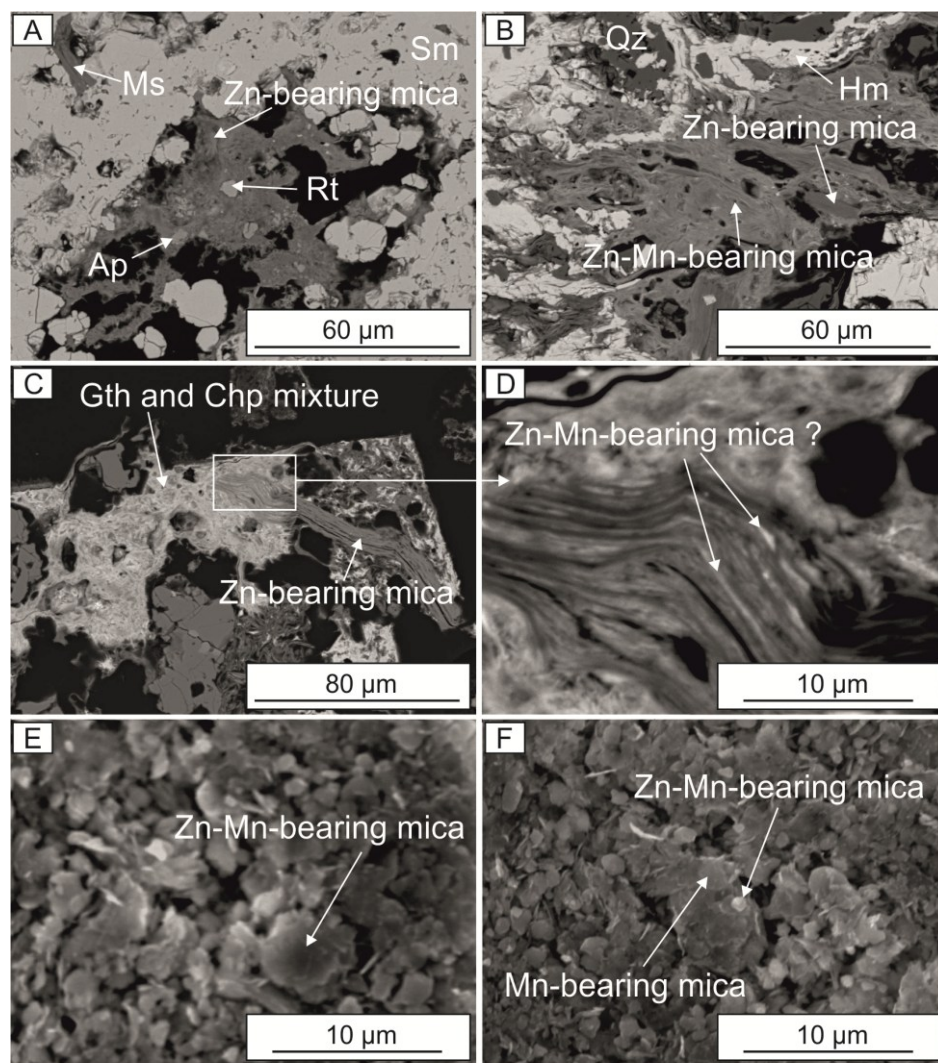


Figure 6.5. Secondary and backscattered electron (BSE) images of Zn-bearing and Zn-Mn-bearing micas in the Cristal samples. (A) A cavity in smithsonite (Sm) filled by a clayey mixture, which surrounds the Zn-bearing mica remnants, as well as rutile (Rt) and apatite (Ap) crystals (sample CR03-3). (B) Hendricksite surrounding a Zn-bearing mica in a hemimorphite (Hm)- and quartz (Qz)-rich sample (CR13-6). (C) Goethite (Gth) and chalcophanite (Chp) surrounding a Zn-bearing mica with possible Zn-Mn-bearing layers (D) (sample CR13-7). (E) and (F) Possible Mn-(hydr)oxides-free powders from the CR07-11_5/5000 sample showing the occurrence of hendricksite flakes.

The EDS analyses of the Bongará samples evidenced also that the smectite recognized in the XRD patterns has a sauconite composition (Table 6.2). The best examples could be

seen in samples CR07-13 and CR03-3 (Figs. 6.6A and B, and Fig. 6.6C, respectively). In the latter, it can be also seen sauconite replacing the Zn-bearing illite.

In the SEM images, the smectite group minerals show flared, “cornflake” or “oak leaf” textures that are commonly covered by thin crusts of micrometric goethite concretions (Fig. 6.6A). The smectites are tightly associated with other flat-lying flakes with scalloped and slightly curled edges. Such textures are generally associated with a mineral with a hybrid illite-smectite morphology (see Keller et al., 1986 for more details), which from EDS analysis results also Zn-bearing (Fig. 6.6B).

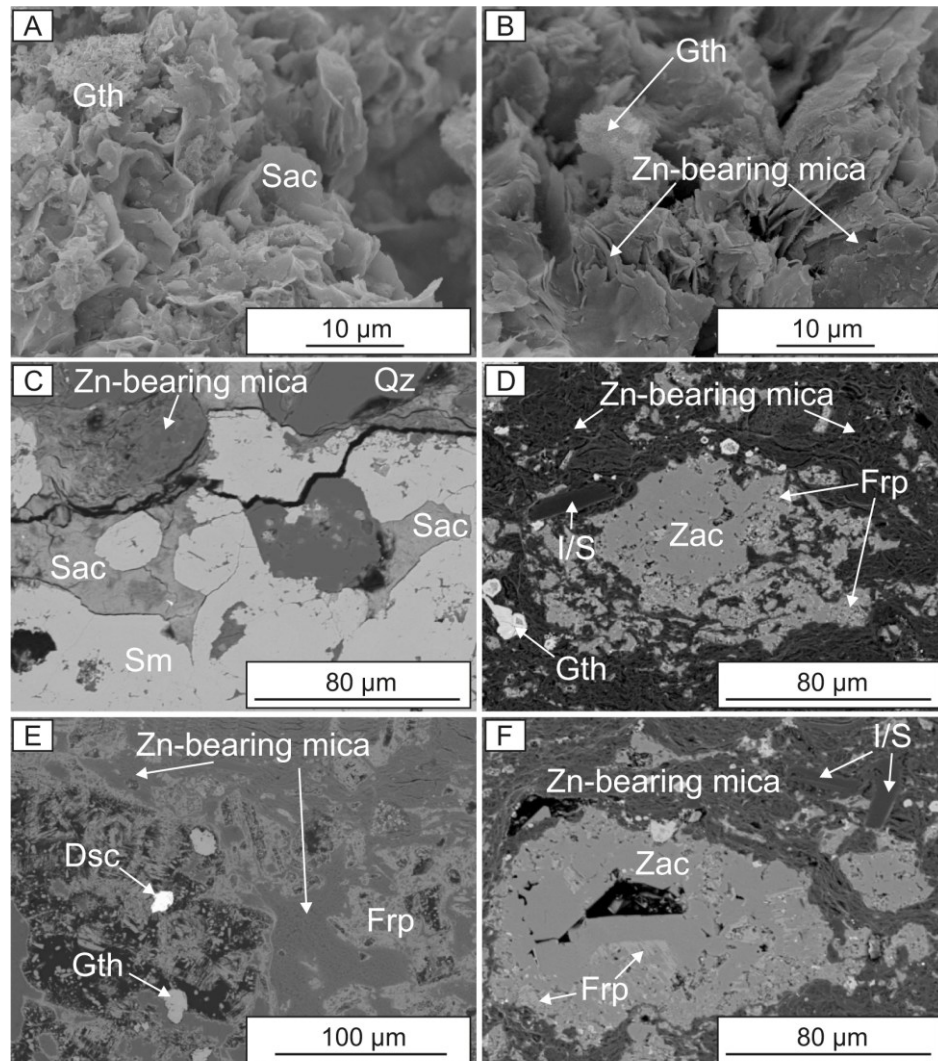


Figure 6.6. Secondary and backscattered electron (BSE) images of clay minerals from Cristal (A, B, C) and Mina Grande (D, E, F) deposits. (A) and (B) 3D images of sauconite (Sac) and interstratified I/S showing “cornflake” (sauconite) and “flat-lying flake” (Zn-bearing illite or I/S) textures. The latter are commonly obliterated by thin crusts of micrometric goethite (Gth) concretions. (C) Sauconite surrounding Zn-bearing mica and filling fractures in smithsonite (Sm) (sample CR03-3). (D, E, F) Zaccagnaite (Zac) replacing fraipontite (Frp), and occurring in cavities of Zn-bearing I/S. Goethite (Gth) and descloizite (Dsc) are commonly found in this mineral assemblage (sample ZB-1).

TABLE 6.1. Chemical composition and structural formulae (apfu) of Zn-bearing micas from the Cristal (CR samples) and Mina Grande (ZB samples) deposits.

Location	Cristal											Mina Grande	
Sample ID	CR03-3	CR03-3	CR03-3	CR03-3	CR07-13	CR07-13	CR13-5	CR13-6	CR13-6	CR13-6	CR13-7	ZB1	ZB1
<i>wt. %</i>													
SiO ₂	48.17	56.84	50.97	53.00	48.60	47.41	47.42	49.94	51.33	43.19	47.25	46.10	47.17
TiO ₂	0.24	0.42	0.13	0.26	0.45	0.45	0.14	0.26	0.33	0.11	0.37	0.17	0.16
Al ₂ O ₃	28.33	22.37	20.34	25.70	29.13	36.35	26.69	29.34	25.54	26.72	25.02	36.84	27.71
MgO	2.12	1.90	2.99	3.48	1.89	0.99	2.22	2.27	3.14	1.67	2.56	-	2.72
MnO	0.22	0.15	0.09	-	-	0.24	1.66	-	0.39	5.75	1.06	0.08	-
FeO _t ^a	4.25	1.83	1.60	1.66	5.06	0.82	3.49	0.79	1.34	0.68	2.48	1.27	1.07
ZnO	0.85	2.82	12.61	1.10	0.06	0.55	0.92	3.83	5.49	8.11	5.85	0.70	9.28
K ₂ O	10.90	7.01	6.04	9.13	10.92	10.16	10.67	8.52	6.60	8.02	8.50	11.64	7.63
CaO	-	0.25	0.60	0.36	0.22	-	0.44	0.80	0.38	0.39	0.17	-	0.30
PbO	-	-	0.15	-	-	-	-	0.49	-	0.40	0.20	0.06	0.24
Total	95.08	93.59	95.54	94.69	96.33	96.97	93.64	96.24	94.55	95.04	93.46	96.87	96.28
<i>apfu</i>													
						on the basis of 11 O							
Si	3.29	3.79	3.55	3.52	3.27	3.09	3.28	3.32	3.46	3.10	3.33	3.04	3.23
Al	0.71	0.21	0.45	0.48	0.73	0.91	0.72	0.68	0.54	0.90	0.67	0.96	0.77
Σ _T	4.00	4.00	4.00	4.00	4.00	4.00	4.00	4.00	4.00	4.00	4.00	4.00	4.00
Al	1.57	1.55	1.22	1.53	1.58	1.88	1.45	1.62	1.49	1.36	1.41	1.90	1.47
Ti	0.01	0.02	0.01	0.01	0.02	0.02	0.01	0.01	0.02	0.01	0.02	0.01	0.01
Mg	0.22	0.19	0.31	0.34	0.19	0.10	0.23	0.22	0.32	0.18	0.27	-	0.28
Mn	0.01	0.01	0.01	-	-	0.01	0.10	-	0.02	0.35	0.06	-	-
Fe	0.24	0.10	0.09	0.09	0.28	0.04	0.20	0.04	0.08	0.04	0.15	0.07	0.06
Zn	0.04	0.14	0.65	0.05	-	0.03	0.05	0.19	0.27	0.43	0.30	0.03	0.47
Pb	-	-	0.003	-	-	-	-	0.01	-	0.01	-	-	-
Σ _O	2.09	2.01	2.28	2.03	2.06	2.08	2.03	2.09	2.20	2.37	2.21	2.01	2.28
Ca	-	0.02	0.05	0.03	0.02	-	0.03	0.06	0.03	0.03	0.01	-	0.02
K	0.95	0.60	0.54	0.77	0.94	0.84	0.94	0.72	0.57	0.73	0.76	0.98	0.67
Σ _i	0.95	0.62	0.59	0.80	0.96	0.84	0.97	0.77	0.59	0.76	0.77	0.98	0.69
Σ _{ch(T)}	-0.71	-0.21	-0.45	-0.48	-0.73	-0.91	-0.72	-0.68	-0.54	-0.90	-0.67	-0.96	-0.77
Σ _{ch(O)}	-0.24	-0.43	-0.19	-0.35	-0.25	0.07	-0.28	-0.16	-0.09	0.11	-0.11	-0.02	0.06
Σ _{ch(I)}	0.95	0.64	0.64	0.83	0.98	0.84	1.00	0.84	0.63	0.79	0.78	0.98	0.71

Note: ^a FeO_t as total iron; - not determined

TABLE 6.2. Chemical compositions and structural formulae (apfu) of trioctahedral mineral species from the Mina Grande (fraipontite) and Cristal (sauconite and Zn-Mn-bearing mica) deposits.

Location	Mina Grande					Cristal		
Sample ID	ZB1		CR03-3			CR07-9	CR13-6	CR13-6
Mineral	Fraipontite		Sauconite			Zn-Mn-bearing mica		
<i>wt. %</i>								
SiO ₂	19.64	16.35	37.78	37.88	40.44	35.99	34.86	38.99
TiO ₂	-	-	0.12	0.12	0.13	0.12	-	0.17
Al ₂ O ₃	20.41	20.46	6.52	5.08	7.11	18.21	20.15	23.13
MgO	0.07	0.05	0.78	0.47	0.75	2.18	1.64	1.67
MnO	0.05	-	-	-	-	9.97	10.89	7.85
FeO _T ^a	0.77	0.32	0.35	0.27	0.11	2.59	1.42	0.66
ZnO	46.67	49.16	37.00	40.24	34.73	19.17	16.85	13.15
CaO	0.04	-	1.52	0.95	1.00	0.38	0.11	0.17
K ₂ O	-	0.01	0.73	0.15	1.15	4.56	5.61	6.86
PbO	-	0.21	-	-	-	-	1.18	0.57
Total	87.65	86.56	84.80	85.16	85.42	93.15	92.71	93.23
<i>apfu</i>	on the basis of 14 O		on the basis of 11 O			on the basis of 11 O		
Si	2.48	2.15	3.52	3.57	3.64	2.92	2.85	2.99
Al	1.52	1.85	0.48	0.43	0.36	1.08	1.15	1.01
Σ _T	4.00	4.00	4.00	4.00	4.00	4.00	4.00	4.00
Al	1.52	1.32	0.24	0.13	0.39	0.66	0.79	1.08
Ti	-	-	0.01	0.01	0.01	0.01	-	0.01
Mg	0.01	0.04	0.11	0.07	0.10	0.26	0.20	0.19
Mn	0.01	0.01	-	-	-	0.68	0.75	0.51
Fe	0.08	0.11	0.03	0.02	0.01	0.18	0.10	0.04
Zn	4.36	4.76	2.54	2.80	2.31	1.15	1.02	0.75
Pb	-	0.02	-	-	-	-	0.03	0.01
Σ _O	5.98	6.26	2.93	3.03	2.82	2.94	2.89	2.59
Ca	0.01	-	0.15	0.10	0.10	0.03	0.01	0.01
K	-	0.03	0.09	0.02	0.13	0.47	0.58	0.67
Σ _I	0.01	0.03	0.24	0.12	0.23	0.50	0.59	0.68
Σ _{ch(T)}	-1.52	-1.85	-0.48	-0.43	-0.36	-1.08	-1.15	-1.01
Σ _{ch(O)}	1.50	1.82	0.09	0.21	0.03	0.55	0.55	0.32
Σ _{ch(I)}	0.02	0.03	0.39	0.22	0.33	0.53	0.60	0.69

Note: ^a FeO_T is total iron; - not determined

In the samples from Mina Grande fraipontite and zaccagnaite, already identified with XRD analyses, have been also detected by SEM-EDS (Table 6.2). Observed in thin section, fraipontite is always texturally associated with Zn-bearing illite or I/S, and/or with zaccagnaite (Figs. 6.6D, E and F). When in association with Zn-bearing illite or I/S, fraipontite occurs as thin halos around the mica grains (Fig. 6.6E), while if associated with zaccagnaite, it can be found as patchy remnants in the latter mineral (Figs. 6.6D and F). Zaccagnaite also turns up as cavity filling, where it shows euhedral crystal shapes. The zaccagnaite-fraipontite association generally occurs in a clayey matrix consisting of Zn-bearing micas. For this reason SEM-EDS analyses do not permit identification of fraipontite in the Cristal mineralization with certainty.

Discussion

The XRPD analyses and the microscopic observations carried out on the samples from the Cristal and Mina Grande deposits have revealed the presence of layered silicates belonging to mica, smectite and kaolinite-serpentine groups. In both deposits, mica that has been firstly classified as muscovite and/or illite by Arfè et al. (in press) is mostly represented by illite or I/S mixed layers. The EDS analyses on the I/S mixed layers have shown that in these phases the Zn and K concentrations are inversely correlated (Table 6.1). This could suggest that in the I/S, Zn is partly hosted by smectite layers characterized by sauconite composition, and that Zn consequently increases as the illite component decreases. Textural observations would suggest that the original illite or I/S mixed layers were of detrital or sedimentary origin (e.g. I/S mixed layers show *Reichweite values* “R”>1, which are commonly produced by diagenetic processes; e.g. Moore and Reynolds, 1997). Looking at the literature (e.g. Mondillo et al., 2015), Zn incorporation in these phyllosilicates could be related either to the same hydrothermal processes responsible for the emplacement of sulfides (Arfè et al., 2017b, in press), or to supergene alteration, which allowed the formation of nonsulfide ores. In both cases, Zn incorporation in the I/S also produced an increase of the smectite (i.e. sauconite) component in the mixed layer. However, we cannot exclude that part of the detected sauconite overgrows the I/S grains, instead of being incorporated into the mixed layers, using the I/S lamellae as a template on which smectite crystallizes directly from fluids, as already observed in other deposits (e.g., Mondillo et al., 2015; Balassone et al., 2017).

In several mica-rich samples, Zn-Mn-bearing phyllosilicates with a chemical composition similar to that of hendricksite were also detected as fine intergrowths between the other phyllosilicates, i.e. Zn-bearing I/S and sauconite. In the $M^{+}-4Si-3R^{2+}$ ternary plot (Fig. 6.7), which is useful to distinguish between dioctahedral and trioctahedral clay types (Meunier, 2005), the compositions of the micas describe the cluster of points “A-B-C”, and are mostly dispersed along the axis “A-B”, which spans between the muscovite and sauconite end-members. In this diagram it is also possible to see that the compositions of Zn-bearing micas (illite or I/S) are closer to the muscovite than to the sauconite end-member, whereas the Zn-Mn-bearing micas are closer to the sauconite than to the hendricksite end-member. This distribution is compatible with the nature of Zn-bearing

micas reported before, which probably consist of illite or I/S, with a high % illite, and sauconite as the smectitic component. A possible explanation of the fact that the compositions of Zn-Mn-bearing micas do not converge exactly toward the hendricksite, can be found in the texture of these phyllosilicates, which being finely intergrown with sauconite and Zn-bearing I/S mixed layers, cannot be analyzed by SEM-EDS with extreme precision. In other words, sauconite, grown over the hendricksite, or directly formed at its expense, can generate considerable bias in the EDS analysis of hendricksite. However, it is important to consider that hendricksite is a mineral typical of Zn-oxidized hypogene mineralizations (Hitzman et al., 2003). In fact, hendricksite has been recognized for the first time in stratiform hypogene deposits (e.g. Franklin mine, New Jersey, USA; Frondel et al., 1966), and in many Zn-bearing skarns (Leavens et al., 2009), where it is derived from high temperature hydrothermal processes ($T > 200^{\circ}\text{C}$). These high temperatures have been corroborated by the unsuccessful attempts to synthesize Zn- and Mn-bearing micas at temperatures lower than 55°C (Perrotta and Gerland, 1975; Choi et al., 2009), which would be typical of a supergene environment (25°C and 1 atm). Therefore, it is likely that also in the Cristal prospect hendricksite formed from hydrothermal fluids, which have emplaced also the sulfide mineralization.

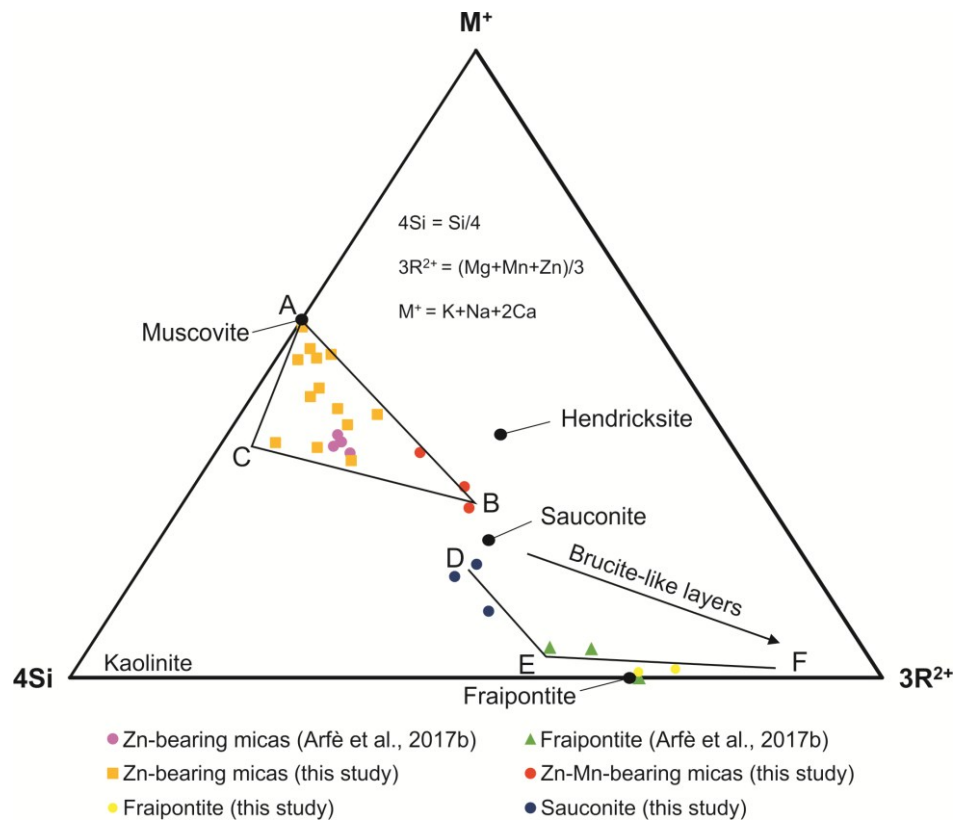


Figure 6.7. $4Si-M^{+}-3R^{2+}$ ternary diagram (Meunier, 2005) showing the chemical compositions of micas and clays identified in the Cristal and Mina Grande samples. Muscovite, hendricksite, sauconite and fraipontite compositions as reported in the IMA database. Due to the compositions of the studied minerals, for the calculation of the $3R^{2+}$ component Mn was used instead of Fe.

The peculiar fraipontite-zaccagnaite association observed at Mina Grande might also be genetically related either to hydrothermal or to supergene processes. In fact, this association was observed in marble quarries of the Carrara basin (Apuane Alps, Italy), where it was deposited through hydrothermal alteration of Zn-bearing sulfides and sulfosalts, in the presence of aluminium-rich fluids (Merlino and Orlandi, 2001). However, zaccagnaite and fraipontite can also form from supergene fluids, as a product of sulfide weathering (e.g. Lozano et al., 2012; Choulet et al., 2016). The XRD analysis of zaccagnaite from the Mina Grande deposit points to the presence of the zaccagnaite 3*R*-polytype, which was firstly identified in the El Soplao karstic caves (Cantabria, Spain), where it was considered as having been formed at ~11°C in a supergene environment (Lozano et al., 2012). The latter formation temperature is very similar to that (~15°C) calculated for some supergene minerals in the Mina Grande deposit (Arfè et al., 2017b), and would therefore be perfectly compatible with the formation of zaccagnaite in a supergene environment at Mina Grande. In the same deposit, however, it was still not possible to definitely establish the nature of fraipontite. In fact, this mineral may have been formed either during the hydrothermal process that generated the sulfides, or in the early stages of supergene alteration, which took place under acidic conditions associated with the alteration of sulfides. In both cases, when the buffering of the carbonate host rock turned the environment from acidic to alkaline (pH >7), fraipontite became unstable and zaccagnaite started to form at its expense.

Conclusions

This study has implemented the data on Zn-bearing phyllosilicates from the Cristal and Mina Grande (Bongará) mineralized areas, also providing a new insight on their genesis. In both deposits several types of phyllosilicates have been detected, which consist of micas and clay minerals. The micas mainly correspond to I/S mixed layers of detrital origin, which have been partly altered or overprinted by sauconite of either supergene or hydrothermal origin. Hendricksite occurring sporadically in the Cristal prospect may be considered a hydrothermal product, formed during the emplacement of sulfides. In the Mina Grande deposit, a peculiar association of fraipontite and zaccagnaite was observed. Even though both these minerals can be either of hydrothermal or supergene origin, the identified zaccagnaite polytype suggests that fraipontite and zaccagnaite are both genetically derived from weathering processes. Ongoing mineralogical investigations carried out by high-resolution transmission electron microscopy (HRTEM) will hopefully better constrain the nature of the Zn-bearing clay minerals in the Bongará district.

Introduction to the Namibian deposits - Why study them

Most issues on the deposits of the Bongará province in Peru have been discussed in the previous chapters. In the next chapters the data on a comparative study on Namibian nonsulfide deposits will be reported. The study on the Namibian ores (Skorpion and Rosh Pinah deposits) has proven interesting, because it was useful to compare supergene profiles generated and developed in tropical areas (Peruvian deposits) with those formed in a humid environment, later evolved under more arid conditions (Namibian deposits).

Weathering conditions in arid climate settings have been extensively studied since in many desert areas (e.g. Northern Chile) economically attractive supergene profiles are superimposed on hypogene ores, as the porphyry-Cu or epithermal deposits. On the contrary, the mineralogical, geochemical and genetic aspects of supergene profiles developed on sulfide protores in completely different climate regimes (humid-tropical) are still poorly investigated. As reported in the Introduction, many Zn-nonsulfide deposits are characterized by fossil supergene profiles that do not allow an accurate analysis of the weathering processes active at the time of enrichment. Therefore, by studying the relatively recent supergene profiles in the Peruvian deposits, where the current weather conditions are not very different from those under which the nonsulfide ores were deposited, it has been possible to obtain new insights on the active weathering processes occurring in tropical areas. The latter processes may be eventually extended to fossil supergene profiles formed under climatic conditions different from the current ones. Indeed, at Skorpion and Rosh Pinah, chemical weathering and soil formation is currently hampered, mostly due to the lack of moisture, even if the same areas have experienced humid-tropical climate regimes in the past, which have controlled the nature of the weathering profiles.

In order to confirm the climatic step-overs and to obtain new data on the climatic conditions at the time of Skorpion and Rosh Pinah sulfide oxidation, the study of these Namibian deposits has been predominantly carried out through stable isotopes geochemistry, with an addition of an investigation on the clay fraction (at Skorpion). Such analysis is even more important than the study on the clay component carried out in the Peruvian supergene profiles, since Zn-smectite (sauconite) represents the main Zn-bearing mineral phase in the Skorpion mine. Compared to the study on Zn-phyllsilicates occurring in the samples from the Bongará province, for which conventional techniques were used to discriminate the possible types of clays, the study on the Skorpion Zn-clays is the first accurate characterization of the mineral sauconite, which has been often quoted in the scientific literature but, despite its economic relevance, has never been mineralogically and geochemically characterized before.

Chapter 7:

New C-O isotopic data on supergene minerals from the Skorpion and Rosh Pinah ore deposits (Namibia): Genetic and paleoclimatic Constraints

Published in "Journal of African Earth Sciences"

Reference: Arfè, G., Boni, M., Balassone, G., Mondillo, N., Hinder, G., Joachimski, M., 2017. New C-O isotopic data on supergene minerals from the Skorpion and Rosh Pinah ore deposits (Namibia): Genetic and paleoclimatic constraints. Journal of African Earth Sciences, 126, 148-158.

Introduction

This study focuses on a comparison between the C-O isotopic geochemistry of carbonate minerals precipitated in the oxidation zone of the Rosh Pinah base metals deposit (Gariep Belt, Namibia) and in the Skorpion nonsulfide Zn mineralization located nearby (Borg et al., 2003) (Fig. 7.1).

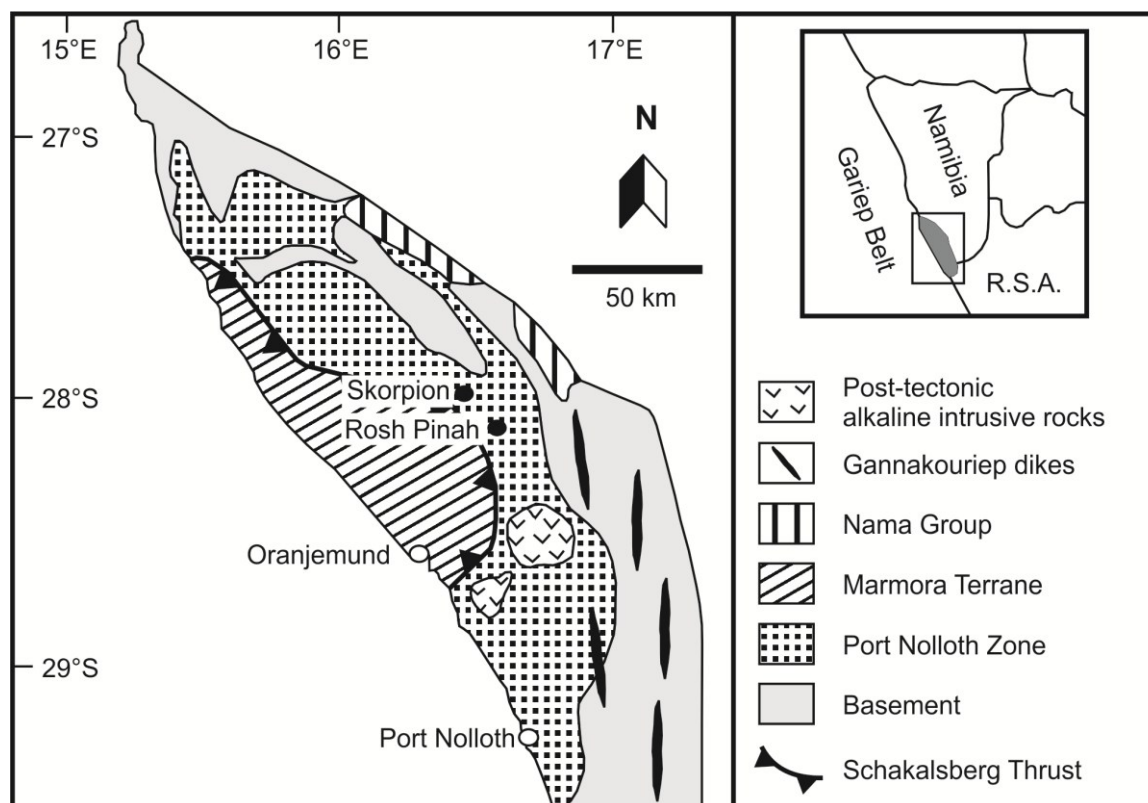


Figure 7.1. Generalized geologic map of the Gariep belt in southern Namibia and northern South Africa. Both Skorpion and Rosh Pinah (filled black circles) are located within the parautochthonous Port Nolloth zone (from Borg et al., 2003; modified).

The Rosh Pinah and Skorpion base metals concentrations together with other smaller occurrences form a major Zn (+Pb and minor Cu) district in southern Africa (Schneider and Walmsley, 2004). The deposits were both subjected to weathering processes that may have started after the end of the pan-African tectonic phase, followed by uplift and denudation and ended with the onset of a strong arid period that began at least in the Oligocene. However, while the mineralization at Skorpion was almost completely transformed into an economically valuable nonsulfide deposit, at Rosh Pinah, the weathered zone has a limited extension and the majority of the primary sulfides have been preserved. Carbon and oxygen isotopes of smithsonite have been measured in order (i) to elucidate the conditions of supergene ore formation and (ii) to identify the sources of the mineralizing fluids. Stable isotopes of calcite have been analysed only in Skorpion. Stable isotope data on Skorpion smithsonites were previously published by Borg et al. (2003) and Kärner (2006), but no data currently exist for the Zn carbonates occurring in the oxidation zone of the Rosh Pinah mine. In this study, we integrate the stable isotope data sets of the Skorpion carbonates and fill the existing gap regarding the carbonate minerals of the supergene zone at Rosh Pinah. The results also add to the interpretation of the post-Gondwanan paleoclimatic evolution in the Gariep Belt.

Geological setting

Regional geological setting

The Late Proterozoic Gariep Belt (Fig. 7.1) is regarded as the southern extension of the Damara orogenic front of central and northern Namibia (Davies and Coward, 1982; Reid et al., 1991; Stanistreet et al., 1991; Gresse, 1994; Frimmel, 2000; Jasper et al., 2000; Frimmel et al., 2002). It is subdivided into an eastern paraautochthonous zone, the so-called Port Nolloth Zone (PNZ), and a western allochthonous zone, the Marmora Terrane. The PNZ evolved from an intracontinental rift to a passive continental margin on the western edge of the Kalahari Craton (Jasper et al., 2000). Regional stratigraphic correlations of the Late Proterozoic rock sequence within the Gariep Belt have been subject of considerable debate and several stratigraphic schemes have been proposed by different authors (e.g. Alchin et al., 2005 and references therein). This is a result of poor, isolated outcrops, complexly deformed rock sequences and rapid lateral facies changes of both metasedimentary and metavolcanic rocks (Kärner, 2006). The Late Proterozoic Gariep rock successions tectonically overly the Palaeoproterozoic basement and correspond to sequences assigned regionally to the Stinkfontein and Hilda Subgroups, which include the Gumchavib, Pickelhaube, and Rosh Pinah formations. The Gariep sequence is genetically related to the progressive opening of a failed intracratonic rift-graben in the east (Rosh Pinah/Skorpion Graben) that was separated by a basement horst from a half graben to the west, which developed into the Adamastor Ocean (Alchin et al., 2005).

The rocks of the PNZ contain stratiform Zn-Pb-Cu-Ag-(±Ba)-sulfide mineralizations in sedimentary and felsic metavolcanic rocks. The best examples are the Rosh Pinah Pb-Zn

(Page and Watson, 1976; Van Vuuren, 1986; Alchin and Moore, 2005) and the Skorpion Zn-Cu deposits (Borg et al., 2003; K€arner, 2006). These base metal deposits (which were attributed to either the VMS or SEDEX types) were formed in an extensional environment during a phase of increased volcanogenic-hydrothermal activity between 740 and 754 Ma (Borg and Armstrong, 2002). The deformation of the ore-bearing units took place during a continental collision and closing of the Adamastor oceanic basin during the Pan-African tectonic phase, 545 million years ago (Alchin and Moore, 2005). The sedimentary and bi-modal volcanic rocks hosting the mineralization have been strongly folded, faulted and overprinted by a lower amphibolite facies metamorphism (Frimmel et al., 1995).

The present landscape of southern Africa is the result of the tectonic processes largely associated with the breakup of Gondwana, which took place after the pan-African tectonic phase (King, 1951). Some of the best summaries of present-day knowledge about the geomorphological evolution of southern Africa and Namibia have been presented by Partridge and Maud (1987) and Partridge (1998), who showed that the macroscale development of the landscape in all of southern Africa, including the Gariep Belt, has occurred in discrete stages. At the end of the Cretaceous, southern Africa and Namibia were transected by a major planation surface, known in the literature as the “African Surface” (related to the African erosion cycle). The maximum peneplanation, coupled with intense lateritic weathering, was reached between the Late Cretaceous and the Oligocene. During the Late Cretaceous-Eocene, a denudation event eroded a 3 km-thick section of southern Africa and Namibia and it reached several hundred km inland (Gallagher and Brown, 1999). The African surface was then rejuvenated and intersected by younger erosion planes, called the post-African I and II surfaces (Partridge and Maud, 1987), which are related to discrete uplifts that took place in the early Miocene and Pliocene. The climate prevailing during the Cretaceous and part of the Eocene was hot and humid (“greenhouse” period, Rust and Summerfield, 1990), but these “tropical” conditions were frequently interrupted by semi-arid periods and ceased almost completely at the end of Eocene. The precise date of the initiation of aridity is, however, a matter of debate (Van Zinderen Bakker, 1975; Ward et al., 1983). Indeed, it is conceivable that aridity may have prevailed since the Early Cretaceous continental fragmentation itself, because dune beds (aeolianites) are interlayered within the Etendeka Lavas in the Huab Basin (Miller, 2008). The Neogene Tsondab Sandstone lithified erg in the southern Namib dates back at least to the early Miocene (but possibly is even older), and overlies wind-sculptured Late Proterozoic rocks (Senut et al., 1994). If we consider the climatic conditions during the Eocene, in pre-Bartonian time (middle Eocene) the climate in the Sperrgebiet was relatively humid and tropical with summer rainfall, but shortly after the Bartonian there are signs of increasing aridity (Pickford et al., 2014).

A typical evolution toward true arid conditions most likely started during the Oligocene (“icehouse”), and lasted up to the Recent. The arid climate conditions were further accentuated and rendered irreversible by the establishment of the cold Benguela current in middle Miocene (Siesser, 1980). These conditions caused the formation of the Namib and Kalahari deserts, where chemical weathering is extremely limited and the denudation

rates of the previously uplifted zones was very slow (Van der Wateren and Dunai, 2001). The Miocene terrace deposits of the Orange River contain calcretes and gypscres, which formed under relatively dry conditions (Roberts et al., 2013), a climatic evolution that has been recognized by Ségalen et al. (2006) based on paleontological evidence. Likewise, through the study of pollen and the stable isotopic composition of plant waxes from a sediment core off Namibia, Hötzel (2013) confirmed an expansion of C4 grasses (which are particularly adapted to dry conditions) during the late Miocene.

Rosh Pinah deposit

The Rosh Pinah deposit is located about 23 km north of the Orange River and 100 km east of the Atlantic Ocean coast (Kindl, 1979). The deposit is one of the major Pb and Zn producers in southern Africa and is operated underground by the Rosh Pinah Zinc Corporation (Pty) Ltd (RPZC). Description of the geology, stratigraphy and geochemistry of the Rosh Pinah mineralization are given by Page and Watson (1976), Van Vuuren (1986), Siegfried (1990), and Wartha and Genis (1992), Frimmel and Board (2000), Jasper et al. (2000), Alchin et al. (2005), Alchin and Moore (2005), Frimmel and Lane (2005). The deposit consists of several orebodies and the Mountain Orebody is the topographically highest mineralization at Rosh Pinah. The morphology of this orebody, i.e., a shallow plunging anticline outcropping to the southeast, was determined by a strong interaction of the ore with meteoric waters. Sulfides and the carbonate gangue were weathered under oxidizing and reducing conditions. The most oxidized ore has the appearance of a cellular, brick-coloured boxwork. It lies in the southwestern area and occurs between section 0 m and section 150 m, both as a horizon locally capping the sulfides, and intercalated within unaltered ore layers (Fig. 7.2A). The leached zones are diffused over the entire orebody and are controlled by areas of preexisting structural weakness (Siegfried, 1990).

Mining has removed much of the surface mineralization that was associated with black to yellow-brown gossans or wad. Although much of the gossan has been mined from the 'B0 orebody, good exposures still occur on the flanks of the open pit. Moderate stripping of the Rosh Pinah gossans on the steep flank of an inselberg has exposed much of the carbonate zone, which contains residual galena at surface (Siegfried, 1990). The most abundant mineral species detected in the gossan are: Fe-oxy-hydroxides, gypsum, cerussite, smithsonite, beudantite, hemimorphite, chrysocolla, azurite, barite and alunite-jarosite. The analyses of some of the most recent gossans showed relatively high amounts of pathfinder elements as Mn (~1000 ppm), Cu (~2000 ppm) and Ba (~5000 ppm), which point to less significant leaching associated with the current arid climate (Andrew, 1984).

Skorpion deposit

The Skorpion deposit (Vedanta Ltd.) is the 8th largest Zn mine in the world and represents a world-class integrated mining and refinery operation. The deposit is situated within the Port Nolloth Zone, in the so-called "Sperrgebiet" (special permit needed for access). The mineralization (21.4 Mt reserves at the beginning of the exploitation, grading 10.6% Zn) is an almost completely weathered shallow body (Fig. 7.2B), mainly

consisting of secondary Zn minerals including carbonates, oxides, phosphates and silicates.

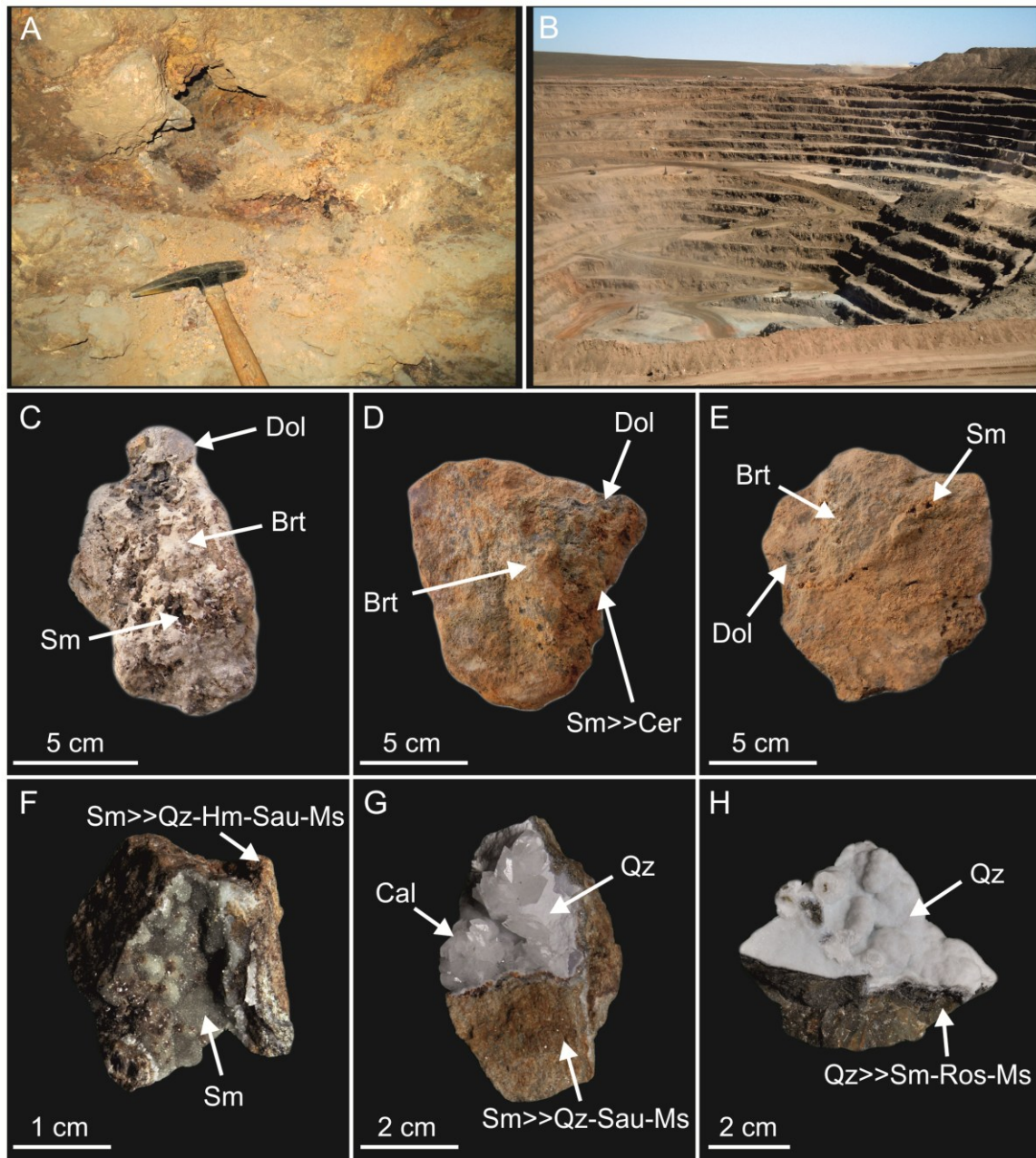


Figure 7.2. (A) Rosh Pinah: oxidation zone at the 400 level below the A Mine pit; (B) Overview of the Skorpion open pit (2015); (C) Rosh Pinah (sample RP8): barite (Brt) needles and smithsonite (Sm) crusts filling vugs in the dolomite (Dol) host rock; (D-E) Rosh Pinah (samples RP3 and RP5): smithsonite veinlets replacing together with barite and cerussite (Cer) the dolomite host rock; (F) Skorpion (sample 6_SK_JH): bothroidal smithsonite occurring as crust on a mixed lithology consisting of smithsonite, quartz (Qz), hemimorphite (Hm), sauconite (Sau) and muscovite (Ms); (G); Skorpion (19_SK_JH): smithsonite replacing host rock, covered by concretionary quartz, followed by euhedral calcite crystals; (H) Skorpion (sample 15_SK_JH): concretionary quartz on a mixture of smithsonite, rosasite (Ros) and muscovite.

The deposit cuts across the deeply weathered metavolcanic rocks of the Rosh Pinah Formation and of the carbonate rocks of the Hilda Subgroup. The Zn-oxidized minerals are mainly hosted by arkoses and subordinately by quartz-sericite schists of volcanic origin. Other rock types associated with the orebody include metamorphic limestones (marbles) and sheared volcanic siliciclastics; no dolomite host rock is known at Skorpion (Borg et al., 2003; Kärner, 2006).

The oxidized orebody is considered to have formed in a paleo-channel, after the supergene alteration of a sulfide-rich primary orebody similar to Rosh Pinah, situated west and underneath the current nonsulfide ores (Borg et al., 2003).

A small outcrop of a crudely banded barite/iron-hydroxide/quartz gossan west of Skorpion, the so-called “discovery outcrop” yielded anomalous metal values of 0.1 - 0.3 % Cu, 0.1 - 2.9 % Pb, 0.1 - 4.1 % Zn, 0.3 - 13.0 % Mn, and 2 - 50 ppm Ag (Kärner, 2006). In some parts of the gossan there is also evidence of strong chemical weathering with formation of kaolinite.

Major ore minerals in the nonsulfide zone at Skorpion include sauconite (the Zn-smectite), smithsonite and hemimorphite (Borg et al., 2003). Other occurring Zn minerals are tarbuttite, scholzite, chalcophanite, hydrozincite, skorpionite and hydrohetaerolite (Kärner, 2006). A new hydrated yttrium-erbium phosphate has been recently discovered and determined as churchite-Y (Y,Er)PO₄·2H₂O (Hinder, 2015).

The nonsulfide orebody at Skorpion is covered by a transported barren regolith, consisting of a surficial layer of wind-blown sand above a massive calcrete layer, below which alluvial interlayered gravels and conglomerates occur. These sediments have been deposited on a palaeo-erosional surface, cut through the host rocks of the Skorpion primary deposit (Kärner, 2006). This erosional discordance is most likely an equivalent of the “Namib Unconformity Surface” mentioned by Partridge and Maud (1987), and dated as Cretaceous-early Tertiary.

Materials and Methods

The study was conducted on 6 gossanous samples from the uppermost levels of the Rosh Pinah mine at the 400 level below the A Mine pit, and on 23 specimens from the Skorpion deposit. The Skorpion samples have been obtained mostly from private collections (A. Johr and G. Hinder) and in limited amount from the mine open pit during a fieldtrip in summer 2014. Before the samples were analysed for C- and O stable isotopes, a petrographic and mineralogical evaluation was carried out, in order to identify mineral textures and paragenesis.

The samples were cut in small slabs for the preparation of polished thin sections used for optical microscopy (OM) and scanning electron microscopy with energy dispersive X-ray spectroscopy (SEM-EDS). Some peculiar pieces of concretions, approximately 5 mm in length, were mounted on stubs using double-sided adhesive tape in order to obtain 3D BSE-SEM images. The remaining material was milled and grinded for mineralogical X-ray powder diffraction (XRPD).

SEM observations were performed on a JEOL JSM5310 at the Department of Earth,

Environment and Resources Sciences (DiSTAR), Università degli Studi di Napoli Federico II (Italy). The analytical conditions were: 20 mm objective lens to specimen working distance, 15 kV accelerating voltage with a tilt angle of 0°. Element mapping and qualitative energy dispersive (EDS) investigations were carried out with the INCA X-stream pulse processor and the 4.08 version Inca software (Oxford Instruments detector), interfaced with the Jeol JSM 5310. The following reference standards were used for quantitative microanalysis: albite (Si, Al, Na), orthoclase (K), wollastonite (Ca), diopside (Mg), almandine (Fe), rutile (Ti), barite (Ba), strontianite (Sr), eskolaite (Cr), rhodonite (Mn), pyrite (S), sphalerite (Zn), galena (Pb), pure silver (Ag), arsenopyrite (As), fluorite (F), apatite (P), sylvite (Cl), pure vanadium (V) and Corning glass (Th, U). Analytical errors are 1% rel. for major elements and 3% rel. for minor elements.

XRPD qualitative analyses were also carried out at DiSTAR, Università degli Studi di Napoli Federico II (Italy), using a Seifert-GE ID3003 diffractometer, with CuK α radiation, Ni-filtered at 40 kV and 30 mA, 3-80 °2 range, step scan 0.02°, time 10 s/step, and the RayfleX (GE) software package; a silicon wafer was used to check the instrumental setting. Sample holder was a zero-background plate of quartz crystal cut and polished 6° of the c-axis.

Stable isotope analyses were conducted at the University of Erlangen-Nuremberg (Germany). Pure carbonate minerals from Skorpion (SK) (16 smithsonites and 5 calcites) and Rosh Pinah (RP) (9 smithsonites and 8 dolomites from the host rock) were separated by handpicking from the bulk samples. The powdered minerals were allowed to react at least for 36 h with 103% phosphoric acid at 70 °C using a GasBench II connected to a ThermoFisher V Plus isotope ratio mass spectrometer. Carbon and oxygen isotope values are reported in per mil relative to Vienna Peedee belemnite (VPDB) and Vienna standard mean ocean water (VSMOW), respectively, by assigning $\delta^{13}\text{C}$ values of +1.95‰ to NBS19 and -46.6‰ to LSVEC and $\delta^{18}\text{O}$ values of -2.20‰ to NBS19 and -23.2‰ to NBS18. Reproducibility was checked by replicate analysis of laboratory standards and was better than $\pm 0.07\text{‰}$ (1 σ) for both carbon and oxygen isotope analyses.

We have used the following isotope fractionation equations to estimate the formation temperatures of smithsonite and calcite:

$$\begin{aligned} 1000 \ln \alpha_{\text{smithsonite-water}} &= 3.10 \cdot (10^6/T^2) - 3.50 & (1; \text{Gilg et al., 2008}) \\ 1000 \ln \alpha_{\text{calcite-water}} &= 2.78 \cdot (10^6/T^2) - 2.89 & (2; \text{O'Neil et al., 1969}) \end{aligned}$$

with T in degree Kelvin.

Oxygen isotope values of smithsonite and dolomite were corrected using the phosphoric acid fractionation factors given by Kim et al. (2007) for calcite, Rosenbaum and Sheppard (1986) for dolomite and Gilg et al. (2008) for smithsonite.

Results

The XRD results of the Skorpion and Rosh Pinah bulk samples used for isotope analyses are given in Table 7.1. The Skorpion specimens mainly consist of smithsonite, calcite, hemimorphite, goethite, and sauconite. Muscovite, quartz, orthoclase, apatite,

chalcophanite, rosasite, hinsdalite and Y-churchite were also detected. In the Rosh Pinah samples, dolomite (host rock) and smithsonite are the most abundant minerals. Traces of cerussite, barite, Ba-rich feldspar, muscovite and quartz are also present, together with ubiquitous goethite.

TABLE 7.1. Semiquantitative XRD analyses of the bulk samples of the Skorpion and Rosh Pinah deposits used for this study.

Sample ID	Dol	Cal	Sm	Cer	Qz	Or	Ms	Sau	Hm	Brt	Ap	Gth
Skorpion												
1_SK_JH	-	X	XXXXX	-	-	-	-	-	-	-	-	-
2_SK_JH	-	XX	XXXXX	-	-	-	-	-	-	-	-	-
3_SK_JH	-	XX	XXXXX	-	-	-	-	-	-	-	-	-
4_SK_JH	-	-	XXXXX	-	-	-	-	-	XXX	-	-	-
5_SK_JH	-	X	XXXX	-	XX	X	X	XX	XXX	-	-	-
6_SK_JH	-	XX	XXXX	-	-	XX	XX	XXX	XX	-	-	XX
8_SK_JH	-	XX	XXXXX	-	-	-	-	-	-	-	-	-
9_SK_JH	-	-	XXXX	-	XX	-	-	XX	XX	-	-	-
10_SK_JH	-	XX	XXXXX	-	-	-	-	-	-	-	-	-
13_SK_JH	-	XX	XXXXX	-	-	-	-	-	-	-	-	-
14_SK_JH	-	XX	XXXXX	-	-	-	-	-	-	-	-	-
18_SK_JH	-	XXXXX	XX	-	-	-	-	-	-	-	-	-
19_SK_JH	-	XXXX	XXXX	-	XXX	-	X	XXX	-	-	-	-
20_SK_JH	-	XXXXX	-	-	XX	-	-	X	-	-	-	-
21_SK_JH	-	XXXX	XXXX	-	XX	-	-	-	XX	-	-	-
22_SK_JH	-	XXXXX	-	-	XX	-	-	-	-	-	-	-
Rosh Pinah												
RP3	XXXX	-	XXX	XX	-	-	-	-	-	XX	-	-
RP4	XXXX	-	XXX	-	-	XX	-	-	-	XX	-	-
RP5	XXXXX	-	XXX	X	-	-	-	-	-	XX	-	-
RP6	XXXXX	-	XXX	X	-	-	X	-	-	-	-	-
RP7	XXXXX	-	XXX	-	-	X	-	-	-	-	-	XX
RP8	XXX	-	XX	-	XX	X	-	-	-	XXXX	X	X

Note: Dol = dolomite; Cal = calcite; Sm = smithsonite; Cer = cerussite; Ros = rosasite; Qz = quartz; Or = orthoclase; Ms = muscovite; Sau = sauconite; Hm = hemimorphite; Brt = barite; Ap = apatite; Gth = goethite; - = not detected (mineral abbreviations from Whitney and Evans, 2010). Mineral abundance inferred by XRD: x < 5 wt%; 5 wt% < xx < 20 wt%; 20 wt% < xxx < 40 wt%; 40 wt% < xxxx < 60 wt%; xxxxx > 60 wt%.

The macro-texture of the oxidized Rosh Pinah samples (Fig. 7.2C) consists of a mixture of brown, goethite-impregnated dolomite, with barite needles and secondary Zn minerals, where smithsonite is prevailing. Smithsonite also patchily replaces the dolomite host rock (Fig. 7.2D, E). In most cases remnants of botryoidal smithsonite, occurring mainly as cavities filling are covered by needle-shaped barite aggregates (Fig. 7.3A). A few (Mg)-smithsonite crystals are nearly rhombohedral (Fig. 7.3B). Smithsonite can occur also as replacement of the (Mn-Fe-Zn)-zoned host dolomite, together with barite and cerussite veinlets cross-cutting the same host rock (Fig. 7.3C, D).

The Skorpion samples consist of concretions of smithsonite, calcite and quartz (Fig. 7.2F,

G, H). Smithsonite (Sm2), which occurs in pseudocolloidal or microcrystalline form with colours ranging from blue-green to white, represents the first mineral to be precipitated in small cavities or as crusts. However, smithsonite occurs also as replacement of the host rock (Sm1), as small, delicate crystals associated with hemimorphite (Fig. 7.3E), or as perfectly rhombohedral crystals covered by microcrystalline quartz (Fig. 7.3F). Calcite (Cal) follows smithsonite in the supergene paragenesis (Fig. 7.2G): it is always crystalline, white and with a rhombohedral shape.

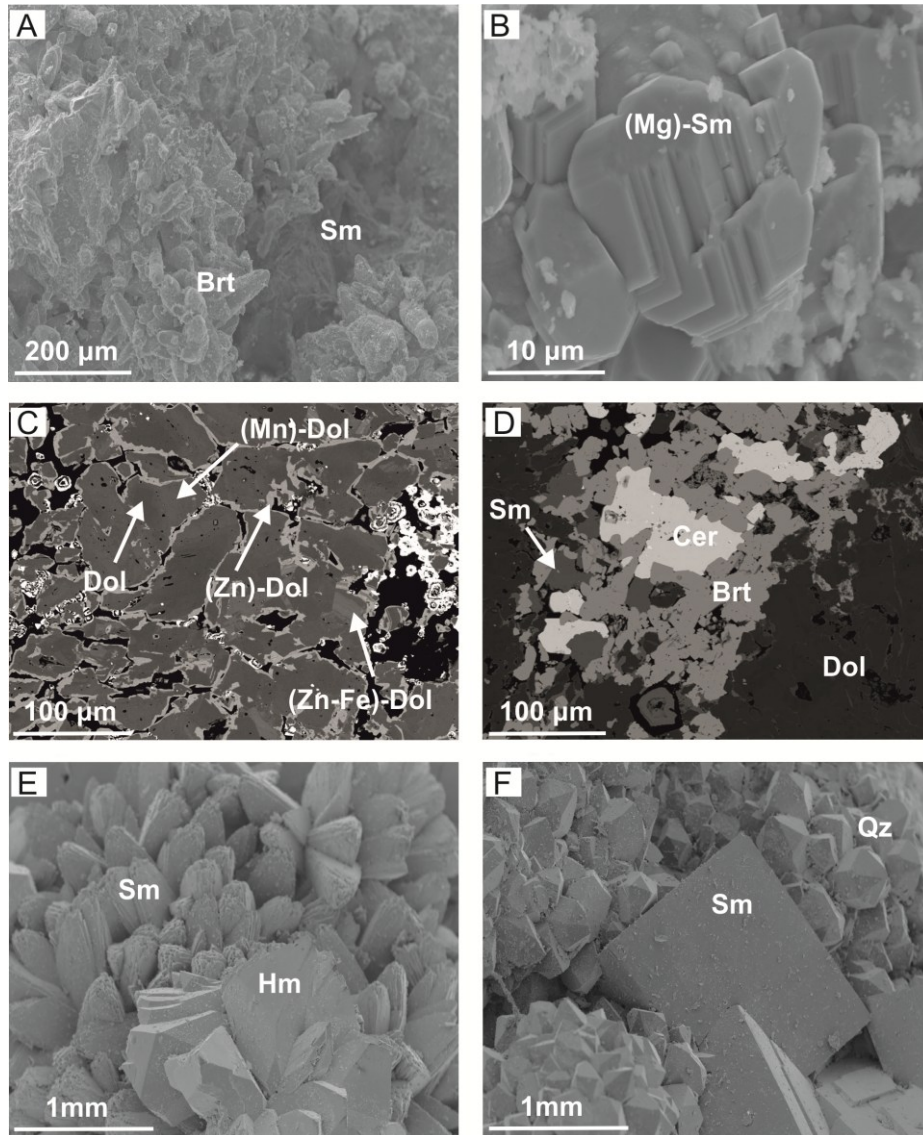


Figure 7.3. Secondary and backscattered electron images of ore and gangue minerals from Skorpion and Rosh Pinah. (A) Rosh Pinah (sample RP4): smithsonite filling a cavity between needle-shaped barite aggregates; (B) Rosh Pinah (sample RP4): Mg-bearing smithsonite in form of nearly rhombohedral crystals; (C,D) Rosh Pinah (samples RP5 and RP3): smithsonite replacing the (Mn-Fe-Zn)-zoned host dolomite, together with barite and cerussite in veinlets; (E) Skorpion (sample 6_SK_JH): crystals of smithsonite growing together with hemimorphite laths; (F) Skorpion (12_SK_JH): rhombohedral crystals of smithsonite associated with bothroids of microcrystalline quartz.

Most Skorpion smithsonites are stoichiometric in composition, but others contain variable amounts of minor and trace elements, as Mg, Fe, Pb and Cu. Smithsonites at Rosh Pinah have significant contents of Fe, Mg and Cu, compared with the Skorpion ones (Table 7.2).

For carbon and oxygen isotope analyses of Skorpion carbonates, we selected 16 botryoidal-colloform (Sm2) and host rock-replacing smithsonite (Sm1) specimens and 5 calcite crystalline agglomerates, which texturally overgrew botryoidal smithsonite. For the Rosh Pinah mine, we chose 9 host rock-replacive smithsonites (Sm1) and 8 dolomites (Dol) from the same host rocks.

TABLE 7.2. Selected chemical composition of smithsonite from Skorpion and Rosh Pinah (SEM-EDS).

Sample ID	Skorpion			Rosh Pinah		
	4_SK_JH	6_SK_JH	7_SK_JH	RP3	RP6	RP6
wt. %						
FeO	0.17	0.35	0.19	-	2.87	0.71
MnO	0.07	-	0.16	0.63	0.47	0.41
MgO	1.95	0.35	0.43	1.80	2.38	2.58
CaO	0.43	0.33	0.19	0.48	0.46	0.49
PbO	-	-	-	1.88	0.46	0.35
ZnO	61.37	61.78	63.26	60.35	55.45	56.99
CuO	-	-	-	-	1.00	1.41
CdO	-	-	0.67	0.34	0.14	0.27
CO ₂ *	35.80	34.25	35.27	35.84	35.68	35.63
Total	99.79	97.06	100.17	101.32	98.93	98.83
on the basis of XCO ₃ (apfu)						
Fe	0.00	0.01	0.00	-	0.05	0.01
Mn	0.00	-	0.00	0.01	0.01	0.01
Mg	0.06	0.01	0.01	0.05	0.07	0.08
Ca	0.01	0.01	0.00	0.01	0.01	0.01
Pb	-	-	-	0.01	0.00	0.00
Zn	0.93	0.98	0.97	0.91	0.84	0.86
Cu	-	-	-	-	0.02	0.02
Cd	-	-	0.01	0.00	0.00	0.00
CO ₃	1.00	1.00	1.00	1.00	1.00	1.00

Note: * Calculated from stoichiometry; - not determined

Skorpion host rock-replacive (Sm1) and botryoidal (Sm2) smithsonites have similar carbon and oxygen isotopic compositions (Fig. 7.4). They are characterized by $\delta^{13}\text{C}$ values varying between -9.1‰ and 0.1‰ VPDB and $\delta^{18}\text{O}$ values between 28.0 to 29.9‰ VSMOW; botryoidal and host rock-replacing smithsonite are slightly different isotopically one from another (Table 7.3, Fig. 7.4). Calcite shows a minor variation in $\delta^{13}\text{C}$ with values ranging from 0 to 1.6‰ VPDB. The $\delta^{18}\text{O}$ values of calcite are between 25.4 and 27.1‰ VSMOW, and thus slightly lower than the $\delta^{18}\text{O}$ values of smithsonite (Fig. 7.4).

The Rosh Pinah smithsonites have $\delta^{13}\text{C}$ values between -2.8 and -1.9‰ VPDB, thus showing a smaller variability compared to the Skorpion smithsonites (Fig. 7.4). The $\delta^{18}\text{O}$ values range from 26.7 to 29.0‰ VSMOW, and are on average close to the $\delta^{18}\text{O}$ values of smithsonites from Skorpion. The host dolomite at Rosh Pinah is characterized by $\delta^{18}\text{O}$ values ranging from 18.7 to 22.0‰ VSMOW and by $\delta^{13}\text{C}$ values of -5.9 to -2.2‰ VPDB (Fig. 7.4).

TABLE 7.3. Carbon and oxygen isotope compositions of smithsonite and calcite from Skorpion, and smithsonite and dolomite from Rosh Pinah.

Sample ID	Analyzed material ID	Mineral phase	$\delta^{13}\text{C}$ (‰ VPDB)	$\delta^{18}\text{O}$ (‰ VSMOW)
Skorpion				
1_SK_JH	1	Sm2	-3.07	28.58
2_SK_JH	2HR	Sm1	-9.14	27.86
	2	Sm2	-7.37	28.31
3_SK_JH	3	Sm2	-8.62	27.99
4_SK_JH	4	Sm2	-2.63	28.72
5_SK_JH	5HR	Sm1	0.13	28.50
	5	Sm2	-2.10	28.71
6_SK_JH	6HR	Sm1	-8.37	28.17
	6	Sm2	-7.50	28.56
8_SK_JH	8	Sm2	-1.74	29.94
9_SK_JH	9HR	Sm1	-2.49	28.60
	9	Sm2	-2.04	29.16
10_SK_JH	10	Sm2	-0.43	29.27
13_SK_JH	13	Sm2	-2.19	29.25
14_SK_JH	14	Sm2	-5.51	28.51
18_SK_JH	18	Cal	1.55	25.83
19_SK_JH	19HR	Sm1	-7.10	27.96
	19	Cal	0.32	27.05
20_SK_JH	20	Cal	-0.02	25.80
21_SK_JH	21	Cal	0.72	26.55
22_SK_JH	22	Cal	0.72	25.39
Rosh Pinah				
RP3	RP3_DA	Dol	-3.42	21.94
	RP3_DB	Dol	-2.73	21.03
	RP3_S	Sm1	-2.61	27.22
RP4	RP4_D	Dol	-4.09	21.98
	RP4_SA	Sm1	-2.05	27.98
	RP4_SB	Sm1	-2.74	28.85
	RP4_SC	Sm1	-2.81	28.87
RP5	RP5_DA	Dol	-3.58	21.90
	RP5_DB	Dol	-2.15	22.09

Note: Sm1 = host rock-replacing smithsonite; Sm2 = botryoidal smithsonite; Cal = vuggy rhombohedral crystals; Dol = host rock-forming dolomite.

TABLE 7.3. Continue....

RP6	RP6_DA	Dol	-3.97	21.49
	RP6_DB	Dol	-4.50	20.77
	RP6_S	Sm1	-2.79	26.73
RP7	RP7_D	Dol	-5.87	18.68
	RP7_SA	Sm1	-1.92	28.88
	RP7_SB	Sm1	-2.18	27.50
RP8	RP8_SA	Sm1	-2.51	28.27
	RP8_SB	Sm1	-2.20	28.99

Note: Sm1 = host rock-replacing smithsonite; Sm2 = botryoidal smithsonite; Cal = vuggy rhombohedral crystals; Dol = host rock-forming dolomite.

Discussion

From textural observations as well as the data reported in previous papers (Borg et al., 2003; Kärner, 2006), there are several evidences that the smithsonite formed in a supergene environment and therefore at relatively low temperatures. We can affirm the same for Skorpion calcite. For example, the felsic metavolcanic rocks hosting the hypogene sulfide mineralisation at Skorpion show supergene alteration and the occurrence of extensive gossanous zones, which are above and lateral to the nonsulfide mineral concentrations (Kärner, 2006). The same can be observed in the highest parts of the Rosh Pinah ore deposit. Moreover, calcite and smithsonite in both deposits are commonly represented by delicate, undeformed, euhedral to subhedral crystals, typical of a low-temperature and low-pressure environment, with textures that are uncommon under high-temperature hydrothermal conditions (Kärner, 2006).

The $\delta^{13}\text{C}$ data of the Rosh Pinah host dolostone determined in this study differ significantly from those reported by Siegfried (1990), who found heavier $\delta^{13}\text{C}$ values (4.2 and 7.7‰ VPDB) in both dolostone and limestone from the hanging wall of the deposit, but are very similar to the values reported by Frimmel and Board (2000) for the lower part of the Pickelhaube Formation (Fig. 7.4), which is an analogue of the Rosh Pinah Formation. The partial overlap between the $\delta^{13}\text{C}$ of smithsonite (-2.8 to -1.9‰ VPDB) and the composition of several host dolomite samples (-5.9 to -2.2‰ VPDB), points to a major contribution of host rock carbon and only a minor influence of isotopically light oxidized organic carbon during smithsonite formation.

The carbon isotope values of smithsonite from Skorpion are relatively comparable to those reported by Borg et al. (2003) and Kärner (2006). The $\delta^{13}\text{C}$ compositions mentioned in the above papers (-8.0 and -4.0 ‰ VPDB) have a smaller variability in comparison with the ratios obtained in this study (-9.1 and 0.1 ‰ VPDB); however, mean values are nearly identical. Carbon isotope analyses carried out by Kärner (2006) on the marbles hosting part of the Skorpion deposit exhibit $\delta^{13}\text{C}$ values of 5.8 and 8.1 ‰ VPDB, which are relatively high when compared with the $\delta^{13}\text{C}$ ratios measured on the Skorpion smithsonites (-9.1 to 0.1 ‰ VPDB, this work). This difference suggests that the contribution of bicarbonate from the oxidation of isotopically light organic carbon during the precipitation of smithsonite was higher than the carbon contribution from the host

rock. The organic carbon could have originated from the graphitic metapelites that are part of the host rocks (Borg et al., 2003), or from Mesozoic/Tertiary sediments/soils rich in organic carbon.

The $\delta^{13}\text{C}$ values of Skorpion calcite (0 to 1.6‰ VPDB) are intermediate between the $\delta^{13}\text{C}$ composition of the host rock and the lower $\delta^{13}\text{C}$ values of smithsonite. For example, in sample 19_SK_JH smithsonite has a $\delta^{13}\text{C}$ composition of -7.1‰ VPDB, whereas the paragenetically younger calcite from the same sample has a value of 0.3‰ VPDB (Table 7.3). This wide difference probably indicates that calcite and smithsonite precipitated during different times from fluids with different carbon isotopic compositions. Moreover, considering the isotopic composition of the host rock, it is likely that calcite carbon represents a mixture of both unidentified isotopically light organic carbon and inorganic carbon from the host marbles.

Previously published $\delta^{18}\text{O}$ data (Borg et al., 2003; Kärner, 2006) for Skorpion smithsonite show a minor variation (27.3 to 28.1‰ VSMOW), with the values being on average lower than those measured in this study (27.9 and 29.9‰ VSMOW). The $\delta^{18}\text{O}$ values of the Rosh Pinah smithsonite (26.7 to 29.0‰ VSMOW) are on average close to the $\delta^{18}\text{O}$ values of Skorpion smithsonite (27.9 and 29.9‰ VSMOW, this study).

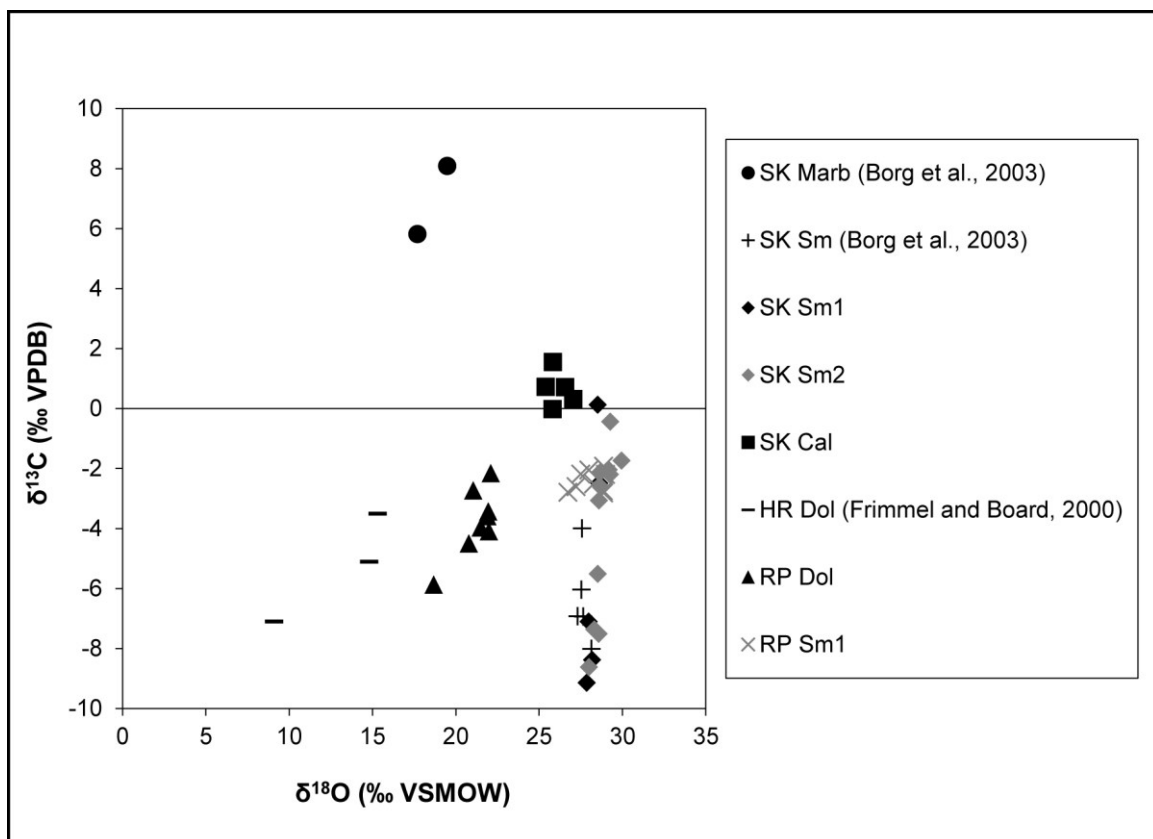


Figure 7.4. $\delta^{13}\text{C}$ vs. $\delta^{18}\text{O}$ compositions of carbonate minerals from Skorpion and Rosh Pinah: Skorpion (Borg et al., 2003) - marble (SK Marb), smithsonite (SK Sm); Skorpion (this study) host rock-replacive smithsonite (SK Sm1), botryoidal smithsonite (SK Sm2), calcite (SK Cal); Rosh Pinah (Frimmel and Board, 2000) - host rock dolomite (HR Dol); Rosh Pinah (this study) - host-rock replacive smithsonite (RP Sm1) and host rock dolomite (RP Dol).

The $\delta^{18}\text{O}$ of carbonate minerals can be used to constrain the temperature or the isotopic composition of the precipitating fluids. Oxygen isotope data for paleogroundwaters or paleometeoric waters, from which the supergene carbonate minerals in the Skorpion and Rosh Pinah deposits should have precipitated, are not available. However, assuming a long-term tectonic and climatic stability in the area, it seems reasonable to assume that the oxygen isotope composition of paleogroundwater was not very different from modern groundwaters. To estimate the formation temperature of Skorpion smithsonite, Kärner (2006) and Gilg et al. (2008) used a $\delta^{18}\text{O}$ value of -6‰ VSMOW, which corresponds to the composition of modern groundwater in the Lüderitz area (Dachroth and Sonntag, 1983). With this assumption, a precipitation temperature of $\sim 17^\circ\text{C}$ was calculated for the Skorpion smithsonites. A more recent study of West et al. (2014) on the isotopic composition of the modern groundwaters across southern Africa, reported $\delta^{18}\text{O}$ values between -5.2 and -4.0 ‰ VSMOW for the Northern Cape area, which is relatively close to the Skorpion-Rosh Pinah district. Moreover, after Kaseke et al. (2016), the oxygen isotope composition of recent precipitation in southern Namibia varies between -5 and -4‰ VSMOW.

Using minimum and maximum $\delta^{18}\text{O}$ values for meteoric waters of -6 ‰ VSMOW (Dachroth and Sonntag, 1983) and -4 ‰ VSMOW (West et al., 2014), formation temperatures have been calculated for smithsonite in both deposits. Considering mean $\delta^{18}\text{O}$ values of 28.6 VSMOW for the smithsonite from Skorpion, their formation temperatures are between 13.6 and 21.5°C (Fig. 7.5A).

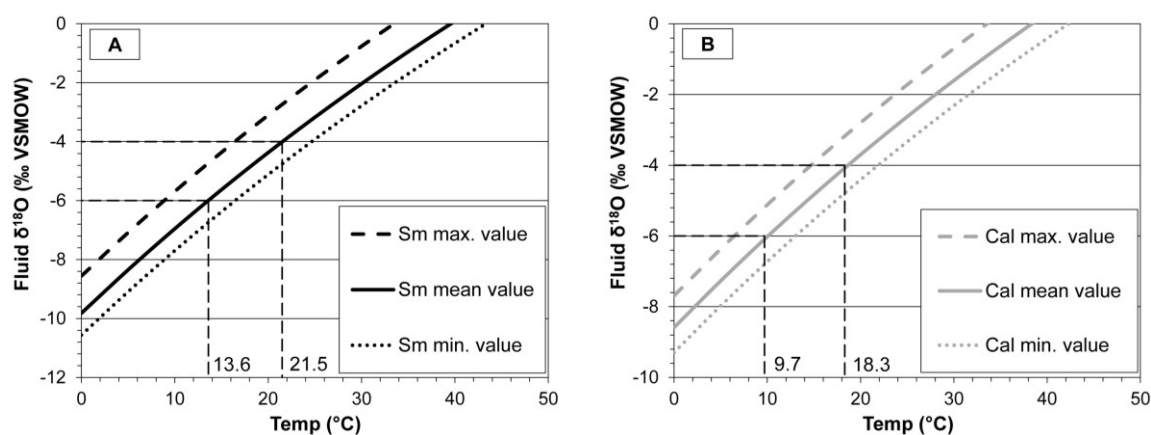


Figure. 7.5. Oxygen isotope equilibrium curves for Skorpion smithsonite (A) according to Gilg et al. (2008) and Skorpion calcite (B) according to O'Neil et al. (1969). Dotted black line represents minimum $\delta^{18}\text{O}$ values of smithsonite (28.0‰ VSMOW) and dotted gray line of calcite (25.4‰ VSMOW), dashed black line represents maximum $\delta^{18}\text{O}$ values of smithsonite (29.9‰ VSMOW) and dashed gray line of calcite (27.1‰ VSMOW) measured in this study. Solid black line indicates mean $\delta^{18}\text{O}$ value of smithsonite, and solid gray line of calcite (VSMOW-Vienna standard mean ocean water). The $\delta^{18}\text{O}$ for the fluid was assumed in both cases to have been between -4 and -6‰ VSMOW (Dachroth and Sonntag, 1983; West et al., 2014).

Then considering a mean value of 28.1‰ VSMOW for Rosh Pinah smithsonites, precipitation temperatures between 15.4 and 23.5°C have been obtained for these

carbonates. These temperatures are partly compatible with modern mean atmospheric temperature of 15-16 °C, measured in the southern coastal area of Namibia by Kaseke et al. (2016).

If we use the same minimum and maximum $\delta^{18}\text{O}$ values for meteoric waters of -6 ‰ VSMOW and -4 ‰ VSMOW to calculate the temperature of Skorpion calcite, the resulting interval is between 9.7 and 18.3 °C. However, this calcite has a carbon isotope composition much more positive than smithsonite. Taking the $\delta^{18}\text{O}$ composition of smithsonite and calcite and assuming a realistic temperature range (Fig. 7.5), it becomes obvious that the fluids widely overlap in their $\delta^{18}\text{O}$ composition. Thus, we argue that both smithsonite and calcite formed in meteoric waters with a comparable oxygen isotopic composition.

The uplift of the Skorpion sulfide protore to a near surface environment and the beginning of weathering can be dated as Late Cretaceous (Kärner, 2006). Weathering was most intense during the Palaeocene and Eocene when climate changed from humid to semi-arid. Additionally, during this long-lasting period, the minerals that were initially formed under a humid climate, e.g. hemimorphite and smithsonite, were progressively replaced by minerals more stable under semi-arid conditions, e.g. sauconite and hydrozincite (Kärner, 2006). In fact, smithsonite formation generally needs a minimum $\log P_{\text{CO}_2(\text{g})} = 0.4$ kPa (Takahashi, 1960; Reichert and Borg, 2008) and forms in a weathering profile preferentially at deeper levels than hydrozincite, or coexists with the latter at near-surface levels, when the soil is water-saturated. Particularly, in arid soils, where the $P_{\text{CO}_2(\text{g})}$ is lower compared to those of humid regions, hydrozincite is more stable than smithsonite. On the other hand, hemimorphite precipitation is favoured at near-surface conditions in comparison with other supergene zinc minerals (e.g. smithsonite and hydrozincite) if $\text{pH} < 7$ and SiO_2 is available. Hydrozincite can also easily replace hemimorphite in a near surface environment following slight variation of the $P_{\text{CO}_2(\text{g})}$, due to their similar stability fields (Takahashi, 1960). A temporary switch from semi-arid to again sub-tropical/semi-humid climate during the Early-Middle Miocene accompanied by a renewed uplift (Burke et al., 2004) may have induced (i) a remobilization of the metals and the precipitation of late “humid” minerals, including kaolinite in the Skorpion gossan, (ii) a partial erosion of the upper part of the Skorpion orebody and (iii) the deposition of boulder beds and fluvial sands over the Skorpion deposit. Karstification of the exposed marble host rock was also associated with this uplift (Kärner, 2006). After this stage, the climate evolved to arid conditions, as testified by calcrete deposits occurring at the top of Miocene fluvial beds. The Pliocene was characterized by an arid climate and normal faulting in the Skorpion-Rosh Pinah area, as testified by red eolian sands covering faulted Miocene sediments (Kärner, 2006). However, the age of the formation of the different mineral phases in both deposits, and especially the age of the main nonsulfides is still uncertain. In order to date the Skorpion weathering phases and related supergene mineralization, the mineral tarbuttite, which is a ubiquitous constituent of the supergene deposit was analysed using the U-Th/He method. Tarbuttite ages revealed a bimodal distribution with maxima at around 50 and 85 Ma, suggesting that Zn-phosphate precipitated during several distinct time intervals between

the Cretaceous and Eocene (Evans et al., 2006). In an unpublished report, Gutzmer (2006) mentioned that Ar-Ar step heating age of the K-bearing mineral romanechite $[(\text{Ba}, \text{H}_2\text{O})_2(\text{Mn}^{+4}, \text{Mn}^{+3})_5\text{O}_{10}]$, sampled in the gossanous upper part of the Skorpion deposit yielded two age clusters referring to late Eocene and middle Miocene.

At Rosh Pinah, smithsonite occurs in the upper levels of the supergene profile and is associated with cerussite. Since Pb is less mobile than Zn, it moves not so far from its original position within the sulfide protore (Hitzman et al., 2003). Therefore, the occurrence of cerussite in the more weathered part of the Rosh Pinah deposit indicates an in situ oxidation in the upper part of the orebody, and would exclude a long lasting leaching process of the sulfides, as it probably occurred at Skorpion.

Integrating the stable isotope data obtained for smithsonite and calcite of Skorpion and for smithsonite at Rosh Pinah with the paleogeomorphological and paleoclimatic evolution of the area as reported in earlier studies, we argue that:

- both the early host rock-replacive smithsonite (Sm1) and the late botryoidal smithsonite (Sm2) were precipitated at comparable temperatures (Fig. 7.4) from fluids depleted in ^{13}C due the remineralisation of organic carbon in soil horizons, either during the Late Cretaceous-Paleocene or early-middle Miocene humid phases. This interpretation is in accord with Kärner (2006), who associated smithsonite formation at Skorpion with more humid climate periods and thick soils overlying the deposit.
- Skorpion calcite (Cal), which precipitated after smithsonite from a host rock bicarbonate-rich fluid, probably formed at a later stage (late Miocene?), when the host marbles were uplifted, karstified and groundwater bicarbonate was dominated by host rock carbonate.
- the similarity of the $\delta^{18}\text{O}$ values of Rosh Pinah and Skorpion smithsonites points to similar ore-forming fluids and/or similar temperature conditions during formation. However, the higher $\delta^{13}\text{C}$ values of Rosh Pinah smithsonite indicate the absence of soils over the deposit at the time of weathering. Considering the limited thickness of the supergene zone over the Rosh Pinah orebody and the occurrence of cerussite, we argue that the weathering processes in this area were active on a shorter period of time, and that smithsonite was not stable in a near-surface environment unless the soil was water-saturated. Consequently, it is likely that Rosh Pinah smithsonite formed at the end of the last semi-humid period (early-middle Miocene). Probably late Miocene aridity and the following Pliocene normal faulting created conditions that were unfavourable (i.e. the deepening of the groundwater table and uplift of the Rosh Pinah orebody over the nearby alluvial plain) for the development of a long-term steady weathering profile.

Thus, supergene alteration resulting in the Skorpion nonsulfide deposit as well as oxidation of the upper parts of the Rosh Pinah sulfide ores probably ended by the late Miocene. Other sulfide, Fe- and Mn-deposits in southern Africa underwent post-Gondwanan supergene enrichments. In fact, we already know that most vanadium ores in Namibia and Zambia (Boni et al., 2007) are related to the formation of the “African erosion surface”. Descloizite (a Zn-plumbo-vanadate) (U-Th)/He ages from several North

Namibia prospects (Otavi Mountainland) range from 60 to 40 Ma, with a weighted mean of 51.1 ± 1.7 Ma (Boni et al., 2007). These ages point to an Early Tertiary period of formation, when climatic conditions must have been firstly humid to allow deep chemical weathering and lateritisation of V-containing Proterozoic volcano-sedimentary successions, followed by semi-arid conditions to favour the precipitation of secondary vanadates. A comparable scenario can be assumed for the Tertiary manganese enrichments in South Africa that have been reported by Van Niekerk et al. (1999).

Conclusions

The area of the Gariep belt, where both Skorpion and Rosh Pinah deposits are located, experienced marked climate changes from Cretaceous onward, most likely from humid-tropical to semi-arid and arid conditions. These climate changes controlled the formation and the nature of the supergene enrichment profiles. The results of this study allow a better characterization of the deep oxidation process that occurred at Skorpion, in comparison with the limited weathering and production of a gossan, typical for the Rosh Pinah deposit. While the comparable oxygen isotope compositions of smithsonite from the two deposits imply similar (meteoric) ore-forming fluids and/or similar temperature conditions during formation of the nonsulfide minerals, the $\delta^{13}\text{C}$ values indicate distinct carbon sources related to a different environmental setting during the formation of Skorpion and Rosh Pinah ore deposits.

In agreement with Kärner (2006), we suggest that Skorpion smithsonite precipitated at an average temperature of 17°C from fluids depleted in ^{13}C , either during the first (Late Cretaceous-Paleocene) or last humid climate phase (early-middle Miocene). Skorpion calcite, which precipitated after smithsonite from a more host rock-buffered system, probably formed during the Miocene, when the host marbles were uplifted, karstified and the groundwater was dominated by bicarbonate from dissolving host rock. The textural relationships between calcite and the other minerals in the deposits suggest that calcite formed at the beginning of the last late Miocene-Pliocene semi-arid period from a fluid whose temperatures ranged from 9.7 to 18.3°C .

Even if the similarity between the $\delta^{18}\text{O}$ composition of Rosh Pinah and Skorpion smithsonite points to similar ore-forming fluids and/or similar conditions during formation, the higher $\delta^{13}\text{C}$ values of the Rosh Pinah smithsonite indicate the absence of an organic carbon-rich soil horizon over this deposit. Combining these data with the limited thickness of the supergene zone over the Rosh Pinah orebody (short-term weathering processes active in this area), it is likely that Rosh Pinah smithsonite, together with the gossan in which it occurs, formed at the end of the early-middle Miocene semi-humid period.

Chapter 8:

Zn-clay minerals in the Skorpion Zn nonsulfide deposit (Namibia): identification and genetic clues revealed by HRTEM and AEM study

Published in “Applied Clay Sciences”

Reference: Balassone, G., Nieto, F., Arfè, G., Boni, M., Mondillo, N., 2017. Zn-clay minerals in the Skorpion Zn nonsulfide deposit (Namibia): Identification and genetic clues revealed by HRTEM and AEM study. Applied Clay Sciences, 150, 309-322.

Introduction

Zn-clays occur in various supergene nonsulfide ores worldwide. In these ores, mainly deriving from the weathering of primary sulfide concentrations, the Zn-clays can be the prevailing economic minerals, or represent minor concentrations in the mineral assemblage (Arfè et al., 2017a; Balassone et al., 2008; Boland et al., 2003; Boni et al., 2009a; Boni and Mondillo, 2015; Borg et al., 2003; Buatier et al., 2016; Choulet et al., 2016; Coppola et al., 2008; Emselle et al., 2005; Frondel, 1972; Hye In Ahn, 2010; Kärner, 2006; Mondillo et al., 2014b, 2015). Zn-clay minerals, formed in slightly acidic to neutral conditions, are also commonly found in contaminated soils at mining and smelting sites (i.e. Manceau et al., 2000; Juillot et al., 2003).

Sauconite (Ross, 1946; Newman and Brown, 1987), which is one of the most common clay minerals in nonsulfide deposits, is a trioctahedral saponite-like smectite with Zn in octahedral coordination. Experimental studies on its synthesis and stability (i.e. Higashi et al. 2002; Klopogge et al. 1999; Pascua et al. 2010; Petit et al. 2008) demonstrated that this Zn-smectite can precipitate from solutions of silicic acid, variously mixed with Zn-compounds (Zn-chloride, Zn-oxide, or Zn-hydroxide) and Na- and Al-compounds, at pH interval of 6-12 and temperatures ranging between 20 and 200 °C.

Among the other Zn-“clay” phases found in nonsulfide ore deposits, we should mention fraipontite (a serpentine-like Zn-clay mineral, Fransolet and Bourguignon, 1975) and baileychlore (a Zn-chlorite, Rule and Radke, 1988). Recently Kaufhold et al. (2015) characterized Zn-smectites from the Silver Coin Mine (USA), while Choulet et al. (2016) and Buatier et al. (2016) have described Zn-clays consisting of interstratified fraipontite/smectite (fraipontite-prevailing), closely associated to willemite in several nonsulfide Zn deposits in the Moroccan High Atlas, which formed by direct precipitation of meteoric and/or hydrothermal fluids. With the increasing quest of mineral resources (and the rising Zn price), mining industries must deal with the complex issues related to the extraction and processing of low grade and/or finely disseminated ores. Clay minerals, including Zn-clays that have been detected in several deposits, can affect the industrial treatment to a various extent (Choulet et al., 2016 and references therein). Hence, their detailed mineralogical study, as well as the investigation of their

crystallization and post-crystallization processes can provide crucial geological information, particularly useful from the perspective of industrial and economic evaluations.

One of the best examples of Zn smectite-rich supergene orebody is the world-class Skorpion mine (Namibia, Vedanta Ltd.) (21.4 Mt ore reserves at the beginning of the exploitation, grading 10.6% Zn). The Skorpion base metals deposit is considered to have been an equivalent of the Rosh Pinah massive sulfides concentration that was subjected to weathering processes, started after the end of the pan-African tectonic phase (Kärner, 2006). The pan-African phase was followed by uplift and denudation, and concluded with the onset of a strong arid period that had its first maximum in Oligocene (Borg et al., 2003; Kärner, 2006; Arfè et al., 2017a). At Skorpion, the trioctahedral Zn-bearing smectite (sauconite) predominates over the other Zn-oxidized minerals (Borg et al., 2003; Kärner, 2006).

The chemical and structural features of sauconite from Skorpion have never examined in detail before; hence, the present research is focused on microtextural observation and chemical analyses on the clay fraction of the supergene nonsulfide ores, carried out for the first time using TEM-STEM and HRTEM investigations. This approach by means of transmission electron microscopy, coupled with high-resolution observations, integrated with other mineralogical and geochemical analyses, allows the investigation of clay textures down to the nanoscale, and consequently a better understanding of their genesis.

Geology of the Skorpion zinc deposit area

The Skorpion zinc deposit (Fig. 8.1A) is hosted by metamorphosed volcano-sedimentary rocks of the Port Nolloth Zone (PNZ), within the late Proterozoic Gariep Belt (Borg et al., 2003). This belt is subdivided into an eastern para-autochthonous zone, the PNZ, and a western allochthonous zone, the Marmora Terrane. The Gariep Belt is regarded as the southern extension of the Damara orogenic front of central and northern Namibia (Davies and Coward, 1982; Reid et al., 1991; Stanistreet et al., 1991; Gresse, 1994; Frimmel, 2000; Jasper et al., 2000; Frimmel et al., 2002). The rocks of the PNZ contain stratiform Zn-Pb-Cu-Ag-(±Ba)-sulfide mineralization in sedimentary and felsic metavolcanic rocks. The best examples are the Rosh Pinah Pb-Zn (Page and Watson, 1976; van Vuuren, 1986; Alchin and Moore, 2005) and the Skorpion Zn-(Cu) deposits (Borg et al., 2003; Kärner, 2006), which were attributed to either the Volcanic-hosted Massive Sulfides (VHMS) or Sedimentary-hosted Massive Sulfides (SHMS) types. The mineral concentrations were formed in an extensional environment during a phase of increased volcanogenic-hydrothermal activity between 740 and 754 Ma (Borg and Armstrong, 2002). The deformation of the ore-bearing units (due to the pan-African tectonic phase) took place during continental collision that produced the closure of the Adamastor oceanic basin 545 million years ago (Alchin and Moore, 2005). The sedimentary and bimodal volcanic rocks hosting the mineralization have been strongly folded, faulted and overprinted by a lower amphibolite facies metamorphism (Frimmel et al., 1995).

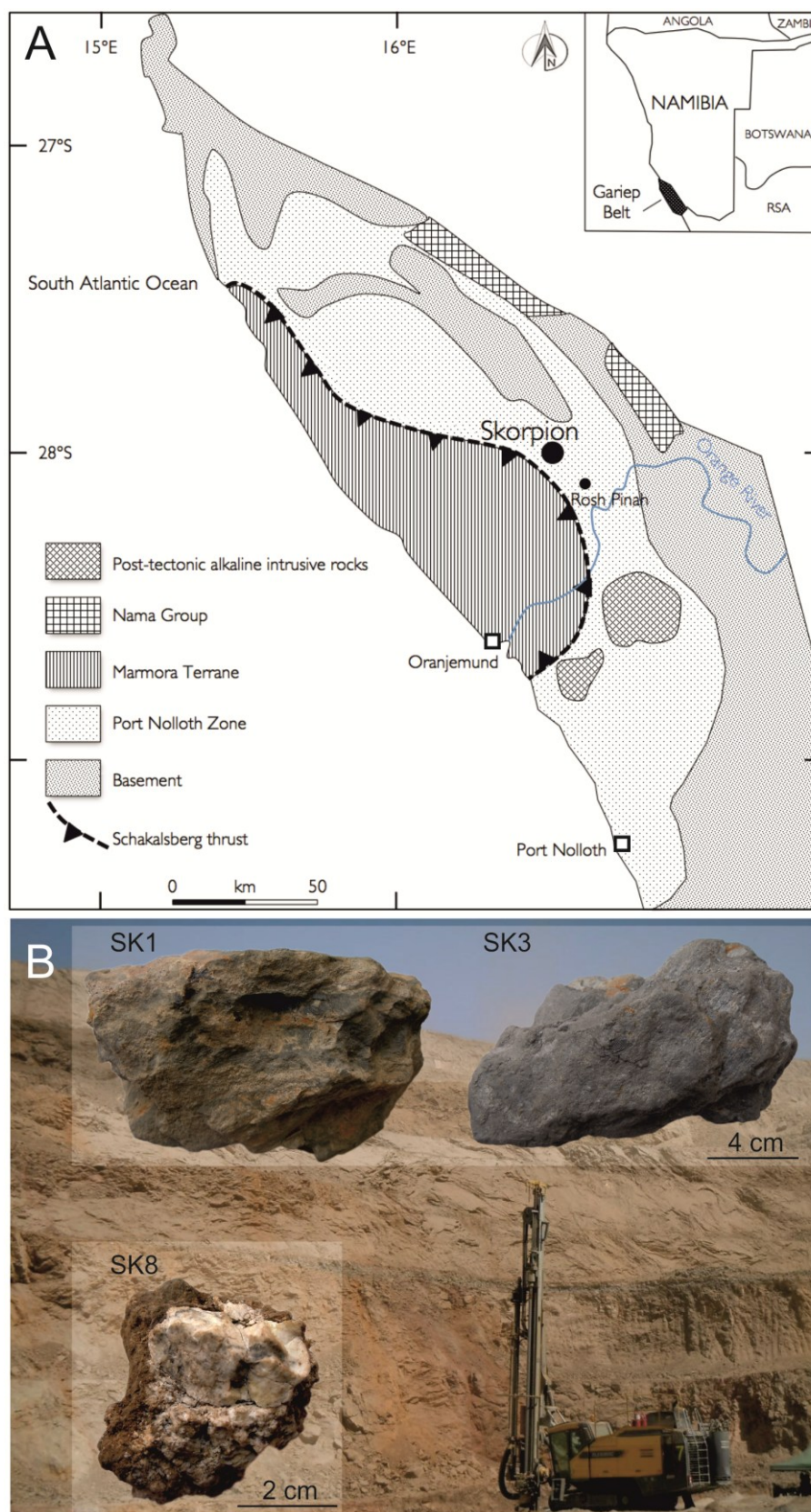


Figure 8.1. (A) Schematic geological map of southern Namibia (modified after Borg et al. 2003 and references therein), with location of the Skorpion deposit in the Gariep belt area. (B) The Skorpion open pit at the date of the sampling (2014), with the samples investigated in this study (see text).

Exhaustive summaries about the geomorphological evolution of southern Africa and Namibia, including the Gariep Belt, which took place after the pan-African tectonic phase (King, 1951), have been presented by Partridge and Maud (1987) and Partridge (1998). The maximum peneplanation, coupled with intense lateritic weathering, causing also part of the Skorpion supergene mineralization, was reached between Late Cretaceous and Oligocene. During Late Cretaceous-Eocene, a denudation event eroded a 3 km-thick section of southern Africa and Namibia, reaching several hundred km inland and producing the so-called “African Erosion Surface” (Gallagher and Brown, 1999). This surface was then rejuvenated and intersected by younger erosion planes, related to discrete uplifts that took place in early Miocene and Pliocene (Partridge and Maud, 1987).

The Skorpion deposit cuts across the deeply weathered Rosh Pinah Formation metavolcanics and the Hilda Subgroup carbonate rocks. The Zn-oxidized minerals are mainly hosted by arkoses and subordinately by quartz-sericite schists of volcanic origin. Other rock types associated with the orebody include limestones and mafic volcanics (Borg et al., 2003; Kärner, 2006). The Skorpion nonsulfide orebody is covered by a transported barren regolith, consisting of a surficial layer of wind-blown sand above a massive calcrete layer, covering a sequence of alluvial interlayered gravels and conglomerates. Great part of the oxidized orebody is considered to have been formed in a paleo-channel, after the supergene alteration of the primary orebody associated to an erosional surface (Borg et al., 2003). This surface is most likely an equivalent of the “African Erosion Surface” dated as Cretaceous-Early Tertiary (Partridge and Maud, 1987). Major ore minerals at Skorpion include not only smithsonite, sauconite and hemimorphite (Borg et al., 2003), but also other Zn minerals like tarbuttite, scholzite, chalcophanite, hydrozincite, skorpionite, and hydrohetaerolite (Kärner, 2006; Arfè et al., 2017a; Balassone et al., 2016; this study). A new hydrated yttrium-erbium phosphate has been recently discovered and determined as churchite-Y, i.e. (Y,Er)PO₄·2H₂O (Hinder, 2015). Based on the stable isotope data of supergene carbonates, Arfè et al. (2017a) suggested that the nonsulfide mineral assemblage precipitated at an average temperature of 17°C, either during the first (Late Cretaceous-Paleocene), or the last humid climatic stage (early-middle Miocene).

The formation process of the Skorpion Zn-bearing supergene minerals, among which sauconite, started from the oxidation of primary (hypogene) sulfides (sphalerite, pyrite, minor chalcopyrite and galena), hosted in late Proterozoic felsic metavolcanic and metasiliciclastic rocks (Borg et al., 2003; Kärner, 2006). The oxidation of primary sulfides (mainly pyrite) within these host rocks produced (i) sulphuric acid, (ii) the release of base metals (Zn²⁺, Pb²⁺ and Cu²⁺) transported in initially acidic solutions, and (iii) insoluble iron hydroxides, which testify high Eh/low pH conditions (Scott 1986, Garrels and Christ 1990). The metal-bearing (Zn-dominated) fluids percolated through the rocks were able to dissolve some of their detrital siliciclastic components. i.e mainly detrital feldspars and micas (as well as the calcitic cements), which provided Si and Al, together with alkaline ions, for sauconite formation. The mineral-water reactions of the hydrolysis processes must have buffered the pH of the supergene fluids, since they produced two strong bases,

namely NaOH and KOH (Sherman 2001). These bases contributed to the buffering/neutralisation of the acid meteoric fluid, which were migrating through the Skorpion metaarkoses. Thus, the supergene fluids became less acidic during the progressive leaching of feldspars from the Late Proterozoic rocks. This neutralisation process played a significant role in the formation of the supergene nonsulfide zinc ore body, giving rise to moderate Eh and pH conditions, favourable for the precipitation of the supergene zinc-bearing minerals, among which sauconite. Its formation requires Eh-pH conditions similar to hemimorphite and smithsonite, i.e. neutral to weak alkaline oxidising conditions, although it can be stable under weak acid conditions (Kärner, 2006, and references therein).

Materials and Methods

The TEM-AEM study was conducted on three samples (SK1, SK3 and SK8), collected from the Skorpion open pit (Fig. 8.1B). Preliminary petrographic and mineralogical analysis was carried out in order to identify the main mineral textures and paragenesis. The samples were characterized by X-ray powder diffraction (XRPD), using a Seifert-GE ID3003 diffractometer, with CuK α radiation, Ni-filtered at 40 kV and 30 mA, 3-80 °2 range, step scan 0.02°, time 10 s/step, and the RayfleX (GE) software package (Dipartimento di Scienze della Terra, dell'Ambiente e delle Risorse, DiSTAR, University of Naples Federico II). The mineral assemblages were also investigated by polished-thin sections used for optical microscopy (OM) and scanning electron microscopy with energy dispersive X-ray spectroscopy (SEM-EDS) (DiSTAR Naples). A JEOL JSM5310 equipped with an Oxford energy dispersive spectrometry (EDS) INCA X-stream pulse processor interfaced with the 4.08 version Inca software has been used. The HRTEM study on thin sections, aimed to investigate the texture of clays at micro- and nano-scale, was performed at the Centro de Instrumentación Científica (CIC) of the University of Granada (Spain). Copper rings were attached to representative selected areas of the matrix of thin sections prepared with Canada balsam and after ion-thinned, using a Fischione Model 1050 ion mill, and carbon coated. Ion milling was performed at 4 kV and $\pm 10^\circ$, until the first hole and $\pm 7^\circ$ during 20 min for final cleaning. We used a Titan TEM with XFEG emission gun, spherical aberration corrector and HAADF detector, working at 300 kV, with a resolution of 0.8 Å in the TEM mode and 2 Å in the STEM mode. EDX spectra for qualitative identification of minerals and chemical maps were obtained using the Super-X system. Quantitative analyses were obtained using albite, biotite, muscovite, spessartine, olivine, titanite, and hemimorphite as standards, measured using the same protocol as samples, to obtain K-factors for the transformation of intensity ratios to concentration ratios according to Cliff and Lorimer (1975).

Taking into account the analytical difficulties in detecting the Na⁺ peak, because of the Na-Zn peaks overlap in the energy-dispersion spectrum, for one sample (SK8) a chemical analysis of the clay fraction (carefully separated and checked for purity by XRD) was carried out by inductively coupled plasma - optical emission (ICP-OES), after a eight-peroxide assay, using a Thermo Jarrell-Ash ENVIRO II ICP (Actlabs, Ancaster). The

uncertainty is less than 3% for major oxides and less than 5% for all other trace elements (for the precision of the method, see actlabs.com).

Results

The mineralogical assemblages of the investigated Skorpion samples, inferred by combined XRPD and SEM-EDS analyses, are always represented by sauconite as main phase (e.g. Fig. 8.2).

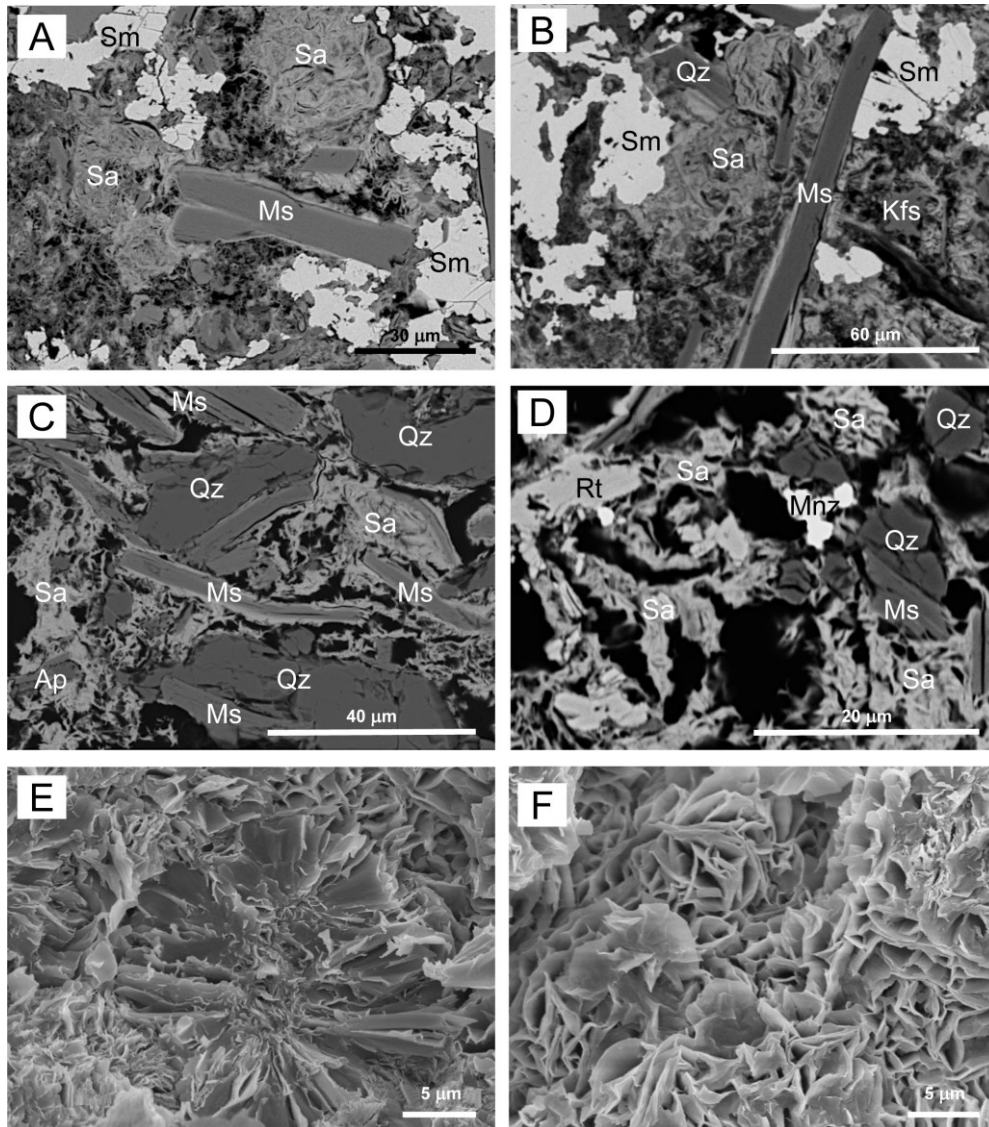


Figure 8.2. (A), (B) BSE micrographs of sauconite-bearing sample SK1, and (C), (D) sample SK3; mineral abbreviations (Whitney and Evans, 2010): Ap, apatite; Kfs, K-feldspar; Mnz, monazite; Ms, muscovite; Qz, quartz; Rt, rutile; Sa, sauconite; Sm, smithsonite. (E), (F) SE micrographs of smectite in sample SK8, respectively from brownish and white (clay-rich) areas (see Fig. 8.1B).

All the X-ray diffraction patterns exhibit the typical peaks of the Zn-smectite, with broad diffraction maxima, indicative of the lack of perfect long-range order due to stacking

faults and/or fine grained crystallite dimension, corresponding to the 001 reflections positioned at about 14.72 Å, and the diagnostic 060 peaks centred at ~1.54 Å. Samples SK1 (Figs. 8.2A, B) and SK3 (Figs. 8.2C, D) also contain minor amounts of smithsonite, quartz, muscovite, K-feldspar and very rare apatite.

Sporadic rutile and monazite were detected only in sample SK3 REE (+Y) phosphates were found also at Skorpion by Kärner (2006), in highly altered gossaneous metasediments at Skorpion as secondary REE minerals. If compared with the other samples, sample SK8 is particularly rich in sauconite; it is composed of dark-brown parts with sauconite and lesser Fe-oxy-hydroxides (Figs. 8.1B and 8.2E), and white parts with prevailing Zn-clay (Figs. 8.1B and 8.2F). Minor content of quartz and muscovite have been also detected.

Microtextures of clays and related minerals

Using ion-milling technique preparation, we were able to observe the mineral fabric of the Zn-clays in the three Skorpion samples which, at low magnification, present similar characteristics and comparable electron diffraction patterns (SAED). The microtextures of the Zn-clays observed in the Skorpion samples at size below 10 µm are very similar to those described by Mondillo et al. (2015) in the Yanque mine (Peru); as a matter of fact, also at Skorpion it was possible to identify the compact clay packages (CCP), as well as the porous clay aggregates (PCA). The CCP type is represented by straight and almost isororiented packets (Figs. 8.3A-D), with a length up to several micrometres and a thickness below ~ 1 µm. The packets can locally pass to slightly curved fibres coexisting with the straight packets, as an epitaxial growth onto mica crystals (Fig. 8.4) or rarely as void fillings. The PCA type consists of very fine-grained packets, with sizes lower than the CCP types, ~ < 400 nm (Figs. 8.3E-H). This microtexture seems to be less frequent in the studied samples than in CCP, and it is occasionally closely related to Fe-hydroxides (Fig. 8.3G).

The electron diffraction patterns of the CCP type are shown in figures 8.5A and B; they correspond to a partially collapsed smectite with spacings of ~ 12 Å between layers, which typically occur as a consequence of TEM vacuum and/or electron irradiation and 5.1 Å in the a^* direction. In figure 8.5C the electron diffraction pattern of mica is shown, which represents the substrate on which CCP smectite grew with an epitaxial mechanism, as discussed afterwards. In this sample (i.e. SK3), the rows have a spacing of 20 Å; lattice fringes with spacings of 20 Å are measured for the same area, which identifies the 2M polytype (Fig. 8.5D). Figures 8.5E and F show the high-resolution images of CCP smectite, with lattice fringes ranging between ~12 and 13 Å. In general, the measured d_{001} values of sauconite vary in a interval of 10.5-13 Å, due to different degrees of collapsing. As reported in Mondillo et al. (2015), the PCA smectite can be also associated with Fe-oxy-hydroxides. Figures 8.6A and B show a HRTEM image with the typical d_{hkl} of hematite; the crystalline domains size are very small and disoriented each other, but it is not really defective.

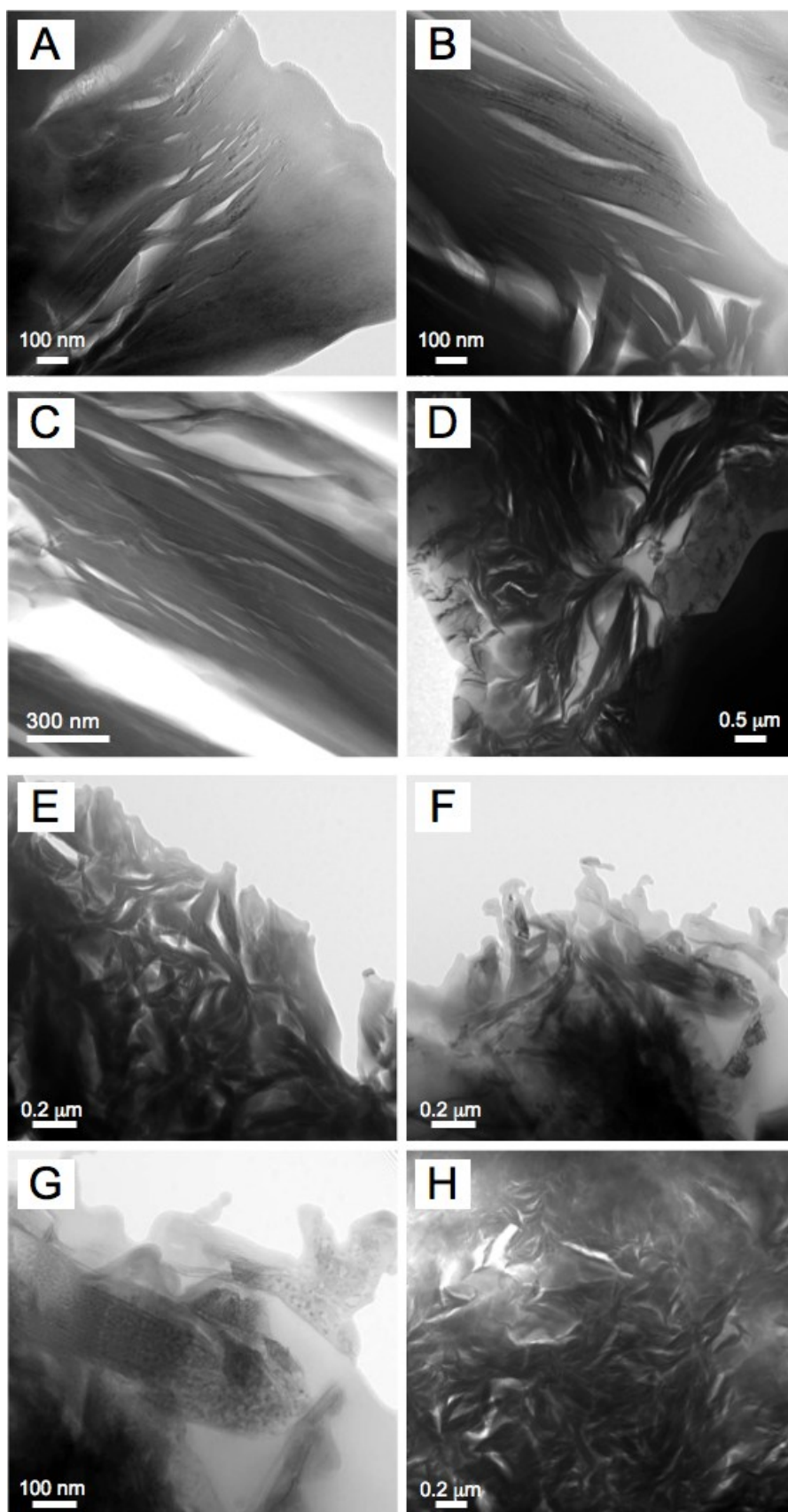


Figure 8.3. Textural images of compact clay packages (CCP): (A), (B), (D) sample SK1; (C) sample SK8. Textural images of porous clay packages (PCP): (E), (F) sample SK1, with (G) enlargement of (F); (H) sample SK8.

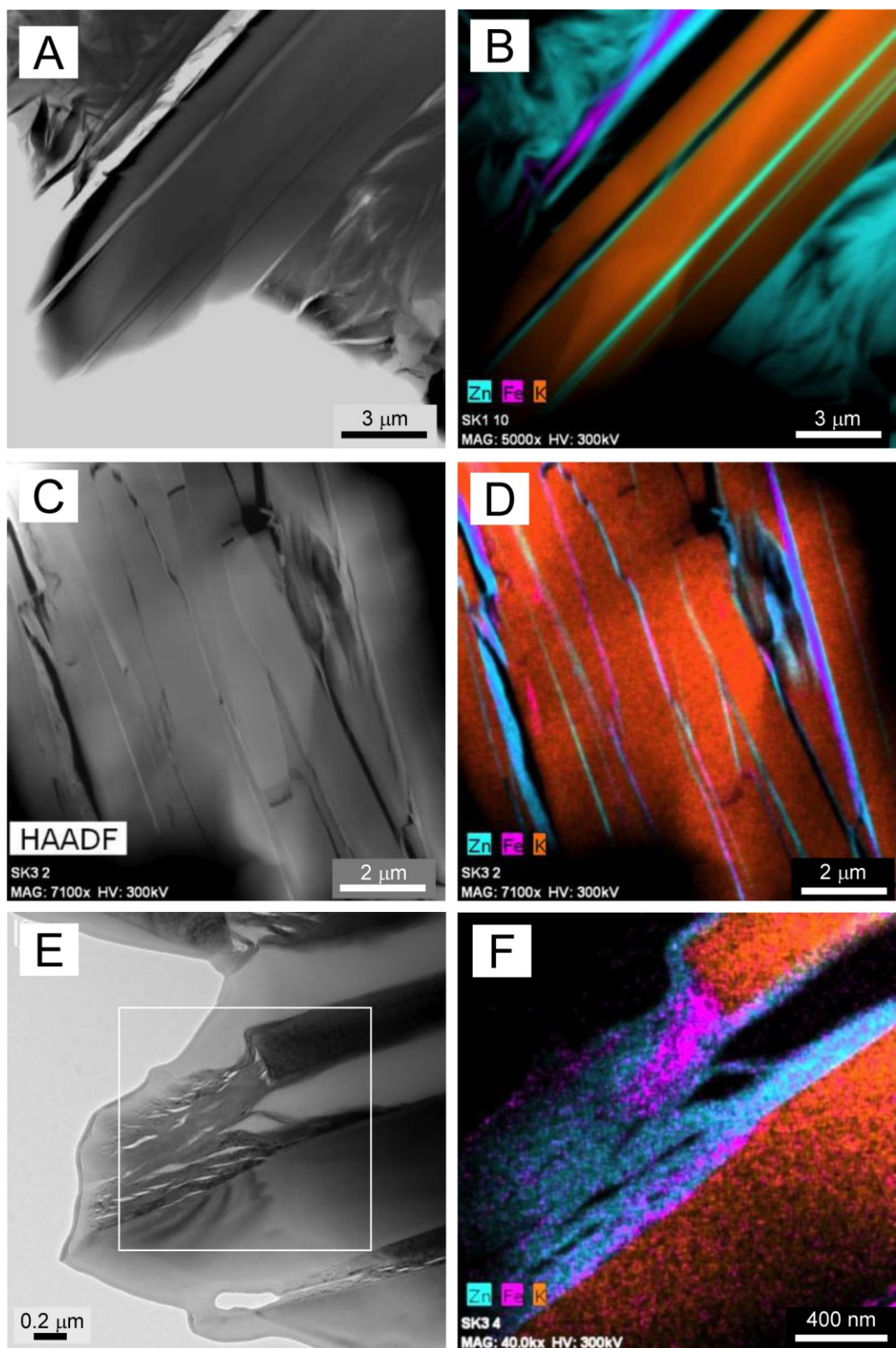


Figure 8.4. Epitaxial growth of smectite onto mica: (A), (B) sample SK1; (C), (D), (E), (F) sample SK3. In (B), (D), (F) STEM-EDX spectra of the investigated areas (on the left) are reported, clearly showing the K-rich mica areas and the Zn-rich saconite ones. (F) Enlargement corresponding to the white frame in (E), where small areas richer in Fe can be also observed (see text).

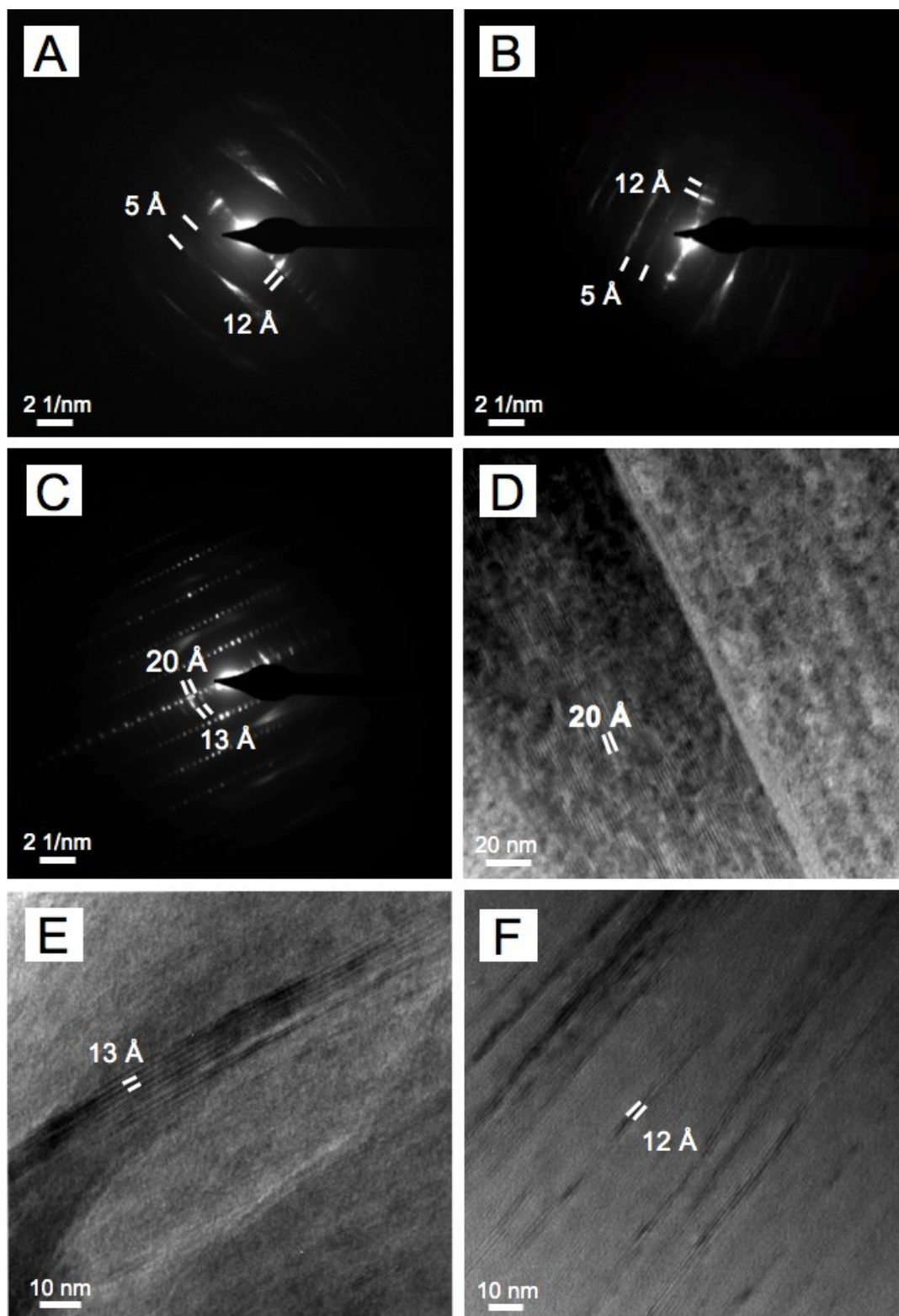


Figure 8.5. (A), (B) Electron diffraction patterns of CCP of sample SK1, shown in Fig. 3A and 3B, respectively. (C) Electron diffraction patterns of mica (20 Å) associated with epitaxial smectite packet (12.5 Å) in sample SK3, and (D) HRTEM image of this mica. (E) HRTEM image of CCP sauconite in sample SK1, showing a close-up view of Fig. 3A. (F) HRTEM image of CCP epitaxial sauconite.

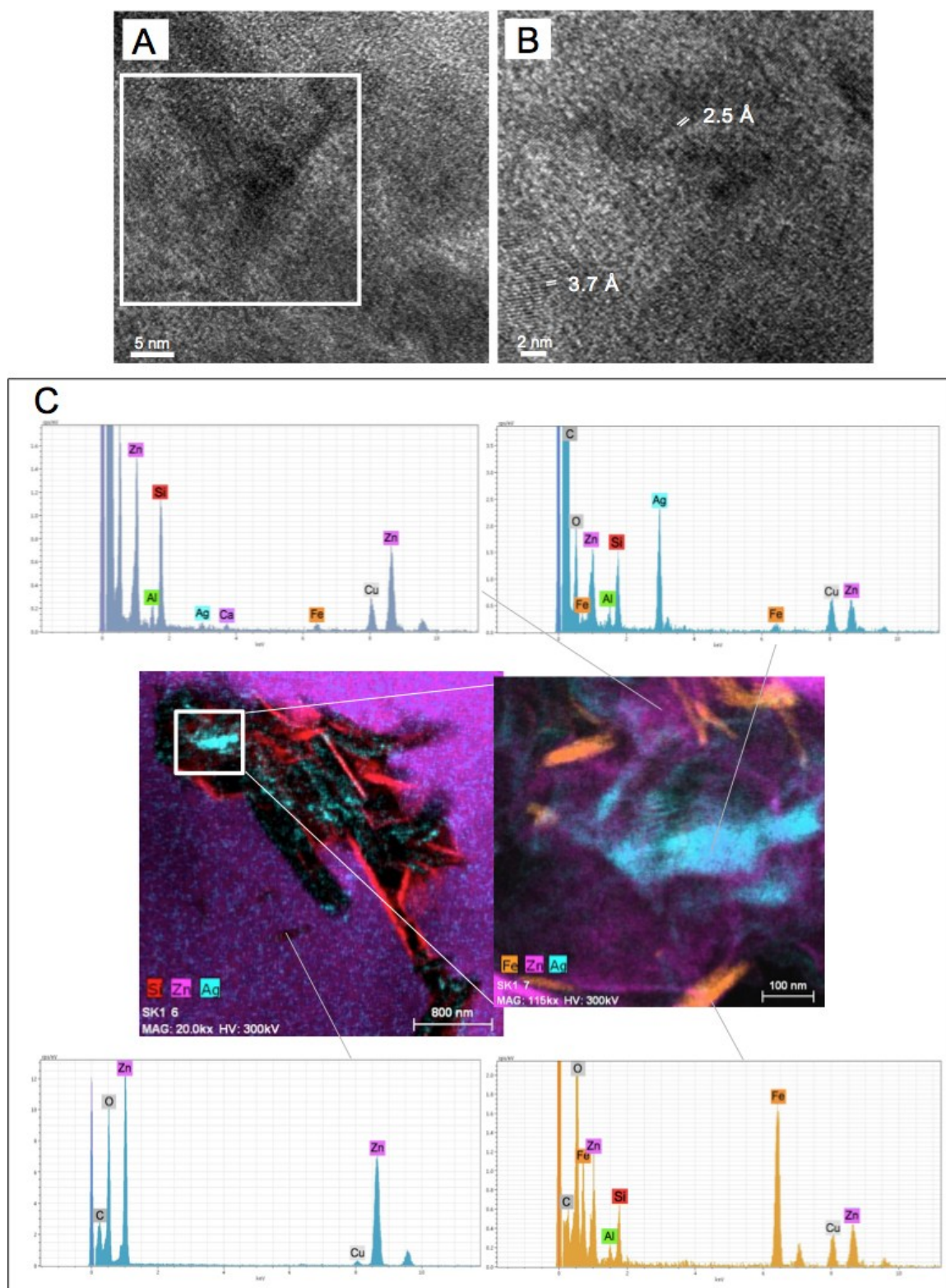


Figure 8.6. (A) HRTEM of nanocrystalline hematite (sample SK1), and (B) enlargement of the area in the white frame. (C) Iron oxy-hydroxides coexisting with PCA smectite in sample SK1, together with Ag-rich areas (see text). Cu peak in the EDX spectra are due to copper ring attached to sample areas (see “Materials and Methods” paragraph).

In figure 8.6C a small amount of native silver retained in the smectite flakes has been also detected in an area where Fe-oxy-hydroxides and sauconite seem to be finely intergrown; Ag is likely attributable to a pure metal instead to a compound, which is simply retained in the smectite flakes.

In figure 8.7 it is shown how iron minerals are disseminated in the smectite interstices. In the same figure, it is worth noting the occurrence of another phase likely interpreted as a Zn-oxide, due to the small C peak, that would allow to exclude a Zn-carbonate. The qualitative EDX spectra show that this mineral also contains a series of metals like Fe, Mn, Co, Ni, Zr, Cd and Pb, not detected elsewhere.

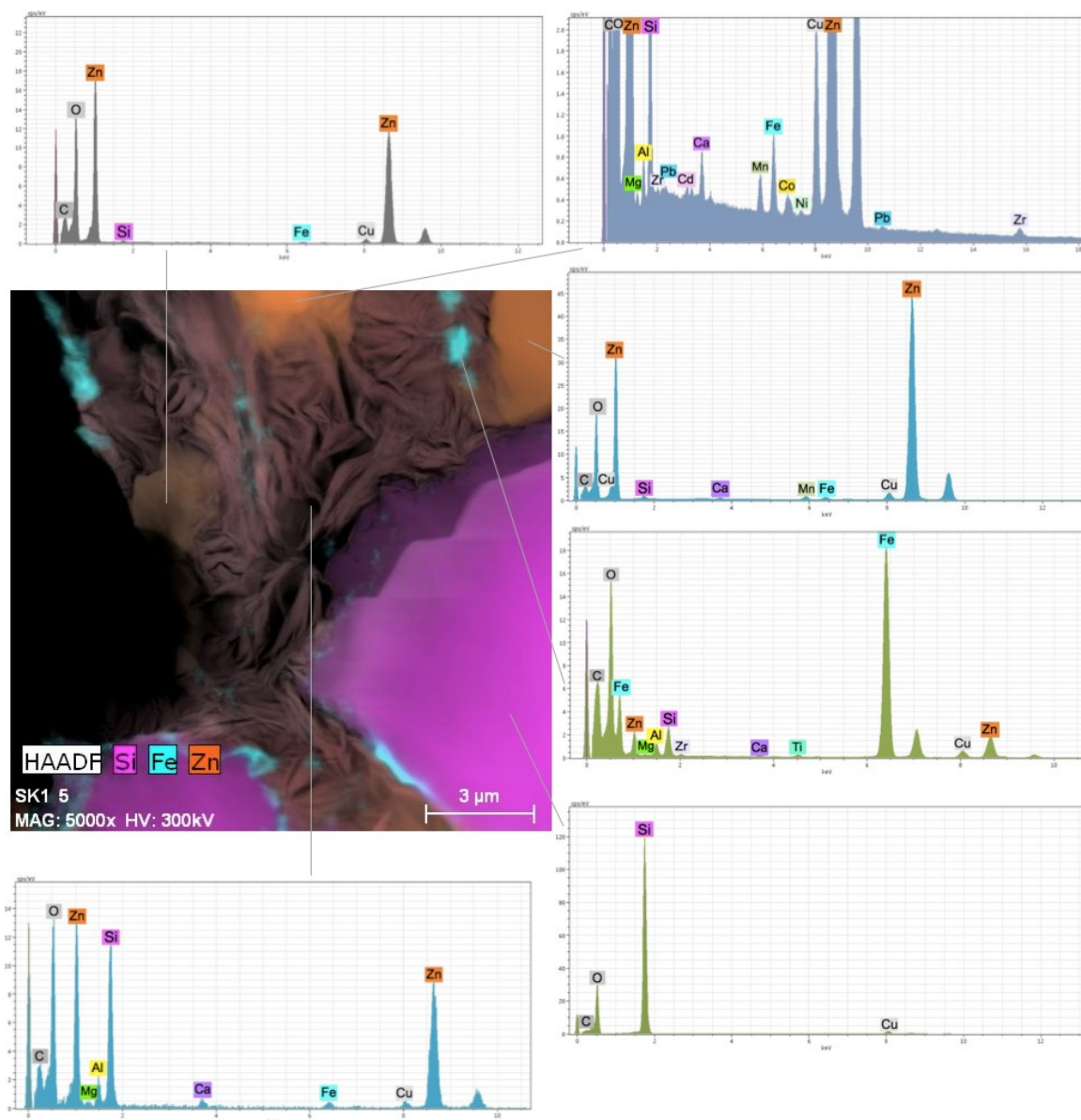


Figure 8.7. Iron oxy-hydroxides coexisting with CCP smectite, together with a Zn-oxide (Cu peak as in Fig. 8.6).

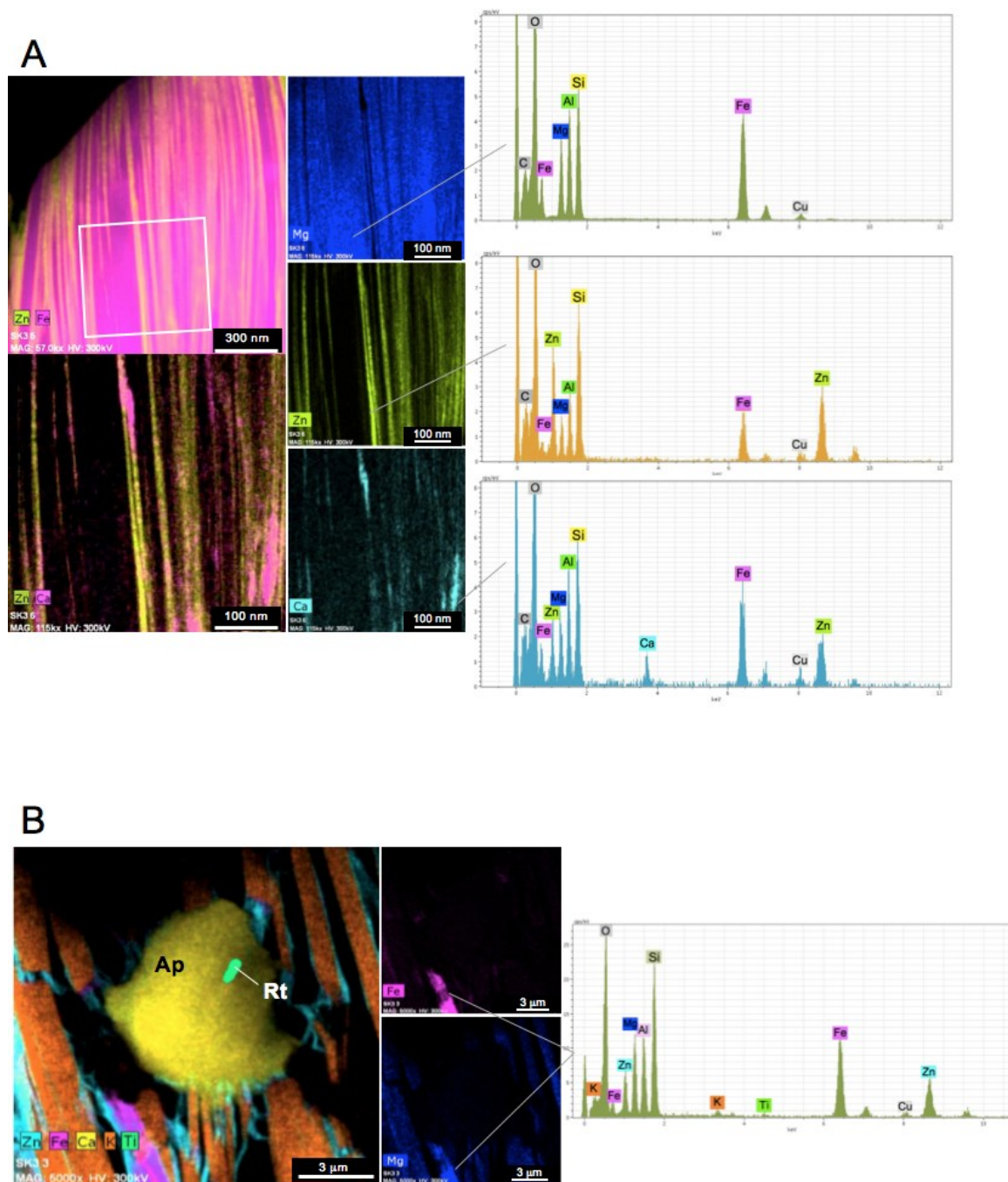


Figure 8.8. (A) Mg-Fe-rich chlorite alternating with saunonite in sample SK3; the upper spectrum corresponds to a Mg-chlorite, the central and lower spectra could be interpreted as a combination of Zn-smectite and a likely Ca-bearing phyllosilicate of composition similar to vermiculite. (B) Mica with smectite in sample SK3; the area indicated by the spectrum could be a baileychlore-type phase (Cu peak as in Fig. 8.6). Mineral symbols as in Fig. 8.2.

Unlike the Peruvian smectite-rich samples (Mondillo et al., 2015), at Skorpion there are chlorites strictly related to smectite. In figure 8.8A the chemical maps of Mg, Fe, Zn and Ca show Fe-Mg chlorite interleaved with smectite. Figure 8.8B shows the occurrence of chlorite with a different composition, which could be ascribed to a possible baileychlore or to a contaminated Fe-Mg chlorite. In figure 8.9 are shown the electron diffraction patterns and the high-resolution images of the chlorite-bearing area of figure 8.8. In the

patterns of figures 8.9A and B, chlorite presents a basal d-spacing of 14 Å. Figures 8.9C and D illustrate the HRTEM images of the lattice fringe spacings of chlorite, thus confirming that d_{chl} of 14 Å is the most common spacing measured in the investigated areas. In some restricted areas, lower d-spacings can be observed, corresponding to individual layers of smectite (Fig. 8.9C). Probably, the frequent open layers observed in HRTEM images, which are due to irradiation effects, correspond to smectitic layers, because this phenomenon is not usual in chlorite while largely affecting smectite. When a two-dimensional resolution is present, chlorite shows an ordered polytype (1 layer) at a local level, but a misorientation among the various packets occurs, which would produce an electron diffraction characteristic of disordered polytypes, as those visible in other images. This appears an ordered polytype at short range, but disordered at long range, a phenomenon not rare in phyllosilicates.

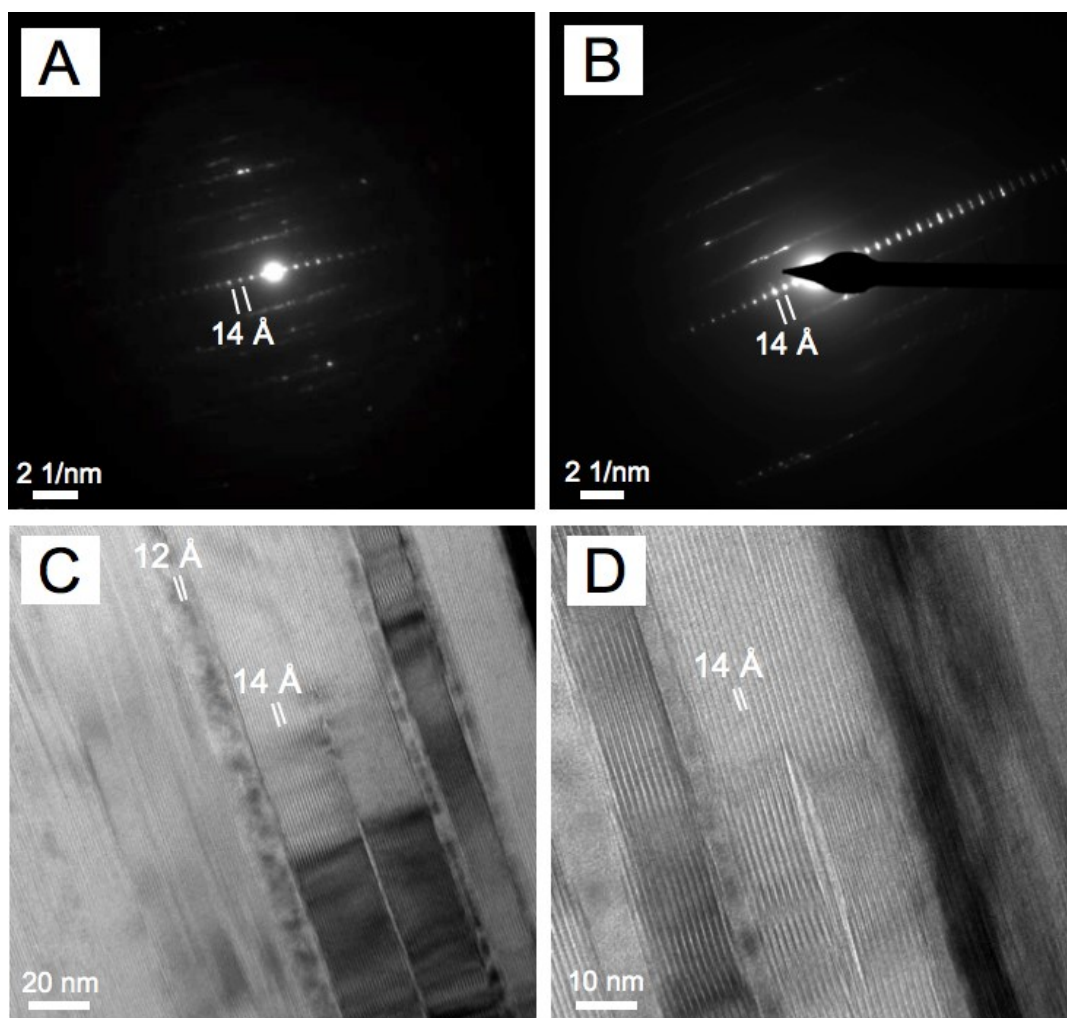


Figure 8.9. (A) Electron diffraction of chlorite in sample SK3. (B) Example of a disordered chlorite polytype. (C) and (D) Lattice fringe images showing predominantly spacing of chlorite; some smectitic layers (12 Å) are shown in (C).

Chemical composition

It is well established that the AEM technique does not determine the absolute chemical composition of a mineral, but only the elemental ratios (i.e. Mondillo et al., 2015). Hence, the structural formulas of smectite and mica were calculated on the basis of 22 negative charges, i.e., $\text{O}_{10}(\text{OH})_2$. According to the accepted stoichiometry of smectites (Güven 1988), Fe, occurring in very small contents (see below), was considered in bivalent form for trioctahedral species like sauconite (see also Buatier et al. 2016, Choulet et al., 2016, Kärner, 2006). However, the occurrence of some Fe^{3+} cannot be excluded. The structural formulae of Skorpion sauconite are shown in table 8.1. Silicon contents vary between 3.15 and 3.66 apfu. The content of the octahedral site is more variable, in an interval of 2.75 and 3.15 apfu; $^{\text{VI}}\text{Al}$, Mg and Fe ranges are 0.00-0.59, 0.00-0.20 and 0.00-0.35 apfu, respectively. Most of the octahedral site is occupied by Zn, variable between 1.95 and 3.08 apfu. Among the interlayer cations, Ca is generally the only component, within a range of 0.05 and 0.19 apfu; K is detected in trace amounts or is absent. In figures 8.10A and B are shown the Zn- $^{\text{VI}}\text{Al}$ -Fe+Mg and $\text{M}^+-4\text{Si}-3\text{R}^{2+}$ ternary plots, respectively; in the first plot it can be seen that the Skorpion sauconites are close to the Zn end-member, unlike the Peruvian specimens that are chemically more variable. Sauconite of this study also partly overlap the compositional field of Kärner (2006). In the plot of figure 8.10B, used to distinguish the dioctahedral from the trioctahedral types (Meunier 2005), our data mainly plot around the theoretical sauconite composition (especially samples SK1 and SK8). The bivariate diagrams of selected elements are reported in figure 8.11A-C. In figure 8.11A is shown the Al vs. Si correlation, where the tetrahedral composition of the studied samples resulted nearly comparable with the Skorpion sauconites analysed by Kärner (2006) and more homogenous in respect to the Peruvian varieties of Mondillo et al. (2015). The same features can be observed in the plot Zn vs. $^{\text{VI}}\text{Al}$ (Fig. 8.11B), which clearly illustrates that the majority of the samples cluster in the area 3.0-2.5 apfu Zn and $^{\text{VI}}\text{Al} < 0.5$ apfu, and that the octahedral site is mainly filled by Zn (Table 8.1 and Fig. 8.10); moreover, a negative correlation between the two octahedral elements can be observed. The diagram Zn/Al vs. Si/Al illustrates a clear positive correlation, with a continuous variation of the two chemical parameters through the data. In this plot, the studied samples resulted more variable if compared with the data of Kärner (2006); this can be clearly explained by considering that the Kärner's data are averages on the bulk samples, while our data refer to many individual (nano)particles. It is worth noting that sample SK8 can be almost considered a Ca-bearing end-member (Table 8.1), being K virtually lacking. This sample is also particularly homogenous (Fig. 8.10 and 8.11), as shown in the chemical map of figure 8.12. ICP-OES analysis was also carried out for sample SK8, in order to check on the Na content, not detectable either by TEM-AEM or by EDS-WDS when also Zn is present. The obtained chemical composition expressed in wt.% is: SiO_2 37.93, Al_2O_3 6.23, FeO 0.01, MgO 0.40, CaO 1.55, Na_2O 0.20, K_2O 0.32, ZnO 38.75, LOI 15.11 (MnO, TiO_2 and P_2O_5 are below detection limits). If reported in term of structural formula based on 22 negative charges (i.e. $\text{O}_{10}(\text{OH})_2$), this composition is perfectly comparable to the compositions obtained by TEM-EDX for the same sample (Table 8.1).

TABLE 8.1. Structural formulae of representative saucnite from Skorpion (Namibia), in atoms per formula unit (apfu), calculated on the basis on 12 O₁₀(OH)₂, obtained by AEM (analyses no. 1-20) and ICP-OS methods (analysis no. 21). See text for further explanations.

sample ID	SK1								SK3				SK8								
no.	1	2	3	4	5	6	7	8	9	10	11	12	13	14	15	16	17	18	19	20	21
Si	3.28	3.26	3.16	3.15	3.24	3.49	3.56	3.29	3.37	3.38	3.58	3.24	3.46	3.45	3.66	3.53	3.43	3.57	3.46	3.46	3.53
Al ^{IV}	0.72	0.74	0.84	0.85	0.76	0.51	0.44	0.69	0.63	0.62	0.42	0.76	0.54	0.55	0.34	0.47	0.57	0.43	0.54	0.54	0.47
Al ^{VI}	0.00	0.04	0.15	0.18	0.24	0.01	0.08	0.00	0.41	0.11	0.13	0.59	0.01	0.09	0.29	0.19	0.01	0.18	0.02	0.06	0.21
Mg	0.06	0.09	0.06	0.14	0.19	0.05	0.07	0.20	0.13	0.17	0.12	0.25	0.00	0.00	0.00	0.00	0.06	0.09	0.04	0.05	0.06
Fe ²⁺	0.16	0.21	0.19	0.19	0.15	0.11	0.11	0.11	0.35	0.12	0.06	0.14	0.00	0.00	0.00	0.00	0.01	0.01	0.01	0.01	0.02
Zn	2.88	2.70	2.76	2.58	2.42	2.85	2.72	2.84	1.95	2.70	2.74	1.77	3.08	2.98	2.57	2.76	3.06	2.72	3.03	2.94	2.66
SO	3.10	3.05	3.15	3.09	3.01	3.03	2.98	3.15	2.84	3.09	3.05	2.75	3.10	3.07	2.86	2.95	3.14	2.99	3.11	3.07	2.95
Ca	0.19	0.19	0.10	0.15	0.17	0.17	0.14	0.18	0.05	0.10	0.07	0.07	0.16	0.16	0.17	0.19	0.14	0.14	0.15	0.17	0.16
K	0.00	0.00	0.00	0.00	0.00	0.00	0.00	0.00	0.07	0.00	0.00	0.38	0.00	0.00	0.00	0.00	0.00	0.00	0.00	0.00	0.04
Na	-	-	-	-	-	-	-	-	-	-	-	-	-	-	-	-	-	-	-	-	0.04
S interlayer	0.19	0.19	0.10	0.15	0.17	0.17	0.14	0.18	0.12	0.10	0.07	0.45	0.16	0.16	0.17	0.19	0.14	0.14	0.15	0.17	0.24
S charge	0.38	0.39	0.20	0.30	0.34	0.33	0.28	0.37	0.18	0.21	0.15	0.52	0.33	0.31	0.33	0.38	0.29	0.27	0.29	0.34	0.40

Note: - Not determined.

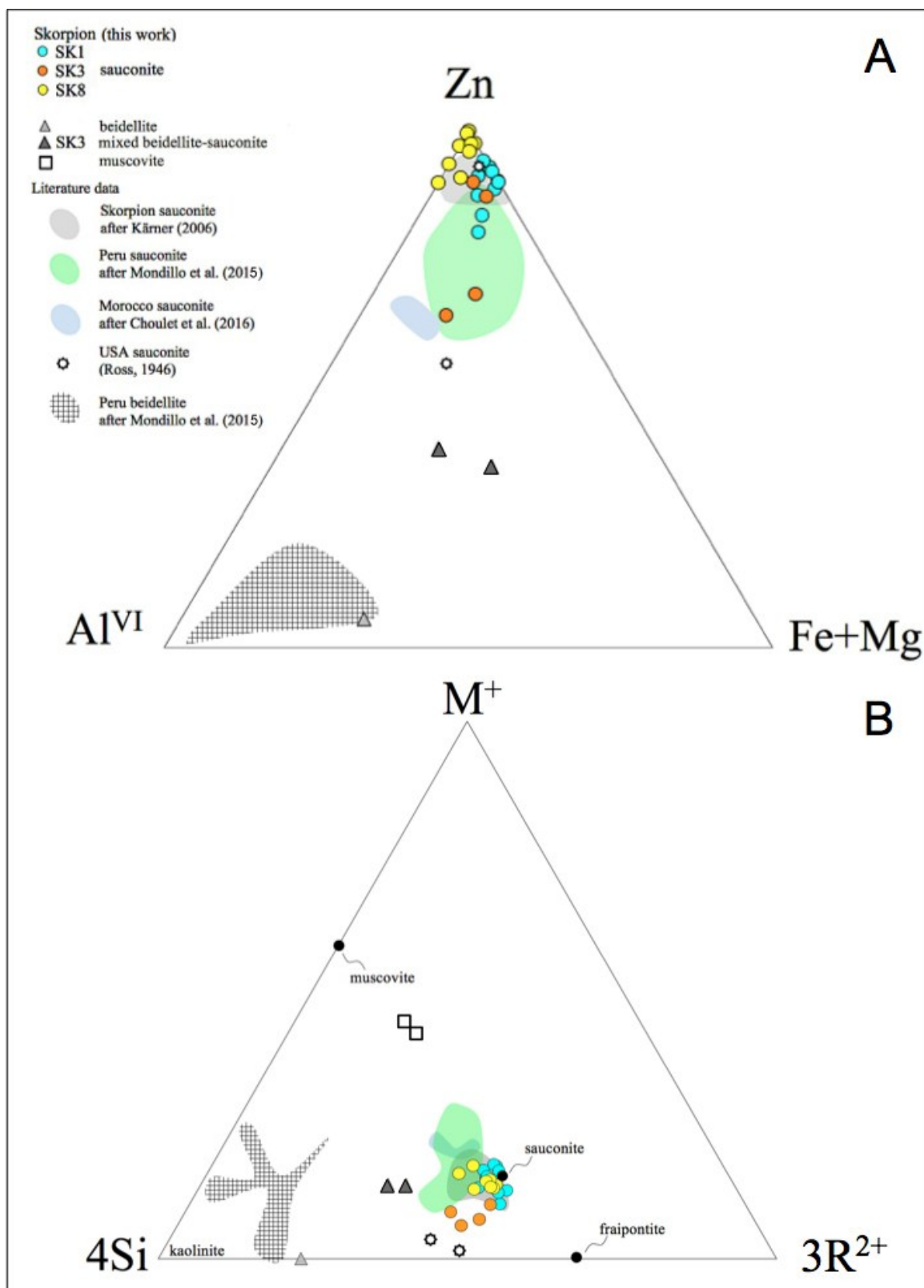


Figure 8.10. (A) Zn-Al^{VI}-Fe+Mg diagram illustrating the octahedral chemical composition of sauconite and beidellite, as well as some examples of mixed compositions (dark grey triangles). (B) 4Si-M⁺-3R²⁺ diagram showing the trioctahedral and dioctahedral phases; the black dots represent the ideal mineral compositions. In both diagrams, our data are compared with literature data.

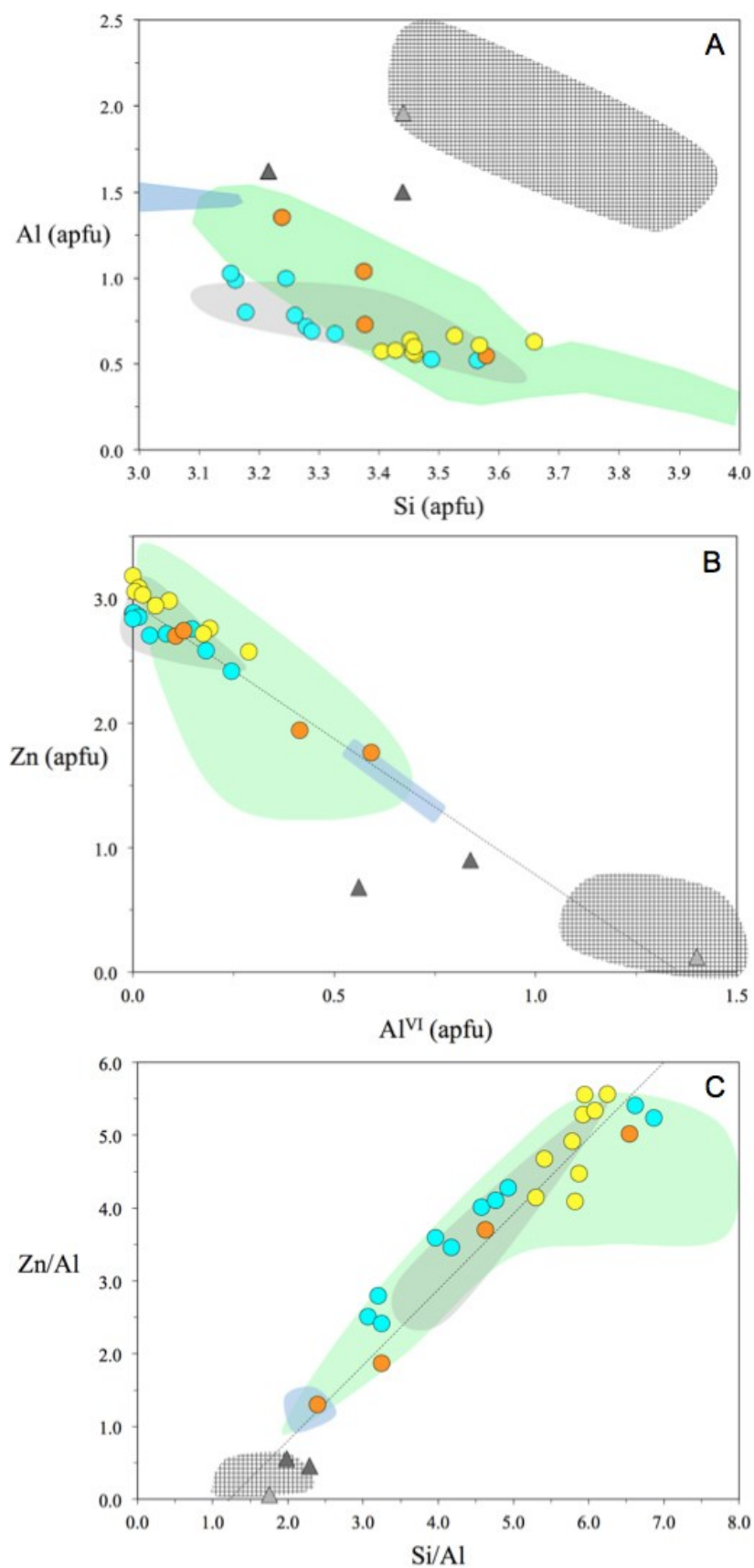


Figure 8.11. Bivariate diagrams, illustrating some chemical features of the Skorpion samples (symbols as in Fig. 8.10).

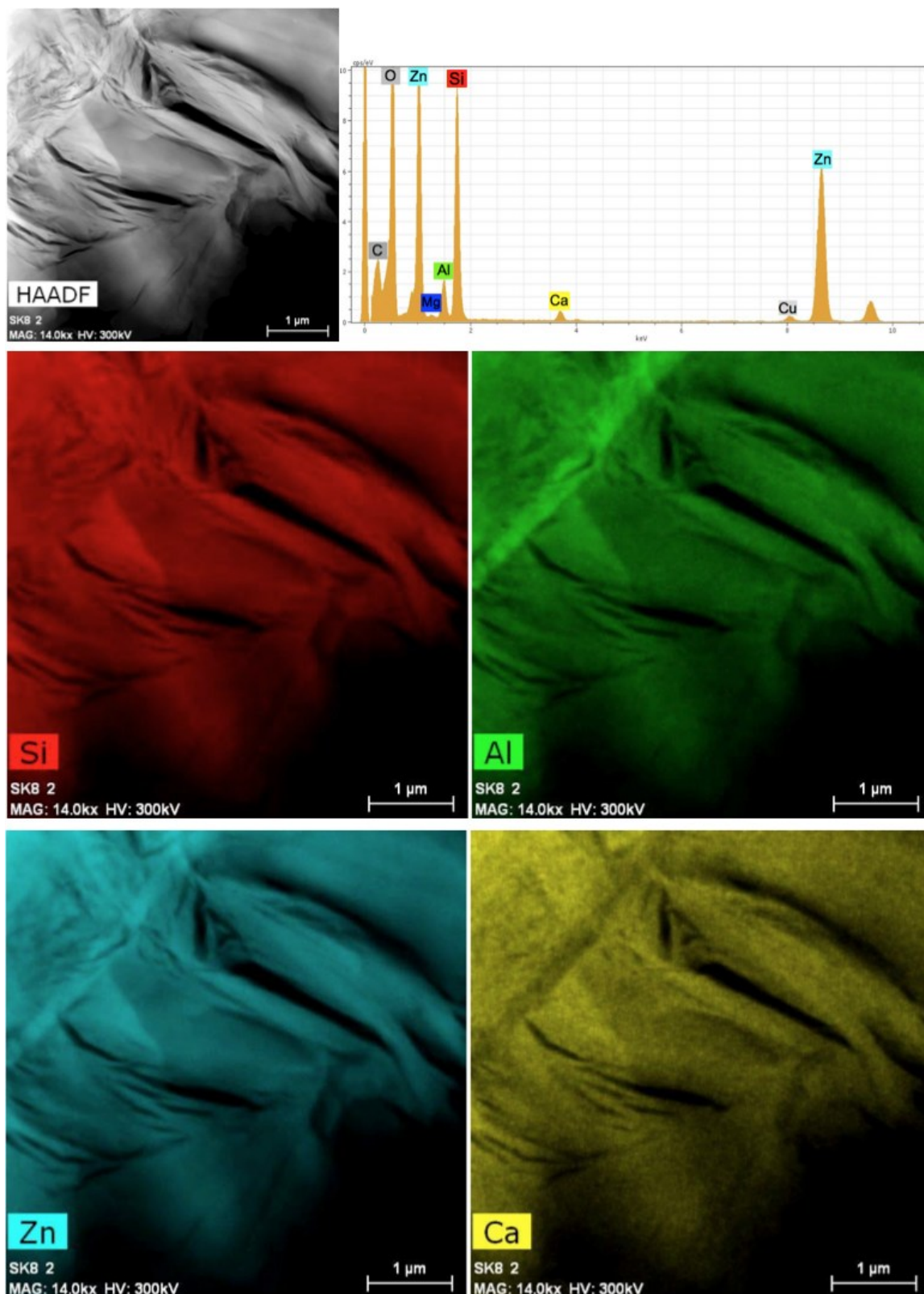


Figure 8.12. HAADF image and chemical mapping of sample SK8.

Contrary to the Peruvian samples, at Skorpion we have detected very limited compositions likely attributable to Zn-beidellite, which was clearly recognized only in sample SK3 (Fig. 8.13). Table 8.2 reports one beidellite-like composition; plotted in Figs. 8.10 and 8.11, this point-analysis falls in the beidellite fields of Mondillo et al. (2015), whereas other analyses (indicated with dark triangles in the cited figures) show a mixed composition between sauconite and beidellite.

TABLE 8.2. Structural formulae of representative beidellite, muscovite and chlorites from sample SK3, in atoms per formula unit (apfu), calculated on the basis on a total of 12 anions ($O_{10}(OH)_2$) for smectites and micas, and 18 anions ($O_{10}(OH)_8$) for chlorites.

Sample ID		SK3				
	beidellite		muscovite			chlorite
Si	3.440	Si	3.206	3.244	Si	2.783
Al ^{IV}	0.560	Al	0.794	0.756	Al ^{IV}	1.217
Al ^{VI}	1.401	Ti	0.053	0.047	Al ^{VI}	1.071
Mg	0.275	Al ^{VI}	1.648	1.590	Mg	1.904
Fe ³⁺	0.378	Mg	0.309	0.389	Fe ²⁺	2.693
Zn	0.122	Fe ³⁺	0.017	0.020	Zn	0.000
SO	2.175	SO	2.027	2.046	Ca	0.000
					K	0.000
Ca	0.000	Ca	0.000	0.000	SO	5.669
K	0.430	K	0.968	1.007		
S interlayer	0.430	S interlayer	0.968	1.007		
S charge	0.430					

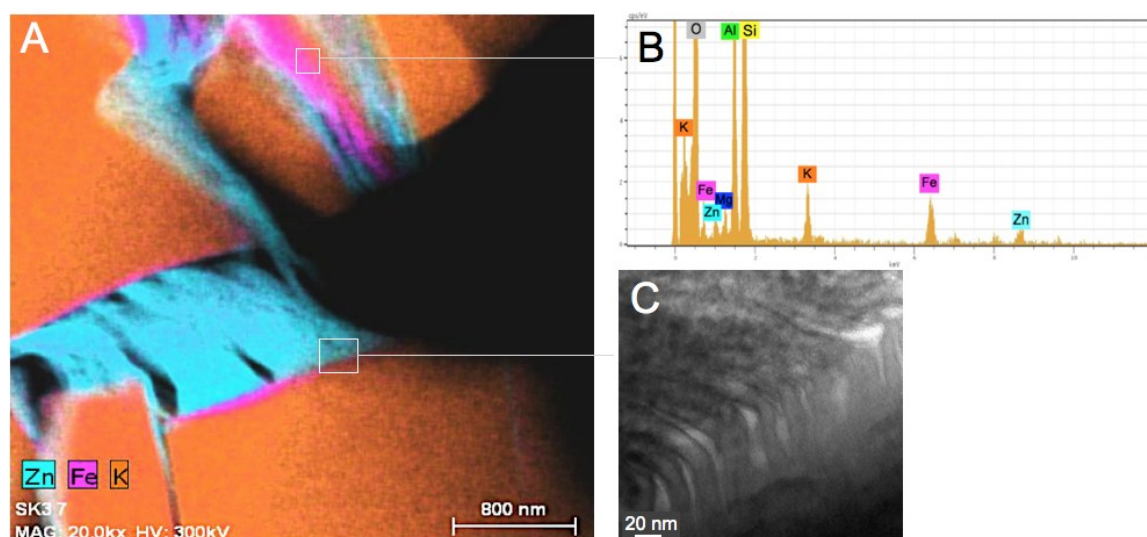


Figure 8.13. (A) Chemical mapping and (B) qualitative EDX spectrum of a possible Zn-bearing beidellite in sample SK3. (C) Enlargement of a transition area smectite-mica.

As illustrated in figures 8.8 and 8.9, chlorite was found in the Skorpion sample SK3. Table 8.2 shows two representative analyses of chlorites; the Fe-Mg chlorite could

correspond to a chamosite, whereas as regards the baileychlore-like compositions, a contamination between sauconite and Fe-Mg chlorite cannot be excluded.

Discussion and conclusions

On the basis of the TEM-HRTEM study of Zn smectite-rich samples from the Skorpion deposit, some specific features can be evidenced for the “sauconite” and related minerals occurring in the nonsulfide orebody, when compared with the Peruvian clay associations reported in Mondillo et al. (2015):

- (i) Skorpion sauconite is chemically more homogeneous if compared with natural sauconites from Yanque and Accha in Peru (Mondillo et al., 2015). In general, the composition of this Skorpion smectite is quite extreme, close to a Ca-rich end-member. Indeed the average composition of sauconite obtained by TEM-AEM corresponds to $\text{Ca}_{0.14}\text{K}_{0.02}(\text{Zn}_{2.7}\text{Mg}_{0.09}\text{Al}_{0.14}\text{Fe}_{0.10})(\text{Si}_{3.4}\text{Al}_{0.6})\text{O}_{10}(\text{OH})_2 \cdot n\text{H}_2\text{O}$. As regards the Na content, very small amounts were detected by ICP-OES in sauconite fraction of sample SK8, carefully selected for purity and with a compositionally homogeneous sauconite, as demonstrated by TEM-AEM investigation. Taking into account that ICP-OES is a bulk analysis, the result is very similar to chemical compositions obtained by TEM-AEM point-analyses. Hence, the Na content is not comparable to the much higher Ca amount, which is the major interlayer cation of the Skorpion smectites. The analysed sauconites do not contain mobile elements like P, which, after the chemical data of Kärner (2006), would be released by the dissolution of apatite and subsequently precipitated as secondary phosphates (this has been rather the case) or retained in the clay structure. Other elements like Ti and REE, which could be similarly incorporated into the clays lattice, have not been detected in the analysed smectites but occur as single minerals, as testified by the occurrence of monazite and rutile observed in the studied samples.
 - (ii) Even though it is demonstrated that the Skorpion sauconite was also formed by replacement of hemimorphite, feldspar and smithsonite (Borg et al., 2003; Kärner, 2006), in the studied samples the relationships between sauconite and micas resulted particularly significant. As a matter of fact, the structural support represented by detrital mica precursors is commonly observed in most samples, also in respect to the Peruvian case. Easy cleavage along the {001} planes of muscovite favored the epitaxial crystallization of Zn smectite on cleavage surfaces, as it has been observed also in other phyllosilicate associations (e.g. kaolinite-mica, Arostegui et al., 2001). This aspect can justify the extreme compositions of the studied samples: in fact, the fluids responsible for the clays deposition did not dissolve the mica crystals of detrital origin, which rather acted as a chemically inactive support. Consequently, the Zn clays are generally scarce in Al and contain very low or no K and Mg.
- In the weathering profiles, alteration progressively affects the existing crystals, starting either from their boundaries and/or from cleavage planes. In the mica

crystals, a volume increase which occurred perpendicularly to the mica lamellae, progressively caused their swelling and deformation that resulted in a sort of “katamorphous” weathering type (Fitzpatrick, 1984, and references therein). This process is enhanced by the fact that plastic smectites tend to flow and therefore to fill newly formed pores and cavities in the surrounding detrital and/or weathered minerals. However, a significant increase in volume can be also the result of the formation of hydrated minerals such as smectite, as well as hemimorphite and hydrozincite. As reported in the isocon diagram by Kärner (2006), a volume increase of 6% can be considered for the supergene Skorpion deposit.

- (iii) In the studied samples, Zn-bearing beidellite was rarely observed in respect to the Peruvian occurrences, and some AEM analyses indicate, at least in part, mixed phases. A formula $[K_{0.43}(Zn_{0.12}Mg_{0.28}Al_{1.40}Fe_{0.38})(Si_{3.44}Al_{0.56})O_{10}(OH)_2 \cdot nH_2O]$ for Zn-beidellite could be nevertheless suggested. The chemical (i.e. K as the only interlayer cation) and textural characteristics of this dioctahedral clay seem to suggest that it formed directly at the expenses of micas, likely as an alteration product; then, beidellite might be formed through a process different from that responsible for the genesis of most sauconites. As shown in figure 8.13, a beidellitic smectite might firstly infiltrate the muscovite crystals; then sauconite crystallization follows, both on the mica cleavage surfaces and as void fillings.
- (iv) Chlorite occurrence, not detected by bulk XRPD analyses, also distinguishes the studied samples. In general, the texture of the investigated chlorite-rich areas by AEM-HRTEM shows the same characteristics as the retrograde alteration of chlorite by smectite, firstly described by Nieto et al. (1994). The genetic relationship with chlorite is different than that with mica: mica is a simple template on which smectite crystallizes directly from fluids. The same fluids, however, were able to cause the chemical alteration of chlorite. This is not strange, as white mica is clearly more resistant than chlorite to chemical alteration. At Skorpion muscovite dominates over other micas within the original host rock; however, small amounts of biotite occur, whose weathering could involve an alteration through mixed layer clay minerals or vermiculite, as proposed by Kärner (2006).
- (v) A possible Zn-oxide (not identified by XRPD) has been recorded in the Skorpion samples only by TEM-EDX; texturally, it seems to have been precipitated later than sauconite and at the same time of Fe-oxy-hydroxides. Even though observed only in sample SK1, this phase seems more capable of capturing various metals than Fe-oxy-hydroxides. According to Paquet et al. (1986), the transition metals released by the destruction of the smectitic crystal lattices can be trapped by oxy-hydroxides and kaolinite during weathering in supergene environment. At Skorpion, Fe-oxy-hydroxides appear to be free of these metals; other trace metals (Co, Ni, Cr, Mn, Fe, Zr, Pb) seem to be concentrated in the Zn-oxide, or to form local enrichments (Ag), not related to oxy-hydroxides frameworks.
- (vi) Fe-oxides (hematite) observed in this study crystallize after clay minerals (meteoric iron), forming very-low size domains.

As pointed out by Mondillo et al. (2015), the occurrence of (lesser) Zn-beidellite,

chlorite, baileychlore, detrital micas and oxides at the micro- and nanoscale also in the case study of Skorpion confirms the complex mineralogical nature of the Zn-nonsulfide smectite-rich (micro)systems, with remarkable implications for mineralogical evaluation and processing.

The microtextures of the clays suggest two possible genetic mechanisms (Mondillo et al. 2015), i.e., smectites can grow on previous phyllosilicates (mica) (CCP texture), and/or directly nucleate and grow from solutions (PCA texture). Even though the geological environment of formation of these deposits is genetically related to supergene processes, a local control by a (likely low temperature) hydrothermal fluid on the precipitation of Zn-smectite should also be considered. Stable isotope measurements of Zn-rich clays of Moroccan Bou Arhous Zn-Pb deposits (Choulet et al., 2016; Buatier et al., 2016) suggest that those Zn clay minerals formed by direct precipitation from fluids, which could be meteoric and/or hydrothermal. Also the TEM study of the Moroccan clays showed the occurrence of bent stacks of parallel platelets (tactoid) with different orientations suggesting direct precipitation from fluids.

At Skorpion, as in other worldwide occurrences, the supergene processes, consisting of surface oxidation at ambient temperatures of primary ore deposits remain the best-envisaged mechanism for the formation of nonsulfide Zn deposits. The Gariep belt area in Namibia, where the Skorpion deposit is located, experienced marked climate changes from Cretaceous onward, most likely from humid-tropical to semi-arid and arid conditions (Arfè et al., 2017a). These climate changes controlled the formation and the nature of the supergene enrichment profile and would have created the most favorable conditions for the formation and variability of the clay minerals in this deposit (Boni and Mondillo, 2015). Typical supergene processes at ambient temperatures with a tendency toward a dryer climate can be considered responsible for the genesis of the Skorpion sauconite, with the possible contribution of low T hydrothermal fluids.

Discussion and Conclusions

The geological, mineralogical and geochemical features of two nonsulfide Zn(Pb) mineralized districts (Bongará and Skorpion-Rosh Pinah), which are located in two different continents, have been described in detail in the previous chapters. The analysis of the results of the study carried out on each deposit has been reported at the end of the respective chapters. Here below a comparison of the two districts will be made, pointing out the characteristics they have in common and their differences, in order to discuss their relationships with the climate conditions during supergene mineralization. In fact, the influence of climate on the geochemical processes that control the ore mineral assemblage under tropical and subtropical regimes is relatively poorly documented in the current literature.

The Mina Grande and Cristal deposits consist of several mineralized zones, where the ore occurs either as Zn-nonsulfides/sulfides in karst cavities (e.g. Mina Grande), or as manto-like replacement bodies (e.g. Cristal). The Zn occurrences are located in carbonate rocks (limestones and dolostones) of the Condorsinga Fm. (Pliensbachian-Toarcian) in the Pucarà Group. In both deposits lead is generally scarce or absent, but interesting germanium amounts have been detected at Cristal. Throughout the area, two phases of karstification of the carbonate rocks that host the ore deposits have been recognized. A most recent (Miocene-Pleistocene) karst landscape is superimposed on the ancient karst morphology, which was developed at the end of sedimentation of the Condorsinga Formation (Lower-to-Middle Jurassic), in association with a period of regional uplift. This older karst activity resulted in a sort of “ground preparation” for the Zn-carrying hydrothermal fluids. Such preparation included a dissolution-related porosity and permeability enhancement that resulted in the development of open cave systems and their infill deposits. The porosity provided channelways and favorable sites for hydrothermal dolomitization and Zn(Pb) mineralization, which both cross-cut and follow the bedding. The younger karst activity is related to the Miocene-Pleistocene uplift and had the effect to remobilize the ores already in situ, thus promoting the deepening of the supergene profiles.

The nonsulfide mineral assemblages of the Mina Grande and Cristal deposits, mostly consisting of smithsonite, hemimorphite and hydrozincite, differ in their average mineral abundances and mineralogical associations. In both deposits minor Zn-phyllosilicates (fraipontite and hendricksite, respectively at Mina Grande and Cristal), and Zn-smectite (sauconite at Cristal) were also found. Fraipontite, which is commonly replaced by supergene zaccagnaite, likely formed during early stage-wallrock supergene replacement processes, during which it replaced I/S mixed layers, of detrital origin. In both Mina Grande and Cristal deposits, the latter minerals were partly altered or overprinted by sauconite of either supergene or hydrothermal origin. The rare hendricksite in the Cristal area could be considered a hydrothermal product, formed during the emplacement of sulfides.

Several stages of alteration and mineral formation, mirrored by the paragenesis of the supergene deposits, have been confirmed by stable isotopic analysis of the newly formed

carbonate minerals. Isotopically distinct smithsonite, hydrozincite and calcite generations have been detected in both deposits. At Mina Grande, early smithsonite was the first product of sulfide oxidation and secondary precipitation, and was partially replaced by early generations of hemimorphite and hydrozincite. At Cristal, the onset of sulfide oxidation likely began in a water-saturated environment under reducing conditions, which favored siderite precipitation. In the Cristal prospect, the first properly “oxidized” mineral phases (e.g. smithsonite) precipitated after siderite, following a transition to a more dynamic hydrogeological system. Such variations of the environmental conditions might have occurred along with the transition from “Pebas” to “Acre” hydrogeological systems (10 Ma; Horn et al., 2010), and with the onset of more relevant periods of uplift (since 14/10 Ma). Late generations of smithsonite, hemimorphite, hydrozincite and calcite can be considered the products of subsequent oxidation phases in both deposits. The latter phases were more intense and prolonged at Mina Grande than at Cristal, since minerals as concretionary calcite and hydrozincite seem to have in the former deposit a more recent precipitation history. This assumption has been also confirmed by the oxygen isotope ratios of the supergene carbonate minerals. Early and late smithsonites from the two deposits have different $\delta^{18}\text{O}$ ratios (Mina Grande: ~ 27 and $\sim 26\text{‰}$ VSMOW, respectively; Cristal: from ~ 25 to $\sim 28\text{‰}$ VSMOW). In particular, the decreasing trend of the $\delta^{18}\text{O}$ ratios from the early to late smithsonites at Mina Grande may suggest several uplift episodes. Such decreasing trend has not been observed in the smithsonite generations of Cristal, leading to the interpretation of a major tectonic stability in this area.

The different host rock (dolostones vs limestones) and the local uplift rates have played an important role in the development of the supergene profiles in the two adjoining minesites. Since the Mina Grande area has been distinctly more uplifted than the Cristal one, being also the latter deposit mainly hosted in dolostones instead of limestones that are the Mina Grande host rocks, the effects of the recent karst activity in the two areas has been completely different. At Cristal, a few remnants of the primary sulfide bodies are still in place, and the nonsulfide mineralogy reflects the near neutral to weak alkaline conditions of supergene environment, in which nonsulfides formed. Conversely, at Mina Grande the hypogene mineralization is completely weathered and eroded, and the nonsulfides mineral assemblage reflects a depositional environment more alkaline than at Cristal. However, the climatic models persisting in this part of the Amazonas from Late Tertiary to Pleistocene also suggest that both the Mina Grande and Cristal supergene mineralizations were related to several weathering episodes that occurred under a climate not very different from today.

The Skorpion and Rosh Pinah Zn(Pb) deposits are hosted in Neoproterozoic rocks that are part of a volcano-sedimentary sequence within the Gariep Belt in southern Namibia. Skorpion is the largest Zn-nonsulfide mineralization ever exploited, and mostly consists of Zn-oxidized minerals (sauconite, smithsonite, hemimorphite, tarbuttite, skorpionite). Sauconite mostly formed by replacement of hemimorphite, feldspar and smithsonite (Kärner, 2006), but minor amounts are also derived from epitaxial crystallization of Zn-

smectite on cleavage surfaces of mica crystals of detrital origin, which acted as a chemically inactive support (Balassone et al., 2017).

The original oxidized interval at the surface of Rosh Pinah was of limited extent and has been now almost completely removed. The most abundant secondary minerals in this mine are smithsonite, cerussite and Fe-(hydr)oxides. The isotopic composition of Skorpion smithsonite shows that the supergene alteration of the sulfide protore was related to typical weathering processes. Skorpion smithsonite is characterized by $\delta^{13}\text{C}$ values strongly variable between 0.1 and -9.1‰ VPDB, and by a small range of $\delta^{18}\text{O}$ values (28.0 to 29.9‰ VSMOW). Calcite shows more limited variations in the $\delta^{13}\text{C}$ values, which are generally positive (0 to 1.6‰ VPDB). The $\delta^{18}\text{O}$ values in calcite are slightly lower than those of smithsonite (25.4 to 27.1‰ VSMOW). The analyses of Rosh Pinah carbonates show that the host dolomites are characterized by $\delta^{18}\text{O}$ values ranging from 18.7 to 22.0‰ VSMOW and by negative $\delta^{13}\text{C}$ values. The carbon isotope ratios of smithsonite, as in Skorpion, are negative but similar to those of the host dolomites. The $\delta^{18}\text{O}$ values are on average the same measured at Skorpion. The similar negative $\delta^{13}\text{C}$ values of smithsonite and dolomite from Rosh Pinah point to the involvement of both organic and host dolomite carbon for smithsonite formation, whereas at Skorpion the involvement of isotopically light organic carbon is considered more probable. However, a similar $\delta^{18}\text{O}$ composition of the smithsonites from the two deposits implies same ore-forming fluids and/or similar conditions during formation. The two deposits formed during two humid, temporally distinct periods characterized by different time spans. The isotope compositions of the carbonates from the Rosh Pinah deposit and its mineral association (e.g. smithsonite and cerussite) suggest that the supergene profile formed here during short-term weathering processes that match with the short-lasting Early-Middle Miocene semi-humid period. On the contrary, the oxidation of the Skorpion sulfide body took place from fluids with marked organic component in the isotope composition, which suggest a well-developed wet environment. Therefore, it is possible that the Skorpion primary orebody was exposed to weathering processes for a time span longer than the period involved in the development of the supergene profile at Rosh Pinah. Such long-lasting wet conditions occurred already during the first (Late Cretaceous-Paleocene) humid climate phase.

This research work has shown how supergene Zn deposits can form in similar conditions and then evolve under extremely variable climate settings that may range from semi-arid/desertic (Skorpion-Rosh Pinah district), to humid/tropical (Bongará district).

The $\delta^{18}\text{O}$ values of the supergene carbonates analyzed in the two mineralized districts considered are relatively constant (between ~25 and 30‰ VSMOW), and they refer to meteoric fluids whose temperatures ranged between ~15 and 25 °C. On the other hand, the comparison between the $\delta^{13}\text{C}$ values of the host rocks and those of supergene carbonates may be indicative of short- or long-terms weathering processes and/or of humid or arid environmental conditions. From the isotopic study performed on the supergene carbonates of the Skorpion, Mina Grande and Cristal deposits, it resulted that long-lasting wet weathering periods are marked by significant differences between the

$\delta^{13}\text{C}$ values of the host rock carbonates and those of smithsonites or supergene calcites. Conversely, similar $\delta^{13}\text{C}$ values are indicative either of short-term weathering processes that occurred in a humid/semi-humid environment (e.g. Rosh Pinah), or of prolonged periods of weathering in semi-arid conditions, where the organic activity may be relatively scarce.

The isotopic compositions of the smithsonites from the Bongará area have revealed that small variations in $\delta^{18}\text{O}$ may indicate extreme environmental changes involving both temperature and $\delta^{18}\text{O}$ composition of the ore-forming supergene fluids. In the tropical zone of Bongará, where climate settings have roughly been the same throughout time, the contemporary variation in temperature and composition of the fluids must be related to the uplift rates. In this relatively mountainous area, for example, the average annual temperatures at altitudes between 1,000 and 2,000 m.a.s.l. lie in the 23°-25°C range, with hot days and temperate-to-fresh evenings and nights. Between 2,000 and 3,600 m, the climate is more temperate, with average annual temperatures of ~ 18°C, which are characterized by strong variations between day and night. It follows that the study of the uplift rates should be as accurate as possible, in order to avoid any wrong interpretation of the isotope data. Therefore, the base metal carbonate minerals from the supergene deposits may provide (paleo)climatic informations, but they are not an exact proxy of the environmental conditions at the time of supergene alteration, if we do not consider a wide series of other geological factors.

Under arid and/or humid climatic conditions, the supergene processes allow the precipitation of an ample suite of minerals that are similar in terms of mineralogical association (e.g. smithsonite, hemimorphite, hydrozincite and sauconite). However, the amounts of such minerals in each deposit might be indicative of a specific climate regime during supergene alteration. To add useful constraints to the paleoenvironmental conditions in supergene mineral formation, the quantitative analysis of the phases occurring in the mineral paragenesis of the ore deposits becomes a fundamental issue. Smithsonite, hemimorphite and hydrozincite are fairly abundant in both Skorpion-Rosh Pinah and Bongará districts, and therefore they are not the best choice minerals to discriminate between humid and arid conditions of formation. On the contrary, an only limited occurrence of smectite group minerals (e.g. sauconite), combined with relatively higher amounts of minerals from the kaolinite group (e.g. fraipontite), would indicate that weathering (Velde, 1985) took place preferably under wet and humid conditions (Sherman, 2001). At Skorpion, great amounts of sauconite formed, replacing other minerals during Eocene-Oligocene, when the area was affected by a (semi)-arid climate (Kärner, 2006 and references therein). In the Bongará district, the pluvial and tropical climate setting has remained unchanged during the entire evolution of the supergene profiles, and therefore sauconite formation has been severely limited.

The mineralogy and geochemistry of the host rock can have also played an important role in determining the geochemical conditions for mineral precipitation in the two above-mentioned districts. For example, silica activity generally controls the formation of both clay minerals and Zn-hydrosilicates (hemimorphite). Smectites, kaolinites and hemimorphite are all stable under elevated silica activity, whereas micas are not.

However, the activity of specific cations (K^+ and Na^+) shifts the equilibrium to one or the other mineral phase (Garrels and Christ, 1990). Kaolinite is stable at low K^+ and Na^+ activities, whereas the medium-to-high activity of these ions is favorable to the stability of smectite and micas. Therefore, arkose-like host rocks (e.g. Skorpion deposit), rather than carbonate ones (e.g. Mina Grande and Cristal deposits) can also control the mineral formation.

The joint role of host rock characteristics and climate in the evolution of a supergene profile is also evident in the genesis of Mina Grande and Cristal deposits. For instance, if we look at the entire mineral assemblage and at the chemistry of peculiar trace elements (e.g. Ge) in both deposits, they show different geochemical signatures. The Mina Grande orebody is the direct expression of an alkaline supergene environment with high runoff rates. In the nearby Cristal prospect, instead, the supergene mineral association consists of several mineral phases that are stable in conditions of lower pH than those acting in the Mina Grande area. The reason of this substantial difference between the two deposits should be attributed mainly to local factors, which are (1) the different host rocks and (2) the variable altitude. A relatively recent study (Teir et al., 2006) on the stability of calcite vs. dolomite in rainwater has revealed that $CO_{2(gas)}$ was more rapidly released from simple calcium carbonate than from calcium-magnesium carbonate in acidic environment. At Cristal, the dolomite host rock did not act as an efficient buffering system for the acidic meteoric waters from which supergene minerals precipitated, due to its major capability to store CO_2 under acidic alteration. On the contrary, at Mina Grande the calcite host rock has favored the maintenance of a limited alkaline pH range, due to the adsorption of excess H^+ (i.e. formation of carbonic acid and bicarbonates) and production of carbonate and bicarbonate ions, if the H^+ concentration is low.

The altitude, which is the other mentioned factor, is probably even more important for the development of the supergene profiles in the Cristal and Mina Grande deposits. Indeed, in the previous chapters it has been reported how the average annual rainfalls in tropical areas are heavily affected by altitude (in the Bongará district average annual rainfalls normally exceed 1,000 mm, with up to 1,800 mm at higher altitudes and as little as 145 mm at lower altitudes). Due to this strong altitude-dependence, the rates of the uplifts under the tropical climate regime become important to determine the initial conditions of weathering for an exposed sulfide protore. Such conditions in tectonic settings such as the fold-and-thrust belt of the Subandean zone may be very different at the district scale. Therefore, the possibility to have sufficiently uplifted areas in this climate setting could result in: (1) poor preservation of sulfide bodies and (2) continuous supply of fresh meteoric water (i.e. reduced acidity of the percolating waters). The latter, along with the lithogeochemistry of the host rock (e.g. calcite over dolomite) allows the development of a supergene profile in a restricted range of pH-Eh conditions that favour the local formation of a limited suite of minerals (commonly Zn-carbonates). Such conditions may be quite alkaline, so that some critical elements like germanium are dispersed in the environment and the possibility to fix them in the supergene minerals is reduced. Conversely, under more acidic conditions (e.g. Cristal area), germanium may be fixed (e.g. absorbed by goethite). Therefore, even if from a metallurgical point of view to have

a restricted suite of minerals is optimal for zinc recovery, the loss of benefits from other by-products elements (e.g. Ge) should be taken into account.

Most likely, the altitude effects are also the main reason of the different clay mineralogy that exists between the Cristal and Mina Grande deposits (e.g. sauconite at Cristal and fraipontite at Mina Grande). The altitude-dependent runoff rates may promote relatively wetter and drier supergene environments. At Cristal, drier conditions relatively to Mina Grande, allowed sauconite formation. On the contrary, fraipontite growth is favoured in the relatively wetter supergene environment of Mina Grande deposit. The amounts of these two minerals compared to other supergene mineral phases (e.g. smithsonite, hemimorphite) occurring in both deposits are very low. The limited growth of fraipontite in the wet Mina Grande deposit would be quite unexpected, but is in agreement with the fact that kaolinite group minerals at 25°C and 1 atm usually occur under more acidic conditions (Garrels and Christ, 1990) than the alkaline ones active during supergene nonsulfide mineralization in this area. At Mina Grande fraipontite formed during the early stages of the sulfides oxidation, when the environment was safely more acidic than the current one, in which fraipontite is not stable. This instability is well documented by the common findings of supergene zaccagnaite replacing fraipontite. This “peculiar” mineral association may be also useful to constrain the genesis of kaolinite group minerals in several environments, since they can also form hydrothermally.

In conclusion, the study carried out on the Bongará (Peru) and Skorpion-Rosh Pinah (Namibia) districts has only partially supported the published theories on the mechanisms that drive the formation of the supergene nonsulfide deposits. In our opinion, the ideas of a few authors (Reichert and Borg, 2008; Reichert, 2009 and Borg, 2015) that see an arid environment as the most favorable scenario for an effective sulfide oxidation process, must be revisited. The present study has significantly improved the knowledge on the supergene deposits formed in tropical weathering regimes, showing at the same time how such deposits can be of high economic interest. Mina Grande and Cristal are two good examples of interesting Zn-nonsulfide concentrations formed under tropical weathering. The observation of a complex coexistence of factors (e.g. the host rock lithotype and runoff rate), and their interplay during sulfide oxidation represents a better understanding of the geochemical processes that control the genesis and preservation of the supergene deposits in modern tropical areas. The data provided by this study on this interesting topic could be applied to other (paleo)weathering profiles worldwide, in order to build more accurate models.

This study has also stressed that the C-O stable isotope analyses are useful to roughly estimate the environmental conditions at the time of supergene oxidation, but they do not provide additional paleoclimate constrains. The attempt to provide paleoclimatic data, without considering the uplift history of the areas considered may result useless. Therefore, a good geological interpretation, and accurate mineralogical and geochemical studies must be combined together in order to provide the right information and determine the constraints for the evolution of the supergene profiles with their mineralization.

Acknowledgements

Above all, I would like to thank my supervisors Prof. Maria Boni, Dr. Nicola Mondillo and Dr. Giuseppina Balassone. Their vast experience and knowledge of the nonsulfide deposits worldwide made my work easier than I thought. However, during my PhD experience there were many obstacles of different nature (scientific, administrative, etc.) that I would not have been able to solve without their continual support and encouragement. Special thanks go to R. de’Gennaro (DiSTAR, Napoli) for his help during SEM analyses. A great thank is also due to Prof. M. Joachimski (GeoZentrum-NordBayern, Erlangen), in whose Laboratory I did part of my isotopic work, who was always ready to help and solve my many doubts.

There are also lots of people I would like to thank for several reasons.

For the research carried out on the Peruvian deposits, I am firstly indebted to the Compañía Minera Pilar del Amazonas, and especially to C. Ushela, for introducing me and my supervisors to the Bongará mineralization. I am also grateful to E. Castro Medrano (formerly Rio Cristal) and L. Oldham (Anglo Peruana) for maps and discussions, and to Zinc One Resources Inc. for allowing publication.

I am indebted to many reviewers for comments and suggestions, which greatly enhanced the quality of my research and rendered my papers more “readable”. Many thanks go to A. Brown (Economic Geology Assistant Editor), G. Borg (Martin Luther University Halle-Wittenberg), D.F. Sangster (Geological Survey of Canada), S. Paradis (Geological Survey of Canada), and to D. Large (Consulting geologist).

For the research carried out on Namibian deposits, I am indebted to the Skorpion and Rosh Pinah personnel, and especially to the mine geologists, for guidance at the minesites and discussion. I am especially grateful to A. Johr (Rosh Pinah) and to G. Hinder (Rosh Pinah Geo Centre), for having provided some of the samples used for analyses.

My great appreciation goes to G. Olivo (Queen's University) and R. Herrington (Natural History Museum of London), who reviewed and evaluated my PhD thesis.

Finally, I would also like to thank Antonella Morelli and my family, for all their love and support.

The research work was supported by Departmental (University of Napoli), funds of M. Boni, G. Balassone and N. Mondillo, and by Ph.D funds to G. Arfè granted by DiSTAR. The Society of Economic Geologists Canada Foundation (SEGCF) supported a Student Research Grant (Project SRG_15-40) to G. Arfè for a fieldtrip to Peru. A limited part of the geochemical analyses were carried out in the frame of a Marie Skłodowska-Curie Individual Fellowship (Project 660885) to N. Mondillo, funded by the European Union’s Horizon 2020 research and innovation program.

References

- Abkhoshk, E., Jorjani, E., Al-Harashsheh, M.S., Rashchi, F., Naazeri, M., 2014. Review of the hydrometallurgical processing of non-sulfide zinc ores. *Hydrometallurgy*, 149, 153-167.
- Ague, J. J., and Brimhall, G.H., 1989. Geochemical modeling of steady state fluid flow and chemical reaction during supergene enrichment of porphyry copper deposits. *Economic Geology*, 84, 506-528.
- Aide, M.T., and Aide, C., 2012. Rare earth elements: their importance in understanding soil genesis. *ISRN Soil Science* 2012.
- Alchin, D.J., Frimmel, H.E., Jacobs, L.E., 2005. Stratigraphic setting of the metalliferous Rosh Pinah Formation and the Spitzkop and Koivib Suites in the Pan-African Gariep Belt, southwestern Namibia. *South African Journal of Geology*, 108, 19-34.
- Alchin, D.J. and Moore, J.M., 2005. A review of the Pan-African, Neoproterozoic Rosh Pinah Zn-Pb deposit, southwestern Africa. *South African Journal of Geology*, 108, 71-86.
- Alcman, A., and Marksteirner, R., 1997. Petroleum systems and structural style in the Santiago fold and thrust belt: A salt related orogenic belt. VI Simposio Bolivariano, *Memorias*, Tomo II, p. 171-186.
- Al Ganad, I., Lagny, P., Lescuyer, J.L., Rambo, C., Touray, J.C., 1994. Jabali, a Zn-Pb-(Ag) carbonate-hosted deposit associated with Late Jurassic rifting in Yemen. *Mineralium Deposita*, 29, 44-56.
- Andrew, R.L., 1984. The geochemistry of selected base- metal-gossans, southern Africa. *Journal of Geochemical Exploration*, 22, 161-192.
- Andrew, A., Godwin, C.I., Sinclair, A.J., 1984. Mixing line isochrons: A new interpretation of galena lead isotope data from southeastern British Columbia. *Economic Geology*, 79, 919-932.
- Anglo Peruana, 2005. A Re-evaluation of the Geology and Mineralization of the Charlotte Bongará Zinc Project, Amazonas, northern Peru: technical report. Anglo Peruana Terra S.A (former Consultora Minera Anglo Peruana S.A.), Lima, Peru, 128 p.
- Aoudjit, H., Robert, M., Elsass, F., Curmi, P., 1995. Detailed study of smectite genesis in granitic saprolites by analytical electron microscopy. *Clay Minerals*, 30, 135-148.
- Arancibia, G., Matthews, S.J., Pérez de Arce, C., 2006. K-Ar and $^{40}\text{Ar}/^{39}\text{Ar}$ geochronology of supergene processes in the Atacama Desert, northern Chile: tectonic and climatic relations. *Journal of the Geological Society of London*, 163, 107-118.
- Arfè, G., Boni, M., Balassone, G., Mondillo, N., Hinder, G., Joachimski, M., 2017a. New C-O isotopic data on supergene minerals from the Skorpion and Rosh Pinah ore deposits

(Namibia): Genetic and paleoclimatic constraints. *Journal of African Earth Sciences*, 126, 148-158.

Arfè, G., Boni, M., Mondillo, N., Aiello, R., Balassone, G., 2016. Supergene alteration in the Capricornio Au-Ag epithermal vein system, Antofagasta Region, Chile. *The Canadian Mineralogist*, 54, 1-25.

Arfè, G., Mondillo, N., Boni, M., Balassone, G., Joachimski, M., Mormone, A., Di Palma, T., 2017b. The karst-hosted Mina Grande nonsulfide zinc deposit, Bongará district (Amazonas region, Peru). *Economic Geology*, 112, 1089-1110.

Arfè, G., Mondillo, N., Boni, M., Joachimski, M., Balassone, G., Mormone, A., Santoro L., Castro Medrano E. The Cristal Zn prospect (Amazonas region, Northern Peru). Part II: An example of supergene zinc enrichments in tropical areas. *Ore Geology Reviews*, (in press).

Arostegui, J., Irabien, M.J., Nieto, F., Sangüesa, J., Zuluaga, M.C., 2001. Microtextures and the origin of muscovite-kaolinite intergrowths in sandstones of the Utrillas Formation, Basque Cantabrian Basin, Spain. *Clays Clay Mineral.*, 49, 6, 529-539.

Attwood, D., 2000. *Soft X-Rays and Extreme Ultraviolet Radiation: Principles and Applications*. Cambridge University Press, Cambridge, 470 p.

Aurischio, C, and Gianfagna, A., 2005. Microanalisi: metodi di rivelazione dei raggi-X a dispersione di energia (EDS) e di lunghezza d'onda (WDS); analisi qualitativa e quantitativa *in* Sequi P., (Eds.). *Metodi di Analisi Mineralogica del Suolo*, 1124.6, 1-37.

Balassone, G., Nieto, F., Arfè, G., Boni, M., Mondillo, N., 2016. New investigations on Zn-clays from Skorpion (Namibia). 35th ICG Cape Town, SA.

Balassone, G., Rossi, M., Boni, M., Stanley, G., McDermott, P., 2008. Mineralogical and geochemical characterization of nonsulfide Zn-Pb mineralization at Silvermines and Galmoy (Irish Midlands). *Ore Geology Reviews*, 33, 168-186.

Balassone, G., Nieto, F., Arfè, G., Boni, M., Mondillo, N., 2017. Zn-clay minerals in the Skorpion Zn nonsulfide deposit (Namibia): Identification and genetic clues revealed by HRTEM and AEM study. *Applied Clay Sciences*, 150, 309-322.

Battaglia-Brunet, F., d'Hugues, P., Cabral, T., Cezac, P., García, J.L., Morin, D. 1998. The mutual effect of mixed Thiobacilli and Leptospirilli populations on pyrite bioleaching. *Mineral Engineering*, 11, 195-205.

Basuki, N.I., 2006. Post-Early Cretaceous MVT Zn-Pb mineralisation, Bongará area, northern Peru: Fluid characteristics and constraints on deposition mechanisms. Ph.D. thesis, Toronto, ON, University of Toronto, 318 p.

Basuki, N.I., and Spooner, E.T.C., 2008. Fluid evolution and flow direction of MVT Zn-Pb related basinal brines, Bongará area, northern Peru: CL and fluid inclusion data [abs.].

Geological-Mineralogical Association of Canada-Society of Economic Geologists-Society for Geology Applied to Mineral Deposits Meeting, Quebec City, 13 p.

Basuki, N.I., Taylor, B.E., Spooner, E.T.C., 2008. Sulfur Isotope Evidence for Thermochemical Reduction of Dissolved Sulfate in Mississippi Valley-Type Zinc-Lead Mineralization, Bongara Area, Northern Peru. *Economic Geology*, 103, 783-799.

Basuki, N.I., and Spooner, E.T.C., 2009. Post-early Cretaceous Mississippi Valley-type Zn-Pb mineralization in the Bongará area, northern Peru: Fluid evolution and paleo-flow from fluid inclusions evidence. *Exploration and Mining Geology*, 18, 25-39.

Baumgartner, R., and Fontboté, L., 2008. Mineral zoning and geochemistry of epithermal polymetallic Zn-Pb-Ag-Cu-Bi mineralization at Cerro de Pasco, Peru. *Economic Geology*, 103, 493-537.

Baumgartner, R., Fontboté, L., Spikings, R., Ovtcharova, M., Schaltegger, U., Schneider, J., Page, L., Gutjahr, M., 2009. Bracketing the age of magmatic-hydrothermal activity at the Cerro de Pasco epithermal polymetallic deposit, Central Peru: A U-Pb and $^{40}\text{Ar}/^{39}\text{Ar}$ study. *Economic Geology*, 104, 479-504.

Bayraktar, I., Aslan, A., Ersayin, S., 1998. Effects of primary slime and clay on selectivity of flotation of sub-volcanogenic complex polymetallic ores. *Trans. Inst. Min. Metal. Sect. B Applied Earth Sciences*, 107, C71-C76.

Belissant, R., Boiron, M.C., Luais, B., Cathelineau, M., 2014. LA-ICP-MS analyses of minor and trace elements and bulk Ge isotopes in zoned Ge-rich sphalerites from the Noailhac-Saint-Salvy deposit (France) Insights into incorporation mechanisms and ore deposition processes. *Geochim. Cosmochim. Acta* 126, 518-540.

Bendezú, R., and Fontboté, L., 2009. Cordilleran epithermal Cu-Zn-Pb-(Au-Ag) mineralization in the Colquijirca district, central Peru: deposit-scale mineralogical patterns. *Economic Geology*, 104, 905-944.

Benavides-Cáceres, V., 1999. Orogenic evolution of the Peruvian Andes: the Andean Cycle. *Society of Economic Geologists Special Publication* 7, 61-107.

Bennetts, D.A., Webb, J.A., Stone, D.J.M., Hill, D.M., 2006. Understanding the salinisation process for groundwater in an area of south-eastern Australia, using hydrochemical and isotopic evidence. *Journal of Hydrology*, 323, 178-192.

Bertin, E.P., 1970, *Principles and Practise of X-ray Spectrometric Analysis*. Plenum, London, 621 p.

Beuchat, S., Moritz, R., Pettke, T., 2004. Fluid evolution in the W-Cu-Zn-Pb San Cristobal vein, Peru: fluid inclusion and stable isotope evidence. *Chemical Geology*, 210, 201-224.

Beuchat, S., Moritz, R., Sartori, M., Chiaradia, M., 2001. High-precision geochronology and structural constraints on ore formation in the Zn-Pb-Ag-Cu Domo de Yauli district,

central Peru, in Piestrzyski et al., (Eds.). Mineral Deposits at the Beginning of 21st Century. Proceed. 6th biennial SGA meeting, 381-384.

Bish, D.L., and Howard, S.A., 1988. Quantitative phase analysis using the Rietveld method. *Journal of Applied Crystallography*, 21, 86-91.

Bish, D.L., and Post, J.E., 1993. Quantitative mineralogical analysis using the Rietveld fullpattern fitting method. *American Mineralogist*, 78, 932-940.

Bissig, T., and Riquelme, R., 2010. Andean uplift and climate evolution in the southern Atacama Desert deduced from geomorphology and supergene alunite-group minerals. *Earth and Planetary Science Letters*, 299, 447-457.

Boland, M.B., Clifford, J.A., Meldrum, A.H., Poustie, A., 1992. Residual base metal and barite mineralization at Silvermines, County Tipperary, Ireland, *in* Bowden, A.A., Earls, G., O'Connor, P.G., and Pyne, J.F., (Eds.). The Irish minerals industry 1980-1990. Irish Association for Economic Geology, Dublin, Ireland, 247-260.

Boni, M., Balassone, G., Arseneau, V., Schmidt, P., 2009a. The nonsulfide zinc deposit at Accha (Southern Peru): geological and mineralogical characterization. *Economic Geology*, 104, 267-289.

Boni, M., Balassone, G., Iannace, A., 1996. Base metal ores in the lower Paleozoic of southwestern Sardinia, in Sangster, D.F., (Eds.). Carbonate-hosted lead-zinc deposits. Society of Economic Geologists Special Publication 4, 18-28.

Boni, M., Gilg, H.A., Balassone, G., Schneider, J., Allen, C.R., Moore, F., 2007. Hypogene Zn carbonate ores in the Angouran deposit, NW Iran. *Mineralium Deposita*, 42, 799-820.

Boni, M., Gilg, H.A., Aversa, G., Balassone, G., 2003. The "Calamine" of SW Sardinia (Italy): geology, mineralogy and stable isotope geochemistry of a supergene Zn-mineralization. *Economic Geology*, 98, 731-748.

Boni, M., and Large, D.E., 2003. Nonsulfide zinc mineralization in Europe. An overview. *Economic Geology*, 98, 715-729.

Boni, M., and Mondillo, N., 2015. The "Calamines" and the "Others": the great family of supergene nonsulfide zinc ores. *Ore Geology Reviews*, 67, 208-233.

Boni, M., Mondillo, N., Balassone, G., 2011. Zincian dolomite: a peculiar dedolomitization case?. *Geology*, 39, 183-186.

Boon, M., and Heijnen, J.J., 1998. Chemical oxidation kinetics of pyrite in bioleaching processes. *Hydrometallurgy*, 48, 27-41.

Boni, M., Schmidt, P.R., De Wet, J.R., Singleton, J.D. Balassone, G., Mondillo, N., 2009b. Mineralogical signature of nonsulfide zinc ores at Accha (Peru): A key for recovery. *International journal of Mineral Processing*, 93, 267-277.

- Boni, M., Terracciano, R., Evans, N., Laukamp, C., Schneider, J. and Bechstädt, T., 2007. Genesis of vanadium ores in the Otavi Mountainland (Namibia). *Economic Geology*, 102, 441-469.
- Borchardt, G., 1989. *Smectites: Madison, USA*, Soil Science Society of America Special Publication, 1, 675-727.
- Borg, G., 2009. The influence of fault structures on the genesis of supergene zinc deposits. *Society of Economic Geologists, Special Publication 14*, 121-132.
- Borg, G., 2015. A Review of Supergene Nonnon- Zinc (SNSZ) Deposits - the 2014 Update, in Archibald S.M. and Piercey S.J. (Eds.). *Current Perspectives of Zinc Deposits*. Irish Association for Economic Geology, Dublin, 123-147.
- Borg, G., and Armstrong, R., 2002. Isotopic SHRIMP age dating of zircons from igneous basement and rhyolitic cover rocks at Skorpion, southern Namibia. *IAGOD Symposium and Geocongress 2002, 11th quadriennial. Extended abstract volume on CD-ROM*, Windhoek, Geological Survey of Namibia.
- Borg, G., Kärner, K., Buxton, M., Armstrong, R., Merwe, S.W., 2003. Geology of the Skorpion supergene Zn deposit, southern Namibia. *Economic Geology*, 98, 749-771.
- Botton, G., 2007. Analytical electron microscopy, in Hawkes, P.W., and Spence, J.C.H., (Eds.). *Science of Microscopy*. Springer, New York, 273 p.
- Brand, W.A., Coplen, T.B., Vogl, J., Rosner, M., Prohaska, T., 2014. Assessment of international reference materials for isotope-ratio analysis. *Pure and Applied Chemistry*, 86, 425-467.
- Brophy, J.A., 2012. Rio Cristal Resources Corporation Bongará zinc project. Technical Report NI 43-101, Canada, Rio Cristal Resources, 104 p.
- Brugger, J., McPhail, D.C., Wallace, M., Waters, J., 2003. Formation of willemite in hydrothermal environments. *Economic Geology*, 98, 819-835.
- Brunton, G., 1955. Vapour pressure glycolation of oriented clay minerals. *American Mineralogist*, 40, 124-126.
- Buatier M., Choulet, F., Petit, S., Chassagnon, R., Vennemann, T., 2016. Nature and origin of natural Zn clay minerals from the Bou Arhous Zn ore deposit. Evidence from electron microscopy (SEM-TEM) and stable isotope compositions (H and O). *Applied Clay Sciences*, 132, 377-390.
- Burke, K., Webb, S.J., Gunnell, Y., 2004. Possible causes and timing of Africa's elevation changes. *Geoscience Africa 2004, Abstract Volume 1*, University of the Witwatersrand, Johannesburg, South Africa, p. 93.
- Catchpole, H., Kouzmanov, K., Putlitz, B., Seo, J.H., Fontboté, L., 2015. Zoned base metal mineralization in a porphyry system: origin and evolution of mineralizing fluids in the Morococha district, Peru. *Economic Geology*, 110, 39-71.

- Cesàro, G., 1927. Sur la fraipontite, silicate basique hydraté de zinc et d'aluminum. *Annales de la Société géologique de Belgique*, 50, 106-110.
- Ceyhan, N., 2003. Lead isotope geochemistry of Pb-Zn deposits from Eastern Taurides, Turkey. Unpublished MSc Dissertation. Graduate School of Natural and Applied Sciences of the Middle East Technical University, Ankara (Turkey), 105 p.
- Chiaradia, M., Fontboté, L., Paladines, A., 2004. Metal sources in mineral deposits and crustal rocks of Ecuador (1°N-4°S): a lead isotope synthesis. *Economic Geology*, 99, 1085-1106.
- Choi, J., Komarneni, S., Grover, K., Katsuki, H., Park, M., 2009. Hydrothermal synthesis of Mn-mica. *Applied Clay Science*, 46, 69-72.
- Choulet, F., Buatier, M., Barbanson, L., Guégan, R., Ennaciri, A., 2016. Zinc-rich clays in supergene non-sulfide zinc deposits. *Mineralium Deposita*, 51, 467-490.
- Church, S.E., LeHuray, A.P., Grant, A.R., Delevaux, M.H., Gray, J.E., 1986. Lead isotopic data from sulfide minerals from the Cascade Range, Oregon and Washington. *Geochimica et Cosmochimica Acta*, 50, 317-328.
- Clauer, N., and Chaudhuri, S., 1992. Isotopic signatures of sedimentary rocks. *Lecture Notes in Earth Sciences*, Springer, Berlin, 43, 529 p.
- Clay, J.E., and Schoonraad, G.P., 1976. Treatment of zinc silicates by the Waelz process. *Journal of the South African Institute of Mining and Metallurgy*, 77(1), 11-14.
- Claypool, G.E., Holser, W.T., Kaplan, I.R., Sakai, H., Zak, I., 1980. The age curves of sulfur and oxygen isotopes in marine sulfate and their mutual interpretation. *Chemical Geology*, 28, 199-260.
- Clifford, J.A., Ryan, P., Kucha, H., 1986. A review of the geological setting of the Tynagh orebody, Co. Galway, in Andrew, C.J., Crowe, R.W.A., Finlay, S., Pennell, W.M., Pyne, J.F., (Eds.). *Geology and genesis of mineral deposits in Ireland*. Irish Association for Economic Geology, Dublin, 419-439.
- Connelly, D., 2011. High clay ores: a mineral processing nightmare part 2. *Australian Journal of Mining* 24, 28-29.
- Cook, N.J., Ciobanu, C.L., Pring, A., Skinner, W., Shimizu, M., Danyushevsky, L., Saini-Eidukat, B., Melcher, F., 2009. Trace and minor elements in sphalerite: A LA-ICPMS study. *Geochimica et Cosmochimica Acta* 73, 4761-4791.
- Coppola, V., Boni, M., Gilg, H.A., Balassone, G., Dejonghe, L., 2008. The "calamine" nonsulfide Zn-Pb deposits of Belgium: Petrographical, mineralogical and geochemical characterization. *Ore Geology Reviews*, 33, 187-210.
- Coppola, V., Boni, M., Gilg, H.A., Strzelska-Smakowska, B., 2009. Nonsulfide zinc deposits in the Silesia-Cracow district, southern Poland: *Mineralium Deposita*, 44, 559-580.

Corrans, R.D., Gewald, H., Whyte, R.M., Land, B.N., 1993. The Skorpion SZ secondary zinc deposit, southwestern Namibia [abs.]. Mining Investment in Namibia Conference, Windhoek, Namibia Department of Mining and Energy, 46-52.

Cross, H.E., Read, F.O., 1970. Waelz treating of complex zinc-lead ores. AIME World Symposium on Mining and Metallurgy of Lead and Zinc, v. 2.

Dachroth, W., and Sonntag, C., 1983. Grundwasserneubildung und Isotopendatierung in Südwestafrika/ Namibia. Zeitschrift der Deutschen Geologischen Gesellschaft, 134, 1013-1041.

Dalheimer, M., 1990. The Zn-Pb-Ag deposits Huaripampa and Carahuacra in the mining district of San Cristobal, central Peru, in Fontboté, L., Amstutz, G.C., Cardozo, M., Cedillo, E., and Frutos, J., (Eds.). Stratabound ore deposits in the Andes. Springer, Berlin, 279-291.

Dalmayrac, B., Laubacher, G., Marocco, R., 1980. Caractères généraux de l'évolution géologique des Andes péruviennes. Travaux et Documents de l'ORSTOM, Paris, 122, 501 p.

Davies, C.J., and Coward, M.P., 1982. The structural evolution of the Gariep arc in southern Namibia (South-West Africa). Precambrian Research, 17, 137-197.

Deer, W.A., Howie, R.A., Zussman, J., 1963. Rock-forming minerals: Sheet silicates. The Mineralogical Society, United Kingdom, 3, 11-30.

de Oliveira, S.B., Juliani, C., Monteiro, L.V.S., 2015. Aspectos da Mineralização de Zn Supergênica Não-Sulfetada do Depósito de Florida Canyon, na Amazônia Peruana. 14º Simpósio de Geologia da Amazônia, Marabá, Brazil (poster).

Dera, G., Pucéat, E., Pellenard, P., Neige, P., Delsate, D., Joachimski, M., Reisberg, L., Martinez, M., 2009. Water mass exchange and variations in seawater temperature in the NW Tethys during the Early Jurassic: evidence from neodymium and oxygen isotopes of fish teeth and belemnites. Earth and Planetary Sciences Letters, 286, 198-207.

de Wet, J.R., and Singleton, J.D., 2008. Development of a viable process for the recovery of zinc from oxide ores. The Journal of the Southern African Institute of Mining and Metallurgy, 108, 253-259.

Dove, P.M., and Rimstidt, J.D., 1994. Silica-water interactions, in Heaney, P.J., Prewitt, C.T., Gibbs, G.V., (Eds.). Silica, Physical Behavior. Geochemistry and Materials Applications: Reviews in Mineralogy, 29, 259-308.

Dowsett, H., Barron, E.J., Poore, R.Z., 1996. Middle Pliocene sea surface temperatures: A global reconstruction. Marine. Micropaleontology, 27, 13-25.

- Dyer, J.A., Trivedi, P., Scrivner, N.C., Sparks, D.L., 2003. Lead sorption onto ferrihydrite. 2. Surface complexation modeling. *Environmental Science and Technology*, 37, 915-922.
- Drever, J.I., 1998. *The Geochemistry of Natural Waters*. Prentice Hall Pub., 436 p.
- Drits, V.A., Sokolova, T.N., Sokolova, G.V., Cherkashin, V.I., 1987. New members of the hydrotalcite-manasseite group. *Clays and Clay Minerals*, 35, 401-417.
- Dufresne, R.E., 1976. Quick leach of siliceous zinc ores. *Journal of Metals*, 28, 8-12.
- Dzombak, D.A., and Morel, F.M.M., 1990. *Surface Complexation Modeling, Hydrous Ferric Oxide*. John Wiley and Sons, New York. 416 p.
- Emmons, S.F., 1901. The secondary enrichment of ore-deposits. *Transactions of the American Institute of Mining and Metallurgical Engineers*, 30, 177-216.
- Emselle, N., McPhail, D.C., Welch, S.A., 2005. Reliance, Flinders Ranges: mineralogy, geochemistry and zinc dispersion around a nonsulfide orebody. *Regolith 2005 - Ten Years of CRC LEME*, 86-90.
- Evangelou, V.P., Sainju, U.M., Huang, X., 1992. Evaluation and quantification of armoring mechanisms of calcite, dolomite and rock phosphate by manganese, in Younos, T., Diplas, P., Mostaghimi, S., (Eds.). *Land Reclamation: Advances in Research and Technology*. American Society of Ag. Engineers, Nashville, TN., 304-316.
- Evans, B.W., and Strens, R.G.J., 1966. Zinc mica from Franklin Furnace, New Jersey [abs.]. *Nature*, 211, 619.
- Evans, N.J., Boni, M., McInnes, B.I.A., McDonald, B.J., 2006. (U-Th)/He Thermochronology of Supergene Base Metal Ores and Implications for Namibian Paleoclimate. 16th Goldschmidt Meeting, 27 Aug-1 Sept, Melbourne, Theme 10, S10-2.
- Faure, G., 1998. *Principles and Applications of Geochemistry*, 2nd edition; Prentice Hall, New Jersey, 600 p.
- Field, C.W., 1966. Sulfur isotopic method for discriminating between sulfates of hypogene and supergene origin. *Economic Geology*, 61, 1428-1435.
- Fitzpatrick, E.A., 1984. *Micromorphology of soils*. Chapman and Hall, London New York, 433 p.
- Flower, B.P., 1999. Warming without high CO₂?. *Nature*, 399, 313-314.
- Fontboté, L., 1990. Stratabound ore deposits in the Pucará basin: An overview. *Society for Geology Applied to Mineral Deposits Special Publication* 8, 253-266.

Fontboté, L., and Gorzawski, H., 1990. Genesis of the Mississippi Valley-type Zn-Pb deposit of San Vicente, Central Peru: Geologic and isotopic (Sr, O, C, S, Pb) evidence. *Economic Geology*, 85, 1402-1437.

Fransolet, A.M., and Bourguignon, P., 1975. Données nouvelles sur la fraipontite de Moresnet (Belgique). *Bulletin de la Société Française de Minéralogie et de Cristallographie*, 98, 235-244.

Frenay, J., 1985. Leaching of oxidized zinc ores in various media. *Hydrometallurgy*, 15(2), 243-253.

Frenzel, M., Hirsch, T., Gutzmer, J., 2016. Gallium, germanium, indium and other trace and minor elements in sphalerite as a function of deposit type - A meta-analysis. *Ore Geology Reviews*, 76, 52-78.

Frimmel, H.E., 2000. The Pan African Gariep belt in southwestern Namibia and western South Africa. *Geological Survey of Namibia Communications*, 12, 197-209.

Frimmel, H.E., and Board, W.S., 2000. Fluid evolution in and around the Rosh Pinah massive sulphide deposit in the external Pan-African Gariep Belt, Namibia. *South African Journal of Geology*, 103, 191-206.

Frimmel, H.E., Fölling, P.G., Eriksson, P., 2002. Neoproterozoic tectonic and climatic evolution recorded in the Gariep Belt, Namibia and South Africa. *Basin Research*, 14, 55-67.

Frimmel, H., Koller, F., Watkins, R.T., Faure, K., 1995. Tectonic history of mafic and ultramafic rocks in the Gariep Belt. *Abstracts Centennial Geocongress, Geological Society South Africa*, 226-229.

Frimmel, H.E., and Lane, K., 2005. Geochemistry of carbonate beds in the Neoproterozoic Rosh Pinah Formation, Namibia: Implications on depositional setting and hydrothermal ore formation. *South African Journal of Geology*, 108, 5-18.

Fron del, C., 1972. *The minerals of Franklin and Sterling Hill - A checklist*. Wiley, New York, 94 p.

Fron del, C., and Ito, J., 1966. Hendricksite, a new species of mica. *American Mineralogist*, 51, 1107-1123.

Fuerstenau, M.C., Jameson, G.J., Yoon, R.-H., 2007. *Froth flotation: a century of innovation*. SME, Englewood, 897 p.

Galán, E., 2006. Genesis of clay minerals, in Bergaya, F., Theng, B.K.G., Lagaly, G., (Eds.). *Developments in clay science: handbook of clay science*. Elsevier, Oxford, 1, 1129-1162.

Gallagher, K., and Brown, R., 1999. The Mesozoic denudation history of the Atlantic margins of southern Africa and southeast Brazil and the relationship to offshore sedimentation, in Cameron, N.R., Bate, R.H., Clure, V.S. (Eds.). The oil and gas habitats of the South Atlantic. Geological Society, London, Special Publications, 153, 41-53.

Garven, G., 1995. Continental-scale groundwater flow and geological processes. *Annual Review of Earth and Planetary Sciences*, 23, 89-117.

Garver, J.I., Reiners, P.R., Walker, L.J., Ramage, J.M., Perry, S.E., 2005. Implications for timing of Andean uplift from thermal resetting of radiation-damaged zircon in the Cordillera Huayhuash, northern Peru. *Geology*, 113, 117-138.

Garrels, R.M., Christ, C.L., 1990. Solutions, minerals, and equilibria. Lones and Bartlett Publishers, Boston, 450 p.

Gat, J.R., 1996. Oxygen and hydrogen isotopes in the hydrologic cycle. *Annual Review of Earth and Planetary Sciences*, 24, 225-262.

Gavelin, S., Parwel, A., Ryhage, R., 1960. Sulfur isotope fractionation in sulfide mineralization. *Economic Geology*, 55, 510-530.

Gerrard, A.J., 1994. Weathering of granitic rocks: Environment and clay mineral formation, in Robinson, D.A. and Williams, R.B.G., (Eds.). Rock weathering and landform evolution. John Wiley & Sons, 3-20.

Ghazban, F., McNutt, R.H., Schwarcz, H.P., 1994. Genesis of sediment-hosted Zn-Pb-Ba deposits in the Irankuh district, Esfahan area, west central Iran. *Economic Geology*, 89, 1262-1278.

Gil, W.R., Baby, P., Marocco, R., Ballard, J.F., 1999. North-south structural evolution of the Peruvian Subandean zone. International Symposium on Andean Geodynamics (ISAG), 4th, June 4, 1999, Göttingen (Germany), Proceedings, 278-282.

Gilg, H.A., Boni, M., Hochleitner, R., Struck, U., 2008. Stable isotope geochemistry of carbonate minerals in supergene oxidation zones of Zn-Pb deposits. *Ore Geology Reviews*, 33, 117-133.

Gilg, H.A., Struck, U., Vennemann, T., Boni, M., 2003. Phosphoric acid fractionation for smithsonite and cerussite between 25 and 72°C. *Geochimica et Cosmochimica Acta*, 67, 4049-4055.

Goldstein, J.I., Newbury, D.E., Echlin, P., Joy, D.C., Romig, A.D., Lyman, C.E., Fiori, C., Lifshin, E., 1992. Scanning Electron Microscopy and X-ray Microanalysis, a text for biologists, materials scientists and geologists. Plenum Press, New York, 820 p.

Gorzawski, H., Fontboté, L., Field, C. W., Tejada, R., 1990. Sulfur isotope studies in the zinc-lead mine San Vicente, central Peru, in Fontboté, L., Amstutz, G.C., Cardozo, M.,

Cedillo, E., Frutos, J. (Eds.). Stratabound Ore Deposits in the Andes. Society for Geology Applied to Mineral Deposits Special Publication 8. Springer, Berlin, 305-312.

Goyne, K.W., Brantley, S.L., Chorover, J., 2010. Rare earth element release from phosphate minerals in the presence of organic acids. *Chemical Geology*, 278 (1), 1-14.

Gnoinski, J., 2007. Skorpion Zinc: optimization and innovation. *Journal of the Southern African Institute of Mining and Metallurgy*, 107, 657-662.

Graham, S. D., Brough, C., Cropp, A., 2015. An Introduction to ZEISS Mineralogic Mining and the correlation of light microscopy with automated mineralogy: a case study using BMS and PGM analysis of samples from a PGE-bearing chromitite prospect [conference paper]. *Precious Metals Conference 2015*.

Gregory-Wodzicki, K.M., 2000. Uplift history of the Central Northern Andes: A review. *Geological Society of America Bulletin*, 112, 1092-1105.

Gresse, P.G., 1994. Strain partitioning in the southern Gariep arc as reflected by sheath folds and stretching directions. *South African Journal of Geology*, 97, 52-61.

Gunnesch K. A., Baumann A., Gunnesch M., 1990. Lead isotope variations across the central Peruvian Andes. *Economic Geology*, 85, 1384-1401.

Gutzmer, J., 2006. Ar-Ar geochronology of Mn⁴⁺ oxihydroxides from the Skorpion Mine, Namibia - implications for ore formation. Unpublished Technical Report to Anglo American Plc, Johannesburg, 23 p.

Güven, N., 1988. Smectites: in *Hydrous Phyllosilicates Exclusive of Micas*, S. W. Bailey, (Eds.). *Reviews in Mineralogy* 20. Mineralogical Society of America, Washington, D.C., 497-560.

Harder, H., 1977. Clay mineral formation under lateritic weathering conditions. *Clay Minerals*, 12, 169-180.

Hartley, A.J., and Rice, C.M., 2005. Controls on supergene enrichment of porphyry copper deposits in the Central Andes: A review and discussion. *Mineralium Deposita*, 40, 515-525.

Hays, P.E., Pisias, N.G., Roelofs, A.K., 1989. Paleooceanography of the eastern equatorial Pacific during the Pliocene: A high resolution radiolarian study. *Paleoceanography*, 4, 57-73.

Hermoza W., P. Baby, N. Espurt, E. Martinez, R. Bolaños, 2006. Lateral variations in the subandean deformation of the Ucayali basin: a complex fold-thrust belt and inverted system. IX simposio Bolivariano, Cartagena de las Indias, Colombia. (abstract volume).

- Hermoza W., P. Baby, N. Espurt, E. Martinez, R. Bolaños, 2007. The Ucayali Sub Andean Basin: a complex fold and thrust belt and inverted system. XIII Congreso Peruano de Geología, Lima (abstract volume).
- Heyl A.V, and Bozion, C.N., 1962. Oxidized zinc deposits of the United States, Part 1. General Geology: US Geological Survey Bulletin, 1135A, 52 p.
- Higashi, S., Miki, K., Komarneni, S., 2002. Hydrothermal synthesis of Zn-smectite. *Clays and Clay Minerals*, 50, 299-305.
- Hill, R.J., 1991. Expanded use of the Rietveld method in studies of phase abundance in multiphase mixtures. *Powder Diffraction*, 6, 74-77.
- Hinder, G., 2015. Sensationeller Neufund von Churchit-(Y) aus der Skorpion Zink Mine in Namibia. *Mineralien-Welt*, 26, 28-29.
- Hitzman, M.W., Reynolds, N.A., Sangster, D.F., Allen, C.R., Carman, C.E., 2003. Classification, genesis, and exploration guides for nonsulfide Zinc deposits. *Economic Geology*, 98, 685-714.
- Hoers, J., 1987. *Stable Isotope Geochemistry*. Springer, Heidelberg, 241 p.
- Hoefs J., 1997, *Stable isotope geochemistry*. Springer, Heidelberg, 201 p.
- Hooghiemstra, H., and Van der Hammen, T., 2004. Quaternary Ice-Age dynamics in the Colombian Andes: Developing an understanding of our legacy. *Philosophical Transactions of the Royal Society of London*, 359 B, 173-181.
- Hoorn, C., 1994. An environmental reconstruction of the palaeo-Amazon River system (Middle to late Miocene, NW Amazonia). *Palaeogeography, Palaeoclimatology, Palaeoecology*, 112, 187-238.
- Hoorn, C., Wesselingh, F.P., Hovikoski, J., Guerrero, J., 2010. The development of the Amazonian mega-wetland (Miocene; Brazil, Colombia, Peru, Bolivia), in Hoorn, C., and Wesselingh, F.P., (Eds.). *Amazonia, landscape and species evolution*. New York, Wiley, 123-142.
- Hötzl, S., 2013. Vegetation development in West Africa of the biosphere shift during late Miocene to (early) Pliocene. Unpublished Dissertation for the Doctoral Degree in Natural Sciences (Dr. rer. nat.) University of Bremen (Germany), 77 p.
- Hye In Ahn, B.S., 2010. Mineralogy and Geochemistry of the Non-sulfide Zn Deposits in the Sierra Mojada District, Coahuila, Mexico. Unpublished Ph.D. Thesis, Austin, USA, University of Texas, 193 p.
- Imasuen, O.I., Tazaki, K., Fyfe, W.S., Kohyama, N., 1989. Experimental transformations of kaolinite to smectite: *Applied Clay Sciences*, 4, 27-41.

Ingwersen, G., 1990. Die sekundären Mineralbildungen der Pb-Zn-Cu-Lagerstätte Tsumeb, Namibia (Physikalisch-chemische Modelle). Diss. Institut für Mineralogie und Kristallchemie, Universität Stuttgart, 232 p.

Instituto Geologico Minero y Metalurgico (INGEMMET), 1995. Geologia de Los Cuadrangulos de Bagua Grande, Jumbilla, Lonya Grande, Chachapoyas, Rioja, Leimebamba y Bolivar: Instituto Geologico Minero y Metalurgico, Boletin 56 Serie A. Carta Geologica Nacional, Peru, 390 p.

Isacks, B.L., 1988. Uplift of the Central Andean Plateau and bending of the Bolivian orocline. *Journal of Geophysical Research*, 93, 3211-3231.

Jacay, J., Sempere, T., Carlier, G., Carlotto, V., 1999. Late Paleozoic-early Mesozoic plutonism and related rifting in the Eastern Cordillera of Peru: International Symposium on Andean Geodynamics, 4th, Göttingen, Proceedings, 358-363.

Jasper, M.J.U., Stanistreet, I.G., Charlesworth, E.G., 2000. Neoproterozoic inversion tectonics, half-graben depositories and glacial controversies, Gariep fold-thrust belt, southern Namibia. *Geological Survey of Namibia Communications*, 12, 187-196.

Jenkyns, H.C., Jones, C.E., Gröcke, D.R., Hesselbo, S.P., Parkinson, D.N., 2002. Chemostratigraphy of the Jurassic system: applications, limitations and implications for palaeoceanography. *Journal of the Geological Society*, 159, 351-378.

Jordan, T.E., Reynolds, J.H., III, Erikson, J.P., 1997. Variability in age of initial shortening and uplift in the Central Andes, 16°-33°30'S, in Ruddiman, W.F., (Eds.). *Tectonic uplift and climate change*: New York, Plenum Press, 41-61.

Juillot, F., Morin, G., Ildefonse, P., 2003. Occurrence of Zn/Al hydrotalcite in smelter-impacted soils from northern France: evidence from EXAFS spectroscopy and chemical extractions. *American Mineralogist*, 88, 509-526.

Kaandorp, R.J.G., Vonhof, H.B., Del Busto, C., Wesselingh, F.P., Ganssen, G.M., Marmorel, A.E., Romero Pittman, L., Van Hinte, J.E., 2003. Seasonal stable isotope variation of the Amazonian fresh water bivalve *Anodontites trapesialis*. *Palaeogeography, Palaeoclimatology, Palaeoecology*, 194 (4), 339-354.

Kaandorp, R.J.G., Vonhof, H.B., Wesselingh, F.P., Pittman, L.R., Kroon, D., van Hinte, J.E., 2005. Seasonal Amazonian rainfall variation in the Miocene Climate Optimum. *Palaeogeography, Palaeoclimatology, Palaeoecology*, 221, 1-6.

Kademli, M., and Gulzoy, O.Y., 2012. The role of particle size and solid contents of feed on mica-feldspar separation in gravity concentration. *Physicochemical Problems of Mineral Processing*, 48(2), 645-654.

Kärner, K., 2006. The metallogensis of the Skorpion Non-sulphide Zinc Deposit, Namibia. Unpublished Ph.D. Thesis, Martin-Luther-Universität Halle-Wittenberg, Germany, 133 p.

- Kaseke, K.F., Wang, L., Wanke, H., Turewicz, V., Koeniger, P., 2016. An analysis of precipitation isotope distributions across Namibia using historical data. *PLOS ONE*, 11, 19 p.
- Kaufhold, S., Färber, G., Dohrmann, R., Ufer, K., Grathoff, G., 2015. Zn-rich smectite from the Silver Coin Mine, Nevada, USA. *Clay Minerals*, 50, 417-430.
- Keller, W.D., 1970. Environmental aspects of clay minerals. *Journal of Sedimentary Petrology*, 40, 798-813.
- Keller, W.D., Reynolds, R.C., Inque, A., 1986. Morphology of clay minerals in the smectite-to-illite conversion series by scanning electron microscopy. *Clays and Clay minerals*, 34, 187-197.
- Kelly, W.C., 1958. Topical study of lead-zinc gossans: State Bureau of Mines and Mineral Resources. New Mexico Institute of Mining and Metallurgy Bulletin 46, 80 p.
- Kim, S.T., Mucci, A., Taylor, B.E., 2007. Phosphoric acid fractionation factors for calcite and aragonite between 25 and 75°C, revisited. *Chemical Geology*, 246, 135-146.
- Kindl, S., 1979. Reconnaissance geological map of the Rosh Pinah and northern Richtersveld areas, 1:50,000, ISCOR geology and exploration dept.
- King, L.C., 1951. South African Scenery. Oliver and Boyd, London, 379 p.
- King, T., 1996. Equatorial Pacific sea surface temperatures, faunal patterns, and carbonate burial during the Pliocene. *Marine Micropaleontology*, 27, 63-84.
- Kittrick, J.A., 1969. Soil minerals in the $\text{Al}_2\text{O}_3\text{-SiO}_2\text{-H}_2\text{O}$ system and a theory of their formation. *Clays and Clay Minerals*, 17, 157-167.
- Klein, G.D., Zúñiga y Rivero, F.G., Hay-Roe, H., Alvarez-Calderon, E., 2011. A Reappraisal of the Mesozoic/Cenozoic Tectonics and Sedimentary Basins of Peru. *Search and Discover Article #10332 (AAPG)*, 55 p.
- Kloprogge, T., Komarneni, S., Amonette, J., 1999. Synthesis of smectite clay minerals: A critical review. *Clays and Clay Minerals*, 47, 529-554.
- Klug, H.P. and Alexander, L.E., 1959. *X-ray Diffraction Procedures*. New York, John Wiley & Sons, 2nd ed. 251 p.
- Kobe, H.W., 1977. El Grupo Pucará y su mineralización en el Peru central: *Sociedad Geologica Peru Boletin*, 55-56, 61-84.
- Kobe, H.W., 1982. El ambiente de la mineralización estratoligada de Zn-Pb-Ag-Ba-Mn-Fe-Cu en los sedimentos de la cuenca occidental del Pucará, Peru central. *Sociedad Geologica Peru Boletin*, 69, 41-69.
- Kobe, H.W., 1990a. Stratabound Cu-(Ag) deposits in the Permian Red-Bed Formation, Central Peru, in Fontbote, L., Amstutz, G.C., Cardozo, M., Wauschkuhn, A., (Eds.). *Stratabound ore deposits in the Andes*. Berlin-Heidelberg, New York, Springer, 113-122.

- Kobe, H.W., 1990b. Metallogenic evolution of the Yauli dome, Central Peru, in Fontboté, L., Amstutz, G.C., Cardozo, M., Wauschkuhn, A., (Eds.). *Stratabound ore deposits in the Andes*. Berlin-Heidelberg, New York, Springer, 267-278.
- Kontak, D.J., Clark, A.H., Farrar, E., Strong, D.F., 1985. The rift associated Permo-Triassic magmatism of the Eastern Cordillera: A precursor to the Andean orogeny, in Pitcher, W.S., Atherton, M.P., Cobbing, J., Beckinsale, R.D., (Eds.). *Magmatism at a plate edge: The Peruvian Andes*. Glasgow, Blackie, and New York, Halsted Press, 36-44.
- Kramers, J.D., Tolstikhin, I.N., 1997. Two terrestrial lead isotope paradoxes, forward transport modelling, core formation and the history of the continental crust. *Chemical Geology*, 139, 75-110.
- Kuhlemann J., Vennemann T., Herlec U., Zeeh S., Bechstädt T., 2001. Variations of sulfur isotopes, trace element compositions, and cathodoluminescence of Mississippi Valley-type Pb-Zn ores from the Drau range, Eastern Alps (Slovenia-Austria): implications for ore deposition on a regional versus microscale. *Economic Geology*, 96, 1931-1941.
- Kulp, J.L., Amstutz, G.C., Eckelmann, F.D., 1957. Lead isotope composition of Peruvian galenas. *Economic Geology*, 52, 914-922.
- Large, D., 2001. The geology of non-sulphide zinc deposits - An overview. *Erzmetall*, 54, 264-274.
- Laubacher, G., 1978. *Géologie de la Cordillère Orientale et de l'Altiplano au nord et nord-ouest du lac Titicaca (Peru)*. Travaux et Documents de l'Office de la recherche scientifique et technique outre-mer (ORSTOM) 95, 217 p.
- Laubacher, G., and Naeser, C.W., 1994. Fission-track dating of granitic rocks from the Eastern Cordillera of Peru: Evidence for Late Jurassic and Cenozoic cooling. *Journal of Geological Society*, 151, 473-483.
- Leach, D.L., Sangster, D.F., Kelley, K.D., Large, R.R., Garven, G., Allen, C.R., Gutzmer, J., Walters, S., 2005. Sediment-hosted lead-zinc deposits: a global perspective, in Hedenquist, J.W. et al. (Eds.). *Economic Geology 100th Anniversary Volume*, Society of Economic Geologists, Inc., Littleton, Co., 561-607.
- Leavens, P. B., Zullo, J., Verbeek, E., 2009. A complex, genthelvite-bearing skarn from the Passaic pit, Sterling Hill mine, Ogdensburg, New Jersey. *Axis*, 5, 1-26.
- LeHuray, A.P., Caulfield, J.B.D., Rye, D.M., Dixon, P.R., 1987. Basement controls on sediment-hosted Zn-Pb deposits: a Pb isotope study of Carboniferous mineralization in central Ireland. *Economic Geology*, 82, 1695-1709.
- LeHuray, A.P., Church, S.E., Koski, R.A., Bouse, R. M., 1988. Pb isotopes in sulfides from mid-ocean ridge hydrothermal sites. *Geology*, 16, 362-365.

- Li, N., and Kyle, J.R., 1997. Geologic controls of sandstone-hosted Zn-Pb-(Sr) mineralization, Jinding deposit, Yunnan Province, China: A new environment for sediment-hosted Zn-Pb deposits, in Rongfu, P., (Eds.). 30th International Geological Congress: Amsterdam, VSP, Proceedings, 9, 67-82.
- Lim, J., 2011. Controlling clay behaviour in suspension: developing a new paradigm for the minerals industry. Ph.D dissertation, University of Melbourne, 187 p.
- Lindgren, W., 1913. Ore deposits. 1st edition. McGraw-Hill, 883 p.
- Loughman, D.L., and Hallam, A., 1982. A facies analysis of the Pucara Group (Norian to Torcian carbonates, organic rich shale and phosphate) of central and northern Peru. *Sedimentary Geology*, 35, 161-194.
- Lozano, R.P., Rossi, C., La Iglesia, Á., Matesanz, E., 2012. Zaccagnaite-3R, a new Zn-Al hydrotalcite polytype from El Soplaio cave (Cantabria, Spain). *American Mineralogist*, 97(4), 513-523.
- Lundberg, J.G., Marshall, L.G., Gurrero, J., Horton, B., Malabarba, M.C.S.L., Wesselingh, F., 1998. The stage of Neotropical fish diversification: A history of tropical South American rivers, in Malabarba, R.E., Reis, R.P., Vari, Z., Lucena, M., Lucena, C.A.S., Eds.). *Phylogeny and classification of Neotropical fishes*. Porto Alegre, Brazil, Edipucrs, 13-48.
- Macfarlane, A.W., 1999. Isotopic studies of Northern Andean crustal evolution and ore metal sources, in Skinner, B.J., (Eds.). *Geology and Ore Deposits of the Central Andes*, Society of Economic Geologists Special Publication 7, 195-217.
- Macfarlane, W., Petersen, U., 1990. Pb Isotopes of the Hualgayoc Area, Northern Peru: Implications for Metal Provenance and Genesis of a Cordilleran Polymetallic Mining District. *Economic Geology*, 85, 1303-1327.
- Machel, H.G., 2001. Bacterial and thermochemical sulfate reduction in diagenetic settings-old and new insights. *Sedimentary Geology*, 140, 143-175.
- Mager, K., Meurer, U., Garcia-Egocheaga, B., Goicoechea, N., Rutten, J., Saage, W., Simonetti, F., 2000. Recovery of zinc oxide from secondary raw materials: New Developments of the Waeltz Process, in 4th international symposium on recycling of metals and engineering materials, Stewart D.L., Stephens R., Daley J.C.(Eds). *The Minerals, Metals & Materials Society 2000*, 329-344.
- Manceau, A., Lanson, B., Schlegel, M.L., Harge, J.C., Musso, M., Eybert-Berard, L., Hazemann, J.L., Chateigner, D., Lamble, G.M., 2000. Quantitative Zn speciation in smelter-contaminated soils by EXAFS spectroscopy. *American Journal of Sciences*, 300, 289-343.
- Manning, T.J., and William, R., 1997. Inductively Coupled Plasma-Atomic Emission Spectrometry. *Chemical Education*, 1-19.

- Maréchal, C.N., Télouk, P., Albarède, F., 1999. Precise analysis of copper and zinc isotopic compositions by plasma-source mass spectrometry. *Chemical Geology*, 156, 251-273.
- Masek, J.G., Isacks, B.L., Gubbels, T.L., Fielding, E.J., 1994. Erosion and tectonics at the margins of continental plateaus. *Journal of Geophysical. Research*, 99, 13941-13956.
- Mathalone, J.M.P., and Montoya, R.M., 1995. Petroleum geology of the sub-Andean basins of Peru: American Association of Petroleum Geologists Memoir, 62, 423-444.
- Matthew, I.G., and Elsner, D., 1977. The processing of zinc silicate ores- a review: *Metallurgical and Materials Transactions B*, 8, 85-91.
- McArthur, J.M., Howarth, R.J., 2004. Strontium isotope Stratigraphy, in Gradstein, F.M., Ogg J.G., Smith, A.G. (Eds.). *A Geological Time Scale*, 96-105.
- Mégard, F., 1968. Geología del cuadrángulo de Huancayo. *Boletín del Servicio de geología y minería*, 18, 123 p.
- Mégard, F., 1978. Étude géologique des Andes du Perou central. *Travaux et Documents de l' Office de la recherche scientifique et technique outre-mer (ORSTOM)*, Paris, 86, 310 p.
- Mégard, F., 1984. The Andean Orogenic Period and its major structures in central and northern Peru. *Journal of the Geological Society*, 141, 893-900.
- Mégard, F., Noble, D.C., McKee, E.H., Bellon, H., 1984. Multiple phases of Neogene compressive deformation in the Ayacucho intermontane basin, Andes of central Peru. *Geological Society of America Bulletin*, 95, 1108-1117.
- Merlino, S., Orlandi, P., 2001. Carraraite and zaccagnaite, two new minerals from the Carrara marble quarries: their chemical compositions, physical properties, and structural features. *American Mineralogist*, 86(10), 1293-1301.
- Meunier, A., 2005. *Clays*. Springer-Verlag Berlin Heidelberg, Germany, 476 p.
- McPhail, D.C., Summerhayes, E., Welch, S., Brugger, J., 2003. The geochemistry of zinc in the Regolith, in Roach, I.C. (Eds.), *Advances in Regolith. CRC for Landscape Environments and Mineral Exploration*, 287-291.
- McSween, H.Y., Richardson, S.M., Uhle, M.E., 2003. *Geochemistry: Pathways and processes*, 2nd edition. Columbia University Press, New York. 432 p.
- Mégard, F., 1978. Étude géologique des Andes du Perou central. *Travaux et Documents de l'Office de la recherche scientifique et technique outre-mer (ORSTOM)*, Paris 86, 310 p.
- Mégard, F., 1984, The Andean Orogenic Period and its major structures in central and northern Peru. *Journal of the Geological Society*, 141, 893-900.

- Mégard, F., 1987. Structures and evolution of the Peruvian Andes, in Schaer, J., and Rodgers, J., (Eds.). *The anatomy of mountain ranges*. Princeton, NJ, Princeton University Press, 179-210.
- Mégard, F., Noble, D.C., McKee, E.H., Bellon, H., 1984. Multiple phases of Neogene compressive deformation in the Ayacucho intermontane basin, Andes of central Peru. *Geological Society of America Bulletin*, 95, 1108-1117.
- Mišković, A., Spikings, R.A., Chew, D.M., Košler, J., Ulianov, A., Schaltegger, U., 2009. Tectonomagmatic evolution of Western Amazonia: Geochemical characterization and zircon U-Pb geochronologic constraints from the Peruvian Eastern Cordilleran granitoids. *Geological Society of America Bulletin*, 121, 1298-1324.
- Miller, R.McG, 2008. *The geology of Namibia*, vol 3. Geological Survey of Namibia, Windhoek, 524 p.
- Mondillo N., Arfè G., Boni M., Balassone G., Boyce A., Joachimski M., Villa I.M. The Cristal Zn prospect (Amazonas region, Northern Peru). Part I: New insights on the sulfide mineralization in the Bongará province. *Ore Geology Reviews*, (in press).
- Mondillo, N., Arfè, G., Herrington, R., Boni, M., Wilkinson, C., Mormone, A., 2018. Germanium enrichment in supergene settings: evidence from the Cristal nonsulfide Zn prospect, Bongará district, northern Peru, DOI: 10.1007/s00126-017-0781-1.
- Mondillo, N., Boni, M., Balassone, G., Grist, B., 2011. In search of the lost zinc: a lesson from the Jabali (Yemen) nonsulfide zinc deposit. *Journal of Geochemical Exploration*, 108, 209-219.
- Mondillo, N., Boni, M., Balassone, G., Joachimski, M., Mormone, A., 2014a. The Jabali Nonsulfide Zn-Pb-Ag Deposit, Western Yemen. *Ore Geology Reviews*, 61, 248-267.
- Mondillo, N., Boni, M., Balassone, G., Villa I.M., 2014b. The Yanque Prospect (Peru): From Polymetallic Zn-Pb Mineralization to a Nonsulfide Deposit. *Economic Geology*, 109, 1735-1762.
- Mondillo, N., Nieto, F., Balassone, G., 2015. Micro- and nano-characterization of Zn-clays in nonsulfide supergene ores of southern Peru. *American Mineralogist*, 100, 2484-2496.
- Monsch, K.A., 1998. Miocene fish faunas from the northwestern Amazonia basin (Colombia, Peru, Brazil) with evidence of marine incursions. *Palaeogeography, Palaeoclimatology, Palaeoecology*, 143, 31-50.
- Montario, M. J., 2006. Thermochronological evidence for Neogene incision of the Rio Pativilca Canyon, northern Peru. M.Sc. thesis, University of Albany, State University of New York, 155 p.
- Montaser, A., 1998. *Inductively Coupled Plasma Mass Spectrometry*. Wiley, New York, 1004 p.

- Monteiro, L.V.S., Bettencourt, J.S., Juliani C., Flávio de Oliveira, T., 2006. Geology, petrography, and mineral chemistry of the Vazante non-sulfide and Ambrósia and Fagundes sulfide-rich carbonate-hosted Zn-(Pb) deposits, Minas Gerais, Brazil. *Ore Geology Reviews*, 28, 201-234.
- Monteiro, L.V.S., Bettencourt, J.S., Juliani C., Flávio de Oliveira, T., 2006. Nonsulfide and sulfide-rich zinc mineralizations in the Vazante, Ambrósia and Fagundes deposits, Minas Gerais, Brazil: Mass balance and stable isotope characteristics of the hydrothermal alterations. *Gondwana Research*, 11, 362-381.
- Moore, J.M., 1972, Supergene mineral deposits and physiographic development in southwest Sardinia, Italy. *Transactions of the Institution of Mining and Metallurgy, Section B*, 71, 59-66.
- Moore, D.M., and Reynolds, R.C. JR., 1997. *X-Ray Diffraction and the identification and Analysis of Clay Minerals* (second edition). Oxford University Press, Oxford, New York, 378 p.
- Mora, A., Baby, P., Roddaz, M., Parra, M., Brusset, S., Hermoza, W., Espurt, N., 2010. Tectonic history of the Andes and sub-Andean zones: Implications for the development of the Amazon drainage basin, in Hoorn, C., and Wesselingh, F.P., (Eds.), *Amazonia, landscape and species evolution: A look into the past*. New York, Wiley, 38-60.
- Moritz, R., Fontboté, L., Spangenberg, J., Rosas, S., Sharp, Z., Fontignie, D., 1996. Sr, C and O isotope systematics in the Pucará basin, Central Peru: Comparison between Mississippi Valley-type deposits and barren areas. *Mineralium Deposita*, 31, 147-162.
- Morrison, J., Brockwell, T., Merren, T., Fourel, F., Phillips, A.M., 2001. On-Line High-Precision Stable Hydrogen Isotopic Analyses on Nanoliter Water Samples. *Analytical Chemistry*, 73, 3570-3575.
- Mortimer, R.J.G., Coleman, M.L., Rae, J.E., 1997. Effect of bacteria on the elemental composition of early diagenetic siderite: implications for paleoenvironmental interpretations. *Sedimentology*, 44, 759-765.
- Naeser, C.W., Crochet, J.Y., Jaillard, E., Laubacher, G., Mourier, T., Sigé, B., 1991. Tertiary Fission-Track ages from the Bagua syncline (Northern Peru). Stratigraphic and tectonic implications. *Journal of South American Earth Sciences*, 4, 61-71.
- Nagao, S., Rao, R., Killey, R., Young, J., 1998. Migration behavior of eu (III) in sandy soil in the presence of dissolved organic materials. *Radiochimica Acta*, 82 (Supplement), 205-212.
- Newman, A.C.D., and Brown, G., 1987. The chemical constitution of clays, in *Chemistry of Clays and Clay Minerals*, A.C.D. Newman, (Eds). John Wiley & Sons, New York, 1-128.

- Nieto, F., Velilla, N., Peacor, D.R., Huertas, M.O., 1994. Regional retyrograde alteration of sub-greenschist facies chlorite to smectite. *Contributions to Mineralogy and Petrology*, 115, 243-252.
- Nimfopoulos, K., Michailidis, K. M., Christofides, G., 1997. Zincian rancieite from the Kato Nevrokopi manganese deposits, Macedonia, northern Greece. *Geological Society London Special Publications*, 119, 339-347.
- Noble, D.C., Silberman, M.L., Mégard, F., Bowman, H.R., 1978. Comendite (peralkaline rhyolites) in the Mitu Group, central Peru: Evidence of Permian-Triassic crustal extension in the Central Andes. *U.S. Geological Survey Journal Research*, no. 6, 453-457.
- Ohmoto, H., and Rye, R.O., 1979. Isotopes of sulfur and carbon, in Barnes, H.L. (Eds.). *Geochemistry of hydrothermal ore deposits*. New York, Wiley-Interscience, 509-567.
- O'Neil, J.R., 1966. Theoretical and experimental aspects of isotopic fractionation, in Valley, J.W., Taylor Jr., H.P., O'Neil, J.R., (Eds.). *Stable isotopes in high temperature geological processes*. Review in *Mineralogy and Geochemistry*, 16, 1-40.
- Osika, R., 1986, Poland, in Dunning, F.W., and Evans, A.M., (Eds.). *Mineral deposits of Central Europe: The Institution of Mining and Metallurgy and the Mineralogical Society*, London, 3, 55-97.
- Page, D.C., and Watson, M.D., 1976. The Pb-Zn deposit of Rosh Pinah Mine, South West Africa. *Economic Geology*, 71, 306-327.
- Palmer, A.N., Palmer, M.V., 1995. Geochemistry of Capillary Seepage in Mammoth Cave. *Proceedings of the 4th Mammoth Cave Science Conference*, Mammoth Cave, KY, p. 119-133.
- Paquet, H., Colin, F., Duplay, J., Nahon, D., Millot, G., 1986. Ni, Mn, Zn, Cr-smectites, early and effective traps for transition elements in supergene ore deposits, in Rodriguez-Clemente & Tardy, Y., (Eds.). *Proceedings of the International Meeting "Geochemistry of the earth surface and processes of mineral formation"*, Granada (Spain), March 1986, 221-229.
- Paradis, S., Keevil, H., Simandl, G.J., Raudsepp, M., 2011. Geology and mineralogy of carbonate-hosted nonsulphide Zn-Pb mineralization in southern (NTS 082F/03) and central (NTS 093A/14E, 15W) British Columbia: Geoscience BC Summary of Activities 2010. *Geoscience BC, Report 2011-1*, 143-158.
- Paradis, S., and Simandl, G.J., 2010. Carbonate-hosted, Nonsulphide Zn-Pb (supergene) Mineral Deposit Profile B09, in *Geological Fieldwork 2010*, British Columbia Geological Survey, Paper 2011-1, 189-194.
- Pascua, C.S., Ohnuma, M., Matsushita, Y., Tamura, K., Yamada, H., Cuadros, J., Ye, J., 2010. Synthesis of monodisperse Zn-smectite. *Applied Clay Science*, 48, 55-59.

- Partridge, T.C., 1998. Of diamonds, dinosaurs and diastrophism: 150 million years of landscape evolution in southern Africa. *South African Journal of Geology*, 101, 167-184.
- Partridge, T.C., and Maud, R.R., 1987. Geomorphic evolution of southern Africa since the Mesozoic. *South African Journal of Geology*, 90, 179-208.
- Paytan, A., Kastner, M., Campbell, D., Thiemens, M.H., 2004. Seawater sulfur isotope fluctuations in the Cretaceous. *Science*, 304, 1663-1665.
- Penrose, R.A.F., 1894. The superficial alteration of ore deposits. *The Journal of Geology*, 30, 288-317.
- Perrotta, A.J., Garland, T.J., 1975. Low Temperature Synthesis of Zinc-Phlogopite. *American Mineralogist*, 60, 152-154.
- Petit, S., Righi, D., Decarreau, A., 2008. Transformation of synthetic Zn-stevensite to Zn-talc induced by the Hofmann-Klemen effect. *Clays and Clay Minerals*, 56, 645-654.
- Pfiffner, O.A., and Gonzalez, L., 2013. Mesozoic-Cenozoic evolution of the Western Margin of South America: Case study of the Peruvian Andes. *Geosciences*, 3, 262-310.
- Pickford, M., Senut, B., Mocke, H., Mourer-Chauviréc, C., Ragea, J.-C., Mein, P., 2014. Eocene aridity in southwestern Africa: timing of onset and biological consequences. *Transactions of the Royal Society of South Africa*, 69, 139-144.
- Poage, M.A., and Chamberlain, C.P., 2001. Empirical relationships between elevation and the stable isotope composition of precipitation and surface waters: Considerations for studies of paleoelevation change. *American Journal of Science*, 301, 1-15.
- Porter, F.C., 1991. *Zinc Handbook: Properties, Processing, and Use in Design*. International Lead Zinc Research Organization. Mechanical Engineering, 73. CRC Press; 1 edition, 629 p.
- Pourret, O., Davranche, M., Gruau, G., Dia, A., 2007. Competition between humic acid and carbonates for rare earth elements complexation. *Journal of colloid and interface science*, 305 (1), 25-31.
- Radke, B.M., and Mathis, R.L., 1980. On the formation and occurrence of saddle dolomite. *Journal of Sedimentary Petrology*, 50, 1149-1168.
- Rehkämper, M., Mezger, K., 2000. Investigation of matrix effects for Pb isotope ratio measurements by multiple collector ICP-MS: Verification and application of optimized analytical protocols. *Journal of Analytical Atomic Spectrometry*, 15, 1451-1460.
- Reich, M., Palacios, C., Vargas, G., Luo, S., Cameron, E.M., Leybourne M.I., Parada, M.A., Zúñiga, A., You, C., 2009. Supergene enrichment of copper deposits since the onset of modern hyperaridity in the Atacama Desert, Chile: *Mineralium Deposita*, 44, 497-504.

- Reichert, J., 2009. A Geochemical Model of Supergene Carbonate-Hosted Nonsulfide Zinc Deposits. Society of Economic Geologists Special Publication 14, 69-76.
- Reichert, J., and Borg, G., 2008. Numerical simulation and a geochemical model of supergene carbonate-hosted non-sulphide zinc deposits. *Ore Geology Reviews*, 33, 134-151.
- Reichert, J., Borg, G., Rashidi, B., 2003. Mineralogy of Calamine Ore from the Mehdi Abad Zinc-Lead Deposit, Central Iran, in Eliopoulos, D.G., et al. (Eds.). *Mineral Exploration and Sustainable Development*. Millpress, Rotterdam, 1, 97-100.
- Reid, C.J., 2001. Stratigraphy and mineralization of the Bongara MVT zinc-lead district, northern Peru. M.Sc. thesis, Toronto, University of Toronto, 179 p.
- Reid, D.L., Ransome, I.G.D., Onstott, T.C. and Adams, C.J., 1991. Time of emplacement and metamorphism of late Precambrian mafic dikes associated with the Pan-African Gariep orogeny, southern Africa: implications for the age of the Nama Group. *Journal of African Earth Sciences*, 13, 531-541.
- Rietveld, H.M., 1969. A profile refinement method for nuclear and magnetic structures. *Journal of Applied Crystallography*, 2, 67-71.
- Rimstidt, J.D., and Vaughan, D.J., 2003. Pyrite oxidation: A state-of-the-art assessment of the reaction mechanism. *Geochimica et Cosmochimica Acta*, 67, 873-880.
- Roberts, D.L., Sciscio, L., Herries, A.I.R., Scott, L., Bamford, M.K., Musekiwa, C. Tsikos, H., 2013. Miocene fluvial systems and palynofloras at the southwestern tip of Africa: Implications for regional and global fluctuations in climate and ecosystems. *Earth-Science Reviews*, 124, 184-201.
- Robinson, B.W., and Kusakabe, M., 1975. Quantitative preparation of SO₂ for ³⁴S/³²S analysis from sulfides by combustion with cuprous oxide. *Analytical Chemistry*, 47, 1179-1181.
- Roh, Y., Zhang, C.L., Vali, H., Lauf, R.J., Zhou, J., Phelps, T.J., 2003. Biogeochemical and environmental factors in Fe biomineralization: magnetite and siderite formation. *Clays and Clay Minerals*, 51 (1), 83-95.
- Rollinson, G., Andersen, J.C.Ø., Stickland, R.J., Boni, M., Fairhurst, R., 2011. Characterization of non-sulphide zinc deposits using QEMSCAN. *Minerals Engineering*, 24, 778-787.
- Rosas, S., 1994. Facies, diagenetic evolution, and sequence analysis along a SW-NE profile in the southern Pucará basin (Upper Triassic-Lower Jurassic), Central Peru. Heidelberg, Ruprecht-Karls-Universität, Heidelberger Geowissenschaftliche Abhandlungen Band 80, 337 p.

- Rosas, S., and Fontboté, L., 1995. Evolución sedimentológica del Grupo Pucará (Triásico superior-Jurásico inferior) en un perfil SW-NE en el centro del Perú. *Sociedad Geológica del Perú*, Vol. Jubilar A. Benavides, 279-309.
- Rosas, S., Fontboté, L., Morche, W., 1997. Vulcanismo de tipo intraplaca en los carbonatos del Grupo Pucará (Triásico superior-Jurásico inferior, Peru central) y su relación con el vulcanismo del Grupo Mitu (Pérmico superior-Triásico). *Congreso Peruano de Geología*, IX, Proceedings, 393-396.
- Rosas, S., Fontboté, L., Tankard, A., 2007. Tectonic evolution and paleogeography of the Mesozoic Pucará basin, central Peru. *Journal of South American Earth Sciences*, 24, 1-24.
- Rose, A.W., Hawkes, H.E., Webb, J.S., 1979. *Geochemistry in mineral exploration*. London, Academic Press, 657 p.
- Rosenbaum, J., and Sheppard, S.M., 1986. An isotopic study of siderites, dolomites and ankerites at high temperatures. *Geochimica et Cosmochimica Acta*, 50, 1147-1150.
- Rosenqvist, T., 2004. *Principles of Extractive Metallurgy*. Tapir Academic Press, Trondheim Norway, 506 p.
- Ross, C.S., 1946. Sauconite - a clay mineral of the Montmorillonite group. *American Mineralogist*, 31, 411-424.
- Rottier, B., Kouzmanov, K., Wälle, M., Bendežú, R., Fontboté, L., 2016. Sulfide replacement processes revealed by textural and LA-ICP-MS trace element analyses: example from the early mineralization stages at Cerro de Pasco, Peru. *Economic Geology*, 111, 1347-1367.
- Roy, D.M., Mumpton, F.A., 1956. Stability of minerals in the system ZnO-SiO₂-H₂O. *Economic Geology*, 51, 432-443.
- Rule, A.C., Radke, F., 1988. Baileychlorite, the Zn end member of the trioctahedral chlorite series. *American Mineralogist*, 73, 135-139.
- Rust, D.J., and Summerfield, M.A., 1990. Isopach and borehole data as indicators of rifted margin evolution in southwestern Africa. *Marine and Petroleum Geology*, 7, 277-287.
- Rutherford, N., 2002. Interaction of pH, redox and solution chemistry in exploration geochemistry. *ALS Chemex News* 2, 2002.
- Sağiroğlu, A., 1988. Cafana (Görgü), Malatya carbonated Zn-Pb deposits. *Bulletin of the Faculty of Eng., Cum. Uni., s. A-Earthsciences*, 5 (1) (in Turkish with English abstract)
- Saini-Eidukat, B., Melcher, F., Lodziak, J., 2009. Zinc-germanium ores of the Tres Marias Mine, Chihuahua, Mexico. *Mineralium Deposita*, 44, 363-370.

- Sangameshwar, S.R., and Barnes, H.L., 1983. Supergene Processes in Zinc-Lead-Silver Sulfide Ores in Carbonates. *Economic Geology*, 78, 1379-1397.
- Sangster, D.F., 1990. Mississippi Valley-type and sedex lead-zinc deposits: A comparative examination. *Transactions of the Institution of Mining and Metallurgy sec. B*, 99, 21-42.
- Santana, I.V., Wall, F., Botelho, N.F., 2015. Occurrence and behaviour of monazite-(Ce) and xenotime-(Y) in detrital and saprolitic environments related to the Serra Dourada granite, Goiás/Tocantins State, Brazil: potential for REE deposits. *Journal of Geochemical Exploration*, 155, 1-13.
- Santoro, L., Boni, M., Herrington, R., Clegg, A., 2013. The Hakkari nonsulfide Zn-Pb deposit in the context of other nonsulfide Zn-Pb deposits in the Tethyan Metallogenic Belt of Turkey. *Ore Geology Reviews*, 53, 244-260.
- Santoro, L., Boni, M., Mondillo, N., Joachimski, M., Woodman, J.A., 2015. A cold supergene zinc deposit in Alaska: The Reef Ridge case. *Geological Society of America Bulletin*, 127, 1534-1549.
- Sass-Gustkiewicz, M., Dzulynski, S., Ridge, J.D., 1982. The emplacement of zinc-lead sulfide ores in the Upper Silesian district-A contribution to the understanding of Mississippi Valley-type deposits. *Economic Geology*, 77, 392-412.
- Savin, S.M., Douglas, R.G., Stehli, F.G., 1975. Tertiary marine paleotemperatures. *Geological Society of America Bulletin*, 86, 1499-1510.
- Scheffer, F., Schachtschabel, P., 2002. *Lehrbuch der Bodenkunde*. Spektrum Akademischer Verlag, Heidelberg, 494 p.
- Schippers, A., 2003. Long-term anaerobic microbial processes in remediated mine tailings. Mitigation of the environmental impact from mining waste (MiMi). MiMi Print, Luleå, Sweden.
- Schneider, J., Melcher, F., Brauns, M., 2007. Concordant ages for the giant Kipushi base metal deposit (DR Congo) from direct Rb-Sr and Re-Os dating of sulphides. *Mineralium Deposita*, 42, 791-797.
- Schneider, G.I.C., and Walmsley, B., 2004. The Sperrgebiet Land Use Plan - An example of integrated Management of Natural Resources. *Communications Geological Survey of Namibia*, 13, 23-32.
- Scotese, C.R., 2001. Atlas of earth history. Paleogeography. PALEOMAP project, Arlington, Texas, 1, 52 p.
- Scott, K.M., 1986. Elemental partitioning into Mn- and Fe-oxides derived from dolomitic shale-hosted Pb-Zn deposits, Northwest Queensland, Australia. *Chemical Geology*, 57, 395-414.

- Ségalen, L., Renard, M., Lee-Thorp, J.A., Emmanuel L., Le Callonnec, L., de Rafélis, M., Senut, B., Pickford, M., Melice, J.-L., 2006. Neogene climate change and emergence of C4 grasses in the Namib, southwestern Africa, as reflected in ratite ^{13}C and ^{18}O . *Earth and Planetary Science Letters*, 244, 725-734.
- Sempere, T., Hérail, G., Oller, J., and Bonhomme, M.G., 1990. Late Oligocene-early Miocene major tectonic crisis and related basins in Bolivia. *Geology*, 18, 946-949.
- Sempere, T., Carlier, G., Soler, P., Fornari, M., Carlotto, V., Jacay, J., Arispe, O., Néraudeau, Cárdenas, J., Rosas, S., Jiménez, N., 2002. Late Permian-Middle Jurassic lithospheric thinning in Peru and Bolivia, and its bearing on Andean-age tectonics. *Tectonophysics*, 345, 153-181.
- Senut, B., Pickford, M., Ward, J., 1994. Biostratigraphie de éolianites néogènes du Sud de la Sperrgebeit (Désert de Namib, Namibie). *Comptes Rendus Académie des Sciences*, 318, 1001-1007.
- Sharp, Z., 2007. *Principles of Stable isotope Geochemistry*. Prentice Hall, New York, 360 p.
- Sharygin, V., 2015. Zincian micas from peralkaline phonolites of the Oktyabrsky massif, Azov Sea region, Ukrainian Shield. *European Journal of Mineralogy*, 27, 521-533.
- Sherman, D.M., 2001. Weathering reactions and soil-groundwater chemistry. *Environmental Geochemistry*. University of Bristol, Unpubl. Lecture Notes 2001/2002, 11 p.
- Siegfried, P.R., 1990. Aspects of the geology of the Mountain orebody, Rosh Pinah mine, Namibia. Unpublished M.Sc. Thesis University of Cape Town, 130 p.
- Siesser, W.G., 1980. Late Miocene origin of the Benguela upwelling system off northern Namibia. *Science*, 208, 283-285.
- Sillitoe, R.H., 2005. Supergene oxidized and enriched porphyry copper related deposits. *Economic Geology 100th Anniversary Volume*, 723-768.
- Sillitoe, R.H., and McKee, E.H., 1996. Age of supergene oxidation and enrichment in the Chilean porphyry copper province. *Economic Geology*, 91, 164-179.
- Singer, P.C., and Stumm, W., 1970. Acidic mine drainage; rate-determining step. *Science*, 167, 1121-1123.
- Singer, A., 1979. Palygorskite in sediments: Detrital, diagenetic and neoformed. A critical review. *Geologische Rundschau*, 68, 996-1008.
- Skarpelis, N., and Argyraki, A., 2009. The geology and origin of supergene ores in Lavrion (Attica, Greece). *Resource Geology*, 59, 1-14.
- Song, X., 1984. Minor elements and ore genesis of the Fankou lead-zinc deposit, China. *Mineralium Deposita*, 19, 95-104.

Song, X., Tan, H., 1996. Geochemical characteristics of the Fankou Pb-Zn deposits, northern Guangdong, South-China, in Sangster, D.F. (Eds.). Carbonate-Hosted Lead-Zinc Deposits, Society of Economic Geologists Special Publication 4, 350-355.

Spangenberg, J.E., Fontboté, L., Macko, S.A., 1999. An evaluation of the inorganic and organic geochemistry of the San Vicente Mississippi Valley type zinc-lead district, central Peru: Implications for ore fluid composition, mixing processes, and sulfate reduction. *Economic Geology*, 94, 1067-1092.

Spangenberg, J.E., Fontboté, L., Sharp, Z.D., Hunziker, J., 1996. Carbon and oxygen isotope study of hydrothermal carbonates in the zinc-lead deposits in the San Vicente district, central Peru: A quantitative modeling on mixing processes and CO₂ degassing. *Chemical Geology*, 133, 289-315.

Spikings, R., Reitsma, M.J., Boekhout, F., Mišković, A., Ulianov, A., Chiaradia, M., Gerdes, A., Schaltegger, U., 2016. Characterisation of Triassic rifting in Peru and implications for the early disassembly of western Pangaea. *Gondwana Research*, 35, 124-143.

SRK Consulting, 2014. NI 43-101 Technical Report Mineral Resources Bongará Zinc Project Amazonas Department, Peru. SRK Consulting (U.S.), Inc., Nevada, USA, 145 p.

Stanistreet, I.G., Kukla, P.A., Henry, G., 1991. Sedimentary basinal response to a late Precambrian Wilson cycle: The Damara orogen and Nama foreland, Namibia. *Journal of African Earth Sciences*, 13, 141-156.

Stavinga, D., Jamieson, H., Paradis, S., Falck, H., 2017. Geochemical and mineralogical controls on metal(loid) mobility in the oxide zone of the Prairie Creek Deposit, NWT. *Geochemistry: Exploration, Environment, Analysis*, 17(1):21

Szekely, T.S., Grose, L.T., 1972. Stratigraphy of the carbonate, black shale, and phosphate of the Pucara' Group (Upper Triassic-Lower Jurassic), central Andes, Peru. *Geological Society of America Bulletin* 83, 407-428.

Takahashi, T., 1960. Supergene alteration of zinc and lead deposits in limestone. *Economic Geology*, 55, 1084-1115.

Taylor, G.R., Day, M., Meredith, K., 2012. Soil degradation due to the destruction of crystalline kaolinite and the formation of X-ray amorphous clays accompanying ephemeral saline groundwater discharge. *Australian Journal of Earth Sciences*, 59, 135-152.

Teir, S., Eloneva, S., Fogelholm, C-J., Zevenhoven, R., 2006. Stability of Calcium Carbonate and Magnesium Carbonate in Rainwater and Nitric Acid Solutions. *Energy Conversion and Management*, 47, 3059-3068.

Thornber, M.R., 1975a. Supergene alteration of sulphides. I. A chemical model based on massive nickel deposits at Kambalda, Western Australia. *Chemical Geology*, 15, 1-14.

- Thornber, M.R., 1975b. Supergene alteration of sulphides. II. A chemical study of the Kambalda nickel deposits. *Chemical Geology*, 15, 116-144.
- Thornber, M.R., and Taylor, G.F., 1992. The mechanisms of sulphide oxidation and gossan formation, in Butt, C.R.M., Zeegers, H., (Eds.). *Regolith exploration geochemistry in tropical and subtropical terrains. Handbook of Exploration Geochemistry*, Elsevier, 4, 119-138.
- Tiller, K.G., and Pickering, J.G., 1974. The synthesis of zinc silicates at 20°C and atmospheric pressure. *Clays and Clay Minerals*, 22, 409-416.
- Valsami-Jones, E., Ragnarsdottir, K.V., Putnis, A., Bosbach, D., Kemp, A.J., Cressey, G., 1998. The dissolution of apatite in the presence of aqueous metal cations at pH 2-7. *Chemical Geology*, 151, 215-233.
- Van der Wateren, F.M., and Dunai, T.G., 2001. Late Neogene passive margin denudation history—cosmogenic isotope measurements from the central Namib desert. *Global and Planetary Change*, 30, 271-307.
- van Geldern, R. and Barth, J.A.C., 2012. Optimization of instrument setup and post-run corrections for oxygen and hydrogen stable isotope measurements of water by isotope ratio infrared spectroscopy (IRIS). *Limnology and Oceanography: Methods*, 10, 1024-1036.
- Van Niekerk, H.S., Gutzmer, J., Beukes, N.J., Phillips, D., Kiviets, G.B., 1999. An $^{40}\text{Ar}/^{39}\text{Ar}$ age of supergene K-Mn oxyhydroxides in a post-Gondwana soil profile on the Highveld of South Africa. *South African Journal of Science*, 95, 450-454.
- Van Zinderen Bakker Snr, E.M., 1975. The origin and palaeoenvironment of the Namib Desert biome. *Journal of Biogeography*, 2, 65-73.
- Van Vuuren, C.J.J., 1986. Regional setting and structure of the Rosh Pinah zinc-lead deposit, South West Africa/Namibia, in Anhaeusser, C.R. and Maske, S., (Eds.). *Mineral deposits of southern Africa*. Geological Society of South Africa, Johannesburg, 2, 1593-1607.
- Velde, B., 1985. *Caly Minerals: A Physico-chemical Explanation of their Occurrence*. Elsevier, 426 p.
- Vicente-Hernández, J., Vicente, M.A., Robert, M., Goodman, B.A., 1983. Evolution des biotites en fonction des conditions d'oxydo-reduction du milieu. *Clay Minerals*, 18, 267-275.
- Villa, I.M., 2009. Lead isotopic measurements in archeological objects. *Archaeological and Anthropological Sciences*, 1, 149-153.
- Villa, I.M., Ruggieri, G., Puxeddu, M., Bertini, G., 2006. Geochronology and isotope transport systematics in a subsurface granite from the Larderello-Travale geothermal system (Italy). *Journal of Volcanology and Geothermal Research*, 152, 20-50.

- Vonhof, H.B., Wesselingh, F.P., Ganssen, G.M., 1998. Reconstruction of the miocene western amazonian aquatic system using molluscan isotopic signatures. *Palaeogeography, Palaeoclimatology, Palaeoecology*, 141, 85-93.
- Ward, J.D., Seely, M.K., Lancaster, N., 1983. On the antiquity of the Namib. *South African Journal of Science*, 79, 175-183.
- Warren, B.E, 1990. X-ray diffraction; New York, Dover Publisher.
- Warren, J., 2000. Dolomite: occurrence, evolution and economically important associations. *Earth-Science Reviews*, 52, 1-81.
- Wartha, R.R., Genis, G., 1992. Lead and zinc. *Mineral Resources of Namibia*. Geological Survey of Namibia, 1-43.
- Wesselingh, F.P., Räsänen, M.E., Irion, G., Vonhof, H.B., Kaandorp, R., Renema, W., Romero Pittman, L., Gingras, M., 2002. Lake Pebas: a palaeoecological reconstruction of a Miocene, long-lived lake complex in western Amazonia. *Cainozoic Research*, 1, 35-81.
- Wesselingh, F.P., and Salo, J.A., 2006. A Miocene perspective on the evolution of the Amazonian biota. *Scripta Geologica*, 133, 439-458.
- West, A.G., February, E.C., Bowen, G.J., 2014. Spatial analysis of hydrogen and oxygen stable isotopes (“isoscapes”) in ground water and tap water across South Africa. *Journal of Geochemical Exploration*, 145, 213-222.
- Whitney, D.L., and Evans, B.W., 2010. Abbreviations for names of rock-forming minerals. *American Mineralogist*, 95, 185-187.
- Wijninga, V.M., 1996. Palaeobotany and palynology of Neogene sediments from the high plain of Bogotá (Colombia). Wageningen, Netherlands, Ponsen and Looingen, BV, 370 p.
- Will, P., Friedrich, F., Hochleitner, R., Gilg, H.A., 2014. Fraipontite in the hydrothermally overprinted oxidation zone of the Preguiça mine, Southern Portugal. Abstract Mid-European Clay Conference, 16-19 September 2014, Dresden, Germany.
- Williams, P.A., 1990. Oxide zone geochemistry. Ellis Horwood Ltd., Chichester, UK, 286 p.
- Wilson, M.J., 1987. Soil smectites and related interstratified minerals: Recent developments, in Schultz, L.G., Van Olphen, H., Mumpton, F.A., (Eds.). *Proceedings of the International Clay Conference*, Denver, 1985. Bloomington, Indiana. The Clay Minerals Society, 167-173.
- Woodward, J.C., Macklin, M.G., Lewin, J., 1994. Pedogenic weathering and relative-age dating of Quaternary alluvial sediments in the Pindus Mountains of northwest Greece, in Robinson, D.A. and Williams, R.B.G., (Eds.). *Rock weathering and landform evolution*. John Wiley & Sons, 259-283.

Workman, A., and Breede, K., 2016. NI 43-101 Technical report on the Bongará zinc project Yambrasbamba area, northern Peru for Zinc One Resources Inc., 137 p.

Wright, C., 2010. Rio Cristal Resources Corporation Bongará Zinc Project: Technical Report NI 43-101. Canada, Rio Cristal Resources Corporation and AMEC (Peru) S.A., 102 p.

Yigit, O., 2009. Mineral deposits of Turkey in relation to Tethyan metallogeny: implications for future mineral exploration. *Economic Geology*, 104, 19-51.

Yilmaz, A., Ünlü, T., Sayili, I.S., 1992. An approach to the origin of Keban Lead-Zinc Mineralizations, Elazığ, Turkey: a preliminary study. *Mineral Resource Exploration Bulletin*, 114, 27-50.

Zartman, R. E., 1974. Lead isotopic provinces in the Cordillera of the western United States and their geologic significance. *Economic Geology*, 69, 792-805.

Zeman, J., 1985. Supergene alteration of sulfides, II. A laboratory electrochemical study. *Scripta Facultatis Scientiarum Naturalium Universitatis Purkynianae Brunensis. Geologia*, 15, 115-136.

Zachos, J.C., Stott, L.D., Lohmann, K.C., 1994. Evolution of early Cenozoic marine temperatures. *Paleoceanography*, 9, 353-387.

Zhang, C.L., Horita, J., Cole, D.R., Zhou, J., Lovley, D.R., Phelps, T.J., 2001. Temperature-dependent oxygen and carbon isotope fractionation of biogenic siderite. *Geochimica et Cosmochimica Acta*, 65(14), 2257-2271.

Zhao, Y.C., Stanforth, R., 2000. Production of Zn powder by alkaline treatment of smithsonite in Zn-Pb ores. *Hydrometallurgy*, 56, 237-249.

Zúñiga y Rivero, F.J., Klein, G.D., Hay-Roe, H., Álvarez-Calderon, E., 2010. The hydrocarbon potential of Peru. BPZ Exploración and Producción S.R.L, Lima, Peru, 338 p.